
The timing and mechanisms of sulfur release by Icelandic flood lava eruptions.

**Holuhraun 2014–15 CE and Laki 1783–84 CE a case
study.**

Catherine Rachael Gallagher



UNIVERSITY OF ICELAND

This dissertation is submitted in partial fulfilment of a degree of
Doctor of Philosophy in Earth Sciences

Department of Earth Sciences, Durham University and Institute of
Earth Sciences, University of Iceland

2021

Advisors

Dr. Kevin W. Burton, Professor of Geochemistry, Durham University, UK

Dr. Thorvaldur Thordarson, Professor of Volcanology and Petrology
University of Iceland

Dr. Bruce Houghton, Gordon A. Macdonald Chair, Professor of Volcanology,
SOEST, University of Hawaii at Manoa, USA

PhD Committee

Dr. Charlotte Vye-Brown, Senior Volcanologist, British Geological Survey, UK

Dr. Richard Brown, Senior lecturer in Volcanology, Durham University, UK

Opponents

Dr. Valentin R. Troll, Professor of Igneous Petrology, Uppsala University, Sweden

Dr. Colin Macpherson, Professor of Geology, Durham University, UK

Abstract

Flood lavas (FL), or high magnitude (1–100 km³) basaltic fissure eruptions have a recurrence interval of 250–500 years in Iceland. These events can produce atmospheric volcanic pollution at tropospheric–stratospheric levels via their sulfur (S) emissions. Current knowledge of the modulating role of shallow conduit processes on the vent activity, as well as the mechanisms and timing of peak S release into the atmosphere, is limited.

This project has two key aims: first, to evaluate the influence of shallow conduit processes on eruption style and dynamics during peak intensities of explosive phases; second, to produce a novel chalcophile stable isotope proxy for the speciation of released S and the redox state of the system upon eruption. Two selected case studies for this project are: (i) the recent low intensity and magnitude end-member, 2014–15 CE Holuhraun, and (ii) a high intensity and magnitude end-member, 1783–84 CE Laki which is well-documented in detailed contemporary accounts.

Micro-textural analysis of the ‘frozen’ outer rinds of pyroclasts from both eruptions, which record the state of the magma prior to fragmentation, identified relative shifts in vesicle number density associated with changes in eruptive intensity. Whole pyroclast textural mapping and in-situ geochemical analysis constrain the modification of the interior of the clasts via post-fragmentation expansion. This process enhanced the contrasts between discrete pre-existing melt domains which mingled prior to eruption. These domains record different shallow conduit histories, in particular contrasting ascent rates, and therefore preserve evidence of equilibrium and disequilibrium vesiculation within the same clast. Zinc and copper stable isotope compositions of lava and tephra from distinct phases of eruptive activity were utilised to fingerprint the mechanisms of S loss. Changes in the efficiency of volatile loss of S can be linked to known changes in vent dynamics, as well as changes in S loss associated with both the evolving transport system, redox conditions at the vent and in the flow field.

The textural and geochemical findings from these two eruptions will help further our understanding of shallow conduit, eruptive and emplacement processes during the many ill-constrained basaltic fissure eruptions of different intensities and magnitudes worldwide.

Útdráttur (Icelandic Abstract)

Flæðibasaltgos, eða stór (1-100 km³) basísk sprungugos, að meðaltali verða á 250-500 ár fresti á Íslandi. Slík gos geta valdið umfangsmikilli mengun í veðra- og/og eða heiðhvolfinu vegna losunar brennisteins gasa. Okkar sýn á stýrihlutverk grunnstæðra gosrásarferla á goshegðun, sem og á ferli og skilvirkni brennisteinsafgösunar út í andrúmsloftið er ófullkomin.

Þetta verkefni hefur tvo meginmarkmið. Í fyrsta lagi, að skoða áhrif grunnstæðra gosrásarferla á goshegðun og gangverk ferlanna á þeim tíma sem ákefð sprengivirkinnar er í hápunkti. Í öðru lagi, að vinna í því að setja saman nýja nálgun til að meta sameindagerð brennisteins og oxunarstig kerfisins við gos. Tvo vel til fallin gos voru valin fyrir þessa rannsókn, nefnilega: (i) gosið í Holuhrauni 2014–15, sem dæmi um aflítið og smátt flæðibasaltgos, og (ii) Skaftáreldar 1783–84 sem dæmi um aflmikið og stærðargráðunni umfangsmeira gos, því að bæði gosin eru vel skráð og rannsökuð.

Greining á míkro-fyrirbærum (gasbólum og örkristöllum) í ysta byrði gjóskukorna, sem storknar samtíma sundrun kvikunnar í gosrásinni, sýnir fylgni á milli gásbólupéttleika og afls sprengigosahrinanna, sem bendir til tengsla á milli afls og hraða afgösunar og blöðrumyndunar. Hins vegar sýnir kortlagning á slíkum míkro-fyrirbærum í þversniði í gegnum gjóskukornin, ásamt greiningu á brennisteinsstyrk, hvernig míkro-veftan í kjarna gjóskukornanna breytist vegna áframhaldandi gas-útpennslu eftir sundrun. Þetta ferli ýkir frekar muninn á hinum ýmsu veftulénunum sem blandast saman efst í gosrásinni fyrir gos. Þessi veftulén eru vitnisburður um breytileg þróunarferli efst í gosrásinni sem tengjast breytilegum rishraða á mismunandi kvikupúlsum, og þess vegna varðveita þau vitnisburð um blöðrumyndun undir efnafræðilegu jafnvægi og ójafnvægi í einu og sama

gjóskukorninu. Styrkur stöðugra samsæta zinks og kopars mælt í gjósku og hrauni frá ákveðnum gosfösum, eru notaðar til þess að rekja ferlin tengd brennisteinslosun. Það er hægt að tengja breytingar á skilvirkni brennisteinslosunar við skráðar breytingar á goshegðun í gígum og við þróun á flutningskerfi hraunsins, sem og oxunarstig kerfisins í gígum og innan hraunsins.

Niðurstöður rannsóknar minnar á þessum tveimur gosum mun án efa hjálpa til við það að auka skilning okkar á þeim ferlum sem eru ráðandi í grunnstæða hluta gosrása, í gígum og við hraunamyndun í flæðibasaltgosum víðsvegar um jörðina.

Table of contents

ABSTRACT	III
ÚTDRÁTTUR (ICELANDIC ABSTRACT)	IV
CHAPTER 1: INTRODUCTION	1
1. 1 INTRODUCTION	1
1. 2 THESIS STRUCTURE	3
CHAPTER 2: PHYSICAL VOLCANOLOGY BACKGROUND	9
2. 1 THE IMPORTANCE OF BASALTIC VOLCANISM	9
2. 2 BASALTIC FOUNTAINING ERUPTIONS	14
2. 2. 1 FISSURE ERUPTIONS: MAGNITUDES AND INTENSITY	15
2. 2. 2 CLASSIFICATIONS OF BASALTIC LAVA FLOW MORPHOLOGIES	24
2. 3 SHALLOW CONDUIT PROCESSES	27
2. 4 ENVIRONMENTAL IMPACT OF FLOOD LAVA ERUPTIONS	31
2. 5 VOLATILES IN BASALTIC MAGMAS	35
2. 6 STABLE ISOTOPES AS TRACERS OF VOLCANIC PROCESSES	36
2. 6. 1 COPPER AND ZINC STABLE ISOTOPES AS TRACERS OF MAGMATIC DIFFERENTIATION AND VOLATILE LOSS	37
2. 7 REFERENCES	42
CHAPTER 3: ICELAND GEOLOGICAL SETTING AND BACKGROUND	58
3. 1 GEOLOGICAL OVERVIEW OF ICELAND	58
3. 2 ICELAND TECTONICS AND GEODYNAMICS	59
3. 3 ICELANDIC VOLCANISM	63
3. 4 SPATIAL AND TEMPORAL DISTRIBUTION OF MAGMA TYPES IN ICELAND	67
3. 5 LARGE VOLUME HOLOCENE BASALTIC FISSURE ERUPTIONS IN ICELAND	69
3. 6 REFERENCES	73
CHAPTER 4: RESEARCH PROJECT CASE STUDIES	80
4. 1 THE 2014–15 CE HOLUHRAUN ERUPTION	80
4. 2 THE SERIES OF EVENTS DURING THE HOLUHRAUN 2014–15 CE FL ERUPTION	84
4. 3 THE 1783–4 CE LAKI FL ERUPTION	95
4. 4 LAKI 1783–84 CE SERIES OF EVENTS	98
4. 5 REFERENCES	106
CHAPTER 5: NE LAKI REVISITED; EVIDENCE FOR ICE-MAGMA INTERACTIONS DURING A SHALLOW SUBGLACIAL FISSURE ERUPTION	112
5. 1 MOTIVATION AND NOVELTY	112
5. 1. 1 BACKGROUND	113
5. 1. 2 PREVIOUS STUDIES	114
5. 1. 3 THE LAKI 1783–84 CE ERUPTION	116
5. 2. METHODS	119
5. 3. INITIAL RESULTS	120

5. 3. 1 THE NEW TEPHRA LAYER FROM FISSURE 7 OR 8.....	120
5. 3. 2 FISSURE 9	122
5. 3. 3 FISSURE 10	123
5. 4 CONCEPTUAL MODEL	136
5. 5 CORRESPONDING TEPHRA LAYER FROM FISSURE 10.	138
5. 6 FUTURE STUDIES	140
5. 7 REFERENCES.....	141

CHAPTER 6: SHALLOW CONDUIT PROCESSES DURING THE HOLUHRAUN 2014–15 CE ERUPTION..... 145

6. 1. 1 INTRODUCTION.....	145
6. 1. 2 PREVIOUS WORK ON LOW-INTENSITY FISSURE ERUPTIONS.....	148
6. 1. 3 GEOLOGICAL SETTING	150
6. 1. 4 A REVIEW OF THE HOLUHRAUN 2014–15 CE EVENT: A LOW-INTENSITY FL ERUPTION.....	150
6. 2. 1. 1 METHODS	156
6. 2. 1. 1 TEXTURAL ANALYSIS	158
6. 2. 1. 2 GEOCHEMICAL GLASS ANALYSIS	163
6. 3. 1 RESULTS HOLUHRAUN:	164
6. 3. 1. 1 DEPOSIT CHARACTERISTICS	164
6. 3. 1. 2 CLAST DENSITY AND BULK VESICULARITY:	166
6. 4. 1 QUALITATIVE TEXTURAL ANALYSIS AND INITIAL INTERPRETATIONS.....	170
6. 4. 2 QUANTITATIVE TEXTURAL ANALYSIS	175
6. 4. 2. 1 VND (N_v).....	175
6. 4. 2. 2 VVD.....	176
6. 4. 2. 3 CVVD	179
6. 4. 3 TEXTURAL HETEROGENEITIES	182
6. 4. 3. 1 (1) PRE-FRAGMENTATION: MELT DIVERSITY AS THE RESULT OF SHALLOW CONDUIT MINGLING	183
6. 4. 3. 2 (2) POST-FRAGMENTATION VESICLE EXPANSION.....	183
6. 4. 4 GLASS GEOCHEMISTRY	188
6. 4. 5 CHANGES IN PROPORTIONS OF TEXTURES THROUGHOUT THE ERUPTION	191
6. 4. 6. 1 INITIAL INTERPRETATIONS OF INTERIOR DOMAIN TEXTURES.....	192
6. 5. 1 INTERPRETATIONS AND DISCUSSION	193
6. 5. 1. 1 EVOLUTION SEEN IN SINGLE PYROCLASTS: VND vs V_G/V_L	194
6. 5. 2 TEMPORAL CHANGES DURING THE ERUPTION	198
6. 6 CONCLUSIONS	205
6. 7 REFERENCES.....	206

CHAPTER 7: SHALLOW CONDUIT PROCESSES DURING THE LAKI 1783–84 CE ERUPTION..... 215

7. 1. 1 INTRODUCTION.....	215
7. 1. 2 PURPOSE.....	217
7. 1. 3 PREVIOUS WORK ON HIGH FOUNTAINING FISSURE ERUPTIONS	217
7. 1. 4 GEOLOGICAL SETTING	219
7. 1. 5 THE 1783–1784 CE LAKI ERUPTION.....	220
7. 2. 1 METHODS	223
7. 2. 2 TEXTURAL ANALYSIS.....	224
7. 2. 3 IMAGE ACQUISITION.....	226
7. 2. 4 GEOCHEMICAL GLASS ANALYSIS	227
7. 3 RESULTS.....	227
7. 3. 1 DEPOSIT CHARACTERISTICS	227
7. 3. 2 CLAST DENSITY AND BULK VESICULARITY	231
7. 3. 3 QUALITATIVE TEXTURAL ANALYSIS AND INITIAL INTERPRETATIONS.....	236
7. 3. 4 QUANTITATIVE TEXTURAL ANALYSIS	244
7. 3. 4. 1 VND.....	244
7. 3. 5 VVD.....	247

7. 3. 6 CVVD	250
7. 3. 7 GLASS GEOCHEMISTRY	253
7. 3. 8 TEMPORAL CHANGES IN TEXTURES THROUGHOUT THE ERUPTION	257
7. 4 INTERPRETATIONS AND DISCUSSION	259
7. 4. 1 VESICLE NUMBER DENSITY (VND) AND VARIATIONS IN MASS ERUPTION RATE (MER)	259
7. 4. 2 V_G/V_L	262
7. 4. 3 INTERPRETATIONS OF OBSERVED TEMPORAL TEXTURAL CHANGES DURING THE ERUPTION	268
7. 5 DISCUSSION	272
7. 5. 1 CORRELATING FOUNTAINING HEIGHTS WITH N+G+C	272
7. 5. 2 TEMPORAL CHANGES IN TEXTURES THROUGHOUT THE ERUPTION, CONDITIONS OF ASCENT/SHALLOW CONDUIT MODEL AND CONDUIT GEOMETRY	274
7. 5. 3 PHREATOMAGMATIC VS MAGMATIC ACTIVITY	276
7. 5. 4 THE INFLUENCE OF LOCAL TECTONICS	279
7. 6 CONCLUSIONS.....	279
7. 7 REFERENCES.....	281

CHAPTER 8: FINGERPRINTING THE MECHANISMS AND TIMING OF S RELEASED ACCOMPANYING FL ERUPTIONS USING NOVEL CHALCOPHILE STABLE ISOTOPE PROXIES289

8. 1 INTRODUCTION	289
8. 1. 1 PREVIOUS WORK ON ZN AND CU ISOTOPIC VARIATIONS OF TERRESTRIAL SAMPLES.....	295
8. 1. 2 GEOLOGICAL SETTING	297
8. 2 METHODS	305
8. 2. 1 SAMPLING METHODOLOGY	305
8. 2. 3 SAMPLE PREPARATION (MAJOR ELEMENTS, TRACE ELEMENTS, CU AND ZN).....	309
8. 3 RESULTS	316
8. 3. 1 COPPER AND ZINC ISOTOPIC SIGNATURES	326
8. 4 DISCUSSION	343
8. 4. 1 ZN ISOTOPE VARIATIONS.....	344
8. 4. 2 CU ISOTOPE VARIATIONS.....	357
8. 4. 3 $\Delta^{66}\text{Zn}$ AND $\Delta^{65}\text{Cu}$ ISOTOPE COVARIATIONS.....	363
8. 5 CONCLUSIONS.....	367
8. 6 REFERENCES.....	368

CHAPTER 9.....382

9. 1 SYNTHESIS AND CONCLUSIONS	382
9. 1. 1 ERUPTIVE ENVIRONMENT.....	382
9. 1. 2 TEXTURAL MATURITY.....	383
9. 1. 4 CHALCOPHILE ISOTOPE VARIATIONS IN ERUPTIVE PRODUCTS	385
9. 2 FUTURE WORK	387

List of tables

Table 2. 1: Holuhraun 2014–15 CE lava morphologies.....	26
Table 5. 1: Laki contemporary accounts.....	140
Table 6. 1: Measured density and calculated bulk vesicularity data set, Holuhraun 2014–15 CE.....	167
Table 6. 2: Vesicle number density data set for Holuhraun 2014–15 CE.....	176
Table 6. 3: EMPA basaltic glass analysis of textural domains, data averages for Holuhraun 2014–15 CE clasts.....	190
Table 7. 1 a and b: Laki 1783–84 CE density and calculated bulk vesicularity data.....	232
Table 7. 2: Vesicle number density data from Laki 1783–84 CE for selected rinds, whole clasts, and interiors.....	246
Table 7. 3: EMPA groundmass glass geochemistry of analysed domains in the Laki 1783–84 CE pyroclasts.....	256
Table 8. 1 Key lava morphologies observed and sampled during Holuhraun 2014–15 CE.....	306
Table 8. 2: Holuhraun tephra Cu and Zn isotopic variations.....	318
Table 8. 3 Holuhraun lava Cu and Zn isotopic variations.....	319
Table 8. 4 Laki tephra Cu and Zn isotopic variations.....	320
Table 8. 5: Laki lava Cu and Zn isotopic variations.....	321
Table 8. 6: International standards Zn and Cu isotopic ratios during analytical runs	322

List of Figures

Figure 1. 1: A schematic diagram demonstrating the effect of eruptive environment on the deposits in the very NE of the Laki cone-row at fissure 10.....	5
Figure 1. 2: Schematic sketch of the evolution of a fissure.....	8
Figure 2. 1: Examples of historic high intensity, Plinian, explosive basaltic eruptions.....	10
Figure 2. 2: A range of basaltic fissure eruption fountaining intensities.....	11
Figure 2. 3: The schematic displaying the effect of the volcanic sulfur release on the stratosphere and troposphere.....	13
Figure 2. 4: The emergent curtain-of-fire Holuhraun 2014–15 CE.....	17
Figure 2. 5: Schematic of the different main types of bubbly melt flow in the shallow conduit during a basaltic eruption.....	19
Figure 2. 6: Examples of the shallow conduit dynamics and resultant styles of vent activity during different types of eruptions.....	21
Figure 2. 7: Schematic demonstrating the deposit characteristics from eruptions of differing intensities.....	22
Figure 2. 8: Photographs of insulated versus open basaltic lava channels and associated lavas flow morphologies.....	25
Figure 2. 9: A schematics of sulfur pollution from the Laki 1783–84 CE eruption.....	32
Figure 2. 10: A schematic of Zn and Cu partitioning behaviour during fissure eruptions.....	39
Figure 3. 1: A broad outline of the epochs spanned by the geology of Iceland.....	59
Figure 3. 2: Map of the NAIP.....	60
Figure 3. 3: Neovolcanic zones, belts and active volcanic systems of Iceland.....	62
Figure 3. 4: A map displaying the location of the current margins of all Holocene lava flows in Iceland.....	64
Figure 3. 5: Schematic of the key components of volcanic systems in Iceland.....	65
Figure 3. 6: Berufjörður, Icelandic Eastfjords, cake layer FL stratigraphy with cross-cutting dyke swarm.....	66
Figure 4. 1: Arctic DEM image of the 2014–15 CE Holuhraun flow field.....	81
Figure 4. 2: The B-V volcanic system.....	82
Figure 4. 3: The Gjálp 1996 CE subglacial eruption, and its jökulhlaup.....	83
Figure 4. 4: The propagation of seismic unrest prior to Holuhraun 2014–15 CE.....	85
Figure 4. 5: This image shows the aerial extent of the small eruption which occurred <48 hours before the 2014–15 CE Holuhraun eruption.....	86
Figure 4. 6: The old Holuhraun craters utilised by 2014–15 CE eruption.....	87
Figure 4. 7: A composite of the growth of the Holuhraun 2014–15 CE lava field.....	89
Figure 4. 8: Field photographs of Holuhraun 2014–15 CE eruptive activity evolving from a curtain-of-fire to discrete vents.....	91
Figure 4. 9: Plot of vent activity and MER, Holuhraun 2014–15 CE.....	93
Figure 4. 10: Volcanic pollution from Holuhraun 2014–15 CE.....	95
Figure 4. 11: The Grímsvötn volcanic system.....	97
Figure 4. 12 Map of the Grímsvötn volcanic system and Laki 1783–84 CE lava flow field.....	99
Figure 4. 13: Schematic of the Laki crater row.....	101
Figure 4. 14: Historical place names of note surrounding the Laki lava field and eruption site.....	104
Figure 5. 1: An ArcticDEM hillshade image of the Laki eruption and surroundings.....	117
Figure 5. 2: A schematic of Laki tephra dispersal and cone eruptive environment.....	118
Figure 5. 3: Thoroddsen 1881–1901 geological map of Iceland.....	118
Figure 5. 4: Field images of Laki tephra deposits.....	121
Figure 5. 5: Field images from the Fissure 9 cone.....	122
Figure 5. 6: Field images from the Fissure 10 SW cone.....	124
Figure 5. 7: Field images of the northern margin of the Fissure 10 SW cone.....	126
Figure 5. 8: ArcticDEM of Fissure 10 and key units. Insets in the top left indicate field location within Iceland.....	127
Figure 5. 9: Un-named peak agglutinated spatter and spatter fed lava sequence at Fissure 10.....	129

Figure 5. 10: Field images of the NE section of the fissure 10 sequences containing pillows and hackly jointed lavas.....	132
Figure 5. 11: Fissure 10 sub-unit correlation along the fissure’s length.....	135
Figure 5. 12: Conceptual model of the subglacial eruptive activity during the Fissure 10 event.....	137
Figure 5. 13: Geographic locations of the local place names that are referred to for the Fissure 10 tephra locations.	139
Figure 6. 1: A georeferenced Landsat 8 real look image from of the Holuhraun 2014–15 CE eruption on the 6 September 2014.....	152
Figure 6. 2: Evolution of the Holuhraun 2014–15 CE vent activity in response to MER and activity vent portions.....	155
Figure 6. 3: Tephra fall sampling locations from the Holuhraun 2014–15 CE eruption.....	157
Figure 6. 4: Key stages of changes in vent activity during Holuhraun 2014–15 CE and their corresponding density samples.....	160
Figure 6. 5: Field images of tephra lenses from Holuhraun 2014–15 CE.....	164
Figure 6. 6: Images of medial fall tephra deposits from Holuhraun 2014–15 CE.....	166
Figure 6. 7: Density histograms versus vent activity comparisons throughout Holuhraun 2014–15 CE.....	168
Figure 6. 8: SEM images of explosive phase pyroclasts, from early September during Holuhraun 2014–15 CE.....	172
Figure 6. 9: SEM images of explosive phase pyroclasts, from late September and October during Holuhraun 2014–15 CE.....	173
Figure 6. 10: Isolated outer rinds of Holuhraun 2014–15 CE pyroclasts.....	174
Figure 6. 11: Vesicle volume distributions from the Holuhraun 2014–15 CE pyroclasts.....	178
Figure 6. 12: Cumulative vesicle by volume distribution of the Holuhraun 2014–15 CE pyroclasts.....	181
Figure 6. 13: Textural domain maps of Holuhraun pyroclasts.....	185
Figure 6. 14: EMPA BSE of early September lapilli and Pele’s hairs from Holuhraun 2014–15 CE.....	186
Figure 6. 15: EMPA BSE images of the increase in microlites in mid-September glassy tephra from Holuhraun 2014–15 CE.....	187
Figure 6. 16: VND against vesicle-to-melt ratio (V_G/V_L) for Holuhraun 2014–15 CE pyroclasts.....	197
Figure 6. 17: (part A) Conceptual model of the evolution of Holuhraun 2014–15 CE’s shallow conduit system.....	203
Figure 6. 18: (part B) Conceptual model of the evolution of Holuhraun 2014–15 CE’s shallow conduit system.....	204
Figure 7. 1: Arctic DEM map of the Laki 1783–84 CE lava field and surrounding locations.....	220
Figure 7. 2: A Schematic of the Laki cone-row with: fissure lengths, activity dates, and associated pyroclast density histograms of explosive phase tephra apron samples.....	222
Figure 7. 3: Laki 1783–84 CE tephra layers in medial soil horizons and proximal tephra apron layering from a single eruptive phase.....	230
Figure 7. 4: A panel compilation of the analysed phases of the Laki 1783–84 CE fissure opening phases.....	235
Figure 7. 5: SEM BSE images of texturally analysed pyroclasts from explosive tephra phases M2 and M4, Laki 1783–84 CE.....	238
Figure 7. 6: SEM BSE images of texturally analysed pyroclasts from explosive tephra phases P3 and M6, Laki 1783–84 CE.....	239
Figure 7. 7: Analysed rinds from M2 and M6 explosive tephra phase clasts, Laki 1783–84 CE.....	240
Figure 7. 8: Textural maps of discrete textural domain proportions in Laki 1783–84 CE pyroclasts.....	243
Figure 7. 9: Vesicle volume distributions from the Laki 1783–84 CE pyroclasts.....	249
Figure 7. 10: Cumulative vesicle by volume distribution of textural analysis of Laki 1783–84 CE pyroclasts.....	252
Figure 7. 11: A comparison plot of time-averaged mass discharge rate against vesicle number density for basaltic fissure eruptions.....	261
Figure 7. 12: SEM BSE images of collapse or outgassing features in P3 and M6 pyroclasts from Laki 1783–84 CE.....	266
Figure 7. 13: VND against vesicle-to-melt-ratio of Laki pyroclasts.....	267

Figure 7. 14: Conceptual model of the evolution of the shallow conduit system during the 1783–84 CE Laki eruption (part A). A conceptual model for the evolution of the shallow conduit system during a single fissure opening phase in the Laki eruption.....	270
Figure 7. 15 Conceptual model of the evolution of the shallow conduit system during the 1783–84 CE Laki eruption (part B).....	271
Figure 7. 16: Conceptual model of the evolution of shallow subglacial activity at fissure 10 during the Laki 1783–84 CE eruption.....	278
Figure 8. 1: A schematic of expected fractionation trends generated by Zn and Cu partitioning into oxidized and reduced S rich phases at magmatic temperatures.....	294
Figure 8. 2: An illustration of Zn and Cu partitioning into oxidized and reduced S rich phases in the shallow conduit alongside S phases.....	295
Figure 8. 3: The temporal evolution of the Holuhraun 2014–15 CE flow field and sample locations.....	300
Figure 8. 4 A georeferenced map of the temporal evolution of the Laki lava field and sample locations.....	303
Figure 8. 5: An outline sketch of the Laki crater row, apron tephra and tephra dispersal axis.....	304
Figure 8. 6: Field images of medial tephra fall from the Holuhraun 2014–15 CE eruption.....	307
Figure 8. 7: Proximal Laki tephra aprons and internal layering and sub-units in medial Laki tephra in soil horizons.....	309
Figure 8. 8: Trace element temporal changes and co-variations in Holuhraun 2014–15 CE tephra and lavas.....	324
Figure 8. 9: Trace element temporal changes and co-variations in Laki 1783–84 CE tephra and lavas.....	325
Figure 8. 10: Caltech $\delta^{66}\text{Zn}$ comparison plot of samples with existing $\delta^{66}\text{Zn}$ data sets.....	327
Figure 8. 11: Caltech $\delta^{65}\text{Cu}$ comparison plot of samples with existing $\delta^{65}\text{Cu}$ data sets.....	328
Figure 8. 12: Holuhraun $\delta^{66}\text{Zn}$ variations, temporal and key major and trace covariations in lavas and tephra.....	334
Figure 8. 13: Laki $\delta^{66}\text{Zn}$ variations, temporal and key major and trace covariations in lavas and tephra.....	335
Figure 8. 14: Holuhraun 2014–15 CE $\delta^{65}\text{Cu}$ variations, temporal and key element covariations.....	338
Figure 8. 15: Laki 1783–84 CE $\delta^{65}\text{Cu}$ variations, temporal and key element covariations.....	339
Figure 8. 16: $\delta^{66}\text{Zn}$ and $\delta^{65}\text{Cu}$ isotope covariations for Holuhraun 2014–15 CE and Laki 1783–84 CE tephra and lavas.....	342
Figure 8. 17: A conceptual model for the generation of $\delta^{66}\text{Zn}$ and $\delta^{65}\text{Cu}$ isotope variations throughout both fissure eruptions.....	345
Figure 8. 18: Temporal $\delta^{66}\text{Zn}$ variations alongside physical volcanological field data sets for Holuhraun 2014–15 CE.....	347

Appendices

- A) Vesicle Number Density and Size Distribution excel calculations: Holuhraun and Laki whole clasts and rinds
- B) Geochemical data sets
- C) Additional vesicularity data



“Some dogs just want to watch the world burn”

Pippin, Volcano Dog, 2014

Declaration

I declare that this thesis, which I submit for the degree of Doctor of Philosophy at Durham University and The University of Iceland, is my own work and not substantially the same as any which has previously been submitted at this or any other university. *Catherine R. Gallagher*

Department of Earth Sciences, Durham University and Institute of Earth Sciences, The University of Iceland May 2021.

Statement of Copyright

© The copyright of this thesis rests with the author. No quotation from it should be published without prior written consent and information derived from it should be acknowledged.

Acknowledgements

First and foremost, I would like to acknowledge the support and encouragement offered to me throughout my research project by my thesis committee and extended supervisory team. I am a better scientist because of them. In particular, I would like to thank my supervisors Kevin Burton, Thorvaldur Thordarson and Bruce Houghton for all of their invaluable advice and support.

To Kevin a special thank you for introducing me to the world of stable isotopes, for the stimulating scientific discussions and for putting up with my ephemeral presence in Durham. To Thor, thanks for introducing me to Icelandic geology, especially Laki, all those years ago as an undergraduate student and for nurturing my interest in academia. To Bruce Houghton, thank you for welcoming me as an extra student with open arms and for introducing me to the world of basaltic fissure eruptions, bubbles, and fluid dynamics. Our many fruitful transatlantic research discussions at all hours of the day and night were extremely motivating!

To Maria Janebo, thank you for somehow managing to balance being such a wonderful friend as well as a great scientific mentor. For your help in field and laboratory as I took my first ash and lapilli samples, as well as tips and tricks for staying sane whilst drawing bubbles. I will be forever grateful for your patience and belief in me. A special thanks goes to Geoff Nowell for all of his help with sample preparation and analysis in the Arthur Holmes laboratory in Durham, and to Paul Savage, thank you for mentoring me during my first days in the laboratory in Durham and then for hosting me in St. Andrews as I completed my analysis. Þóra Björg, the GIS guru, you have been so helpful with all of my blunders, what would I do without you?

This research would not have been possible without the help of so many excellent and valued people in the field over many summers, who helped hunt for Laki tephra all over southern Iceland, as well as digging pits and lugging samples around both Laki and Holuhraun. A special thanks goes to Þóra Björg, Maria, Rob, Katrín, Will and of course the tephra pit digging volcano dog, Pippin.

Special thanks to the IES eruption team for the incredible experience of witnessing and working together on the 2014–15 CE Holuhraun flood lava eruption, it's one of my favourite memories and it was such a pleasure to work with you all. I have endless gratitude towards the 'Eldfjallafræði og Náttúruvárhópur' at IES for the countless opportunities to work on various fieldwork projects all over the country. This has vastly expanded my knowledge of volcanism in general, as well as enabling me to develop a specialist knowledge of Icelandic geology and volcanology. Living in Iceland, and being part of this team, has allowed me the privilege of working on two active eruption sites during my time here, with the latest Geldingardalsgos, at Fagradalsfjall, still ongoing as I submit this thesis. At this point it is also prudent to give a nod to the IES sink or swim attitude to 4x4 driving in the field here, which gave me an unparalleled level of experience and training on Icelandic "roads" in obscure corners in the highlands to access the previously inaccessible. I am forever indebted to Steini for coming to my rescue to replace the car that wasn't so lucky along the way in the Skaftá, allowing us a precious extra sampling day!

Thank you to the “women in the wild”, who adventured all over Iceland with me and taught me the meaning of Petta Reddast and how to embrace it. For long coffee filled mornings when the weather conditions were not in our favour and for prioritising all the opportunities for climbing, running, hiking, skiing and grasping adventures with both hands when they came. Throughout my PhD experience it’s been these parallel outdoor activities with such an amazing group of strong and skilled mountaineering women that kept my morale high. Erla, Elísabet, Sydney, Gro and Holly you’ve done more than you could ever know to keep me smiling and happy through all of this. To the dawn patrol thanks for all of the morning hikes and coffee on Esjan before work (not as often as we hoped), but I’d love to continue this tradition!

To the very welcoming and wonderful friends I made in Durham thank you for making my time there thoroughly enjoyable, despite the endless lab work: Kate, Emma, Erin, Kate, Liz, Edward, Jordan, Fienke and Kathy. Having such great company and friendship from my lovely colleagues in Askja, both in the office and corridors, made coming into work in the dark winters much more enjoyable. A special thank you to the people who made everything about this place brighter: Hannah, Matylda, Maria, Maja, Daniel, Paavo, Eemu, Maarit, Becca, Deirdre, Martin, Óli, Nína, Julia, Vincent, Joaquín, Greta, Dave, Jake, Michelle, Ade, Sandra, Iwona, Jónas, Simon, and Hrönn and to anyone I’ve overlooked.

To my friends back home who have graciously accepted my long absences and sudden reappearances, dropping in and out of their lives, whilst living on this dark rock in the Atlantic who always welcome me back with open arms. To my oldest and dearest friend Emily, who once told me I’d end up on this path before I’d even realised it myself. For her constant support and love, from thousands of kilometres away, I am eternally grateful.

Rob deserves special thanks, for just about everything really! For the continued love and support, the endless encouragement and for being a truly amazing adventure companion, second only to Pippin. For travelling all over this country and the world with me in pursuit of expanding our knowledge in volcanology but also all of the different mountain adventures. Our journey, and every aspect of it, has meant the world to me.

Last, but not least, I would like to thank my family. To my father and mother for holding the strings as I took my first steps down the winding road that led me here, and for inspiring me to live outside of my comfort zone and push myself when I didn’t think I could in every aspect of my life. To my Mum who continues to love, support and encourage me with every fibre of her being, I am eternally grateful and humbled. I wish my father could have seen the path this eventually led me down, but hopefully you would have been proud, Dad.

This project was funded by NERC via the IAPETUS DTP programme, with the final years supported by The University of Iceland teaching assistant grant as well as a research position in the EVE project provided by Thorvaldur Thordarson and Ármann Höskuldsson. Funding from the Watanabe Trust Fund enabled an informative and productive time as visiting researcher hosted by The University of Okayama, Misasa campus, Japan, carrying out analytical work.

Bean san oíche Artach

Ar Scáth a Chéile a Mhaireann Na Daoine

Strokkur Geyser strafed the sky,
And ploughed and sowed the inner eye.

'21' by Patrick Joseph Gallagher

'Yet often the mountain gives itself most completely when I have no destination,
when I reach nowhere in particular, but have gone out merely to be with the
mountain as one visits a friend with no intention but to be with them.'

Nan Shepherd, The Living Mountain

A handful of Earth

Dick Gaughan

Contemporary account describing the Laki 1783–84 CE eruption

'All that day and night the thunderous crashing was so great that everything shuddered and shook, and the earthquakes made every timber crack again and again. The entire area between Árjall and the uplands of Skaftártunga appeared as one great conflagration and the fire was still churning in the orifice mentioned earlier. With several companions I went over to the canyon. The flood of fire flowed with the speed of a great river swollen with meltwater on a spring day. In the middle of the flood of fire great cliffs and slabs of rock were swept along, tumbling about like large whales swimming, redhot and glowing'

Steingrímsson, 1788

'...the face of the Earth became white. Grass withered down to the roots like it had been burned. Milking cows and milch ewe lost their yield. Due to the haze and the mist the sun was blood red in colour... this could be called the grass burning summer or the sulphuric summer...'

Pétursson, 1784

'...the flow of lava was so intense that no one had experienced such enormity and people thought that this would be their last day alive...'

Pálsson, 1784

Dedication

For my mother

Chapter 1: Introduction

1. 1 Introduction

Flood lavas (FL: or high magnitude ($>1-100 \text{ km}^3$) basaltic fissure eruptions) are the building blocks of Iceland. Whilst events of this magnitude are uncommon, with an eruptive frequency of 1 in 250–500 years, they are commonly associated with substantial atmospheric volcanic pollution at tropospheric–stratospheric levels due to their relatively high sulfur (S) content. Sulfur, more particularly sulfuric aerosols, is the only volcanic species that has been observed to perturb the radiative balance of the atmosphere, over timescales of weeks to years, despite occurring in minor proportions in volcanic plumes relative to H_2O and CO_2 , alongside halogens and toxic levels of certain trace metals. Flood lava eruptions in Iceland are capable of posing a hemisphere-wide hazard causing environmental pollution, indirect and direct impacts on human health, and climatic forcing (Loughlin et al., 2012). Nevertheless, due to the low frequency of such eruptions, our knowledge of the mechanisms and timing of S loss at peak eruptive intensity and thus peak atmospheric loading during these events is confined to a few focused case studies. This project has two key aims: (1) to evaluate the modulating role of shallow conduit processes on eruption styles during FL eruptions, and on the dynamics of explosive activity during periods of peak intensity; (2) to evaluate novel chalcophile stable isotope proxies, to trace the speciation of S released to the atmosphere during magma degassing and fragmentation, combined with existing analytical techniques to improve our understanding of the redox of basaltic systems upon eruption. As well as identifying the mechanisms of syn-eruptive S loss at the vents, this approach also addresses the mechanisms of syn-emplacement S loss in the lava flow field and its transport system. Only two FL eruptions have been documented in historical times in Iceland with any detail and form the case studies for this project: a lower intensity and low magnitude eruption, 2014–15 CE Holuhraun, documented with modern scientific tools; and the high-intensity and high magnitude eruption, 1783–84 CE Laki, recorded in detailed contemporary accounts and subsequent studies.

Detailed textural analysis of pyroclasts from both eruptions indicate that only the outer rinds of these samples provide a close approximation to the melt at fragmentation. Vesicle number densities of outer rinds for both eruptions are similar suggesting that the high intensity, sub-Plinian nature, of the Laki fountaining was driven by other criteria not captured in these pyroclasts. The clast interiors have been modified by post fragmentation expansion. Rather than over-printing the clast's existing primary textures it has enhanced them, highlighting textural heterogeneities driven by distinct domains within the clasts. These discrete domains are derived from melt packages that experienced different shallow conduit histories, capturing both disequilibrium and equilibrium processes before mingling prior to fragmentation. The proportions of which vary temporally and are associated with changes in mass eruption rate (MER) in both eruptions. A volatile supersaturated, disequilibrium process, that generated domains of ultra-vesicular foam with very low S glass contents is present in pyroclasts from both eruptions suggesting rapid ascent rates through the shallow conduit. For all cases where this texture is present the pyroclasts in question were erupted during peak periods in MER during both eruptions. A shallow glacial eruptive environment, identified for the first time by this project, in the NE of the Laki cone-row appears to suppress volatile exsolution as well as being associated with this rapid ascent texture suggesting some degree of additional overburden pressure.

This is the first study to identify relative variations in chalcophile (Cu and Zn) stable isotopes in a large range of basaltic eruptive products, which occur in response to eruptive intensity and therefore changes in syn-eruptive degassing efficiency as well as changes in redox. These isotopes are also clearly sensitive to syn-emplacement volatile loss in response to the evolution of the thermal insulation of the lava flow field and redox changes in this environment. In addition, increases in sulfide content are detected, both petrologically and through relative variations in Cu elemental concentrations and Cu isotopic variations throughout the eruption. This is linked to density-driven settling of immiscible sulfides in the lava pond which are then preferentially incorporated into the lava flow transport system fed by the lava pond. Variations in these isotopic data sets highlight the importance of sampling strategy with respect to fully understanding the physical volcanological processes, as well as the evolution of activity during the eruption.

This is only the second study of pyroclasts from flood lava eruptions in Iceland, and it covers both low- and high-intensity end-members of these high magnitude events. It permits comparisons of shallow conduit processes at both ends of the intensity spectrum. Unlike Eldgjá 939 CE, these eruptions are very well constrained, and thus diversity can be identified on very fine scales isolating key features not previously recognised. For example, the 2014–15 CE Holuhraun eruption provides an unparalleled data set where a precise eruption chronology, isotopic variations, and textural diversity can be linked with precision and a high degree of confidence.

Regardless of the spectrum of magnitudes over which these events occur basaltic fissure eruptions maintain similar eruptive vent dynamics and emplace the same eruptive products. Therefore, the textural, in-situ geochemical, and isotopic findings from these eruptions extend to basaltic eruptions of varying magnitudes and intensities worldwide. Of particular interest is the possibility of applying these techniques to flood basalt (FB) events that are order of magnitude larger than their smaller counterparts, the FL, as the high-intensity eruptive phases from FB events are capable of delivering significant S loads to stratospheric levels. Consequently, FB events have significant climatic and environmental impacts as well postulated associations with mass-extinction events. This work advances our understanding of shallow conduit processes during all basaltic fissure eruptions, regardless of magnitude, identifying the mechanisms of S loss, as well as understanding the controls on the timing of peak intensity eruptive phases.

1. 2 Thesis structure

This research project addresses several key aspects of basaltic fissure eruptions: from variations in shallow conduit processes; to changes in eruptive environment; and the timing and mechanisms of syn-eruptive and syn-emplacement sulfur (S) loss in high- and low-intensity FL eruptions.

The following is a short summary and context for the key aims, areas of focus, and methods for each aspect of the project, which form four distinct chapters (Figures 1.1 and 1.2):

- (1) Initial interpretations of the eruptive environment in the very NE of the Laki fissure system, a reclassification of deposits from sub-aerial to intra- and sub-glacial.
- (2) Shallow conduit processes during a low-intensity, low-volume, end-member FL eruption: Holuhraun 2014–15 CE a case study.
- (3) Shallow conduit processes during a high-intensity, high-volume, end-member flood lava eruption: Laki 1783–84 CE a case study.
- (4) Tracing the peak periods of S release to the atmosphere, and speciation of exsolved volatiles and immiscible phases, during both aforementioned historical FL eruptions; using moderately volatile chalcophile isotope compositions as a proxy for sulfur loss in explosive and cone tephra phases. This method also tracks the changes in redox conditions in the flow field and within the transport system with its changing levels of insulation.

Chapter 2: Outlines an overview of background to the physical volcanology addressed by this research project, highlighting where this study adds to the current state of knowledge.

Chapter 3: Provides an overview of Icelandic geology, its volcanic systems and their geochemistry, FL eruptions throughout geological time, as well as an overview of historical examples of Icelandic FL eruptions and previous pertinent isotopic studies of these events.

Chapter 4: Introduces the case study FL eruptions: 2014–15 CE Holuhraun and 1784–84 CE Laki and provides a detailed overview of previous work.

Chapter 5: Presents the initial results from re-mapping the deposits from fissures 7–10 of the Laki eruption, at its NE extent, with a focus on a proposed reclassification of fissure 10 from a sub-aerial magmatic phase to a phreatomagmatic shallow subglacial eruption which became dry and ice-confined as activity progressed (Figure 1. 1). This chapter forms a short field observations report, providing contextualisation of the samples analysed in chapters 6, 7, and 8.

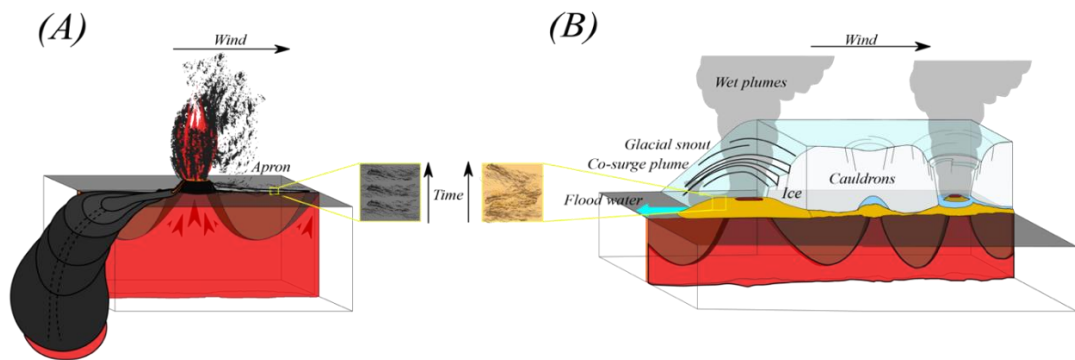


Figure 1. 1: A schematic diagram demonstrating the effect of eruptive environment on the deposits in the very NE of the Laki cone-row at fissure 10. (A) displays an established sub-aerial fissure, with an area of active vents exhibiting fountaining behaviour that creates sheet-like, apron phase, explosive tephra deposits as well as building a scoria cone and lava feeding the flow field. (B) Displays a once shallow subglacial fissure that has melted through the ice. This activity creates laterally confined fine-ash rich tuff cones, through magma-ice or external water interactions, formed by coeval fall units and pyroclastic density currents. This is recorded as cross-bedded sequences of repeating units, some of which are rich in accretionary lapilli and armoured clasts. The stratigraphy also suggests local water level fluctuates later on in this fissure's eruptive activity, changing to purely dry magmatic activity towards the latter stages of the fissure's activity.

Chapter 6: Investigates the state of the magma immediately prior to fragmentation through micro-textural analysis of the vesicle population in the outer rinds of the Holuhraun 2014–15 CE pyroclasts. Detailed whole clast textural mapping identified discrete domains, which mingled prior to fragmentation and were modified by post fragmentation expansion which enhanced pre-existing domain textures. Textural analysis and in-situ geochemical analysis quantified the diversity of clasts present. The implications of their preservation are discussed in terms of recording distinct melt packages, which experienced contrasting shallow conduit histories resulting in pyroclasts containing both equilibrium and disequilibrium textures (Figure 1. 2).

Chapter 7: Applies the same approach to the micro-textural analysis used in Chapter 6 to the vesicle populations in pyroclasts erupted during high-intensity, fissure opening and fountaining phases in the Laki 1783–84 CE FL eruption. Lower vesicle number densities (N_v^m) than expected were identified in the outer rinds of the Laki pyroclasts, giving values similar to the outer rinds of the Holuhraun clasts. This suggests that in the Laki eruption, other fragmentation criteria such as inertia, stress, strain, and larger bubbles not captured and recorded in analysed pyroclasts are potentially playing a more dominant role in the Laki magma fragmentation than during Holuhraun, which has more typical N_v^m values for its time-averaged discharge rate.

Distinct domains of equilibrium and disequilibrium textures, recording the existence of melt packages that experienced contrasting shallow conduit histories prior to mingling, are also present in the Laki pyroclasts. Varying proportions of these domains throughout the Laki eruption correspond to known increases in lag time between high intensity eruptive fissure opening phases, temporal variations in MER, as well as differences in eruptive environment (Figures 1. 1 and 1. 2). The geochemical discrepancies between textural domains are more pronounced in the Laki pyroclasts than those analysed in the Holuhraun samples. In-situ geochemical analysis also highlights the effect of a shallow subglacial eruptive environment in the NE of the Laki fissure, where ice or glacial meltwater provides the means to suppress the exsolution of volatiles recorded in texturally mature pyroclasts (Figure 1. 1).

Chapter 8: Geochemical analysis of a suite of eruptive products from the Holuhraun 2014–15 CE and Laki 1783–84 CE FL events, with a focus on characterising the spatial and temporal variations in copper and zinc isotope compositions throughout the eruption. This approach identified peak periods of volatile loss, associated with peak eruptive intensities where volatile degassing was more efficient, as well as fingerprinting the signature of different vent activity and transport systems on the eruptive products (Figures 1. 1 and 1. 2). Copper and zinc isotope variations indicate that cone building phase tephra, which are often the only samples that can be collected from the vent activity in older eruptions, display no resolvable variation in Zn values. Therefore, if these were analysed for unconstrained historic or much older events through geological time, they would not document peak phases of oxidised volatile loss due to eruptive intensity; instead, they would display very little variation and thus cannot be used to identify peak phases in eruptive intensity. Notably, compound flow fields also present complications in terms of sampling and interpreting isotopic data sets with the subsequent burial of youngest flows, channel migration, and resurfacing of the flow field obscuring syn-emplacement trends in the data set. Eruptions such as Laki 1783–84 CE, where multiple vents can feed one channel system during different phases of their eruptive intensity, present additional complications further obscuring syn-eruptive trends in the flow field data set. Future studies of this nature should place emphasis on physical volcanological constraints in

terms of eruptive history prior to sampling older or less well-constrained historical eruptions.

Chapter 9: Provides a research project synthesis, as well as interdisciplinary conclusions and a framework of suggestions for future work within these research fields.

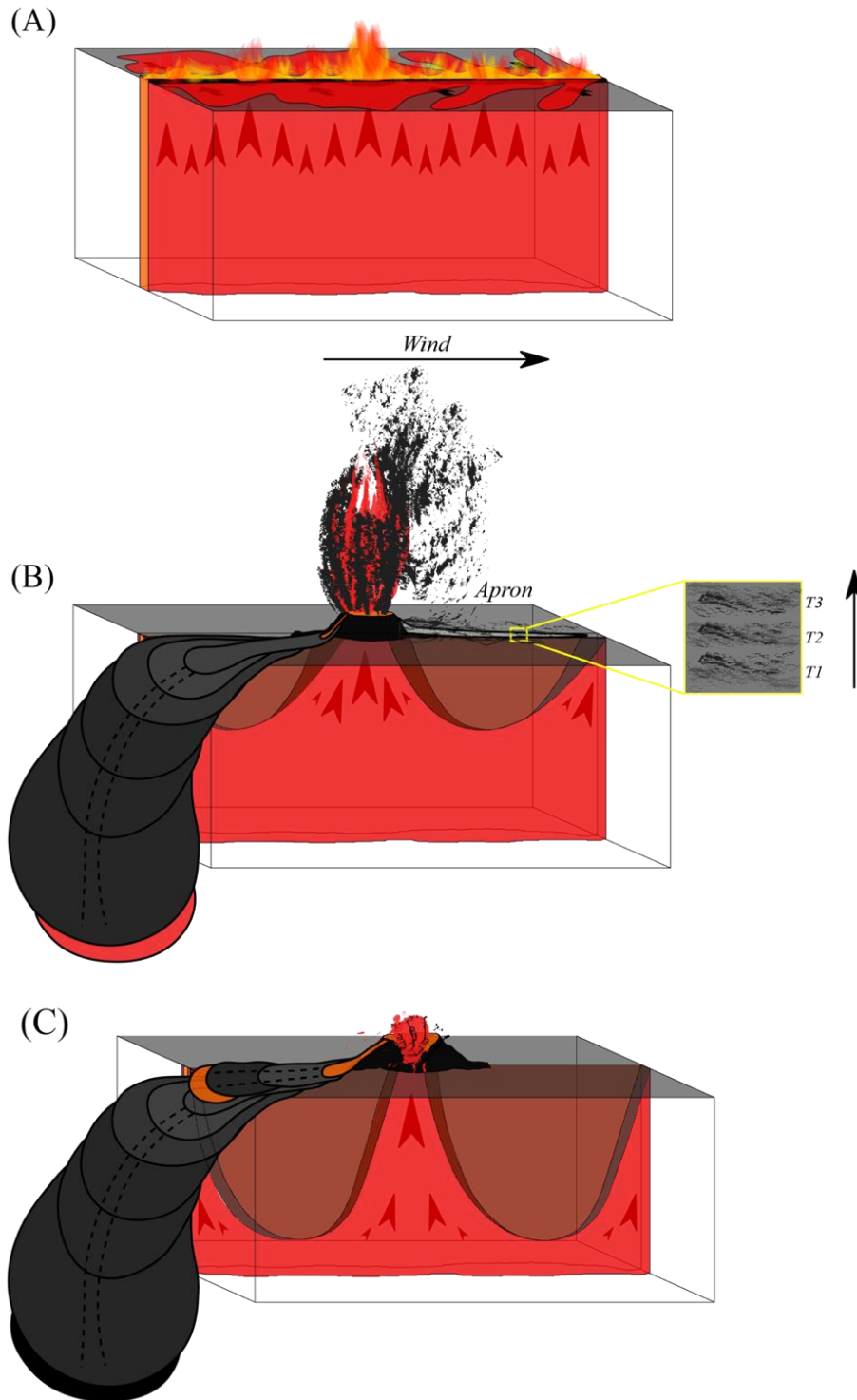


Figure 1. 2: Schematic sketch of the evolution of a fissure. Phase (A) represents the emergent fissure opening phases where activity occurs continuously along the entire fissure associated with <50 m high vent activity and sheet lavas with no defined dominant transport system. These are referred to as the first lava arrivals in Chapter 8. Phase (B) activity devolves onto discrete vents, and during phases of waxing MER with intense fountaining creating sheet-like, explosive apron phase, tephra deposits, as well as lava feeding an established transport system, the location of which is highlighted by the dashed line where it is thermally insulated, with the strongest hydraulic head of any phase of the fissure's lifespan. Explosive phase tephra is the focus of Chapters 6 and 7, and defines a clear sub-group in Chapter 8. Lowland versus highland lavas and their transport systems indicated by the dashed black lines, as schematically shown here as distal and proximal lavas, are highlighted as a subgroup in Chapter 8. Phase (C) lower intensity vent activity, associated with periods of lower MER, which may occur between episodic increases in MER or during the waning phases of the eruption. The cone building tephra phase and later lavas are the focus of another sub-grouping in Chapter.

Chapter 2: Physical volcanology background

2.1 The importance of basaltic volcanism

Basaltic volcanism is the dominant type of volcanic activity on Earth; indeed, 70 % of Earth's crust is basaltic in composition, the majority of which is generated along mid-ocean ridges (Mckenzie and Bickle, 1988) that crisscross the vast submarine expanse of the planet's surface. Volcanic activity in this submarine environment has a lower viscosity due to suppression of volatile exsolution both via higher hydrostatic pressures than at atmospheric levels as well as experiencing the higher bulk modulus of water relative to air, creating higher confining pressures. This produces effusive eruptions, with suppressed explosive intensity, of basaltic magmas with high volatile contents (Cas and Simmons, 2018). They form compound lava flows emplaced pillow-by-pillow or lobe-by-lobe. Subaerially, the same magmas are not subject to high confining pressures upon eruption, so the volatiles in these magmas can exsolve, enabling these eruptions to release volatiles to the atmosphere. Subaerial basaltic volcanism occurs across the whole spectrum of tectonic environments and makes up over 95% of Earth's intracontinental volcanism (Crisp, 1984). These eruptions encompass a wide range in eruptive styles, magnitudes, intensities, and mass eruption rates (MER), emplacing a diverse and inextricably linked continuum of eruptive products.

Whilst subaerial basaltic eruptions commonly occur as effusive events, due to the low viscosity of basaltic melts, basaltic volcanism is not entirely effusive. Fountaining or Strombolian explosive eruptive activity is a common manifestation of basaltic eruptive behaviour, but it is also pertinent to note that basaltic eruptions are amongst the most vigorous, high-intensity and high magnitude eruptions in historical times i.e., sub-Plinian to Plinian (e.g., Etna 122 CE, 2011 CE, 2013 CE, Grímsvötn 2011 CE, Oshima-Miharayama 1986 CE, Katla 1918 CE, Mt. Tarawera 1886 CE, Eldgjá 936 CE, Vatnaöldur 871 CE, and Veiðivötn 1477 CE) (Figure 2. 1).

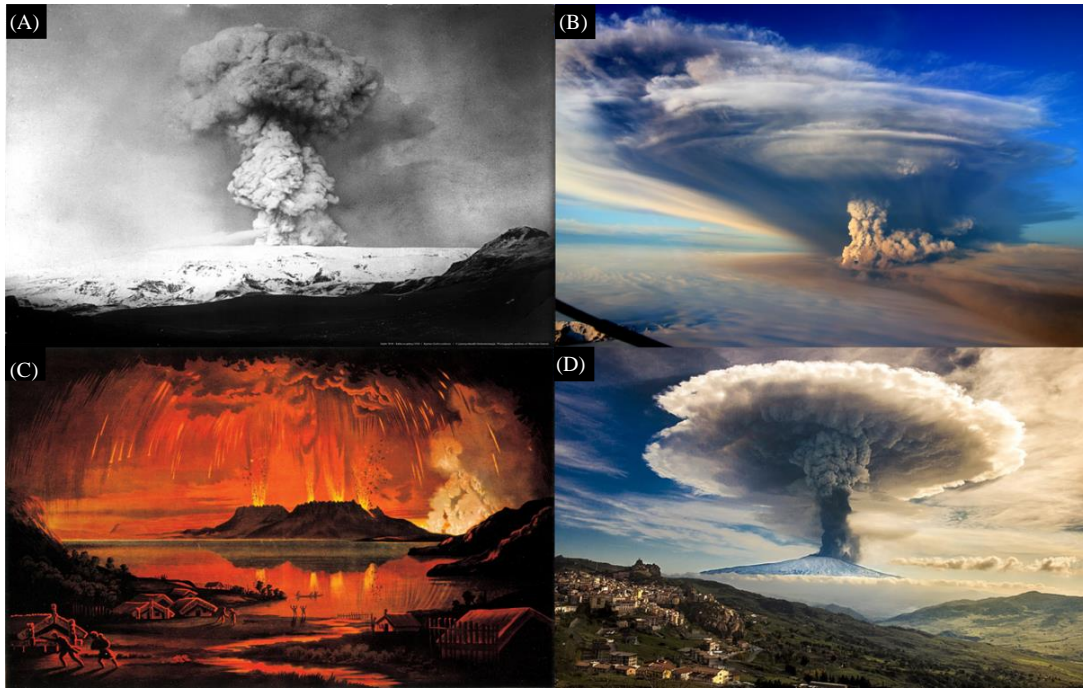


Figure 2. 1: Plinian basaltic eruptions. Examples of historic high intensity, Plinian, explosive basaltic eruptions. (A) Katla 1918 (NordVulk), (B) Grimsvötn 2011 (FutureVolc), (C) An artist's impression of the Tarawera 1886 CE eruption (NZ, national museum gallery), (D) Etna 2013 CE (Fernando Famiani, photographer).

Basaltic fissure eruptions are the most common form of basaltic volcanism, with nearly all volcanoes having basaltic fissures with various stages of maturity (Walker, 1993; Gudmundsson, 1995; Walker, 1999). Explosive eruptive style during basaltic fissure eruptions can vary from a <50 m high curtain-of-fire, often associated with an emergent phase, to sub-Plinian–Plinian (>1400 m) fountaining intensities, and a whole spectrum in between, depending on the life span and MER of the magma in question (Figure 2. 2).

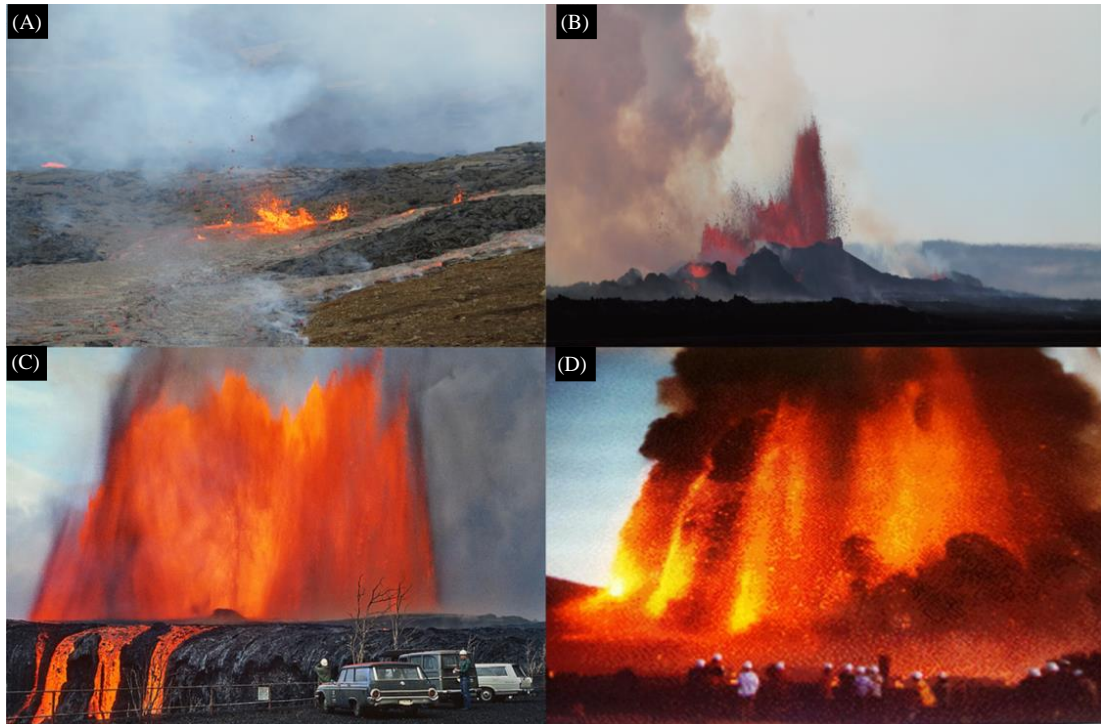


Figure 2. 2: Range of basaltic fissure eruption fountaining intensities. These images are taken from different examples of historical fountaining events of different intensities and stages of activity. From the top left: (A) Emergent fissure opening phase Geldingardalsgos, Fagradalsfjall, 2021 CE, <5 m high, (author's own photograph); (B) Holuhraun 2014–15 CE at highest MER, 170 m, on the 7 September 2014 (author's own photograph); (C) Mauna Ulu 1969 CE, one of its moderate-high fountaining episodes (USGS); (D) Oshima 1986 CE, sub-Plinian fountaining episode 1,600 m high (OVO).

Until the early 1980s, no examples of Plinian basaltic eruptions had been documented (Williams et al., 1983), with Walker (1984) being the first to cite Tarawera 1886 CE as a basaltic Plinian event based on unpublished data. Thus, only in the last few decades has there been a shift to high eruptive intensities being considered for basaltic eruptions (Sparks, 1978; Wilson, 1980) with the knowledge that higher viscosities are not essential for Plinian eruptions and that other parameters play a significant role (Williams, 1983; Parfitt, 2004). This has led to detailed mapping of deposits from basaltic sub-Plinian–Plinian eruptions, both historic and prehistoric, on a global scale. Until recently, parameterisation and modelling of processes that result in explosive events have focused predominantly on high viscosity magmas. It is only in the past few decades that research has started to quantify the result of complex feedbacks in the shallow conduit that modulate changes in eruptive dynamics in basaltic explosive eruptions. Consequently, basaltic eruptions of all magnitudes are now known to display highly variable, episodic, and rapidly fluctuating eruptive styles and intensities over their eruptive lifespans.

The dominant volatile species dissolved in basaltic magmas are H₂O, followed by CO₂, with lower concentrations of sulfur (S), halogen species, Cl and F, and associated metal complexes. Due to the earlier subsurface degassing of CO₂, the eruptive emissions volatile budget from a volcanic eruption does not feature a strong CO₂ flux (Schmidt and Robock, 2015); instead, they predominantly consist of H₂O and S. For basaltic eruptions the S budget is around an order of magnitude higher than explosive silicic magma eruptions (Devine et al., 1984) resulting in a higher amount of emitted toxic gases loaded into the atmosphere upon eruption. Despite the relatively low eruptive concentrations of S this is the only volcanic volatile species that has been observed to perturb the radiative balance of the atmosphere (Schmidt and Robock, 2015). If these relatively volatile rich eruptions have a high mass eruption rate (MER), resulting in an explosive event, this enables more efficient upper troposphere and stratospheric level injections of the eruptive plume (Thordarson et al., 1996; Thordarson and Self, 2003; Self et al., 2014; Schmidt et al., 2015). Consequently, they can trigger environmental, atmospheric, and climatic perturbations, which can be both on a local and hemisphere-wide scale. Sustained high-intensity and high-volume fountaining events, i.e., high-intensity FL eruptions, can support eruption plumes that are capable of delivering more volatiles to the tropopause/stratosphere boundary where their S aerosols have a longer lifespan, posing a real hazard to the climate in terms of cooling and disruptions of hemispheric weather systems (Figure 2. 3).

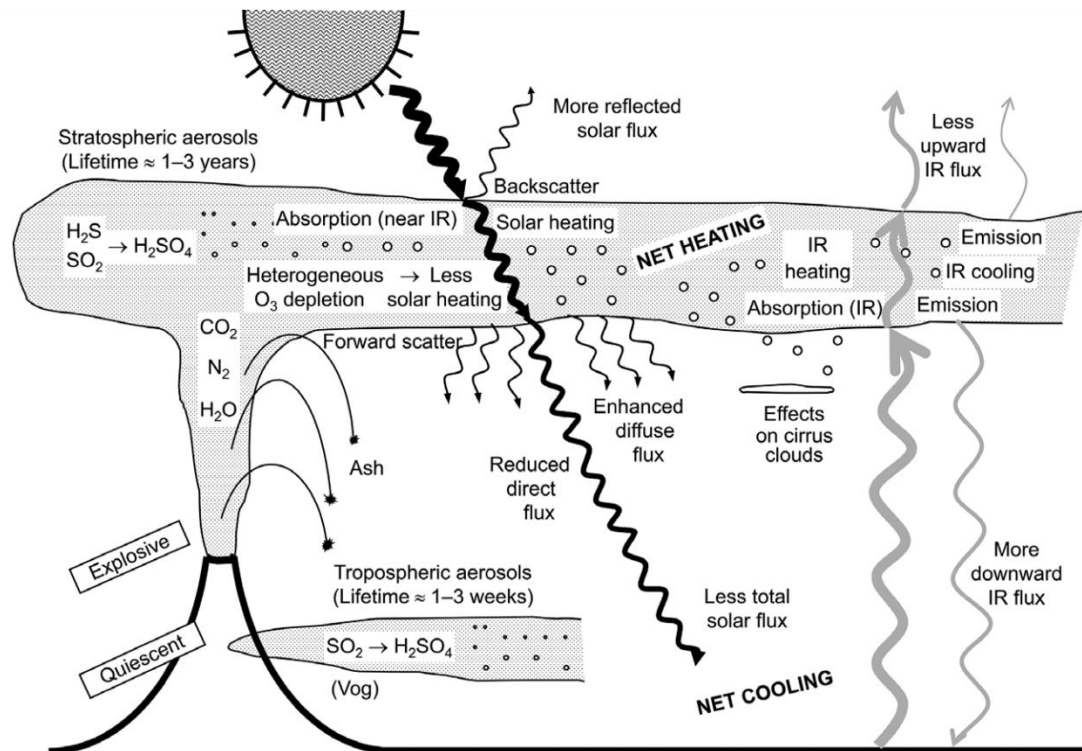


Figure 2. 3: The effect of the volcanic sulfur release on the stratosphere and troposphere. A schematic sketch taken from Schmidt and Robock (2015) displays the chemical reactions of the volcanic plume and its volatiles. Of interest for this project is how the sulfur present in the plume matures from volatiles to aerosols, as well as the relative lifespan of these aerosols in environments of differing humidity (stratosphere, dry; troposphere, higher humidity).

Recently the wider volcanological, political, and economic communities have recognised the implications of long-lived toxic gas hazards posed by FL fountaining events for both health/environmental and climatic perspectives (Schmidt et al., 2016). Of particular relevance to this study are European geographical areas, where governments such as the United Kingdom have added gas-rich FL, “Laki-type” eruptions, to its top three risks on the National Risk Register of Civil Emergencies in 2012 (Loughlin, 2012). A “Laki-type” eruption is defined as producing fountaining activity at the vents of sub-Plinian intensities and thus a sulfur and metal-rich plume that reaches at least the troposphere-stratosphere boundary (see Chapters 4, 5, and 7). These events are much rarer than the infamous Eyjafjallajökull eruption, which caused widespread disruption of air traffic in the northern hemisphere in 2010, despite being a relatively low magnitude event. Whilst it gained so much interest due to the necessary shut down of air traffic as safe volcanic ash volume limits were reassessed and established, ash from Grímsvötn 2011 did not trigger the same headline news. Grímsvötn 2011 was a higher magnitude and higher intensity event

(Petersen et al., 2012; Sigmarsson et al., 2013), but a combination of a short main eruptive phase and westerly to southerly winds at high altitudes (Petersen et al., 2012) meant the ash caused less disruption to aviation.

2. 2 Basaltic fountaining eruptions

Lava fountaining eruptions, producing incandescent and sustained jets of pyroclastic material, are evocative of explosive eruptions at Kīlauea, Hawai‘i, but typify explosive activity at basaltic volcanoes worldwide regardless of tectonic environment. Eruptions of this nature span a large range in magnitude as well as intensity, style, and MER. To fully understand the variability in these explosive events, a number of parameters influencing the rising magma need to be considered, such as: decompression rate; fluid dynamics; geochemistry and thus viscosity; volatile budget and redox; behaviour of volatiles on ascent; the mechanisms of degassing, outgassing; and the effect of conduit geometry. This results in complex feedbacks and rapid fluctuations, which correspond to changes in eruptive dynamics generating textural diversities in the erupted pyroclasts.

Weak fountaining events devolve from an emergent phase of laterally near-continuous “curtain-of-fire” fountaining to discrete vents, each producing near-vent, coarse-grained pyroclastic fall deposits. If vent localisation occurs in-step with the waxing phase of the eruption, where the magma discharge is still increasing, fountaining intensity and height increase. These more intense phases can produce medial and distal tephra fall, which can form discontinuous or continuous layers depending on the timescales of activity. Episodic phases of higher MER, and therefore higher intensity fountaining, is a common feature of fissure eruptions; once activity has devolved to discrete vents, it can result in intense phases of moderate-high fountaining e.g., Kīlauea in Hawaii: Kīlauea Iki 1959 CE (Richter et al., 1970; Stovall et al., 2011, 2012), Mauna Ulu 1969–74 CE (Parcheta et al., 2013; Swanson et al., 1979) Pu‘u‘Ō‘ō 1983–86 CE (Wolff et al., 1988; Mangan and Cashman, 1996; Heliker et al., 2003; Heliker and Mattox, 2003). A similar reduction in MER followed by a surge in fountaining intensity took place within the 2014–15 Holuhraun event in September 2014, linked to changes in MER (Bonny et al., 2018).

High intensity basaltic fountaining events are usually confined to summit eruptions through cylindrical conduits e.g., Etna 2007 (Andronico et al., 2008, 2014) and 2013 (Calvari et al., 2018) with fountain heights during the latter reaching sub-Plinian intensities and recorded fountaining heights between 800–1,500 m. However, high fountaining activity also occurs during basaltic fissure eruptions, producing jets >400 m (Houghton et al., 2016). These are typical of Hawaiian style activity with notable historical examples occurring at Kīlauea: Kīlauea Iki 1959 CE (Richter et al., 1970; Stovall et al., 2011, 2012), Mauna Ulu 1969-74 CE (Parcheta et al., 2013; Swanson et al., 1979), Pu'u'Ō'ō 1983-86 CE (Wolff et al., 1988; Mangan and Cashman, 1996; Heliker et al., 2003; Heliker and Mattox, 2003). The highest documented historical eruption fountain heights from a short-lived and small volume fissure eruption were recorded in 1986 CE at Oshima Volcano, Japan, reaching 1,600 m (Sumner, 1998); Plinian intensities were documented at another short-lived historical fissure eruption at Mt. Tarawera, New Zealand 1886 CE (Carey et al., 2007). For all of these eruptions, the highest lava fountaining occurred once the eruptive activity concentrated from a curtain of fire onto discrete vents on the fissure in question. The timescale for reaching peak intensity varies for eruptions of this nature and can take minutes–hours (Richter et al., 1970) or days (Witt et al., 2018). All of these eruptions also displayed rapid fluctuations in eruptive behaviour resulting in pulsating episodes of activity throughout. An understudied and rare manifestation (in historical times) of high-intensity fountaining eruptions are FL eruptions, emplacing > 1 km³ of eruptive products within timescales of months–years with episodic high intensity eruptive phases. Only two eruptions of this nature have occurred in the last 2000 years, both in Iceland: Eldgjá 936 CE and Laki 1783–84 CE. Both displayed sub-Plinian–Plinian fountaining activity reaching heights of >1.4 km (Thordarson et al., 2003a). A smaller magnitude and weaker intensity end-member of FL occurred in 2014–15, also in Iceland, at Holuhraun displaying low–moderate, <170 m, (Houghton et al., 2016) fountaining heights (Figure 2. 2).

2. 2. 1 Fissure eruptions: magnitudes and intensity

Fissure eruptions exhibiting explosive eruptive behaviour occur over a wide range of intensities and magnitudes, as well as volcano-tectonic settings. Eruptive intensities vary from Hawaiian to Plinian fountaining, displaying episodic and rapid

fluctuations in eruptive style, due to rapid feedbacks in shallow conduit processes, which also switch between steady and unsteady vent activity, are a common feature of explosive basaltic fissure eruptions.

Fissure eruptions build a small amount of topography around the vent site, consisting of spatter cones and ramparts, near-vent clastogenic lava flows as well as channels feeding advancing lava flows. If the eruptive duration of the vent activity continues past the emergent fissure opening ‘curtain-of-fire’ phase and concentrates down onto discrete vents along with waxing MER, the eruption may form scoria cones, spatter ramparts, and sheet-like medial tephra aprons associated with more vigorous-intensity activity. Focal points of activity develop along active fissures due to choke points within the conduit subsurface geometry in response to differing flow rates. This is dictated by variable subsurface conduit geometry, with narrower areas shutting down and wider areas allowing a higher flow rate which is thermally erosive (Head et al., 1996; Moreland et al., 2019). This process causes convection cells to develop within the conduit as high flow rates and descending degassed melt concentrate into certain areas (Jones et al., 2020).

The duration, and therefore magnitude, of basaltic fissure eruptions can range from small fissure eruptions generated over tens of minutes to a few hours of activity, creating vastly different surface landforms in terms of area and volume. For example, the proximal eruptions at Piton de La Fournaise (La Réunion) 1972 CE 2–6 and 7–9 November fissure eruptions from creating very small lava fields of 0.02 km^3 during 2–4 days minutes eruption (Peltier et al., 2009), when compared to early Holocene Icelandic shield lava eruptions which produce 10s–100s of km^3 of lava over prolonged periods of time (decades–hundreds of years). The latter also starts as a fissure eruption and concentrates down to a central vent producing effusive, i.e., very low energy, activity from a main lava pond, which feeds an insulated transport system which flows to endogenously emplaced pāhoehoe lava lobes at the flow fronts.

The explosive intensity, and therefore style of eruptive activity, during a fissure eruption, is primarily dictated by MER and shallow conduit processes such as bubble nucleation, expansion, coalescence, and outgassing (Gonnermann and Manga, 2003).

Explosive basaltic activity spans a large range from low energy to high energy events, resulting in a spectrum of the style of vent activity from weaker intensity Hawaiian and Strombolian events, to higher intensity Vulcanian, sub-Plinian, Plinian events in the case of magmatic eruptions. In the case of eruptions involving external water, i.e., ice, surface liquid water bodies or aquifers, Surtseyan or Phreato-Plinian activity classifications are applied due to the finer grained nature of the tephra produced. Throughout the lifetime of an active fissure eruption it can display several styles in vent activity. Rapid transitions between types of vent activity or fluctuations in intensity occur as a result of feedbacks within the shallow conduit, coupled with waxing and waning of the MER, which can occur episodically throughout the eruption.

Initial vent activity, during the opening phase of the fissure, is typified by an emergent ‘curtain-of-fire’ stage (<50 m in height) along the entire active fissure or fissures (Houghton et al., 2021) (Figure 2. 4). This emergent phase transitions, either over the course of days (Witt et al., 2018) or in some high intensity and high cases tens of minutes (Sumner et al., 1998), into more intense explosive activity.



Figure 2. 4: Curtain-of-fire Holuhraun 2014–15 CE. On the 31 August 2014, the Holuhraun 2014–15 CE eruption re-initiated, with emergent curtain-of-fire fountaining activity stretching for 1.5 km. Author photograph.

The style of explosive activity that ensues is strongly dependent on the manner the volatiles ascend through the shallow conduit and can be roughly grouped into two categories: sustained or unsteady discharge eruptions of differing intensities. The classifications, and the corresponding behaviour of melt and bubbles in the shallow conduit, for that style of eruption, are as follows:

- (1) Fountaining eruptions: Often referred to as Hawaiian fountaining eruptions, are typified by a sustained magma discharge, forming continuous incandescent jets at the surface. Whilst the discharge is maintained for hours–days, the MER, and therefore the intensity of the fountaining during the eruption can fluctuate, sometimes episodically creating pulses of more intense phases. Fountaining eruptions have higher ascent rates when compared to effusive activity or, indeed, Strombolian-style events (see (2) below). As a result, the volatile and melt phases remain coupled through the shallow conduit, taking the form of a heterogeneous but continuous stream of gas. This can occur as a form of a churn flow (lower gas flux) or annular flow (higher gas flux) in the shallow conduit (Houghton and Gonnerman, 2008), producing high-powered gas jets at the surface (Gonnerman, 2015) (Figure 2. 5).

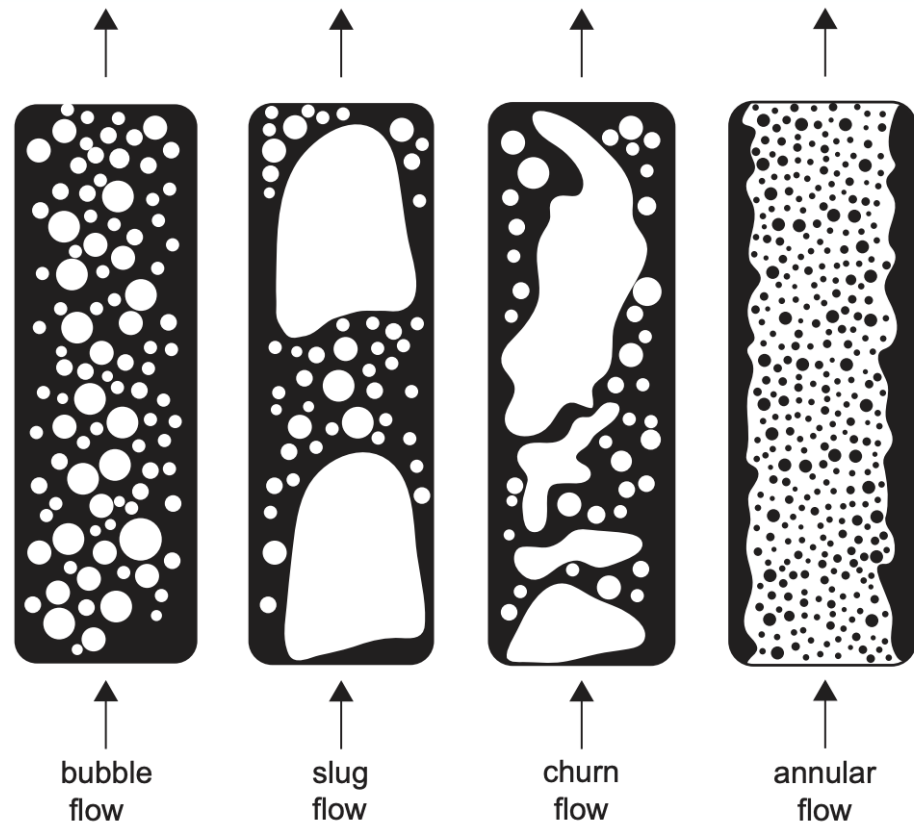


Figure 2. 5: Houghton and Gonnerman, 2008. Schematic of the different main types of bubbly melt flow in the shallow conduit during a basaltic eruption, bubbles are shown in white with the melt in black.

This style of eruptive activity is often regarded as weak, producing Hawaiian style fountaining, which can be divided into three different sub-classifications, as defined by Houghton et al., 2016: low <100 m, moderate 100–400 m and high >400 m. However, fountaining can reach sub-Plinian to Plinian intensities (Thordarson and Self, 1996; Sumner 1998; Thordarson et al., 2003; Bonnaccorso et al., 2014; Moreland et al., 2019; Spina et al., 2021). Fountaining events are distinguished from Strombolian explosions by their longer durations (>300 s), Houghton et al., 2016. Parfitt and Wilson, 1999 suggested that basaltic sub-Plinian–Plinian eruptions are a more intense form of Hawaiian and Strombolian events, with higher ascent rates, based on their similar dynamics. However, when analysing basaltic pyroclasts from weak–high intensity events, a limited number of studies have demonstrated distinct differences in vesicle number densities versus mass eruption rates (Houghton et al., 2004; Sable et al., 2006). This suggests that another criterion must be

invoked for lower viscosity melts (Papale, 1999), i.e., microlite rich and therefore more viscous basaltic melts such as 122BC Etna and Tarawera 1886 CE (Sable et al., 2006).

(2) Strombolian eruptions: Forming normal, major, or violent Strombolian explosions and rarer paroxysms are typified by an unsteady magma discharge, creating short bursts of explosive activity. This classification is based on eruptions at Stromboli, and further verification of whether it is applicable to Strombolian eruptions elsewhere is necessary (Houghton et al., 2016). Unsteady explosive activity is the result of large slugs, conduit-filling bubbles, which have a higher rise rate than their parental melt and thus decouple, ascending more quickly through the shallow conduit. As they burst explosively at the surface, incandescent globules of melt are scattered around the vent area. Individual Strombolian explosions, lasting for between 15 ± 6 s, consist of sub-second pulses of meter-diameter gas pockets (Gaudin et al., 2014a; 2014b; Taddeucci et al., 2015) (Figure 2. 6), rather than one individual slug. The three varieties of Strombolian explosions have a comparatively shorter duration relative to Hawaiian eruptions but vary in mass discharge rate, with paroxysms overlapping with Hawaiian discharge rates (Houghton et al., 2016). Paroxysms, the more intense style of Strombolian explosivity, e.g., Stromboli 2019 (Giordano and Astis, 2021), also referred to as Vulcanian eruptions, are shorter-lived than Strombolian eruptions, which have milder explosions and usually last for days building thick scoria cones and fall deposits dispersed away from the vent (Walker 1973; Calvari and Pinkerton 2004; Pioli et al., 2008; Giordano and Astis, 2021). Paroxysms, due to their higher intensity, produce more fine ash from the higher degree of fragmentation the magma undergoes.

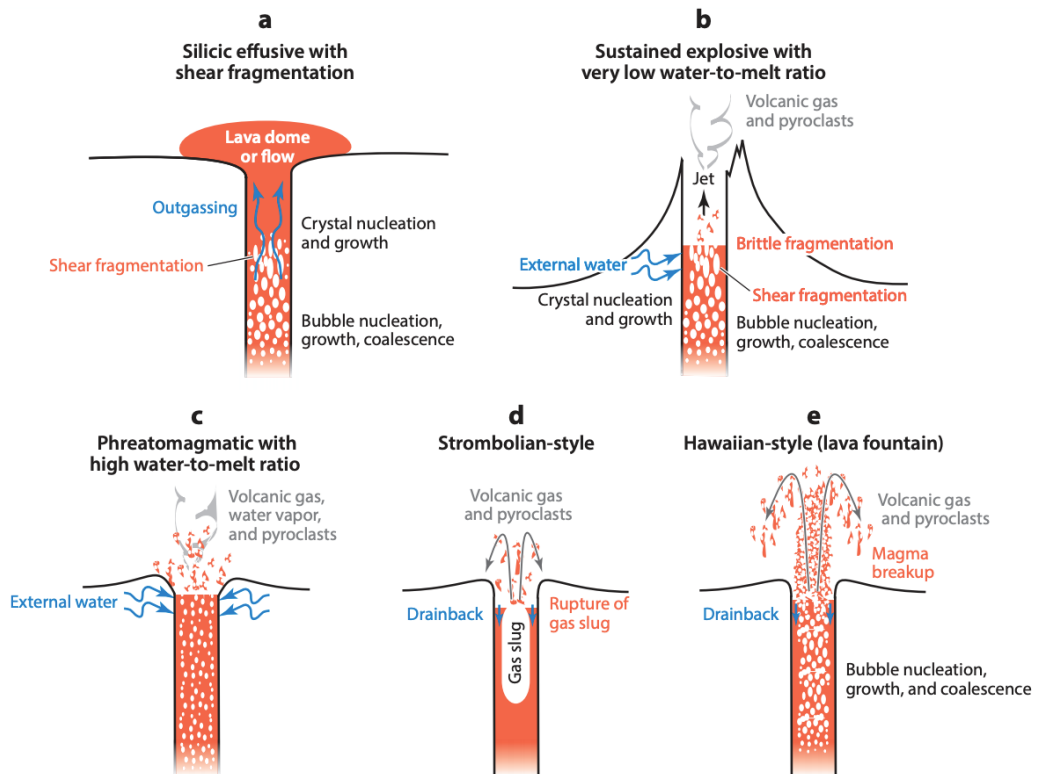


Figure 2. 6: Gonnerman, (2015). Examples of the shallow conduit dynamics and resultant styles of vent activity during different types of eruptions: a) Effusion of high viscosity melt, not discussed here. b) Sustained explosive eruptions, with a low water-to-melt ratio, of a magma with a high viscosity or experiencing high shear rates, or both. c) Phreatomagmatic explosive eruptions, with high water-to-melt ratios, where the external water granulates the eruptive pyroclasts and flashes explosively to steam d) Strombolian-style eruptions, where large gas slugs formed by coalescence of smaller bubbles or clusters of smaller bubbles, which travel together as a slug, decouple from the melt and travel through the shallow conduit with a higher rise rate and burst at the surface causing discrete explosions. e) Hawaiian-style fountaining eruptions, which can form sustained or un-sustained vent activity, occur due to high shallow conduit ascent rates of a coupled melt and gas phase, which form powerful gas jets carrying at the surface.

(3) Phreatomagmatic events: These involve the addition of external water to the melt in the shallow conduit prior to or post fragmentation, as the result of the magma penetrating an aquifer, erupting underneath a glacier, a surface water lake, or the sea. Magma-water interactions result in phreatomagmatic fragmentation producing a finer-grained deposit; with the extent of its influence on the fragmentation intensity depending on the ratio of external water to magma and the timescales involved. Lower intensity phreatomagmatic fragmentation does not add explosivity to the system, with the eruptive intensity dictated by magmatic fragmentation processes only, external water induces thermal granulation through hydro-fractures disintegrating the melt (Kokelaar, 1986; Moreland et al., 2020). Another mode of phreatomagmatic fragmentation is a fuel-coolant interaction, driven by steam film generation and collapses at the external water to magma

interface and subsequent flash boiling of the water to produce explosive activity (Zimanowski et al., 2015 and references therein; Moreland et al., 2020). Based on the degree of tephra dispersal, the phreatomagmatic realm is divided into Surtseyan, after their Icelandic namesake, which erupted off the coast of South Iceland in 1963 CE, Phreato-Plinian type eruptions, named after the C-phase of the Askja 1875 CE eruption.

The seminal publication by Walker (1973), a widely accepted classification, which categorizes the eruptive intensity of a basaltic event based on the characteristics of its tephra deposit, gives a best estimate of the intensity of older, remote, and/or undocumented basaltic events, which have a preserved tephra layer. Walker (1973) uses the following two characteristics of the resultant tephra deposits: (1) dispersal of ejecta, as a proxy for MER, i.e., how quickly the deposit thins away from the vent; and (2) the fragmentation indices, i.e., the degree of fines as a weight percent. These two criteria generally separate the styles of eruptive activity (Figure 2. 7).

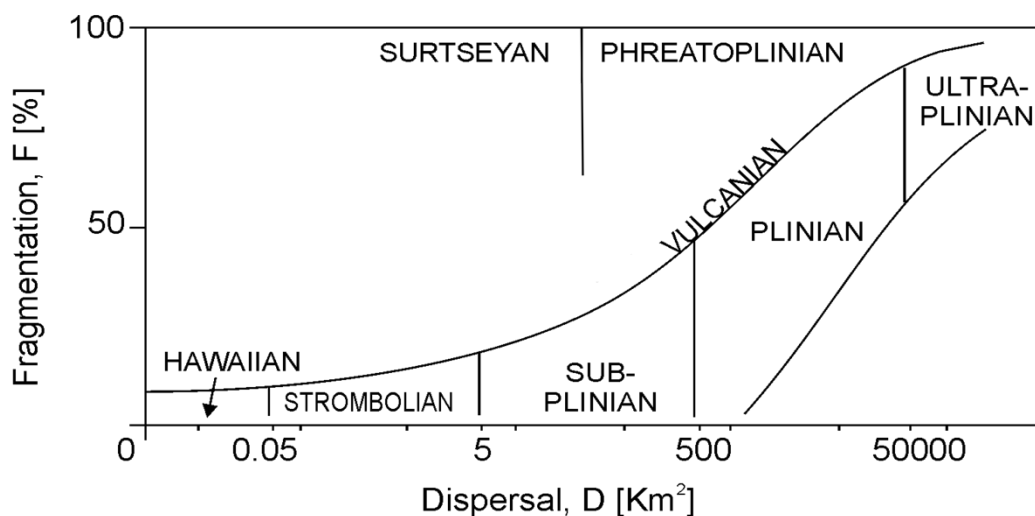


Figure 2. 7: Eruptive intensity deposit characteristic schematic taken from Walker (1973). The initial classification of explosive volcanism using: D, dispersal index, which is a measure of how quickly the mapped isopach of the tephra dispersal from an eruption or eruptive phases thins away from its source vents; and F, fragmentation index, which measures how fine-grained said deposit is. Note that this initial classification categorises Hawaiian eruptions at the low-intensity end-member of eruptive styles. However, fountaining eruptions span the scale from Hawaiian to sub-Plinian–Plinian intensities.

However, the caveats in this classification that need to be addressed are: (1) that all Hawaiian and Strombolian activity is regarded as weak, (2) without a known timeframe that tephra deposition occurred within, demarcations between the eruptive styles cannot be identified from the deposits alone in order to distinguish between

transient paroxysm explosions versus sustained activity types e.g., Hawaiian and Strombolian or Vulcanian and sub-Plinian events. These two sticking points currently hinder the ability of the scientific community to characterise and classify activity at certain volcanoes for the purposes of future hazard forecasting, as well as the understanding of the driving forces between these different eruptions (Houghton et al., 2016; Bonadonna et al., 2012). Further complications exist when Hawaiian fountaining activity is considered in isolation, as it is typically regarded as weak intensity eruptive activity. Instead, it spans a range from weak emergent phases with fountains reaching 50 m in height to sub-Plinian to Plinian eruptive intensities producing fountains reaching >1400 m. High intensity fountaining at Kīlauea produces fountains of >500 m in height (Houghton et al., 2016) and fountaining events of sub-Plinian to Plinian intensities produce fountains reaching >1400 m in height, e.g., Eldgjá 936 CE, Laki 1783–84 CE, Oshima 1984 CE, and Etna 2011, 2014, 2015, and 2021 CE (Sumner, 1998; Larsen, 2000; Andronico et al., 2005, 2014; Bonnaccorso et al., 2014; Carbone et al., 2016; Moreland et al., 2019; Spina et al., 2021). A recent study by Spina et al., (2021) called for fountaining activity, given the wide spectrum it spans in terms of intensity in nature, to be given its own classification outside of effusive versus explosive activity classifications.

Other layers of complexity addressed by the Walker (1973) classifications include rapid transitions between eruptive intensities at basaltic volcanoes. These have been frequently observed as reoccurring episodic transitions to higher intensity activity phases separated by periods/phases of weaker intensity activity. This has been observed at Kīlauea in Hawaii: Kīlauea Iki 1959 CE (Richter et al., 1970; Stovall et al., 2011, 2012), Mauna Ulu 1969-74 CE (Swanson et al., 1979; Parcheta et al., 2013) Pu'u'Ō'ō 1983-86 CE (Wolff et al., 1988; Mangan and Cashman, 1996; Heliker et al., 2003; Heliker and Mattox, 2003) whilst also occurring at central volcanoes as Etna and Stromboli (Spampintao et al., 2012). Transitions between explosive styles throughout fissure eruptions, i.e., from Hawaiian to Strombolian, have been observed during eruptions at Heimaey 1973 CE or the Great Tolbachik Fissure, 1975 CE (Parfitt, 2004). In contrast, the opposite occurred during some 21st century summit eruptions at Etna (Spampintao et al., 2012), which displays increased frequency in Strombolian activity (e.g., rapid Strombolian activity) prior to the onset of sustained fountaining (Andronico et al., 2005, 2014). The Walker (1973)

classification better suits point source eruptions, and not fissure eruptions with multiple discrete vents within one fissure or several active fissures, e.g., Eldgjá 936 CE, Vatnaöldur 871 CE, Veiðivötn 1477 CE, Laki 1783–84 CE and Tarawera 1886 CE.

Houghton et al. (2016) call for a particular focus on mapping historical deposits from eruptions with well-documented vent activity from Etna, Kīlauea, and Stromboli which were not included in the original Walker (1973) classification. As well as detailed fieldwork and data sets from other basaltic volcanoes to build a detailed database from which to extract quantitative demarcation characteristics that can be applied to less classical and complicated deposits.

Analysis of Strombolian versus Hawaiian deposits in the field at a componentry level might also provide extra information for eruptive style differentiation since Hawaiian deposits are rich in achneliths, which reflecting the presence of the sustained gas stream phase in the fountaining jet which fuses the very outer skin of the lapilli pyroclasts (Houghton et al., 2016; Taddeucci et al., 2015).

2. 2. 2 Classifications of basaltic lava flow morphologies

Basaltic lava flows are defined by the end-member morphotypes of pāhoehoe and ‘a’ā, but also feature a spectrum of hybrid morphotypes such as slabby, rubbly, and spiny pāhoehoe (Table 2. 1, Figure 2. 8) (Keszthelyi et al., 2000, 2004, 2006; Thordarson, 2013; Harris et al., 2017). The morphology of the lava flows that these basaltic eruptions produce varies as a function of the rheological properties of the melt upon eruption, modified by syn-eruptive degassing, the MER, and associated vent dynamics, as well as the slope on which the lava flows are emplaced. In turn, these processes influence the type of transport system that develops and the thermal efficiency of that transport system as it becomes more established and matures, which dictates the morphology of the lavas produced at the active fronts. In general, more intense eruptive activities with a higher MER will form more open-channelled transport systems emplacing rubbly pāhoehoe to ‘a’ā lavas, whereas more thermally efficient closed transport systems feed a spectrum of pāhoehoe depending on the stage of the eruption (Figure 2. 8).

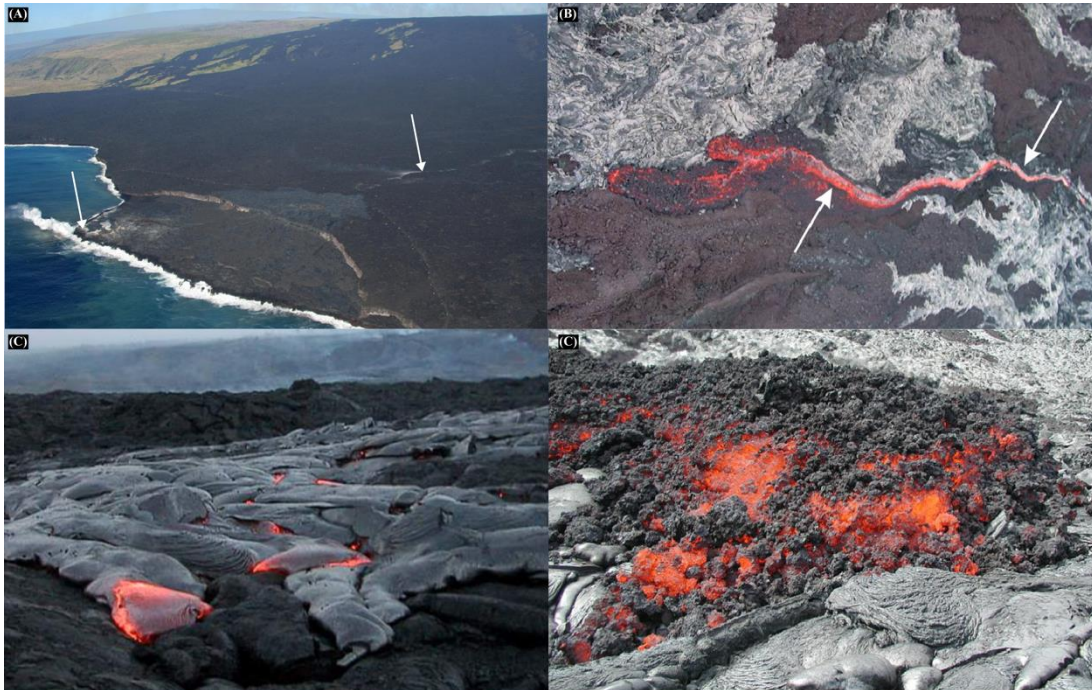


Figure 2. 8: Photographs of insulated versus open basaltic lava channels and associated lavas flow morphologies. (A) An aerial image of an active pāhoehoe closed transport system, with the active lava channel location indicated by white arrows. (B) An aerial planar image of an active 'a'ā open transport system, with the active lava channel location indicated by white arrows. (C) Pāhoehoe flow lobes at the advancing active margins. (D) 'A'ā flow front at the active flow margin. Images courtesy of Dr. Thorvaldur Thordarson, taken on fieldwork in Hawaii.

In the case of Icelandic basaltic fissure eruption fed lavas, the following morphologies are associated with certain phases of the event: (1) slabby pāhoehoe flows are concentrated at near vent areas, these are common at the start of eruptions as lava floods away from the emergent phase fountains, unconfined, before a clear transport system develops. (2) 'A'ā fed by open-channels during higher MER phases of an eruption, this flow type is also more common on steeper slopes. (3) Rubbly pāhoehoe, frequently associated with the similar vent dynamics as 'A'ā lavas, but has a more thermally efficient transport system, and can also occur as outbreaks from an 'A'ā during deflating and new frontal lobe emplacement. These are lost as the active 'A'ā front then advances over them. (4) Spiney pāhoehoe, associated with a lower MER during the waning phases of the eruption occurring as squeeze outs from the very end of the lava flow field. These are very viscous and have a higher emplacement temperature, potentially associated with the latent heat of crystallisation due to their very degassed nature and associated syn-eruptive and emplacement microlite content (Table 2. 1).





	'A'a	Rubby pāhoehoe	Slabby pāhoehoe	Spiney pāhoehoe
Description	A lava with brecciated flow tops and bases. The breccia consists of jumbles of blocky lava and irregular-shaped clinker.	A flow characterised by a flow top of pāhoehoe crustal rubble and a pāhoehoe base. The crustal rubble is up to several decimetre in size.	A flow characterised by a flow top of crustal slabs and a pāhoehoe base. The slabs are up to metres across and several decimetres thick.	A flow with a coherent crust, undisrupted at meter scale and with a spinose surface and characterised by longitudinal grooves and ridges over a flow field scale. Flows never display large amounts of volume growth via inflation.
Emplacement	The clinker is formed by viscous tearing of the chilled lava crust. The clinker is rafted towards the flow front where it is dislodged from the front in <i>caterpillar-track</i> motion (Keszthelyi and Self, 1998). 	Can be two-fold (1) Pulses of lava disrupt the immature crust of a pāhoehoe flow, that is brecciated and transported on top of the flow (Keszthelyi et al., 2004; Guilbaud et al., 2005). (2) Breakout picks up loose breccia from the a'a flow that is carried on top of the flow. 	Pulses of lava disrupt a mature crust of an inflated pāhoehoe flow and forms heaps of slabby clasts that raft on top of the flow (Macdonald, 1967; Swanson, 1973; Self et al., 2000; Harris et al., 2017). 	Surface is formed by very slow but evident viscous tearing of the microlite rich lava in a break-out which as it oozes out and tears forms very fine Pele's Hair like spines on the surface. This flow type is susceptible to over inflation of, creating flower structures with outer surfaced turn 180°. It is often unpreserved over aerial scales. 
T°C (FLIR)	Ca. 995	Ca. 1005	Ca. 1050	Ca. 1015
Velocity	≈ 30-60 m/hr	≈ 10-30 m/hr	≈ 400 - 800 m/hr	1-2m/day
1st observed	1 st of September/ 2 nd eruption day	1st of September	31 st of August /1 st day of eruption	November 6th
Location	Active flow front.	Marginal and frontal break out.	Marginal and frontal break out. Primarily in proximal areas	Marginal and frontal break out. Associated with lower discharge.
Video	20140906_1523_GBMP	20140904_2221_GBMP	20140831_2033_RA	041114_1627_CRG

Table 2. 1: Holuhraun 2014–15 CE lava morphologies. The primary active lava flow morphologies observed during the Holuhraun 2014–15 CE eruption, and their key characteristics as noted in the field by the IES eruption team or during post-processing of FLIR images and time-lapse videos.

During the Holuhraun 2014–15 eruption, resurfacing events occurred in areas around the active transport system, as well as utilising older transport systems, emplacing pāhoehoe flows which were predominantly comprised of spiny pāhoehoe over the original lava morphologies emplaced earlier in the eruption. This process can be observed from aerial images of other Icelandic basaltic fissure eruptions.

There is a large range in magnitude of basaltic fissure eruptions, with the smallest occurring as hour-long events feeding minor lava flows, with the other end of this spectrum characterised by months- to years-long FL events in historical times, to decade-long eruptions emplacing flood basalt provinces. However, regardless of the spectrum of magnitudes, these events occur over, basaltic fissure eruptions maintain similar eruptive vent dynamics and emplace the same eruptive products.

2.3 Shallow conduit processes

Basaltic magmas at depth in the crust contain volatiles in solution, and the solubility of these volatiles is dependent on several variables: pressure, melt composition, oxygen fugacity and consequently volatile saturation and speciation (Wallace and Anderson, 2000). The dominant volatile species are CO₂ and H₂O; the former reaches saturation, i.e., can exsolve from the melt to a separate vapour phase, at depths of 25 km or more and has a much lower limit of solubility in basaltic magmas (Pan et al., 1991; Dixon, 1997; Papale, 1999; Shishkina et al., 2010; Hartley et al., 2017). Consequently, CO₂ does not play a dominant role in the shallow conduit dynamics of the magma, whereas the more soluble volatile species, H₂O, along with the more minor species S, Cl and F (Thordarson et al., 1996), which predominantly exsolve at much shallower crustal depths (Schilling et al., 1980; Wallace and Carmichael, 1992; Carroll and Webster, 1994; Dixon and Stolper, 1995; Dixon et al., 1995; Webster et al., 1999).

The exsolution of water into a separate vapour phase occurs over a short period of the melt's history, during its ascent through the shallow conduit, prior to eruption. The vapour phase takes the form of bubbles which nucleate and grow via decompression driven growth and via diffusion of exsolving volatiles through the melt to nucleation sites; nucleation can occur homogeneously or heterogeneously. If the ascent rate of the magma is high, leading to high-volatile supersaturation

conditions in the melt, this can subsequently result in a burst of homogeneous nucleation within the melt due to the high interfacial energy between vapour and melt occurring as a disequilibrium process (Mangan and Sisson, 2000; Mourtada-Bonnefoi and Laporte, 2004). Whereas heterogeneous nucleation can occur at lower supersaturations, and therefore at closer to equilibrium conditions at lower ascent rates, if preferential nucleation sites are available (e.g., phenocryst surfaces in phyric melts), producing lower interfacial energy between vapour and solids (Gardner et al., 1999; Gardner and Denis, 2004).

These bubbles expand in size as a result of continuing ascent-driven decompression and diffusion (Parfit and Wilson, 2008). This occurs over a short timespan (seconds) (Gardner et al., 1996) during ascent through the shallow conduit via diffusion of volatiles from the surrounding melt into existing bubbles, as well as internal gas expansion. The rate of growth of these bubbles is dictated by a number of factors: (1) the volatile content of the melt immediately surrounding the bubble; (2) the diffusion rate from melt into the bubble; and (3) the viscous resistance of the melt (Prousevitch et al., 1993; Toramaru, 1995; Gonnermann and Manga, 2007).

Bubble size can also be increased by coalescence, a process that also modifies the shape of the bubbles, which is a function of the radii of the two bubbles in question, termed the linear collision efficiency (a dimensionless quantity). This determines whether or not two bubbles can coalesce or if their size differences are too great (Sahagian, 1985; Sahagian et al., 1989). Coalescence occurs whereby the confining pressure exerted on neighbouring bubbles by the surrounding melt is lower than the pressure exerted by the gas inside of the bubbles themselves. This causes melt-films in between the two bubbles to eventually thin to a critical film thickness, which is dependent on liquid viscosity, surface viscosity, density and surface tension (DeVries, 1972; Narsimhan and Ruckenstein, 1986a; 1986b; Mangan and Cashman, 1996). After this critical film thickness is reached it causes the bubble walls to rupture and the bubbles to merge, which can be triggered by a range of processes (Gonnermann and Manga, 2013 and references therein). In basaltic magmas the critical thickness of melt-films which allows for coalescence in response to bubble growth is 0.5 μm (Cashman and Mangan, 1994; Klug and Cashman, 1996; Castro et al., 2012). In low viscosity magmas, the melt from ruptured films assimilates to the

new bounding bubble walls and can cause a domino effect, triggering the collapse of surrounding bubbles. Correspondingly, the bubble number density of the melt decreases. Coalescence requires longer timescales (tens of seconds) than growth (Gardner et al., 1996), which is achieved through a slower ascent rate of the melt.

In low viscosity magmas, the vapour phase can decouple from the melt phase during ascent and gradually separate from the melt, moving faster through the conduit establishing open-system degassing or outgassing (Figure 2. 6) (Thordarson et al., 1996). All of these shallow conduit processes have a modulating role on the style of eruptive activity at the vent, if the melt has high ascent velocities, similar to the rise velocities of the bubbles, the vent activity will be more explosive. Early exsolution of CO₂ may increase the buoyancy enough to enable rapid ascent rates (Sable et al., 2006). However, if the bubbles have a higher rise velocity, the gas-phase can be concentrated towards the top of the rising magma column, and if the system is rising fast, this will result in a short-lived but high intensity explosive fountaining phase (to a large extent a gas-jet) followed by longer-lasting effusive phase e.g., Laki 1783–84 CE, Eldgjá 939 CE and Oshima 1986 CE eruptions. Dragging behind this gas-/bubble-rich top is a column of partly degassed magma, which does rise more slowly and ends up being erupted to produce lava. If outgassing occurs, this results in effusive eruptive activity at the surface or magma stalling in the conduit forming a dense plug, e.g., Eyjafjallajökull 2010. Rapid feedbacks in the conduit and changes in bubble evolution and ascent rates cause eruptive activity to change and fluctuate, resulting in unsteady or sustained eruptions.

Fragmentation of a magma is the process by which it transitions from a two-phase fluid with dispersed bubbles, or for phyrlic magmas a three-phase, fluid with dispersed bubbles and crystals, to a gas jet carrying fragments of the melt in question through the shallow conduit. For basaltic versus silicic magmas, the processes which induce fragmentation are fundamentally different, enabling lower viscosity mafic magmas to fragment at much lower bubble volume fractions than their higher viscosity silicic counterparts.

For silicic magmas, the process of fragmentation is achieved through brittle failure due to high tensile stress on the framework of melt-films between bubble walls in

response to a pressure build-up by the volatiles inside the bubbles. This requires a minimum critical volume fraction of bubbles to be reached, around 70–75 % (Sparks, 1978), although depending on whether the melt is also experiencing shearing this can be as low as 64% (Gardner et al., 1996, 1999).

However, in low viscosity basaltic melts, fragmentation at much lower critical volume fractions can be induced by four additional criteria: (1) inertial, pull-apart, fluid dynamic forces; (2) strain-rate; (3) potential energy; and (4) stress (Gonnermann and Manga, 2007; Namiki and Manga, 2008; Rust and Cashman, 2011). For explosive basaltic eruptions, laboratory experiments and numerical modelling have shown that the rates and timing of processes such as decompression, degassing, vesicle nucleation, growth, coalescence and outgassing, in the shallow conduit, are critical for the development of different eruptive styles (Namiki and Manga, 2006; Gonnermann and Manga, 2007; 2008; Houghton et al., 2016). In the case of very crystal-rich basaltic magmas, with a higher viscosity and complex three-phase interactions, decoupling of vapour and melt phases to decouple is subdued significantly, resulting in higher explosivity when coupled with high MERs.

Qualitative and quantitative analysis of basaltic pyroclasts have demonstrated a wide range of vesicle number densities (VND), size distributions (VSD) and volume distributions (VVD) for explosive basaltic eruptions with vastly different eruptive styles and evolution of activity (Cashman and Mangan, 1994; Polacci et al., 2006; Sable et al., 2006; Lautze and Houghton, 2008; Costantini et al., 2010; Stovall et al., 2011; 2012; Parcheta et al., 2013; Holt et al., 2019). This microtextural fingerprint preserved in the pyroclast captures the melt framework at the time of fragmentation, thus providing a window into the shallow conduit. From these pyroclasts, the timing, rates, and temporal evolution of shallow conduit processes can be established and the modulating influences on the style of vent activity upon eruption, and even to some degree spatial evolution in a cross-section of the conduit itself, can be assessed. Post fragmentation modification of the bubble population in pyroclasts from low viscosity melt eruptions occurs due to the thermal gradient present within the clasts as a result of the insulating effect the fountains themselves have (Mangan and Cashman, 1996; Parcheta et al., 2013; Stovall et al., 2011; 2012; Porritt et al., 2012; Cashman and Scheu, 2015; Holt et al., 2019), causing expansion and in some cases coalescence.

2. 4 Environmental impact of Flood Lava eruptions

The volatile budget from a volcanic eruption predominantly consists of CO₂ and H₂O, with lower concentrations of sulfur (S), halogen species and associated metals (Schmidt and Robock, 2015; Ilyinskaya et al., 2021). However, CO₂ and H₂O are thought to have a negligible impact on atmospheric chemistry due to their high background abundances (Wignall, 2001; Self et al., 2005; Self et al., 2008); hence, despite the relatively low eruptive concentrations of S, this is the only volcanic volatile species that has been observed to perturb the radiative balance of the atmosphere over short-lived timescales 1–3 years (Schmidt et al., 2012; Schmidt and Robock, 2015). Initially, SO₂ and H₂S are the most abundant S species present in the volcanic plume (Wallace and Edmonds, 2011), but H₂S rapidly converts to SO₂, which subsequently undergoes a conversion to sulfate aerosols (SO₄²⁻). These aerosols absorb near-IR radiation and scatter it away from Earth's surface, inducing a surface cooling effect and creating thermal gradients that modify meteoric conditions (Robock, 2000; Robock and Oppenheimer, 2003; Edmonds and Mather, 2017). If injected into the stratosphere, the life span of both SO₂ (hours) and SO₄²⁻ (days) increases to weeks and months–years respectively, due to slower removal processes associated with lower water vapour contents, i.e., the humidity environment at stratospheric levels, thereby increasing their associated climatic and environmental impact (Figure 2. 9).

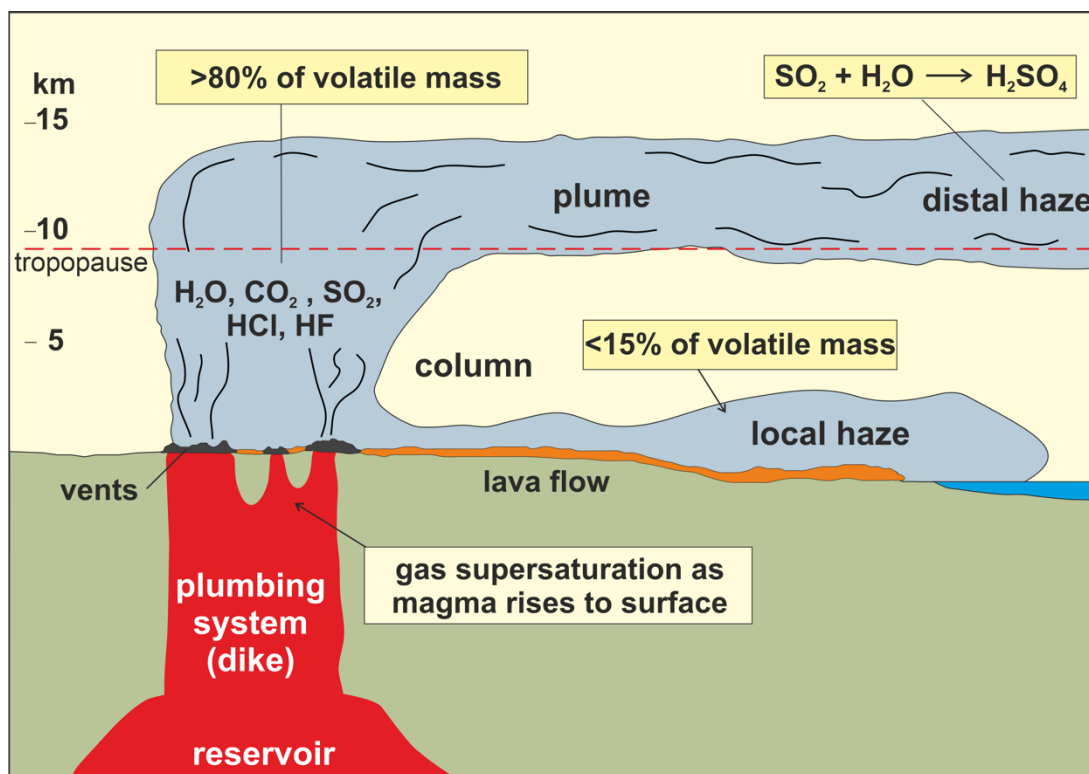


Figure 2. 9: Sulfur pollution from the Laki 1783–84 CE eruption. Schematic courtesy of Dr. Thorvaldur Thordarson of the 1783–84 CE Laki FL eruption and its associated volcanic plume. The image highlights coeval tropospheric injection of volatiles, creating a S and halogen rich localised vog, as well as the injection of volatiles into the stratosphere. In both cases, S gases undergo a conversion as the plume matures to S aerosols. In the dry stratospheric environment, the S is present as a longer-lived distal haze that had a hemisphere-wide impact.

Large and sustained injections of volcanic S can induce significant environmental degradation and health hazards through a tropospheric sulfur and halogen rich vog (Figures 2. 3 and 2. 9), acid rain (Thordarson and Self, 1993; Thordarson et al., 1996; Robock, 2000; Oman et al., 2006a; 2006b) and climatic perturbations that can last for 1–3 years through upper troposphere-lower stratospheric sulfur aerosol loading (Thordarson and Self, 1993; Thordarson et al., 1996; Robock, 2000; Robock and Oppenheimer, 2003; Thordarson et al., 2001; Thordarson and Self, 2001, 2003; Thordarson et al., 2003b; Self et al., 2005; Schmidt et al., 2010; Oppenheimer et al., 2011; Schmidt et al., 2011; Wallace and Edmonds, 2011; Black et al., 2014a, 2014b; Black and Manga, 2017). Climatic perturbations are manifest as a three-fold effect: (i) surface cooling; (ii) moderation of the planetary airflow via changing the equator to pole temperature gradient; and (iii) low-level volcanic pollution (Thordarson and Self, 2003; Oman et al., 2006a, 2006b; Thordarson et al., 2009).

Of particular interest are basaltic magmas, which produce a volatile load about an order of magnitude higher than explosive silicic eruptions (Devine et al., 1984).

Explosive basaltic eruptions are easily capable of stratospheric injection levels, e.g., Fontana 60 ka, 122 BC Etna, Tarawera 1886 CE, Krakatoa 1883 CE (basaltic andesite), Katla 1918 CE and Grímsvötn 2011 CE but are generally short-lived compared to their effusive counterparts. However, large-volume basaltic FL eruptions produce convective volcanic plume heights capable of stratospheric volatile loading. This is coupled with their higher magnitude, that requires longer periods of eruptive activity and a higher MER for the more explosive phases which reach the stratosphere. Eruptions of this magnitude can therefore inject volatiles into the atmosphere for prolonged periods of time, and into the stratosphere through repeated high-intensity explosive fissure opening phases, e.g., Eldgjá 936 CE and Laki 1783–84 CE (Thordarson and Self, 1993; Woods, 1993; Thordarson et al., 1996; Moreland et al., 2019). The larger end-members of this style of eruption are Flood Basalts (FB; $>100 \text{ km}^3$), hundreds to thousands of these events result in the formation of continental flood basalt provinces (CFBs) or large igneous provinces (LIPs), which have a postulated association with the mass extinction events that punctuate Earth's geological record (Courtillet et al., 1999; Rampino and Stothers, 1988) although more recent atmospheric modelling studies have cast doubt over these earlier claims addressing the limiting time-scales of stratospheric volatile loading during these events (Schmidt et al., 2015). Consequently, modelling the S dispersal from volcanic plumes within the atmosphere and calculating the total atmospheric S burdens for previous eruptions, including FLs (both historical and through geological time), to improve hazard and environmental assessments has been a key research focus over recent decades (Thordarson et al., 1996; Thordarson and Self, 2001; Thordarson et al., 2001, 2003b; Self et al., 2005, 2006, 2008; Oppenheimer et al., 2011; Schmidt et al., 2011; Loughlin et al., 2012; Schmidt and Robock, 2015; Ilyinskaya et al., 2017).

Nevertheless, the total atmospheric S budget of ancient LIPs, comprising of hundreds to thousands of individual FB eruptions which build the province, remains notoriously difficult to reconstruct in absolute terms. This is due to the large uncertainties associated with the total duration of LIP construction, which can occur over several million years, although their peak production period generally appears to be shorter, i.e., 0.5–1 Ma (Hofmann et al., 1997; Courtillet and Renne, 2003; Chenet et al., 2007, 2008). However, the time between individual eruptions is on the

order of hundreds–thousands of years (Thordarson and Self, 1996) therefore the frequency of these eruptions is too low to create a cumulative climatic impact from the atmospheric volatile loading (volcanic forcing) during the total LIP construction. Instead, atmospheric perturbations occur only in response to individual eruptions or a series of closely spaced events. For example, in the case of a Roza like event, part of the Columbian River Basalt Group (CRBG) province, which is thought to have been active for 10–20 years, the atmospheric effects of the sulfur loading can only last a maximum of 2–3 years beyond the duration of the individual event (Thordarson et al., 1996, 1998). On geological time-scales the immense volume of lava emplaced via FB eruptions occurs over relatively limited periods of time, indicating that MER, and therefore the volatile flux, from these individual eruptions during their peak eruptive intensity were fairly high (Rampino and Stothers, 1988; Stothers and Rampino, 1990; Self et al., 1996; Courtillot et al., 1999; Wignall, 2001; Jolley and Widdowson, 2005; White and Saunders, 2005; Self et al., 2005, 2006, 2008; Chenet et al., 2009; Oppenheimer et al., 2011 and references therein; Black et al., 2012, 2014a, 2014b; Schmidt and Robock, 2015). Each FB event is, in turn, made up of discrete pulses of eruptive activity, which start explosively, reaching sub-Plinian–Plinian intensities which can inject volatiles into the stratosphere, and subsequently waning into effusive activity that last years to decades (Brown et al., 2014; Thordarson and Self, 1998). Hence the environmental and climatic impact associated with LIPs is down to individual eruptions, but it is not straightforward to obtain information on the size and duration of these events, although some of them most likely lasted for decades (Thordarson and Self 1998; Schmidt et al., 2015). Each of these units within the LIP formation is separated by periods of hiatus in eruptive activity, sometimes reflected in the presence of palaeosols; again, like other timescales in these events, these hiatus periods are of unknown length and may be localised with activity occurring elsewhere in the system (Self et al., 1996; Widdowson, 1996; Widdowson and Cox, 1996; Widdowson et al., 1997; Chenet et al., 2009; Sayyed, 2014). The pattern and duration of these phases of explosive activity, capable of stratospheric injection, throughout a FB eruption, is also relatively unconstrained; with only two examples exist of well-studied explosive tephra fall phases, both of which are part of the Columbia River Basalt Group province (CRBG) FB event: The Roza Member and the Grande Ronde Member phases (Swanson et al., 1975; Barry et al., 2010; Brown et al., 2014, 2015). Some

studies have noted a potentially more volatile and particulate rich plume from the earliest explosive eruptive phase as a result of volatile saturation (Vye-Brown et al., 2013; Brown et al., 2014). Established techniques which rely on comparing S in eruptive glasses with a pre-eruptive S content from melt inclusions, e.g. the so-called petrological method (Devine et al., 1984; Devine and Island, 1984), which is commonly used to establish the S-budget for volcanic eruptions, is not always applicable, for example to aphyric magmas or for phyric magmas where melt inclusions have undergone post entrapment modifications or alteration. This is the case for many ancient FB eruptions; therefore, empirical or proxy methods are applied using whole rock FeO_t contents (Óskarsson et al., 1984; Thordarson and Self, 1996; Thordarson et al 2003; Self et al., 2005; Blake et al., 2010; Black et al., 2012, 2014a, 2014b) to back-calculate pre-eruptive S contents before applying the petrological method to erupted glass S values.

Regardless of magnitude, basaltic fissure eruptions maintain similar eruptive styles, nature, and eruptive products. It is, therefore, reasonable to improve our understanding of the climatic and environmental impacts of FB events using smaller scale FL eruptions, which serve as well-documented, modern analogues to their larger counterparts.

2. 5 Volatiles in Basaltic Magmas

The partitioning of sulfur between magmatic fluids and melts controls the volatile budget of magmas and sulfur load released on volcanic degassing (Webster and Botcharnikov, 2011). Due to the complex behaviour of S in melts, modelling of this S partitioning between vapour-melt phases must include the effects of T, P, melt composition, and oxygen and S fugacities (Scaillet and Pichavant, 2005; Moretti and Baker, 2008; Wallace and Edmonds, 2011; Barnes, 2012). The redox of the silicate melts in question, prior to eruption, is particularly important, as oxygen fugacity ($f\text{O}_2$) has a strong influence on their total S budget and the distribution of S between the melt and liquid/gas phase by controlling the amount of dissolved S that a melt can carry at depth before the melt becomes S saturated (Wallace and Carmichael, 1992). In reduced conditions, the melt contains less dissolved S, as the S^{2-} ions present have a lower solubility compared to S^{6+} , which is present in oxidising

conditions, so the S present is driven into a gas or immiscible liquid phase; in intermediate conditions, both S^{2-} and S^{6+} are present. At saturation, a liquid or vapour phase, rich in sulfur, co-exists with the silicate melt, e.g., immiscible sulfide or sulfate liquid. Several studies have also noted that oxidised melts contain some of their S budget in an S excess gas/sulfate fluid phase, which is not recorded by pre-eruptive S content and therefore not included in eruptive S outgassing calculations (Oppenheimer et al., 2011). Upon decompression, experimental data demonstrates that S strongly partitions into the gas phase (Edmonds and Mather, 2017), which is especially the case for reduced conditions e.g., MORB where S^{2-} becomes even less soluble in the melt phase. Sulfur solubility and redox state are key parameters for modelling volcanic forecasting, but the magma ascent rate, and whether the system is experiencing open or closed degassing (is the exsolved vapour retained entirely until eruption or partially lost) must also be considered (Metrich and Mandeville, 2010; Wallace and Edmonds, 2011). Rapid ascent rates inhibit redox evolution for vapour-melt-fluid systems as they cannot equilibrate on these timescales, instead the melt is driven to S saturation. Melts at depth can be driven to S saturation in response to crystallisation, this saturated state is retained until the melt reaches shallower pressures; causing S degassing to be controlled by the existing vapour-melt partitioning (Wallace and Edmonds, 2011). This in turn makes the redox state of flood basalts, both prior to and upon eruption, very important for environmental assessments as it can increase their atmospheric S yield above the suggested values from petrological methods (Oppenheimer et al., 2011).

2. 6 Stable isotopes as tracers of volcanic processes

The advent of high resolution and high precision mass spectrometry (i.e., TIMS or ICP-MS-MC) has enabled the rapid growth of an emerging field in the application of novel, non-traditional, stable isotope systems that can fractionate in response to a number of processes leaving a distinct geochemical and cosmochemical fingerprint. These stable isotopes can be used to trace the magmatic or surface processes involved in both the formation, differentiation and evolution of Earth and other planets in our Solar System.

As this field of study continues to develop, it provides new perspectives across a broad spectrum of geological processes by constraining the elemental budget estimates for specific reservoirs, how isotopes fractionate as mass moves from one to the other, as well as the conditions which drive fractionation, e.g., oxygen fugacity. The cause of variations of some of these novel-stable isotopes in terrestrial igneous rocks is limited by our current understanding of the mass-dependant fractionation mechanisms of these systems at magmatic temperatures (Wang et al., 2017). Not only is it important to understand the effects of magmatic processes for terrestrial samples, with respect to establishing robust bulk silicate Earth (BSE) values for the novel stable isotope systems; it is also important for samples from other planetary bodies or meteorites, as they will all have potentially undergone some isotopic fractionation during magmatic processes (Chen et al., 2013; Chen, 2014).

2. 6. 1 Copper and Zinc stable isotopes as tracers of magmatic differentiation and volatile loss

Of particular interest to this study are the stable isotopes of the chalcophile transition metals, copper (Cu) and zinc (Zn) which are moderately volatile (Herzog et al., 2009; Chen et al., 2013) at atmospheric pressures. The natural abundances, in terrestrial samples, of the different isotopes for Cu and Zn are as follows:

Copper has two stable isotopes ^{63}Cu (69.17 %) and ^{65}Cu (30.83 %). Zinc has five stable isotopes ^{64}Zn (48.6%), ^{66}Zn (27.9 %), ^{67}Zn (4.1%), ^{68}Zn (18.8%), ^{70}Zn (0.6%).

The expected response for Zn and Cu isotopes is dictated by the dominant valence state, i.e., speciation, of S present in the melt in question i.e., as S^{2-} or S^{6+} . In turn, S speciation is controlled by temperature, pressure, water content and oxygen fugacity ($\text{Fe}_{2+}/\text{Fe}_{3+}$, SO_2/S_2 redox buffers) (Sakai et al., 1982; Ueda and Sakai, 1984; Burgisser and Scaillet, 2007; Marini et al., 2011). S is an important component within basaltic systems that exhibits volatile behaviour; S occurs as a dissolved volatile species, as a segregated vapour phase, as well as within minerals and immiscible melts (De Moor et al., 2013). The transition between sulfide and sulfate valence states, i.e., S^{2-} or S^{6+} , occurs over a narrow range of oxygen fugacity ($f\text{O}_2$) values around the Fayalite-Magnetite-Quartz (FMQ) interval between oxidised and

reduced conditions. Therefore, the oxygen fugacity of the magma in question directly controls the amount of sulfur present in solution in the melt at sulfur saturation; in reduced conditions S saturates at 1400 ppm and starts to exsolve as immiscible sulfides or a reduced S species vapour phase. Whereas, in an oxidised silicate melt, S saturates at much higher concentrations (7500 ppm), forming sulfate fluid or vapour phases (Wallace and Carmichael, 1994; Jugo, 2005b).

As sulfur segregates into separate gas or fluid/sulfide melt phases, which develop as the melt is driven to S saturation during ascent driven decompression, a corresponding mass-dependant fractionation of the chalcophile isotopes Cu and Zn is expected due to their affinity with S and their volatile nature. In basaltic magmas Cu has a high partition coefficient between sulfides and the silicate matrix (Peach et al., 1990; Luguet et al., 2003; Li et al., 2009; Collins et al., 2012), and it preferentially partitions into immiscible sulfide phases as a major element component, as the basaltic melt evolves via fractionation or crustal assimilation in the shallow crust (Sun et al., 2004; Halter et al., 2005; Zajacz and Halter, 2009; Collins et al., 2012). Copper has a high partition coefficient for chalcopyrite, which is often identified as a minor phase in Icelandic FL basaltic eruptive products as a quenched immiscible melt resulting from sulfur saturation of the magmas prior to eruption. Whereas Zn preferentially partitions, as a trace element component, into olivine, with a partition coefficient of 1 (Deer et al., 2013). Icelandic FL lavas and associated tephra have a consistently low phenocryst content (generally <10%), within which olivine is a common, but subordinate, phenocryst or crystal mush glomerocryst phase. Therefore, for a small increase in the percentage of immiscible chalcopyrite present in a FL lava flow or tephra the bulk elemental Cu concentration increases notably. Whereas, unless the olivine content of a lava flow or tephra increases significantly, which cannot occur with the addition of a small percentage increase of crystal mush glomerocrysts (xenocrysts) or a density stratified magma storage zone which creates an increase in phenocrysts (to 20%) throughout the eruption, this is not the case for Zn.

It is hypothesised that as a melt migrates from a crustal storage reservoir to a shallow conduit setting prior to an eruption, the chalcophile stable isotope volatiles exsolve from the melt in response to decompression. If the melt in question is oxidised, i.e.,

higher oxygen fugacity, light Zn isotope will preferentially partition into the oxidised S rich gas phase or sulfate fluid phase present. Therefore, as a magma fragments and degasses SO_2 during an eruption, the volatile loss of light Zn could also take place, leaving the residual melt with a heavy $\delta^{66}\text{Zn}$ signature (Luck et al., 2005; John et al., 2008; Herzog et al., 2009; Chen et al., 2013; Chen, 2014). In a reduced setting where S is lost as H_2S in a volatile phase, the heavy Cu isotope will partition into a Cu chloride complex (e.g. Cu_3Cl_3) vapour or fluid phase (Candela and Holland, 1984; Williams et al., 1995; Liu et al., 2002; Hack and Mavrogenes, 2006; Simon et al., 2006) leaving the residual melt depleted in the heavy Cu isotope and thus has an isotopically lighter $\delta^{65}\text{Cu}$ signature (Halter et al., 2005; Markl et al., 2006; Moynier et al., 2006; Seo et al., 2007; Li et al., 2009; Savage et al., 2015). In a reduced setting, S can also segregate into FeS_2 rich immiscible sulfide melt, lost as a particulate phase, preferentially incorporating the light Cu isotope, leaving the residual melt with an isotopically heavier $\delta^{65}\text{Cu}$ signature (Figure 2. 10, also see Figure 8. 1 in Chapter 8).

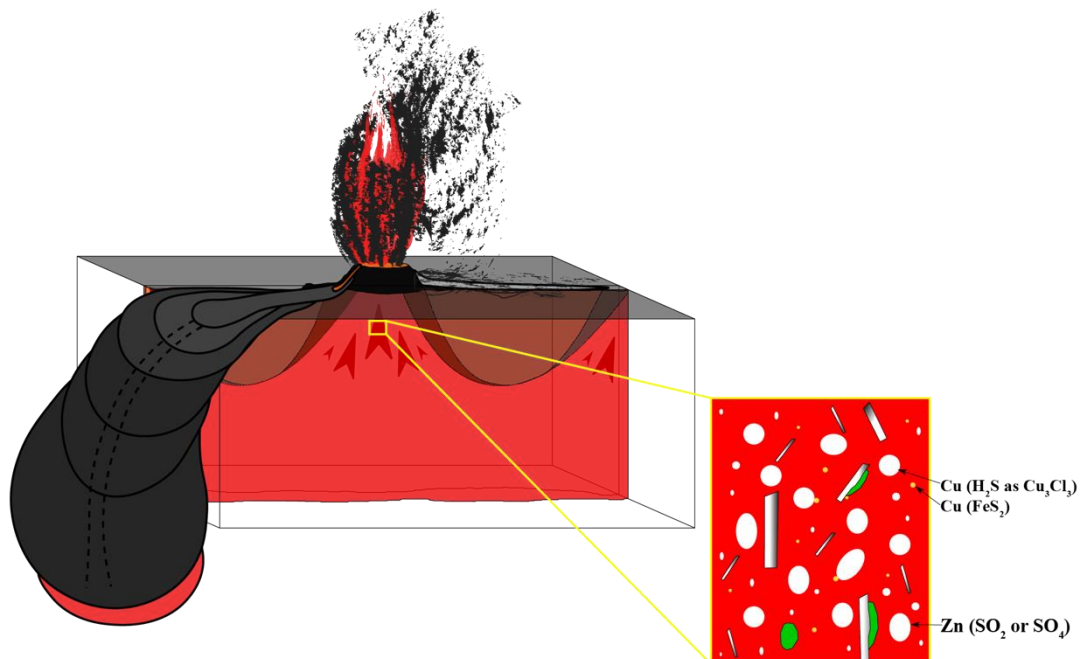


Figure 2. 10: Zn and Cu partitioning behaviour during eruptions. Schematic of a basaltic fissure eruption, and its eruptive products, with its shallow conduit system in cross-section. The inset displays a package of melt rising through the shallow conduit: melt is shown in red, bubbles in white, immiscible sulfide phases in yellow, plagioclase crystals in greyscale and olivine or pyroxene in green. This inset also highlights the partitioning behaviour of Cu and Zn during ascent, depending on the redox conditions of the system and which S species are present, which in turn results in the mass-dependant fractionation of these two stable isotope systems.

The majority of previous novel-stable isotope studies focussed on fingerprinting the Cu and Zn isotopic signature of BSE and tracing the effects of magmatic differentiation, hydrothermal and ore-forming processes on these stable isotope systems at both a bulk sample and mineral separate level for geological samples as well as evaporation and condensation processes during planetary and lunar processes (Herzog et al., 2009; Telus et al., 2012; Chen et al., 2013; Chen, 2014; Liu et al., 2015; Savage et al., 2015; Doucet et al., 2016; Liu et al., 2016; Mahan et al., 2017; Sossi et al., 2015; 2018; Wang et al., 2017). Whilst at a planetary formation and differentiation scale, the volatile behaviour of Zn and Cu has been well demonstrated (Moynier et al., 2006, 2010; Paniello, 2012; Day and Moynier, 2014), with volatile loss or evaporation identified as the only process which can induce Zn isotope fractionation, with a magnitude of 1‰ for $\delta^{66}\text{Zn}$. How residual eruptive products record Cu and Zn mass-dependant fractionation during the shallow crustal history of a melt and during an eruption is currently poorly constrained, this remains fairly speculative despite potentially providing important constraints on the mechanisms of gas release and speciation of volatiles present before atmospheric disassociation. In this regard, the relative enrichment and depletion of heavy or light Cu and Zn isotopes in residual eruptive products could potentially indicate the speciation of S lofted into the atmosphere as a gas or particulate phase upon eruption.

The current limitations of the existing data sets are at least in part due to sampling strategy, with each previous study consisting of either: (1) low sample number focusing on characterising several complementary aspects of the volcanic system from a broad-scale perspective, and not one eruption in particular (Wang et al., 2019); or (2) samples analysed in isolation, e.g. Pele's hairs $\delta^{66}\text{Zn}$ fingerprint and compared with other planetary body samples (Herzog et al., 2009), rather than products from the same eruption; and (3) comparing of samples from unrelated parts of the lava field that may have been emplaced by very different eruptive vent activity. The latter is particularly important, as lava flow fields are often compound, with multiple vents emplacing separate lava flow branches simultaneously or discrete vents emplacing lava flows during distinct stages of the eruption associated with changes in eruption style and therefore degassing. Large scale late-stage lava flow resurfacing events have been observed in recent eruptions, e.g., Holuhraun 2014–15 CE (Pedersen et al., 2017), which complicates retrospective sampling as the

association between active channel migration, eruptive style as the association of the resultant lava surface, and the emplacement dynamics is unclear. Therefore, unless the eruptive style and lava emplacement history are well understood either through on-site documentation or thorough detailed volcanological studies of the eruption products, discerning sampling sites that can be directly associated with a certain stage of the eruption or with each other is extremely difficult and directly impacts the nature of the $\delta^{65}\text{Cu}$ and $\delta^{66}\text{Zn}$ isotope variations observed.

Chen et al. (2013) found no variation of $\delta^{66}\text{Zn}$ values when comparing the S (ppm), Zn (ppm) and SiO_2 (wt %) concentrations in a suite of eruptive products from Hekla, a stratovolcano in Iceland, and its associated fissure system. This study highlights the aforementioned sampling issues well, as these eruptive products span over 6000 years of Hekla's eruptive history with only 1–2 samples from each eruption; these were initially collected for a different study (Savage et al., 2011) to characterise the SiO_2 variations within the volcanic system and the associated fractionation of Si isotopes. The melts in question are geochemically unrelated and have undergone different degrees of magmatic differentiation, mixing and mingling with other magmas, and different initial S concentrations and redox conditions, as well as having experienced different eruptive/emplacement dynamics and therefore different degassing extents. As the sampling neither spans an eruptive time-series from a single eruption at Hekla, nor a suite of eruptive products from one eruption, e.g., tephra and differing lava morphologies associated with different transport systems, the same set is unsuitable for the analysis of degassing induced isotope fractionation. The culmination of which is a data set that displays a high degree of scatter and no convincing volatile loss trends; however, the variations in the data set cannot be simply explained by modelling of fractional crystallisation processes (Chen et al., 2013).

The same study did, however, find a strong covariance between Zn content and $\delta^{66}\text{Zn}$ in Kīlauea Iki 1959 CE tephra and lava lake core samples due to the affinity of this element in olivine (Deer et al., 2013), a mineral which Hawaiian lavas generally have in abundance. The olivine content, and therefore Zn (ppm) concentration, increased with depth in the lava lake due to density stratification of the lava lake during and post-eruption.

This thesis aims to adopt an improved sampling strategy to overcome these limitations, isolating the effect of shallow conduit disequilibrium processes and emplacement dynamics, to understand behaviour of the novel-stable isotopes Cu and Zn in response to degassing. This will be done by focusing on the eruptive products from two historical, well-documented and geochemically homogeneous, OIB FL eruptions: Laki 1783–84 CE and Holuhraun 2014–15 CE, which fed compound lava flow fields with dynamic transport systems as well as episodic periods of tephra fall during their more explosive phases. This will add to the handful of studies that currently exist to help identify whether and under which circumstances Zn and Cu are useful tracers of volatile loss in magmatic systems and their eruptive products (Liu et al., 2016; Wang et al., 2017). Samples from young basaltic eruptions provide an insight into how these isotopes behave as a magma evolves without the complications of examining older exhumed volcanic rocks that have been subject to secondary geological processes such as: hydrothermal alteration, weathering, or metamorphism; which overprint this initial imparted magmatic isotope signature as well as elemental concentrations. This is particularly important for Zn isotopes, which are readily overprinted by surface weathering.

2.7 References

- Andronico, D., Branca, S., Calvari, S., Burton, M., Caltabiano, T., Corsaro, R. A., Carlo, P. D., Garfi, G., Lodato, L., Miraglia, L., Murè, F., Neri, M., Pecora, E., Pompilio, M., Salerno, G. and Spampinato, L. (2005), A multi-disciplinary study of the 2002–03 Etna eruption: Insights for a complex plumbing system, *Bulletin of Volcanology*, 67, 314– 330, doi:10.1007/s00445-004-0372-8.
- Andronico, D., Scollo, S., Caruso, S. and Cristaldi, A. (2008). “The 2002-03 Etna Explosive Activity: Tephra Dispersal and Features of the Deposits.” *Journal of Geophysical Research: Solid Earth* 113(4).
- Andronico, D., Scollo, S., Cristaldi, A. and Lo Castro, M. D. (2014). Representivity of incompletely sampled fall deposits in estimating eruption source parameters: a test using the 12–13 January 2011 lava fountain deposit from Mt. Etna volcano, Italy. *Bulletin of Volcanology*, 76, Article number: 861. doi:10.1007/s00445-014-0861-3
- Barnes, S. (2012) Sulfur in Magmas and Melts: Its Importance for Natural and Technical Processes, Economic Geology. Behrens, H. and Webster, J. D. (Editors). In: Sulfur in magmas and melts. *Reviews in Mineralogy and Geochemistry*, 73, doi:10.2113/econgeo.107.4.737.
- Black, B. A., Elkins-Tanton, L. T., Rowe, M. C., and Ingrid Peate, I. U. (2012). Magnitude and Consequences of Volatile Release from the Siberian Traps. *Earth and Planetary Science Letters*, (317–318), pp. 363–373.
- Black, B. A., Lamarque, J. F., Shields, C. A., Elkins-Tanton, L. T., and Kiehl, J. T.

- (2014a). Acid Rain and Ozone Depletion from Pulsed Siberian Traps Magmatism. *Geology*. 42, (1) pp. 67–70.
- Black, B. A., Hauri, E. H., Elkins-Tanton, L. T. and Brown, S. M. (2014b). Sulfur isotopic evidence for sources of volatiles in Siberian Traps magmas. *Earth and Planet Science Letters*. 394, pp. 58-69
- Black, B.A., and Manga. M. (2017). Volatiles and the tempo of flood basalt magmatism. *Earth and Planetary Science Letters* (458) pp. 130-140; doi:10.1016/j.epsl.2016.09.035.
- Blake, S., Self, S., Sharma, K., and Sephton, S. (2010). Sulfur Release from the Columbia River Basalts and Other Flood Lava Eruptions Constrained by a Model of Sulfide Saturation. *Earth and Planetary Science Letters*. 299 (3–4). Pp. 328–38.
- Bonaccorso, A., Calvari, S., Linde, A. and Sacks, S. (2014). Eruptive processes leading to the most explosive lava fountain at Etna volcano: The 23 November 2013 episode. *Geophysical Research Letters*. 41, (14), pp. 4912-4919
- Bonadonna, C., and Costa, A. (2012). Estimating the volume of tephra deposits: A new simple strategy. *Geology*, 40, pp. 415–418. doi:10.1130/G32769.1
- Bonny, E., Thordarson, T., Wright, R., Höskuldsson, A., and Jónsdóttir, I. (2018). The Volume of Lava Erupted During the 2014 to 2015 Eruption at Holuhraun, Iceland: A Comparison Between Satellite- and Ground-Based Measurements. *Journal of Geophysical Research: Solid Earth*, 123, (7) pp. 5412–5426. doi.org/10.1029/2017JB015008
- Burgisser, A., and Scaillet, B. (2007). Redox evolution of a degassing magma rising to the surface. *Nature*, 445 (7124), pp. 194–197. doi.org/10.1038/nature05509
- Brown, R. J., Blake, S., Thordarson, T., and Self, S. (2014). Pyroclastic edifices record vigorous lava fountains during the emplacement of a flood basalt flow field, Roza Member, Columbia River Basalt Province, USA. *Bulletin of the Geological Society of America*, 126 (7–8), pp. 875–891. doi:10.1130/B30857.1
- Brown, R. J., Thordarson, T., Self, S. and Blake, S. (2015). Disruption of tephra fall deposits caused by lava flows during basaltic eruptions. *Bulletin of volcanology*. 77 (10). pp. 90. https://doi.org/10.1007/s00445-015-0974-3
- Calvari, S., Cannavò, F., Bonaccorso, A., Spampinato, L., and Pellegrino, A. G. (2018). Paroxysmal Explosions, Lava Fountains and Ash Plumes at Etna Volcano: Eruptive Processes and Hazard Implications. *Frontiers in Earth Science*. 6. doi:10.3389/feart.2018.00107
- Candela, P. A. and Holland, H. D. (1984). The partitioning of copper and molybdenum between silicate melts and aqueous fluids. *Geochimica et Cosmochimica Acta*. 48, pp. 373-380
- Carbone, D., Zuccarello, L., Messina, A., Scollo, S. and Rymer, H. (2016). Balancing bulk gas accumulation and gas output before and during lava fountaining episodes at Mt. Etna. *Nature Scientific Reports*. 5. 18049. doi:10.1038/srep18049
- Carey, R. J., Houghton, B. F., Sable, J. E., & Wilson, C. J. N. (2007). Contrasting grain size and componentry in complex proximal deposits of the 1886 Tarawera basaltic Plinian eruption. *Bulletin of Volcanology*. 69 (8), pp. 903–926. doi: 10.1007/s00445-007-0117-6
- Carroll, M. R. and Webster, J. D. (1994). Solubilities of sulfur, noble gases, nitrogen, chlorine, and fluorine in magmas. Chapter 7, In: Carroll, M. R. and Holloway, J. R. (1994). Volatiles in magmas. *Mineralogical Society of America Reviews in Mineralogy*. 30. pp. 231-279.

- Cas, R. A. F. and Simmons, J. M. (2018). Why Deep-Water Eruptions Are So Different From Subaerial Eruptions. *Frontiers in Earth Science*. 6, 198. doi:10.3389/feart.2018.00198
- Cashman, Katharine V. and Mangan, Margaret T.. "Chapter 11b. Physical aspects of magmatic degassing II. Constraints on vesiculation processes from textural studies of eruptive products". In: Volatiles in Magmas, edited by Michael R. Carroll and John R. Holloway, Berlin, Boston: De Gruyter, 2018, pp. 447-478. doi:10.1515/9781501509674-018
- Cashman, K. V. and Scheu, B. (2015). Chapter 15 – Magmatic Fragmentation. In: The Encyclopedia of Volcanoes (Second Edition). Sigurdsson, H. (Editor). pp. 459-471. doi:10.1016/B978-0-12-385938-9.00025-0
- Castro, J. M., Burgisser, A., Schipper, C. I. and Mancini, S. (2012). Mechanisms of bubble coalescence in silicic magmas. *Bulletin of Volcanology*. 74, pp. 2339–2352
- Chen, H. (2014). Unpublished PhD thesis. Zinc and Copper Isotopic Fractionation during Planetary Differentiation. Washington University in St. Louis.
- Chen, H., Savage, P. S., Teng, F. Z., Helz, R. T., and Moynier, F. (2013). Zinc isotope fractionation during magmatic differentiation and the isotopic composition of the bulk Earth. *Earth and Planetary Science Letters*, 369–370, pp.34–42. doi:10.1016/j.epsl.2013.02.037
- Chenet, A. L., Quidelleur, X., Fluteau, F., Courtillot, V., & Bajpai, S. (2007). 40K-40Ar dating of the Main Deccan large igneous province: Further evidence of KTB age and short duration. *Earth and Planetary Science Letters*, 263 (1–2), 1–15. doi:10.1016/j.epsl.2007.07.011
- Chenet, A. L., Fluteau, F., Courtillot, V., Gérard, M., & Subbarao, K. V. (2008). Determination of rapid Deccan eruptions across the Cretaceous-Tertiary boundary using paleomagnetic secular variation: Results from a 1200-m-thick section in the Mahabaleshwar escarpment. *Journal of Geophysical Research: Solid Earth*, 113(4). doi: 10.1029/2006JB004635
- Chenet, A. L., Courtillot, V., Fluteau, F., Gérard, M., Quidelleur, X., Khadri, S. F. R., Subbarao, K. V., and Thordarson, T. (2009). Determination of rapid Deccan eruptions across the Cretaceous-Tertiary boundary using paleomagnetic secular variation: 2. Constraints from analysis of eight new sections and synthesis for a 3500-m-thick composite section. *Journal of Geophysical Research: Solid Earth*, 114 (6). doi:10.1029/2008JB005644
- Collins, S. J., MacLennan, J., Pyle, D. M., Barnes, S. J. and Upton, B. G. J. (2012). Two phases of sulphide saturation in Réunion magmas: Evidence from cumulates. *Earth and Planetary Science Letters*. 337–338, pp. 104-113
- Costantini, L., Houghton, B. F., and Bonadonna, C. (2010). Constraints on eruption dynamics of basaltic explosive activity derived from chemical and microtextural study: The example of the Fontana Lapilli Plinian eruption, Nicaragua. *Journal of Volcanology and Geothermal Research*, 189(3–4), 207–224. https://doi.org/10.1016/j.jvolgeores.2009.11.008
- Courtillot, V., Jaupart, C., Manighetti, I., Tapponnier, P. and Besse, J. (1999). On causal links between flood basalts and continental breakup. *Earth and Planetary Science Letters*, 166 (3–4), pp. 177–195. doi:10.1016/S0012-821X(98)00282-9
- Courtillot, V. E. and Renne, P. R. (2003). On the ages of flood basalt events. *Comptes Rendus Geoscience*. 335, (1), pp. 113–140. doi:10.1016/S1631-0713(03)00006-3
- Crisp, J. A., (1984). Rates of magma emplacement and volcanic output. *Journal of*

- Volcanology and Geothermal Research*, 110 (3-4), pp. 265-280.
- Day, J. M. D. and Moynier, F. (2014). Evaporative fractionation of volatile stable isotopes and their bearing on the origin of the Moon. *Philosophical Transactions of the Royal Society*. 371, (2024), A.3722013025920130259 doi:10.1098/rsta.2013.0259
- Deer, W. A., Howie, R. A. and Zussman, J. (2013). An introduction to rock forming minerals. Mineralogical Society of Great Britain and Ireland. doi:10.1180/DHZ
- Devine, J.D., Sigurdsson, H., Davis, A. N. and Self, S. (1984) Estimates of sulfur and chlorine yield to the atmosphere from volcanic eruptions and potential climatic effects. *Journal of Geophysical Research*. 89. pp. 6309–6325
- Devine, D., and Island, R. (1984). Estimates of Sulfur and Chlorine yield to the atmosphere from volcanic eruptions and potential climatic effects. *Journal of Geophysical Research*, 89, 6309–6325.
- de Moor, J. M., Fischer, T. P., Sharp, Z. D., King, P. L., Wilke, M., Botcharnikov, R. E., Cottrell, E., Zelenski, M., Marty, B., Klimm, K., Rivard, C., Ayalew, D., Ramirez, C. and Kelley, K. A. (2013). Sulfur degassing at Erta Ale (Ethiopia) and Masaya (Nicaragua) volcanoes: Implications for degassing processes and oxygen fugacities of basaltic systems. *Geochemistry, Geophysics and Geosystems*. 14, (10). pp. 4076-4108.
- deVries, A. J. (1972). Morphology, coalescence, and size distribution of foam bubbles. In: Lemlich R (Editors) Adsorptive Bubble Separation Techniques. Academic Press, New York, pp. 7-31
- Dixon, J. E. (1997). Degassing of alkalic basalts. *American Mineralogist*, 82, pp. 368-378.
- Dixon, J. E. Stolper, E. M. and Holloway, J. R. (1995). An experimental study of H₂O and carbon dioxide solubilities in mid-ocean ridge basaltic liquids. Part I: Calibration and solubility results. *Journal of Petrology*, 36, pp. 1607–1631.
- Dixon, J.E. and Stolper, E.M. (1995) An experimental study of H₂O and carbon dioxide solubilities in mid-ocean ridge basaltic liquids. Part II: Application to degassing of basaltic liquids. *Journal of Petrology*, 36, pp. 1633–1646.
- Doucet, L. S., Mattielli, N., Ionov, D. A., Debouge, W., and Golovin, A. V. (2016). Zn isotopic heterogeneity in the mantle: A melting control? *Earth and Planetary Science Letters*, 451, pp. 232–240. doi:10.1016/j.epsl.2016.06.040
- Edmonds, M., and Mather, T. A. (2017). Volcanic sulfides and outgassing. *Elements*, 13 (2), pp.105–110. doi:10.2113/gselements.13.2.105
- Giordano, G. and De Astis, G. (2021). The summer 2019 basaltic Vulcanian eruptions (paroxysms) of Stromboli. *Bulletin of Volcanology*, 83, 1. doi:10.1007/s00445-020-01423-2
- Gonnermann, H. M., and Manga, M. (2007). The fluid mechanics inside a volcano. *Annual Review of Fluid Mechanics*, 39, pp. 321–356. doi:10.1146/annurev.fluid.39.050905.110207
- Gonnermann, H. M. and Manga, M. (2003). Explosive volcanism may not be an inevitable consequence of magma fragmentation. *Nature*, 426, pp. 432–435
- Gonnermann, H. M. and Manga, M. (2013). Dynamics of magma ascent in the volcanic conduit. In: Modeling Volcanic Processes: The Physics and Mathematics of Volcanism. Fagents, S. A., Gregg, T. K. P. and Lopes. R. M. C. (editors)
- Gonnermann, H. M. (2015). Magmatic Fragmentation. *Annual Reviews in Earth and Planetary Science*. 43. pp. 431-458. doi:10.1146/annurev-earth-060614-105206
- Gardner, J. E., Thomas, R. M. E., Jaupart, C., and Tait, S. (1996). Fragmentation of

- magma during Plinian volcanic eruptions. *Bulletin of Volcanology*, 58(2–3), pp. 144–162. doi:10.1007/s004450050132
- Gardner, J.E., Hilton, M., and Carroll, M.R. (1999). Experimental constraints on degassing of magma: Isothermal bubble growth during continuous decompression from high pressure. *Earth and Planetary Science Letters* 168, pp. 201–218. doi:10.1016/S0012-821X(99)00051-5
- Gardner, J.E., and Denis, M.-H. (2004). Heterogeneous bubble nucleation on Fe-Ti oxide crystals in high-silica rhyolitic melts. *Geochimica et Cosmochimica Acta*, 68, pp. 3587–3597. doi:10.1016/j.gca.2004.02.021
- Gaudin, D., Moroni, M., Taddeucci, J., Scarlato, P., and Shindler, L. (2014a), Pyroclast tracking velocimetry: A particle Tracking Velocimetry-based tool for the study of Strombolian explosive eruptions, *Journal Geophysics Research: Solid Earth*, 119, pp. 5369– 5383, doi:10.1002/2014JB011095.
- Gaudin, D., Taddeucci, J., Scarlato, P., Moroni, M., Freda, C., Gaeta, M. and Palladino, D. M. (2014b), Pyroclast Tracking Velocimetry illuminates bomb ejection and explosion dynamics at Stromboli (Italy) and Yasur (Vanuatu) volcanoes, *Journal Geophysics Research: Solid Earth*, 119, pp. 5384– 5397, doi:10.1002/2014JB011096.
- Gudmundsson, A. (1995). Ocean-ridge discontinuities in Iceland. *Journal of Geology Society London*, 152, pp. 1011-1015
- Guilbaud, M. N., Self, S., Thordarson, T., and Blake, S. (2005). Morphology, surface structures, and emplacement of lavas produced by Laki, A.D. 1783-1784. *Special Paper of the Geological Society of America*, 396, pp. 81–102. doi:10.1130/0-8137-2396-5.81
- Hack, A. C. and Mavrogenes, J. A. (2006). A synthetic fluid inclusion study of copper solubility in hydrothermal brines from 525 to 725 °C and 0.3 to 1.7 GPa. *Geochimica et Cosmochimica Acta*, 70, (15), pp. 3970-3985. doi:10.1016/j.gca.2006.04.035
- Halter, W. E., Heinrich, C. A., and Pettke, T. (2005). Magma evolution and the formation of porphyry Cu-Au ore fluids: Evidence from silicate and sulfide melt inclusions. *Mineralium Deposita*, 39(8), 845–863. doi:10.1007/s00126-004-0457-5
- Hartley, M. E., Shorttle, O., MacLennan, J., Moussallam, Y., and Edmonds, M. (2017). Olivine-hosted melt inclusions as an archive of redox heterogeneity in magmatic systems. *Earth and Planetary Science Letters*, 479, pp. 192–205. doi:10.1016/j.epsl.2017.09.029
- Harris, A. J. L., Rowland, S. K., Villeneuve, N. and Thordarson, T. (2017). Pāhoehoe, ‘a‘ā, and block lava: an illustrated history of the nomenclature. *Bulletin of Volcanology*, 79, 7
- Head III, J. W., Wilson, L. and Smith, D. K. (1996). Mid-ocean ridge eruptive vent morphology and substructure: Evidence for dike widths, eruption rates, and evolution of eruptions and axial volcanic ridges. *Journal of Geophysical Research*. 101, (B12). pp. 28265-28280
- Heliker, C., and Mattox, T. N. (2003). The first two decades of the Pu‘u ‘Ō‘ō-Kūpaianaha eruption: Chronology and selected bibliography. *US Geological Survey Professional Paper*, 1676, pp. 1–20.
- Heliker, C., Swanson, D. A., Takahashi, T. J., Norton, G. A., Survey, U. S. G., and Paper, P. (2003). The Pu ‘ u ‘ Ō ‘ ö-Kūpaianaha Eruption of Kilauea Volcano , Hawai ‘ i : The First 20 Years *US Geological Survey Professional Paper*.1676.
- Herzog, G. F., Moynier, F., Albarède, F., and Berezhnoy, A. A. (2009). Isotopic and

- elemental abundances of copper and zinc in lunar samples, Zagami, Pele's hairs, and a terrestrial basalt. *Geochimica et Cosmochimica Acta*, 73(19), pp. 5884–5904. doi:10.1016/j.gca.2009.05.067
- Hofmann, C., Courtillot, V., Féraud, G., Rochette, P., Yirgu, G., Ketefo, E., and Pik, R. (1997). Timing of the Ethiopian flood basalt event and implications for plume birth and global change. *Nature*, 389 (6653), pp. 838–841. doi:10.1038/39853
- Holt, S. J., Carey, R. J., Houghton, B. F., Orr, T., McPhie, J., and Feig, S. (2019). Eruption and fountaining dynamics of selected 1985–1986 high fountaining episodes at Kīlauea volcano, Hawai'i, from quantitative vesicle microtexture analysis. *Journal of Volcanology and Geothermal Research*, 369, pp. 21–34. doi:10.1016/j.jvolgeores.2018.11.011
- Hon, K., Kauahikaua, J., Denlinger, R. and Mackay, K. (1994). Emplacement and inflation of pahoehoe sheet flows: Observations and measurements of active lava flows on Kīlauea Volcano, Hawaii. *Geological Society of America Bulletin*. 106. pp. 351-370.
- Houghton, B. F., Wilson, C. J. N., Del Carlo, P., Coltelli, M., Sable, J. E. and Carey, R. (2004). The influence of conduit processes on changes in style of basaltic Plinian eruptions: Tarawera 1886 and Etna 122 BC. *Journal of Volcanology and Geothermal Research*, 137, (1–3), 30, pp. 1-14
- Houghton, B. F., and Gonnermann, H. M. (2008). Basaltic explosive volcanism: Constraints from deposits and models. *Chemie Der Erde*, 68 (2), pp. 117–140. doi:10.1016/j.chemer.2008.04.002
- Houghton, B. F., Taddeucci, J., Andronico, D., Gonnermann, H. M., Pistolesi, M., Patrick, M. R., Orr, T. R., Swanson, D. A., Edmonds, M., Gaudin, D., Carey, R. J., and Scarlato, P. (2016). Stronger or longer: Discriminating between Hawaiian and Strombolian eruption styles. *Geology*, 44(2), pp. 163–166. doi:10.1130/G37423.1
- Houghton, B. F., Tisdale, C. M., Llewellyn, E. W., Taddeucci, J., Orr, T. R., Walker, B. H. and Patrick, M. R. (2020). The Birth of a Hawaiian Fissure Eruption. *Journal of Geophysical Research: Solid Earth*, 126, . doi:10.1029/2020JB020903
- Ilyinskaya, E., Schmidt, A., Mather, T. A., Pope, F. D., Witham, C., Baxter, P., Jóhannsson, T., Pfeffer, M., Barsotti, S., Singh, A., Sanderson, P., Bergsson, B., McCormick Kilbride, B., Donovan, A., Peters, N., Oppenheimer, C., and Edmonds, M. (2017). Understanding the environmental impacts of large fissure eruptions: Aerosol and gas emissions from the 2014–2015 Holuhraun eruption (Iceland). *Earth and Planetary Science Letters*, 472, pp. 309–322. doi:10.1016/j.epsl.2017.05.025
- Ilyinskaya, E., Mason, E., Wieser, P.E., Holland, L., J. Liu, E. J., Mather, T. A., Edmonds, M., Whitty, R. C. W., Elias, T., Nadeau, P. A., Schneider, D., McQuaid, J. B., Allen, S. E., Harvey, J., Oppenheimer, C., Kern, C. and Damby, D. (2021). Rapid metal pollutant deposition from the volcanic plume of Kīlauea, Hawai'i. *Nature Communications in Earth Environment*. 2. 78, doi:10.1038/s43247-021-00146-2
- John, S. G., Rouxel, O. J., Craddock, P. R., Engwall, A. M., and Boyle, E. A. (2008). Zinc stable isotopes in seafloor hydrothermal vent fluids and chimneys. *Earth and Planetary Science Letters*, 269 (1–2), pp. 17–28. doi:10.1016/j.epsl.2007.12.011
- Jugo, P.J., Luth, R.W., and Richards, J.P., 2005a, Experimental data on the

- speciation of sulfur as a function of oxygen fugacity in basaltic melts. *Geochimica et Cosmochimica Acta*. 69. pp. 497–503.
- Jugo, P.J., Luth, R.W., and Richards, J.P., 2005b. An experimental study of the sulfur content in basaltic melts saturated with immiscible sulfide or sulfate liquids at 1300°C and 1.0 GPa. *Journal of Petrology*. 46. pp. 783–798
- Jolley, D. W., & Widdowson, M. (2005). Did Paleogene North Atlantic rift-related eruptions drive early Eocene climate cooling? *Lithos*. 79 (3-4 special issue), pp. 355–366. doi:10.1016/j.lithos.2004.09.007
- Jones, Thomas J., and Llewellyn, E. W. (2020). Convective tipping point initiates localization of basaltic fissure eruptions. *Earth and Planetary Science Letters*. 1. 116637. doi:10.1016/j.epsl.2020.116637
- Keszthelyi, L. and Self, S. (1998). Some physical requirements for the emplacement of long basaltic lava flows. *Journal of Geophysical Research: Solid Earth*. 103. (B11) pp. 27447-27464. doi:10.1029/98JB00606
- Keszthelyi, L., McEwen, A. and Thordarson, T. (2000). Terrestrial analogs and thermal models for Martian flood lavas. *Journal of Geophysical Research, Planets*. 105. (E6), pp. 15027-15049. doi:10.1029/1999JE001191
- Keszthelyi, L., Thordarson, T., McEwen, A., Haack, H., Guilbaud, M., Self, S. and Rossi, M. J. (2004). Icelandic analogs to Martian flood lavas. *Geochemistry, Geophysics, Geosystems*. 5. (Q11), 014. doi:10.1029/2004GC000758.
- Keszthelyi, L., Self, S. and Thordarson, T. (2006). Flood lavas on Earth, Io and Mars. *Journal of the Geological Society*, 163, pp. 253-264, doi:10.1144/0016-764904-503
- Klug, C., and Cashman, K. V. (1994). Vesiculation of May 18, 1980, Mount St. Helens magma. *Geology*. 22 (5), pp. 468–472. doi:10.1130/0091-7613(1994)022<0468:VOMMSH>2.3.CO;2
- Kokelaar, P. (1986). Magma-water interactions in subaqueous and emergent basaltic volcanism. *Bulletin of Volcanology*. 48: pp. 275–289. doi:10.1007/BF01081756
- Larsen, G. (2000) Holocene eruptions within the Katla volcanic system, south Iceland: characteristics and environmental impact. *Jökull*. 49. 1–28.
- Lautze, N. C., and Houghton, B. F. (2008). Single explosions at Stromboli in 2002: Use of clast microtextures to map physical diversity across a fragmentation zone. *Journal of Volcanology and Geothermal Research*. 170. (3–4), pp. 262–268. doi:10.1016/j.jvolgeores.2007.10.011
- Liu, W., Brugger, J., McPhail, D.C. and Spiccia, L. (2002). A spectrophotometric study of aqueous copper(I)-chloride complexes in LiCl solutions between 100 °C and 250 °C. *Geochimica et Cosmochimica Acta*. 66, pp. 3615-3633
- Li, W., Jackson, S. E., Pearson, N. J., Alard, O., and Chappell, B. W. (2009). The Cu isotopic signature of granites from the Lachlan Fold Belt, SE Australia. *Chemical Geology*, 258 (1–2), pp. 38–49. doi:10.1016/j.chemgeo.2008.06.047
- Liu, S. A., Huang, J., Liu, J., Wörner, G., Yang, W., Tang, Y. J., Chen, Y., Tang, L., Zheng, J., and Li, S. (2015). Copper isotopic composition of the silicate Earth. *Earth and Planetary Science Letters*, 427, pp. 95–103. doi:10.1016/j.epsl.2015.06.061
- Liu, S. A., Wang, Z. Z., Li, S. G., Huang, J., and Yang, W. (2016). Zinc isotope evidence for a large-scale carbonated mantle beneath eastern China. *Earth and Planetary Science Letters*, 444, pp. 169–178. doi:10.1016/j.epsl.2016.03.051
- Loughlin, S. C., Aspinall, W. P., C, V.-B., Baxter, P. J., Braban, C., M, H., Schmidt, A., Thordarson, T., and Witham, C. S. (2012). Large-Magnitude Fissure Eruptions in Iceland: Source Characterisation. *British Geological Survey*

- OpenFile Report*, pp. 1–136.
- Luck, J. M., Othman, D. Ben, and Albarède, F. (2005). Zn and Cu isotopic variations in chondrites and iron meteorites: Early solar nebula reservoirs and parent-body processes. *Geochimica et Cosmochimica Acta*. 69 (22), pp. 5351–5363. doi:10.1016/j.gca.2005.06.018
- Luguet, A., Lorand, J.-P., Seyler, M. (2003). A coupled study of sulfide petrology and highly siderophile element geochemistry in abyssal peridotites from the Kane Fracture Zone (MARK area, Mid-Atlantic ridge). *Geochimica et Cosmochimica Acta*. 67. pp. 1553-1570
- Macdonald, G. A. (1967). Forms and structures of extrusive basaltic rocks. In: Hess HH, Poldervaart A (editors) *The Poldervaart Treatise on rocks of basaltic composition*. Interscience, New York, pp. 1–61
- Mahan, B., Siebert, J., Pringle, E. A., and Moynier, F. (2017). Elemental partitioning and isotopic fractionation of Zn between metal and silicate and geochemical estimation of the S content of the Earth's core. *Geochimica et Cosmochimica Acta*. 196. pp. 252–270. doi:10.1016/j.gca.2016.09.013
- Mangan, M. T., and Cashman, K. (1996). The structure of basaltic scoria and reticulite and inferences for vesiculation, foam formation, and fragmentation in lava fountains. *Journal of Volcanology and Geothermal Research*. 73. (1–2) pp. 1–18.
- Mangan, M. and Sisson, T. (2005). Evolution of melt-vapor surface tension in silicic volcanic systems: experiments with hydrous melts. *Journal of geophysics*. pp. 110. doi:10.1029/2004JB003215
- Markl, G., Lahaye, Y. and Schwinn, G. (2006). Copper isotopes as monitors of redox processes in hydrothermal mineralization. *Geochimica et Cosmochimica Acta*, 70. pp. 4215–4228
- Marini, L., Moretti, R. and Accornero, M. (201). Sulfur Isotopes in Magmatic-Hydrothermal Systems, Melts, and Magmas. Its importance for natural and technical processes. Behrens, H. and Webster, J. D. (Editors). In: Sulfur in magmas and melts. *Reviews in Mineralogy and Geochemistry*. 73. pp. 423-492. doi:10.2138/rmg.2011.73.1
- Martin, E., Paquette, J. L., Bosse, V., Tiepolo, M., Sigmarsson, O. (2011). Geodynamics of rift–plume interaction in Iceland as constrained by new $^{40}\text{Ar}/^{39}\text{Ar}$ and in situ U–Pb zircon ages. *Earth and Planetary Science Letters*. 311. (1–2), pp. 28-38
- McKenzie D. and Bickle M. J. (1988). The volume and composition of melt generated by extension of the lithosphere. *Journal of Petrology*. 29. pp. 625-679
- Metrich, N. and Mandeville, C. W. (2010). Sulfur in Magmas. *Elements*. 6. (2), pp. 81–86. <https://doi.org/10.2113/gselements.6.2.81>
- Moreland W.M, Thordarson T, Houghton B.F. and Larsen G, (2019). Driving mechanisms of subaerial and subglacial explosive episodes during the 10th century Eldgjá fissure eruption, southern Iceland. *Volcanica*.
- Moretti, R. and Baker, D. R. (2008). Modeling the interplay of $f\text{O}_2$ and $f\text{S}_2$ along the FeS-silicate melt equilibrium. *Chemical Geology*. 256. (3–4), pp. 286-298
- Mourtada-Bonnefoi, C. C., and Laporte, D. (2004). Kinetics of bubble nucleation in a rhyolitic melt: An experimental study of the effect of ascent rate. *Earth and Planetary Science Letters*. 218. (3–4), pp. 521–537. doi:10.1016/S0012-821X(03)00684-8
- Moynier, F., Albarède, F., and Herzog, G. F. (2006). Isotopic composition of zinc, copper, and iron in lunar samples. *Geochimica et Cosmochimica Acta*. 70. (24),

- pp. 6103–6117. doi:10.1016/j.gca.2006.02.030
- Moynier, F., Abe, M. and Telouk, P. (2010). Experimental and theoretical investigation of isotope fractionation of Zn. *The Journal of Physical Chemistry A*.
- Namiki, A., and Manga, M. (2006). Influence of decompression rate on the expansion velocity and expansion style of bubbly fluids. *Journal of Geophysical Research: Solid Earth*. 111. (11), pp. 1–17. doi:10.1029/2005JB004132
- Namiki, A., and Manga, M. (2008). Transition between fragmentation and permeable outgassing of low viscosity magmas. *Journal of Volcanology and Geothermal Research*. 169. (1–2), pp. 48–60. doi:10.1016/j.jvolgeores.2007.07.020
- Narsimhan, G. and Ruckenstein, E., 1986a. Hydrodynamics, enrichment and collapse in foams. *Langmuir*. 2. pp. 230-238.
- Narsimhan, G. and Ruckenstein, E., 1986b. Effect of bubble size distribution on the enrichment and collapse in foams. *Langmuir*. 2. pp. 494-508.
- Óskarsson, N., Grönvold, K. and Larsen, G. (1984). The haze produced by the Laki eruption. (In Icelandic). In: Einarsson, T., Guðbergsson, G. M., Gunnlaugsson, G. A., Rafnsson, S. and Þórarinnsson, S. (Editors.) *Skaftáreldar 1783-1784 :Ritgerðir og Heimildir*. pp. 67-80. Mál og Menning: Reykjavík.
- Oman, L., Robock, A., Stenchikov, G.L. et al. (2006a). Modeling the distribution of the volcanic aerosol cloud from the 1783–1784 Laki eruption. *Journal of Geophysical Research*. 111. D12209.
- Oman, L., Robock, A., Stenchikov, G.L. and Thordarson, T. (2006b). High-latitude eruptions cast shadow over the African monsoon and the flow of the Nile. *Geophysical Research Letters*. 33. L18711.
- Oppenheimer, C., Scaillet, B. and Martin, R. S. (2011). Sulfur degassing from volcanoes: source conditions, surveillance, plume chemistry and earth system impacts (Chapter 13), In: *Sulfur in Magmas and Melts: Its Importance for Natural and Technical Processes*. Behrens, H and Webster, J. D. (Editors). *Reviews in Mineralogy and Geochemistry*. Volume 73: pp. 363 - 422
- Papale, P. (1999). Modeling of the solubility of a two-component H₂O+CO₂ fluid in silicate liquids. *American Mineralogist*. 84. (4), pp. 477-492
- Pan, V., Holloway, J. R. and Hervig, R. L. (1991). The pressure and temperature dependence of carbon dioxide solubility in tholeiitic basalt melts. *Geochimica et Cosmochimica Acta*. 55 (6), pp. 1587-1595
- Paniello, R. C., Day, J. and Moynier, F. (2012). Zinc isotope evidence for the origin of the Moon. *Nature*. 490. (7420). pp. 376-9. doi:10.1038/nature11507
- Parcheta, C. E., Houghton, B. F., and Swanson, D. A. (2013). Contrasting patterns of vesiculation in low, intermediate, and high Hawaiian fountains: A case study of the 1969 Mauna Ulu eruption. *Journal of Volcanology and Geothermal Research*. 255. pp. 79–89. doi:10.1016/j.jvolgeores.2013.01.016
- Parfitt, E. A. (2004). A Discussion of the mechanisms of explosive basaltic eruptions. *Journal of Volcanology and Geothermal Research*. 134. (1–2), pp. 77-107
- Parfitt, Elisabeth A. and Wilson, Lionel (2008). *Fundamentals of physical volcanology*. Blackwell, Malden, Mass. ISBN 0632054433
- Peach, C. L., Mathez, E.A. and Keays, R.R. (1990). Sulfide melt-silicate melt distribution coefficients for noble metals and other chalcophile elements as deduced from MORB – Implications for partial melting. *Geochimica et Cosmochimica Acta*. 54. pp. 3379-3389

- Pedersen, G. B. M., Höskuldsson, A., Dürig, T., Thordarson, T., Jónsdóttir, I., Riishuus, M. S., Óskarsson, B. V., Dumont, S., Magnusson, E., Gudmundsson, M. T., Sigmundsson, F., Drouin, V. J. P. B., Gallagher, C., Askew, R., Gudnason, J., Moreland, W. M., Nikkola, P., Reynolds, H. I., and Schmith, J. (2017). Lava field evolution and emplacement dynamics of the 2014–2015 basaltic fissure eruption at Holuhraun, Iceland. *Journal of Volcanology and Geothermal Research*. 340. pp. 155–169. doi:10.1016/j.jvolgeores.2017.02.027
- Peltier, A., Bachèlery, P. and Staudacher, T. (2009). Magma transport and storage at Piton de La Fournaise (La Réunion) between 1972 and 2007: A review of geophysical and geochemical data. *Journal of Volcanology and Geothermal Research*. 184. pp. 93–108
- Petersen, G. N., Björnsson, H., Arason, P. and von Löwis, S. (2012). Two weather radar time series of the altitude of the volcanic plume during the May 2011 eruption of Grímsvötn, Iceland. *Earth System Science Data*. 4. pp. 121–127, doi:10.5194/essd-4-121-2012.
- Pioli, L., Erlund, E., Jognson, E., Cashman, E., Wallace, P., Rosi, M., Delgado Granados, H. (2008). Explosive dynamics of violent Strombolian eruptions: The eruption of Parícutin Volcano 1943–1952 (Mexico). *Earth and Planetary Science Letters*. 271. (1–4), pp. 359–368
- Polacci, M., Corsaro, R. A., and Andronico, D. (2006). Coupled textural and compositional characterization of basaltic scoria: Insights into the transition from Strombolian to fire fountain activity at Mount Etna, Italy. *Geology*. 34 (3), pp. 201–204. doi:10.1130/G22318.1
- Porritt, L. A., Russell, J. K., and Quane, S. L. (2012). Pele’s tears and spheres: Examples from Kilauea Iki. *Earth and Planetary Science Letters*. 333–334. pp. 171–180. doi:10.1016/j.epsl.2012.03.031
- Proussevitch, A., Sahagian, D. L. and Anderson, A.T. (1993). Dynamics of diffusive bubble growth in magmas: isothermal case. *Journal of Geophysical Research*. 98. pp. 22283–22307
- Proussevitch, A. and Sahagian, D.L. (1996). Dynamics of coupled diffusive and decompressive bubble growth in magmatic systems. *Journal of Geophysical Research*. 101. pp. 17447–17455
- Rampino, M. R., and Stothers, R. B. (1988). Flood basalt volcanism during the past 250 million years. *Science*. 241 (4866), pp. 663–668. doi:10.1126/science.241.4866.663
- Richter, D. H., Eaton, J. P., Murata, K. J., Ault, W. U., & Krivoy, H. L. (1970). Chronological Narrative of the 1959–60 Eruption of Kilauea Volcano, Hawaii. *USGS Professional Paper*. 537-E. doi:10.1016/0198-0254(80)95902-6
- Robock, A. (2000). Volcanic eruptions and climate. *Reviews of Geophysics*, Volume 38, Issue 2, pp. 191–219. <https://doi.org/10.1029/1998RG000054>
- Robock, A. and Oppenheimer, C. Editors. (2003). *Volcanism and the Earth’s Atmosphere*, *Geophysical Monograph*. 139. American Geophysical Union, Washington, DC, 360 pp
- Rust, A. C., and Cashman, K. V. (2011). Permeability controls on expansion and size distributions of pyroclasts. *Journal of Geophysical Research: Solid Earth*, 116 (11), pp. 1–17. doi:10.1029/2011JB008494
- Sable, Julia E., Houghton, B. F., Del Carlo, P., and Coltelli, M. (2006). Changing conditions of magma ascent and fragmentation during the Etna 122 BC basaltic Plinian eruption: Evidence from clast microtextures. *Journal of Volcanology and Geothermal Research*. 158. (3–4), pp. 333–354.

doi:10.1016/j.jvolgeores.2006.07.006

- Sahagian, D. L. (1985). Bubble migration and coalescence during the solidification of basaltic lava flows. *The Journal of Geology*. 93. pp. 205–211
- Sahagian, D. L., Anderson, A. T. and Ward, B. (1989). Bubble coalescence in basalt flows: comparison of a numerical model with natural examples. *Bulletin of Volcanology*. 52. pp. 49–56. doi:10.1007/BF00641386
- Sakai, H., Casadevall, T.J. and Moore, J.G. (1982). Chemistry and isotope ratios of sulfur in basalts and volcanic gases at Kilauea volcano, Hawaii. *Geochimica et Cosmochimica Acta*. 46. pp. 729-738
- Savage, P. S., Georg, R. B., Williams, H. M., Burton, K. W. and Halliday, A. N. (2011). Silicon isotope fractionation during magmatic differentiation. *Geochimica et Cosmochimica Acta*. 75. (20), pp. 6124-6139
- Savage, P., Moynier, F., Chen, H., Shofner, G., Siebert, J., Badro, J., and Puchtel, I. S., (2015). Copper isotope evidence for large-scale sulphide fractionation during Earth's differentiation. *Geochemical Perspective Letters*. 1. pp. 53–64.
- Sayed, M. R. G. (2014). Flood basalt hosted palaeosols: Potential palaeoclimatic indicators of global climate change. *Geoscience Frontiers*. 5. (6), pp. 791–799. doi:10.1016/j.gsf.2013.08.005
- Scaillet, B., and Pichavant, M., 2005, A model of sulphur solubility for hydrous mafic melts: Application to the determination of magmatic fluid compositions of Italian volcanoes: *Annals of Geophysics*. 48. pp. 671–698.
- Schilling, J.-g., Bergeron, M. B. and Evans, R. (1980). Halogens in the mantle beneath the North Atlantic. *Philosophical Transactions of the royal society of America*. 297. (1431). doi: 10.1098/rsta.1980.0208.
- Schmidt, A. (2015). Chapter 15 'Volcanic Gas and Aerosol Hazards from a Future Laki-Type Eruption in Iceland'. In: *Volcanic Hazards, Risks and Disasters*. Editor(s): John F. Shroder, Paolo Papale. doi: 10.1016/B978-0-12-396453-3.00015-0.
- Schmidt, A., Carslaw, K. S., Mann, G. W., Wilson, M., Breider, T. J., Pickering, S. J., and Thordarson, T. (2010). The impact of the 1783-1784 AD Laki eruption on global aerosol formation processes and cloud condensation nuclei. *Atmospheric Chemistry and Physics*. 10. (13), pp. 6025–6041. doi:10.5194/acp-10-6025-2010
- Schmidt, Anja, Ostro, B., Carslaw, K. S., Wilson, M., Thordarson, T., Mann, G. W., and Simmons, A. J. (2011). Excess mortality in Europe following a future Laki-style icelandic eruption. *Proceedings of the National Academy of Sciences of the United States of America*. 108. (38), pp. 15710–15715. doi:10.1073/pnas.1108569108
- Schmidt, A., Carslaw, K. S., Mann, G. W., Rap, A., Pringle, K. J., Spracklen, D. V., Wilson, M., and Forster, P. M. (2012). Importance of tropospheric volcanic aerosol for indirect radiative forcing of climate. *Atmosphere Chemistry Physics*. 12. pp. 7321–7339, doi:10.5194/acp-12-7321-2012, 2012.
- Schmidt, A., Leadbetter, S., Theys, N., Carboni, E., Witham, C. S., Stevenson, J. A., Birch, C. E., Thordarson, T., Turnock, S., Barsotti, S., Delaney, L., Feng, W., Grainger, R. G., Hort, M. C., Höskuldsson, Á., Ialongo, I., Ilyinskaya, E., Jóhannsson, T., Kenny, P., Mather, T. A., Richards, N. A.D. and Shepherd, J. (2015). Satellite detection, long-range transport, and air quality impacts of volcanic sulfur dioxide from the 2014–2015 flood lava eruption at Bárðarbunga (Iceland). *Journal of Geophysical Research: Oceans*. 120. pp. 9739–9757. doi:10.1002/2015JC011107.

- Schmidt, A., and Robock, A. (2015). Volcanism, the atmosphere and climate through time. *Volcanism and Global Environmental Change*. pp. 195–207. doi:10.1007/9781107415683.014
- Schmidt, A., Skeffington, R., Thordarson, T., Self, S., Forster, P. M., Rap, A., Ridgwell, A., Fowler, D., Wilson, M., Mann, G. W., Wignall, P. B. and Carslaw, K. S. (2016). Selective environmental stress from sulphur emitted by continental flood basalt eruptions. *Nature Geoscience*. 9. pp. 77–82. doi:10.1038/ngeo2588
- Self, S., Thordarson, T., and Widdowson, M. (2005). Gas Fluxes from Flood Basalt Eruptions. *Elements*, 1(5), 283–287. <https://doi.org/10.2113/gselements.1.5.283>
- Self, Stephen, Widdowson, M., Thordarson, T., and Jay, A. E. (2006). Volatile fluxes during flood basalt eruptions and potential effects on the global environment: A Deccan perspective. *Earth and Planetary Science Letters*. 248, (1–2), pp. 518–532. doi:10.1016/j.epsl.2006.05.041
- Self, Stephen, Blake, S., Sharma, K., Widdowson, M., and Sephton, S. (2008). Sulfur and Chlorine in Late Cretaceous. *Science*. 319. pp. 1654–1657.
- Self, S., Schmidt, A. and Mather, T. A. (2014). Emplacement characteristics, time scales, and volcanic gas release rates of continental flood basalt eruptions on Earth. in Keller, G., and Kerr, A.C., eds., *Volcanism, Impacts, and Mass Extinctions: Causes and Effects: Geological Society of America Special Paper*. 505. pp. 319–337. doi:10.1130/2014.2505(16).
- Seo, J.H., Lee, S.K., Lee, I. (2007) Quantum chemical calculations of equilibrium copper (I) isotope fractionations in ore-forming fluids. *Chemical Geology*. 243. pp. 225-237.
- Shishkina, T. A., Botcharnikov, R. E., Holtz, F., Almeev, R. R. and Portnyagin, M. V. (2010). Solubility of H₂O- and CO₂-bearing fluids in tholeiitic basalts at pressures up to 500 MPa. *Chemical Geology*. 277. pp. 115-125
- Sigmarsson, O., Haddadi, B., Carn, S., Moune, S., Gudnason, J., Yang, K. and Clarisse, L. (2013). The sulfur budget of the 2011 Grímsvötn eruption, Iceland. *Geophysical Research Letters*. 40. (23), pp. 6095-6100. doi: 10.1002/2013GL057760.
- Simon, A. C., Pettke, T., Candelac, P. A., Piccolic, P. M. and Heinrich, C. A. (2006). Copper partitioning in a melt–vapor–brine–magnetite–pyrrhotite assemblage. *Geochimica et Cosmochimica Acta*. 70. (22), pp. 5583-5600
- Sossi, P. A., Halverson, G. P., Nebel, O., and Eggins, S. M. (2015). Combined separation of Cu, Fe and Zn from rock matrices and improved analytical protocols for stable isotope determination. *Geostandards and Geoanalytical Research*, 39. (2), 129–149. doi:10.1111/j.1751-908X.2014.00298.x
- Sossi, P. A., Nebel, O., O’Neill, H. S. C., and Moynier, F. (2018). Zinc isotope composition of the Earth and its behaviour during planetary accretion. *Chemical Geology*. 477. pp. 73–84. doi:10.1016/j.chemgeo.2017.12.006
- Sparks, R. S. J. (1978). The dynamics of bubble formation and growth in magmas: a review and analysis. *Journal of Volcanology and Geothermal Research*. 3. pp. 1-38
- La Spina, G., Arzilli, F., Llewellyn, E. W., Burton, M. R., Clarke, A. B., de’ Michieli Vitturi, M., Polacci, M., Hartley, M. E., Di Genova, D., and Mader, H. M. (2020). Explosivity of basaltic lava fountains is controlled by magma rheology, ascent rate and outgassing. *Earth and Planetary Science Letters*. 1. 116658. doi:10.1016/j.epsl.2020.116658
- Stothers, R. B., and Rampino, M. R. (1990). Periodicity in flood basalts, mass

- extinctions, and impacts; A statistical view and a model. In: *Global Catastrophes in Earth History; An Interdisciplinary Conference on Impacts, Volcanism, and Mass Mortality*, Virgil L. Sharpton, Peter D. Ward (Editors). *Geoscience World*.
- Stovall, W. K., Houghton, B. F., Gonnermann, H., Fagents, S. A., and Swanson, D. A. (2011). Eruption dynamics of Hawaiian-style fountains: The case study of episode 1 of the Kilauea Iki 1959 eruption. *Bulletin of Volcanology*. 73. (5), pp. 511–529. doi:10.1007/s00445-010-0426-z
- Stovall, W. K., Houghton, B. F., Hammer, J. E., Fagents, S. A., and Swanson, D. A. (2012). Vesiculation of high fountaining Hawaiian eruptions: Episodes 15 and 16 of 1959 Kīlauea Iki. *Bulletin of Volcanology*. 74. (2), pp. 441–455. doi:10.1007/s00445-011-0531-7
- Sun, W.D., Arculus, R.J., Kamenetsky, V.S., Binns, R.A. (2004) Release of gold-bearing fluids in convergent margin magmas prompted by magnetite crystallization. *Nature*. 431. (7011), pp. 975-978.
- Sumner, J. M. (1998). Formation of clastogenic lava flows during fissure eruption and scoria cone collapse: The 1986 eruption of Izu-Oshima Volcano, eastern Japan. *Bulletin of Volcanology*. 60 (3), pp. 195–212. doi:10.1007/s004450050227
- Swanson, D. A. (1973). Pahoehoe Flows from the 1969–1971 Mauna Ulu Eruption, Kilauea Volcano, Hawaii. *GeoScience World, America Bulletin*. 84. (2): pp. 615–626. doi:10.1130/0016-7606(1973)84<615:PFPTMU>2.0.CO;2
- Swanson, D. A., Wright, T. L. and Helz, R. T. (1975). Linear vent systems and estimated rates of magma production and eruption for the Yakima basalt of the Columbia plateau. *American Journal of Science*. 275. pp. 877-905
- Swanson, D. A., Duffield, W. A., Jackson, D. B., and Peterson, D. W. (1979). Chronological narrative of the 1969-71 Mauna Ulu eruption of Kilauea Volcano, Hawaii. *U.S. Geological Survey Professional Paper*. 1056, 55 p.
- Taddeucci, J., Edmonds, M., Houghton, B., James, M. R. and Vergnolle, S. (2015). Chapter 27 - Hawaiian and Strombolian Eruptions. In: *The Encyclopedia of Volcanoes (Second Edition)*. Sigurdsson, H., Houghton, B., McNutt, S. R., Rymer, H. and Stiz, J. pp. 485-503
- Telus, M., Dauphas, N., Moynier, F., Tissot, F. L. H., Teng, F. Z., Nabelek, P. I., Craddock, P. R., and Groat, L. A. (2012). Iron, zinc, magnesium and uranium isotopic fractionation during continental crust differentiation: The tale from migmatites, granitoids, and pegmatites. *Geochimica et Cosmochimica Acta*. 97. pp. 247–265. doi:10.1016/j.gca.2012.08.024
- Thordarson, T. and Self, S. (1993). The Laki (Skaftár Fires) and Grímsvötn eruptions in 1783-1785. *Bulletin of Volcanology*. 55. (4), pp. 233–263. doi: 10.1007/BF00624353
- Thordarson, Th., Self, S., Óskarsson, N., and Hulsebosch, T. (1996). Sulfur, chlorine, and fluorine degassing and atmospheric loading by the 1783-1784 AD Laki (Skaftár Fires) eruption in Iceland. *Bulletin of Volcanology*. 58. (2–3), pp. 205–225. doi:10.1007/s004450050136
- Thordarson, T. and Self, S. (1998). The Roza Member, Columbia River Basalt Group: A gigantic pahoehoe lava flow field formed by endogenous processes? *Journal of Geophysical Research*. 103. (B11), pp. 27411-27445.
- Thordarson, T, and Self, S. (2001). Real-time observations of the Laki sulfuric aerosol cloud in Europe during 1783 as documented by Professor S. P. van Swinden at Franeker, Holland. *Jokull*. 50. pp. 65–72.

- Thordarson, T., Miller, D. J., Larsen, G., Self, S. and Sigurdsson, H. (2001). New estimates of sulfur degassing and atmospheric mass-loading by the 934 AD Eldgja eruption, Iceland. *Journal of Volcanology and Geothermal Research*. 108. pp. 33-54
- Thordarson, T. and Self, S. (2003). Atmospheric and environmental effects of the 1783-1784 Laki eruption: A review and reassessment. *Journal of Geophysical Research, Atmospheres*. 108. 4011
- Thordarson, T., Larsen, G., Steinthorsson, S., and Self, S. (2003a). The 1783–1785 AD Laki-Grímsvötn eruptions II: appraisal based on contemporary accounts. *Jökull*. 53. pp. 11–47.
- Thordarson, T., Self, S., Miller, D. J., Larsen, G. and Vilmundardóttir, E. G. (2003b) Sulphur release from flood lava eruptions of the Veiðivötn, Grímsvötn and Katla volcanic systems, Iceland. In: C Oppenheimer, DM Pyle and J Barclay (eds.) *Volcanic Degassing*. pp. 103-121. *The Geological Society of London*.
- Thordarson, T. (2013) Hraun (Lava). In: *Náttúruvá á Íslandi, Höfundar (Reykjavik)*, pp. 105–129. (In Icelandic).
- Thordarson, T., Rampino, M., Keszthelyi, L. and Self, S. (2009) Effects of megascale eruptions on Earth and Mars. In: M.G. Chapman and L. Keszthelyi (Editors), *Preservation of random megascale events on Mars and Earth: Influence on Geological History*. *Geological Society of America Special Paper*. 453. pp. 37-53.
- Toramaru, A. (1995). Numerical study of nucleation and growth of bubbles in viscous magmas. *Journal of Geophysical Research*. 100. (B2), pp. 1913–1931.
- Ueda, A. and Sakai, H. (1984) Sulfur isotope study of Quaternary volcanic rocks from the Japanese island arc. *Geochimica et Cosmochimica Acta*. 48. pp. 1837-1848.
- Vye-Brown, C., Gannoun, A., Barry, T. L., Self, S., and Burton, K. W. (2013). Osmium isotope variations accompanying the eruption of a single lava flow field in the Columbia River Flood Basalt Province. *Earth and Planetary Science Letters*. 368. pp. 183–194. doi:10.1016/j.epsl.2013.02.003
- Walker, G. P. L. (1973) Explosive volcanic eruptions — a new classification scheme. *Geol Rundsch*. 62. pp. 431–446. doi:10.1007/BF01840108
- Walker, G. P. L., Self S, Wilson L (1984) Tarawera 1886, New Zealand — A basaltic plinian fissure eruption. *Journal of Volcanology Geothermal Research*. 21. pp. 61–78. doi:10.1016/0377-0273(84)90016-7
- Walker, G.P.L. (1964) Geological investigations in eastern Iceland. *Bulletin Volcanologique*. 27. (1), pp. 351-363
- Walker, G.P.L. (1993) Basaltic-volcano systems. *Geological Society, London, Special Publications*. 76, pp. 3-38
- Walker, G.P.L. (1999) Volcanic rift zones and their intrusion swarms. *Journal of Volcanology and Geothermal Research*. 94 (1-4), pp. 21-34
- Wallace, P., and Carmichael, I. S. E. (1992). Sulfur in basaltic magmas. *Geochimica et Cosmochimica Acta*. 56. (5), pp. 1863–1874. doi:10.1016/0016-7037(92)90316-B
- Wallace, P. J., and Edmonds, M. (2011). The sulfur budget in magmas: Evidence from melt inclusions, submarine glasses, and volcanic gas emissions. *Reviews in Mineralogy and Geochemistry*. 73. pp. 215–246. doi:10.2138/rmg.2011.73.8
- Wang, Z. Z., Liu, S. A., Liu, J., Huang, J., Xiao, Y., Chu, Z. Y., Zhao, X. M., and Tang, L. (2017). Zinc isotope fractionation during mantle melting and constraints on the Zn isotope composition of Earth's upper mantle. *Geochimica*

- et Cosmochimica Acta* 198. pp. 151–167. doi: 10.1016/j.gca.2016.11.014
- Wang, Z., Park, J. W., Wang, X., Zou, Z., Kim, J., Zhang, P., and Li, M. (2019). Evolution of copper isotopes in arc systems: Insights from lavas and molten sulfur in Niuatahi volcano, Tonga rear arc. *Geochimica et Cosmochimica Acta*. 250. pp. 18–33. doi:10.1016/j.gca.2019.01.040
- Webster, J. D., Kinzler, R. J. and Mathez, E. A. (1999). Chloride and water solubility in basalt and andesite melts and implications for magmatic degassing. *Geochimica et Cosmochimica Acta*. 63. (5), pp. 729-738
- Webster, J. D., & Botcharnikov, R. E. (2011). Distribution of sulfur between melt and fluid in S-O-H-C-Cl-bearing magmatic systems at shallow crustal pressures and temperatures. *Reviews in Mineralogy and Geochemistry*. 73. pp. 247–283. doi: 10.2138/rmg.2011.73.9
- White, R. V., & Saunders, A. D. (2005). Volcanism, impact and mass extinctions: Incredible or credible coincidences? *Lithos*. 79. (3-4 special issue). pp. 299–316. doi:10.1016/j.lithos.2004.09.016
- Widdowson, M. and Cox, K.G. (1996). Uplift and erosional history of the Deccan Traps, India: Evidence from laterites and drainage patterns of the Western Ghats and Konka Coast. *Earth and Planetary Science Letters*. 137. pp. 57–69.
- Widdowson, M., Walsh, J. N. Subbarao, K. V. (1997). The geochemistry of Indian bole horizons: Palaeoenvironmental implications of Deccan intravolcanic palaeosurfaces. *Geological Society London Special Publications*. 120. (1), pp. 269-281. doi:10.1144/GSL.SP.1997.120.01.17
- Wignall, P. B. (2001). Large igneous provinces and mass extinctions. *Earth Science Reviews*. 53.(1–2), pp. 1–33. doi:10.1016/S0012-8252(00)00037-4
- Williams, S. N. (1983). Plinian air-fall deposits of basaltic composition. *Geology*. 11. pp. 211-214
- Williams, T.J., Candela, P.A. and Piccoli, P.M. (1995). The partitioning of copper between silicate melts and two-phase aqueous fluids: an experimental investigation at 1 kbar, 800 °C and 0.5 kbar, 850 °C. *Contributions to Mineralogy Petrology*. 121. pp. 388-399
- Wilson, L. (1980). Relationships between pressure, volatile content and ejecta velocity in three types of volcanic explosion. *Journal of Volcanology and Geothermal Research*. 8. (2–4), pp. 297-313
- Witt, T., Walter, T. R., Müller, D., Guðmundsson, M. T., and Schöpa, A. (2018). The Relationship Between Lava Fountaining and Vent Morphology for the 2014–2015 Holuhraun Eruption, Iceland, Analyzed by Video Monitoring and Topographic Mapping. *Frontiers in Earth Science*. 6. doi:10.3389/feart.2018.00235
- Woods, A.W. (1993). A model of the plumes above basaltic fissure eruptions. *Geophysical Research Letters*. 20. (12), pp. 1115–18.
- Wolfe EW, Neal CA, Banks NG, Duggan TJ (1988) Geologic observations and chronology of eruptive events. In: Wolfe EW (ed) The Pu'u 'O'o Eruption of Kilauea Volcano, Hawaii: Episodes 1 Through 20, January 3, 1993, Through June 8, 1984. *USGS Professional Papers*. 1463. pp. 1–97
- Zajacz, Z. and Halter, W. (2009). Copper transport by high temperature, sulfur-rich magmatic vapor: Evidence from silicate melt and vapor inclusions in a basaltic andesite from the Villarrica volcano (Chile). *Earth and Planetary Science Letters*. 282. (1), pp. 115-121. DOI: 10.1016/j.epsl.2009.03.006
- Zimanowski, B., Büttner, R., Dellino, P., White, J. D. L. and Wohletz, K. H. (2015). Magma–Water Interaction and Phreatomagmatic Fragmentation. Chapter 26, In:

The Encyclopedia of Volcanoes (Second Edition), pp. 473-484. doi:
10.1016/B978-0-12-385938-9.00026-2.

Chapter 3: Iceland geological setting and background

3.1 Geological overview of Iceland

The subaerial portion of the Iceland Basalt Plateau's geological history spans two geological Periods: the Quaternary (0–2.58 Ma) and the early part of the Neogene (2.58–16 Ma).

These two geological Periods can be subdivided into Epochs which are more descriptive in terms of periods of warmer or colder climates and major glaciations, which affect the landforms both erosively but also shaping sub-glacially erupted volcanic products. There are five geological epochs represented by the landmass of Iceland: the Anthropocene (<1950 CE); the Holocene (>1950 CE–0.0117 Ma); the Pleistocene (0.781–2.58 Ma); the Pliocene (2.58–5.333 Ma); and the latter half of the Miocene (5.333–16 Ma) (Figure 3. 1).

However, there are also informal but very common classifications used within the research community that work on Icelandic geology, which are a mixture of these epochs. These are probably the result of localised differences in the initiations colder climates, and therefore evidence of glaciations, in Iceland compared to other nearby landmasses, e.g., southern Europe, and are outlined as follows: the Late Pleistocene (0.0117–0.781 Ma); the Plio-Pleistocene (0.781–3.3 Ma) as set out by Sæmundsson (1979).

The samples analysed in this project are from two historical eruptions in Iceland that span both the late Holocene and Anthropocene epochs. The following subsections lay out the current understanding of Icelandic tectonics, volcanism, and geochemistry as a foundation to the interpretations made in later chapters in this thesis regarding the samples analysed in this study from specific eruptions and their associated volcanic systems.

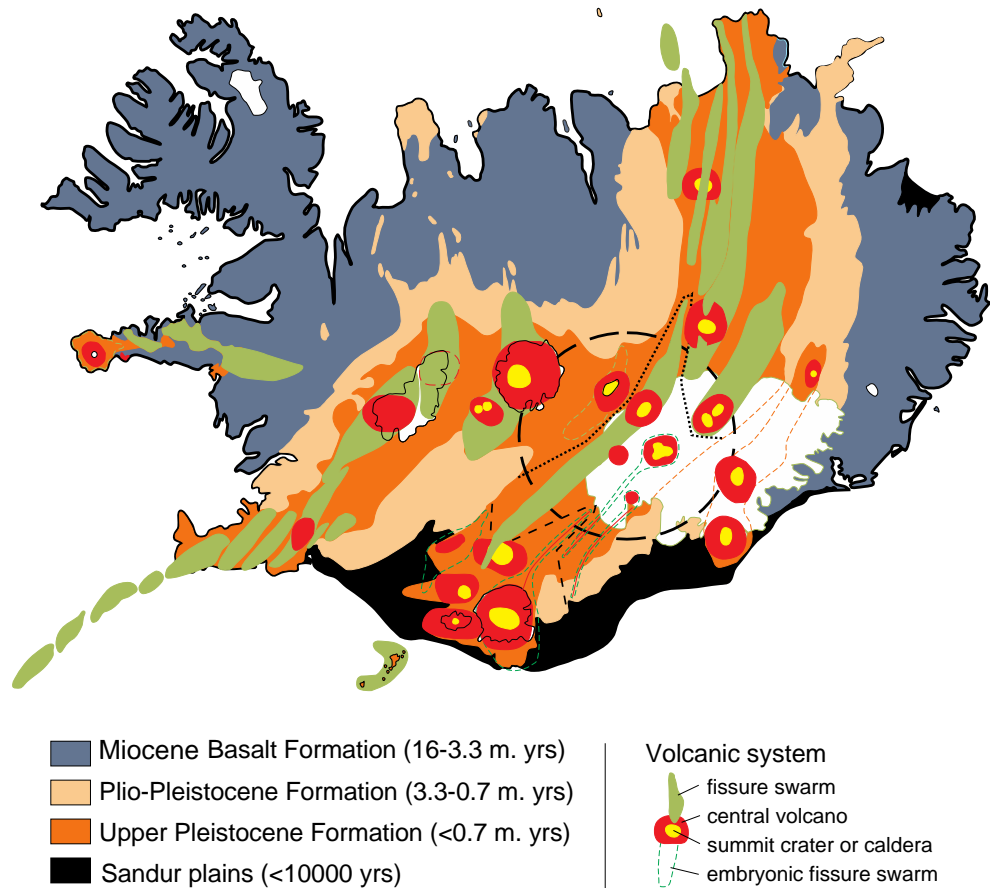


Figure 3. 1: A broad outline of the epochs spanned by the geology of Iceland. This indicates the rough ageing of Icelandic rock formations towards its periphery in response to the spreading of the plate boundaries which cross the island. The location of active volcanism, indicated focal points of activity and delineated by volcanic systems, is confined to the neovolcanic zones. It should be noted that the majority of the volcanic systems in the propagating rift in S–SE Iceland have an embryonic fissure swarm.

3. 2 Iceland tectonics and geodynamics

The Iceland Basalt Plateau (IBP) rises 300 m above the surrounding seafloor (Malinverno, 1990), covering a total area of 350,000 km². It lies at the centre of the North Atlantic Igneous Province (NAIP), which formed during a significant rifting event triggered by the Iceland mantle plume during the Paleogene. The NAIP is dominated by flood basalt volcanism and numerous, now extinct, mature volcanic centres, forming a Large Igneous Province (LIP), which stretches between eastern Greenland and north-west Scotland (British Paleogene Igneous Province, BPIP) (Figure 3. 2).

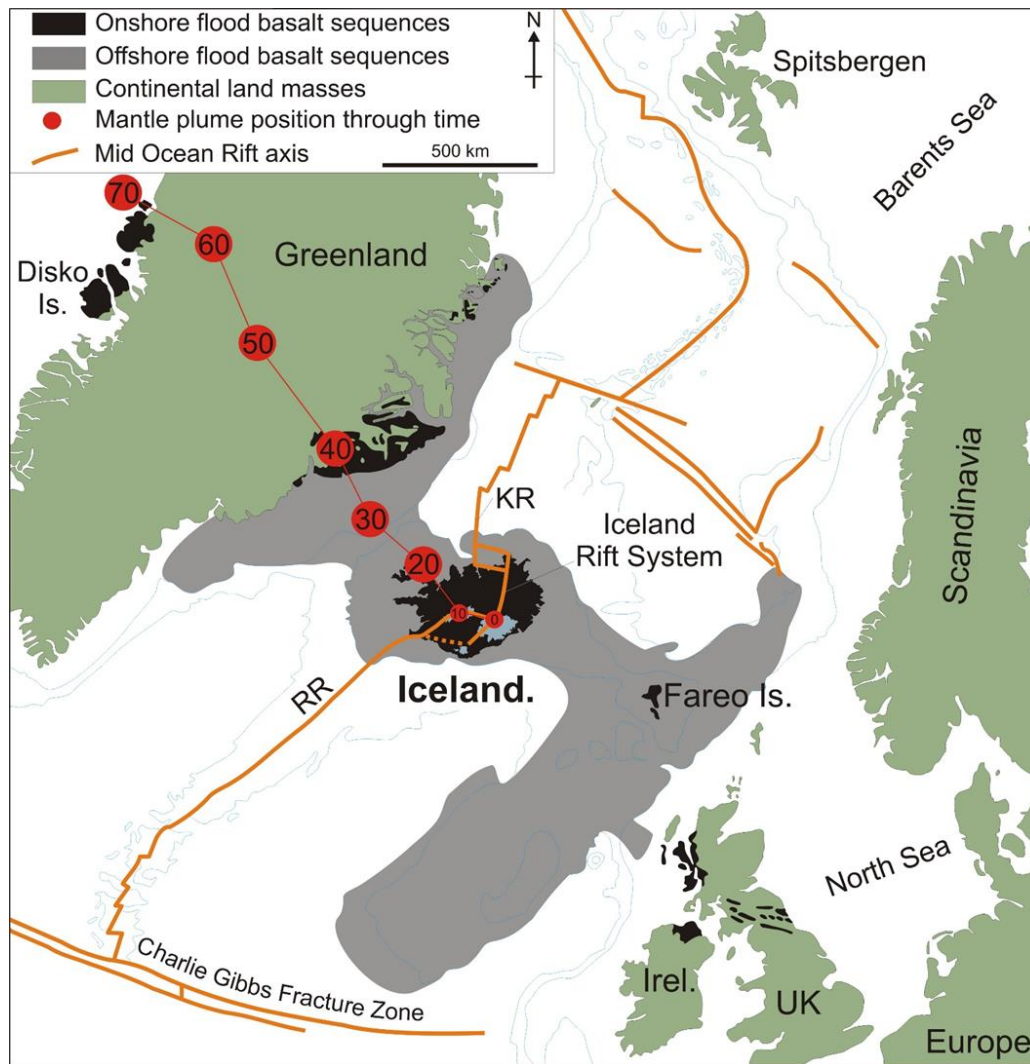


Figure 3. 2: NAIP. Map of the NAIP taken from Thordarson and Larsen (2007), edited from Saunders et al. (1997), that displays the temporal evolution of the NAIP and the locations of the Iceland mantle plume through time and the associated volcanism throughout the area in response to its presence. The current location of the Iceland mantle plume is SE Iceland underneath eastern Vatnajökull.

Iceland is the only currently volcanically active region in the IBP; its existence is a manifestation of the interplay of the Mid-Atlantic Ridge (MAR) and the Iceland mantle anomaly, more widely referred to as the Iceland mantle plume. The interaction between the two has generated a thermally buoyant and subaerial portion of oceanic crust that results from the unusually high melt production (Helgason, 1985; Martin et al., 2011), that also displays a distinctive enriched geochemical and isotopic signature, typical of ocean island basalt (OIB) compared to normal Mid-Ocean Ridge Basalt (MORB). This signature varies both spatially across the island, believed to be a consequence of differing proportions of a geochemically heterogeneous mantle, within the expected values

for plume (Rasmussen et al., 2020) vs MORB melt in different parts of the asthenosphere, but also temporally across the NAIP in general (Spice et al., 2016). In total, 103,300 km² of the NAIP forms the subaerial portion of Iceland, with the remainder creating a shallow submarine shelf around the volcanic island extending 50–200 km from the coastline (Thordarson and Larsen, 2007). This makes Iceland not only the largest subaerial landmass on the MAR, but also the largest subaerial landmass within the entirety of the global mid-ocean ridge system.

Tectonically the island behaves as an extension of the mid-ocean ridge system that it sits astride of, bounded by the submarine MAR junctions of the Reykanes Ridge (RR) to the south and the Kolbeinsey Ridge (KR) to the north. The island itself is roughly bisected by a series of axial rifts and intraplate belts, which delineate the current plate boundary across the island and accommodate spreading (Figures 3. 2 and 3. 3). Crisscrossing the island from SW to the NE are three main axial zones: the Western Volcanic Zone (WVZ); the Mid-Iceland Belt (MIB); and the Northern Volcanic Zone (NVZ). The Eastern Volcanic Zone (EVZ) is a younger proto-axial rift that propagates from the southern margin of the NVZ and runs parallel with the WVZ extending towards the SW.

Connecting these axial zones to the submarine RR and KR to the south and north are volcanic belts and seismic zones. The Reykjanes Volcanic Belt (RVB), which extends from the submarine RR to the southern margin of the WVZ, contains a series of distinct volcanic systems containing only fissure swarms. The RVB has a strong strike-slip component to its tectonic fabric and is thought to be either an oblique axial rift or a leaky transform zone (Clifton et al., 2003; Clifton and Kattenhorn, 2006; Einarsson, 2008). Connecting the WVZ with the proto-axial rift of the EVZ is the South Iceland Seismic Zone (SISZ), which is a leaky transform zone with limited volcanism, that manifests as en-échelon N-S trending right-lateral strike-slip faults (Ward, 1971; Einarsson et al., 1981; Einarsson and Eiríksson, 1982; Stefánsson et al., 1993; Gudmundsson, 1995; Árnadóttir et al., 2001; Einarsson, 2008).

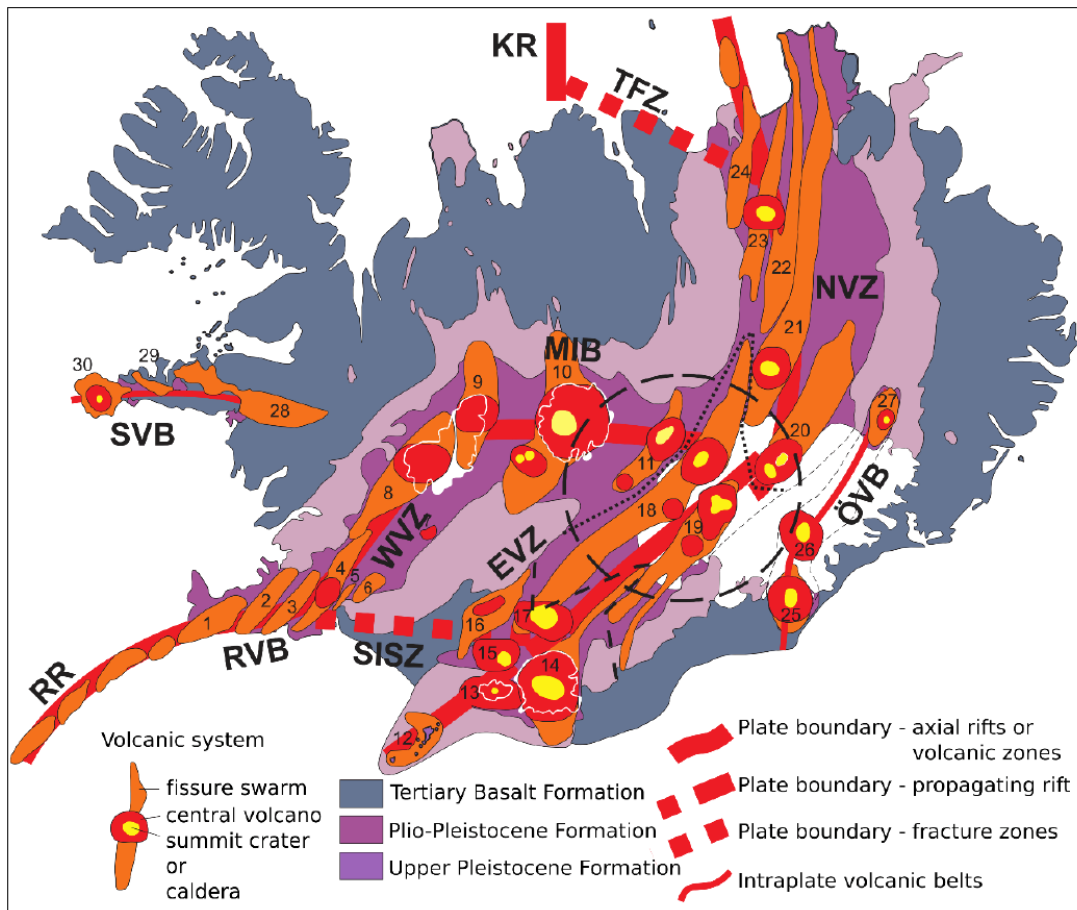


Figure 3. 3: Neovolcanic zones, belts and active volcanic systems of Iceland. A map illustrating the distribution of key geological formations, volcano-tectonic structures and distribution of volcanic systems (see key for details). Also shown are the 11 different active zones or belts of Iceland (neovolcanic zones), the abbreviations are as follows: RR, Reykjanes Ridge; RVB, Reykjanes Volcanic Belt; SISZ, South Iceland Seismic Zone; WVZ, West Volcanic Zone; MIB, Mid-Iceland Belt; EVZ, East Volcanic Zone; NVZ, North Volcanic Zone; TFZ, Tjörnes Fracture Zone; KR, Kolbeinsey Ridge; ÖVB, Öræfi Volcanic Belt; SVB, Snæfellsnes Volcanic Belt. The numbered volcanic systems are as follows: The Reykjanes Volcanic Zone: (1) Reykjanes–Svartsengi, (2) Krísvúik, (3) Brennisteinsfjöll; West Volcanic Zone: (4) Hengill, (5) Hrómundartindur, (6) Grímsnes, (7) Geysir, (8) Prestahnjúkur, (9) Langjökull; Mid-Iceland Belt: (10) Hofsjökull, (11) Tungnafellsjökull; East Volcanic Zone: (12) Vestmannaeyjar, (13) Eyjafjallajökull, (14) Katla, (15) Tindfjöll, (16) Hekla–Vatnafjöll, (17) Torfajökull, (18) Bárðarbunga–Veidivötn, (19) Grímsvötn; North Volcanic Zone: (20) Kverkfjöll, (21) Askja, (22) Fremrinámur, (23) Krafla, (24) Þeistareykir; Öræfajökull Volcanic Belt: (25) Öræfajökull, (26) Esjufjöll, (27) Snæfell; Snæfellsnes Volcanic Belt: (28) Ljósufjöll, (29) Helgrindur, (30) Snæfellsjökull. The large open circle indicates the approximate centre of the Iceland mantle plume, as depicted by Wolfe et al. (1997) (Thordarson and Larsen, 2007). The axial rifts are typified by tholeiitic geochemistries; the propagating tip of the EVZ indicated by the dashed line has transitional to alkalic geochemistries indicative of immature rifting. The northern part of the EVZ is a more established rifting regime and is typified by enriched tholeiitic geochemical signatures. Intraplate volcanic systems such as those on the Öræfajökull Volcanic Belt and Snæfellsnes Volcanic Belt also have transitional or alkalic geochemistries due to more small scale, deeper melting, as rifting occurs through thicker, older, crust. The volcanic systems can be seen to develop parallel to the stress regime of the zone they develop in whilst also having the geochemical signature, which indicates the maturity of the rifting they developed within.

At the northern boundary of the island, the NVZ is connected to the submarine southern boundary of the KR by the Tjörnes Fracture Zone (TFZ), occurring as a series of right-lateral strike-slip faults with an oblique normal faulting component.

As neither the MAR nor the Iceland plume are wholly stationary, the location of active rifting and volcanism through geological time in Iceland has migrated or jumped. Although in general, the rocks increase in age towards its peripheral margins, the plume is drifting towards the southeast relative to the MAR (Helgason, 1984). This has gradually pulled the axial rifting zones eastwards towards the plume head, triggering relocations of dominant spreading and volcanism zones through rift jumps, with new propagating rift zones gradually taking over from older axial rifting zones (Saemundsson, 1974; Johannesson, 1980; Óskarsson et al., 1985; Furman et al. 1992; Hardarson et al., 1997; Kempton et al., 2000; Martin et al., 2011). The current plume head location is thought to be in the SE of the island, under the Vatnajökull ice cap (Fitton et al., 1997; Wolfe et al., 1997).

As a consequence of this dynamic tectonic environment distinct intraplate volcanic belts have formed, which lie outside of the well-defined axial rift zones (Figure 3. 3) of which there are two active examples: the Öräfi Volcanic Belt (ÖVB); and the Snæfellsnes Volcanic Belt (SVB). Early studies hypothesised that the ÖVB, an intraplate belt, is the site of a mostly dormant rift zone that intersects with a fracture zone. However, more recent studies have suggested that it represents an embryonic rift at the fringe of the mantle plume (Hards et al., 2000; Peate et al., 2010). SVB is thought to represent the relicts of an older rift zone, active before 6 Ma, which was overtaken by the current WVZ (Jakobsson et al., 2008; Peate et al., 2010). The SVB is still active due to the topography of the lithosphere underneath it as mantle plume material is channelled westwards beneath this old rift.

3. 3 Icelandic volcanism

Active volcanism in Iceland is confined to discrete volcanic systems, which have a distinct volcano-tectonic architecture, within the active axial zones and intraplate belts (Figures 3. 3–3. 5). Eruptions occur either at a central volcano, a focal point of more evolved magmatism, or along linear vent structures in its associated fissure swarm, which only feature more primitive, mafic magmatism (Figure 3. 5) (Jakobsson, 1974, 1978, 1979a, 1979b; Jakobsson and Gudmundsson, 2008; Jakobsson et al., 2008; Sæmundsson, 1979; Jóhannesson and Sæmundsson, 1998; Thordarson and Höskuldsson, 2008; Thordarson and Larsen, 2007; Jóhannesson

2014; Jóhannesson and Sæmundsson 2009; Pálmasson and Sæmundsson 1974; Gudmundsson, 2000; Hjartardóttir et al., 2009; Hjartadóttir and Einarsson, 2011). Holocene lava flows stretch from these fissure systems and central volcanoes (Figure 3. 4) with flow directions dictated by topography and extents by critical flow length and MER (Walker, 1973).

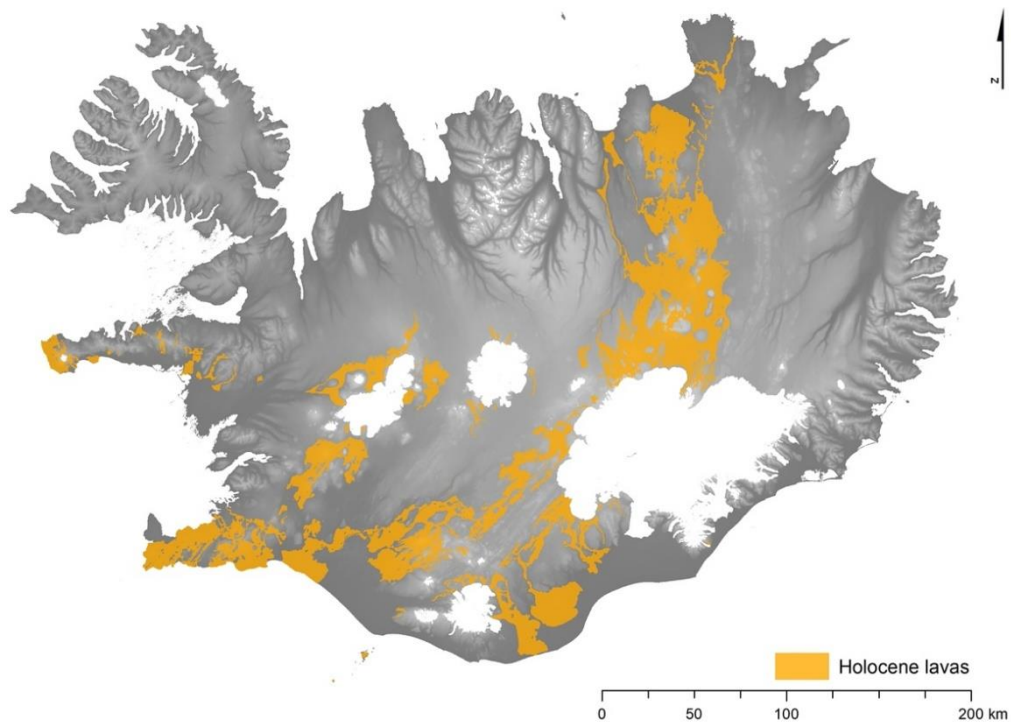


Figure 3. 4: Holocene lavas. A map displaying the location of the current margins of all Holocene lava flows in Iceland. Open source shapefile taken from Náttúrufræðistofnun Íslands (The Icelandic Institute of Natural History, overlain on an opensource hillshade DEM outline of Iceland.

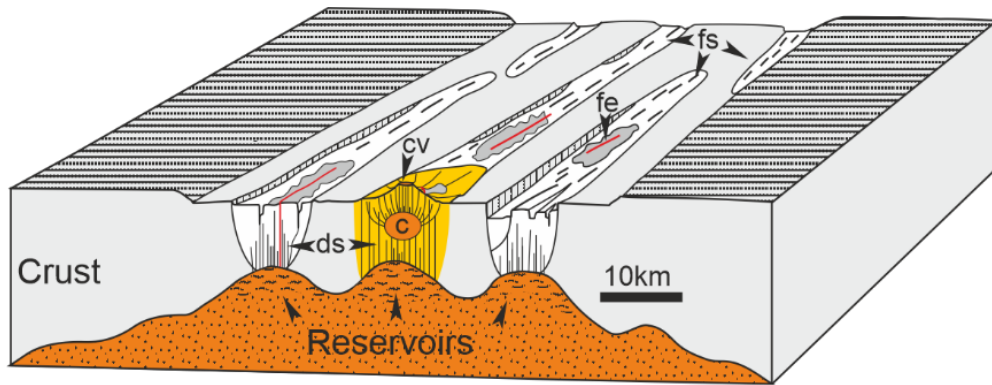


Figure 3. 5: Schematic of volcanic systems in Iceland consisting of a central volcano (cv) and/or a fissure swarm (fs), taken from Hartley and Thordarson, 2013. These simplified schematics all display architecture of the surface and subsurface structures of volcanic systems in Iceland along the neovolcanic zones, highlighting key features such as dyke swarms (ds), magma reservoirs, and dyke feeding fissure eruptions (fe). Older dykes in the dyke swarms are shown in grey, with active dykes highlighted in red in cross section. The surface expression of dykes are shown in the same colour scheme, with active dykes feeding cone row and lava flow field system depicted as a red line in the middle of the lava flow field (the latter is shown as a darker grey free form shape). Melt or magma reservoirs are shown in orange, with a larger storage zone shown at depth and a smaller concentrated storage zone (C) as part of the central volcanic plumbing system. Silicic magmatism, located at activity focal points (i.e., central volcanoes), is highlighted in yellow.

Volcanic systems are not just the fundamental component of the modern neovolcanic zones in Iceland; their older counterparts constructed the now eroded Pleistocene-Neogene sequences. The emblematic layer-cake, plateau basalt sequences sourced from fissure (dyke) swarms that volumetrically dominated the Neogene volcanic successions relative to the products of central volcanoes (Walker, 1959, 1993; Thorarinnsson and Tegner 2009). The fissure swarm is the subaerial expression of the associated subsurface intruding dyke swarm beneath it. Where the dyke swarm has been exhumed, its presence and extent can be confined by a $>2\%$ dyke density in the lava pile (Walker, 1963b) (Figure 3. 6). These archetypical successions show that the majority of the Icelandic plateau was constructed by recurrent, predominantly effusive, basaltic flood lava eruptions ($>1-100 \text{ km}^3$; FL), creating large lava flow fields originating from linear vents within the fissure swarms of the volcanic systems (Thordarson and Höskuldsson 2008). The overall architecture of volcanic systems from the Neogene to the present day remains largely the same, with FL eruptions representing the major contributor to the construction of the Iceland Basalt Plateau (e.g. Walker, 1959, 1993; Thordarson and Höskuldsson, 2008); FL eruptions can therefore be thought of as the building blocks of Iceland.



Figure 3. 6: Berufjörður, Icelandic Eastfjords, cake layer FL stratigraphy with cross-cutting dyke swarm, dyke locations within the lava pile have been highlighted in yellow. Image provided by Dr. Robert Askew.

Volcanic systems in Iceland have a typical life-span of 0.5–1.5 million years, and there are at least 30 volcanic systems in Iceland that are considered to be currently active (Pálmason and Sæmundsson, 1974; Jakobsson, 1974; Saemundsson 1978; 1979; Jakobsson et al., 1978). Although, the exact number of active volcanic systems and the delineation between adjacent systems is still an active debate, as highlighted by the 2014–2015 CE Holuhraun eruption. This eruption, and the two previous historical Holuhraun eruptions, have the geochemical signature of the Bárðabunga-Veiðivötn system but erupted in a geographical region belonging to the southern branch of Askja fissure swarm (Figure 3. 3) (Hartley, 2012; Hartley and Thordarson, 2013; also see Chapter 4, Figures 4. 1 and 4. 2). Of the 30 volcanic systems mapped out in figure 3. 3, 20 have fissure swarms of varying maturity: 7 have well-developed mature-moderately mature swarms which occur as a high density elongated narrow fissures, e.g., Bárðabunga-Veiðivötn; and 4 can be regarded as embryonic with an isolated single fissure or a few discrete fissures, e.g., Þórðarhyrna-Grímsvötn. Nineteen out of 30 volcanic systems feature a central volcano, the source of more evolved magmatism within the system, although several volcanic systems without a

central volcano in the RVB have a well-established geothermal system suggesting long-lived shallow magma storage zones.

Throughout historical times, that is, since Iceland was settled around 870 CE, 8 km³ of magma has been erupted in Iceland, which gives an average of 20 events per century. The volcanic systems within the EVZ have been the most prolific in terms of eruptive activity, producing 82 % of Iceland's volumetric magma output. Of the total volume, given as dense rock equivalent (DRE), of melt erupted across all volcanic systems during historical times, 79 % were basaltic, 16 % intermediate, and 5 % silicic magmas. Notably, volumetrically FL eruptions have accounted for approximately 54 % of this total historic magma output, regardless of magma composition, even though these events are purely mafic in composition. The vast compound lava flow fields produced by sizable events often extending beyond the limits of the volcanic system they originated from (Thordarson and Larsen, 2007; Figure 3. 4).

3. 4 Spatial and temporal distribution of magma types in Iceland

The interaction between the MAR and Iceland mantle plume underneath Iceland has generated a thermally buoyant and subaerial portion of oceanic crust, that results from the unusually high melt production (Helgason, 1985; Sigmarsson et al., 2008; Martin et al., 2011). As a consequence of the coincidence of these two geological components, many magmas erupted in Iceland display a distinctive radiogenic isotope signature, as well as an enriched trace and rare earth element geochemical and radiogenic isotopic signature, more akin to Ocean Island Basalts (OIBs), compared to normal Mid-Ocean Ridge Basalts (MORB). The magmas erupted from neovolcanic systems within the axial zones and intraplate belts display a spectrum of this enrichment and differing radiogenic isotope signatures, as well as a distinct fingerprint of recycled oceanic crust sourced from the deep mantle (Rasmussen et al., 2020).

Generating MORBs is achieved by partial melting of the upper mantle in a mature rifting environment, as a consequence of upwelling asthenosphere to shallow levels, which undergoes adiabatic decompression, causing the mantle geotherm to intersect

the mantle solidus. Generating magmas with an OIB geochemistry is generally thought to require an elevated thermal anomaly within the mantle, a mantle plume, generated at the core-mantle boundary creating a perturbation in normal upper mantle column geotherm as it rises through the mantle enabling the volcanic systems above to sample a heterogeneous array of distinct mantle end-member/component geochemistries. Ocean island basalts display a wide range in radiogenic isotopes (e.g., Sr-Nd-Hf-Pb-Os isotopic ratios) that lie on a spectrum from MORB towards several distinct mantle components based on the relative difference in high or low radiogenic isotope ratios of the different end-members (Hémond et al., 1993; Thirlwall, 1995; Thirlwall et al., 2004; Thirlwall et al., 2006; Shorttle et al., 2013). Ocean island basalts sometimes have a long-lived primordial He/He isotope signature indicative of a deep mantle reservoir (Hilton et al., 2000; Graham, 2002; Jackson et al., 2017), as well as distinct recycled oceanic crust isotopic signatures (Sun and McDonough, 1989; Chauvel and Hémond, 2000; Kempton et al., 2000; Kokfelt et al., 2003, 2006; Kobayashi et al., 2004; Sobolev et al., 2007; Peate et al., 2010; Weis et al., 2011); in some cases mixing of different melts in the mantle is also preserved in the eruptive phenocryst record (Winpenny and MacLennan, 2011).

Volcanic systems that lie upon the mature axial rifts in Iceland erupt magmas of tholeiitic OIB geochemistry, which are generated by well-established large-scale rifting. Off-rift, intraplate volcanism, e.g., SVB and ÖVB, has an alkalic OIB geochemistry and is relatively more enriched in incompatible elements compared to tholeiitic magmas. Alkalic magmas in Iceland are thought to sample deeper levels, small-scale, melts of where only an enriched and more fusible source can melt. This deeper level melting can occur in areas of incipient rifting through thicker older crust (e.g., ÖVB). It is therefore unsurprising that as the EVZ, a proto-axial rift, is traced to the southwest from its well-established northern boundary to the actively propagating tip, which is rifting through older Icelandic crust, it displays a geochemical signature trending from tholeiitic to transitional-alkalic. The SVB and ÖVB are also characterised by a distinct isotopic fingerprint with low $^{143}\text{Nd}/^{144}\text{Nd}$ and high $^{87}\text{Sr}/^{86}\text{Sr}$ (Hémond et al., 1993).

The samples used in this study are taken from axial rifting localities, close to the plume head. The novel chalcophile isotope systems are used in this study to explore

volatile loss of these magmas and volatile speciation, and lie within the OIB field for the limited data sets available for these novel isotopes.

3. 5 Large volume Holocene basaltic fissure eruptions in Iceland

Throughout the Holocene and Anthropocene, FL eruptions $>1 \text{ km}^3$ – 100 km^3 reoccur with a frequency of 250 years. They occur as two main end-members creating two very morphologically different physical volcanological landforms: (1) years–to–century long low-discharge events forming very low angled, symmetrical, lava shields; and (2) months-to-years long higher-discharge events, fed by a linear fissure, with an initial short-lived explosive phase giving way to an effusive phase creating a vast compound flow field. The flow fields from these higher discharge, shorter life-span events, display a diverse spectrum of Pāhoehoe crust morphology types due to changes in vent activity, local topography, or localised transitions in the transport systems, produce slight changes in temperature and or rheology.

There are two different sources for these large volume, long-lived, basaltic events: (1) Deep crustal storage reservoirs which experience recharge events from mantle-derived injections, these recharge events produce magmas that are geochemically and isotopically relatively heterogeneous, and also control the timescales of the event (Sinton et al., 2005); and (2) large-volume, differentiated shallower crustal magma reservoirs built up prior to the onset of eruptive activity producing geochemically and isotopically homogeneous magmas (Guilbaud et al., 2007; Métrich et al., 1991; Bindeman et al., 2006; Passmore et al., 2012), are relatively shorter lived i.e. months–years as their supply is more limited (Sigmarsson et al., 1991; Passmore, 2009; Passmore et al., 2012). For both of these cases, the size of the volcanic eruption is controlled by the availability of magma, i.e., storage reservoir capacity and the cooling rate of the magma in question (Head et al., 1996).

At depth, melt crystallisation often produces an interconnected framework of minerals (i.e. a crystal mush) in a shallow crustal storage reservoir, which record (through their entrapped melt inclusions) the temporal evolution of magma mixing and mingling, and the depths at which this occurred. A recent study by Caracciolo et al., (2020), focussing on fissure eruptions in Bárðarbunga-Veiðivötn volcanic system

in Iceland from the last glacial period (Weichselian) to the present day, indicates that inclusions from the erupted crystal mush melt display a much wider compositional range than erupted lavas, in particular, more evolved compositions in more recent times. In general, the melt inclusion compositions in the crystal mush samples and mush glomerocrysts are more primitive than the erupted host magma and its phenocryst cargo (Passmore, 2009; Passmore et al., 2012).

Lava shields are only found in the Icelandic geological record in the early-mid Holocene >3000 BP (Hjartarson, 2003; Sinton et al., 2005), extending radially 28 km from the vent in all directions with a very gentle slope aspect generated by decades–century timescales of lava effusion fed by a sustained lava lake (Thordarson and Sigmarsson, 2008; Thordarson and Hoskuldsson, 2008). Contrastingly, higher-discharge, fissure-fed LF create compound flow fields through months–years of eruptive activity. These flow fields, which extend up to 100 km from the vents, occur throughout the Holocene and Anthropocene. Fissure-fed FL are a common feature of the EVZ, though not exclusively, as they also occur within the WVZ and NVZ. These events are some of the largest of this type of eruption on Earth in postglacial times (Thordarson and Hoskuldsson, 2008). The length ‘limit’ of <100 km measured in these lava flow fields indicate that there is perhaps a critical flow length to these endogenously emplaced, compound, basaltic FL flow fields. The exception to this rule is the largest of these events, the 8600 BP Þjorsá eruption, sourced from a fissure eruption in the Bárðarbunga-Veiðivötn system (although its exact source vents are unknown), which produced a flow field with a total length of 130 km.

During historical times, i.e., in the last 1140 years in Iceland, there have been 5 high-discharge FL events: Eldgjá 939 CE (~20 km³); Hallmundarhraun 950 CE (~8 km³); Frambruni-Dyngjuháls 13th century (~4 km³); Laki 1783–84 CE (~15 km³); and Holuhraun 2014–2015 CE (~1.2 km³). All of these volumes are stated as DRE and, with the exception of Holuhraun, all volumes are approximate due to exposure limitations and unknown pre-eruption topographic heights. Eldgjá, Frambruni-Dyngjuháls and Laki account for over 55 % of the volumetric magma output of EVZ in historical times, whilst Hallmundarhraun accounts for 70 % of the RVB-WVZ historical output. The youngest of these events, Holuhraun, which sits at the boundary of the NVZ and EVZ, either marginally increases the EVZ volumetric

magma output or accounts for ~50 % of the NVZ historical volumetric magma output.

Of these eruptions, two are high magnitude and high discharge FL events: Eldgjá 939 CE and Laki 1783–84 CE; so, whilst their eruptive products are, as the name suggests, predominantly lava, they also produced a significant tephra layer during their high discharge i.e., sub-Plinian to Plinian, explosive phases. The tephra produced during the explosive phase is preserved in the soil horizons surrounding the eruption and along the dispersal axis of the plume into distal regions. This layer can be traced through isopach mapping, lines of equal thickness, from the source to the extremities of preservation in order to determine a volume estimate. However, internal stratigraphy and how it varies within the tephra layer in the medial and proximal soil horizons can also be used to identify the source vent(s) for this tephra, and to determine the sequence of eruptive activity. This has been done in detail for the first 15 km of the Laki fissure (Thordarson, 1990; Thordarson and Self, 1993; Thordarson, 2003; Thordarson and Self, 2003; Thordarson et al., 2003) and for a portion of the Eldgjá deposit (Larsen, 2000; Moreland et al., 2019).

As previously stated, FL eruptions produce a sulfur and trace metal rich volatile plume from the vent, but they also produce a similar localised haze in the region of the flow field. Whilst the former can produce significant and widespread atmospheric and environmental pollution, which, if injected into the stratosphere, can trigger cooling events lasting for several years. The localised toxic sulfur, halogen and trace metal haze can produce significant localised pollution of the hydro- and eco-systems causing devastating local impacts (Ilyinskaya et al., 2021). With volcanic trace metal concentrations exceeding toxic trace metal quantities and also anthropogenic pollution levels in certain areas (Ilyinskaya et al., 2021; Mason et al., 2021). This includes a significant risk to Icelandic population centres, alongside the potential for the lava flows from these events to reach cities, towns or farmsteads. This is particularly pertinent for the capital region in the SW of the country, which is at risk from FL from both the WVZ and RVB. A lava flow from the latter of these would also be close enough to a large geothermal power plant utilised by the capital region as well as being of close proximity to the international airport at Keflavík, posing a significant additional financial risk (Andréasdóttir, 2018). Therefore,

understanding the processes that drive the explosive phases of these events, and the mechanisms of volatile loss from them, has the potential to improve understanding of the associated hazards and risks. Out of the 5 historical FL eruptions, quantitative textural data exists for the erupted pyroclasts from one of these events, Eldgjá 939 CE (Moreland et al., 2019), the explosive activity and tephra produced has been documented and assessed for only two of these eruptions: Eldgjá 939 CE (Moreland et al., 2019; Thordarson et al., 2001; Thordarson, et al., 2003a), and Laki 1783–84 CE (Thordarson, 1990; Thordarson and Self, 1993; 2003; Thordarson et al., 1996; Thordarson et al., 2003a; 2003b), the flow field emplacement analysed and documented for 2 out of 5 events: Laki 1783–84 CE (Guilbaud et al., 2007) and Holuhraun 2014–15 CE (Pedersen et al., 2017). Both the Hallmundarhraun 950 CE (Jóhannesson, 1989) and Frambruni-Dyngjuháls, 13th century (Hjartarson, 2004), eruptions lack detailed tephra and flow field studies. For this reason, this study concentrates on two of the more well-studied historical FL events: the Laki 1783–84 CE and Holuhraun 2014–2015 CE eruptions. Better constraints of their peak explosive phases, the evolution of eruptive style at the vents, and fluctuations in shallow conduit process which modulate the style of eruptive activity will, in principle, help us to understand the hazards that these rarer historical events pose. Furthermore, contemporary accounts of the Laki eruption, on-site observations and detailed documentation of the Holuhraun eruption gives an unprecedented time-series of events for a FL event. For both of these eruptions, there is a wealth of previous studies focussing on: the geochemistry and petrology of the eruptive products; the volatile burden of the eruptions; and the morphology of the lava flows emplaced and their associated transport systems. In the case of Laki, Thordarson et al., 2003a mapped out the total volume of the Laki tephra erupted through isopachs as well as the total volume for the first 6 of 10 total eruptive fissures.

Whilst FL eruptions are at least an order of magnitude smaller than flood basalts (FB; $>100 \text{ km}^3$ – $10,000 \text{ km}^3$), they provide an excellent modern analogue for these larger events as, regardless of magnitude, these eruptions produce similar eruptive products and display similar spatial and temporal evolution in eruptive behaviour dictated by MER.

3. 6 References

- Árnadóttir, T., Hreinsdóttir, S., Gudmundsson, G., Einarsson, P., Heinert, M. and Völksen, C. (2001). Crustal deformation measured by GPS in the South Iceland Seismic Zone due to two large earthquakes in June 2000. *Geophysical Research Letters*. 28. (21), pp. 4031-4033
- Andréasdóttir, Þ. B. (2018). Masters thesis. Volcanic hazard and risk assessment at Reykjanes, vulnerability of infrastructure. The University of Iceland.
- Askew, R. A. (2020). Ph.D thesis. Breiðdalur Central Volcano. What came first: The Central Volcano or The Fissure Swarm? The University of Iceland.
- Bindeman, I. N., Sigmarsson, O., and Eiler, J. (2006). Time constraints on the origin of large volume basalts derived from O-isotope and trace element mineral zoning and U-series disequilibria in the Laki and Grímsvötn volcanic system. *Earth and Planetary Science Letters*. 245 (1–2), pp. 245–259. doi:10.1016/j.epsl.2006.02.029
- Caracciolo, A., Bali, E., Guðfinnsson, G. H., Kahl, M., Halldórsson, S. A., Hartley, M. E. And Gunnarsson, H. (2020). Temporal evolution of magma and crystal mush storage conditions in the Bárðarbunga-Veiðivötn volcanic system, Iceland. *Lithos*. pp. 352–353. 105234. Doi:10.1016/j.lithos.2019.105234
- Chauvel, C. and Hémond, C. (2000). Melting of a complete section of recycled oceanic crust: Trace element and Pb isotopic evidence from Iceland. *Geochemistry, Geophysics, Geosystems*, 1 (2).
- Clifton, A. E. and Kattenhorn, S. A. (2006). Structural architecture of a highly oblique divergent plate boundary segment. *Tectonophysics*. 419. (1–4), pp. 27–40
- Clifton, A. E., Pagli, C., Jónsdóttir, J. F., Eythorsdóttir, K. and Vogfjörð, K. (2003). Surface effects of triggered fault slip on Reykjanes Peninsula, SW Iceland *Tectonophysics*. 369. pp. 145–154.
- Einarsson, P. and Eiríksson, J. (1982). Earthquake fractures in the districts Land and Rangárvellir in the South Iceland seismic zone. *Jökull*. 32. pp. 113–120.
- Einarsson, P., Foulger, G., Stefánsson, R., Björnsson, S. and Skaftadóttir, Þ. (1981). Seismicity pattern in the South Iceland seismic zone. In: Earthquake Prediction: An International Review, Volume 4. Simpson, D. and Richards, P.G. (Editors), *American Geophysical Union*. pp. 141–151.
- Einarsson, P. (2008). Plate boundaries, rifts and transforms in Iceland. *Jökull*. 58. pp. 35-58.
- Fitton, J. G., Saunders, A.D., Norry, M. J., Hardarson, B. S. and Taylor, R. N. (1997). Thermal and chemical structure of the Iceland plume. *Earth and Planetary Science Letters*. 153. (3–4), 2, pp. 197–208.
- Furman, T., Meyer, P. S. and Frey, F. (1992). Evolution of Icelandic central volcanoes: evidence from the Austurhorn intrusion, southeastern Iceland. *Bulletin of Volcanology*. 55. pp. 45–62. Doi:10.1007/BF00301119
- Graham, D. W. (2002). Noble Gas Isotope Geochemistry of Mid-Ocean Ridge and Ocean Island Basalts: Characterization of Mantle Source Reservoirs. *Reviews in Mineralogy and Geochemistry*. 47 (1), pp.247–317. doi: https://doi.org/10.2138/rmg.2002.47.8
- Gudmundsson, A. (2000). Dynamics of volcanic systems in Iceland: example of tectonism and volcanism at juxtaposed hot spot and mid-ocean ridge systems. *Annual Review of Earth Planetary Science*. 28. pp. 107–140
- Gudmundsson, A. (1995). Ocean-ridge discontinuities in Iceland. *Journal of the*

- Geological Society*. 152. pp. 1011–1015, doi:10.1144/GSL.JGS.1995.152.01.22
- Guilbaud, M.-N., Blake, S., Thordarson, T. and Self, S. (2007). ‘Role of Syn-eruptive Cooling and Degassing on Textures of Lavas from the AD 1783-84 Laki Eruption, South Iceland’. *Journal of Petrology*. 48. pp.1265–1294.
- Hardarson, B.S., Fitton, J.G., Ellam, R.M. and Pringle, M.S. (1997). Rift relocation – a geochemical and geochronological investigation of a paleo-rift in NW Iceland. *Earth and Planetary Science Letters*. 153. pp. 181–196.
- Hards, V. L., Kempton, P. D., Thompson, R. N and Greenwood, P. B. (2000). The magmatic evolution of the Snæfell volcanic centre; an example of volcanism during incipient rifting in Iceland. *Journal of Volcanology and Geothermal Research*. 99. (1–4), pp. 97–121. Doi:10.1016/S0377-0273(00)00160-8
- Hartley, M. E. (2012). Ph.D thesis. Postglacial volcanism and magmatism on the Askja volcanic system, North Iceland. The University of Edinburgh.
- Hartley, M. E., and Thordarson, T. (2013). The 1874-1876 volcano-tectonic episode at Askja, North Iceland: Lateral flow revisited. *Geochemistry, Geophysics, Geosystems*. 14. (7), pp. 2286–2309. Doi:10.1002/ggge.20151
- Head III, J. W., Wilson, L. and Smith, D. K. (1996). Mid-ocean ridge eruptive vent morphology and substructure: Evidence for dike widths, eruption rates, and evolution of eruptions and axial volcanic ridges. *Journal of Geophysical Research*. 101. (B12). pp. 28265–28280
- Helgason, J. (1984). Frequent shifts of the volcanic zone in Iceland. *Geology*. 12. pp. 212–216.
- Helgason, J. (1985). Shifts of the plate boundary in Iceland: Some aspects of Tertiary volcanism. *Journal of Geophysical Research, Solid Earth*. 90. (B12), pp. 10084–10092
- Hémond, C., Arndt, N. T., Lichtenstein, U., Hofmann, A. W., Óskarsson, N. and Steinthorsson, S. (1993). The heterogeneous Iceland plume: Nd-Sr-O isotopes and trace element constraints. *Journal of Geophysical Research, Solid Earth*. 98. (B9), pp. 15833–15850
- Hilton, D. R., Thirlwall, M. F., Taylor, R. N., Murton, B. J. and Nichols, A. (2000). Controls on magmatic degassing along the Reykjanes Ridge with implications for the helium paradox. *Earth and Planetary Science Letters*. 183 (1/2). pp. 43–50. [https://doi.org/10.1016/S0012-821X\(00\)00253-3](https://doi.org/10.1016/S0012-821X(00)00253-3)
- Hjartardóttir, Á. R., Einarsson, P., and Sigurdsson, H. (2009). The fissure swarm of the Askja volcanic system along the divergent plate boundary of N Iceland. *Bulletin of Volcanology*. 71. (9), pp. 961–975. Doi:10.1007/s00445-009-0282-x
- Hjartardóttir, Á. R., and Einarsson, P. (2012). The Kverkfjöll fissure swarm and the eastern boundary of the Northern Volcanic Rift Zone, Iceland. *Bulletin of Volcanology*. 74. (1), pp. 143–162. Doi:10.1007/s00445-011-0496-6
- Hjartarson, Á. (2003). Ph.D thesis. Post Glacial Lava production in Iceland. Orkustofnan report. Geological Museum of Denmark and ÍSOR.
- Hjartarson, Á. (2004). Hraunin í Bárðardal. *Náttúrufræðingurinn*. 72. (3-4). pp. 155–163.
- Ilyinskaya, E., Mason, E., Wieser, P.E., Holland, L., J. Liu, E. J., Mather, T. A., Edmonds, M., Whitty, R. C. W., Elias, T., Nadeau, P. A., Schneider, D., McQuaid, J. B., Allen, S. E., Harvey, J., Oppenheimer, C., Kern, C. and Damby, D. (2021). Rapid metal pollutant deposition from the volcanic plume of Kīlauea, Hawai‘i. *Nature Communications in Earth Environment*. 2. 78. doi:10.1038/s43247-021-00146-2
- Jackson, M. G., Konter, J. G. and Becker, T. W. (2017). Primordial helium entrained

- by the hottest mantle plumes. *Nature*. 542(7641), pp. 340–343.
- Jóhannesson H (1989) The age of Hallmundarhraun lava. (Aldur Hallmundarhrauns í Borgarfirði). *Fjölrit Náttúrufræðistofnunar Íslands*. 9. pp. 1–12. (In Icelandic)
- Jóhannesson, H. and Sæmundsson, K. (1998) Geological Map of Iceland, 1:500,000. Bedrock Geology Icelandic Institute of Natural History and Iceland Geodetic Survey, Reykjavík.
- Jóhannesson, H. and Sæmundsson, K. (2009) Geological Map of Iceland. 1:600.000. Tectonics. Náttúrufræðistofnun Íslands, Reykjavík (1st edition).
- Jones, T. J., and Llewelin, E. W. (2020). Convective tipping point initiates localization of basaltic fissure eruptions. *Earth and Planetary Science Letters*. 1. 116637. Doi:10.1016/j.epsl.2020.116637
- Jóhannesson, H. (2014) Geological Map of Iceland. 1:600.000. Bedrock. Náttúrufræðistofnun Íslands, Reykjavík. (In Icelandic)
- Jóhannesson, H. (1980). Jarðlagaskipan og þróun rekbelta á Vesturlandi Náttúrufræðingurinn, 50, pp. 13–31. (In Icelandic)
- Jakobsson, S. P. (1974). Eldgos við Eldeyjarboða. Museum of Natural History, Department of Geology and Geography.
- Jakobsson, S. P. (1978) Environmental factors controlling the palagonisation of the surtsey tephra, Iceland. *Bulletin of the Geological Society. Denmark*. 27. Special Issue. pp 91–105.
- Jakobsson, S.P. (1979) Petrology of recent basalts of the Eastern Volcanic Zone, Iceland. *Acta Naturalia Islandica*. 26, pp. 103.
- Jakobsson, S.P. (1979b) Outline of the petrology of Iceland. (Ágrip: Um bergfræði Íslands). *Jökull*. 29. pp. 57–73 (English full version) and pp. 96–99 (Icelandic text only).
- Jakobsson, S.P., Jónsson, J. and Shido, F. (1978) Petrology of the Western Reykjanes Peninsula, Iceland. *Journal of Petrology*. 19. pp. 669–705
- Jakobsson, S., Jonasson, K., Sigurðsson, A. (2008) The three igneous rock series in Iceland: a review. *Jökull*. 58. pp.117–138.
- Jakobsson, S.P. and Gudmundsson, M.T. (2008). Subglacial and intraglacial volcanic formations in Iceland. *Jökull*, 58, pp. 179–197.
- Kobayashi, K., Tanaka, R., Moriguti, T., Shimizu, K. and Nakamura, E. (2004). Lithium, boron, and lead isotope systematics of glass inclusions in olivines from Hawaiian lavas: evidence for recycled components in the Hawaiian plume. *Chemical Geology*. 212 (1–2), pp. 143–161.
- Kokfelt, T.F., Hoernle, K. and Hauff, F. (2003). Upwelling and melting of the Iceland plume from radial variation of ^{238}U – ^{230}Th disequilibria in postglacial volcanic rocks. *Earth and Planetary Science Letters*. 214(1-2), pp. 167–186.
- Kokfelt, T. F., Hoernle, K. A. J., Hauff, F., Fiebig, J., Werner, R. and Garbe-Schoenberg, D. (2006). Combined trace element and Pb–Nd–Sr–O isotope evidence for recycled oceanic crust (upper and lower) in the Iceland mantle plume. *Journal of Petrology*. 47 (9), pp. 1705–1749.
- Kempton, P. D., Fitton, J. G., Saunders, A. D., Nowell, G. M., Taylor, R. N., Hardarson, B. S. and Pearson, G. (2000). The Iceland plume in space and time: a Sr–Nd–Pb–Hf study of the North Atlantic rifted margin. *Earth and Planetary Science Letters*. 177. (3–4), pp. 255–271
- Larsen, G. (2000). Holocene eruptions within the Katla volcanic system, south Iceland: characteristics and environmental impact. *Jökull*. 49, pp. 1–28.
- Malinverno, A. (1990). A quantitative study of the axial topography of the Mid-

- Atlantic Ridge. *Journal of Geophysical Research, Solid Earth*. 95. (B3), pp. 2645–2660
- Martin, E., Paquette, J. L., Bosse, V., Tiepolo, M., Sigmarsson, O. (2011). Geodynamics of rift–plume interaction in Iceland as constrained by new $^{40}\text{Ar}/^{39}\text{Ar}$ and in situ U–Pb zircon ages. *Earth and Planetary Science Letters*. 311. (1–2), pp. 28–38
- Moreland W.M, Thordarson T, Houghton B.F. and Larsen G, (2019). Driving mechanisms of subaerial and subglacial explosive episodes during the 10th century Eldgjá fissure eruption, southern Iceland. *Volcanica*. 2 (2).
- Mason, E., Wieser, P.E., Liu, E.J., Edmonds, M., Ilyinskaya, E., Whitty, R. C. W., Mather, T. A., Elias, T., Nadeau, P. A., Wilkes, T. C., McGonigle, A. J. S., Pering, T. D., Mims, F. M., Kern, C., Schneider, D. J. and Oppenheimer, C. (2021). Volatile metal emissions from volcanic degassing and lava–seawater interactions at Kīlauea Volcano, Hawai’i. *Nature Communications in Earth Environment*. 2. 79. Doi:10.1038/s43247-021-00145-3
- Métrich, N., Sigurdsson, H., Meyer, P. S. and Devine, J. D. (1991). The 1783 Lakagigar eruption in Iceland: geochemistry, CO₂ and sulfur degassing. *Contributions to Mineralogy and Petrology*. 107. pp. 435–447.
- Óskarsson, N., Grönvold, K. and Larsen, G. (1984). The haze produced by the Laki eruption. (In Icelandic). In: Einarsson, T., Guðbergsson, G. M., Gunnlaugsson, G. A., Rafnsson, S. and Þórarinnsson, S. (Editors.) *Skaftáreldar 1783-1784: Ritgerðir og Heimildir*. pp. 67–80. Mál og Menning: Reykjavík.
- Óskarsson, N., Steinthorsson, S. and Sigvaldason, G.E. (1985). Iceland geochemical anomaly: origin, volcanotectonics, chemical fractionation and isotope evolution of the crust. *Journal of Geophysical Research*. 90. pp. 10011–10025
- Pálmason, G. and Sæmundsson, K. (1974) Iceland in Relation to the Mid-Atlantic Ridge. *Annual Review of Earth and Planetary Sciences*. 2. (1), pp. 25–50
- Passmore, E. (2009). Ph.D Thesis, University of Edinburgh. ‘Feeding large eruptions: crystallization, mixing and degassing in Icelandic magma chambers’.
- Passmore, E., MacLennan, J., Fitton, G. and Thordarson, T. (2012). Mush disaggregation in basaltic magma chambers: Evidence from the AD 1783 Laki Eruption. *Journal of Petrology*. 53. (12). pp. 2593–2623. Doi:10.1093/petrology/egs061
- Rasmussen, M. B., Halldórsson, S. A., Gibson, S. A. and Guðfinnsson, G. H. (2020). Olivine chemistry reveals compositional source heterogeneities within a tilted mantle plume beneath Iceland. *Earth and Planetary Science Letters*. 531. 116008
- Pedersen, G. B. M., Höskuldsson, A., Dürig, T., Thordarson, T., Jónsdóttir, I., Riishuus, M. S., Óskarsson, B. V., Dumont, S., Magnusson, E., Gudmundsson, M. T., Sigmundsson, F., Drouin, V. J. P. B., Gallagher, C., Askew, R., Gudnason, J., Moreland, W. M., Nikkola, P., Reynolds, H. I., and Schmith, J. (2017). Lava field evolution and emplacement dynamics of the 2014–2015 basaltic fissure eruption at Holuhraun, Iceland. *Journal of Volcanology and Geothermal Research*. 340. pp. 155–169. Doi:10.1016/j.jvolgeores.2017.02.027
- Peate, D. W., Breddam, K., Baker, J. A., Kurz, M. D., Barker, A. K., Prestvik, T., Grassineau, N., Skovgaard, A. C. (2010). Compositional Characteristics and Spatial Distribution of Enriched Icelandic Mantle Components. *Journal of Petrology*. 51. (7), pp. 1447–1475. Doi:10.1093/petrology/egq025
- Sæmundsson, K. (1974) Fissure swarms and central volcanoes of the neovolcanic zones of Iceland. *Geological Society America Bulletin*. 85. pp. 495–504

- Sæmundsson, K. (1978) Fissure swarms and central volcanoes of the neovolcanic zones of Iceland. *Geological Journal Special Issues*. 10. pp. 415–432
- Sæmundsson, K. (1979) Outline of the geology of Iceland. *Jökull*. 29. pp. 7–28
- Shorttle, O., Maclennan, J., & Piotrowski, A. M. (2013). Geochemical provincialism in the Iceland plume. *Geochimica et Cosmochimica Acta*. 122, pp. 363–397.
- Sigmarsson, O., Condomines, M., Grönvold, K., and Thordarson, T. (1991). Extreme Magma homogeneity in the 1783-84 Lakagigar eruption: origin of a large volume of evolved basalt in Iceland. *Geophysical Research Letters*. 18. (12), pp. 2229–2232.
- Sigmarsson, O., Maclennan, J. and Carpentier, M. (2008). Geochemistry of igneous rocks in Iceland: a review. *Jökull*. 58. pp. 139–160
- Sinton, J., Grönvold, K. and Sæmundsson, K. (2005). Postglacial eruptive history of the Western Volcanic Zone, Iceland. *Geochemistry, Geophysics, Geosystems*. 6. (12), Q12009, doi:10.1029/2005GC001021.
- Sobolev, A.V., Hofmann, A.W., Kuzmin, D.V., Yaxley, G.M., Arndt, N.T., Chung, S.L., Danyushevsky, L.V., Elliot, T., Frey, F.A., Garcia, M.O., Gurenko, A.A., Kamenetsky, V.S., Kerr, A.C., Krivolutsкая, N.A., Matvienkov, V.V., Nikogosian, I.K., Rocholl, A., Sigurdsson, I.A., Sushchevskaya, N.M. and Teklay, M. (2007). The amount of recycled crust in sources of mantle-derived melts. *Science*. 316 (5823), pp. 412–417.
- Spice, H. E., Fitton, J. G. and Kirstein, L. A. (2016). Temperature fluctuation of the Iceland mantle plume through time. *Geochemistry, Geophysics, Geosystems*. 17. pp. 243–254, doi:10.1002/2015GC006059.
- Stefánsson, R., Bödvarsson, Slunga, R., Einarsson, P., Jakobsdóttir, S. S., Bungum, H., Gregersen, S., Havskov, J., Hjelle, J. and Korhonen, H. (1993). Earthquake prediction research in the South Iceland Seismic Zone and the SIL Project. *Bulletin of the Seismological Society of America*. 83. (3), pp. 696–716
- Sun, S. S. and McDonough, W. F. (1989). Chemical and Isotopic Systematics of Oceanic Basalts: Implications for Mantle Composition and Processes. In: Saunders, A. D., Norry, M. J. (Editors). *Magmatism in the Ocean Basins. Journal of the Geological Society of London, Special Publications*. 42, pp. 313–345. <https://doi.org/10.1144/GSL.SP.1989.042.01.19>
- Thirlwall M.F. (1995). Generation of Pb isotopic characteristics of the Iceland plume. *Journal of the Geological Society of London*. 152, pp. 991–996. doi.org/10.1144/GSL.JGS.1995.152.01.19
- Thirlwall, M. F., Gee, M. A. M., Taylor, R. N., Murton, B. J. (2004) Mantle components in Iceland and adjacent ridges investigated using double-spike Pb isotope ratios. *Geochimica et Cosmochimica Acta*, 68 (2), pp. 361–386 doi:10.1016/s0016-7037(03)00424-1
- Thirlwall, M. F., Gee, M. A. M., Lowry, D., Matthey, D. P., Murton, B. J. and Taylor, R. N. (2006). Low $\delta^{18}\text{O}$ in the Icelandic mantle and its origins: Evidence from Reykjanes Ridge and Icelandic lavas. *Geochimica et Cosmochimica Acta*, 70(4), pp. 993–1019.
- Thorarinnsson, S. and Tegner, C. (2009). Magma chamber processes in central volcanic systems of Iceland: constraints from layered gabbro of the Austurhorn intrusive complex. *Contributions to Mineralogy and Petrology*. 158. pp. 223–244.
- Thordarson, T. (1990). Masters thesis. The eruption sequence and the eruption behaviour of the Skaftár Fires, 1783–85, Iceland: characteristics and distribution of eruption products. University of Texas at Arlington.

- Thordarson, T. (2003). The 1783–1785 AD . Laki-Grímsvötn eruptions I: A critical look at the contemporary chronicles. *Jökull*. 53. pp. 1–10.
- Thordarson, T. and Self, S. (1993). The Laki (Skaftár Fires) and Grímsvötn eruptions in 1783-1785. *Bulletin of Volcanology*. 55. (4), pp. 233–263. doi:10.1007/BF00624353
- Thordarson, Th., Self, S., Óskarsson, N., and Hulsebosch, T. (1996). Sulfur, chlorine, and fluorine degassing and atmospheric loading by the 1783–1784 AD Laki (Skaftár Fires) eruption in Iceland. *Bulletin of Volcanology*. 58. (2–3), pp. 205–225. doi:10.1007/s004450050136
- Thordarson, T., Miller, D. J., Larsen, G., Self, S. and Sigurdsson, H. (2001). New estimates of sulfur degassing and atmospheric mass-loading by the 934 AD Eldgja eruption, Iceland. *Journal of Volcanology and Geothermal Research*. 108. pp. 33–54
- Thordarson, T. and Self, S. (2003). Atmospheric and environmental effects of the 1783–1784 Laki eruption: A review and reassessment. *Journal of Geophysical Research-Atmospheres*. 108, 4011
- Thordarson, T, Larsen, G., Steinthorsson, S., and Self, S. (2003a). The 1783–1785 AD Laki-Grímsvötn eruptions II: appraisal based on contemporary accounts. *Jökull*. 53. p. 11–47.
- Thordarson, T., Self, S., Miller, D. J., Larsen, G. and Vilmundardottir, E. G. (2003b) Sulphur release from flood lava eruptions of the Veiðivötn, Grímsvötn and Katla volcanic systems, Iceland. In: C Oppenheimer, DM Pyle and J Barclay (eds.) Volcanic Degassing. pp. 103–121. *The Geological Society of London*.
- Thordarson, T. and Larsen, G. (2007). Volcanism in Iceland in historical time: Volcano types, eruption styles and eruptive history. *Journal of Geodynamics*, 43. (1), pp. 118–152. Doi:10.1016/j.jog.2006.09.005
- Thordarson, T. and Höskuldsson, Á. (2008). Postglacial volcanism in Iceland. *Jökull*. 58. pp. 197–228.
- Thordarson, T. and O. Sigmarsson 2008. Effusive activity in the 1963–67 Surtsey eruption, Iceland: flow emplacement and growth of small lava shields. In: Thordarson, T., G. Larsen, S. Self, S. Rowland and Á. Höskuldsson eds. Studies in Volcanology: The Legacy of George Walker. *The Geological Society of London Special Publications*., in press.
- Walker, G. P. L. (1959) Geology of the Reydarfjörður area, eastern Iceland. *Quarterly Journal of the Geological Society London*. 114. pp. 367–91.
- Walker, G.P.L. (1963) The Breiddalur central volcano, eastern Iceland. *Quarterly Journal of the Geological Society of London*. 119. Pp. 29–63
- Walker, G. P. L. (1973). Length of lava flows. *Philosophical Transactions of the Royal Society*. 274. pp.107–118.
- Walker, G.P.L. (1964) Geological investigations in eastern Iceland. *Bulletin Volcanologique* 27 (1). pp. 351–363
- Walker, G.P.L. (1993) Basaltic-volcano systems. *Geological Society, London, Special Publications*. 76. pp. 3–38
- Weis, D., Garcia, M. O., Rhodes, J., Jellinek, M and Scoates, J. S. (2011). Role of the deep mantle in generating the compositional asymmetry of the Hawaiian mantle plume. *Nature Geoscience*, 4, pp. 831–838. doi.org/10.1038/ngeo1328
- Winpenny, B. and MacLennan, J. (2011). A partial record of mixing of mantle melts preserved in Icelandic phenocrysts. *Journal of Petrology*. 52 (9), pp. 1791–1812, https://doi.org/10.1093/petrology/egr031

- Wolfe, C. J., Bjarnason, I. T., VanDecar, S. C. and Solomon, S. C. (1997). Seismic structure of the Iceland mantle plume. *Nature*. 385. pp. 245–247
- Ward, P. L. 1971: New Interpretation of the Geology of Iceland. *Geological Society of America Bulletin*. 82. pp. 2991–3012

Chapter 4: Research project case studies

4.1 The 2014–15 CE Holuhraun eruption

The 2014–15 CE Holuhraun FL eruption is an event of significance, as it provided a rare opportunity to witness, for the first time with modern scientific equipment, a typical example of the type of eruption that is the main contributor to building the Icelandic plateau basalt succession. The 2014–15 CE event at the Holuhraun fissure lasted 6 months, from 31 August 2014 to 27 February 2015. Hartley and Thordarson (2013) have inferred from field, satellite, and aerial data, combined with historical accounts of eruptions in this area with an unknown origin, that the Holuhraun fissure has been active 3 times in the last 230 years. Producing as many compound lava flow fields on the Dyngjusandur glacial outwash plain in the central highlands of Iceland, north of the Vatnajökull icecap, and the Dyngjujökull outlet glacier. The first eruption in 1797 CE created a 2 km fissure 15 km south of Askja, 1862–1864 CE along a fissure that starts 23 km south of Askja and extends below Dyngjujökull (Jónsson, 1945; Thórarinsson and Sigvaldason, 1972; Hartley and Thordarson, 2013), the 2014–15 CE erupted through the same vents as the first eruption (Figure 4. 1).

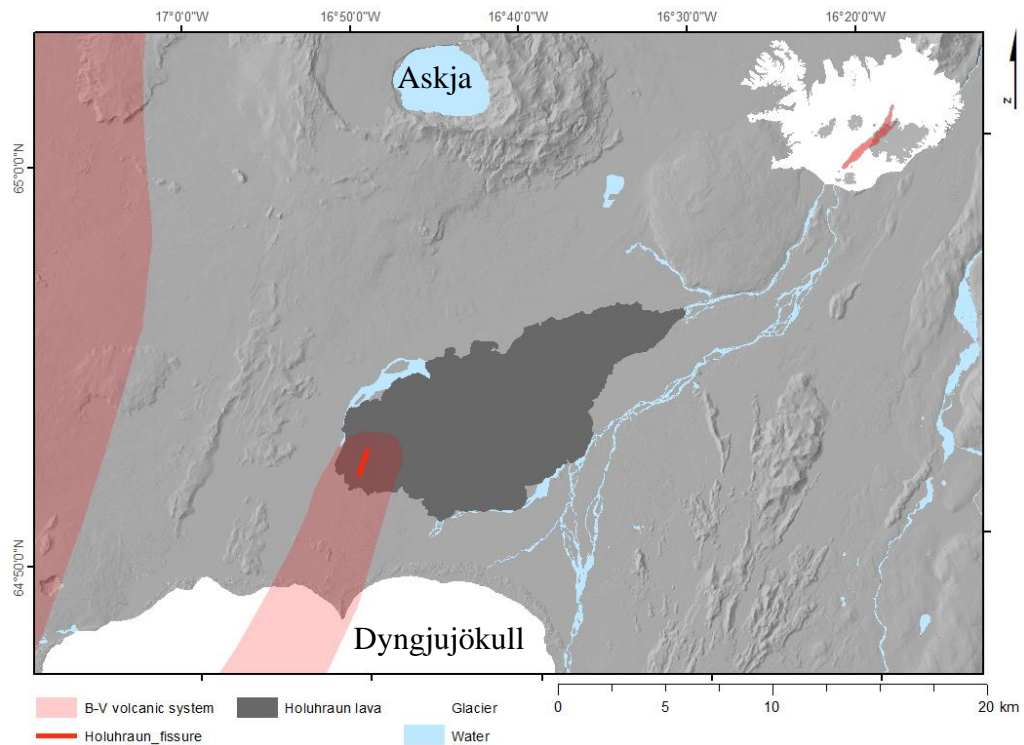


Figure 4. 1: Arctic DEM image of the 2014–15 CE Holuhraun flow field. Arctic DEM hillshade of the area surrounding the Holuhraun 2014–15 CE lava flow field, with the new proposed Bárðarbunga–Veiðivötn (B-V) fissure swarm (Hartley and Thordarson, 2013; Pedersen et al., 2017) shown in light red. Askja and Dyngjujökull, the outlet glacier from the Vatnajökull ice-cap are labelled for reference. The grey outlined box in the inset of Iceland (top righthand of the figure) indicates the geographic locations of the 2014–15 Holuhraun eruption within the island, with the large-scale important features such as the B-V fissure swarm, shown in red, and Vatnajökull, shown in grey, highlighted for reference. The location of the 2014–15 CE Holuhraun fissure, part of which was reactivated during this event, having previously fed older historical lava fields in the area (Holuhraun 1 and 2), is highlighted by a bright red line.

The Holuhraun fissure is situated within the Northern Volcanic Zone at the southern end of the Askja volcanic system (Hartley and Thordarson, 2013; Pedersen et al., 2017). Geochemical and isotopic studies of its products, from the 1790s, 1860s and 2014–15 CE eruptions, indicate geochemically and isotopically indistinguishable and homogeneous magmas. Their geochemical fingerprint is suggestive of affinities to the magma produced in the Bárðarbunga–Veiðivötn (B-V) rather than the Askja volcanic system (e.g., Hartley and Thordarson, 2013; Sigmarsson and Halldórsson, 2015; Halldórsson et al., 2018). This led Hartley and Thordarson (2013) to suggest that the two systems are overlapping or interfingering and that the exact boundaries between the two are not well defined (Figure 4. 2). This is not an uncommon finding, the minor explosive phase of the Gjálp 1996 CE subglacial fissure eruption (Gudmundsson et al., 1997), which occurred geographically within the B-V system, but has a geochemical and isotopic signature of the Grímsvötn volcanic system (Steinthorsson et al., 2000).

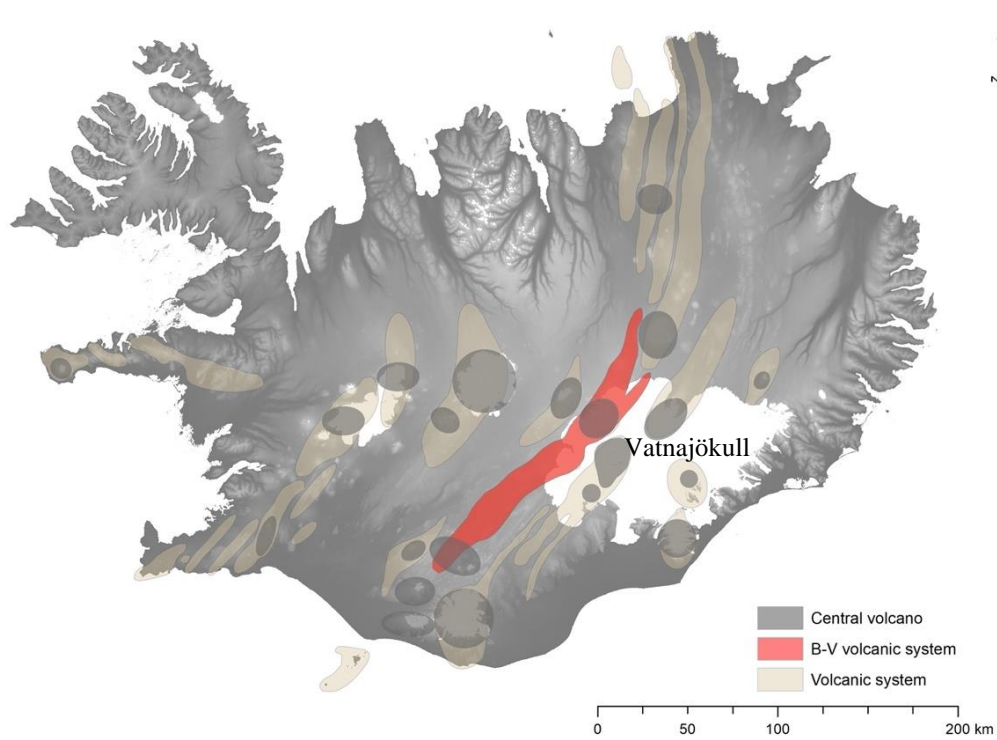


Figure 4. 2: The B-V volcanic system. A hillshade DEM map of Iceland, with the active volcanic systems outlined in light grey and cream-brown and glaciers in white. The location of the B-V volcanic system is highlighted in red, and the new interfingering northern boundary of its fissure swarm can be clearly observed south and west of Askja volcanic system (Askja lies immediately to the NE of B-V, although the fissure swarm of the latter can also be seen to the west of the Askja system). The B-V fissure swarm can be observed to span subaerial environments either side of its subglacial portion under the Vatnajökull ice-cap.

This subglacial fissure eruption, which occurred under >800 m of ice, triggered a large jökulhlaup in the area (Figure 4. 3); the activity was predominantly effusive, with a small weakly explosive phase which created an approximately 4.5 km high plume when it eventually melted through the ice above.

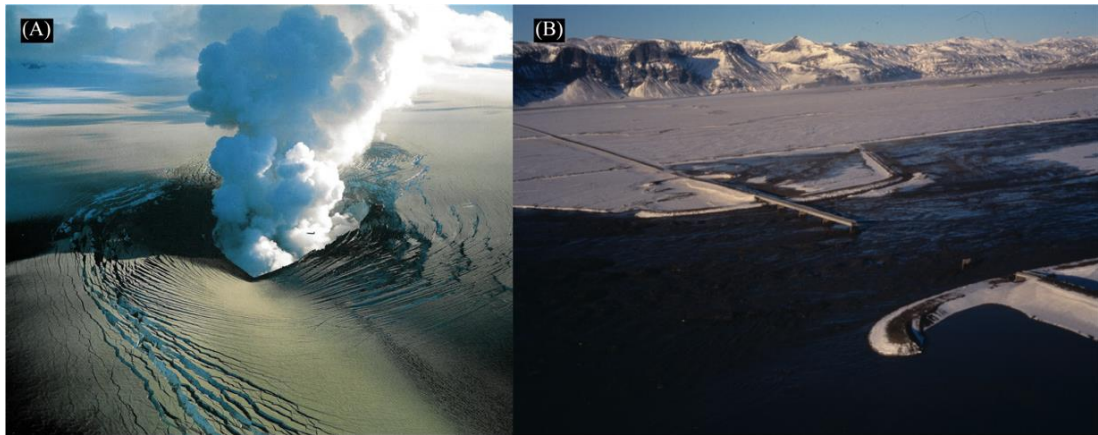


Figure 4. 3: The Gjalp 1996 CE subglacial eruption, and its jökulhlaup. Aerial images of the weakly explosive phase of the sub-glacial 1996 CE Gjalp eruption (shown in A), associated with the Grímsvötn volcanic system, which triggered a large jökulhlaup. The associated jökulhlaup destroyed infrastructure in the SE Iceland lowlands (shown in B), with the flood destroying the only road bridge across this part of the south coast of Iceland; which connects the south coast towns both with the south western towns and the capital region, but also with the east fjörds).

The B-V volcanic system is entirely basaltic, extending up to 190 km long and up to 25 km wide (Figures 3. 3 4. 1 and 4. 2). It has a well-developed fissure swarm which is partially ice-covered and extends to the NNE and SW of its two central volcanoes: Bárðarbunga and Hamarinn, which lie underneath the Vatnajökull ice cap. Bárðarbunga is the only one of the two that contains a known caldera (Figure 3. 3; Gudmundsson and Högnadóttir, 2007). Hamarinn is the only area within the B-V system that has a significant geothermal system, which is associated with jökulhlaup hazards in the Kaldavísl river, and while it is seismically active, Hamarinn is not linked to any Holocene eruptions. However, like Bárðarbunga, its subaerially exposed rocks, found on the NNW flanks, and the subglacially erupted ridge Fögrufjöll (extending to the SW), are basaltic. Within the ice-covered portion of the system, phreatomagmatic activity dominates the Holocene eruptive record, although events that did not reach outside of the ice to form a layer in the soil horizons surrounding Vatnajökull result in an incomplete tephrochronology record of its total activity, with only around 1 in 4 eruptions being preserved.

Of the two fissure swarm branches, to the NNE and SW, eruptions in the NNE portion are less well characterised (Figure 4. 2). Effusive fissure eruptions, producing large lava fissure fed flows and shields, are the dominant type of eruption on the subaerial fissure swarm in the B-V system throughout the Holocene. The system is responsible for the Þjórsá lava field, the largest Holocene lava flow in Iceland, reaching 130 km in length and $>20 \text{ km}^3$, as well as the $\sim 15 \text{ km}^3$

Trölladyngja shield volcano. Phreatomagmatic activity is not limited to the subglacial portion of the system; high water tables and retreating ice-margins throughout the Holocene resulted in a series of explosive fissure eruptions, which interacted with external water bodies to form tuff cone-rows. Two very large and explosive phreatomagmatic fissure eruptions occurred in historical times: Vatnaöldur 877 CE (5 km³) and Veiðivötn 1477 CE (10 km³), the latter of which dispersed tephra as far as Sweden and Ireland. In total, the B-V system has yielded at least 26 confirmed eruptions over the last 1000 years. Twenty-two of these occurred within the ice-covered portion of the system (e.g., Thordarson and Larsen, 2007). The most recent, the Holuhraun 2014–15 CE FL eruption, occurred in the subaerial portion of the fissure swarm and erupted a lava flow field of 1.2 km³ in volume (Thordarson et al., 2020; Bonney et al., 2018) (Figure 4. 2).

Detailed in-situ imaging, mapping and sampling of the eruptive products of the 2014–15 CE FL event at Holuhraun was carried out by the IES eruption team, and external collaborators, throughout the eruption. This was coupled with comprehensive deformation, tremor and seismicity measurements (Sigmundsson et al., 2014; Ágústsdóttir et al., 2016; Hjartardóttir et al., 2016; Eibl et al., 2017), in-situ volcanic gas surveys (Ilyinskaya et al., 2017; Pfeffer et al., 2018), satellite S plume measurements and forecast modelling (Schmidt et al., 2015), as well as petrological and geochemical studies of a large sample suite that spans the entire eruption (Bali et al., 2018; Halldórsson et al., 2018; Hartley et al., 2018). This has yielded an unparalleled data set for this rare type of eruption.

4. 2 The series of events during the Holuhraun 2014–15 CE FL eruption.

On 15 August, 2014, seismic activity was recorded beneath the north-eastern flank of the Bárðarbunga central volcano (Sigmundsson et al., 2014). By the 16th, the frequency of these earthquakes increased significantly, along with the formation of three new earthquake clusters: (1) beneath the Kistufell region at the northern edge of Vatnajökull, (2) beneath the eastern half of Bárðarbunga caldera, which, during the course of the day, propagated some 5 km to the southeast, (3) centred beneath the region 12 km to the east of the Bárðarbunga caldera and separated from the propagating second cluster by ~3 km wide aseismic zone. It was this third cluster of

earthquakes that became the earthquake swarm that propagated >40 km to the north, along a lineament, over the next nine days (until 25 August 2014) (Figure 4. 4).

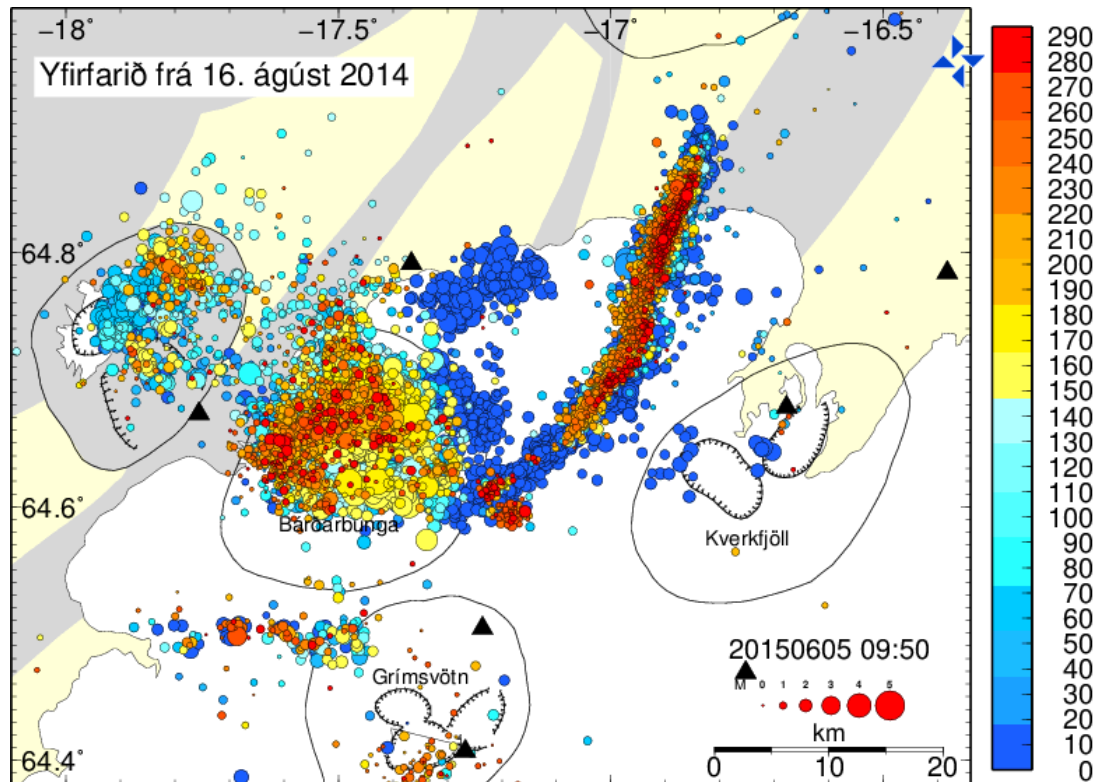


Figure 4. 4: The propagation of seismic unrest prior to Holuhraun 2014–15 CE. Figure taken from Veðurstofnun Íslands (The Icelandic Met Office), which indicates the propagation of seismic activity preceding the Holuhraun 2014–15 CE fissure eruption from the 16 August 2014 until the 5 June 2015 spanning a 4 month cooling period after the eruption had finished. The colour of the seismic events indicates age, with the oldest shown in dark blue (from 16 August 2014), which grades to the youngest shown in red; a legend for the colour scheme and the number of days since the seismicity started listed to the right of the map. The pathway of the dyke, as well as related seismicity in the area, is seen clearly by the linear feature stretching to the NE of the Bárðarbunga Caldera. The surrounding volcanic systems and their calderas are shown for geographical orientation and reference.

Three shallow ice-depressions, ice-cauldrons, appeared on the surface of the outlet glacier, Dyngjufjökull, above the swarm as it propagated northwards. These are hypothesised to be the result of small effusive subglacial eruptions, one of which included the intrusion of a dyke 50 m into the ice (Reynolds et al., 2017). The swarm remained in the same position from 25–29 August, when the first visible eruption took place through the vent system of the 1797 CE Holuhraun eruption, about 6–7 km north of the margins of the outlet glacier Dyngjufjökull (Sigmundsson et al., 2014; Ágústsdóttir et al., 2016; Hjartardóttir et al., 2016; Pedersen et al., 2017;

Reynolds et al., 2017; Bali et al., 2018). This was a minor, short, stop-start eruption, along a 600 m long fissure, and lasted only 4–5 hours.



Figure 4. 5: This image shows the aerial extent of the small eruption which occurred <48 hours before the 2014–15 CE Holuhraun eruption. IES eruption team image. The eroded and partially sandur covered older Holuhraun 1 red and brown crater row with the black and still steaming small lava flow field Holuhraun 2014–15 episode 1 extending for 600 m along the original crater row feeding a small lava flow field starting to cover the Holuhraun 1 lava.

The magma utilised the pre-existing ‘monogenetic’ fissure formed during the AD 1797 Holuhraun event, with new spatter starting to cover the older cones. Fountain fed lava flows emplaced shelly pāhoehoe lava flows, utilising older lava channel levees (Figures 4. 5 and 4. 6).

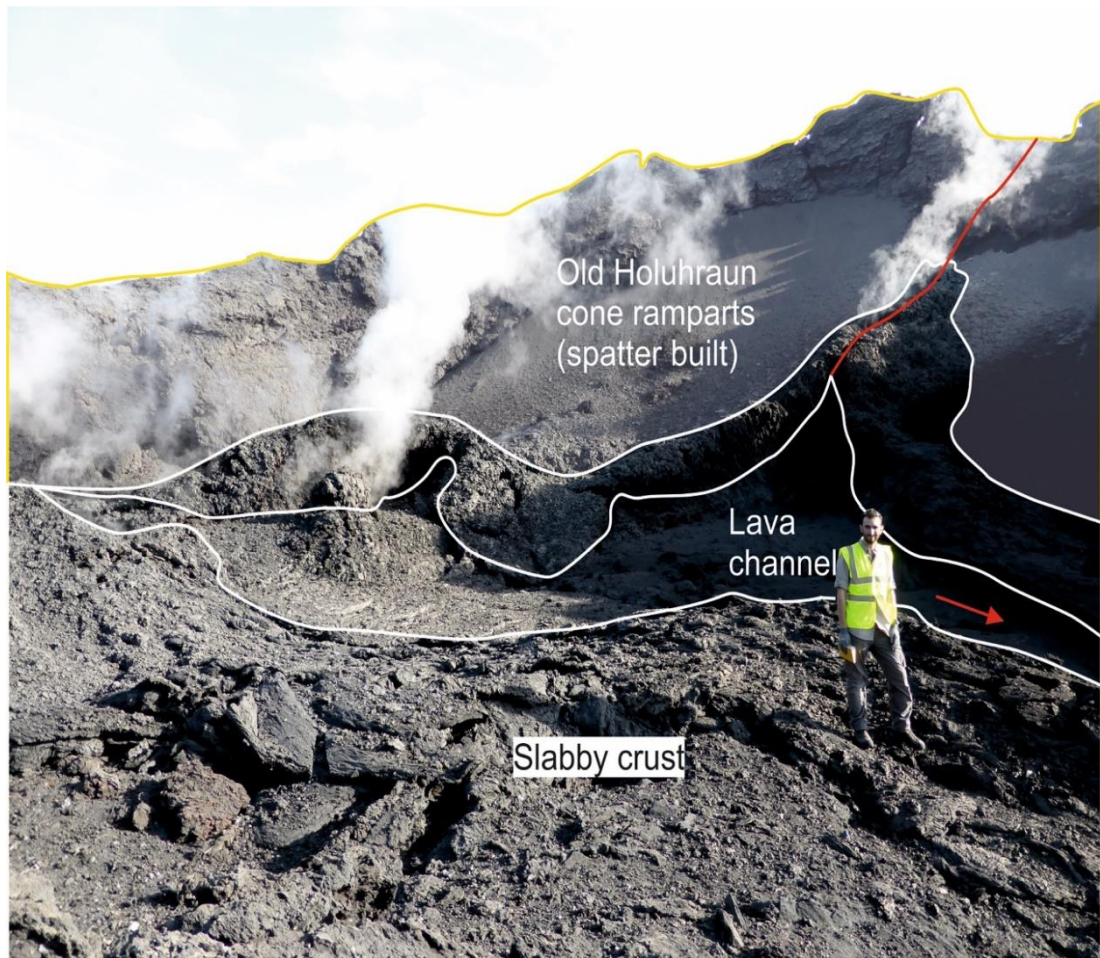


Figure 4. 6: The old Holuhraun craters utilised by 2014–15 CE eruption. IES eruption team image. A field team member stands inside one of the old Holuhraun 1 craters where the Holuhraun 2014–15 CE eruption utilised existing fissure cracks, ramparts, and channels to emplace new slabby pāhoehoe lava flows.

The earthquake swarm was still ongoing when the main eruption began through the same vent system on 31 August 2014 (Figure 4. 4), lengthening the active fissure by 1.8 km. The majority of the eruptive activity at Holuhraun was effusive, feeding a compound lava flow field constructed through several lava branches emplaced in a clockwise fashion, each creating local topography which diverted the next to the E-SE (Figure 4. 6). In total, the eruption created an 83.8 km² basaltic flow field with a volume of 1.2 km³ dense rock equivalent (DRE), making this event the largest FL eruption in Iceland for 230 years, since the 1783–1784 CE Laki eruption. The flow field was emplaced on a flat glacial outwash plain, with a regional slope of ~1° to the NE. Despite this lack of local topographical influence on the lava transport system and lava flows, the eruption emplaced a spectrum of pāhoehoe lava flow morphologies which can be linked directly to the style of eruptive activity at the vent and the evolution of the transport system (Table 2.1): (1) slabby pāhoehoe flows

were emplaced in the initial fissure opening phases which are now buried under subsequent activity, and near the vents throughout the eruption, (2) rubbly pāhoehoe flows, which make up the majority of the flows emplaced during the eruption, and (3) spiny pāhoehoe, initially emplaced as very microlite rich, higher temperature (probably due to the latent heat of crystallisation), squeeze-outs from November onwards. Spiny pāhoehoe is also the dominant lava morphology emplaced during the resurfacing events towards the end of the eruption, which were fed by reactivation of older lava tube systems and break-outs (Pedersen et al., 2017). Pedersen et al., (2017) mapped out the evolution of the transport system and flow field in full, using aerial and ground images and satellite data sets, and more details of the main distribution centres and transport systems can be found there. In September an exponential decrease in mass eruption rate (MER) followed by a resurgence phase with a waxing MER during the period of the 16–20 September, following the low point on 15 September (Bonny et al., 2018), is also associated with a substantial lateral expansion of the flow field (Eibl et al., 2017; Pedersen et al., 2017). This expansion of the flow field is thought to have been triggered by branching within the main lava channel leading to formation of a series of new lava flows (Pedersen et al., 2017). Thus, initiating the construction of a composite lava flow field (Figure 4. 7) fed by a branching transport system. Prior to this change in vent activity, and the number of active vents (see Chapters 6 and 8), the eruption fed one main lava flow branch through a focussed transport system. Throughout this major rifting event and FL eruption, substantial seismic activity was continually recorded at the Bárðarbunga central volcano, associated with caldera floor collapse (Gudmundsson et al., 2016; Riel et al., 2015).

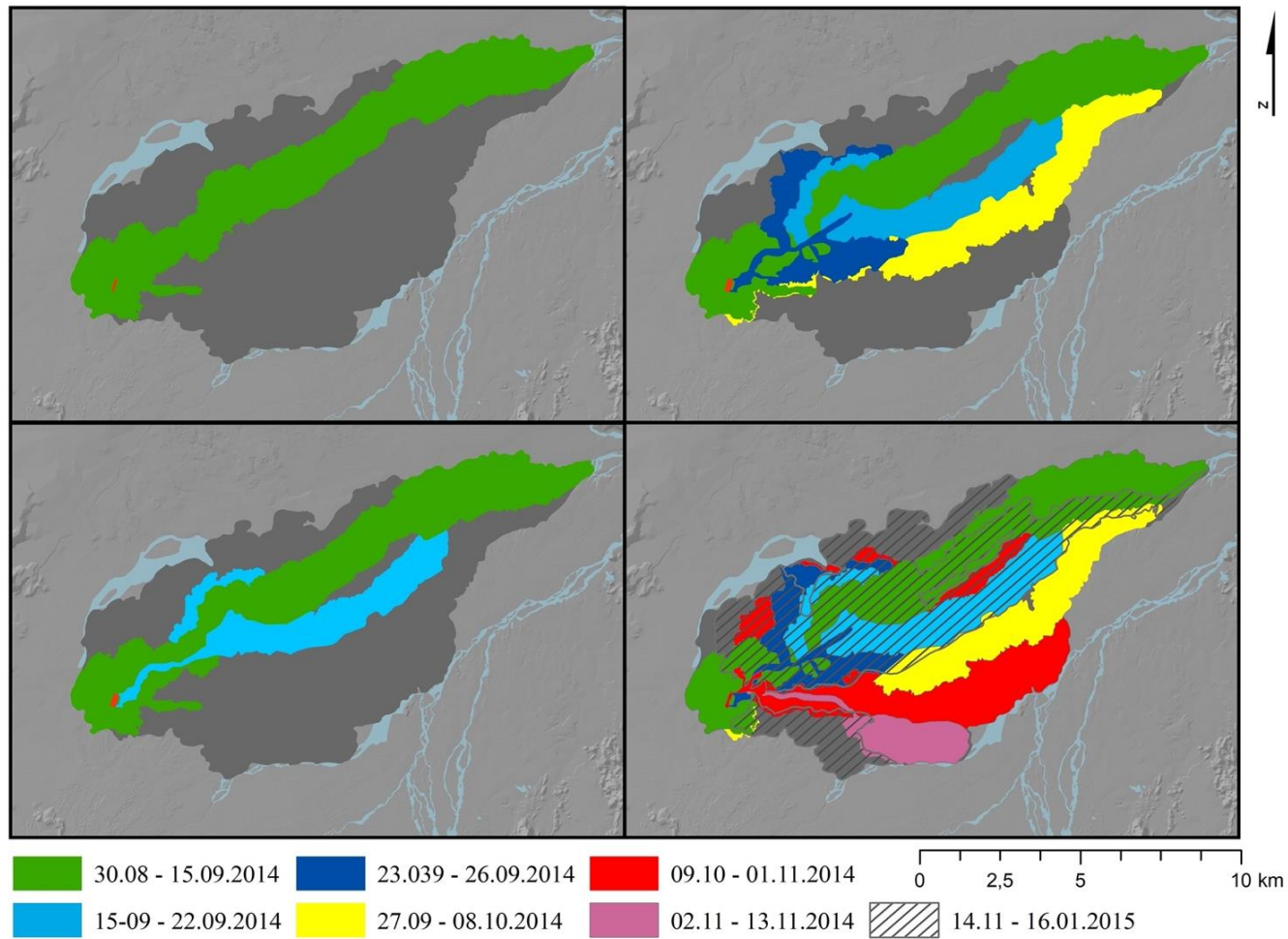


Figure 4. 7: A composite of the growth of the Holuhraun 2014–15 CE lava field. Outline of the 2014–15 CE Holuhraun flow field after the 27 February 2015 shown in grey, overlain on top of an Arctic DEM hillshade of the sandur it erupted onto. Four time periods are displayed, with their associated emplaced lava branches, to highlight the branching nature of flow emplacement, which is predominantly emplaced in a clockwise fashion. The initial branching of the flow field occurs on the 15 September 2014 occurs coevally with changes in vent activity.

The varieties in morphologies present in the Holuhraun 2014–15 CE lava flow field and their association with both the evolution of vent activity and the lava transport systems has drawn much attention in recent studies; both as an evolution of the first FL observed with modern equipment, but also due to the parallels of morphologies and the applications that can be applied to planetary volcanism, or lava and river water interactions in regard to extra-terrestrial biological interests (Pedersen et al., 2017; Dundas et al., 2020; Aufaristama et al., 2019; Voigt et al., 2020, 2021). In contrast, the explosive activity and its evolution through the eruption has not been well documented or analysed, although changes in MER have been analysed in detail (Bonny et al., 2018).

However, the evolution of the explosive activity from the eruption, i.e., fountaining behaviour, has not been published in full, aside from the IES eruption team daily–weekly field observation reports (not open to the public) and a study by Witt et al., (2018) which analyses the evolution of fountaining during vent localisation in the first 4 days of the eruption. The following is a short summary of this activity both in terms of vent locations and the style of eruptive activity, as well as the temporal localisation of activity.

During the first week of the Holuhraun eruption, the initial emergent phase fountaining devolved from a weakly explosive laterally near-continuous “curtain-of-fire”, along the entire length of the 1.8 km long fissure, onto eruption at discrete vents (Figure 4. 8). Localisation occurred in the area of the vent where the initial emergent phase activity was more vigorous, which tends to be in the middle portion of the active fissure segments. On average, during the emergent phase, along the entire length of the fissure, typical fountaining heights were <50 m. However, the location of what later became the focal point of activity throughout the duration of the eruption, the main vent Baugur, in its embryonic phase, had fountaining heights 71.5 ± 0.4 m (Witt et al., 2018). Five discrete vents formed during the period of activity localisation, and were given the nicknames: Norðri, Suðri, Krakki, Heimasætan and Baugur (Figure 4. 8).

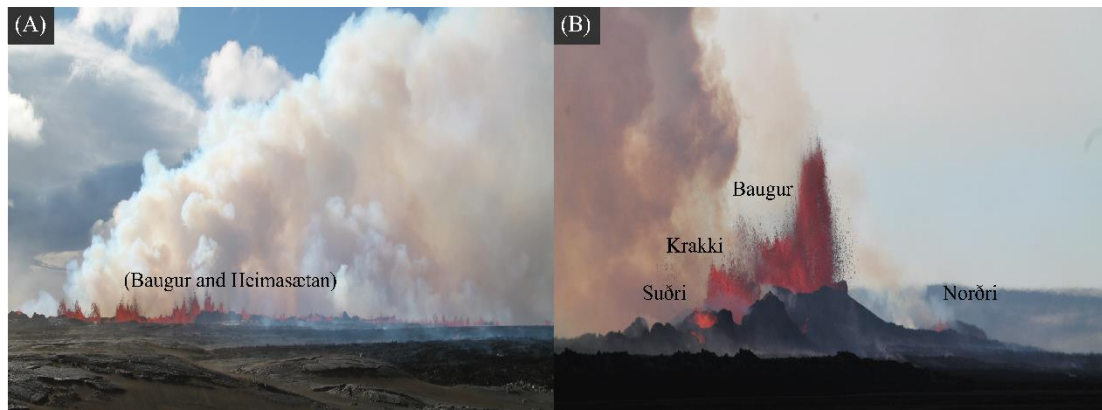


Figure 4. 8: Holuhraun 2014–15 CE curtain-of-fire to discrete vents. Field photographs taken by the author during Holuhraun 2014/15 CE eruption, capturing (A) the emergent fountaining phase on day 1 and (B) the peak MER and highest fountaining phase on the 6–9 September 2014 CE. The initial location of Baugur and Heimasætan are shown in (A) for reference to highlight the increase in intensity of vent activity at these locations over time as shown in (B). It should be noted that the field images are taken from different locations with $>150^\circ$ between the angles of the cameras.

In the case of Holuhraun, vent localisation occurred in-step with the waxing phase of the eruption, where the magma discharge was still increasing, and corresponding fountaining intensity and height increased. Calculated time-averaged MER, taken from integrated satellite and ground-based data, indicates an increase from $150 \text{ m}^3\text{s}^{-1}$ to $560 \pm 85 \text{ m}^3\text{s}^{-1}$ occurred over the course of the first 8–9 days of the eruption (Bonny et al., 2018); as a result, fountaining height increased to 160–170 m. Medial tephra fall, consisting of isolated lapilli clasts and ash, was predominant during this period, although it continued to occur intermittently throughout September to November during the 6-month long event. However, due to its small volume, which also fell directly onto a glacial outwash plain, a substrate consisting of black sand and rocks, the tephra from this eruption was not preserved as it did not form a discrete layer. Instead, the samples that were collected as they fell are the only preserved tephra fall from this event excluding thin traceable lenses in the vent region, which cannot be directly linked to a particular phase of activity. Notably, during the peak the highest intensity fountaining phase of this eruption associated with highest MER, the eruption produced a large amount of Pele’s hairs from 6–8 September. During this initial phase seismic activity reduced somewhat from 31 August–5 September and had more-or-less disappeared following a small eruption that took place on a short fissure 1.5 km south of the main active vent system on 5 September 2014 (Pedersen et al., 2017) (Figure 4. 7). This formed a separate smaller lava flow, emplaced within the graben, bounded by two large normal faults.

Following this, the magma discharge exponentially decreased to $30 \pm 5 \text{ m}^3\text{s}^{-1}$ over a period of 8 days (Bonny et al., 2018), with the lowest MER recorded on 15 September. All active vents, with the exception of the main vent Baugur, which displayed significantly reduced fountaining heights (maximum of 70 m), shut down (including the vent for the secondary smaller flow field to the south) after the 16 September (Figure 4. 9). This reduction of MER and intensity did not mark the end of the eruption; instead, like many other basalt fountaining events, Holuhraun was displaying episodic changes in MER. After this lull in activity, a resurgence of more vigorous activity caused by a second waxing MER was observed on 17 September. This steadily increased until fountaining intensity peaked on 2 September, corresponding to a secondary MER peak at $440 \pm 65 \text{ m}^3\text{s}^{-1}$. Following this secondary waxing phase, the MER decreased in an exponential manner between 20–30 September and a lava pond formed in the main vent, Baugur (Figure 4. 9). This had a modulating effect on vent activity which shifted from intermittent fountaining to vigorous boiling by early October (Figure 4. 9). Throughout October occasional, explosive, large-bubble-bursting activity resembling a spurt of fountaining created sporadic medial tephra fall. On 8 October, measurements by the IES eruption team on the ground, and from overflight photographs, record bubble bursts of around 1–1.5 times the rampart height ($>50 \text{ m}$) (Figure 4. 9). From early to late November, the lava lake activity reduced to steady boiling, punctuated by large bubble bursting activity, with a maximum bubble diameter of 50 m recorded on 18 November. By December, the bubble bursting events had ceased, and a steady-state, rolling boil activity took over (Figure 4. 9). The level of the pond dropped steadily throughout February until the eruption ended on 27 February 2015. This late-stage, rolling boil of the lava pond, is linked to large scale resurfacing events across the complex compound flow field (Pedersen et al., 2017).

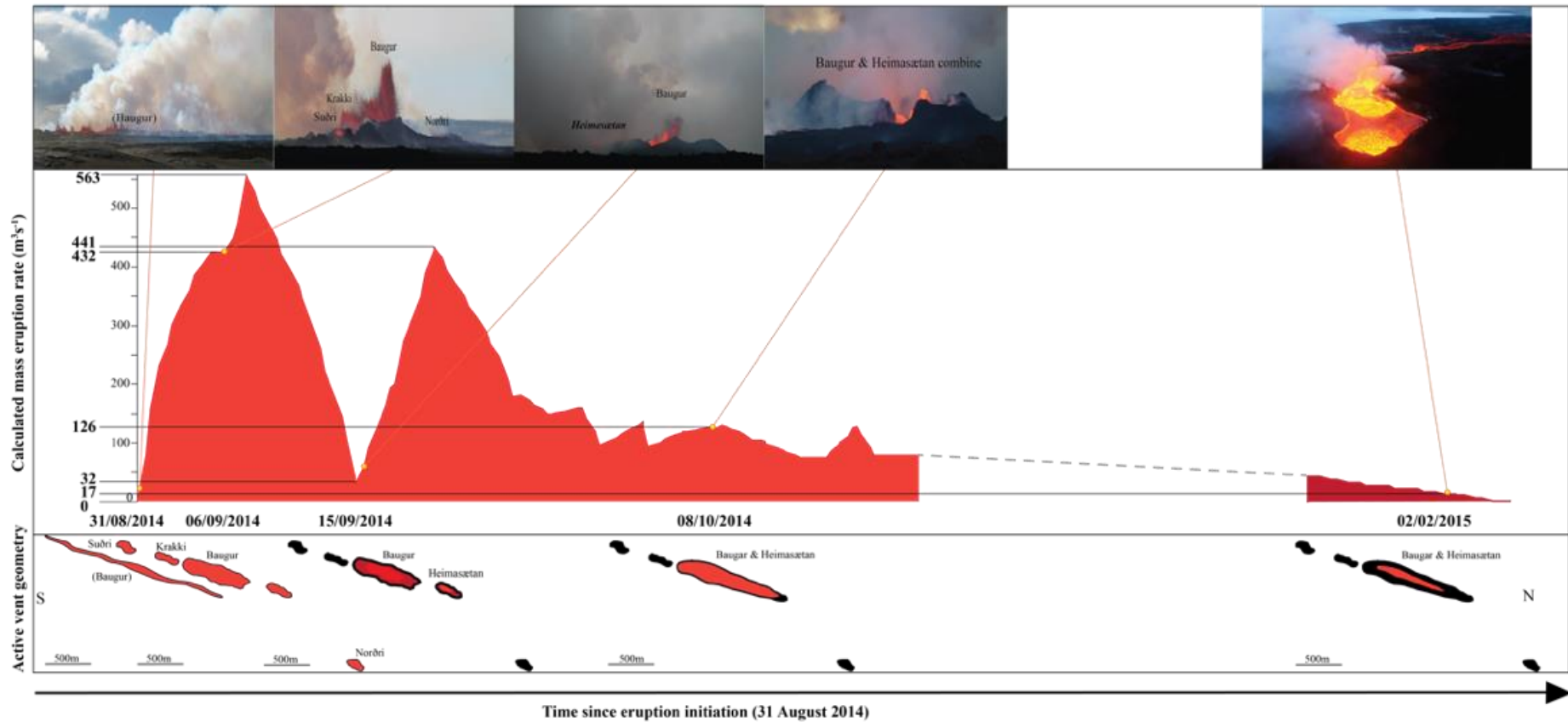


Figure 4. 9: Vent activity and MER, Holuhraun 2014–15 CE. The style and intensity of vent activity during Holuhraun 2014 –15 CE (IES eruption team images) (top panel), and associated Time-Average MER from Bonny et al. (2018) (middle panel) and active vents along the Holuhraun fissure (bottom panel).

The Holuhraun 2014–15 CE event was one of the most polluting eruptions in the last century (Gíslason et al., 2015; Pfeffer et al., 2018; Schmidt et al., 2015), emitting approximately 9.6Mt of SO₂ (Pfeffer et al., 2018) (Figure 4. 10). Thordarson et al., 2020 use preliminary unpublished data, used the petrological method and two-stage degassing model, to estimate that the 2014–15 Holuhraun magma carried 9 Mt, rather than 9.6 Mt, of S to the surface, releasing 7.55 Mt into the atmosphere in total: 6.55 Mt at the vents into the plume, and 1.15 Mt into a localized haze from the lava flow field. The 2014–15 Holuhraun eruption emitted more than the combined atmospheric load of over 20 years of eruptive activity produced by Kīlauea, as recorded by USGS from 1977–1997 CE, and more than the 1991 CE eruption of Pinatubo (Sutton et al., 2001). It was the most polluting event since the 2000–2003 CE eruption of Miyake-jime in Japan (Kazahaya et al., 2004). The atmospheric S levels exceeded the legal limits (for SO₂ this is calculated using a 10-minute mean air quality 500 mg/m³) set by the World Health Organisation (WHO) and Icelandic health standards, monitored throughout the event at the eruption site (IES eruption team gas meter readings, Gíslason et al., 2015; Pfeffer et al., 2018; Schmidt et al., 2015). Nevertheless, the overall wider environmental impact of the eruption was lessened due to several factors: (1) The remote location, which enabled dilution of the plume before it reached population centres in Iceland, despite locally exceeding WHO SO₂ safety levels twice in mid-late September (Figure 4. 10). At this time, air quality monitoring stations in Iceland recorded SO₂ levels >1400 mg/m³ in the north and eastern Iceland (Schmidt et al., 2015). (2) The 2014–15 event was a low-intensity flood lava event; the vent activity during the 2014–15 event supported a 1–3 km high gas-rich plume entirely confined to the lowermost troposphere (Schmidt et al., 2015; Pfeffer et al., 2018). As they drifted away, these plumes generated detectable SO₂ levels in neighbouring European countries, although it only surpassed WHO air quality limits in Ireland for 1 hour on 6 September (Schmidt et al., 2015). This timing coincides with the period of highest magma discharge during the eruption (Bonny et al., 2018), as well as the concentration of activity onto discrete vents generating the highest lava fountaining heights (unpublished IES, eruption team field observations). (3) The eruption took place during the Icelandic winter, thereby slowing the reaction converting SO₂ to SO₄²⁻, due to the low sunlight levels and drier atmospheric conditions (Pfeffer et al., 2018).

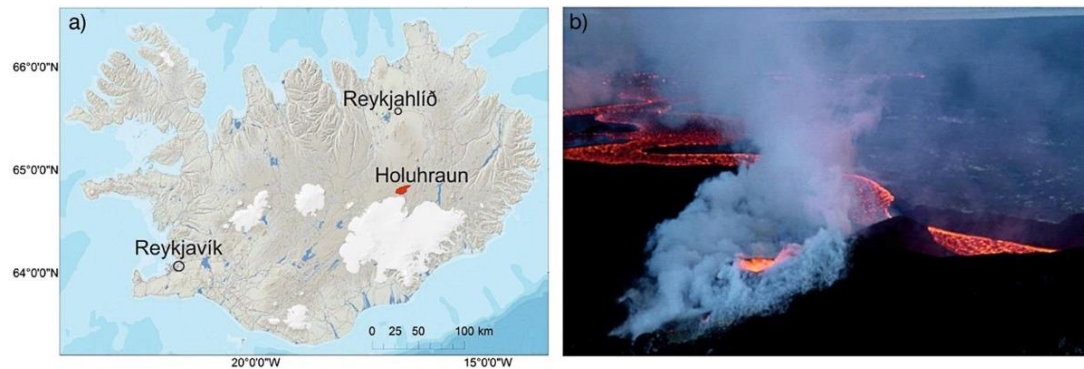


Figure 4. 10: Volcanic pollution from Holuhraun 2014–15 CE. This figure was taken from Ilyinskaya et al., 2017. a) Location map of the Holuhraun eruption site (lava flow extent shown by red colour), and the two populated areas in this study: Reykjavík city capital area, population 120,000; and Reykjavhlíð town, population 300. b) Holuhraun eruption during the January 2015 field campaign. During this period, the activity was exclusively effusive. The width of the lava channel is ~50 m.

4. 3 The 1783-4 CE Laki FL eruption

The Laki 1783–84 CE fissure eruption, started on 8 June 1783 and lasted for 8 months; early Icelandic literature refers to this event as Skaftáreldar, which translates as the Skaftár Fires. Fires is a common name for prolonged fissure fed eruptive activity in Iceland, and the Skaftá, a large glacial river which runs from Skaftárjökull, an outlet glacier from the SW of the Vatnajökull ice-cap, through the Síða highlands to the lowlands in South Iceland is the namesake for this fissure eruption. The canyon calved by the Skaftá, channelled the western branches of the lava flow from the Laki fissures down the same path as the river itself from in the Síða highlands to the lowlands. There the lavas, that flowed down this western canyon, and spread out over the Síða plains, gradually encroaching on nearby farmsteads and into the outskirts of a larger local settlement, Kirkjubærklaustur. The Hverfisfljót canyon to the east of the town, which runs from Síðujökull, another SW outlet glacier of the Vatnajökull ice-cap, on the eastern margin of the Síða highlands, is also utilised by lava flows later in the eruption. The combination of the later timing of these lava flows, and because they were emplaced further away from Kirkjubærklaustur than the Skaftá results in the name for the eruption primarily being associated with the Skaftá.

The eruption is mentioned by two additional names in Icelandic literature, each referring specifically to the direct physical volcanological products it formed: (1)

Lakagígar, which translates as ‘the Laki crater-row’ refers to the mixed phreatomagmatic and magmatic pyroclastic cone-row, which takes its name from the mountain Laki, an older hyaloclastite formation, which the crater row bisects as eruptive activity propagated step-wise through it from the SW–NE, (2) the suffix -*hraun*, which translates to lava, is added, with *Skaftáreldahraun* referring directly to the lava flow field created by the Laki fissure eruption. Historical accounts documenting seismic and eruptive activity in Iceland date back to the early stages of settlement. However, the detailed contemporary accounts for the Laki eruption (compiled into *Eldrít*, the book of fire), mostly comprised of eye-witness accounts from Jón Steingrímsson, a local priest in Kirkjubærklaustur (Steingrímsson 1783a; 1783b; 1788; 1901; Steingrímsson and Ólafsson, 1783), make it one of the earliest well-documented volcanic eruptions in Iceland. It is also an event of significance as prior to the advent of the Laki eruption, and until the 2014–15 CE Holuhraun eruption, there is no other such meticulous documentation of a flood lava event. Whilst the Eldgjá FL event occurring after settlement is 4 times the size of Laki in terms of volume, there is little contemporary documentation of the event itself in the Icelandic records, which were sent to the Danish crown as the settlers wanted others to continue emigrating to Iceland.

The 1783–84 CE Laki fissure eruption is part of the Grímsvötn-Þórðarhyrna volcanic system, which sits at the northern end of the Eastern Volcanic Zone (EVZ) and is the most extensively ice-covered system in Iceland. The Laki fissure represents a branch of its 10–15 km wide and 80 km long embryonic fissure swarm which extends to the SW of the central volcano (Jakobsson, 1979, Thordarson and Self 1993; icelandicvolcanos.is) (Figure 4. 11) and it is one of only two Holocene eruptions to occur on the ice-free portion of the system along with Lambagígar.

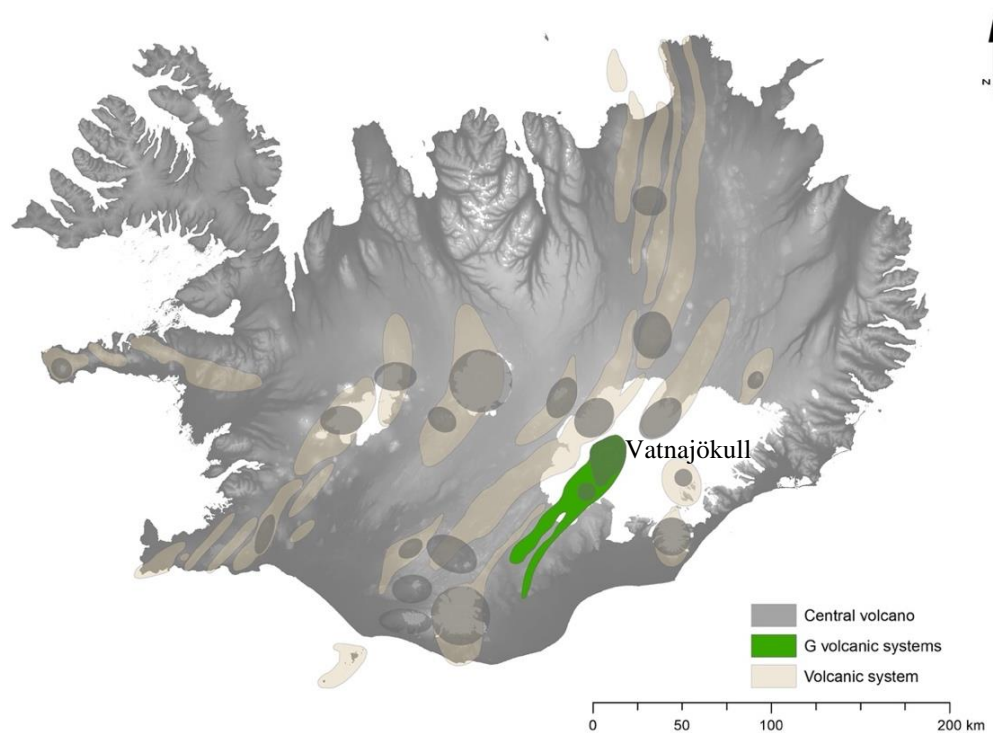


Figure 4. 11: The Grímsvötn volcanic system. A hillshade DEM map of Iceland, with the active volcanic systems outlined in light cream-brown. Ice-caps and glaciers are shown in white. The Grímsvötn volcanic system is highlighted in green can be seen extending to the SE from the Vatnajökull ice-cap.

The volcanic system contains two subglacial volcanic centres with caldera complexes: Grímsvötn and Þórðarhyrna (G-Þ). Grímsvötn has a 50 km² subglacial composite caldera complex, and throughout historical times (the last 1100 years in Iceland), has erupted with a frequency of 1 eruption every 10 years. The majority of the system's volcanism is basaltic, with basaltic andesite, dacite, rhyolite outcropping as nunataks linked to the system's second central volcano. The eruptive frequency of the Þórðarhyrna central volcano, which lies to the SW of this system, is less well constrained with current estimates of 2 eruptions per 500 years with the last occurring in 1903 CE. Due to the subglacial nature of both of volcanic centres, the system is dominated by phreatomagmatic explosive activity (from weakly explosive events, e.g., 2004, up to Plinian intensities e.g., 2011 CE VEI 4) or subglacial fissure eruptions, e.g., Gjálp 1996 CE with jökulhlaups frequently associated with periods of volcanic unrest. As with B-V weaker intensity events at G-Þ, which do not produce tephra fall which reaches outside of previous glacial margin extents throughout the Holocene, are not preserved in the pre-historic soil stratigraphy. As is the case for

earlier historical eruptions in Iceland, eruptive events at G-Ð were poorly recorded by the local population or information was lost through records not surviving through to the present day.

4. 4 Laki 1783–84 CE series of events

The 1783–84 CE Laki eruption lasted for 8 months in total, starting on the 8 June 1783 CE preceded by several weeks of increasing seismicity in the area (Erikksson 1783) and lasting until the 7 February 1784 CE, and occurred in an episodic fashion through 10 distinct explosive fissure opening phases (Thordarson and Self., 1993) (Figure 4. 13). This fissure forming period was also part of a larger volcano-tectonic episode involving the Grímsvötn central volcano that lasted for more than 2 years (Steingrímsson 1788, Einarsson, 1984; Thorarinsson, 1984; Thordarson and Self 2003b) (Figure 4. 12). The 1783–84 CE Laki eruption is the second largest FL event in Icelandic history, after the 939 CE Eldgjá event, and created a compound lava flow field with a total area of 600 km² and a volume of 14.7 km³ (Figure 4. 12), additionally the event produced 0.4 km³ DRE of tephra.

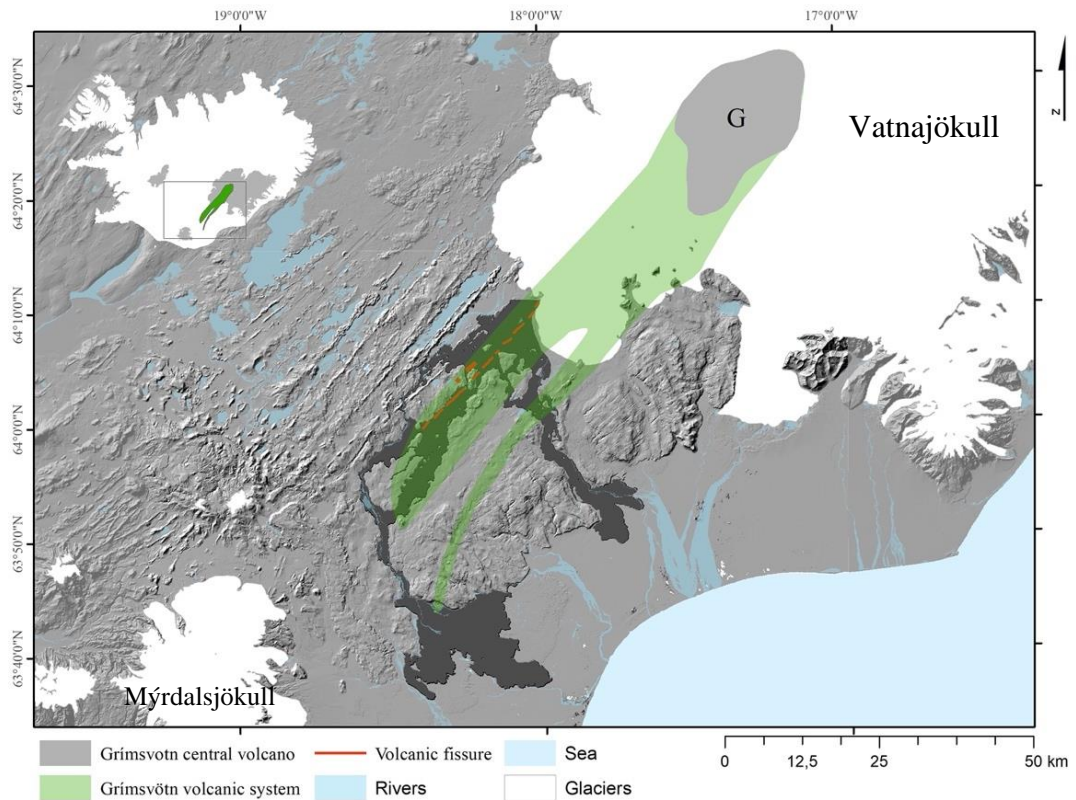


Figure 4. 12 Map of the Grímsvötn volcanic system and Laki 1783–84 CE lava flow field. Arctic DEM hillshade of the area surrounding the Laki 1783–84 CE lava flow field (dark grey), with the embryonic Grímsvötn (G) fissure swarm shown in light green. The grey box in inset of Iceland indicates Holuhraun geographic location within the island, with the large scale important features such as the G fissure swarm, shown in green and Vatnajökull and Mýrdalsjökull shown in grey for reference. The Laki fissure can be seen in 10 distinct en-echelon fissures (shown as red lines), stretching from the SW to the NE of the lava field towards Vatnajökull. The small Lambagigar fissure system, which lies slightly to the north of the extensive Laki fissure system is also highlighted by red lines for comparison.

The timing of fissure opening phases and explosive activity is well constrained by the aforementioned historical accounts, as well as by detailed tephrochronology studies (Thordarson 1990; Thordarson and Self 1993; Thordarson, 2003; Thordarson and Self, 2003; Thordarson et al., 2003). By combining field observations with contemporary accounts, these studies revealed that the Laki cone row was formed by 10 sequentially erupting en-echelon fissures, as activity propagated, in a step-wise fashion, from the SW Síða highlands NE towards Vatnajökull. Each fissure opening phase was preceded by increasing seismicity, before a high-discharge explosive phase of sub-Plinian intensity fountaining occurred, which lasted for approximately 0.5–1 day, before waning into less vigorous fountaining and effusive activity. The tephra fall from this explosive phase produced a proximal sheet-like apron as well as distally dispersing ash creating traceable internal stratigraphy in the Laki tephra layer in the proximal and medial soil horizons, which varies along strike showing the dominance of the more proximal cones, indicating the migration of activity from the

SW-NE. Some fissures created marker units, e.g., magmatic units, which are Pele's hair rich at the base, or more rare phreatomagmatic units which are fine ash rich. The differences between Laki tephra layers have enabled the evolution of eruptive activity, recorded by this sequence, to be more easily deciphered along strike as well within the isopach maps for individual fissures as well as the Laki tephra layer as a whole. The field tephrochronology datasets combined with historical observations of documented ash fall, timing and duration of ash fall, ash colour, and wind direction in Eldrít to create a near-complete understanding of the succession.

In total, the distinct 10 eruptive fissures created a 29.5 km long mixed magmatic and phreatomagmatic crater row. The crater row stretches 11 km to the SW and 16 km to the NW of the Laki hyaloclastite mountain; as the fissure eruption dissected this pre-existing geological feature, the rifting created a large graben, accompanied by small craters (Figure 4. 13). In earlier literature, the Laki fissure is recorded as being a 27 km long geological feature; however, this study has revised this length, to 29.5 km, with improved aerial photographs and increasing the fissure length to the northeast (see Chapter 5).

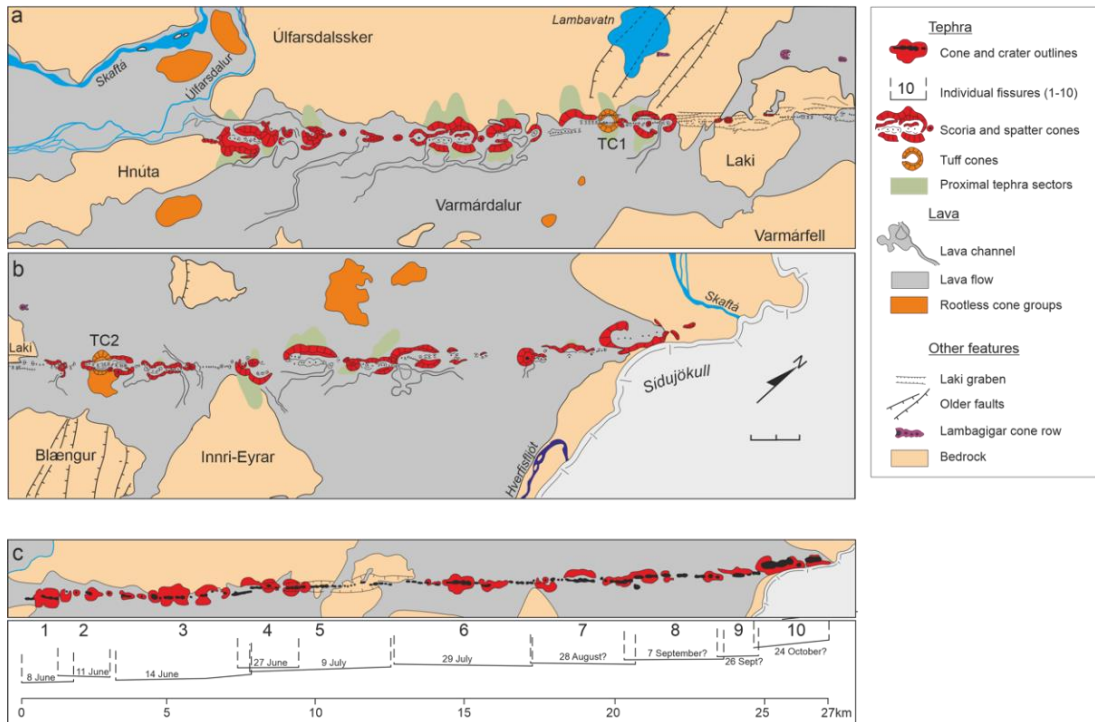


Figure 4. 13: Laki crater row. This figure is taken from Thordarson and Self (1993); the top two panels (a and b) are combined to make a schematic map (not to scale) of the Laki cone-row and surroundings from the SW (a) to the NE (b). The explosive tephra deposits are shown in light green, the magmatic crater forming cone deposits are highlighted in red and the tuff-cones are highlighted in orange. The Laki lava flow field itself is shown in grey, and the rootless cone groups associated with it are highlighted in orange. Pre-eruptive topographic hyaloclastite features, which now stand proud of the flow field, are shown in cream/pale orange. The location of the graben through Mt. Laki is denoted by light grey lines. The lowest panel is a schematic sketch of the entire fissure and its surroundings, this time in less detail, but with the addition of brackets below the fissure, which indicate the location and dates of the ten distinct fissure opening episodes.

After the fissure opening phase, explosive vent activity transitioned into prolonged (days-weeks) effusion feeding a large compound lava field, which exhibits a spectrum of pāhoehoe crust morphologies. The lavas predominantly flowed southwards from the fissures towards the lowlands, channelled through two pre-existing glacial river calved canyons, the Skaftá canyon to the west and the Hverfisfljót canyon to the east, creating two main flow branches which bound the Síða district. The compound pāhoehoe flow field developed a mature tube system, enabling lava to be transported whilst undergoing only minor amounts of cooling and, therefore, minimal further crystallisation of microlites, to the active flow fronts (Guildbaud et al., 2007) up to 90km from the vent in some cases.

The Eldrít accounts document lava surge, discharging down these canyons, occurring shortly after the onset of eruptive activity during a fissure opening phase. The initial

two lava surges covered 6–16 km/day, which dropped to 2–3 km/day for fissures 3–10 (Thordarson and Self, 1993), with these speeds calculated using the onset of explosive activity, initial evidence of water pollution denoted by people living downstream in the lowlands and subsequent drying up of the riverbeds before the lava fronts themselves were visible (Sigurdsson, 1982; Thordarson and Self, 2001; Thordarson et al., 2003a). Contemporary accounts also documented specific lava arrivals at inhabited lowland areas, when coupled with field observations such as changes in lava crust morphology, as well as mapped lava tubes and outbreaks; this enables an accurate understanding of the evolution of the lava flow field and emplacement dynamics. Such a high-resolution determination of the temporal and spatial evolution of the lava flow field means subsequent sampling of lava fronts linked to specific known dates of activity is very accurate. The lava flow field is predominantly rubbly pāhoehoe, but several morphologies are observed and can be explained by localised changes in transport systems or topography (Guilbaud et al., 2007). The Laki lava flow, like the Eldgjá lava flow, advanced over marshy ground creating rootless cones as the lava lobes inflate and eventually, under their own weight, crack the basal crust enabling interactions between the lavas and the wetland in both the mid-highlands and the lowlands of the Síða area.

The processes generating episodic eruptive activity, creating 10 discrete fissure opening events, each of which follows the same pattern; a peak mass-eruption rate which then exponentially declines within the first 24 hours, are not well understood. Timescales of magma migration from the storage zone to eruption, using Fe-Mg diffusion chronometry of olivine phenocrysts from the Laki eruptive products from different fissure opening episodes matches the timescales outlined in contemporary accounts well (Hartley et al., 2016). Thordarson and Self (1993) suggest that the episodic nature of the Laki eruption cannot be linked to separate inflation and deflation events of the reservoir that fed the eruption. Instead, they hypothesise that non-linear flow through the linear conduit that fed the eruption could result in a variable flow rate generating a rheological spectrum; however, this has not been examined further.

Thordarson and Self (1993) agreed with the initial geological mapping of the very northern section of Laki by Thoroddsen, 1881–1901, and the hypothesis initially

outlined by Jakobsson (1979) that the lavas, now attributed to fissure 10 from the Laki eruption erupted through a geologically older hyaloclastite linear feature. However, Chapter 5 of this thesis will go through several lines of evidence that refute this hypothesis, outlining new field evidence, collated over 4 summers of field campaigns which found evidence for magma-ice interactions and ice-confined deposits.

Six inhabited areas in this county, spread roughly between both canyons (Skaftá and Hverfisfljót), directly south, southeast and east of the fissure itself, which were affected the most by the hazards from the eruption are given the nickname 'Fire Districts' (Holm, 1784). From east to west these are: Álftaver, Skaftártunga, Meðalland, Landbrot, Síða (where Kirkjubærklaustur lies) and Fljótshverfi. Additionally, whilst not inhabited, two livestock grazing pastures of importance, as they are used throughout the late spring and summer, were also affected: (1) Álftaversafréttur, the area east of Álftaver extending towards Hólmsá, a river near Mýrdalsjökull, up to Brytalæki in the north and (2) Síðumannafréttur, the area of heathland extending from the geologically older escarpment directly above the Síða district to the east, northeast and northwest, to the Laki fissures themselves in the mid-highlands (Figure 4. 14)

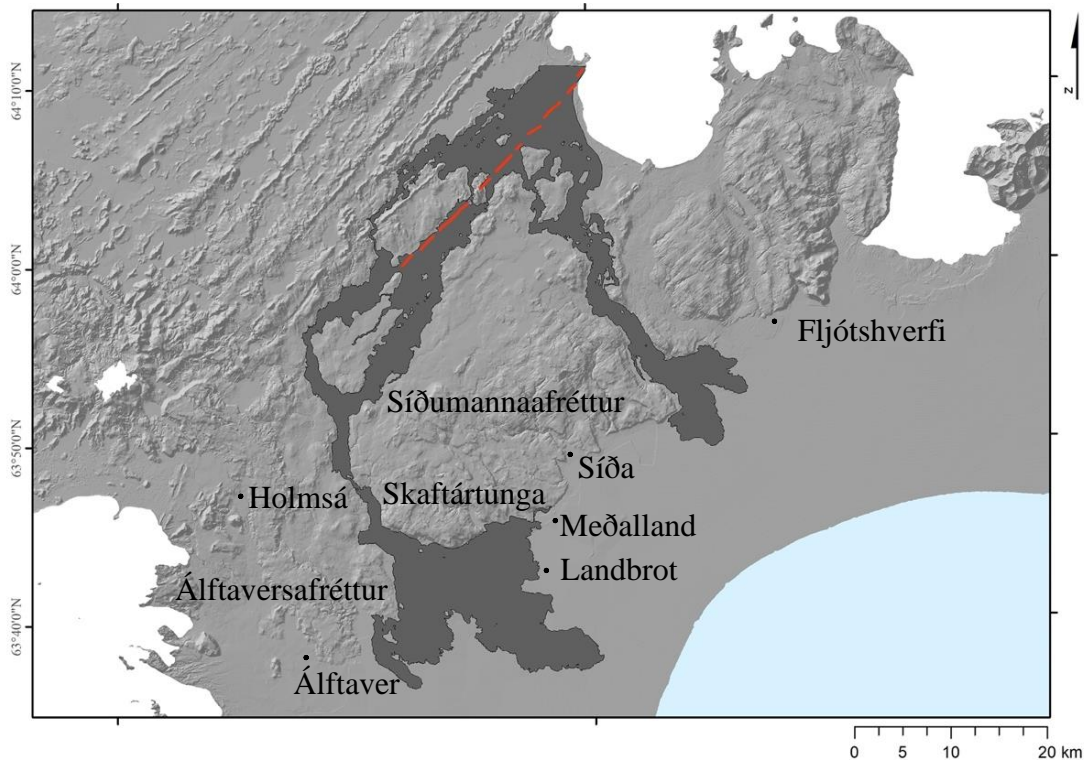


Figure 4. 14: Historical place names of note surrounding the Laki lava field and eruption site. Place names, previously inhabited or currently inhabited and farmed that are referred to in the Eldrít accounts, as well as geographic Icelandic place names where tephra samples were taken.

Previous geochemical studies

The Laki eruptive products are classified as quartz-normative tholeiite. Sigmarsson et al. (1991), noted that the whole-rock geochemical analysis eruptive products are homogeneous in their major element compositions and display uniform U, Th, Pb and O isotopic signatures. However, small scale whole rock variations, of statistical significance, were observed by Passmore et al. (2012) in some regions of the flow field, which were interpreted as varying amounts of crystal mush included in the whole rock samples. Whilst this is important, the geochemical heterogeneity it causes is relatively small, and samples with much higher crystal contents were avoided in the samples analysed in this PhD research project. However, like most Icelandic FL's, the Laki eruptive products contain <10% phenocrysts and crystal mush glomerocrysts, and are therefore classified as aphyric; again, this also evolves with time with more phenocrysts erupted towards the end of the eruption.

A wide range in phenocryst compositions has been observed in the Laki eruptive products by several studies (Métrich et al. 1991; Bindeman et al. 2006; Guilbaud et al., 2007; Passmore, 2009; Passmore et al., 2012; Neave et al., 2013). Passmore et al., 2012 observed that the crystal composition becomes more primitive throughout the eruption, correlating with the eruptive products originating from later erupting fissures. Detailed studies of trace element variations both within zoned crystals and in melt inclusions in this crystal cargo (Neave et al., 2013) indicated that the compositions observed could not be generated by the evolution of a primary melt along the liquidus. Instead, they record a high degree of mixing of a diverse set of both depleted and enriched mantle melts with different crystallisation histories (which generate their distinct compositions). These melts simultaneously mix and crystallise in a mid-crustal (15 km) storage reservoir, eventually generating the Laki carrier liquid. The crystal mush generated in this mid-crustal storage reservoir is partially disaggregated as the Laki carrier melt migrated through the crust to shallower storage zones prior to eruption.

Many of the studies of Laki have focussed on its environmental impact, through underpinning of its total volatile budget, in particular, the S, Cl, and F content of the melt and the degree of syn-eruptive and syn-emplacement degassing. This was carried out to identify the eruption's total atmospheric volatile load, using the difference in volatile contents between melt inclusions and glassy eruptive tephra and lava selvages. These values have been used as model inputs to gain constraints on the environmental and climatic impact of an FL eruption within Europe today with its higher population densities and well-developed infrastructure, which are all fragile and at risk from an event like this (Loughlin, 2012; Schmidt et al., 2015). More recently, studies have concentrated on identifying the redox conditions of the Laki melt within the crustal storage zone at depth, using XANES to fingerprint the oxygen fugacity (fO_2) of glassy melt inclusions within phenocrysts. The fO_2 of the melt prior to eruption influences the volatile content at saturation of the melt itself; this concentration limit and speciation dictates the evolution of volatile exsolution as well as the phases present. Analysis of melt inclusions in phenocrysts from rapidly quenched erupted tephra indicates that the Laki melt prior to eruption was oxidised (Hartley et al., 2017).

Holuhraun 2014–15 CE and Laki 1783–84 CE represent two end-member styles of fountaining activity for high magnitude basaltic fissure eruptions: low–moderate and sub-Plinian intensity fountaining, with only the Eldgjá FL eruption surpassing this activity at sub-Plinian–Plinian activities. Analysis of the modulating role of shallow conduit processes on eruptive intensity and temporal evolution of this throughout an eruption’s lifespan, as well as the mechanisms of volatiles release, i.e., the speciation of volatiles lost during syn-eruptive and syn-emplacement degassing, had not yet been undertaken on either the Holuhraun or Laki eruptive products before this project. Initial analysis in the eruptive activity in response to changes in the eruptive environment as Laki propagates from the SW to the NE has been undertaken for the Laki melt and surface lake at the P1 cone site in the southern fissure (Decker, 2017). However, newly revealed outcrops in the very NE of the fissure system, due to the response of the local outlet glacier Síðujökull to climate change, has enabled previously unknown and inaccessible portions of the Laki fissure eruptive cones to be sampled and studied. A summary of initial findings and interpretations can be found in Chapter 5, as the change from magmatic to shallow sub-glacial–ice-confined eruptive environment directly influences interpretations of the processes occurring during this stage of the eruption both texturally and geochemically.

4. 5 References

- Ágústsdóttir, T., Woods, J., Greenfield, T., Green, R. G., White, R. S., Winder, T., Brandsdóttir, B., Steinthórsson, S., and Soosalu, H. (2016). Strike-slip faulting during the 2014 Bárðarbunga- Holuhraun dike intrusion, central Iceland. *Geophysical Research Letters*. 43. pp. 1495–1503.
- Aufaristama, M., Hoskuldsson, Á., Ulfarsson, M.O., Jonsdottir, I., and Thordarson, T. (2019). The 2014–2015 Lava Flow Field at Holuhraun, Iceland: Using Airborne Hyperspectral Remote Sensing for Discriminating the Lava Surface. *Remote Sensing*, 11 (5), pp. 476.
- Bali, E., Hartley, M. E., Halldórsson, S. A., Gudfinnsson, G. H., and Jakobsson, S. (2018). Melt inclusion constraints on volatile systematics and degassing history of the 2014–2015 Holuhraun eruption, Iceland. *Contributions to Mineralogy and Petrology*. 173. (2). doi:10.1007/s00410-017-1434-1
- Bindeman, I. N., Sigmarsson, O., and Eiler, J. (2006). Time constraints on the origin of large volume basalts derived from O-isotope and trace element mineral zoning and U-series disequilibria in the Laki and Grímsvötn volcanic system. *Earth and Planetary Science Letters*. 245. (1–2), pp. 245–259. doi:10.1016/j.epsl.2006.02.029
- Bonny, E., Thordarson, T., Wright, R., Höskuldsson, A., and Jónsdóttir, I. (2018). The Volume of Lava Erupted During the 2014 to 2015 Eruption at Holuhraun,

- Iceland: A Comparison Between Satellite- and Ground-Based Measurements. *Journal of Geophysical Research: Solid Earth*. 123. (7), pp. 5412–5426. doi:10.1029/2017JB015008
- Decker, Z. (2017) Masters Thesis. The University of Iceland ‘Episode 4 of the 1783–84 Laki eruption: conduit processes and eruption dynamics of phreatomagmatic phase 1’
- Dundas, C. M., Keszthelyi, L., Lev, E., Rumpf, M. E., Hamilton, C. W., Höskuldsson, Á., Thordarson, T. (2020). Lava–water interaction and hydrothermal activity within the 2014–2015 Holuhraun Lava Flow Field, Iceland. *Journal of Volcanology and Geothermal Research*, 408, doi.org/10.1016/j.jvolgeores.2020.107100.
- Eibl, E. P. S., Bean, C. J., Jónsdóttir, I., Höskuldsson, A., Thordarson, T., Coppola, D., Witt, T., and Walter, T. R. (2017). Multiple coincident eruptive seismic tremor sources during the 2014–2015 eruption at Holuhraun, Iceland. *Journal of Geophysical Research: Solid Earth*. 122. (4), pp. 2972–2987. doi:10.1002/2016JB013892
- Einarsson T, Guðbergsson GM, Gunnlaugsson GA, Rafnsson S, Þórarinnsson S (1984) Skaftáreldar 1783-1784: Ritgerðir og Heimildir. Mál og Menning: Reykjavík, 442.
- Eiríksson, J. (1783). Abstract from Erichsens writings, dated July 11, 1783 at Fljótastöðum Vestur-Skaftafells County. In: Einarsson, T., Guðbergsson, G. M., Gunnlaugsson, G. A., Rafnsson, S. and Þórarinnsson, S. (eds.) Skaftáreldar 1783-1784: Ritgerðir og Heimildir. pp. 274-276. Mál og Menning Reykjavík.
- Gíslason, S. R., Stefánsdóttir, G., Pfeffer, M. A., Barsotti, S., Jóhannsson, T., Galeczka, I., Bali, E., Sigmarsson, O., Stefánsson, A., Keller, N. S., Sigurdsson, Bergsson, B., Galle, B., Jacobo, V. C., Arellano, S., Aiuppa, A., Jónasdóttir, E. B., Eiríksdóttir, E. S., Jakobsson, S., G.H. Guðfinnsson, G. H., Halldórsson, S. A., Gunnarsson, H., Haddadi, B., Jónsdóttir, I., Thordarson, T., Riishuus, M., Högnadóttir, T., Dürig, T., Pedersen, G. B. M., Höskuldsson, Á. and Gudmundsson, M. T. (2015). Environmental pressure from the 2014-15 eruption of Barðarbunga volcano, Iceland. *Geochemical Perspectives Letters*. 1. (1), pp. 84–93. doi:10.7185/geochemlet.1509
- Gudmundsson, M.T., Sigmundsson, F. and Björnsson, H. (1997). Ice-volcano interaction of the 1996 Gjalp subglacial eruption, Vatnajökull, Iceland. *Nature*. 389, pp. 954-957
- Gudmundsson, M. T., Jónsdóttir, K., Hooper, A., Holohan, E. P., Halldórsson, S. A., Ófeigsson, B. G., Cesca, S., Vogfjörð, K. S., Sigmundsson, F., Högnadóttir, T., Einarsson, P., Sigmarsson, O., Jarosch, A. H., Jónasson, K., Magnússon, E., Hreinsdóttir, S., Bagnardi, M., Parks, M. M., Hjörleifsdóttir, V., Pálsson, F., Walter, T. R., Schöpfer, M. P. J., Heimann, S., Reynolds, H. I., Dumont, S., Bali, E., Gudfinnsson, G. H., Dahm, T., Roberts, M. J., Hensch, M., Belart, J. M. C., Spaans, K., Jakobsson, S., Gudmundsson, G. B., Fridriksdóttir, H. M., Drouin, V., Dürig, T., Aðalgeirsdóttir, G., Riishuus, M. S., Pedersen, G. B. M., van Boeckel, T., Oddsson, B., Pfeffer, M. A., Barsotti, S., Bergsson, B., Donovan, A., Burton, M. R. and Aiuppa, A. (2016). Gradual caldera collapse at Bárðarbunga volcano, Iceland, regulated by lateral magma outflow. *Science*. 353. (6296), aaf8988. doi:10.1126/science.aaf8988
- Guilbaud, M.-N., Blake, S., Thordarson, T. and Self, S. (2007). ‘Role of Syn-eruptive Cooling and Degassing on Textures of Lavas from the AD 1783-84 Laki Eruption, South Iceland’. *Journal of Petrology*. 48. pp.1265-1294.

- Halldórsson, S. A., Bali, E., Hartley, M. E., Neave, D. A., Peate, D. W., Guðfinnsson, G. H., Bindeman, I., Whitehouse, M. J., Riishuus, M. S., Pedersen, G. B. M., Jakobsson, S., Askew, R., Gallagher, C. R., Guðmundsdóttir, E. R., Gudnason, J., Moreland, W. M., Óskarsson, B. V., Nikkola, P., Reynolds, H. I., Schmidt, J. and Thordarson, T. (2018). Petrology and geochemistry of the 2014–2015 Holuhraun eruption, central Iceland: compositional and mineralogical characteristics, temporal variability and magma storage. *Contributions to Mineralogy and Petrology*. 17. (3) 8, pp. 1–25. doi:10.1007/s00410-018-1487-9
- Hartley, M. E., and Thordarson, T. (2013). The 1874-1876 volcano-tectonic episode at Askja, North Iceland: Lateral flow revisited. *Geochemistry, Geophysics, Geosystems*. 14. (7), pp. 2286–2309. doi:10.1002/ggge.20151
- Hartley, M. E., Morgan, D. J., MacLennan, J., Edmonds, E. and Thordarson, T. (2016). Tracking timescales of short-term precursors to large basaltic fissure eruptions through Fe–Mg diffusion in olivine. *Earth and Planetary Science Letters*. 439. pp. 58-70. doi:10.1016/j.epsl.2016.01.018
- Hartley, M. E., Shorttle, O., MacLennan, J., Moussallam, Y., and Edmonds, M. (2017). Olivine-hosted melt inclusions as an archive of redox heterogeneity in magmatic systems. *Earth and Planetary Science Letters*, 479, 192–205. <https://doi.org/10.1016/j.epsl.2017.09.029>
- Hartley, M. E., Bali, E., MacLennan, J., Neave, D. A., and Halldórsson, S. A. (2018). Melt inclusion constraints on petrogenesis of the 2014–2015 Holuhraun eruption, Iceland. *Contributions to Mineralogy and Petrology*. 173. (2), pp. 1–23. doi:10.1007/s00410-017-1435-0
- Hjartardóttir, Á. R., Einarsson, P., Gudmundsson, M. T., and Högnadóttir, T. (2016). Fracture movements and graben subsidence during the 2014 Bárðarbunga dike intrusion in Iceland. *Journal of Volcanology and Geothermal Research*. 310. pp. 242–252. doi:10.1016/j.jvolgeores.2015.12.002
- IES eruption team field reports. Háskóli Íslands, Institute of Earth Sciences and The Icelandic Metrological Office (Veðurstofa Íslands). Accessed (17/03/2021) from: <https://en.vedur.is/earthquakes-and-volcanism/articles/nr/3071>
- IMO Holuhraun eruption reports. The Icelandic Metrological Office (Veðurstofa Íslands). Accessed (17/03/2021) from: <https://en.vedur.is/earthquakes-and-volcanism/articles/nr/3071>
- Ilyinskaya, E., Schmidt, A., Mather, T. A., Pope, F. D., Witham, C., Baxter, P., Jóhannsson, T., Pfeffer, M., Barsotti, S., Singh, A., Sanderson, P., Bergsson, B., McCormick Kilbride, B., Donovan, A., Peters, N., Oppenheimer, C., and Edmonds, M. (2017). Understanding the environmental impacts of large fissure eruptions: Aerosol and gas emissions from the 2014–2015 Holuhraun eruption (Iceland). *Earth and Planetary Science Letters*. 472. pp. 309–322. doi:10.1016/j.epsl.2017.05.025
- Jakobsson, S.P. (1979). Petrology of recent basalts of the Eastern Volcanic Zone, Iceland. *Acta Naturalia Islandica*. 26. 103.
- Jónsson, O. (1945). Ódáðhraun I-III. Bókaútgáfan Norðri, Akureyri. 1276. pp.
- Kazahaya, K., ; Shinohara, H., Uto, K., Odai, M., Nakahori, Y., Mori, H., ; Iino, H. Miyashita, M. and Hirabayashi, J. (2004). Gigantic SO₂ emission from Miyakejima volcano, Japan, caused by caldera collapse. *Geology*. 32. (5), pp. 425–428. doi:10.1130/G20399.1
- Loughlin, S. C., Aspinall, W. P., C, V.-B., Baxter, P. J., Braban, C., M, H., Schmidt, A., Thordarson, T., and Witham, C. S. (2012). Large-Magnitude Fissure

- Eruptions in Iceland: Source Characterisation. *British Geological Survey OpenFile Report*, pp. 1–136. <http://www.bgs.ac.uk/research/volcanoes/LakiEruptionScenarioPlanning.html%0Apapers3://publication/uuid/E5A6AE4C-D7D6-4563-AD7C-4B53F7033815>
- Métrich, N., Sigurdsson, H., Meyer, P. S. and Devine, J. D. (1991). The 1783 Lakagigar eruption in Iceland: geochemistry, CO₂ and sulfur degassing. *Contributions to Mineralogy and Petrology*. 107. pp. 435-447.
- Neave, D. A., Passmore, E., MacLennan, J., Fitton, G. and Thordarson, T. (2013). Crystal-Melt Relationships and the Record of Deep Mixing and Crystallization in the AD 1783 Laki Eruption, Iceland. *Journal of Petrology*. 54. (8), pp.1661-1690.
- Passmore, E. (2009). Unpublished Thesis, University of Edinburgh. ‘Feeding large eruptions: crystallization, mixing and degassing in Icelandic magma chambers’.
- Passmore, E., MacLennan, J., Fitton, G. and Thordarson, T. (2012). Mush disaggregation in basaltic magma chambers: Evidence from the AD 1783 Laki Eruption. *Journal of Petrology*. 53. (12). pp. 2593–2623. doi:10.1093/petrology/egs061
- Pedersen, G. B. M., Höskuldsson, A., Dürig, T., Thordarson, T., Jónsdóttir, I., Riishuus, M. S., Óskarsson, B. V., Dumont, S., Magnusson, E., Gudmundsson, M. T., Sigmundsson, F., Drouin, V. J. P. B., Gallagher, C., Askew, R., Gudnason, J., Moreland, W. M., Nikkola, P., Reynolds, H. I., and Schmith, J. (2017). Lava field evolution and emplacement dynamics of the 2014–2015 basaltic fissure eruption at Holuhraun, Iceland. *Journal of Volcanology and Geothermal Research*, 340, pp. 155–169. doi:10.1016/j.jvolgeores.2017.02.027
- Pfeffer, M. A., Stefánsdóttir, G., Bergsson, B., Barsotti, S., Galle, B., Ilyinskaya, E., Spina, A. La, Sigurðardóttir, G. M., and Jónasdóttir, E. B. (2015). Ground-based measurements of the emission rate and composition of gases from the Holuhraun eruption. *EGU Abstract*. 17. 7373.
- Pfeffer MA, Bergsson B, Barsotti S, Stefánsdóttir G, Galle B, Arellano S, Conde V, Donovan A, Ilyinskaya E, Burton M, Aiuppa A, Whitty RCW, Simmons IC, Arason Þ, Jónasdóttir EB, Keller NS, Yeo RF, Arngrímsson H, Jóhannsson Þ, Butwin MK, Askew RA, Dumont S, Von Löwis S, Ingvarsson Þ, La Spina A, Thomas H, Prata F, Grassa F, Giudice G, Stefánsson A, Marzano F, Montopoli M, Mereu L. (2018) change in text. Ground-Based Measurements of the 2014–2015 Holuhraun Volcanic Cloud (Iceland). *Geosciences*. 8. (1), 29. doi:10.3390/geosciences8010029
- Riel, B., Milillo, P., Simons, M., Lundgren, P., Kanamori, H. and Samsonov, S. (2015). The collapse of Bárðarbunga Caldera, Iceland. *Geophysics Journal International*. 202. pp. 446-453. doi:10.1093/gji/ggv157
- Reynolds, H.I., Gudmundsson, M.T., Högnadóttir, T. et al. Subglacial volcanic activity above a lateral dyke path during the 2014–2015 Bárðarbunga-Holuhraun rifting episode, Iceland. *Bulletin of Volcanology*. 79 (38). doi:10.1007/s00445-017-1122-z
- Schmidt, A. (2015). Chapter 15 ‘Volcanic Gas and Aerosol Hazards from a Future Laki-Type Eruption in Iceland’. In: *Volcanic Hazards, Risks and Disasters*. Editor(s): John F. Shroder, Paolo Papale. doi:10.1016/B978-0-12-396453-3.00015-0.
- Schmidt, A., Leadbetter, S., Theys, N., Carboni, E., Witham, C. S., Stevenson, J. A., Birch, C. E., Thordarson, T., Turnock, S., Barsotti, S., Delaney, L., Feng, W., Grainger, R. G., Hort, M. C., Höskuldsson, Á., Ialongo, I., Ilyinskaya, E.,

- Jóhannsson, T., Kenny, P., Mather, T. A., Richards, N. A.D. and Shepherd, J. (2015). Satellite detection, long-range transport, and air quality impacts of volcanic sulfur dioxide from the 2014–2015 flood lava eruption at Bárðarbunga (Iceland). *Journal of Geophysical Research: Oceans*. 120. pp. 9739–9757. doi:10.1002/2015JC011107.
- Sigmundsson, F., Hooper, A., Hreinsdóttir, S., Vogfjörð, K. S., Ófeigsson, B. G., Heimisson, E. R., Dumont, S., Parks, M., Spaans, K., Gudmundsson, G. B., Drouin, V., Árnadóttir, T., Jónsdóttir, K., Gudmundsson, M. T., Högnadóttir, T., Fridriksdóttir, H. M., Hensch, M., Einarsson, P., Magnússon, E., Samsonov, S., Brandsdóttir, B., White, R. S., Ágústsdóttir, T., Greenfield, T., Green, R. G., Hjartardóttir, Á. R., Pedersen, R., Bennett, R. A., Geirsson, H., la Femina, P. C., Björnsson, H., Pálsson, F., Sturkell, E., Bean, C. J., Möllhoff, M., Braiden, A. K. and Eibl, E. P. S. (2014). Segmented lateral dyke growth in a rifting event at Bárðarbunga volcanic system, Iceland. *Nature*. 517. (7533). doi:10.1038/nature14111
- Sigmarsson, O., and Halldórsson, S. A. (2015). Delimiting Baroarbunga and Askja volcanic systems with Sr- and Nd-isotope ratios. *Jökull*. 65. pp. 17–28.
- Sigurdsson H (1982) Volcanic pollution and climate: the 1783 Laki eruption. *EOS*. 63. pp. 601-602
- Steinthorssona, S., Hardarson, B. S., Ellam, R. M. and Larsen, G. (2000) Petrochemistry of the Gjalp-1996 subglacial eruption, Vatnajökull, SE Iceland. *Journal of Volcanology and Geothermal Research*. 98. (1–4), pp. 79-90
- Steingrímsson, J. (1788). A complete description on the Síða volcanic fire, dated November 24 1788 at Prestbakki In: Safn til Sögu Islands. IV. pp. 1-57: Copenhagen.
- Sutton, A. J., Elias, T., Gerlach, T.M. and Stokes, J.B. (2001). Implications for eruptive processes as indicated by sulfur dioxide emission from Kīlauea volcano, Hawai'i, USA, 1979-1997. *Journal of Volcanology and Geothermal Research*. 108. pp. 283–302.
- Thorarinsson, S. (1984). The Laki Fires. In: Einarsson, T., Guðbergsson, G. M., Gunnlaugsson, G.A., Rafnsson, S. and Þórarinnsson, S (eds.) Skaftáreldar 1783-1784: Ritgerðir og Heimildir. pp. 11-36. Mál og Menning: Reykjavík.
- Thórarinnsson, S. and Sigvaldason, G. E. (1972). Eruption in Askja, 1961 – a preliminary report. *American Journal of Science*. 260, pp. 641-651.
- Thordarson, T. (1990). Unpublished masters thesis. The eruption sequence and the eruption behaviour of the Skaftár Fires, 1783-85, Iceland: characteristics and distribution of eruption products. University of Texas at Arlington.
- Thordarson, T. and Self, S. (1993). The Laki (Skaftár Fires) and Grímsvötn eruptions in 1783-1785. *Bulletin of Volcanology*. 55. (4), pp. 233–263. doi:10.1007/BF00624353
- Thordarson, T. (2003). The 1783 – 1785 A . D . Laki-Grímsvötn eruptions I: A critical look at the contemporary chronicles. *Jökull*. 53, pp. 1–10.
- Thordarson, T. and Self, S. (2003). Atmospheric and environmental effects of the 1783-1784 Laki eruption: A review and reassessment. *Journal Of Geophysical Research-Atmospheres*. 108. 4011
- Thordarson, T, Larsen, G., Steinthorsson, S., and Self, S. (2003). The 1783–1785 AD Laki-Grímsvötn eruptions II: appraisal based on contemporary accounts. *Jökull*. 53. pp. 11–47.
- Thordarson, T., and Larsen, G. (2007). Volcanism in Iceland in historical time: Volcano types, eruption styles and eruptive history. *Journal of Geodynamics*.

43. (1), pp. 118–152. doi:10.1016/j.jog.2006.09.005
- Thordarson, T. (2020). Sulfur output by the 2014–15 flood lava eruption at Holuhraun, N-Iceland. *Goldschmidt 2020 abstract*. doi:10.46427/gold2020.2594
- Voigt, J. R. C., Hamilton, C. W., Scheidt, S. P., Achilles, C. N., Dundas, C. M., Keszthelyi, L. P., Münzer, U. and Whelley, P. L. (2020). Platy Terrain within the 2014–2015 Holuhraun Lava Flow-Field: An Analog for Martian Flood Lavas. *In Lunar and Planetary Science Conference*. (No. 2326, p. 2358).
- Voigt, J. R. C., Hamilton, C. W., Scheidt, S. P., Münzer, U., Höskuldsson, Á., Jónsdóttir, I., Thordarson, T. (2021). Geomorphological characterization of the 2014–2015 Holuhraun lava flow-field in Iceland, *Journal of Volcanology and Geothermal Research*, 419, 107278, doi.org/10.1016/j.jvolgeores.2021.107278.
- Witt, T., Walter, T. R., Müller, D., Guðmundsson, M. T., and Schöpa, A. (2018). The Relationship Between Lava Fountaining and Vent Morphology for the 2014–2015 Holuhraun Eruption, Iceland, Analyzed by Video Monitoring and Topographic Mapping. *Frontiers in Earth Science*, 6. doi:10.3389/feart.2018.00235

Chapter 5: NE Laki revisited; evidence for ice-magma interactions during a shallow subglacial fissure eruption.

5.1 Motivation and Novelty

Many aspects of explosive subaerial phreatomagmatic and subglacial eruptive activity globally are well constrained and characterised (Höskuldsson and Sparks, 1997; Gudmundsson et al., 2004; Tuffen, 2007; Jakobsson and Gudmundsson, 2008; Wilson et al., 2009; Tuffen et al., 2010; Jude-Eton et al., 2012; Magnússon et al., 2012; Edwards et al., 2015; Gudmundsson, 2015; Moreland et al., 2019). When it comes to sub-glacially formed volcanic edifices, Iceland has the largest variety of such formations worldwide, given the extensive glacial cover during the Pleistocene and the frequent volcanic activity (Kjartansson, 1943; Jones, 1969; Smellie et al., 2002; Tuffen et al., 2002; Schopka et al., 2006). Most studies have been based on mapping Pleistocene formations or observations of the eruptions that have occurred since the 1990s. One type of relatively uncharacterised volcanic formations affected by ice are those formed under very thin glaciers, usually at or within the ice margin. It is thought that these formations may display several forms of hybrid activity where magma-water interaction and ice-confinement may play a role.

Understanding the nature and morphology of shallow subglacial and intra-glacial ice-confined deposits in the geological record can, in turn, help improve maps of paleo ice-extents (Höskuldsson et al., 2006; Edwards et al., 2015; Smellie, 2018). Combining aerial photographs, field mapping and models of previous ice extents enables these shallow intraglacial edifices to be well constrained and understood. These techniques are used to ground-truth remote sensing data sets, such as the high resolution ArcticDEM, further improving recognition of these structures, and thus paleo ice-extents, in other countries/continents (Edwards et al., 2015; Smellie, 2018). Another topical application of this is using these high confidence morphological data sets from Earth and relating them to Martian ice-magma edifices to estimate past ice thickness on Mars and help constrain its paleo-climate variations (Edwards et al., 2009; Edwards et al., 2015; Smellie and Edwards; 2016; Smellie, 2018). All of these

previous studies called for an improved understanding of terrestrial analogues, and as of yet, the current studies of ice-magma interactions in the geological record do not include any examples of historical fissure eruptions through a shallow ice margin, as they are either unpreserved or inaccessible.

Wilson et al. (2009) note that no examples of shallow subglacial fissure eruptions that do not break immediately through the ice have been directly observed and, due to their setting and unconsolidated nature, no resultant products have been preserved. Nevertheless, they hypothesised this type of eruption would result in explosive activity, forming stratified tuff cones or rings, comprised of interbedded fall and surge tephra deposits, as well as generating meltwater floods

5. 1. 1 Background

To date, one reasonably detailed study has been conducted on an historic fissure eruption through a thin (<100 m) glacial margin, the 1969 CE event on Deception Island, Antarctica (Smellie, 2002). This eruption benefits from eye-witness accounts and detailed seismicity measurements. However, the eruptive products showed no evidence of external ice interaction; instead, they suggest a weak ‘dry’ or magmatic, Hawaiian or Strombolian, mechanism (Smellie, 2002) with catastrophic drainage of meltwater at the start of the event curtailing ice-magma interactions (Baker et al., 1975; Smellie, 2002). Eruptions like this will also not leave a record that can be easily interpreted as subglacial (Smellie, 2002), with the added complication of material being lost through glacial erosion as the Mount Pond glacier still surrounds these vents. Evidence of older, historical and pre-historic, shallow intra-glacial eruptions exist on Deception Island Antarctica, but they are only partially visible in-situ, or preserved as fragments at the marine termini of outlet glaciers (Baker et al., 1975; Smellie, 2002; Wilson et al., 2009). This locality, therefore, offers little or no opportunity to fully map and understand well-constrained ice-magma activity sequences.

Wilson et al. (2009) hypothesise that, at the onset of a shallow subglacial eruption, a mature magmatic foam interacts with meltwater generated by the abrupt melting of

the overlying ice. The magma-meltwater/ice interactions that ensue produce a fine-ash-rich deposit composed of interbedded tephra fall and pyroclastic density current deposits. This is not dissimilar to the results from a previous study of the medial-distal fall units from the subglacial fissures of the Eldgjá eruption (939 CE), where a mature magmatic foam interacts with the overlying glacier generating a fine-ash-rich plume (Moreland et al., 2019). If the meltwater can drain easily away from the subglacial eruptive activity, or the vents can lithify, isolating the conduit from the external water source, the eruption style may change from phreatomagmatic to magmatic effusive activity (Wilson et al., 2009).

If an historical example of activity of this nature was well documented and understood better constraints and understanding could be applied to much older eruptions in the geological record using the well-known ‘The present is key to the past’ principle (Sir Charles Lyell). Examples of transitional or fini-glacial deposits have been highlighted in the Icelandic geological record, e.g., Hestfjall (<14.7 ka) (Sinton et al., 2005; Eason et al., 2015), but questions remain about the source of water for these events, with a lack of definitive ice- and ocean- margins at the time (Sinton et al., 2005).

5. 1. 2 Previous studies

Recent studies of historical phreatomagmatic volcanism in Iceland, i.e., in the last 1100 years, are largely confined to explosive events at subglacial central volcanoes, e.g., Oræfajökull 1363 CE and 1727 CE, Katla 1625 CE, 1755 CE and 1918 CE, Grímsvötn 2004 CE and 2011 CE, and Eyjafjallajökull 2010 CE, focused on mapping tephra dispersal and associated jökulhlaups for hazard assessments. However, there are only two examples of historic subglacial fissure eruptions in Iceland: Eldgjá 939 CE and Gjalp 1996 CE and due to locations of these eruptive fissures the vent products are inaccessible due to the ice now covering these areas once more. As Eldgjá 939 CE eruption was a high intensity, high magnitude FL event, the extensive medial and distal phreatomagmatic deposits from its subglacial phase provide some insight into the evolution of the subglacial portion of the eruption (Larsen, 1979; Miller., 1989; Larsen, 2000; Thordarson et al., 2001; Moreland et al., 2019), and are well preserved in soil horizons; across South Iceland.

Whilst still currently submerged, the location of the Eldgjá fissures under Kötlujökull was identified through radio-echo sounding (Björnsson et al., 2000). Gjálp 1996 CE was a much lower intensity and low magnitude eruption (see Chapter 4, Figure 4. 3), that occurred under much thicker ice. Whilst there are no publications of the mapped extent of its tephra layer, the tephra deposit itself is only accessible near the eruption site in profiles through the ice, or cropping out in outlet glaciers at the margins of Vatnajökull (Larsen, G. personal. communication). It is distinguished from other Grímsvötn tephra layers in these localities through its basaltic Icelandite geochemistry (Sigmarsson et al., 2000; Sigmarsson et al., 2015). There is only one existing study of an intra-glacial, ice-confined, historic fissure eruption in Iceland: the silicic effusive 950 AD Skerin Ridge eruption, within the Eyjafjalljökull volcanic system (Óskarsson, 2009).

The Earth is venturing into uncharted territory as climatic change continues to adversely impact its glaciers, ice-caps, and ice-sheets. In Iceland, the retreat of its glaciers, in response to climate change, will reveal outcrops sub-glacially erupted formations and their stratigraphy as they emerge from the outlet glacier margins. Due to their eruptive environment, outcrops from historical shallow subglacial eruptions which occurred under the ice-extents mapped for the little Ice Age would become more rapidly accessible. These outcrops would present a key opportunity to map the eruptive sequences. Understanding the morphology of these shallow sub-glacially erupted outcrops will help us locate future areas of interest in other terrestrial localities, whilst also providing the opportunity for datasets like these to be used to improve the scientific understanding of shallow ice-magma interactions on other planets. The latter of which has significant implications for the identification of Martian glacio-volcanic edifices (Edwards et al., 2009; Smellie and Edwards, 2016).

Recent findings from the initial mapping of previously unidentified and unmapped sequences of the NE portions of the Laki 1783–84 CE fissure eruption, South Iceland, and reassessment of the tephra stratigraphy from this eruption suggest that the eruptive activity propagated underneath the outlet glacial Síðujökull. As the fissure propagated to the NE from a subaerial to subglacial eruptive environment it transitioned from magmatic to ice-confined phreatomagmatic sequences providing

the first opportunity to analyse and document the eruptive products from a shallow sub-glacial fissure eruption on Earth.

5. 1. 3 The Laki 1783–84 CE eruption

On 8 June 1783 CE a fissure eruption, Skaftáreldar (The Skaftár Fires) from now on referred to as Laki 1783–84 CE, started which would become the second largest flood lava eruption in historical times in Iceland. It lasted for 8-months, with activity propagating from the SW–NE in 10 distinct fissure opening phases across the Síða highlands, south Iceland, eventually creating Lakagígar, a 29.5 km long mixed cone row which stretches to the SW and the NE of the subglacially erupted hyaloclastite landform, Mt. Laki, the crater row's namesake (Figure 5. 1). The combination of the climatic and ecological impact of a Laki-type eruption, the rarity of high magnitude, flood lava (FL), events which have an eruptive frequency of 1 in 250–500 years in Iceland, and proximity of Iceland to mainland Europe has resulted in this eruption being the subject of a wealth of detailed scientific studies over the last decades and thus its sequence of activity fairly well defined. The main focus of these previous studies has been to fully characterise and constrain the eruptive sequences and timescales by: (1) defining the sequence of eruptive activity through tephrochronology (Thordarson and Self, 1993); (2) characterising tephra dispersal from a sub-Plinian fountaining intensity event (Thordarson and Self, 1993; Thordarson et al., 2003a); and (3) calculating the atmospheric volatile flux and the eruptions climatic or environmental impacts (Thordarson et al., 1996; Thordarson and Self, 2003; Thordarson et al., 2003b; Schmidt et al., 2015). Several studies have characterised the eruption's geochemistry and petrology to understand its plumbing system (Passmore, 2009; Passmore et al., 2012; Neave et al., 2013, 2017); as well as texturally analysing the microlite contents of the lava flows it emplaced to understand the evolution of its transport system and consequently the lava flow morphologies produced (Guilbaud et al., 2007).

However, it is only the first 15 km of the 29.5 km long crater row that constitutes the 'well-defined' portion of the eruption. Whilst several studies analysed lava flows sourced from the northern craters, there are still question marks over the intensity and type of vent activity from fissure episodes 7–10 which erupted after late August

during the Laki 1783–84 CE eruption.; and also, whether they were explosive enough to generate tephra fall in the Síða highlands or lowlands. The first 15 km of the crater row is comprised of 6 fissure opening episodes, and corresponding explosive tephra production, that occurs between 8 June–30 July which is dominantly magmatic, but phreatomagmatic activity in the form of two tuff cones associated with localised surface water bodies have been identified as tuff-cones within the cone row (Thordarson and Self, 1993). The relatively unstudied northern fissures of Laki are probably the result of a combination of factors: (1) inaccessibility issues to sample eruptive deposits on the northern side of Mt. Laki; and (2) the poorly preserved tephra stratigraphy proximity which becomes an increasing issue towards Síðujökull (a SW outlet glacier of Vatnajökull) because of the dynamic erosive and depositional glacial outwash environment (Figures 5. 1 and 5. 2).

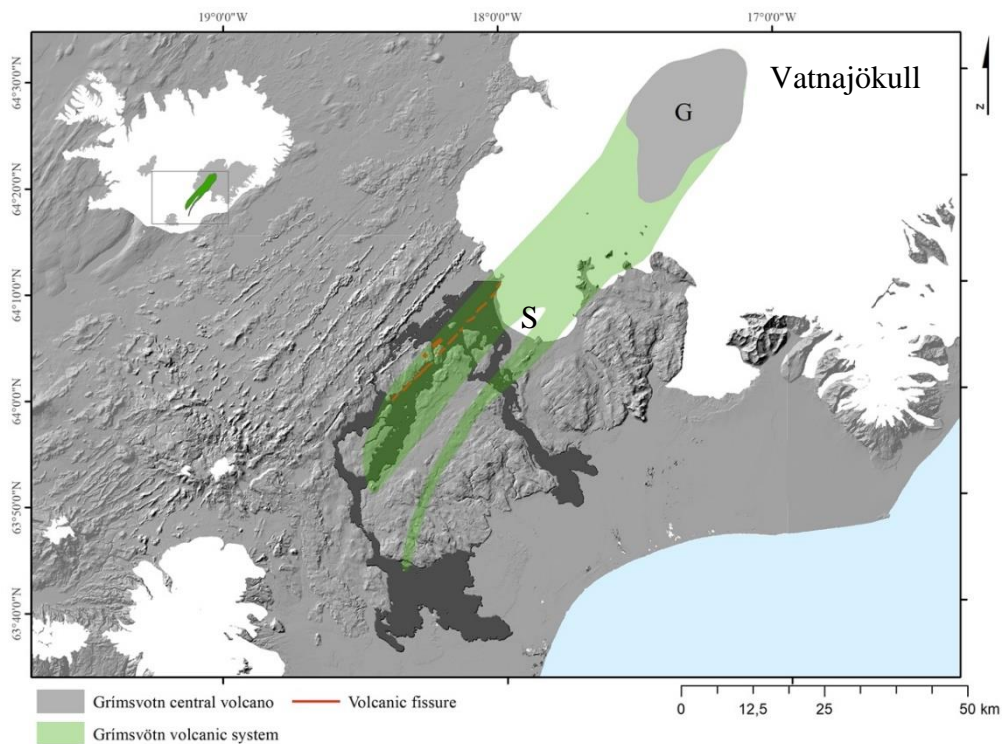


Figure 5. 1: The Laki eruption and surroundings. ArcticDEM hillshade image, with a dark grey outline of the total area of the Laki lava field, which spread from the Síða highlands to the lowlands through deep glacial river canyons, towards the sea shown in light blue. The location of the Grímsvötn central volcano is highlighted in grey, with its associated embryonic fissure swarms shown in pale green. Vatnajökull ice-cap can be seen depicted in white, with the outlet glacier which Laki propagated underneath, Síðujökull (S), at the southern boundary of the NE of the fissures. The location of the Laki fissure swarm is shown in red, alongside Lambaggar to the N of the extensive Laki fissure. An inset of Iceland with the Grímsvötn system highlighted in green is provided for geographic reference.

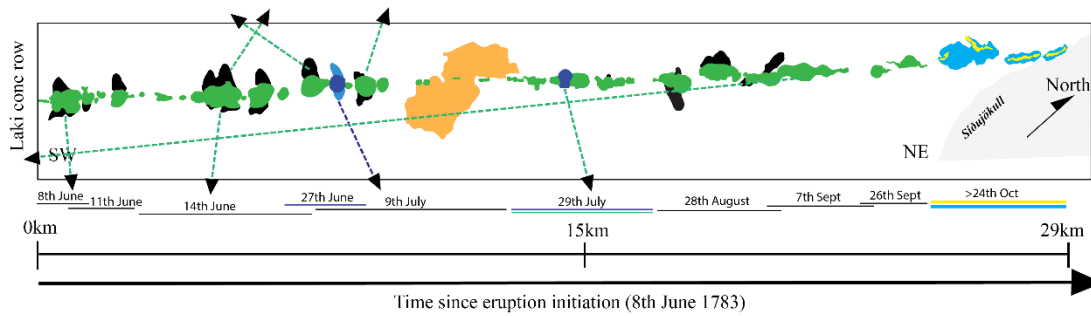


Figure 5. 2: Laki tephra dispersal and cone eruptive environment. Schematic sketch (to scale) depicting the Laki cone-row, its tephra apron deposits and their associated fissure opening episode dates. Green cones and black tephra aprons, and black fissure opening episode lines, indicate magmatic activity, whereas phreatomagmatic activity is shown by different scales of blue. Interactions between magma-external water from surface lake phreatomagmatic deposits are down in dark blue with a lighter blue apron, with the proposed subglacial magma-ice activity shown in turquoise at the very NE of the Laki cone row. Proposed spatter fed ice-confined lavas or tuff mantling spatter fed lavas, which lie above the subglacially generated phreatomagmatic sequences, are mapped in yellow.

Initial geological maps of Iceland by Thorvaldur Thoroddsen classify the pale tephra cones and capping lavas from fissure 10, of the Laki 1783–84 CE cone-row, as an older hyaloclastite sequence emerging from Síðujökull which is drawn distinctively curving around the fissure 10 cones in 1901 CE (Figure 5. 3). An early study of the proximal lava flows which cap the SW cone of fissure 10, were initially interpreted as a separate eruption at Fljótsoddi (Jakobsson, 1979), but were remapped through analysis of aerial photographs as belonging to the Laki 1783–84 CE (Thordarson and Self, 1993; Thordarson and Self, 2003), which was later confirmed by geochemical and petrological analysis (Passmore, 2009; Passmore et al., 2012).

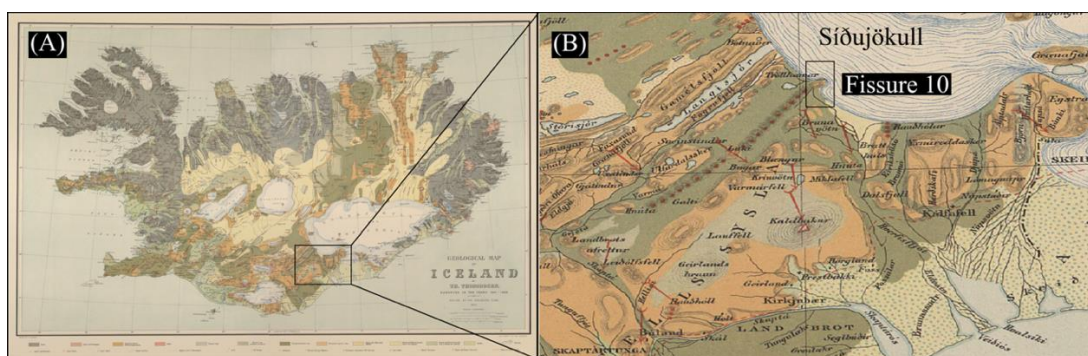


Figure 5. 3: Thoroddsen 1881–1901 geological map. Images of the original geological map from Thoroddsen 1881–1898 taken from the National Museum of Iceland. (A) Displays the map in its entirety, with the location of the inset (B) shown by a black box. (B) Focuses on the section of the map covering the area surrounding the Laki eruption. The margin of Síðujökull can be seen to clearly, and purposefully, curve around the edge of what this study proposes is fissure 10 of the Laki eruption rather than the older hyaloclastite sequence it is mapped as here. The area of interest inside of image (B) is highlighted by a black box.

However, analysis of the tephra cones beneath these capping lavas at the very SW of fissure 10, or indeed the sequences which extend to the NE from this locality, have not been mapped or sampled to assess the sequence of eruptive activity; nor to confirm that they were also part of the Laki 1783–84 CE fissure 10 eruptive episode.

5.2 Methods

Field mapping: Detailed in-situ field mapping campaigns were undertaken from 2016–2020, which underpins this chapter, enabling an initial reconstruction of eruptive events in the last 3–4 Laki fissures (Fissures 7/8, 9 and 10) and identifying the relationship of units relative to each other. Field mapping was also used to constrain the morphology of the deposits along strike and any variations with stratigraphic height, which enables an assessment of the influence of increasing ice-thickness or meltwater interaction along the fissure, and throughout the eruption.

For fissure 7/8, sampling pits were dug through the medial-distal tephra apron sequence to ensure all of the deposit was logged and reworked capping material was excluded. Key visible changes in stratigraphic height in the apron sequences were sampled as distinct units to capture changes in eruptive style, degassing and intensity over the explosive phases, as well as to record any geochemical changes. Mapping and sampling of fissures 9 and 10 was carried out on the accessible northern side where large cross-sections through the crater sequences provide excellent field relationships. The inaccessible, steep, but excellently exposed, southern faces were photographed in high resolution from the Síðujökull glacier itself to piece together a complete and clear sequence of activity. Initial morphological analysis of this crater row along strike was also carried out in 2018–19 with the advent of the open-source ArcticDEM.

Imaging: The crater row is inaccessible to the S, due to the actively calving and unstable front of Síðujökull, and the mouth of the large glacial river Hverfisfljót. The glacier has only recently fully receded from the SE/S side of the cones revealing steep-sided walls with poorly developed and over steepened talus slopes, compared to its northern aspect. The steep-sided faces of the cones provide excellent cross-sections from which to piece together the sequence of activity. Because of the

inaccessibility of these steep active rockfall area they were imaged using a 45-megapixel camera from Síðujökull itself <1 km from the fissure 10 cone row.

Remote sensing mapping: Analysis of aerial photographs of the north of Laki from Landmælingar Íslands (The National Land Survey of Iceland) taken from overflights from 1945 CE onwards were utilised alongside the high resolution ArcticDEM. The combination of these two remote-sensing mapping methods, enabled rough paleo-ice extent estimates in SW-Vatnajökull in the late 1700s by using crater formation morphology and presence of dated quaternary deposits. They also provide insight into the evolution of the deposits through post-eruptive processes; that is how these sequences weather in the dynamic, erosive environment, resulting in their current morphology.

Sample analysis: Samples from three key units were petrologically, geochemically and texturally characterised using microscopy, XRF, BSE SEM images, and EMPA analysis to assess the effect of external water on the eruptive dynamics, event intensity, degassing, and or early quenching.

5. 3 Initial results

This brief overview section is structured following the temporal evolution of the last 3–4 Laki fissures as traced along the strike of the cone-row from the SW (fissure 7) to the NE (fissure 10) (Figure 5. 2).

5. 3. 1 The new tephra layer from fissure 7 or 8.

Two extensive tephra aprons associated with fissure 7/8 opening phases were located to the north-northeast of the crater row; they clearly originate from these fissures as they decrease in thickness northwards and are not associated with rootless cones or sandur plain deposits closer to the glacier margin further to the NE. The surrounding lava has been deflected by the topographical high they create, indicating the explosive activity occurred before the lavas at this locality. They consist of 3 distinct primary units of fine-coarse lapilli supported with subordinate fine-course ash, which sit on top of a soil horizon; these will be referred to as G1-3 of the M5 explosive

tephra apron (Figure 5. 4). The top 3 centimetres of the deposit were excluded from sampling due to evidence of reworking. The units are distinguished by internal changes in grainsize within the deposit, with G2 containing a lower proportion of coarse lapilli with a higher percentage of fine lapilli and ash when compared with G1 and G3. Lapilli grains have three components: (1) black scoria, (2) golden pumice (3) achneliths on top of the soil horizon. According to contemporary accounts, a vent opening phase for fissures 7 and 8 occurred on 28 August 1783 CE but isn't associated with tephra fall in the Síða district; these accounts suggested lava surges dominated this phase. On 7 September 1783 CE activity producing tephra fall occurs in the lowlands from fissure 7/8, which corresponds to the location of M5. A discrepancy in the dates during this time could also be a factor of wind direction; the M5 tephra apron deposits stretch northwards, suggesting a northern prevailing wind direction which would limit the tephra fall into the upwind area during any explosive phases.

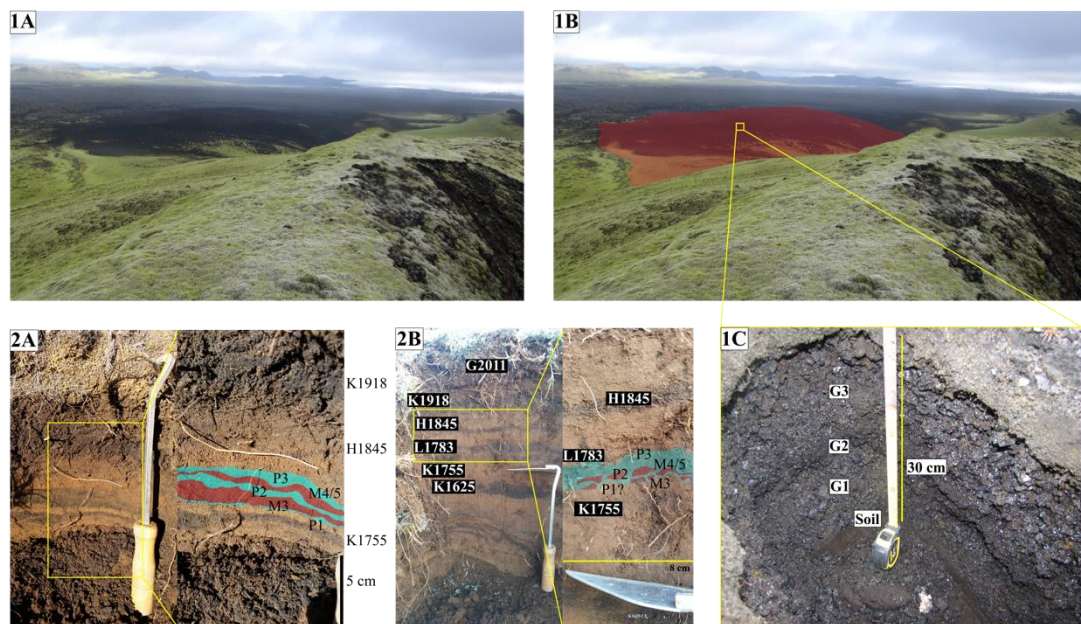


Figure 5. 4: Laki tephra deposits. (1A) extensive black M5 apron tephra layer extending north-eastwards away from the green moss-covered crater, outlined in (1B) with red for clarity, with the inset outline for (1C) indicated by a yellow box. (1C) A tephra pit through the edge of M5 explosive apron tephra fall deposit to the soil layer underneath, 3 distinct layers with different grainsizes G1–3 (labelled) can be observed. (2A and B) Medial soil horizons in the Síða highlands, with coloured overlays highlighting distinct tephra magmatic (red) and phreatomagmatic (blue) sub-units within the Laki 1783–84 CE tephra layer, which are also labelled. Katla 1755 CE, Hekla 1845 CE, Katla 1918 CE, and Grímsvötn 2011 CE are labelled for reference

5. 3. 2 Fissure 9

This cone is only partially preserved due to erosion and moraine deposition as the glacier, Síðujökull, surged in advances and retreats over the area resulting in extensive moraine deposition in the area (Figure 5. 5, panels B and C), which has either completely removed the southern parts of this cone or obscures the remaining deposit (Figure 5. 5, panel C). The half cone which still exists on the northern side of the fissure is black, with a similar morphology to P1 and P2 consisting of golden pumice, no achneliths are found in this cone sequence. In the centre of the cone isolated agglutinated spatter sequences exist, with traces of ramparts and spatter fed flows towards the NE, NW and N of the cone (Figure 5. 5, panel A and B).

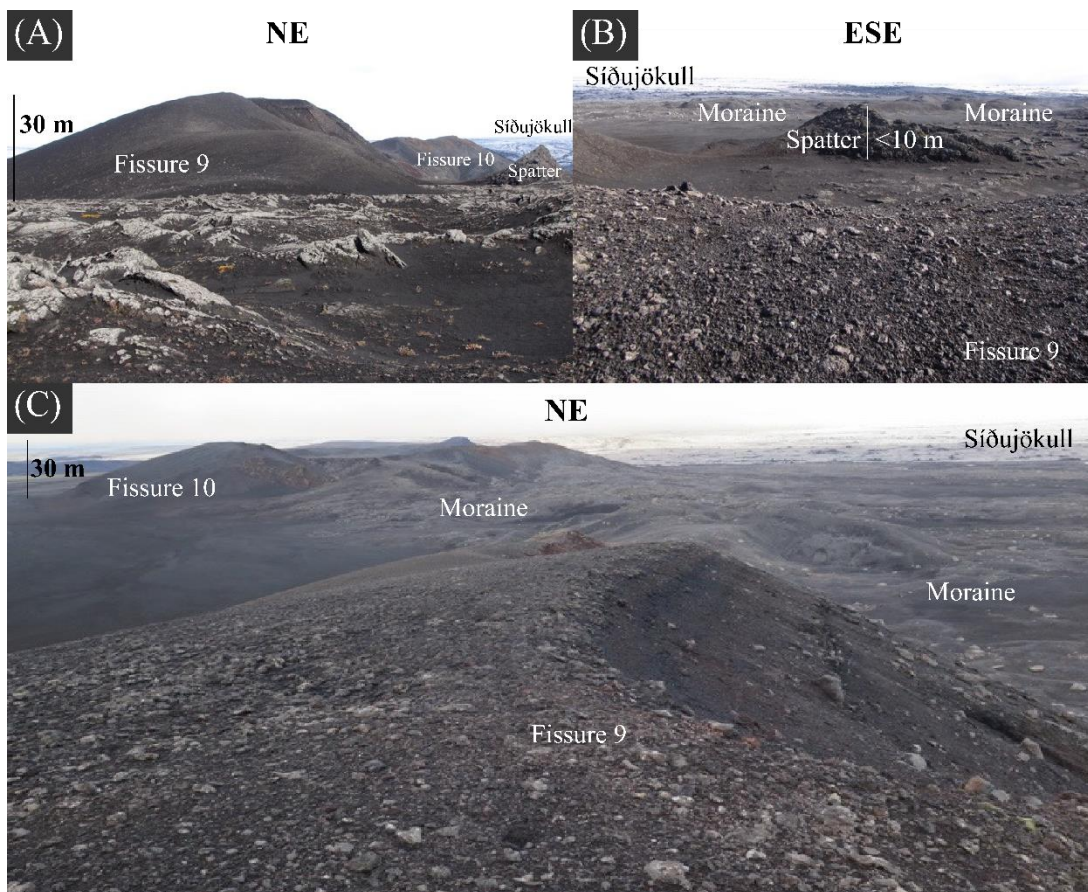


Figure 5. 5: Fissure 9. Field images from the Fissure 9 cone, displaying dry magmatic activity fed sequences with spatter ramparts and close to vent shelly lava flows (upper images). The crater has been eroded on its southern margin by the Síðujökull glacier, which has deposited extensive moraine over the SW of the area (lower image). Looking to the NE from fissure 9 on the lower image, the fissure 10 SW tuff cone can be observed from a distance and again, extensive moraine affects the margin of fissure 10.

5. 3. 3 Fissure 10

To the NE of fissure 9 lies the cone group of fissure 10; as previously mentioned, these deposits were initially mapped as older hyaloclastite deposits (Thoroddsen, 1881–1901; Jakobsson, 1979). The most SW of these has been partially destroyed on its S-SE aspect either by the 1993 glacial surge of Síðujökull or earlier glacial erosion (Figure 5. 6, panels A and D), however, unlike fissure 9, it maintains a recognisable cone-like crater structure on all sides despite the till layer covering most of its surface. The erosion of the S/SE aspect of the crater has revealed a well lithified, fine-grained bedded, tuff containing layers rich in juvenile basaltic lapilli (Surtseyan style outcrop, e.g., Hrossaborg, N. Iceland). This sequence is capped in parts of the cone by spatter fed lava flows (both on the external and internal cone slopes; Figure 5. 6, panel B), with small-scale lava channel transport systems preserved. These mantling spatter flows create pockets of topography unaffected by the glacial surges or fluvial erosion on their lee side, enabling partial preservation of magmatic tephra from the wanes stages of spatter fed activity. Samples from this phase of the eruption are referred to as the sixth magmatic phase of the eruption, M6 (Figure 5. 6, panel C). M6, where it is preserved on the SW face of the cone as a primary deposit, consists of layers of lapilli with a scoracious or achnelith appearance; M6 also has a medium-course ash matrix, golden pumice is absent in the M6 deposits, and the clasts are generally denser than the other Laki magmatic tephra. These deposits, where preserved, are too small to have classified units within them although faint bedding is observed.

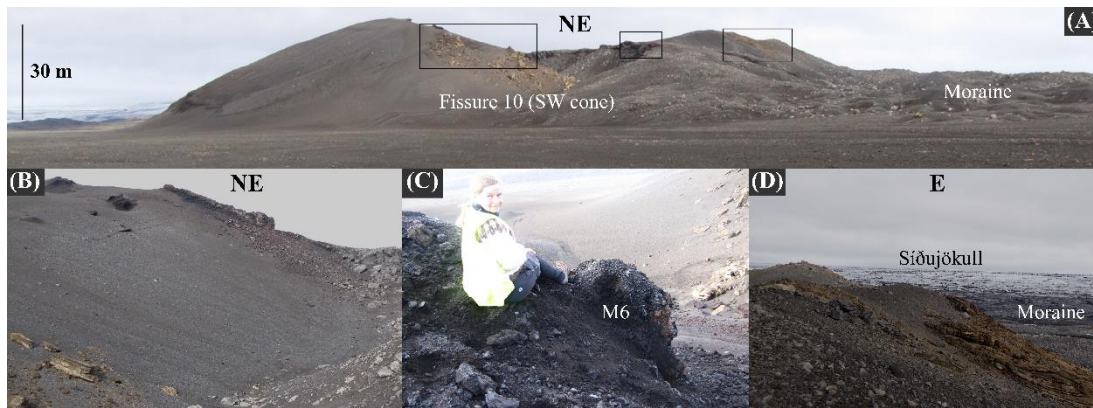


Figure 5. 6: Fissure 10. Field images from the Fissure 10 SW cone, displaying brown tuff sequences capped by dry magmatic spatter fed activity (lower left image). This magmatic activity also deposited a small amount of tephra fall in the area, preserved in topographic lows near the margins of the lava flows (lower centre image). The fissure 10 cone has been eroded on its southern margin by the Síðujökull glacier, leaving clear brown lithified tuff sequences at the surface (lower right image).

If viewed in isolation, the well-lithified nature of the lapilli tuff at the SE of this cone would match the initial interpretations from the reconnaissance mapping efforts by Thorodsson (1881–1901) and Jakobsen (1979), which classified this as an older hyaloclastite sequence. However, when tracing the cone sequences along its northern margins, a 30 m cross-section through the crater exists due to erosion from a once extensive glacial river system that flowed over the Fljótsoddi and into the Skaftá; revealing a pale brown, fresh, and unconsolidated tuff-cone beneath the rheomorphic, spatter fed, lava flows. This sequence is referred to as P3 in Chapters 7 and 8 (Figure 5. 7). The braided river system that once flowed over this area has been re-routed to the SSE, due to the glaciers in the area retreating; now flowing behind the fissure 10 cones and terminal moraine deposits of Síðujökull into Hverfisfjót, leaving all of the northern sides of the cone accessible (Figure 5. 7, panel A).

P3 predominantly consists of a pale cross-bedded tuff (litho facies, CBT-p), a pyroclastic tuff deposit characterised by low angled cross-bedding dominated pale brown, dark grey and cream ash rich sequences. The cross-bedded sets are typified by four recurring sub-facies (Figure 5. 7, panels A–D): (1) fine light-brown ash layers with no internal structures; (2) dark fine-medium ash layers (5–8 cm) with lenses/internal fine-scale cross-beds <1 cm of coarse ash (plagioclase and olivine rich); (3) light brown-cream fine-ash layers (5 mm–8 cm), rich in accretionary lapilli and armoured clasts, these occur on their own and sometimes at the top of sub facies

(1); (4) massive, matrix supported, light brown-cream fine-ash containing 20–40 % golden pumices and (5) matrix supported light brown-cream fine-ash, with lapilli sized golden pumice proportion increasing towards the top of the unit whilst remaining matrix supported.

Occasionally within this sequence, horizontally bedded golden pumice and scoria lapilli clast supported units (litho-facies Ln) of varying thickness (5–30 cm) occur as distinct normally graded units between separate recurring packages of CBT-p (Figure 5. 7, panels C and D).

Initial interpretations: The CBT-p litho-facies was probably produced during pulsating eruptive activity from a wet plume. Low-angled cross bed sets suggest aggradational deposition by pyroclastic surges, which are preserved to varying degrees. Accretionary lapilli units represent the end of the pulse, falling out from the co-surge plume. They are, however, missing in some sets, suggesting either that the surge travelled further, and the co-surge plume fall out was deposited elsewhere; or, it has been removed by the next passing erosive surge. Some accretionary lapilli, sub-unit 3, have also clearly deformed on impact to make exaggerated ellipsoids with a flattened base. Sub-units (4) and (5) have a component of plume fall tephra mixed into surge deposits. All sub-sets contain a high percentage of highly vesiculated sideomelane glass either as fine-ash or golden pumice clasts suggesting they are comprised of a mature, full vesiculated, magmatic foam. The Ln litho-facies was probably produced during periods of coeval tephra fall and surge dominated deposition from the eruption. The sequence is preserved so well here due to the protective capping spatter lava sequences which acted as a barrier to fluvial and glacial erosion.

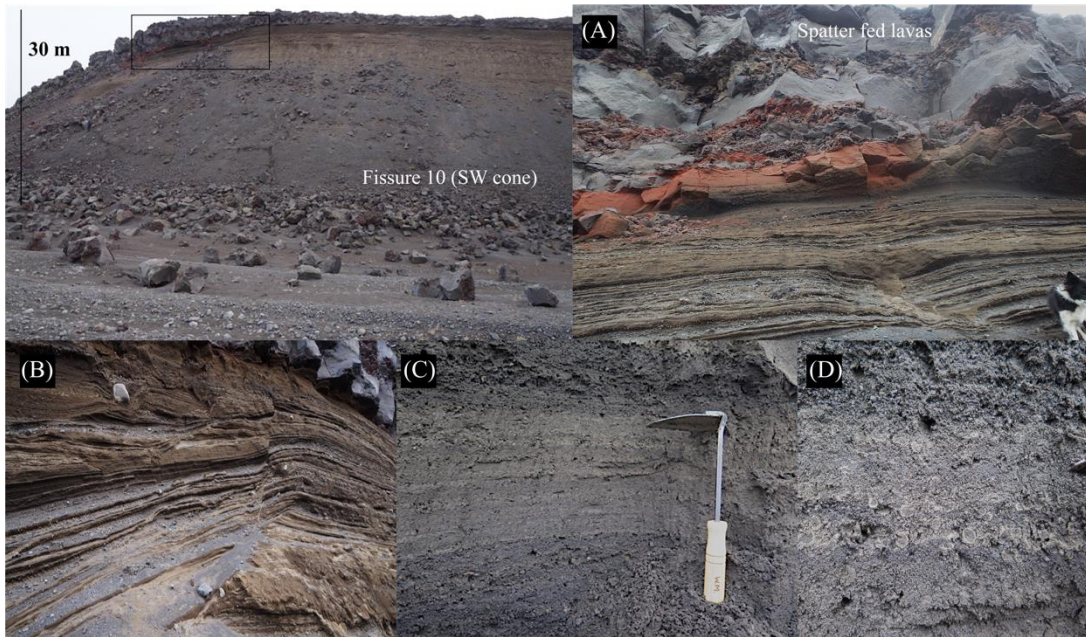


Figure 5. 7: P3, CBT-p, and spatter fed lavas. Field images from the Fissure 10 SW cone, on its northern margin where a complete 30 m cross-section is accessible through a light brown tuff sequence which is capped by spatter fed lavas (top left image). A person wearing red, inside of the inset location box, is shown for scale. (A) focuses on the top of the sequence where the tuff sequence can be observed to squeeze up through the spatter fed lavas in places and in others could interbed with it, although the steep exposure limits the view from below. (B) highlights the syn-eruptive faulting through the sequence as well as very large, rounded fluvial origin bombs throughout the sequence. (C and D) display the thin repeating beds of lighter brown and dark brown and black units; the light brown layers are often rich in accretionary lapilli (D).

Ballistics (litho-facies B) occur throughout the CBT-p litho facies. These comprise of juvenile basaltic fragments (5 mm–20 cm) and lithic (5 mm–20 cm) bombs. In the very SW of fissure 10 where CBT-p and Ln dominate the sequence, there are additional, notable, large armoured lithics (10–20 cm) present; they have a sub-rounded to rounded, smooth morphology armoured ballistics (Figure 5. 7, panel B). Sub-angular and rounded lithics (10–20 cm) are present throughout the sequence, occasionally draped in a coating of magmatic juvenile spatter.

Initial interpretations: Further evidence of a wet sediment environment is found through the presence of large lithic and juvenile bombs creating clear sags in the pyroclastic cross-beds beneath. Large armoured sub-rounded ballistics of all sizes are seen throughout the sequence, which are potentially indicative of clasts of a glacial river or tillite deposit origin being incorporated into the eruption from the substrate immediately below.

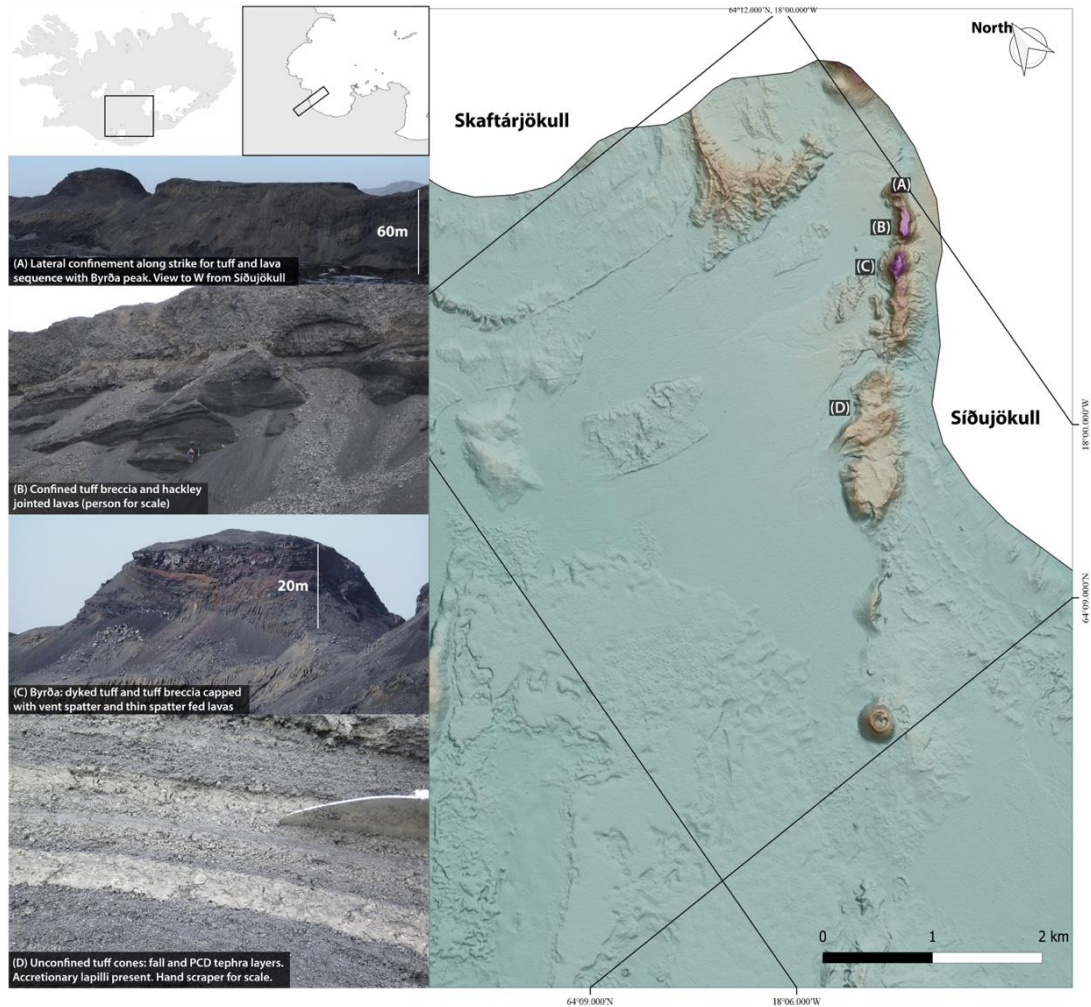


Figure 5. 8: ArcticDEM of Fissure 10 and key units. Insets in the top left indicate field location within Iceland. To the right is an Arctic DEM of Northern Laki fissure (artificial hillshade, with elevating grading from relatively lower areas in green, through to brown, with the highest peaks shown in purple). The proximal outlet glaciers Skaftárjökull and Síðujökull, from Vatnajökull, are shown in white. The field images to the left correspond to letters on the DEM, and the images themselves show clear examples of different sequences along the fissure indicating an intra-glacial eruptive setting.

This sequence of tuff and lavas continues when tracing the fissure 10 cone sequences to the NE towards an un-named peak within these cones, which is the highest of the fissure 10 cone sequence at 747 m a.s.l (Figure 5. 8). However, there are subtle changes in the sequences: (1) the large-scale morphology of the deposits becomes more elongated than the tuff cones and spatter lava sequences in the very SW (Figure 5. 8); (2) the thin veneer spatter-fed, rheomorphic flow lobes of rubbly-spiney pahoehoe lava flow sequences (with units varying from 0.2–0.5 m) become more dominant and thicken (0.5–4 m) towards the SW away from the peak (Figure 5. 9; panels A and C). Oxidised red and black agglutinated spatter sequences with thin lenses of black scoria become more dominant in this sequence, occurring as layers

(0.2–3 m thick) between the lava flows, also occurring as over thickened (1–5 m) units towards the SW (Figure 5. 9, panels C and E). When viewed from Síðujökull looking northwards, feeder dykes cutting through the CBT-p connecting to these flows above can clearly be observed, at the boundary between the flows and the CBT-p sequences, extensive oxidisation can be observed. The exposed basal crust of the over thickened lava flow unit, which extends to the SW of the un-named peak, reveals rounded lithics preferentially picked out and preserved by the base of the lava as it flows over the CBT-p units (Figure 5. 9, panels D and E).

The faulting can be observed in CBT-p layers to the SW of the un-named peak beneath the spatter lavas at this locality, which tapers when traced downwards through the unit. In places, the CBT-p litho-facies can be observed between the lobes of the first 4 m of the spatter fed lavas (Figure 5. 7, panel A).

Initial interpretations

The increase of angular lithics in the CBT-p at this locality suggests a vent widening event, when considered alongside the extensive spatter and spatter fed flows which bake and oxidise the tuff directly below, suggesting a proximal vent locality where eruptive activity transitions from a wet to dry environment. This could occur either as the conduit isolates itself from the water source or the surrounding water can drain away either as a flood or into faults in the area. Tapering of faulting in the CBT-p units is suggestive of faulting caused by loading of the wet sequence by the spatter lavas above. The presence of the CBT-p within the lava units above indicates either possible squeeze structures due to loading of the wet sediment below as the lava flows above advance over it or continued episodic pulses of phreatomagmatic activity as the vent initially struggles to isolate itself from the water source. Both of these hypotheses require the lava and tuff sequences to occur during the same eruption and not the lava interacting with a well-lithified older hyaloclastite sequence.

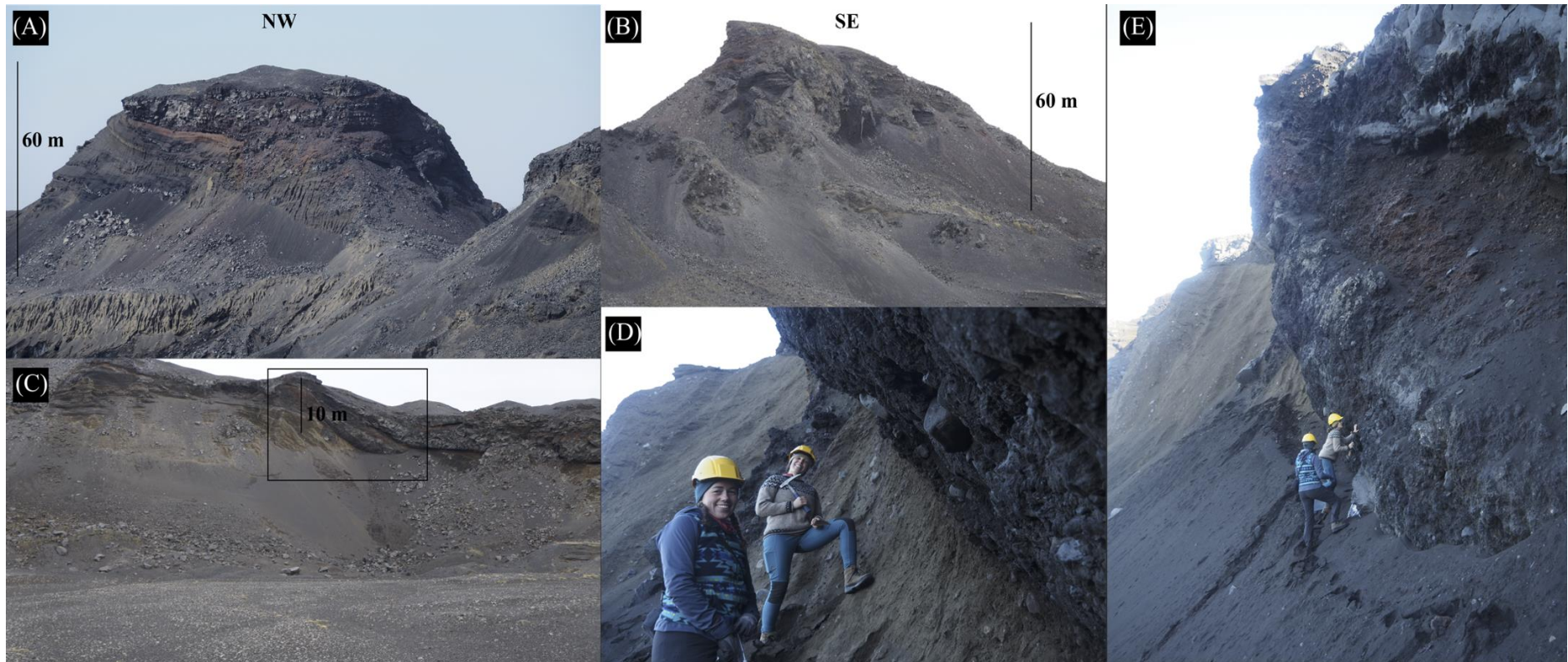


Figure 5. 9: Un-named peak agglutinated spatter and spatter fed lava sequence. Field images of the un-named peak and the surround sequences at fissure 10. This locality is roughly halfway along fissure 10. (A) Viewing the un-named peak from the SE to the NW, displays the transition from bedded light brown tuff into spatter fed flows well, with the boundary displaying extensive oxidation beneath the lava and spatter sequences. A feeder dyke at a 30° angle can be seen to intersect the flows above the sediments. (B) displays the same sequence as viewed from the NW looking to the SE, with a clear erosional scarp at the NE edge of the un-named peak. (C) highlights the over thickened spatter fed flows and spatter sequence to the SW of the un-named peak. (D) is in the black box highlighted in (C) and displays the base of the spatter fed flows which have preferentially mantled and picked up the rounded fluvial bobs in the sequence. The tuff unit below is rich in angular lithics indicating a vent widening event as this edifice becomes dominant through this phase of the eruption. (E) shows the same unit as (D) viewed from further away with an extensive and oxidised spatter unit above.

Continuing to the NE, the fissure 10 cone sequences continue to be elongated but are still multi-faceted, oscillating between the CBT-p and a new litho-facies unit: dark cross-bedded tuff (CBT-d). This sequence consists of low-angled cross-bedded dull black or matt grey unconsolidated lapilli tuff (Figure 5. 10, panel D). These cross-bedded sets are typified by three main recurring sub-facies: (1) matrix supported black coarse-ash (2–10 cm); (2) matrix supported dull/matt grey/black layers rich in scoracious lapilli (0.5–15 cm); and (3) massive, clast supported matt black-dull dark grey lapilli–bomb units (5–100 cm) (Figure 5. 10, panel D).

Spatter fed isolated thin lobes with thick agglutinated spatter “crusts” are observed throughout the CBT-d. These thin lobes have a hackly morphology, which extends from the core through the agglutinated spatter crusts and throughout the spatter crusts themselves. These are best exposed at the very northern end of the fissure. The agglutinated spatter crusts also contain very rounded, vesicular, grey basaltic lithics in places 2–3 cm in size. When this sequence is observed from Síðujökull looking northwards, the oscillating CBT-d and CBT-p units display erosive contacts throughout (Figure 5. 10, panel B).

Above these tuff units in the NE of fissure 10, the cone sequence does not contain thin oxidised rheomorphic flows and agglutinated spatter observed in the SW of fissure 10. Instead, stratigraphically above the CBT-p and d units, there is initially a thin (30–40 cm) layer of fine-coarse grained sands, containing sub-units of laminated fine-ash to clays (<1 cm) (Figure 5. 10, panel E). These sequences are followed by a unit above which contains small (30–50 cm) basaltic pillows or small lobes with thick quenched outer rims interbedded with a fine-grained glassy matrix (Figure 5. 10, panels C and E). This sequence is capped by a 10–15 m thick, massive, hackly jointed lava flow which occurs immediately above the pillows in some localities; but in other places, another repeated CBT-p unit and thin (1–3 m) rheomorphic lava lobes, with less irregular columns, and a smooth continuous base and top crust occur in-between the two (Figure 5. 10, panel A–C).

The thick hackly lava flow has a morphologically varied base; across most of the unit it exhibits bulbous/rounded pillow lava-like basal structures, but in places this is replaced by a smooth pahoehoe base. Small scale faulting of the CBT-p and d units

as well as thin lava flows can be observed which tapers out 10 m below the thick hackly lava. The top of the hackly jointed lava flow has been eroded away. No oxidisation of the CBT-p and d units can be observed in the NE of Fissure 10 (Figure 5. 10, panels B–E), unlike in the SW where thin spatter units cap the tuff units (Figure 5. 7, panel A).

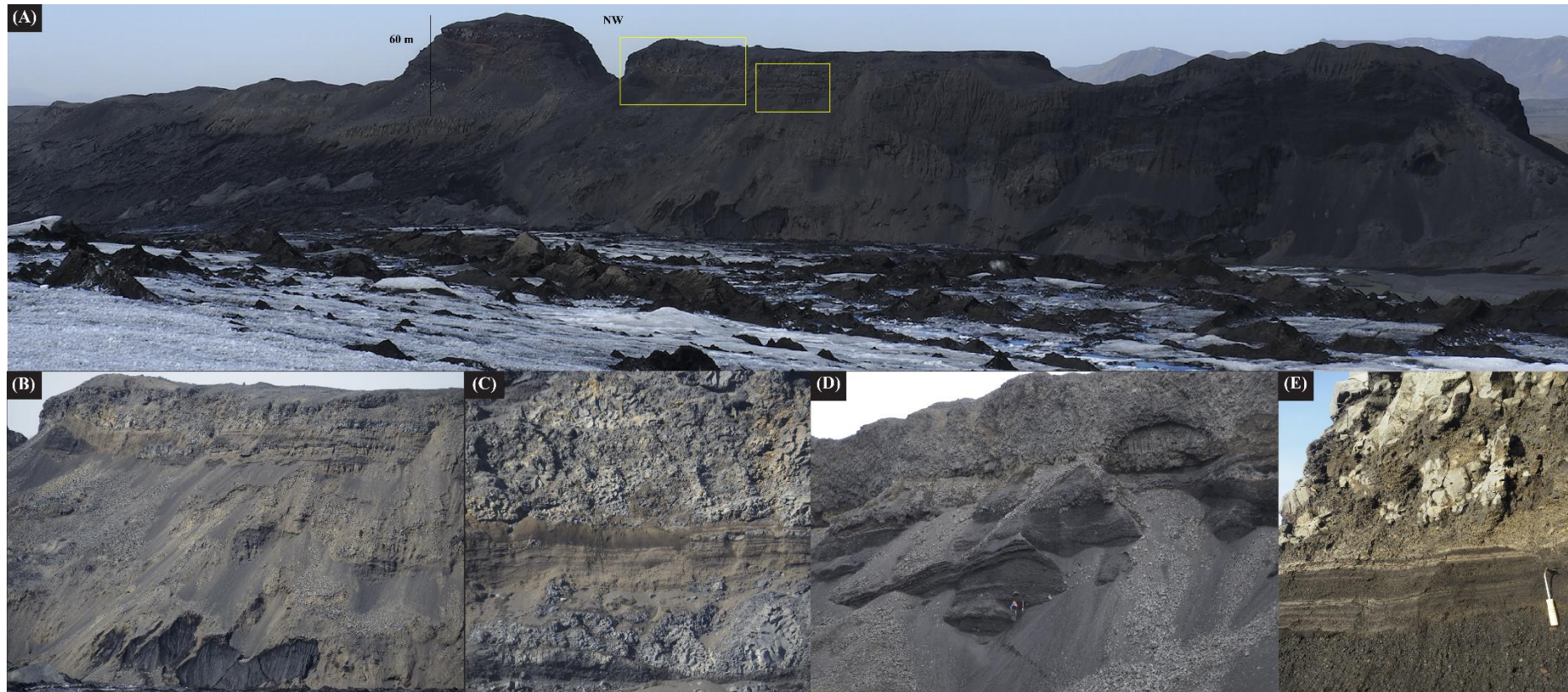


Figure 5. 10: NE of fissure 10, CBT-d, pillows and hackly lavas. Field images of the NE section of the fissure 10 sequences. (A) is taken from Síðujökull looking to the NW, capturing the elongated nature of these sequences compared to those SW of the unnamed peak. The yellow boxes indicate the locations of (B and C), (D) is at the same stratigraphic height on the northern aspect of the same ridge. (B) highlights the erosional contacts between the CBT-p and -d units which can be observed well from the glacier itself. This image also captures syn-eruptive faulting displacing tuff, and small lava flows underneath the large hackly lava, which caps the sequence. (C) Small pillow-like morphology lava units occur prior to the thick capping hackly lavas, with the latter displacing a basal crust suggestive of being emplaced into soft sediments as it sags into the tuff below and squeezes structures occur in places. (D) when the units are viewed from the NW looking to the SE, the CBT-d seems to dominate the sequences under the hackly lavas with better exposure than the cones southern margin. (E) occurs at the boundary between the large hackly lava and the CBT-d in image (D); at this boundary small pillow-like lava lobes and evidence of standing calm water can be found in the form of multiple fine clay-silt varves, which occur repeatedly in-between layers of fine-medium coarseness tephra.

Initial interpretations:

The CBT-d litho-facies was also probably produced during pulsating eruptive activity from a wet plume, producing a roughly bedded sequence with large low angled cross bed sets throughout. However, unlike the CBT-p unit, eruptive activity transitions into semi-stable effusive, dry activity several times throughout the CBT-d unit, producing small spatter fed lobes which are then rapidly quenched, giving them a hackly morphology, due to the presence of a fluctuating water level throughout this period of the eruption which these small lobes are interacting with. Above the CBT-d unit water can accumulate, with evidence of a possible standing water body indicated by the small sedimentary sequence containing very fine grain varves; this would also suggest a period of quiescence in eruptive activity at this locality in fissure 10, allowing such fine material to settle in layers. Small pillows or lobes above this also support the hypothesis of a considerable standing water body for a period of time during the eruption. This transitions into units that indicate both wet and dry eruptive activity, creating a sequence of initially thin hackly lavas interbedded with CBT-p units and capped by a substantial hackly jointed lava flow. The base of the large capping lava varies from a hackly jointed undulating base to rounded half pillows that squeeze into the soft sediments below (Figure 5. 10, panel C); in two places, this appears to have triggered syn-eruptive faulting in the tuff and thin lava sequences below which is accompanied by slumping and infilling of the hackly jointed bulbous/pillow-like base of the capping lava. When tracing the units to the NE there are increasing proportions of CBT-d and hackly lavas (Figure 5. 11).

All of the lavas NE of the high un-named peak appear to either be laterally confined or their margins have been eroded away, suggesting the environment they were emplaced into restricted their lateral development. The walls of these sequences, especially on their SE margins, do not have well-developed talus slopes; instead, they are over-steepened (Figure 5.10, panels A and B), extremely unstable with frequent rock-falls and debris slides. The top of the fissure 10 deposits have extensive extensional linear cracks which follow the same strike as the cone sequences. Both of these observations suggest an unstable sequence that has recently had its surrounding lateral support, which it formed against, removed.

A variety of intrusions can be identified throughout the fissure 10 eruptive sequences that fall roughly into three main types: (A) Dykes that cross-cut the sequence at <50 degrees and are best exposed towards the NE end of the fissure when viewed from Síðujökull looking northwards (Figure 5. 10, panel A). These are <1 m–2 m in thickness but their contact boundary cannot be assessed accurately from a remote distance. (B) Feeder dykes: two of these are present in the sequence with a very clearly visible contact. One feeds the spatter lavas at the un-named peak and the other one feeds the thick hackly jointed lava (C) A third type is pillow-like intrusions/hackly jointed intrusions, possibly associated with feeder dykes, but again the contact is not visible from such a distance, and they are potentially small lava lenses (Figures 5. 10, panels A and B; and 5. 11).

The entire sequence of fissure 10 from the SW–NE is mantled by a thin (<0.5 m) clast supported layer of primary glaciogenic till material. It consists predominantly of sub-angular-rounded clasts and a clay-rich matrix, it also contains larger sub-rounded blocks; which represents the extent of glacier re-advance after the eruption had finished over the Laki sequences. It is also present in/on the SW-S slopes of the fissure as well, as ice only receded from this region in 2015. The sequence on the northern side of fissure 10, is also clearly shorter in height than the exposure on the southern margins, indicating that glacial flood and moraine deposits bury a significant portion of the fissure sequence on the northern side. The top of the thickest lava unit has been removed and there is a thin layer of glacial till in its place.

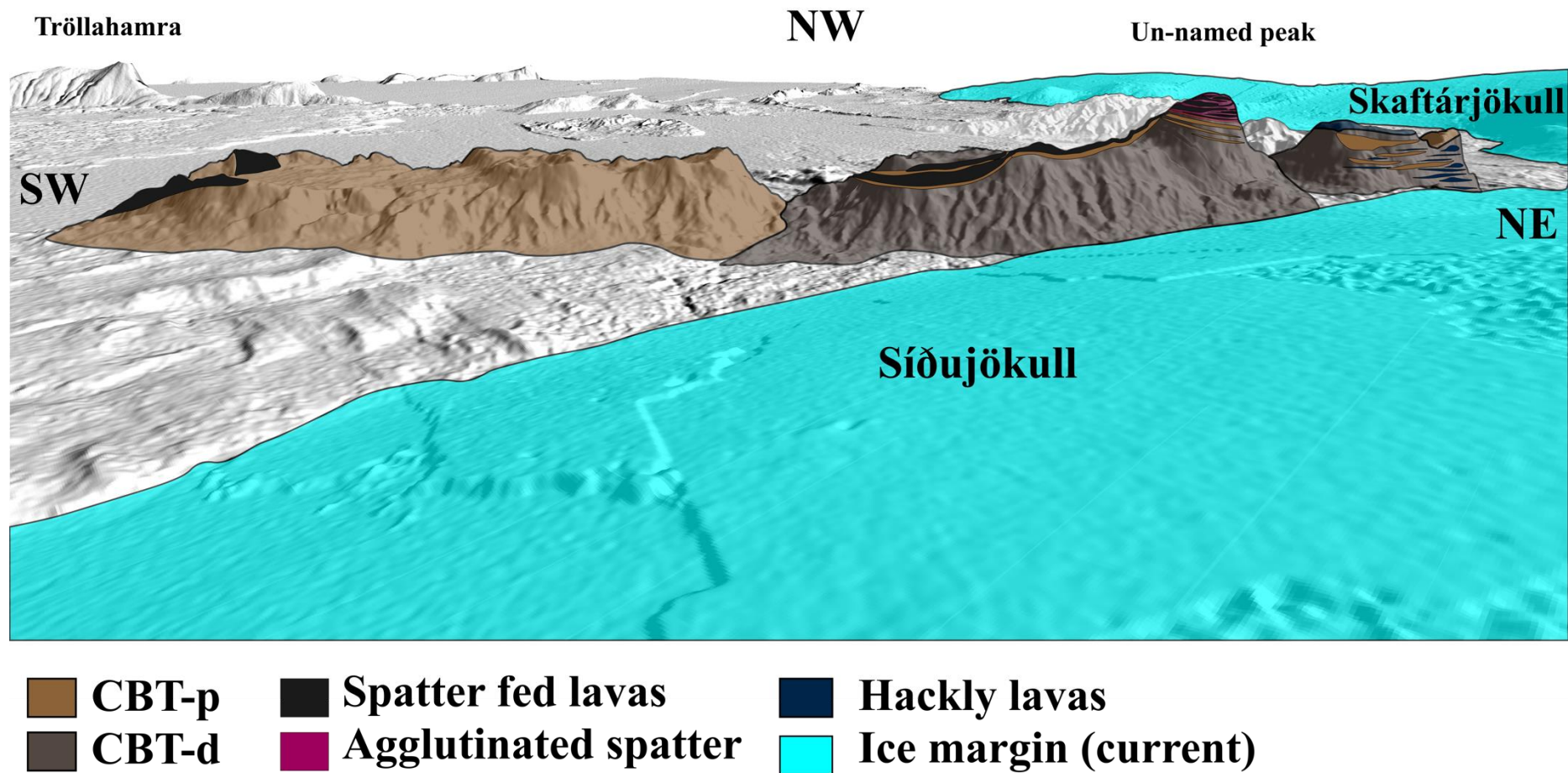


Figure 5. 11: Fissure 10 sub-unit correlation along the fissure's length. Arctic DEM V3Geo 3D map of the north of Laki with the initial units identified by geological mapping indicated by the colours noted in the legend. Sub-units are correlated across the cones from fissure 10 from the SW to the NE, which becomes increasingly ice-confined with evidence of episodic water level changes.

5. 4 Conceptual model

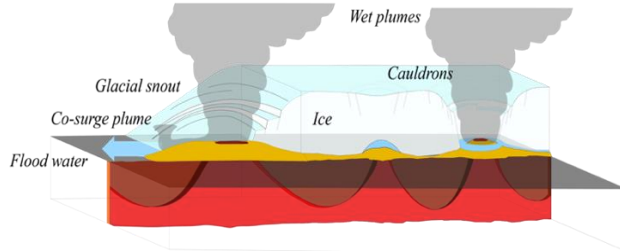
Upon further field mapping examination of the Laki 1783–84 CE fissure closer to the glacier, the Laki deposits reveal a much more complex history of events than previously assumed; phreatomagmatic deposits are found to dominate this region, displaying clear evidence of magma-glacier interactions. This also suggests that in the 1800s the extent of Síðujökull and Skaftájökull would have been much greater than observed today, reaching the northern edge of the Laki lava field in this area extending towards the Skaftá at the NE edge of Tröllahamar (Figure 5. 11), not similar to recent glacial margins which has previously been suggested in recent studies (Björnsson and Pálsson, 2008).

The working hypothesis for the eruptive environment of fissure 10 is an eruption in a shallow sub-glacial environment, where the effects of the increasing influence of ice-confinement and external water due to magma-ice interactions can be observed when tracing the fissure from the SW to the NE (Figures 5. 11 and 5. 12). This is seen both in the morphology of the sequences and their increasingly elongated nature, as well as in the units within which the sequences are comprised of increasing proportions of CBT-d and hackly lavas (Figures 5. 8 and 5. 11). The water level throughout the eruption fluctuates as the eruption melts through the ice and flooding drains the vent areas periodically (Figure 5. 12). Due to cauldrons forming above the erupting fissure prior to it breaking through the ice, the highest peak in fissure 10 is at a stratigraphic height which is removed from ice or water-magma interactions and only effusive activity is observed at the top of its crater (Figures 5. 10–5. 12).

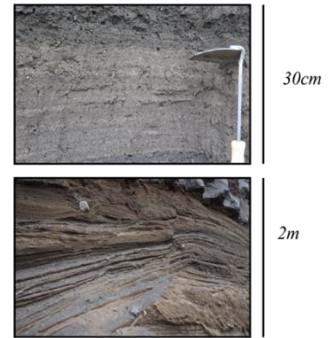
Subglacial and ice-confined case: P3 & M6

1: Shallow subglacial fissure eruption activity form bedded tuff cones.

At the snout of the glacier unconfined x-bedded tuff cones form, activity triggers jökulhlaups which drain from the glacier snout. Under thicker ice, tuff cones are ice-confined. Co-surge plume deposits accretionary lapilli in the interbedded surge and plume fall units.

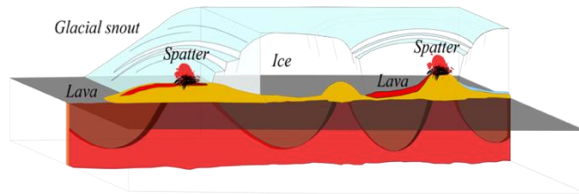


Tuff x-bed surge and fall units

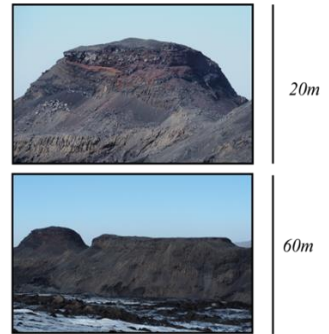


2: Tuff lithification enables vent isolation from water source, magmatic activity ensues.

At the glacier snout spatter fed lavas and dense scoria mantle the tuff sequences, magmatic activity (within the glacier margins) produces lavas that are laterally ice-confined.

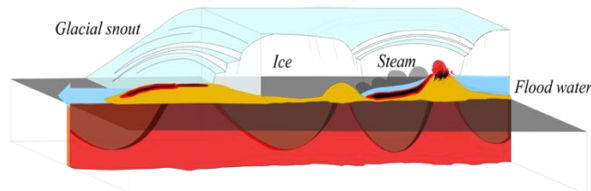


Transition to ice confined magmatic activity and capping spatter



3: Water pressure builds under the glacier, causing jökulhlaups

Flood water flows over active ice-confined lavas resulting in hackley jointed morphologies



Hackley jointed lava and jökulhlaup

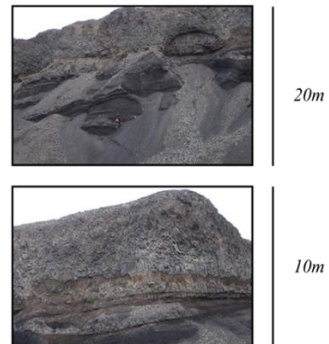


Figure 5. 12: Conceptual model of subglacial eruptive activity during the shallow subglacial-subaerial eruptive phase during the fissure 10 event. Part of schematic outline modified after Moreland et al., 2019. A fissure opens below the tongue of Síðujökull. At the glacier margin, the craters are not confined laterally by the ice, forming ellipsoidal tuff cones comprising of pyroclastic surge layers cross-cutting each other. Where the ice is thicker, cauldrons form above this portion of the fissure with a body of meltwater below them; when the internal hydrostatic pressure reaches a high enough level, a jökulhlaup escapes from this region of the fissure. Subsequent activity in this area is magmatic, although further north along the fissure eruptive activity continues to melt the surrounding glacier and episodic jökulhlaups drain towards the snout of the glacier to the SE and disrupt the cooling of spatter fed lava flows giving them hackley (rapid and disorganised) columnar jointing.

5. 5 Corresponding tephra layer from Fissure 10.

When tracing medial tephra stratigraphy from the northern fissure segments in the highlands SE of the Laki crater row, it became apparent from Geirlandsheiði, across Kaldbakur to the Illugilshnúkar/Núpafjallsendi area of Núpahraun there is a traceable third phreatomagmatic unit that occurs towards the end of the eruption, sourced from the N or NE of this location as it thickens in this direction (Figure 5. 4). This was initially assumed to be from Grímsvötn, the central volcano associated with the Laki fissure swarm as the Laki eruption represents the main eruptive activity which is part of a 2-year-long (May 1783 CE–May 1785 CE) volcano-tectonic episode of unrest within the Grímsvötn-Þórðarhyrna volcanic system. Contemporary accounts documented 7 distinct explosive events to the N/NE of the eastern Síða district (Austur-Landnorðursgjá), which have been postulated to be summit eruptions from Grímsvötn central volcano (Thordarson and Self, 1993; Thordarson et al., 2003a; Thordarson and Self, 2003). However, distinct tephra fall units from the central volcano do not exist within the stratigraphy possibly due to weak explosive activity producing small amount of tephra fall (e.g., Grímsvötn 2004), which would not extend past the glacier margins, and therefore would not be preserved in the soil record. As the Laki eruption represents a high-intensity FL end-member, it is also possible that the layers from Grímsvötn are simply mingled with the dominant tephra fall from the crater row itself and are not distinguishable.

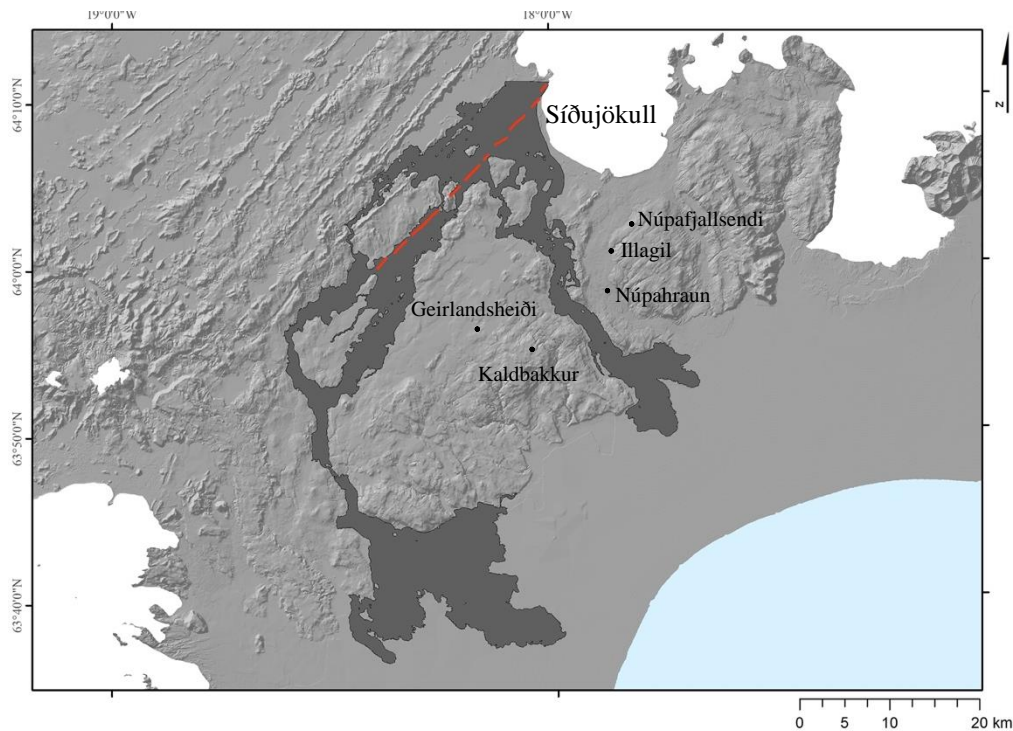


Figure 5. 13: Geographic locations of the local place names that are referred to for the Fissure 10 tephra locations.

Contemporary accounts note several interesting things which could be linked to the eruptive activity at fissure 10 (Table 5. 1). An increased sulfuric stench in the Hverfisfljót canyon occurs in late October, followed by an intense eruptive episode, which was postulated to be from Grímsvötn, with observations of pale-brown sandy ash blowing down from the highlands after this episode. However, the rough triangulation, which uses lowland sightings of eruptive activity from several farms, to suggest this was Grímsvötn (Thordarson et al., 2003), could easily indicate eruptive activity at the location of fissure 10, which would only be a degree or two off the location of Grímsvötn itself. Documentation of a very intense period of earthquakes in late November, and observations of another column of fire, from the rough location of fissure 10, might also suggest that fissure 10 could be comprised of two distinct eruptive episodes in October and November rather than one.

Proposed activity	Contemporary accounts evidence	Ground-truthing
Jökulhlaup on the 24 October 1783 at the start of the N. fissure opening phase	24 October 1783: This day, earthquakes started again, and strong acrid (sulfuric) stench was emitted from the east-northeast	Investigate tephra and flood sequences in riverside flood level soil sections.
Explosive phreatomagmatic tuff cones and tephra layer (active for 5 days?)	25 October 1783: A huge column of fire rose from the Austur-Landnorðursgjá, and sandy ash fell in the Síða district. The same day an intensive lava surge emerged from the Hverfisfljót gorge continuing for five days .	This was also initially proposed to be Grímsvötn but could be the tuff cones and more confined craters. This can be investigated by creating a detailed isopach and TGSD data set. Did this activity continue for longer than 5 days, as contemporary accounts suggest?
Byrða eruption further into Sídujökull, 24 November 1783?	24 November 1783: the fire column was seen to rise above Mt. Kaldbakur. In early December, the activity started to dwindle.	Use field mapping and imagery to assess whether the entire fissure segment was active at the same time, or do we see evidence of separate fissure opening phases?

Table 5. 1: Laki contemporary accounts. Collation of hypothesised activity at fissure 10 with the corresponding supporting contemporary accounts, as well as methods to ground-truth these hypotheses.

5. 6 Future studies

The following research questions could be addressed through 3D mapping, grainsize analysis, detailed geochemical and petrological analysis as well as magnetometer surveys:

- 1) What degree of influence does the increasing involvement of ice have on eruptive style and activity along the propagating fissure?
- 2) Were all vents along the fissure active simultaneously, or were there several opening phases. Assess the timescales for this eruptive phase, e.g., is 5 days (Table 5. 1) reasonable?
- 3) Is the source of the tephra layer identified in the Síða highlands from this shallow sub-glacial activity or from the more geochemically evolved Grímsvötn central volcano tephra?
- 4) Did the meltwater create a jökulhlaup(s), or if there was sufficient groundwater storage capacity for it to have drained into the bedrock as it is speculated to have done after the Holuhraun subglacial eruptions of 2014 (Reynolds et al., 2016).
- 5) Where was the glacier edge at the time of the eruption and how did the ice thickness change with distance along the ice-confined fissure?

- 6) Can these sequences be used as an analogue for astrobiological colonisation, as the fissure 10 acts as a time capsule with ice only recently retreating fully from its NE margin? With dead ice still observed in most of the southern margins in the NE section of the fissure and around the un-named peak.

Complementary research veins in the future could also include: (1) heat transfer/ice melting models for the settings of ice-confinement of lavas partly or fully emplaced sub-glacially; (2) modelling of fragmentation and degassing of eruptive material in a partly subglacial setting; (3) investigations into how common these features are around Vatnajökull, as Eldgígur in Djúpá is potentially similar; (4) detailed petrological analysis could be carried out to investigate cooling textures and magma water and sulfur contents to ascertain the degree of volatile suppression due to early quenching of magma feeding this portion of the Laki eruption; and (5) tephra sampling to further improve a well-defined isopach map and TGSD of the later eruptive sequences of Laki could be carried out to understand the activity in the NE of the cone-row better.

5.7 References

- Baker, P.E. McReath, I. Harvey, M.R. Roobol, M.J. and Davies, T.G. (1975) The geology of the South Shetland Islands: V. Volcanic evolution of Deception Island. *British Antarctic Survey Science Reports*. 78. p. 81
- Björnsson, H. and Pálsson, F. (2008). Icelandic glaciers. *Jökull*. 58. pp. 365–386.
- Björnsson H., F. Pálsson, M. T. Guðmundsson 2000. Surface and bedrock topography of the Mýrdalsjökull ice cap, Iceland: The Katla caldera, eruption sites and routes of jökulhlaups. *Jökull*. 49. pp. 29–46.
- Bonadonna, C. Genco, R. Gouhier, M. Pistolesi, M. Cioni, R. Alfano, A. Hoskuldsson, A. Ripepe, M. (2011). Tephra sedimentation during the 2010 Eyjafjallajökull eruption (Iceland) from deposit, radar, and satellite observations. *Journal of Geophysical Research, Solid Earth*. 116. (B12).
- Eason, D.E. Sinton, J.M. Grönvold, K. and Kurz, M.D. (2015). Effects of deglaciation on the petrology and eruptive history of the Western Volcanic Zone, Iceland. *Bulletin of Volcanology*. 77. pp. 47
- Edwards, B.R. Tuffen, H. Skilling, I.P. and Wilson, L. (2009) ‘Introduction to Special Issue on Volcano-Ice Interactions on Earth and Mars: the state of the science’ *Journal of Volcanology and Geothermal Research*. 185. (4), pp. 247–250.
- Edwards, B.R., Gudmundsson, M.T. and Russell, J.K. (2015) ‘Glaciovolcanism’. In: Sigurdsson, H., Houghton, B., Rymer, H., Stix, J., McNutt, S. (Eds.), *The Encyclopedia of Volcanoes*, pp. 377–393.
- Gudmundsson, M.T., Sigmundsson, F., Björnsson, H., and Högnadóttir, T., (2004)

- The 1996 eruption at Gjalp, Vatnajökull ice cap, Iceland: efficiency of heat transfer, ice deformation and subglacial water pressure. *Bulletin of Volcanology*. 6. pp. 46–65
- Gudmundsson, M.T. (2005) Subglacial volcanic activity in Iceland (Chapter 6) In: *Developments in Quaternary Science 5. Iceland: Modern processes, Past Environments*. Editors: Caseldine, C.J. Russell, A., Hardardóttir, J., and Ó. Knudsen, pp. 127-151.
- Guilbaud, M.-N., Blake, S., Thordarson, T. and Self, S. (2007). ‘Role of Syn-eruptive Cooling and Degassing on Textures of Lavas from the AD 1783-84 Laki Eruption, South Iceland’. *Journal of Petrology*. 48. pp.1265-1294.
- Höskuldsson, A. and Sparks, R.S.J. (1997) Thermodynamics and fluid dynamics of effusive subglacial eruptions. *Bulletin of Volcanology*. 59. pp. 219–230.
- Höskuldsson, A. Sparks, R.S.J. and Carroll, M. R. (2006) Constraints on the dynamics of subglacial basalt eruptions from geological and geochemical observations at Kverkfjöll, NE-Iceland. *Bulletin of Volcanology*. 68. pp. 689–701.
- Jakobsson, S.P. (1979) Petrology of recent basalts of the Eastern Volcanic Zone, Iceland. *Acta Naturalia Islandica*. 26. 103.
- Jakobsson, S.P. and Gudmundsson, M.T. (2008). Subglacial and intraglacial volcanic formations in Iceland. *Jökull*. 58. pp. 179-197.
- Jones, J.G. 1969. Intraglacial volcanoes of the Laugarvatn region, south-west Iceland. *International Quarterly Journal of the Geological Society London*. 124. pp.197-211.
- Jude-Eton, T. C. Thordarson, T. Gudmundsson, M.T. Oddsson, B. (2012). Dynamics, stratigraphy and proximal dispersal of supraglacial tephra during the ice-confined 2004 eruption at Grímsvötn Volcano, Iceland. *Bulletin of Volcanology*. 74. pp. 1057–1082.
- Kjartansson, G. 1943. Árneshingasaga I. *Yfirlit og jarðsaga*. pp.1-183. (In Icelandic)
- Larsen., G. (1979). About the age of the Eldgjá lavas. *Náttúrufræðingurinn*, 49 (1979), pp. 1-26
- Larsen, G. (2000) Holocene eruptions within the Katla volcanic system, south Iceland: characteristics and environmental impact. *Jökull*. 49. pp. 1–28.
- Neave, D. A., Passmore, E., MacLennan, J., Fitton, G. and Thordarson, T. (2013). Crystal-Melt Relationships and the Record of Deep Mixing and Crystallization in the AD 1783 Laki Eruption, Iceland. *Journal of Petrology*. 54. (8), pp.1661-1690.
- Neave, D. A., Buisman, I. and MacLennan, J. (2017). Continuous mush disaggregation during the long-lasting Laki fissure eruption, Iceland. *American Mineralogist*. 102. (10), pp. 2007–2021. doi:10.2138/am-2017-6015CCBY
- Magnússon, E., Gudmundsson, M.T., Sigurdsson, G., Roberts, M.J., Höskuldsson, F. and Oddsson, B. (2012). Ice-volcano interactions during the 2010 Eyjafjallajökull eruption, as revealed by airborne radar. *Journal of Geophysical Research*. 117. (B07405).
- Miller D. J. (1989). Unpublished PhD thesis. The 10th Century eruption of Eldgjá, southern Iceland. Nordic Volcanological Institute, Reykjavík
- Moreland W.M, Thordarson T, Houghton B.F. and Larsen G, (2019). Driving mechanisms of subaerial and subglacial explosive episodes during the 10th century Eldgjá fissure eruption, southern Iceland. *Volcanica*.
- Óskarsson, B. V. (2006) Unpublished thesis. The University of Iceland. ‘The Skerin ridge on Eyjafjallajökull, south Iceland: Morphology and magma-ice interaction

in an ice-confined silicic fissure eruption.’

- Reynolds, H.I. Gudmundsson, M.T. Högnadóttir T, Magnússon, E. Pálsson, F. (2017). Subglacial volcanic activity above a lateral dyke path during the 2014–2015 Bárðarbunga-Holuhraun rifting episode, Iceland. *Bulletin of Volcanology*. 79. 38.
- Passmore, E. (2009). Unpublished Thesis, University of Edinburgh. ‘Feeding large eruptions: crystallization, mixing and degassing in Icelandic magma chambers’.
- Passmore, E., MacLennan, J., Fitton, G. and Thordarson, T. (2012). Mush disaggregation in basaltic magma chambers: Evidence from the AD 1783 Laki Eruption. *Journal of Petrology*. 53. (12). pp. 2593–2623. doi:10.1093/petrology/egs061
- Schopka, H.H., Gudmundsson, M.T. Tuffen, H. (2006). The formation of Helgafell, a monogenetic subglacial hyaloclastite ridge: Sedimentology, hydrology and volcano-ice interaction. *Journal of Volcanology and Geothermal Research*. 152. pp. 359-377.
- Schmidt, A. (2015). Chapter 15 ‘Volcanic Gas and Aerosol Hazards from a Future Laki-Type Eruption in Iceland’. In: Volcanic Hazards, Risks and Disasters. Editor(s): John F. Shroder, Paolo Papale. doi:10.1016/B978-0-12-396453-3.00015-0.
- Sigmarsson, O., Karlsson, H.R. and Larsen, G. (2000). The 1996 and 1998 subglacial eruptions beneath the Vatnajökull ice sheet in Iceland: contrasting geochemical and geophysical inferences on magma migration. *Bulletin of Volcanology*. 61. pp. 468–476.
- Sigmarsson, O., Carpentier, M. and Larsen, G. (in prep). New constraints on Grímsvötn magmatic system inferred from ice-kept historical tephra.
- Sinton, J.M., Grönvold, K. and Sæmundsson, K. (2005) Postglacial eruptive history of the Western Volcanic Zone, Iceland. G3, Vol. 6, 12.
- Smellie, J. L. (2002) The 1969 subglacial eruption on Deception Island (Antarctica): events and processes during an eruption beneath a thin glacier and implications for volcanic hazards. *Geological Society, London, Special Publications*. 202. pp. 59–79
- Smellie, J.L. and Edwards, B.R. (2016). Glaciovolcanism on Earth and Mars: Products, Processes and Paleoenvironmental Significance. Cambridge: Cambridge University Press.
- Smellie, J.L. (2018) Glaciovolcanism: A 21st century proxy for paleo-ice. Chapter 10 In: Past Glacial Environments (second edition), pp. 335–375.
- Steingrímsson, Rev. J. (1907) Fullkomið rit um Síðveld (original manuscript transcribed). The National Archive of Iceland. In: Thórgunnar Skúladóttir (Editor) ‘Fires of the Earth, The Laki Eruption 1783-1784. (1998). The University of Iceland Press and the Nordic Volcanology Institute.
- Steingrímsson J (1783a) A short compendium of the recent volcanic outburst in western part of Skaftafell county, dated at Prestbakki July 4, 1783. In: Einarsson, T., Guðbergsson, G.M., Gunnlaugsson, G.A., Rafnsson S. and Þórarinnsson, S. (editors.) Skaftáreldar 1783-1784: Ritgerðir og Heimildir. pp. 272-274. Mál og Menning: Reykjavík 1984.
- Steingrímsson, J. (1783b). Abstract from a letter to Reverend Bjarni Jónsson, dated August 31 1783 at Prestbakki. In: Safn til Sögu Islands. IV. pp. 69-70: Copenhagen.
- Steingrímsson, J. (1788) A complete description on the Síða volcanic fire, dated November 24 1788 at Prestbakki In: Safn til Sögu Islands. IV. pp. 1-57:

Copenhagen.

- Steingrímsson, J. and Ólafsson, S. (1783). A simple, but true narrative of the eruption in Skaftafell county in the year 1783, dated November 24 1788 at Kirkjubæjarklauster. In: Safn til Sögn Islands. IV. pp. 58-69: Copenhagen (in Icelandic).
- Thordarson, T. and Self, S. (1993). The Laki (Skaftár Fires) and Grímsvötn eruptions in 1783-1785. *Bulletin of Volcanology*. 55. pp.233-263.
- Thordarson, T. and Self, S. (2003). Atmospheric and environmental effects of the 1783-1784 Laki eruption: a review and reassessment. *Journal of Geophysical Research*. 108.
- Thordarson, T., Self, S., Oskarsson, N. and Hulsebosch, T. (1996). Sulfur, chlorine, and fluorine degassing and atmospheric loading by the 1783-1784 AD Laki (Skaftár Fires) eruption in Iceland. *Bulletin of Volcanology*. 58. pp.205-225.
- Thordarson, T., Miller, D.J., Larsen, G., Self, S. and Sigurdsson, H. (2001). New estimates of sulfur degassing and atmospheric mass-loading by the 934 AD Eldgjá eruption, Iceland. *Journal of Volcanology and Geothermal Research*. 108. (1-4), 15, pp. 33-54
- Thordarson, T., Larsen, G., Steinthorsson, S., and Self, S. (2003a). The 1783–1785 AD Laki-Grímsvötn eruptions II: appraisal based on contemporary accounts. *Jökull*. 53. pp. 11–47.
- Thordarson, T., Self, S., Miller, D. J., Larsen, G. and Vilmundardóttir, E. G. (2003b) Sulphur release from flood lava eruptions of the Veiðivötn, Grímsvötn and Katla volcanic systems, Iceland. In: C Oppenheimer, DM Pyle and J Barclay (eds.) Volcanic Degassing. pp. 103-121. *The Geological Society of London*.
- Thoroddsen, T. (1881–1898). Geological Map of Iceland. Edited by the Carsberg Fund, 1901.
- Tuffen, H., Pinkerton, H., McGarvie, D.W., Gilbert, J.S. 2002. Melting of the glacier base during a small-volume subglacial rhyolite eruption: evidence from Bláhnúkur, Iceland. *Sedimentary Geology*.149. pp.183-198.
- Tuffen, H. (2007) Models of ice melting and edifice growth at the onset of subglacial basaltic eruptions. *Journal of Geophysical Research*. 112. (B03203).
- Tuffen, H. Owen, J. and Denton, J.S. (2010) Magma degassing during subglacial eruptions and its use to reconstruct palaeo-ice thicknesses. *Earth-Science Reviews*. 99. (1-2): pp. 1-18
- Wilson, L. Smellie, J.L. and Head, J.W. (2009) Volcano-ice interactions. In: Modeling Volcanic Processes: The Physics and Mathematics of Volcanism. Fagents, S., Gregg, T. K. P. and Lopes, R. M. (Editors) pp. 275-299. doi:10.1017/CBO9781139021562.013

Chapter 6: Shallow conduit processes during the Holuhraun 2014–15 CE eruption

6.1 Introduction

Volcanism in Iceland is confined to the active axial zones and intraplate belts and localised in distinct volcanic systems. Eruptions occur either at a volcanic system's central volcano or along linear vent structures in its associated fissure swarm (Jakobsson, 1979a, 1979b; Thorarinsson et al., 1959; Pálmasson and Sæmundsson 1974; Sæmundsson, 1974, 1978, 1979; Jóhannesson and Sæmundsson, 1998, 2009; Gudmundsson, 2000; Thordarson and Larsen, 2007; Jakobsson et al., 2008; Jakobsson and Gudmundsson, 2008; Thordarson and Hoskuldsson, 2008; Hjartardóttir, 2008; Hjartardóttir et al., 2009, 2012; Hjartardóttir and Einarsson, 2012; Jóhannesson 2014). Volcanic systems are not just the fundamental building blocks of the modern neovolcanic zones in Iceland; their older counterparts constructed the now eroded Pleistocene-Neogene sequences. The emblematic layer-cake, plateau basalt sequences volumetrically dominated the Neogene volcanic successions relative to the products of central volcanoes (Walker, 1963, 1964, 1993; Thorarinsson et al., 1959). These successions show that the Icelandic plateau was constructed by recurrent, predominantly effusive, basaltic flood lava eruptions ($>1-100 \text{ km}^3$; FL), creating large lava flow fields originating from linear vents within the fissure swarms (Thordarson and Hoskuldsson, 2008). The overall architecture of volcanic systems from the Neogene to the present remains largely the same, with flood lava eruptions as the major contributor to the construction of the Iceland Basalt Plateau (e.g., Walker, 1963, 1964, 1993; Thordarson and Höskuldsson, 2008) which can therefore be thought of as the building blocks of Iceland. The 2014–15 CE Holuhraun flood lava eruption is an event of significance as it provided a rare opportunity to witness, for the first time with modern scientific equipment, a typical example of the type of eruption that is the main contributor to the Icelandic plateau basalt succession.

The Holuhraun 2014–15 CE eruption represents the low-magnitude and low-intensity end-member of FL events, associated with semi-sustained and weak fountaining. Weak fountaining events devolve from an emergent phase of laterally near-continuous “curtain-of-fire” fountaining to discrete fountains, through localised vents, each producing near-vent, coarse-grained pyroclastic fall deposits. If this occurs during the waxing phase of the eruption, mass eruption rate and fountain height increase. These more intense phases can produce sheet-like medial and distal tephra fall, which can form discrete lobes or sheets depending on the timescales of activity. Episodic fountaining is a common feature once activity has devolved to discrete vents, it can result in intense short-lived phases of moderate-high fountaining e.g., Kīlauea in Hawaii: Kīlauea Iki 1959 CE (Richter et al., 1970; Stovall et al., 2011, 2012), Mauna Ulu 1969–74 CE (Swanson et al., 1979; Parcheta et al., 2013) Pu’u’Ō’ō 1983–86 CE (Mangan and Cashman, 1996; Wolfe et al., 1988; Heliker et al., 2003; Heliker and Mattox, 2003). A similar reduction in MER followed by a surge in fountaining intensity took place within the 2014–15 Holuhraun event in September 2014, linked to changes in mass eruption rates (MER) (Bonny et al., 2018).

Over short time scales, many basaltic fissure eruptions display highly variable and rapidly fluctuating eruptive styles and intensities (Orr et al., 2015; Houghton et al., 2020). This variability is the result of complex feedbacks in the shallow conduit that modulate changes in eruptive dynamics, which in turn is recorded in the micro-textures in erupted pyroclasts, namely vesicle number densities, shapes and sizes (Cashman and Mangan, 1994; Mangan and Cashman, 1996; Shea et al., 2010). Multiple processes play a role in these feedbacks, where the most important are changes in microlite crystal content and volatile behaviour upon ascent, mass-ascent rate, fluid dynamic aspects such as coupling or decoupling of melt and bubbles, crystal content of the magma, conduit geometry and conduit wall stability. In this study we focus on the relative influences of volatile degassing in the shallow conduit, during the relatively short ascent history of the magma prior to fragmentation, from the perspective of bubble nucleation, growth, coalescence and outgassing during a basaltic fissure eruption and how these processes may relate to changes in eruptive behaviour and style at the surface (Mangan et al., 1993;

Cashman and Mangan, 1994; Mangan and Cashman, 1996; Sparks, 2003; Houghton and Gonnermann, 2008; Shea et al., 2010; Houghton et al., 2020).

The 2014–15 CE event at Holuhraun was the largest eruption to occur in Iceland in 240 years (i.e., since the 1783–84 CE Laki eruption). In-situ detailed imaging, mapping and sampling of the eruptive products was carried out continuously throughout the 2014–15 CE Holuhraun eruption. This, coupled with comprehensive deformation and seismicity measurements including the subset of syn-eruptive tremor (Sigmundsson et al., 2014; Ágústsdóttir et al., 2016; Hjartardóttir et al., 2016; Eibl et al., 2017), in-situ volcanic gas surveys (Ilyinskaya et al., 2017; Pfeffer et al., 2018), satellite sulfur (S) measurements and modelling of plumes (Schmidt et al., 2015), and ground-based time-averaged mass eruption rates (Bonny et al., 2018), have yielded an extensive data set for this infrequent type of eruption. The erupted pyroclasts from lava fountaining phases at the 2014–15 Holuhraun event provide a unique chance to analyse how the shallow conduit modulates eruptive style and intensity, using the pyroclasts micro-textures as indicators of fragmentation and post-fragmentation conditions. Samples from various phases and times of the eruption reveal relatively homogeneous magma composition throughout (Bali et al., 2018; Halldórsson et al., 2018; Hartley et al., 2018), thus precluding these parameters from playing a significant role in changing eruptive behaviour.

To date only one micro-textural study exists for an FL eruption, the Eldgjá 939 CE event in Iceland (Moreland et al., 2019), which, unlike Holuhraun, was a high-discharge and high-magnitude event. Due to scarcity of events of this size, a comprehensive data set on the explosive mechanisms of large fissure eruptions is lacking. Therefore, the study of the Holuhraun pyroclasts enables characterisation of vesiculation processes during a low-intensity Icelandic FL for comparison with Eldgjá 939 CE. It also provides an ideal testing ground to assess whether vesicle number density in low intensity basaltic fountaining is a proxy for eruptive intensity and hence magma rise rates.

The observed variety of microtextural fingerprints identified by this study in a single lapilli clast and how these evolve with time throughout an eruption highlights the importance of quantitatively analysing the outer rinds, in isolation, if present, of

pyroclasts from low viscosity melts. This provides accurate VND data sets for the state of the melt prior to fragmentation, rapidly quenched and unaffected by post fragmentation expansion, which can be used as a better proxy for explosivity in a variety of styles of basaltic eruptions. The discrete textural domains identified by small scale textural mapping of heterogeneities in basaltic pyroclasts also capture changing shallow conduit processes, which are responsible for rapid fluctuations in eruptive styles during fissure eruptions.

6. 1. 1 Previous work on low-intensity fissure eruptions

The transition between effusive and explosive eruptions, or different intensity phases within a single eruption, are dictated by the magma's ability to break into discrete liquid pieces (fragment) and the ability of gas bubbles to rise through the magma column and escape (outgas). Fragmentation occurs at a threshold in the shallow conduit where a continuous melt containing dispersed bubbles fragments, and transforms to a continuous gas carrying liquid pyroclasts. The processes that induce fragmentation of magmas are fundamentally different for basaltic versus silicic melts. These differences enable low viscosity magmas (basalts) to fragment at much lower bubble volume fractions than higher viscosity melts. Silica rich melts fail in brittle fashion at high tensile stress associated with a minimum bubble fraction of 70–75 %, which is typical for higher viscosity melts where the melt films between bubbles rupture due to internal gas pressure within the bubbles (McBirney and Murase, 1970; Zhang, 1999). Although if the melt experiences processes that are governed by the viscoelasticity properties of the melt, e.g., shearing this can occur at slightly lower vesicularities down to 64 % (Webb and Dingwell, 1990a, 1990b; Gardner et al., 1996; Papale, 1999; Gonnermann and Manga, 2003; Tuffen et al., 2003). For basaltic magmas, which have a lower viscosity allowing both bubble outgassing and easier bubble expansion under decompression as viscosities do not reach those required to retard bubble expansion (Thomas et al., 1994; Barclay et al., 1995; Gardner et al., 2000; Namiki and Manga, 2008), fragmentation is governed purely by fluid mechanics (Namiki and Manga, 2008). There are four additional ways to induce fragmentation at lower bubble fractions in lower viscosity melts: (1) inertial, pull-apart, fluid dynamic forces (if the inertia forces acting on the expanding melt, driven by bubble expansion, is greater than surface tension stress which

viscous forces dictate, fragmentation can occur), (2) strain-rate (where bubbles grow faster than the surround melt can transform, pushing the melt across the glass transition), (3) potential energy (which is related to the initial pressure in the bubbles, that can drive gas expansion) (4) stress (where bubbles rupture when the tensile strength of the melt is exceeded) (Gonnermann and Manga, 2007; Namiki and Manga, 2006, 2008; Rust and Cashman, 2011). For explosive basaltic volcanism, laboratory experiments and numerical modelling have shown that the timing and degree of processes like decompression, degassing, vesicle nucleation, growth, coalescence and outgassing, occurring over short timescales in the shallow conduit as magma ascends, are the key in the development of different eruptive styles (Gonnermann and Manga, 2007; Namiki and Manga, 2006, 2008; Houghton et al., 2016). Quantitative micro-textural analysis of eruptive pyroclasts is a powerful tool that fingerprints the timing, rates, and temporal evolution of these shallow conduit processes, throughout an eruption as they exert modulating influences on the style of eruption. A wide range of vesicle number densities (VND), size distributions (VSD) and volume distributions (VVD) have been identified by studies on basaltic eruptions which display vastly different eruptive styles and progression of activity (Cashman and Mangan, 1994; Polacci et al., 2006; Sable et al., 2006, 2009; Lautze and Houghton, 2008; Costantini et al., 2010; Stovall et al., 2011, 2012; Parcheta et al., 2013; Houghton et al., 2016; Holt et al., 2019). The 2014–15 event at Holuhraun represents the low end-member in terms of explosivity for prolonged and sustained fountaining eruptions. This event exhibited a variety of eruptive styles and a time-dependent evolution in terms of eruption intensity.

Some fountaining basaltic fissure eruptions display episodic and rapid fluctuations in eruptive behaviour that are associated with changes in MER throughout the lifespan of the event. Good examples of this type of activity were documented during the low-moderate-high fountaining episodes of Pu‘u‘Ō‘ō 1983–86 CE (Mangan et al., 1993; Cashman and Mangan, 1994; Mangan and Cashman, 1996; Holt et al., 2019), as well as the lower-transitional fountaining observed during Mauna Ulu 1969 CE (Parcheta et al., 2013), Kīlauea Iki 1959 CE eruption (Richter et al., 1970; Stovall et al., 2011, 2012). The 2014–2015 CE event at Holuhraun is no exception, with two documented distinct episodes that can be linked to changes in time-averaged MER (Figures 6. 1 and 6. 2). The processes affecting the magma in the shallow conduit

during these episodes of resurgence are not well constrained. However, as demonstrated below, the micro-textural diversity of tephra clasts produced at various times during the 2014–15 event at Holuhraun does shed some light on the triggers for sudden changes in eruptive style.

6. 1. 2 Geological setting

In Iceland, volcanic systems — composed of a central volcano or a fissure swarm or both — are a fundamental component of the volcanic succession. In general, whilst recurring small magnitude eruptions are common at central volcanoes, the majority of the eruptive volume of volcanic systems is produced by large magnitude events, i.e., FL eruptions, on the fissure swarms. These FL events are the archetypical eruptive activity that can be thought of as the building blocks of Iceland, occurring with a frequency of approximately 250–500 years. Five FL eruptions have taken place in Iceland in historical times: Eldgjá 939 CE ($\sim 20 \text{ km}^3$), Hallmundarhraun 950 CE ($\sim 8 \text{ km}^3$), Frambruni-Dyngjuháls 13th century CE ($\sim 4 \text{ km}^3$), Laki 1783–84 CE ($\sim 15 \text{ km}^3$) and Holuhraun 2014–15 CE (1.2 km^3) (Miller, 1989; Thordarson and Self, 1993; Thordarson, 2003; Thordarson et al., 2003a; Sinton et al., 2005; Thordarson and Larsen, 2007; Pedersen et al., 2017; Moreland et al., 2019). Together these five FLs account for more than half (54 %) of the total historical erupted volume of magmas in Iceland and 64 % of the mafic eruptions (Thordarson and Larsen, 2007). Whilst events of this magnitude are infrequent in Icelandic geological history, their volatile and aerosol atmospheric loadings have the potential to have a devastating climatic and environmental impact (e.g., Thordarson et al., 1996; Thordarson and Self, 2001; Thordarson and Self, 2003; Thordarson et al., 2003b; Schmidt et al., 2010; Schmidt et al., 2011; Loughlin et al., 2012).

6. 1. 3 A review of the Holuhraun 2014–15 CE event: A low-intensity FL eruption.

The 2014–15 CE event at the Holuhraun fissure lasted for 6 months (31 August 2014 to 27 February 2015). It produced a 1.2 km^3 dense rock equivalent (DRE) volume (Bonny et al., 2018) basaltic lava flow emplaced over 84 km^2 (Pedersen et al., 2017) at Dyngjúsandur, in the central highlands of Iceland (Figure 6. 1). The eruption

occurred along a fissure that has erupted three times: first in 1797–98 CE, then 1867 CE, and again in 2014–15 CE, with the youngest event partially covering old vents and lavas. Although this fissure is located within the southern branch of the Askja fissure swarm, the eruption products of these events are geochemically and isotopically linked to the magmas erupted on the adjacent Bárðarbunga-Veiðivötn system, highlighting the complexity of the regional tectonics and associated magmatism (Hartley and Thordarson, 2013; Sigmarsson and Halldórsson, 2015; Hjartardóttir et al., 2016; Halldórsson et al., 2018). The Holuhraun 2014–15 CE event is the only historic FL eruption that is well-documented, directly observed, but represents only the weakest, low intensity, end-member of the spectrum of this high-magnitude eruptive activity.

Eruptive activity progressed as follows: after a minor stop-start episode lasting only 4 hours on 29 August, along a small 600 m long fissure, activity resumed on 31 August and the fissure reached a total length of 1.8 km. Initially, the activity was typified by a continuous curtain of fire along the entire length of the fissure (Figures 6. 3 and 6. 4) with typical fountain heights of <50 m (Figures 6. 2 and 6. 4). The maximum fountain height was 71.5 ± 0.4 m along the middle portion of the fissure (Witt et al., 2018), where the main vent Baugur would later develop. This initial activity had a calculated time-averaged MER, taken from integrated satellite and ground-based data, of $150 \text{ m}^3\text{s}^{-1}$ (Bonny et al., 2018). Fountaining heights after the first 3 days were measured by the IES eruption field team using a clinometer and are reported below as the height above the crater rampart. The highest point of the rampart was 75 m throughout September and early October. From 1–4 September eruptive activity focused onto discrete vents (Witt et al., 2018), in-step with an increase in MER, from 150 to 270 ± 40 to $405 \pm 60 \text{ m}^3\text{s}^{-1}$ (Bonny et al., 2018), as the eruption continued to wax. This increase in MER in conjunction with vent localisation resulted in increased lava fountain heights, ≥ 125 m from 2–4 September (IES eruption team field reports). Vent localisation occurred at the fissure segments where the highest fountains were seen during the curtain-of-fire phase of activity (Figures 6. 2 and 6. 4).

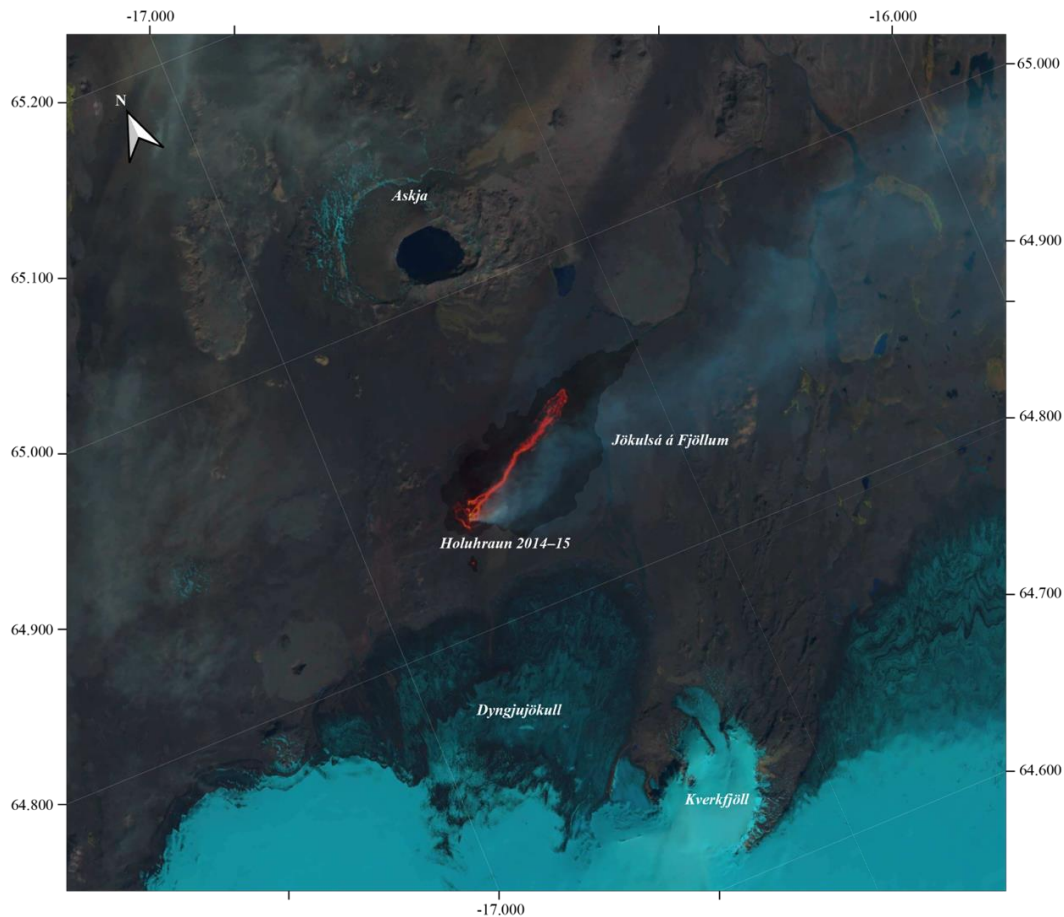


Figure 6. 1: A georeferenced Landsat 8 real look image from of the Holuhraun 2014–15 CE eruption on the 6 September 2014. The active vent system and lava fields are visible, with the final aerial extent of the Holuhraun 2014–15 CE lava field (black) overlaid on the image. The first incandescent lava branch can be seen travelling to the ENE, which finished on the 15 September as branching of the flow field started. For reference, geographical features of note in the surrounding area such as the Askja and Kverkfjöll central volcanoes, Dyngjufjökull, and Jökulsá á Fjöllum provided for orientation. Inset of Iceland, with the outlines of volcanic systems and glaciers outlined for reference, with Bárðarbunga (B) and Askja (A) central volcanoes labelled to highlight their regional location.

The five principal vents were given the names: Norðri, Suðri, Krakki, Heimasætan and Baugur (Figures 6. 2 and 6. 4). The time-averaged MER peaked on 7–8 September at $560 \pm 85 \text{ m}^3\text{s}^{-1}$ (Bonny et al., 2018), corresponding to the highest recorded fountains at $\sim 160\text{--}170 \text{ m}$. Notably, during this time (i.e., 6–8 September), a large amount of Pele’s hair was produced by the fountains. Following this, the magma discharge dropped rapidly to $30 \pm 5 \text{ m}^3\text{s}^{-1}$ over 8 days (Bonny et al., 2018), with the lowest flux recorded on 15 September, corresponding to a fountain height of 70 m and a period of reduced seismicity (IMO Holuhraun eruption reports). This coincided with changes along the fissure in terms of active vents, as all but the main vent Baugur (Figures 6. 2 and 6. 4) shut down after 16 September. Coincidentally, the Baugur vent displayed drastically reduced fountaining intensity. There is a

resurgence on 17 September, with fountain intensity peaking on 20 September during a secondary peak in MER at $440 \pm 65 \text{ m}^3\text{s}^{-1}$. This waxing during 16–20 September, following the low point on 15 September, is also associated with substantial lateral expansion of the flow field (Eibl et al., 2017; Pedersen et al., 2017). The expansion was triggered by branching within the main lava channel leading to the formation of a series of new lava flows (Pedersen et al., 2017), thus initiating the construction of a composite lava flow field (Figure 6. 1).

The MER then decreased in an exponential manner over 20–30 September, and consequently a lava pond formed in the main vent, Baugur, which had a modulating effect on vent activity which shifted from intermittent fountaining to vigorous roiling by early October. Throughout October occasional bursting activity of large, decoupled, bubbles created sporadic medial tephra fall. On 8 October, the IES eruption team on the ground, and overflights, recorded bubble bursts to heights of around 1–1.5 times the rampart height ($>50 \text{ m}$) (Figures 6. 2 and 6. 4). From early to late November the lava lake activity was reduced to steady roiling, punctuated by large bubble bursts with a maximum diameter of 50 m recorded on 18 November. The bubble bursting events had ceased by December and steady state, rolling roiling activity, takes over. The level of the pond dropped steadily throughout February until the eruption ended on 27 of February 2015. This late-stage boiling of the lava pond, was accompanied by large scale resurfacing events across the complex, compound flow field (Pedersen et al., 2017).

Holuhraun 2014–15 CE was one of the most polluting eruptions in the last century (Gíslason et al., 2015; Schmidt et al., 2015; Stefánsson et al., 2017; Pfeffer et al., 2018), emitting approximately 9.6 Mt of SO_2 (Pfeffer et al., 2018) into the atmosphere. However, new estimates by Thordarson et al., 2020, using the final lava field volume and two-stage degassing method calculations, suggest that the eruption carried 9 MT of SO_2 from depth, but not all of this was lofted into the atmosphere. Instead, approximately 70 % of the volatiles outgassed at the vents via syn-eruptive degassing (6.4 MT) entering the eruptive plume, and 13% was exsolved from the lava field during emplacement (1.15 MT), creating a local ground haze; in total, this method estimates 7.5 MT of SO_2 . The atmospheric SO_2 levels at the eruption site exceeded the legal limits, several times, for air quality ($>500 \text{ }\mu\text{g}/\text{m}^3$ for over 10

minutes) set by the World Health Organisation (WHO) and Icelandic health standards (IES eruption field team gas meter readings; Gíslason et al., 2015; Schmidt et al., 2015; Pfeffer et al., 2018).

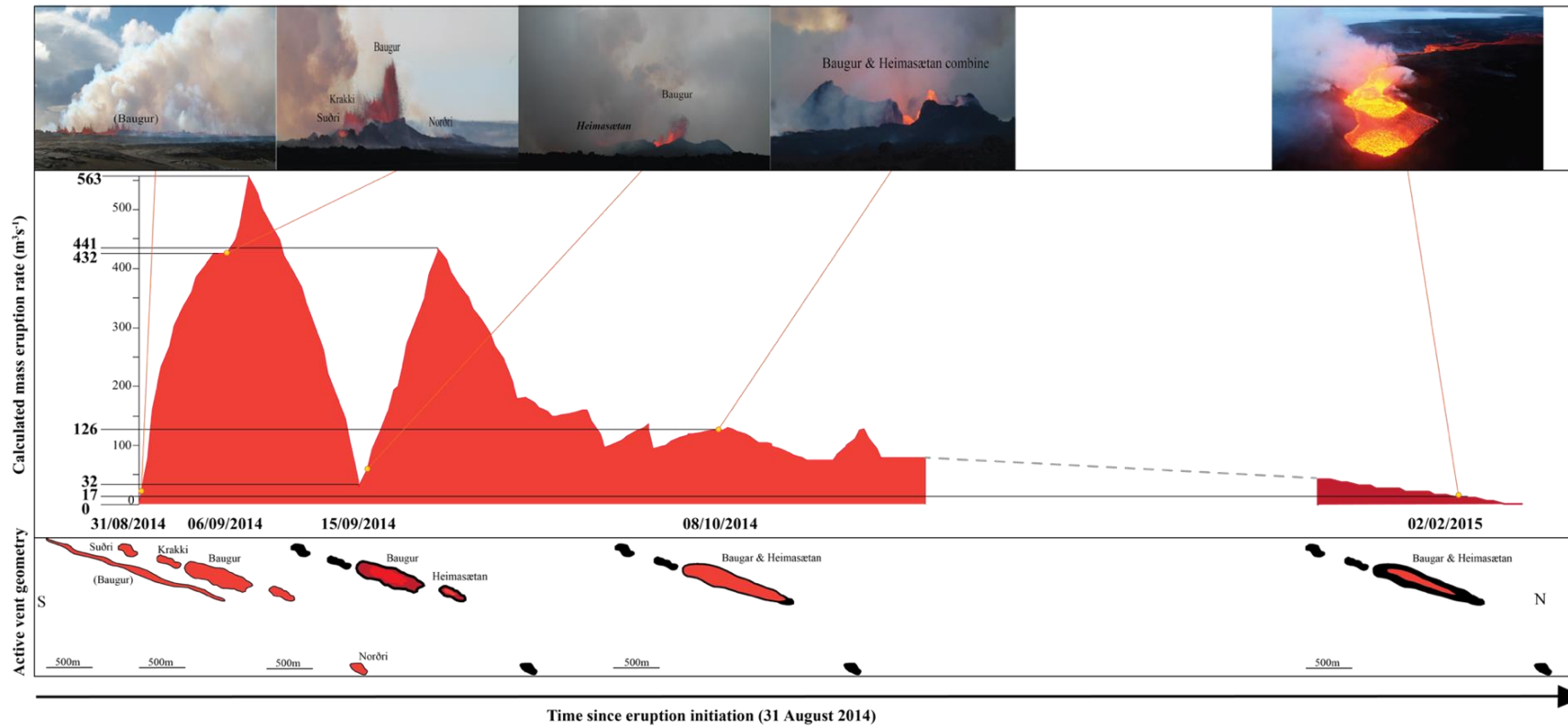


Figure 6. 2: Evolution of the Holuhraun 2014–15 CE vent activity in response to MER and activity vent portions. This is a compilation panel indicating the evolution of several aspects of the Holuhraun eruption (y-axis) through time (x-axis). The active vent geometry (bottom panel) can be seen to concentrate onto discrete vents and subsequently widen throughout the eruption; the active vents are shown in orange. Blacked out vents are no longer active and the darker red zone inside the active on 17 of September 2014 indicates the period between the 15–17 September where the eruptive activity reduced. The middle panel displays calculated MER (Bonny et al., 2018) throughout the eruption. Black lines with key discharge rates are provided for reference. The dotted line represents the average MER from October–February which is not included to emphasise the variations in MER over a short period of time at the start of the eruption. In the top panel the corresponding style of eruptive activity can be seen; photographs are taken from different angles due to the evolution of the lava field restricting access. Orange lines link the calculated MER to the vent activity at the time the image was taken.

In the first months, vent activity produced 1–3 km high gas-rich plumes that were confined to the lowermost troposphere (Pfeffer et al., 2018; Schmidt et al., 2015). Yet these plumes triggered SO₂ levels of >1400 µg/m³ at air quality monitoring stations in north and east Iceland on several occasions (Schmidt et al., 2015). Elevated SO₂ levels were also detected in neighbouring European countries, but only surpassed WHO air quality limits in Ireland for 1 hour on 6 September (Schmidt et al., 2015). This timing coincides with the period of highest MER during the eruption (Bonny et al., 2018).

6.2 Methods

To capture changes in shallow conduit processes that modulated eruption dynamics throughout the Holuhraun 2014–15 CE eruption, pyroclasts erupted during known and well-documented phases of explosive eruptive activity were sampled. Pyroclasts were collected in-situ, often as they fell, from the surface of the glacial outwash plain within a few kilometres of the source vents (Figures 6. 3, 6. 5 and 6. 6). Each sample consisted of at least 100 clasts between 16–32 mm. Nine samples, which span the period of tephra-producing fountain activity from 1 September to 12 November, were collected for clast density/vesicularity analysis. A locally dispersed tephra deposit close to the crater erupted in February, towards the end of the eruption, was also analysed, bringing the sample total to ten.

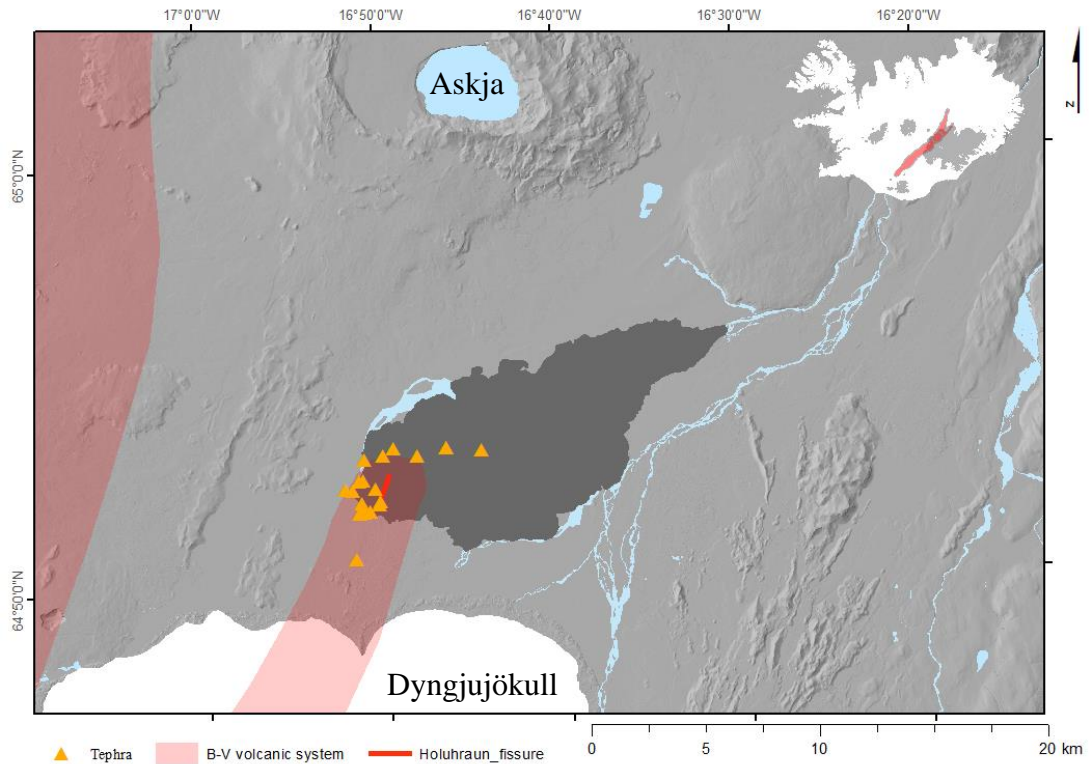


Figure 6. 3: Tephra fall sampling locations from the Holuhraun 2014–15 CE eruption. Arctic DEM hillshade image of Holuhraun 2014–15 CE flow field, highlighted in dark grey, and area surrounding the eruption. The locations of proximal and medial tephra fall samples which were analysed in this study are indicated by orange triangles. The new proposed Bárðarbunga-Veiðivötn (B-V) fissure swarm (Hartley and Thordarson, 2013; Pedersen et al., 2017) shown in light red. Askja and Dyngjujökull, the outlet glacier from the Vatnajökull ice-cap are labelled for reference. The grey outlined box in the inset of Iceland (top righthand of the figure) indicates the geographic locations of the 2014–15 Holuhraun eruption within the island, with the large-scale important features such as the B-V fissure swarm, shown in red, and Vatnajökull, shown in grey, highlighted for reference. The location of the 2014–15 CE Holuhraun fissure, part of which was reactivated during this event, having previously fed older historical lava fields in the area (Holuhraun 1 and 2), is highlighted by a bright red line.

Clast density measurements were carried out on the 100 largest clasts from each sample, following the procedure of Houghton and Wilson (1989). First, samples were cleaned in an ultrasonic bath to remove any fine particles and dried in an oven at 40°C for at least 48 hours. Then, the clasts were weighed individually ($\omega_{\text{clast}}^{\text{D}}$, dry weight), and each clast was wrapped in polyethylene film (parafilm) to waterproof them and the amount used recorded (ω_{parafilm}). Finally, each clast was immersed in deionised water, suspended in a wire cage, with a ballast of known and consistent weight (ω_{ballast}) and weighed again ($\omega_{\text{clast}}^{\text{W}}$, wet weight).

The density of each clast (ρ_{clast}) was then calculated using Archimedes' principle following:

$$\rho_{\text{clast}} = \frac{\omega_{\text{clast}}^{\text{D}}}{\omega_{\text{clast}}^{\text{D}} - (\omega_{\text{clast}}^{\text{W}} - \omega_{\text{ballast}} + \omega_{\text{parafilm}})}$$

(Eq. 1)

A dense rock equivalent (DRE) value of 2830 kg m^{-3} for a Holuhraun basalt calculated from major element concentrations was used when converting measured bulk density to density-derived vesicularity (ϕ) following:

$$\phi = (1 - (\rho_{\text{clast}} / \text{DRE}) * 100$$

(Eq. 2)

6. 2. 1 Textural Analysis

Three clasts of modal density, which were representative of the componentry present within the modal clasts, were chosen from each of the ten bulk density histograms, together with outlier clasts representing the minimum and maximum density, to be made into polished thin sections for textural analysis. In total, 28 clasts were made into polished sections, and initial qualitative petrological and microtextural observations were carried out to characterise which clasts are most representative of the textural diversity of each sample. Four out of 28 clasts, which best captured the array of textures present and accurately represented the average proportions of these textures within the modal clasts, were selected for quantitative vesicle size distribution and number density analysis and carbon coated with a thickness of $250 \mu\text{m}$. The vesicle abundance and size distribution for these pyroclasts provide windows into shallow conduit processes by providing a snapshot of the vesiculation state at the time of quenching, during and following fragmentation, which can be used to extrapolate the relative rates and significances of bubble nucleation, and free growth, as well as the roles of vesicle coalescence and outgassing (Cashman and Mangan, 1994; Mangan and Cashman, 1996).

The four clasts chosen for detailed textural analysis were also intended to represent the key stages of activity as the eruption evolved, with most of this evolution

occurring in the first six weeks of the eruption. The samples and the activity they represent are as follows (Figures 6. 2 and 6. 4):

- 1) 1 September: an open and continuous curtain of fire along a 1.8 km long fissure that has been active for 24 hrs.
- 2) 6 September: the most vigorous activity (highest recorded fountains) producing large quantities of tephra rich in Pele's hair and tears. The vent geometry had changed during the initial 7 days of the eruption as choke points developed and activity concentrated at discrete vents/focal points. The same volume funnelled through a narrower outlet enables higher fountaining.
- 3) 17 September: This sample represents the denser material erupted after a period of reduced seismic and eruptive activity at Holuhraun, during the re-initiation of subdued fountaining activity (which is greatly reduced in comparison with earlier September activity 6 September both in size and in explosivity).
- 4) 8 October: Subdued activity typified by bubble bursting that reaches above the lower-most sections of the crater ramparts formed around the discrete vents. Reticulite and minor amounts of isolated Pele's hair were still produced despite a lack of fountaining. Despite the reduction in explosivity at the vents, the lava discharge rate remained high.

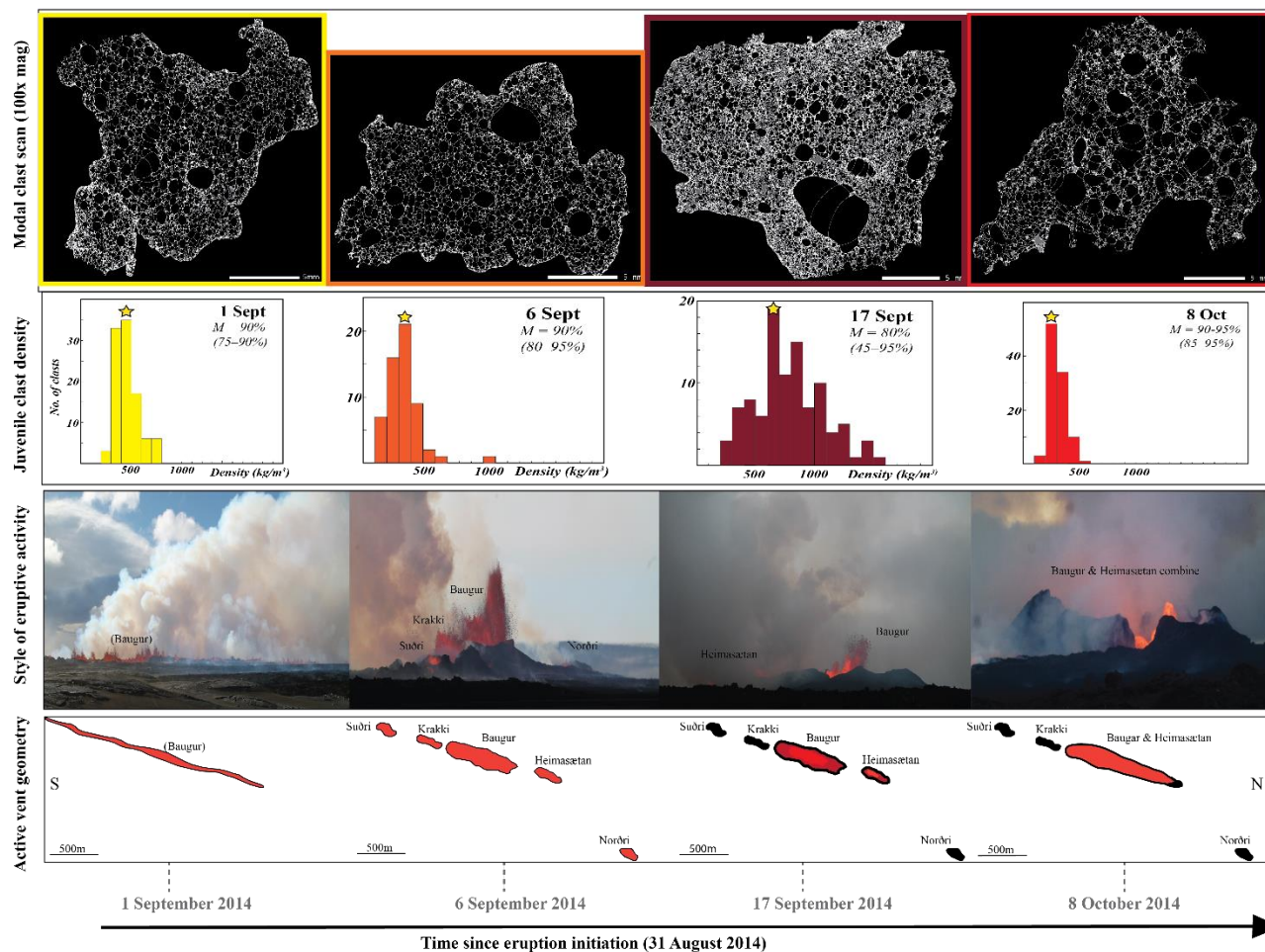


Figure 6. 4: Key stages of changes in vent activity during Holuhraun 2014–15 CE and their corresponding density samples. This is a compilation panel indicating the evolution of several aspects of the Holuhraun eruption (y-axis) through time (x-axis). The bottom and lower middle panels are the same as Figure 6. 2. The upper middle panel displays lapilli pyroclast density histograms, which correspond to the imaged activity in panel 2. The yellow star indicates the modal clasts selected for image analysis. The images in the very top panel display the decoalesced analysed modal clast analysed from each of these eruptive phases.

A JEOL-JSM-7001F Schottky Emission Scanning Electron Microscope at The Institute for Planetary Materials, Okayama University, Japan, was used to collect Back-Scatter Electron (BSE) images from each polished thin section. To fully capture textural variations of the vesicle populations, which span several orders of magnitudes, nests of overlapping images at different magnifications were taken. The pyroclasts from the Holuhraun eruption are texturally complex and display a high degree of melt heterogeneity with domains characterised by distinct vesicle populations (for further details, see the Result section of this Chapter). In order to represent the observed textural heterogeneity within the Holuhraun clasts accurately, the method of Shea et al. (2010) was modified to map the whole thin section area with 100x magnification BSE images collected with a 60 % overlap. Internal SEM software (Mapxml) or software derived from UAV aerial image mapping (pix4D, using manual tie-points) was used to stitch the images without distortion into a whole clast map. The 100x full-pyroclast map replaces the flatbed scan and 50x magnifications in the Shea method, whereas the 250x and 500x magnification nest structures remain unchanged (Figures 6. 8 and 6. 9). The 250x and 500x magnifications were collected on a tabletop Hitachi TM3000 SEM at The University of Iceland. The number of higher magnification images range from six to twelve depending on the heterogeneity of the sample, with more images taken for samples displaying a higher degree of textural complexity. Images for the higher magnifications were positioned to capture the relative proportions of different domains within the clast to ensure the data set included adequate numbers of nests to characterise each type of identified domain individually.

The 100x BSE maps vary in total area (mm^2), and therefore, a different scaling factor was used for each individual map; these range from 281.6–546.0 (pixels/mm) depending on the area of the clast itself. For the 250x and 500x magnification BSE images the areas, and thus scaling factors, are consistent, 0.42 mm^2 (1706.7) and 0.11 mm^2 (3410) respectively.

All raw BSE images were converted manually into binary images using Adobe Photoshop by converting all vesicles to black and the melt/interstitial glass to white. Phenocrysts and microlites, where present, were converted to grey in an additional layer which was analysed separately. Thin melt walls between vesicles were

reinforced to a 3 px width where necessary, and any melt films broken during the thin section and polishing process were redrawn to capture, as closely as possible, the true vesicle distribution and number density present in the magma immediately preceding fragmentation. The images were manually “decoalesced” by reconstructing the natural curvature of the bubble walls that separated vesicles present prior to the last stage of coalescence when these walls were ruptured (Klug and Cashman, 1994).

The images were then analysed with the free, open-source image processing software ImageJ (Schneider et al., 2012), which measures the vesicle number density (VND, number of individual bubbles) and 2D vesicle size distribution (VSD, the size of individual bubbles) in each image. The total melt area of each image was calculated by removing the percentage area taken up by crystal content. The area of each vesicle was then recalculated to give the diameter of an equivalent circle, and the data was binned using geometric bin sizes (equivalent diameter multiplied by $10^{0.1}$). The number of vesicles per unit area, N_A , was calculated using the combined reference area of the image in that magnification. Due to the nested structure of image sets, some vesicles appear in more than one magnification; therefore, a cut-off point for N_A was chosen for each magnification to ensure no vesicle was counted twice during a transition from one magnification to the next. The cut-offs between magnifications were chosen to minimise any abrupt jumps in areal vesicularity. To ensure pixel size and shape were captured accurately, we superimposed a lower cut-off diameter of 5.9 μm in the 500x image, equivalent to 20x20 pixels. Some studies of silicic tephra have used 4.0 μm and 20x20 pixels, but the SEM used for the high magnification images for this study does not achieve that resolution. However, the bubble populations in these (and other) basaltic tephra are markedly coarser than those of silicic pumices. Most of the bubble population in these low viscosity basaltic samples was captured before this cutoff, and processing bubbles of a smaller size than 5.9 μm would be a trade-off between resolution and number statistics. In several samples, the smaller N_A bins have gaps between 5.9 and 10.0 μm , therefore when comparing data sets in terms of cumulative vesicularity relative to vesicle size and N_{V_m} and mass eruption rate, the data sets are truncated at 10.0 μm to enable compatibility in the comparisons between the Holuhraun samples. Additional 250x

and 500x nests were processed to prevent empty bins so the data set could be compared with other eruptions; however, these gaps persist.

Following the stereological method of Sahagian and Proussevitch (1998), the 2D vesicles per unit area, N_A , can be converted to the number per unit volume, N_V . This method assumes that all vesicles analysed are spherical, and does not account for their natural morphologies, however for lower viscosity eruptions (e.g., basaltic melts), the assumption of spherical morphology is generally close to reality. It also adjusts for the probability that not all vesicles will be cross-sectioned at their maximum diameter and therefore may be larger than they appear in 2D by using a dimensionless alpha-value conversion coefficient (α). The original α -values were calculated for 12 classes by Sahagian and Proussevitch (1998) and were later extended for 32 size classes (calculated by K. Cashman). N_V was then scaled with reference to melt volume (N_{V_m}) to account for the volume occupied by the vesicles themselves. To avoid misleading volumetric vesicle number densities, as a result of the method or variability within the sample in 3D space when converting the samples from 2D to 3D, the image derived N_V is scaled to the bulk vesicularity derived from density measurements.

6. 2. 2 Geochemical Glass Analysis

Major element and volatile concentrations of basaltic glass from Holuhraun were determined by electron microprobe analysis (EMPA), at The University of Iceland, using a JEOL JXA-8230 SuperProbe. This was carried out on the same thin sections used for SEM textural analysis in order to be able to assess the degree of spatial geochemical homogeneity within each clast compared to textural observations.

All data in this study is reported with a 1σ error and was collected over multiple analytical sessions. Ten to twenty points were collected per textural zone analysed, using an acceleration voltage of 15 kV, corresponding to a 10 nA beam current with a diameter of 10 μm . The reference standard used was A-99, a Smithsonian Microbeam Standard, consisting of natural basaltic glass from Kīlauea, Hawai'i (Makaopuhi Crater); this was analysed 5–10 times at the start and end of each

analysis run. The instrument was stable throughout the analysis run, and therefore no drift correction was applied. All analyses with total mass sums below 98 % were discarded.

6. 3. Results Holuhraun

6. 3. 1 Deposit characteristics

Preserved tephra from the Holuhraun 2014–15 CE eruption is generally confined to the vent region, with very thin lenses preserved on near-vent lavas beyond the host scoria cones. The fountaining activity in September formed the majority of the 10–75 m high spatter ramparts that built up around the vents. The ramparts and associated tephra fall deposits are comprised of repeating subunits of spatter-bomb-rich horizons intercalated with units dominated by golden pumice and scoria, with subordinate juvenile lava and bedrock lithics that extend up to a maximum of 20 m beyond the ramparts (Figure 6. 5).



Figure 6. 5: Tephra lenses from Holuhraun 2014–15 CE. Relict tephra lenses, visible as a light sandy brown material extending from the crater slope, and into the dark lava field. Where it sits on top of the lava, small rubbly piece of the lava crust stand proud of the lenses. Pippin, the small border collie, for scale.

However, it is the small amount of preserved medial tephra fall produced by Holuhraun which is the focus of this study. This is represented by isolated ash to lapilli sized clasts, as well as Pele's hairs and tears, deposited directly onto a glacial outwash plain consisting of basaltic sand and rocks. Due to the low intensity of this eruption, the Holuhraun medial tephra did not form a thick layer, and because of the depositional environment it is now eroded. Thus, the characteristics described below are from in-situ field documentation made by the IES eruption team (IES eruption team field reports). Medial tephra fall (fine ash and Pele's hairs) was observed up to 14 km from the vent. Medial tephra fall was most common during the peak eruptive intensity periods in September; however, it also persisted to a lesser extent throughout October and November. Complications caused by the continually expanding lava flow field, resulted in tephra sampling only being possible when it fell beyond the flow field boundary. The following observations are made from tephra collected onsite on plastic sheeting placed on the ground. This intermittent, and now eroded, tephra fall was predominately comprised of elongated lapilli (1–6.4 cm) to small fluidal bombs (6.4–10 cm) (Figures 6. 5 and 6. 6). This deposit also contains (i) golden pumice (1–4cm), with a maximum observed size of 9–10 cm, (ii) Pele's hairs and Pele's tears (<0.5 cm) and (iii) a minor fraction of fine-medium ash. Fluidal lapilli clasts collected from medial tephra fall deposits associated with specific vent activity were selected for this study. Both golden pumice lapilli and fluidal lapilli samples, 16–32 mm in size, were included in the 100–120 clasts collected for analysis for this study.



Figure 6. 6: Images of medial fall tephra deposits from Holuhraun 2014–15 CE. Field images (captured by Bergún Arna Óladóttir) of golden pumice, achneliths (fused outer surface golden pumice clasts), Pele's tears and hairs on the dark Sandur, comprised of basaltic ash and rounded rock fragments from the glacial outwash plain. The size of golden pumice and achneliths varies from ash to large lapilli.

6. 3. 2 Clast density and bulk vesicularity

The average clast density for samples of the Holuhraun 2014–15 tephras ranged from 300–730 kg m⁻³, corresponding to an average vesicularity of 72–90 % with errors reported to 1 std (Table 6. 1). The clast density modal range of the tephra is 200–300 to 600–700 kg m⁻³, corresponding to the modal vesicularity range of 75–80 to 90–95 %.

Table 6. 1: Measured density and calculated bulk vesicularity data set, Holuhraun 2014–15 CE.

	Av. Density (kg m ⁻³)	1 std	Av. Ves.	1 std	Distribution	Ves. Range	Min. Ves.	Max. Ves.	Modal Density (kg m ⁻³)	Modal Ves.
1 Sept	450	±12	84%	±4	Unimodal (slight +ve skew)	18%	72%	90%	400–500	85– 90%
2 Sept	420	±13	85%	±5	Unimodal (slight +ve skew)	21%	69%	90%	300–400	85– 90%
6 Sept	310	±14	88%	±5	Unimodal (slight +ve skew)	31%	64%	95%	300–400	85– 90%
9 Sept	450	±11	84%	±4	Unimodal (slight - ve skew)	21%	74%	94%	400–600	80– 85%
17 Sept	730	±29	72%	±10	Polymodal (+ve skew)	49%	44%	93%	600–700	75– 80%
8 Oct	290	±7	90%	±2	Unimodal (tight)	12%	82%	93%	200–300	85– 95%
16 Oct	410	±13	85%	±5	Unimodal (tight)	23%	73%	96%	400–500	80– 85%
4 Nov	300	±12	89%	±4	Unimodal (tight)	32%	62%	93%	200–300	85– 90%
12 Nov	280	±6	90%	±2	Unimodal (tight)	11%	86%	96%	200–300	85– 90%
12 Feb	550	±30	79%	±10	Unimodal (+ve skew)	54%	38%	92%	400–500	85– 90%

Table 6. 2: Measured density and calculated bulk vesicularity data set, Holuhraun 2014–15 CE. Measured density and calculated bulk vesicularity data. Shorthand used in the table is as follows: Av. = Average; Ves. = vesicularity; std = standard deviation; +ve = positive and -ve = negative. Min. = minimum; Max. = maximum; Sept. = September; Oct. = October; Nov. = November and Feb. = February.

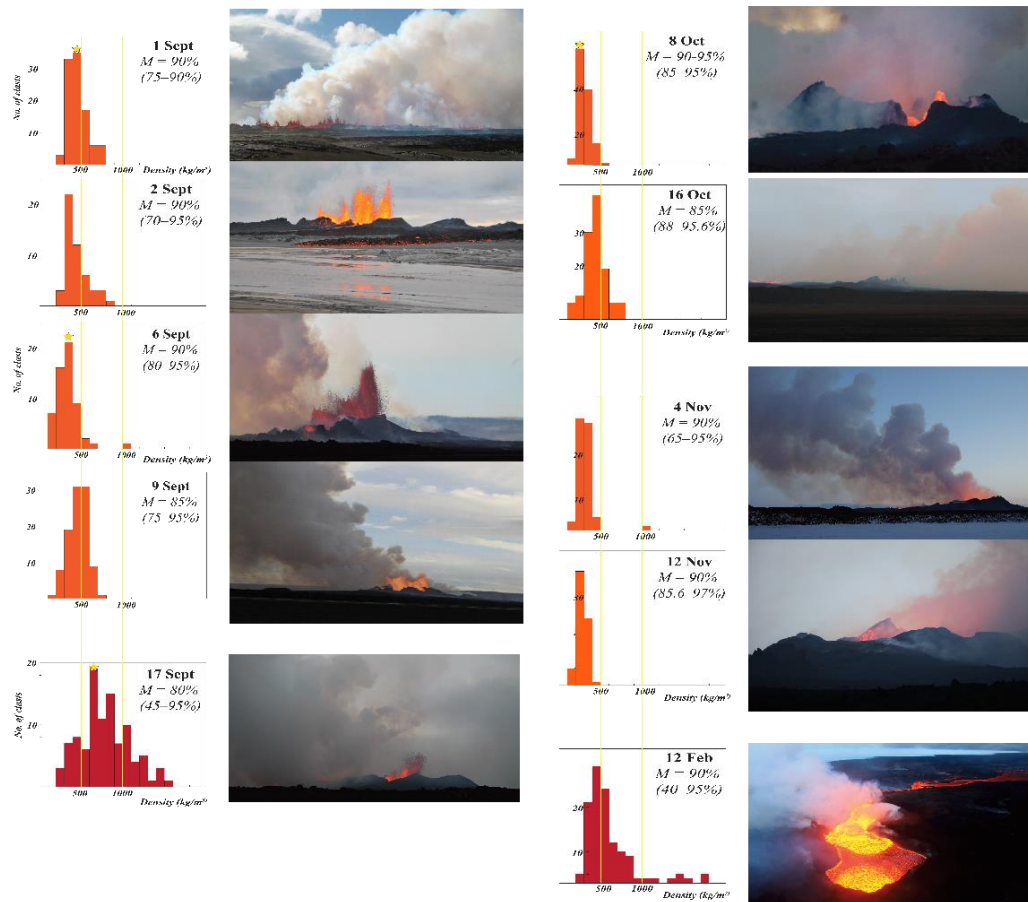


Figure 6. 7: Density histograms versus vent activity comparisons throughout Holuhraun 2014–15 CE. Representative density histograms with matching eruption images. Most density histograms are displayed in orange, save 17 September 2014 and 12 February 2014 which are highlighted in dark red, this is due to the more complicated density distribution of these samples and the general higher proportions of denser clasts in these samples. Yellow lines at 500 and 1000 (kg/m³) density permit comparison between samples. Vesicularity ranges and modal values for each sample are listed in the upper right corner.

For the first 9 days the eruptive intensity increased driven by a waxing mass-discharge rate which peaked on 8 September. This occurred in step with fountaining activity focusing onto discrete vents in the first five days of the eruption, with the highest fountaining heights reached on 6–7 September. The clast density of the tephra erupted during this period are all unimodal with a slight positive skew. The modal density of samples from this period shows a subtle shift towards decreasing density 400–500 kg m⁻³ to 300–400 kg m⁻³ corresponding to a slight (5 %) increase in average vesicularity over time from 84–88 %, with 6 September displaying the highest vesicularity of this subgroup (Table 6. 1; Figure 6. 7). From 9 September the mass-discharge exponentially decreased until 15–16 September, where magma discharge calculations show that the eruption almost came to a halt (Bonny et al., 2018), followed by a short resurgence of more intense activity from 17–20

September. The samples capturing this sharp decrease in discharge and fountaining height on 9 September, showed a marginal increase in density to 400–600 kg m⁻³ (i.e., decrease in vesicularity), whilst maintaining a unimodal distribution but now with a slightly negative skewed distribution (Table 6. 1; Figure 6. 7). The sample of 17 September, representing the tephra fall from the onset of resumed activity, captured an abrupt change in the erupted pyroclasts after this stop-start event. The clast density histogram has a complicated almost poly-modal, saw-toothed distribution which spans a wide range from 200–1600 kg m⁻³, with modal density of 600–700 kg m⁻³ and an average vesicularity of 72 %, equal to a drop of >10 % in overall vesicularity (Table 6. 1; Figure 6. 7).

The two October clast density samples correspond to decoupled bubble bursting activity, documented by the IES eruption team, on 8 and 16 October. These samples display a tight unimodal distribution, with modal density peaks at 200–300 and 400–500 kg m⁻³ respectively and corresponding average vesicularities of 90 % and 85 %. While the 16 October clast population displays an increase of density compared to that of 8 October, and spans a broader range, both samples have a tight unimodal distribution (Table 6. 1, Figure 6. 7). Field observations note an increase in vent degassing on 15–16 October which obscures the vent itself from view with periodic incandescent bubble bursts partially visible, making observations of vent activity difficult. Throughout late October and early November activity intensity is subdued to a rolling boil with large bubble bursts. Density samples taken during this period, on 4 and 11 November, have densities of 200–300 kg m⁻³, a 50 % decrease when compared to 16 October values and an increase in vesicularity from ~84 % to ~89 %. However, with the exception of two rare dense outlier clasts in 4 November samples, the density histograms from this period have tight unimodal distributions.

On 12 February, a tephra fall deposit limited to the immediate surroundings of the main vent, Baugur, was sampled. This was only possible due to the reduction in intensity of vent activity towards the end of the eruption, with mid-February vent activity characterised by an outgassing lava pond with a steadily declining lava level (Figure 6. 7). The clasts of this sample have a modal density of 400–500 kg m⁻³ and an average vesicularity of ~79 %. As with the other clast density samples from this

event, except the 17 September sample, the clasts have a unimodal distribution, but it is negatively skewed, with a pronounced, very dense tail. The clasts of 12 February sample contain a relatively high abundance of both mature euhedral microlites, dendritic microlites and a higher proportion of phenocrysts than the other samples in thin section, however, this was not quantified.

6. 4. 1 Qualitative textural analysis and initial interpretations

All clasts are composed of sideromelane, limited changes in phenocryst proportions, with varying microlite contents, tachylite is absent. All of the Holuhraun clasts display cores with mature and internally heterogeneous bubble textures surrounded by a more rapidly quenched, immature outer rind vesicle population.

The maturity of the vesicle population increases inwards from the outer margin in a semi-symmetrical arrangement (Figures 6. 8–6. 10 and 6. 13); two or three concentric zones are recognised:

- (a) Outer rind: The unbroken portions of the outermost margins of each clast are characterised by a narrow, albeit in some places discontinuous, melt-rich rind containing only small vesicles (Figures 6. 8–6. 10 and 6. 13).
- (b) Interior rind: Extending inwards from the rind in each clast are laterally discontinuous pockets of melt, characterised by small to medium-sized vesicles. These are present in two out of the four clasts analysed, from 1 and 17 September.
- (c) Inner mature foam: The interior of the clast is typified by heterogeneous vesicle populations, sometimes forming sharply delineated textural domains of contrasting vesicle number and size. Large vesicles are only found within the mature interior and are generally concentrated towards the centre of the clast.

This semi-concentric zoning of vesicle maturity has been demonstrated by several studies of Kīlauea pyroclasts to be indicative of post-fragmentation expansion of the interior vesicle population (Mangan and Cashman, 1996; Porritt et al., 2012; Stovall et al., 2011, 2012; Parcheta et al., 2013; Holt et al., 2019). This process reflects

ongoing vesiculation after the primary fragmentation of the magma and zonation is due to thermal gradients within the cooling pyroclasts, within the fountain, which generate different length and time scales for continued vesicle growth and development to maturity. Consequently, only the rapidly quenched outer rind is the most representative of the vesicle distribution of the melt at fragmentation, and as such the quantitative textural analysis carried out by this study concentrates on outer rinds.

It is important to note that the post-fragmentation expansion of the interior of the pyroclasts (Figures 6. 10) has emphasised pre-existing, primary, textural contrasts not easily observed in the rind, highlighting evidence of magma mingling and mixing in the shallow conduit, which is addressed in full in the discussion (see Figures 6. 8–6. 10 and 6. 13). Due to the smaller nature of the unmodified vesicle populations in the rinds, distinct textural domains with different vesicle populations are harder to distinguish in the rind itself although small scale vesicle clusters or melt rich regions are visible (Figure 6. 10).

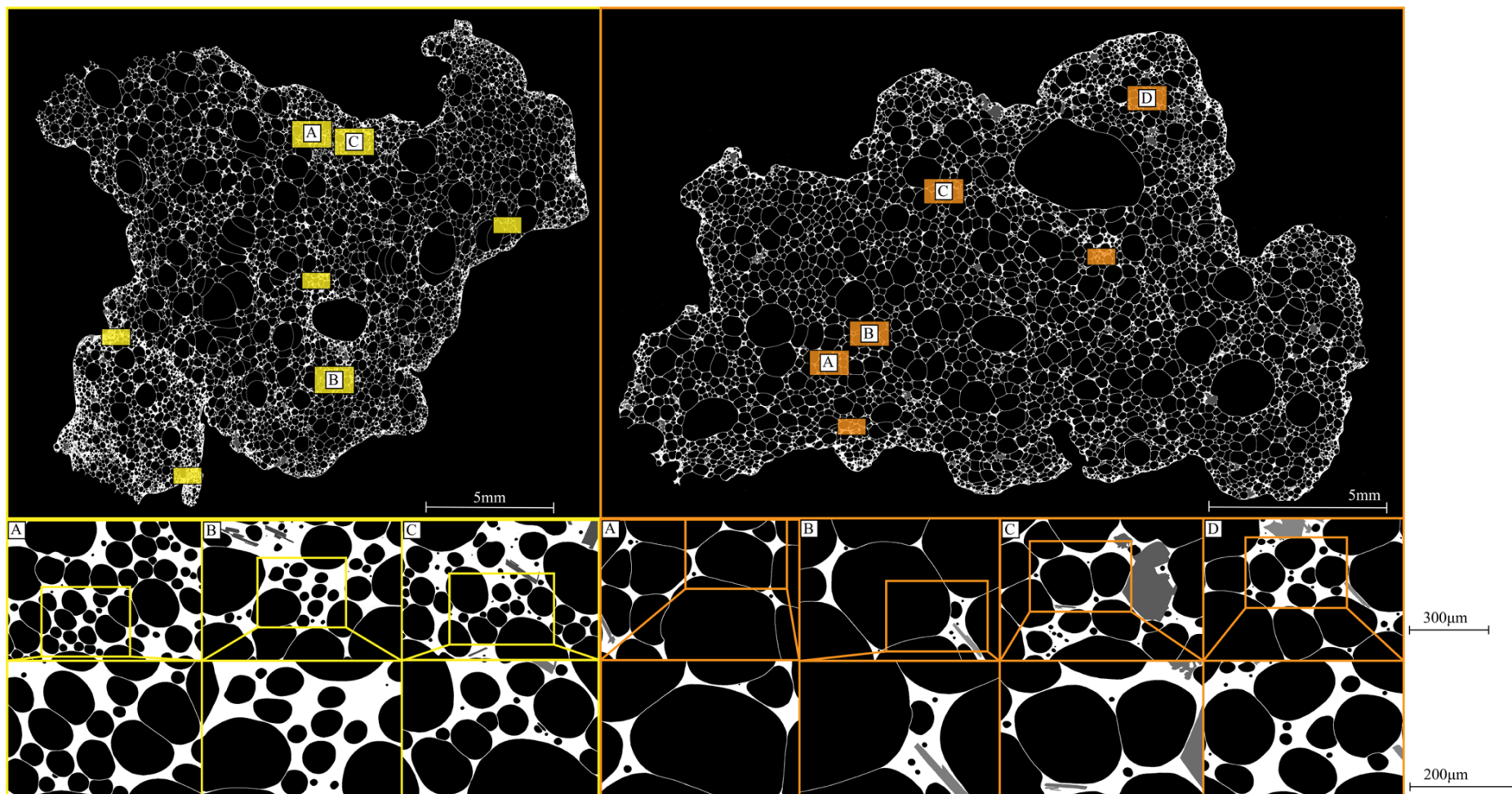


Figure 6. 8: SEM images of explosive phase pyroclasts, from early September during Holuhraun 2014–15 CE. This figure indicates the distribution of 250x and 500x magnification nests on 1 of September 2014 (left hand) and 6 September 2014 (right hand) clasts. Underneath are SEM images at 250x and 500x that display examples of the main textures found within the clasts. The location of the 500x magnification is indicated by a coloured box in the 250x images.

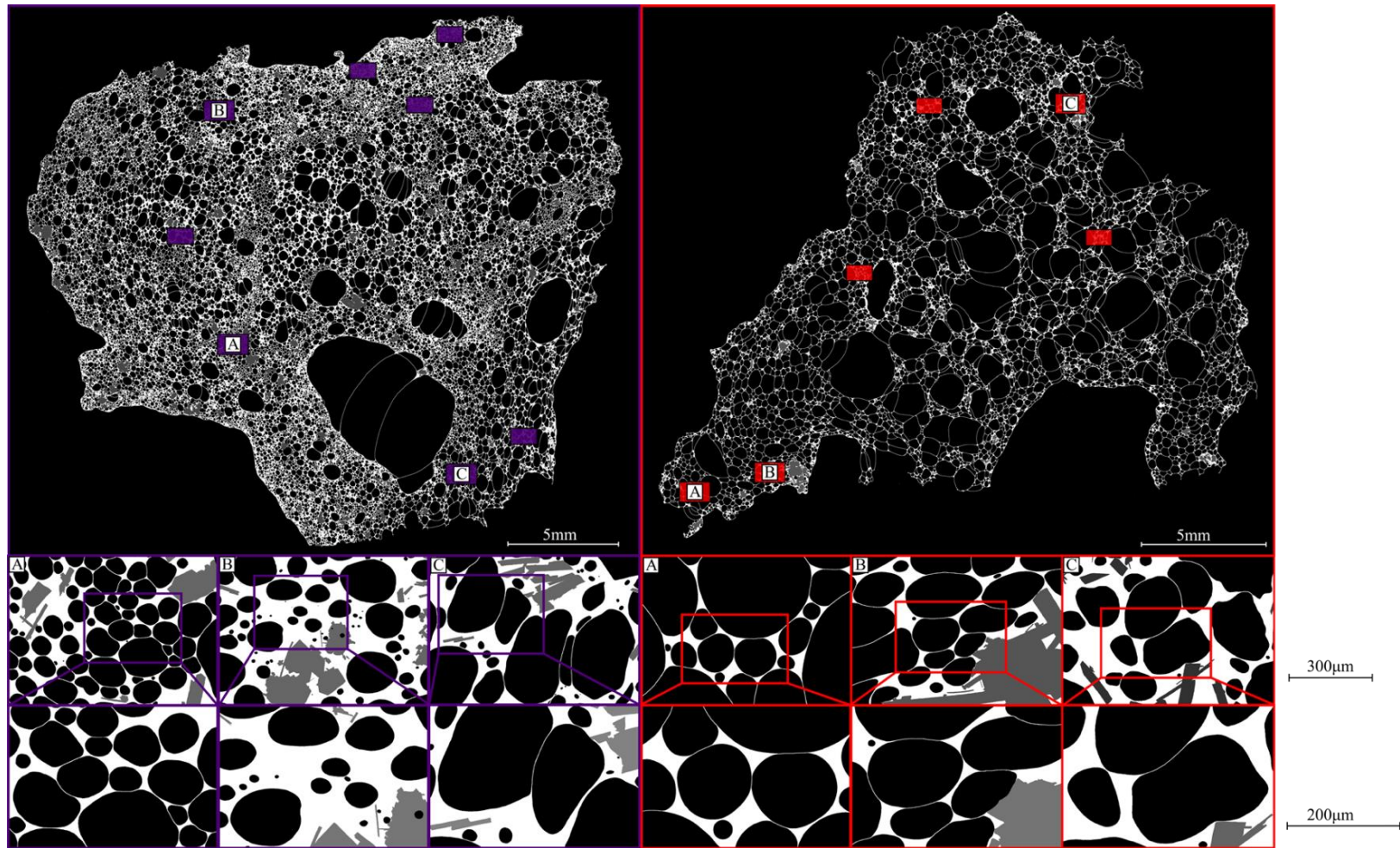


Figure 6. 9: SEM images of explosive phase pyroclasts, from late September and October during Holuhraun 2014–15 CE. Indicates the distribution of 250x and 500x magnification nests on the 17 September (left hand) and 8 October (right hand) clasts. Underneath are SEM images at 250x and 500x that display examples of the main different textures found within the clasts. The location of the 500x magnification is indicated by a coloured box in the 250x images.

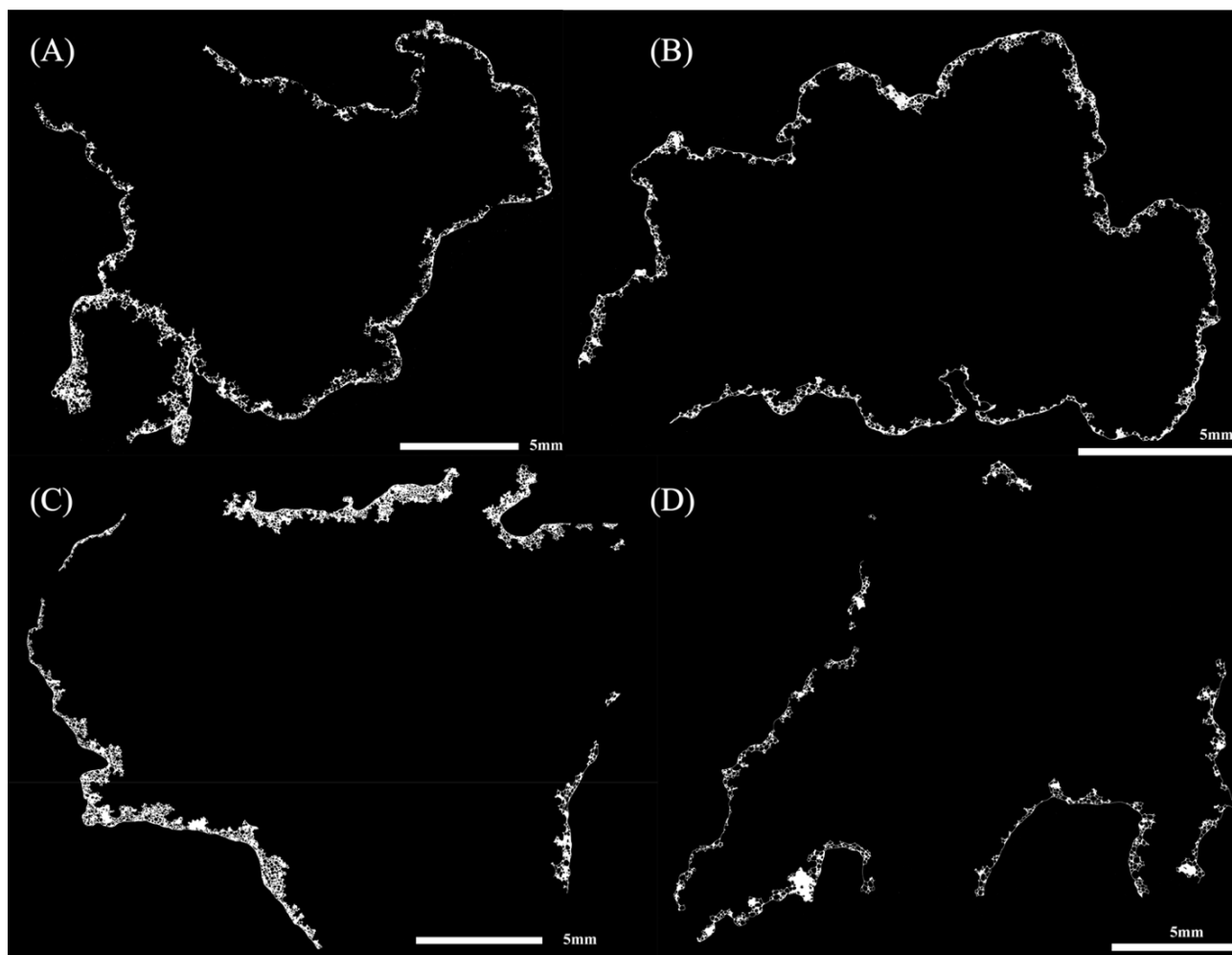


Figure 6. 10: Isolated outer rinds of Holuhraun 2014–15 CE pyroclasts. Outlines of the analysed melt rinds from ImageJ, the melt rich rinds are shown in white with any bubbles in black on a black background. From the top left across (A) 1 September, (B) 6 September, bottom left across (C) 17 September 2014 and (D) 8 October 2014. These plots demonstrate the thickness of the rind in each sample; notably, the 1 September 2014 and 17 September 2014 have thicker rinds than the other samples.

6. 4. 2 Quantitative textural analysis

Quantitative vesicle distributions were measured on the rinds from the 1, 6 and 17 September as well as on the 8 October. Whole clast vesicle distribution data is also provided for comparison in the following quantitative textural analysis:

6. 4. 2. 1 VND (N_V)

All of the Holuhraun rinds have low vesicularity, calculated from the ImageJ thin-section data sets, which range from 31–47 %, and is approximately 40% lower than the calculated vesicularity for the whole clasts (Table 6. 2). Rind vesicle number densities (N_V) for the golden pumices throughout the Holuhraun eruption range 4.43×10^3 – $5.10 \times 10^3 \text{ mm}^{-2}$. When these values are adjusted to be referenced to the melt (N_V^m), the corresponding values fall into a range of 1.77×10^3 – $9.73 \times 10^3 \text{ mm}^{-3}$ (Table 6. 2). Whole-clast N_V values display a lower range than the rinds from 7.74×10^2 – $4.43 \times 10^3 \text{ mm}^{-3}$, which when adjusted to N_V^m display an increase to 9.00×10^3 – $2.22 \times 10^4 \text{ mm}^{-3}$ which is higher than the outer rinds. When the interior textures are isolated, using the difference between the rind and whole clasts, their N_V^m values range from 4.87×10^3 – $1.35 \times 10^4 \text{ mm}^{-3}$ which is consistently higher than the rind.

Table 6. 2: Density and vesicularity data for all of the texturally analysed pyroclasts from the Holuhraun eruption.

Sample	Date Erupted	Days into eruption	Density (g/cm ³)	Vesicularity	V _G /V _L ^b	N _A (mm ⁻²)	N _V (mm ⁻³)	N _V ^m (mm ⁻³)
AH01092014 rind	1 Sept 2014	2	N/A	41.1 ^a	0.752541	123	5.10E+03	8.70E+03
AH01092014	1 Sept 2014	2	0.48	83.2	4.952381	113	3.74E+03	2.22E+04
AH01092014 interior ^c	1 Sept 2014	2	N/A		4.199840			1.35E+04
AH06092014 rind	6 Sept 2014	7	N/A	38 ^a	0.600000	121	4.43E+03	7.15E+03
AH06092014	6 Sept 2014	7	0.48	86.7	6.518797	64	2.61E+03	1.96E+04
AH06092014 interior ^c	6 Sept 2014	7	N/A		5.918797			1.25E+04
AH17092014 rind	17 Sept 2014	18	N/A	30.5 ^a	0.438849	146	6.76E+03	9.73E+03
AH17092014	17 Sept 2014	18	0.7	75.4	3.065041	93	3.60E+03	1.46E+04
AH17092014 interior ^c	17 Sept 2014	18	N/A		2.626192			4.87E+03
TT08102014 rind	8 Oct 2014	39	N/A	46.97 ^a	0.885725 06	58	9.38E+02	1.77E+03
TT08102014	8 Oct 2014	39	0.24	91.4	10.62790 7	30	7.74E+02	9.00E+03
TT08102014 interior ^c	8 Oct 2014	39	N/A		9.742181 94			7.23E+03

Table 6. 3: Vesicle number density data set for Holuhraun 2014–15 CE.

^a Calculated vesicularity using ImageJ BSE SEM images for rinds where density derived bulk vesicularity ascertained from the whole clast could not be used.

^b Calculated vesicle-to-melt ratio (V_G/V_L) is calculated after Gardner et al., 1996 using the formula = (Ves_{fraction}/(1- Ves_{fraction}))*(1/(1-Phenocryst_{fraction})), using the calculated bulk vesicularity values for the whole clast, alongside Image J calculated values from thin section for the rind vesicularity and crystal content (see supplementary material, appendix A: Holuhraun Clasts).

^c Interior values are roughly calculated using the difference between the rind and whole clast V_G/V_L and N_V^m (mm³).

6. 4. 2. 2 VVD

Vesicle volume distributions (VVD) (Figure 6. 11) show the volume fractions contained within vesicle size bins. All Holuhraun rinds have a tight unimodal distribution, with a slight negative skew and a fine tail.

In all of the September rinds, vesicles with equivalent diameters from 0.06–0.3 mm account for approximately >90 % of the void space present; for the 8 October clast, this range is displaced to vesicles with equivalent diameters of 0.09–0.5 mm. The 1

and 6 September have a modal peak volume fraction at 0.2 mm; this decreases to 0.1 mm for the 17 September, increasing again on the 8 October to 0.3 mm.

Both the 1 and 6 September rinds have a very similar overall size distribution, with a larger volume fraction contributing to the greater modal peak for the 1 September clast, which contains a higher proportion of rind. The greater proportion of rind in the 1 September clast is created by this sample consisting of two separate, smaller clasts, which fused together (Figure 6. 8). The size distribution of the 6 September clast, whilst nearly identical to the 1 September, has a more subdued peak, and an extended fine tail. The 17 September clast has a near-normal distribution, a skewness of zero, which is very common in growth driven size distributions. It has a reduced fine tail when compared to the rest of the Holuhraun samples; it also contains a smaller modal peak. The 8 October clast has a negative skew similar to the 1 and 6 September, although not as marked. It has a unimodal size distribution; however, this drops off abruptly in the large vesicle sizes relative to the other samples.

Despite the interior textural heterogeneity, the whole clasts size distributions display a similar broadly unimodal distribution with a slight negative skew and fine tails, with some subtle variations on that theme. Notably, the whole clast modal peaks are larger and are consistently offset from the rinds to a larger bubble size, approximately by a factor of 3–4. Whilst the whole clasts display broader ranges in equivalent vesicle diameter and with more exaggerated modal peaks than the rinds, the overall shape of the rinds vs whole clast histograms are very similar (Figure 6. 11). This is likely reflecting the post-fragmentation expansion of a pre-existing melt diversity within which internally homogeneous domains, of contrasting vesicle size and number density distributions, coexist with oversized coalesced bubbles. Post-fragmentation expansion appears to be the dominant process, the influence of continued bubble nucleation appears to be negligible. For the whole clasts' VVD's, the vesicle range accounting for the bulk, i.e., 90 %, of the void space is 0.1–1.4 mm.

Holuhraun

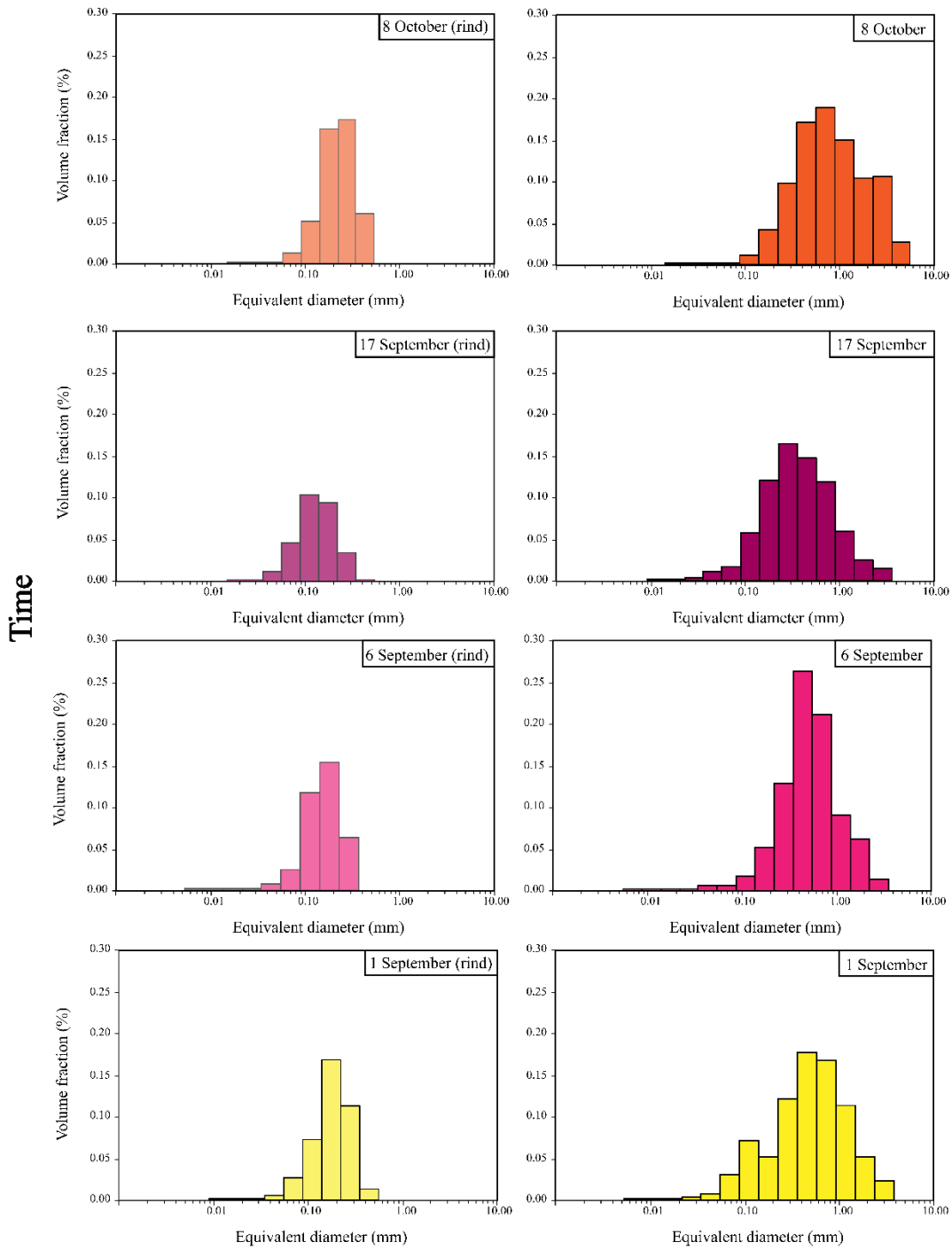


Figure 6. 11: Vesicle volume distributions. Vesicle volume distributions show the volume fraction (%) weighted by their vesicle size bins (mm). The whole clast data is plotted on the right side of the figure with the corresponding rinds on the left. The data is presented from the bottom upwards in a would-be stratigraphic time sequence.

6. 4. 2. 3 CVVD

Cumulative vesicle by volume distribution vs equivalent vesicle diameter plots (Figure 6. 12) produces sigmoidal curves that provide the means for more direct comparisons of bubble populations between samples than VVD.

Rinds: All of the rinds for the Holuhraun clasts have steep-sloped sigmoid curves, where at least 70% of the cumulative vesicle volume is represented by a narrow vesicle distribution with an equivalent diameter range within 0.10–0.20 mm. This trend suggests that the vesicle populations in the rinds are generated by one phase of nucleation and growth. However, there are subtle differences in the rind samples, which are as follows:

The 6 September rind, which represents the melt erupted during a waxing MER phase and peak fountaining intensity at the vent, has the steepest sigmoid curve. This trend is driven by a tight range in the size of the vesicle population, from 0.09–0.17 mm, above the 25 percentile of the cumulative vesicle volume. The smaller vesicle populations, 0.01–0.07 mm, in the 6 September rind follows the same distribution as the other September rinds. The 1 and 17 September rinds display the widest range in vesicle population equivalent diameters/size, from 0.75–0.25 mm, generating two relatively shallower, but different, curves. In the 1 September rind between <0.02–0.04 mm the curve rises slightly above the other samples, from 2–3 % cumulative vesicle volume and between 0.08–0.09 mm its curve becomes steeper. These subtle changes in slope could be generated by two phases of nucleation, but as noted in the VVD data set this can be attributed to the high proportion of rind in this sample. At equivalent size diameters >0.04 mm the 1 September rind has a lower proportion of smaller vesicles than the other September rinds, with the populations above the 86 per centile marginally offset towards relatively larger sizes. The 17 September rind, below 25 percentile the population features a higher proportion of smaller vesicles, between 0.05–0.09 mm, than any of the other Holuhraun rinds, suggesting a different growth time for this population. This sample contains the highest proportion of rind in the analysed Holuhraun samples. The 8 October rind has a tight distribution driven by 90 % of its population, which range from 0.09–0.11 mm in size. It features, by far, a larger vesicle size population creating a curve that is consistently

offset towards larger vesicle equivalent diameters sizes relative to the other rinds (Figure 6. 12). The 95 percentile, >0.11 mm, is the only section of this curve that intersects the other rinds.

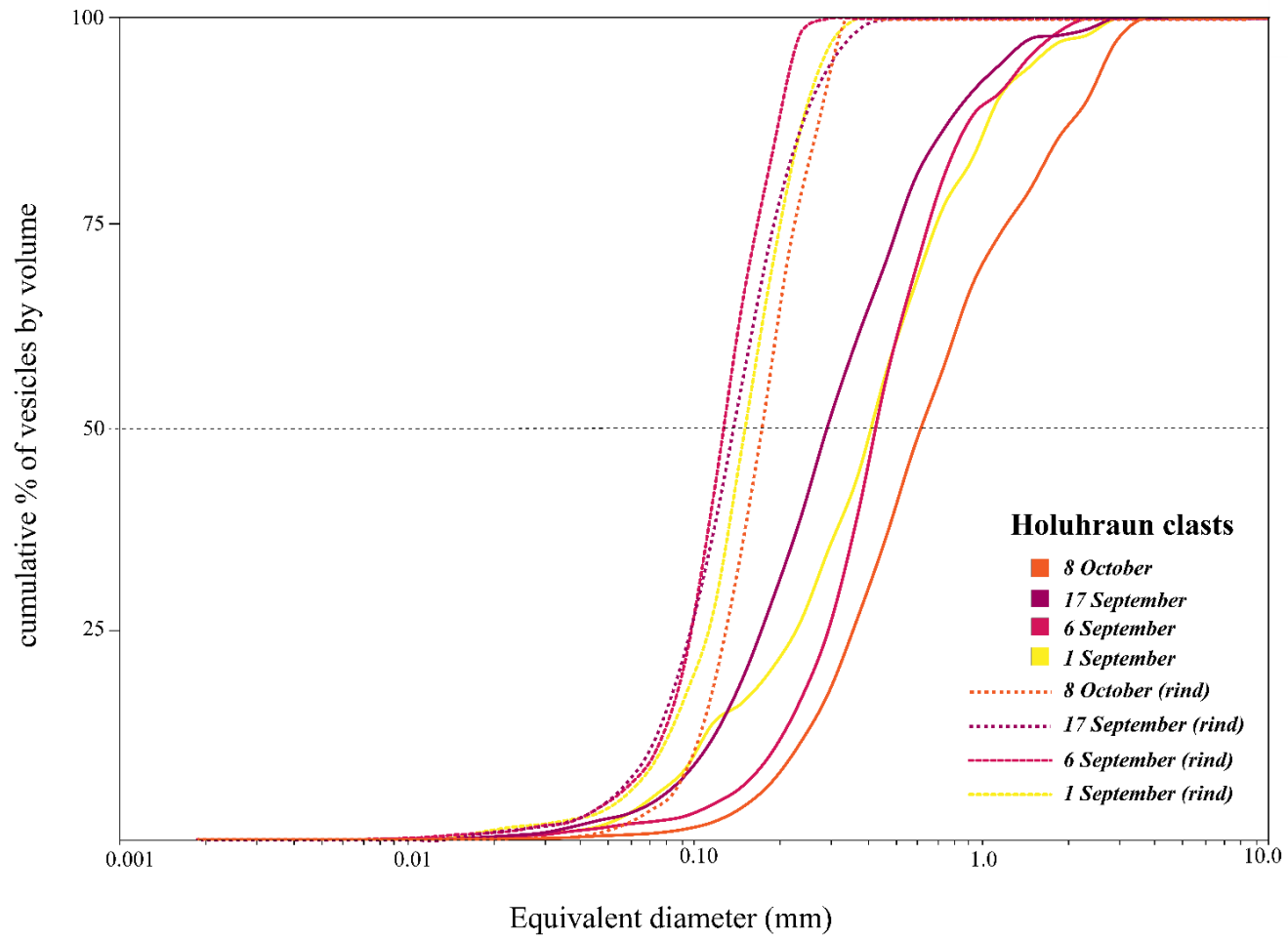


Figure 6. 12: Cumulative vesicle by volume distribution for the Holuhraun 2014–15 CE pyroclasts. Cumulative vesicle by volume distribution vs equivalent vesicle diameter plots produce curves that enable better direct comparisons between samples than VVD histograms. Here the rind data is plotted as dashed lines and the whole clasts as continuous lines of the same colour as the rinds.

Whole clasts: The whole clasts sigmoid curves have a markedly shallower gradient when compared to their rinds. The whole clast curves are offset from the rinds towards larger equivalent diameter vesicle size bins. As previously noted in the VVD section (Figure 6. 12), this relative offset, in the size of the vesicle populations present, between the rinds and the whole clasts is by a factor of 3–4. This is an expected outcome of the contrasting immature vesicle population in the rind and the mature, heterogeneous, interior clast vesicle textures. Where the mature interior domains have undergone further post-fragmentation modification via growth, coalescence and further, although limited, nucleation. The whole clast CVVD sigmoid curves display clear evidence of multiple coalescence events in all analysed clasts, recorded by slight increases in the larger equivalent diameter vesicle populations above the 70 percentile.

Samples which contain a higher percentage of interior rind display either small distinct bulges below the 20 percentile, e.g., 1 September, or a shallower curve in general e.g., 17 September.

6. 4. 3 Textural heterogeneities

The Holuhraun pyroclasts display an exceptional degree of textural diversity present in both a subdued fashion in the outer rinds and much more clearly in the interior of the clasts (Figures 6. 8–6. 10 and 6. 13). Regions within the rinds and interiors of the clasts are composed of several distinct textural domains, which are internally homogeneous. Each domain is delineated by traceable fluidal boundaries (Figure 6. 13), indicating that these different melt domains were hot and easily mingled when they came into contact with each other. Evidence of quenching at the domain boundary contacts or aligned microlite orientations at domain boundaries are absent in all clasts (Figures 6. 8, 6. 10 and 6. 13). The processes creating the forms of textural heterogeneity in the Holuhraun pyroclasts occur at two different stages in the eruption history:

6. 4. 3. 1 (1) Pre-fragmentation: melt diversity as the result of shallow conduit mingling

The first stage occurs in the shallow conduit and is preserved intact only in the texturally immature outer rinds of the Holuhraun clasts, which are more rapidly quenched upon fragmentation and thus representative of the vesicle distribution within the melt in the shallowest conduit. The outer rind is characterised by small round bubbles, which are dispersed heterogeneously in melt containing moderate crystal contents. The outer rind forms the fluidal outer boundary of the clasts, highlighted in yellow in Figure 6. 13, and passes sharply into the interior textures. There are two exceptions: the 1 and 17 September, where this gradient is more gradual. Analysis of the outer rind at higher magnifications identified that distinct regions with different vesicle size distributions, as well as variable melt and crystal proportions, are present on a micro-scale, in all of the Holuhraun rinds (Figures 6. 8–6. 10 and 6. 13). The boundaries between different micro-scale domains are fluidal, and evidence of quenching is absent (Figures 6. 8–6. 10 and 6. 13). As the outer rinds are representative of the vesicle distribution within the melt at fragmentation, this indicates that the melt contained texturally distinct melt domains prior to fragmentation.

This evidence is consistent with the mingling of texturally distinguishable melts, with different shallow conduit histories generated by different bubble nucleation and growth rates in separate melts in the shallow conduit prior to fragmentation. This mingling event(s) creates a heterogeneous primary melt texture when viewing the rind in general as a whole. This primary range of textures is the starting point from which the textures listed below mature during post-fragmentation modification.

6. 4. 3. 2 (2) Post-fragmentation vesicle expansion

Despite the significant post-fragmentation modification of the vesicle population within the interior of the clasts, boundaries of the pre-existing, textural domains are not only preserved but contrasts within the domains are accentuated and enhanced by second stage post-fragmentation vesiculation. This is observed as differing degrees of bubble maturity in the inner rind and interior mature foam as the existing vesicle

populations expanded. This continued vesiculation occurs over seconds during transport of the basaltic pyroclasts within the hot, and thermally insulating, core of fountains, resulting in the interior of the clast experiencing later quenching than the rind allowing further expansion of the interior before the glass transition is reached. The result is a shift towards larger vesicle sizes, as shown in the VND, VVD and CVVD data sets.

A common terminology for interior clast textural end-members was developed. This terminology broadly groups the internally homogeneous vesicle morphologies into three types of domains within the heterogeneous samples, shown in colour coded clast maps (Figure 6. 13). The ranges stated below in bubble wall thickness, and bubble size distributions are specific to the clasts quantitatively examined in this study.

- 1) Mature vesicle texture: occurs only in the interior of clasts. It is characterised by a heterogeneous bubble size population and high degrees of coalescence, with relatively thick vesicle walls. It contains moderate proportions of microlites varying in size, indicating several populations (Figures 6. 13 and 6. 14).
- 2) Ultra-vesicular foam texture: occurs as elongate domains which cross-cut other textural boundaries in the interior of the clast. It is characterised by a relatively uniform population of small bubbles, closely packed with thin walls and very few microlites. A less well-developed, version of this texture exists in the interior rind and in places in the interior of the 17 September clast that is melt-rich and thus displays thicker melt walls and abundant small bubbles. It is not possible to trace this texture into the outer rind (Figure 6. 13).
- 3) Very mature, melt- and crystal-rich texture: occurs only in the interior of the clast. It is bubble-poor with thick bubble walls and very mature, well-developed, rounded vesicles. In the ÁH17092014 clast, this texture contains a higher concentration of mature euhedral and immature swallow-tailed lath microlites ($< 100 \mu\text{m}$) (Figures 6. 13–6. 15).

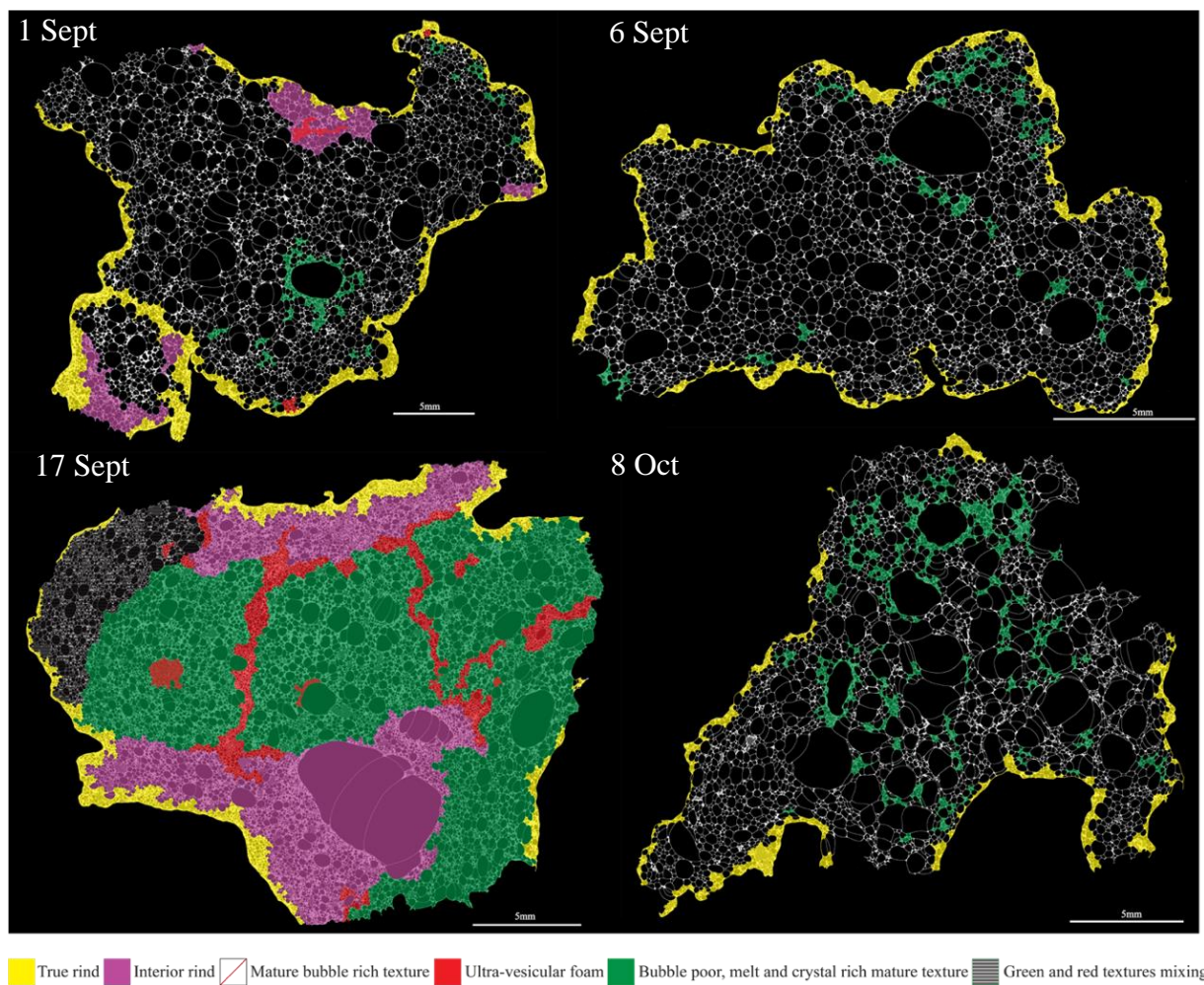


Figure 6. 13: Textural domain maps of Holuhraun pyroclasts. Maps corresponding to textural descriptions of both the semi-symmetrical radial thermal gradients within the clast that create: (A) The outer rind shown in yellow, (B) interior rind shown in pink and (C) Mature inner foam, which can be sub-divided into three textures: (1) Mature melt (no colour) (2) Ultrafoam shown in orange and (3) Very mature melt, bubble poor and crystal-rich shown in green.

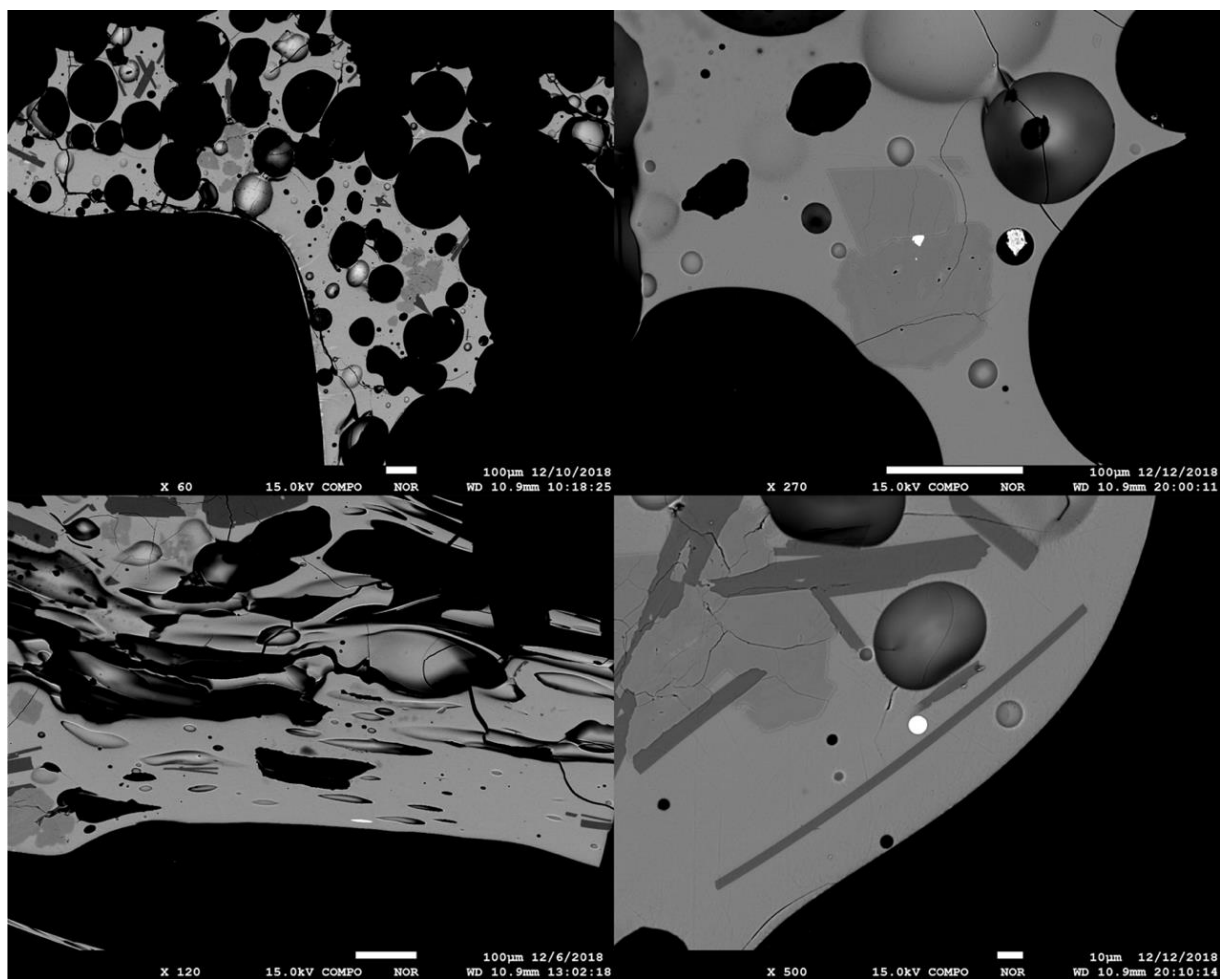


Figure 6. 14: EMPA BSE of early September lapilli and Pele's hairs from Holuhraun 2014–15 CE. EMPA BSE images of early September lapilli or Pele's hairs. Displaying the microlite poor nature of the glass erupted in the first waxing phase of Holuhraun vent activity. BSE images are greyscale, with epoxy filled vesicles appearing black/dark grey, volcanic glass as light grey and crystal phases (plagioclase, clinopyroxene, olivine) are different shades of grey depending on their chemical composition. Quenched fluid phases (e.g., sulfides) are bright white and rounded. The lighter/brighter grey-white phases, such as sulfide have a higher atomic number.

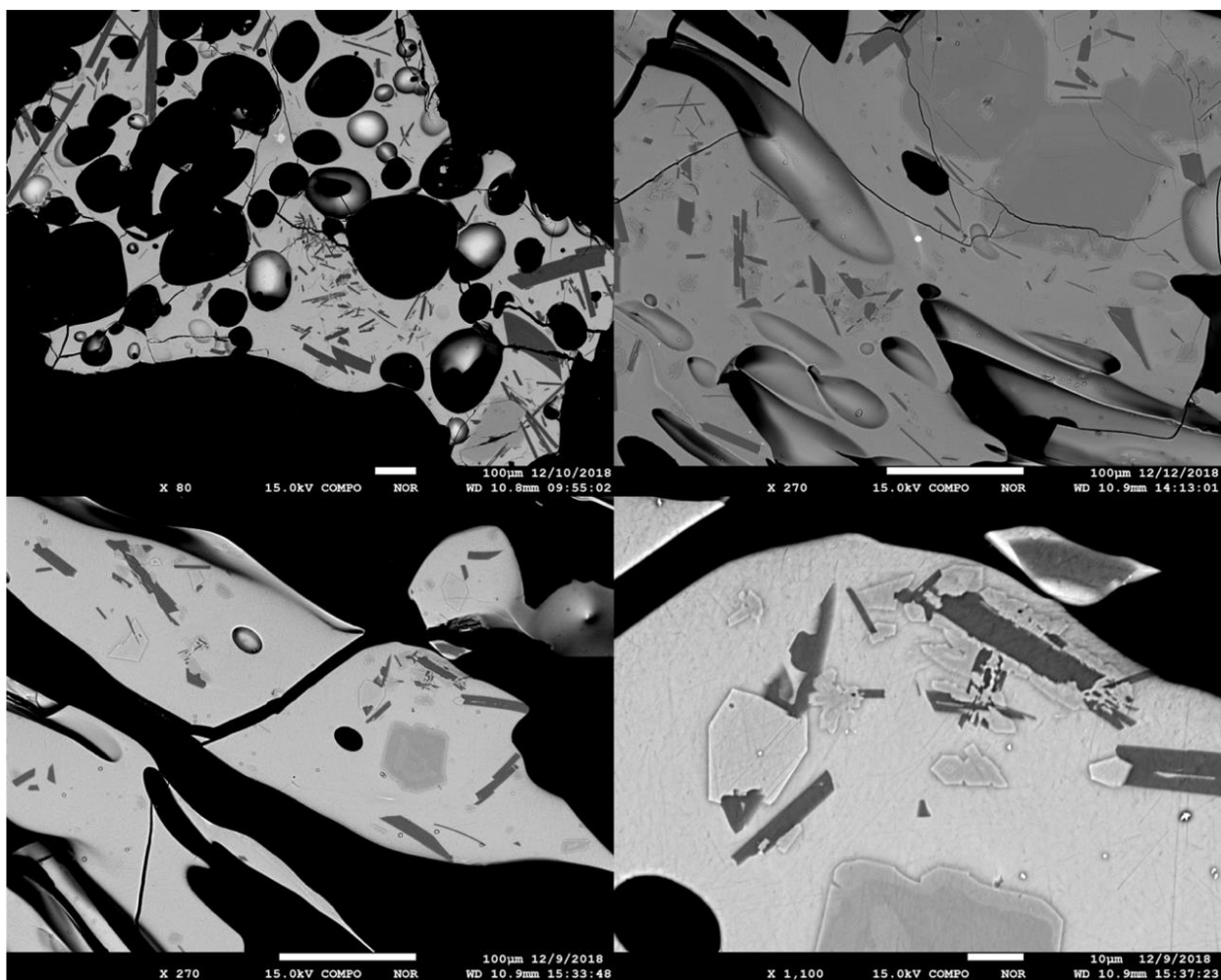


Figure 6. 15: EMPA BSE images of the increase in microlites in mid-September glassy tephra from Holuhraun 2014–15 CE. Mid-September (15–18 September) lapilli glass EMPA BSE images from the low MER to resurgence stop-start event. More mature microlite populations (zoned and euhedral) are visible in these mid-September samples are present, indicating more time for maturation of these microlites. They also occur in a similar glomerocryst morphology of interlocking different crystals, but on a microscale.

6. 4. 4 Glass geochemistry

To ascertain if these different textural end-members were linked to geochemical variations within the melts mingling in the shallow conduit during the Holuhraun eruption, glasses were analysed, by EMP, from the thin sections of 1 and 17 September clasts which contain the largest degree of textural variety. The domains mapped out and texturally analysed in the quantitative and qualitative results sections were targeted for analysis of major element and volatile element concentrations, e.g., sulfur (S) and chlorine (Cl). For each clast, 20 separate points were analysed for the rind, and 10 separate points for the inner rind and each of the interior domains; averages are reported in Table 6. 3 (see supplementary material, appendix B: Holuhraun EMPA bubble data, for the full data set). The ultra-vesicular foam (domain 2) is an exception with 7–9 points averaged, as its thin bubble walls resulted in some analysis associated with a high elemental S error and low totals, which were therefore discarded.

Major element and S concentrations in the 1 and 17 September samples indicate that the 17 September melt was slightly more evolved than 1 September, with a consistently elevated S concentration in all rinds and domains. This slight geochemical difference corresponds to an increased microlite content (of approximately 7 %) in the 17 September sample when compared to the 1 September, elevating the matrix glass S content and producing slightly more evolved compositions. When the S value is corrected to account for the change in microlite content (Thordarson et al., 1996; also see Table 6. 3), the difference is approximately 20–35 ppm. Considering each clast in isolation, the major element geochemistry of the glass is identical; however, slight variations are observed in volatile element compositions between the rind, inner rind, mature and very mature domains. The outer rinds of the 1 and 17 September clasts display the highest S concentrations of all of the analysed regions in the Holuhraun pyroclasts. However, whilst there are slightly lower average S concentrations in the inner rinds and interior domains of the clasts, this difference is statistically indistinguishable compared to the outer rinds. Notably, the ultra-vesicular foam displays the lowest S concentration in both samples. Whilst this is statistically insignificant in the 1 September clast, the same

trend is more apparent in the 17 September clast, where there is markedly lower S concentration in the ultra-vesicular foam, as well as in the embryonic ultra-vesicular foam in the inner rind in this sample (Table 6. 3).

Table 6. 3: Basaltic glass analysis summary for 1 and 17 September clast domains.

Clast	Texture	SiO ₂	TiO ₂	Al ₂ O ₃	FeO	MnO	MgO	CaO	Na ₂ O	K ₂ O	P ₂ O ₅	Totals	S ppm	S ^a ppm
1 Sept	Rind	50.3	1.94	13.62	13.07	0.23	6.27	11.22	2.31	0.22	0.19	99.44	421	/
	Inner Rind	50.0	1.92	13.61	13.17	0.22	6.29	11.24	2.42	0.22	0.21	99.41	407	/
	Mature	49.8	1.95	13.61	13.18	0.22	6.41	11.23	2.47	0.21	0.19	99.40	395	/
	Very Mature	49.9	1.93	13.61	13.26	0.22	6.33	11.28	2.44	0.22	0.20	99.51	407	/
	Ultra-vesicular foam	49.9	1.95	13.64	12.97	0.22	6.30	11.18	2.48	0.22	0.21	99.21	385	/
17 Sept	Rind	49.9	2.07	13.36	13.66	0.23	6.04	10.93	2.34	0.23	0.20	99.12	435	407
	Inner Rind	49.7	2.05	13.32	13.77	0.23	6.05	11.04	2.51	0.23	0.20	99.22	391	365
	Very Mature	49.6	2.05	13.26	13.82	0.23	6.06	11.02	2.51	0.23	0.23	99.16	431	402
	Ultra-vesicular foam	49.5	2.10	13.34	13.69	0.23	6.10	10.98	2.54	0.23	0.21	98.99	355	331
	Mixed	49.7	2.11	13.16	14.06	0.25	6.04	10.95	2.52	0.24	0.22	99.33	435	414

Table 6. 4: EMPA basaltic glass analysis of textural domains, data averages for Holuhraun 2014–15 CE clasts. EMPA basaltic glass analysis of Holuhraun clasts. All data is an average of several analyses, see Supplementary data for the full data set (appendix B: Holuhraun EMPA bubble data). All Major oxide data is reported in weight percent, with totals as the percentage sum of all oxides and volatiles measured. S, measured as parts per million, is the only volatile reported here; see supplementary data for full S data set. S^a = S concentration corrected for the difference in microlite contents between the 1 and 17 September samples, calculated for 17 September only with 1 September S microlite content used as a baseline. Using the formula $S/(1+\text{crystalfraction})$ after Thordarson et al., 1996. The increase in microlite crystal fraction from the 1 to the 17 September clasts is approximately 0.07.

6. 4. 5 Changes in proportions of textures throughout the eruption

The degree of textural diversity present in the clasts varies throughout the eruption and will be considered in depth in the discussion section. Critically, whilst pronounced proportional variations in textural diversity are observed temporally throughout Holuhraun, the proportions of textural domains present within clasts from a specific density sample display minor variations. Additional observations from photomicrographs of clasts not quantitatively analysed can be found in the supplementary material (appendix C: Holuhraun photomicrographs).

The proportion of immature vesicle textures (A and B) are similar in the 6 September and 8 October, despite contrasting vent activity intensity; however, the 1 and 17 September rinds and interior rinds are markedly thicker. In the 1 September clast this is arguably due to two clasts that have fused together, in the bottom left corner, creating fused outer rinds separating the two. Their smaller individual clast sizes would lower the interior thermal gradients, creating higher proportions of the outer and inner rind as the clast in its entirety cooled faster, limiting the development of the interior foam (Figures 6. 8–6. 10 and 6. 13). In the 17 September clast, the thick outer and inner rinds are generated again by the interior foam development being curtailed by the interior of the clast reaching the glass transition faster, but the cause is different: low intensity fountaining limits the time this clast experienced thermal insulation.

In general, the majority of interiors of the analysed and imaged Holuhraun clasts are dominated by the mature vesicle texture (domain type 1; Figure 6. 13; also see supplementary material, appendix C), captured in various stages of maturity passing into the clast interior (Figures 6. 8–6. 10 and 6. 13), which is produced by a common early shallow conduit history for much of the melt, prior to fragmentation. This dominates the early stage of the eruption as seen in the 1 and 6 September clasts at around 95 %, and reappears in the 8 October clast, but is proportionally reduced to 80–85 %. Notably it is completely absent in the 17 September clast, which in general has a markedly different texture to the Holuhraun clasts that pre- and post- date this sample.

Temporally throughout the eruption there are fluctuations in the proportions of very mature and ultra-vesicular foam domains, which evolved from melts with contrasting vesiculation histories (differing nucleation and growth rates) and subsequently mingled with the more dominant melt prior to fragmentation (Figures 6. 8–6. 10 and 6. 13). The very mature vesicle foam (domain type 3) is the most prevalent in the 17 September sample where it makes up 85 % of the clast, although it is present as a subordinate texture in small seams of melt- and crystal-rich magma totaling no more than 5% of the clast, increasing to 15–20 % in the 8 October clast. The ultra-vesicular foam (domain type 2) occurs only in two samples: 1 September, where it occurs as two small pockets totaling <5 % and in the 17 September clast where it is <15 %.

Changes in textural proportions in clast interiors are not coupled by a variations in clast componentry, all samples are achneliths with golden pumice interiors, or the clast phenocryst populations. Phenocryst contents are low in all samples but vary slightly from <2 % in the 1 and 6 September clasts, which are also microlite-poor when compared to the 17 September and 8 October clasts. The texturally distinct 17 September clast does have the higher whole sample modal density and pronounced shift in density distribution. The 17 September clast is also more crystal-rich, as displayed by the very mature texture domains and rinds, with a markedly higher proportion of euhedral mature microlites and swallow-tailed laths as well as a larger proportion of phenocrysts (~5 %) when compared to the earlier September clasts. This higher phenocryst content, although still within the aphyric classification, continues for the rest of the eruption and is seen in the samples collected after 17 September, including 8 October.

6. 4. 6. 1 Initial interpretations of interior domain textures

Mature vesicle texture: Whilst this texture is mature, with respect to the rind, the degree of coalescence and bubble morphologies indicate that there has been no relaxation time, implying that this is a disequilibrium texture. The vesicle population is fairly heterogeneous, displaying evidence of several vesicle coalescence, nucleation and growth events that are well underway and are associated with clear

shearing and deformation of the vesicle morphologies present. This indicates that the vesicles have not had extended time to relax prior to cooling. The microlite population present is not mature, mostly consisting of swallow-tailed laths, but euhedral or zoned microlites are absent. Both the vesicle texture and microlite population support a fast ascent rate, not as rapid as the ultra-vesicular foam, with fast microlite crystallisation associated with volatile loss.

Ultra-vesicular foam texture: This texture consists of incipient-semi well-ordered open-celled, polyhedral, foam (Mangan and Cashman, 1996) comprising of small, rounded, bubbles. It represents a disequilibrium process, whereby rapid ascent rates permit a high degree of volatile supersaturation, generating a late-stage, short-lived, relatively homogeneous, burst_nucleation event (Houghton and Gonnermann, 2008). It occurs both as pockets of well-developed foam in the mature vesicle texture (domain type B), or as bands migrating through the very mature texture (domain type C), creating a mingled pattern, both in a mature and embryonic form (which is relatively melt rich with thicker bubble walls and smaller, rounded, bubbles) and in some places it has mixed completely with the mature vesicle texture (domain type B).

Very mature, melt- and crystal-rich texture: This texture contains strikingly smooth, elliptical, vesicle populations present in this texture, which probably reflect abundant time for bubble relaxation, back to simple shapes, prior to fragmentation. This process requires longer residence time in the shallow conduit to ensure sufficient time elapses to allow complete relaxation. It also has a higher microlite content than domain types A and B, with its rounded vesicles associated with a mature, coarse, euhedral microlite population. It is, therefore, interpreted as a mature equilibrium texture, which didn't ascend as rapidly as domain types A and B.

6. 5. 1 Interpretations and discussion

In basaltic pyroclasts from fountaining events, vesicle number densities and size distributions in the rapidly quenched rinds can reveal information about the nucleation, growth, coalescence of bubbles during the timescales of magma ascent through the shallow conduit with interior textures providing information on the post-

fragmentation modification of the primary vesicle textures (Mangan and Cashman, 1996; Stovall et al., 2011, 2012; Parcheta et al., 2013; Holt et al., 2019). Therefore, we infer that the bubble population present in the Holuhraun pyroclast rinds is the closest approximation of the melt textures immediately prior to fragmentation. The magma rapidly quenched upon fragmentation, creating a limited opportunity for the bubble population to be modified by subsequent growth and coalescence. All of the rinds have a low vesicularity (Table 6. 2), > 30 % lower than the minimum bubble fraction (~70 %) required for fragmentation, suggesting that other processes such as: (1) inertial forces, (2) strain-rate, (3) potential energy (4) stress (Namiki and Manga, 2006, 2008; Gonnermann and Manga, 2007; Rust and Cashman, 2011) induced melt fragmentation in the Holuhraun eruption.

Analysis of the whole Holuhraun clasts at 100x magnification, with additional 250x and 500x nests, has facilitated the acquisition of a comprehensive statistical representation of the textural heterogeneity of the entire clast at all scales. This enables the isolation of both the interior and the rind textural fingerprints, allowing a direct comparison between the VND and VSD present. This detailed fine-scale mapping is key to documenting the relationship between the rind and the interior of individual pyroclasts. Which, in turn, is pivotal in understanding the processes that enabled the development of textural diversity present both up to fragmentation in the rapidly quenched rind and the post-fragmentation textural over-printing in a thermally insulating fountain interior (Cashman and Mangan, 1994; Mangan and Cashman, 1996).

6. 5. 1. 1 Evolution seen in single pyroclasts: VND vs V_G/V_L

To examine the varying influence of competing shallow conduit processes of nucleation, growth, coalescence, and outgassing of bubbles temporally, a plot of VND against vesicle-to-melt ratio (V_G/V_L) (Gardner et al., 1996) can be used. Each process imparts a characteristic textural signature when plotted in VND against V_G/V_L space. (Figure 6. 12). This visualisation is better at identifying trends in the smaller bubble populations than in the CVVD plots, due to smaller bubbles contributing a negligible part of the total volume resulting in a minimal impact to the

CVVD curve and thus being poorly represented. The rind and interior have distinctly different textural signatures and plot in separate VND and V_G/V_L space (Figure 6. 16); thus, the suggested trajectory between them is used to distinguish which post-fragmentation processes have a dominant influence on the interior clasts.

The September rinds plot in very similar VND vs V_G/V_L space, with only subtle differences, the 1 and 17 September rinds have higher N_V^m values than 6 September (Figure 6. 12 and Table 6. 2). These relative shifts between sample rinds could indicate that the 1 and 17 September rinds underwent slightly more vigorous nucleation (Figure 6. 16). The 6 September has a much higher MER than the 1 and 17 September eruptive activity, so it is unlikely that this sample is offset due to a slower ascent rate. There is evidence for this in the presence of small proportions of the ultra-vesicular foam domains in the 1 and 17 September rinds (see Figures 6. 8–6. 10 and 6. 13). The increase in offset towards nucleation in VND vs V_G/V_L space equates to larger proportions ultra-vesicular foam domains in the 17 September samples compared to the 1 September. The 8 October rind is offset by nearly an order of magnitude towards lower N_V^m values suggesting that it experienced longer residence times in the shallow conduit, which would promote coalescence, a process occurring over tens of seconds rather than growth (seconds) (Mangan et al., 1993). The documented decrease in MER (calculated by Bonny et al., 2018) from 20 September, which is associated with waning vent activity from fountaining into vigorous bubble bursting in October, supports this conclusion. This decrease in ascent rate adds in a few crucial seconds of delay in the time this melt package resides in the shallow conduit, causing a reduction in N_V^m . The slight vertical displacement occurs because of a slight increase in V_G/V_L , which could indicate that some growth also contributes to the 8 October rind bubble textures.

Whilst the whole clast and interior values, which reflect a combination of varying proportions of different domains with no common ascent history, hold no primary volcanological significance in V_G/V_L and N_V^m space, they are discussed here for reference when compared to the rinds. All Holuhraun whole clast values are offset, from their associated rind, on a trajectory that indicates growth/growth and nucleation has modified the heterogeneous primary clast textures post-fragmentation from their original rind values. The result of which increases both the V_G/V_L as well

as the N_V^m values (Figure 6. 16) prior to the interior of the clast reaching the glass transition. When the clast interior textures are isolated from the whole clast dataset, the increase of both the V_G/V_L as well as the N_V^m of the clast interiors is less, and the trajectory of the path from rind-interior is steeper, indicating that growth is the more dominant process that has modified these internal textures post-fragmentation from their primary rind textures (Figure 6. 16). The exception is the interior texture of the 17 September clast, which is both offset from the rind to a lesser extent than in the case of the other Holuhraun samples, but notably, this offset is in the direction of growth and coalescence in V_G/V_L and N_V^m space, indicating these processes dominated the post-fragmentation modification of the 17 September clast interior. The lower degree of displacement from the primary rind values supports thin section observations which note the presence of a thick rind and extensive interior rind in the 17 September clast. This textural data suggests that this clast experienced a lower thermal gradient and quenched faster than the early September pyroclasts. This is in agreement with field observations of reduced vent activity from the 15–17 September, associated with a drop to near cessation levels in activity and subsequent resurgence of MER; the clasts erupted after this period would spend less time in a thermally insulating fountain during less intense vent activity phases.

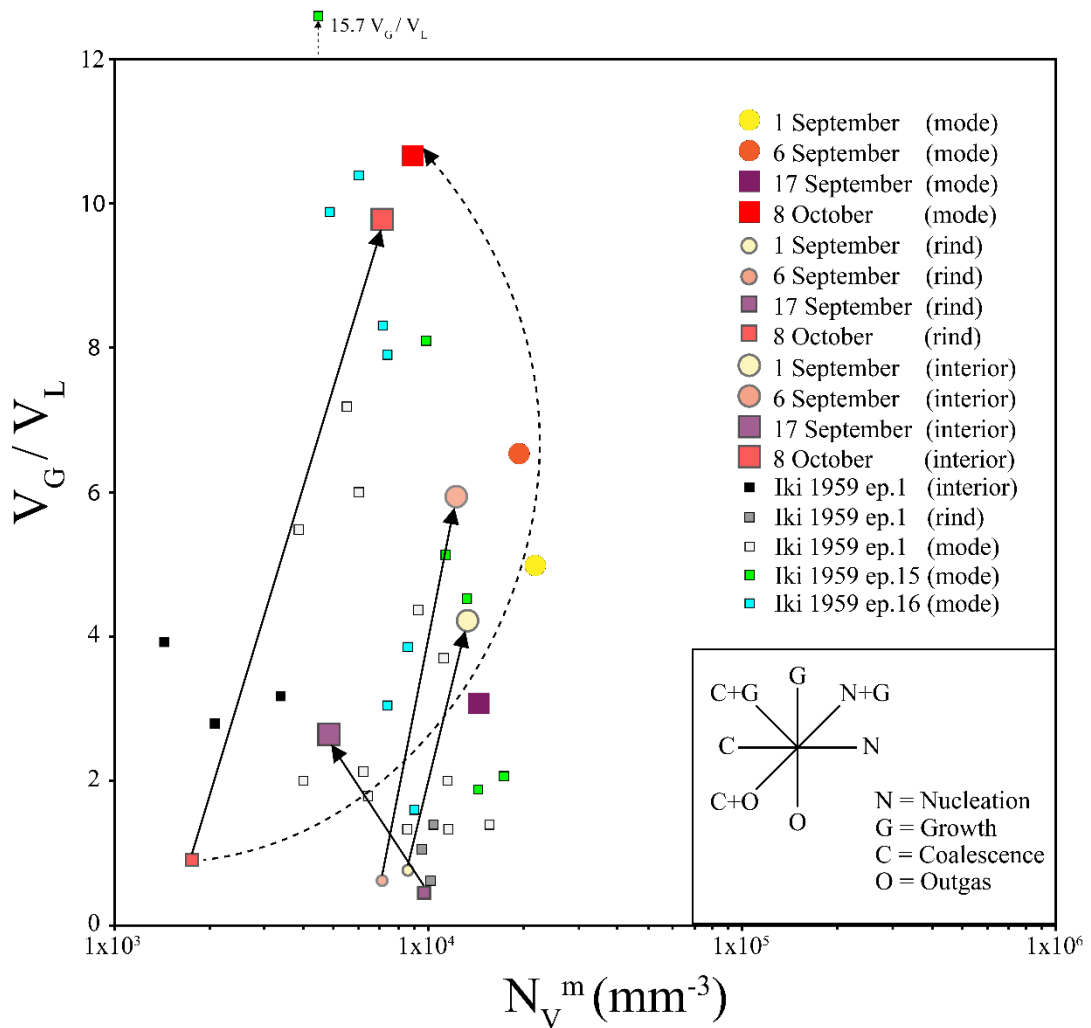


Figure 6. 16: VND against vesicle-to-melt ratio (V_G/V_L) for Holuhraun 2014–15 CE pyroclasts. VND against vesicle-to-melt ratio (V_G/V_L) (Gardner et al., 1996) after Stovall et al. (2011). This plot distinguishes the data sets from rinds (opaque symbols) from their whole clast counterparts (brightly coloured symbols of the same colour). Dark black lines indicate assumed trends from the rinds to the whole clasts. The dashed line for the 8 October is a suggested trend trajectory to account for the clear blooming coalescence event, which is underway captured by this whole clast. The compass inset refers to the different processes governing the trajectory line angle between the clasts' rinds and whole clasts as well as between each other. Kīlauea Iki 1959 CE pyroclast data from Stovall et al. (2011 and 2012) for episodes 1, 15 and 16 are plotted for reference.

A change in vent activity by late September-early October to intermittent fountaining and vigorous boiling with large bubble bursting events did not create a similar shift in interior texture for the 8 October clast as observed in the 17 September clast. Instead, it followed along a more extended trajectory reflecting free growth or growth and nucleation. However, despite the evolution of most of the Holuhraun clasts in V_G/V_L and N_V^m space, very clear micro-textural evidence of coalescence is present in all clasts, which may hint at a curved evolutionary trajectory that cannot be deciphered from these plots alone (Figure 6. 16). The 8 October clasts exhibit an

excellent example of a frozen coalescence event, indicated by very mature and convoluted vesicle textures in thin section (Figures 6. 8–6. 10 and 6. 13). The general trend of interior textures being principally modified by growth or growth and nucleation is interesting as Stovall et al. (2011, 2012) and Parcheta et al. (2013) both observed a decreasing N_v^m from the rind to the core for the clasts suggesting growth and coalescence played a more dominant role in these eruptions at Kīlauea (Figure 6. 16). These observed trends in Hawaiian pyroclasts are much more similar to what is observed in the 17 September clast from Holuhraun.

6. 5. 2 Temporal changes during the eruption.

Some interior domain textures, e.g., A and C are clearly genetically related to the quenched rind. It is also apparent that domain texture B is not clearly identifiable in the outer rind but can be traced into the interior rind in places (Figures 6. 8–6. 10 and 6. 13). Therefore, the rind data set only provides an average of 3 different melt domains which have experienced different ascent rates, as they cannot be separated accurately, although changes in bubble proportions and microlites on a micro-scale can be observed. There are, however, distinct changes in the proportions of the rind textures throughout the eruption that indicate key changes in the ascent rate and, therefore, the onset of nucleation, growth, and coalescence of bubbles. Due to the vesicular nature of the Holuhraun and Hawaiian pyroclast rinds, it is unlikely that they represent a fused outer skin of the clasts due to remelting with hot magmatic gases post-fragmentation. It seems, therefore, appropriate to assume they are proportional to eruptive intensity and ascent rate.

The flow regime as magma ascends through a shallow linear conduit is complicated by the morphology of the subsurface geometry, orientation and variegation of the fissure (Parcheta et al., 2015a, 2015b, 2016). This is because these parameters generate different degrees of interaction, in terms of viscosity and velocity gradients, between the dyke and conduit walls since natural heterogeneity is not reflected in the geometric simplifications made for input parameters in models. This may cause significant delays for melt packages at the outer areas of the dyke and not others, e.g., the centre, where the velocity would be highest, generating textural

heterogeneity in the Holuhraun samples, manifested as the difference between the mature and very mature vesicle textures (domain types A and C). Another possibility to generate the observed difference between the mature and very mature textures is a subsurface convective flow regime in the dyke with heterogeneous and chaotic mingling of fresh upwelling melt and cooler downwelling, degassed, melt blebs with mature textures including microlites (Landi et al., 2008; Francalanci et al., 2012; Jones and Llewellyn, 2020). Degassed, unerupted, magma would be denser and would, therefore, sink and potentially mingle but not completely mix with fresh, buoyant, melts at a later stage during the eruption. This would produce mature melt textures which are bubble poor and with euhedral, zoned, microlites. The EMP geochemical analysis, however, does not support this latter hypothesis with the very mature melt domains displaying statistically insignificant variations in S content, not consistent with degassed downwelling melts despite its very mature microlite population. Therefore, subtle differences in ascent rates could develop the textural variations that are more likely to be associated with velocity profile differences across the width of the dyke, exacerbated by variations in its sub-surface geometry.

However, this hypothesis does not explain the presence of the ultra-vesicular foam on 1 and 17 September or dominance of the very mature texture on 17 September (Figure 6. 13). These are more likely to be controlled by episodic changes in MER throughout the Holuhraun eruption (IES eruption team field reports; Bonny et al., 2018).

Ultra-vesicular foam texture (domain type B) is an enhanced relic of a primary texture melt package that has undergone rapid ascent, driven to volatile supersaturation, triggering a homogeneous burst of nucleation and resulting in more efficient degassing (a lower S content of the glass in this domain). In the Holuhraun eruption, the ultra-vesicular foam textures occur mainly in the samples from 17 September, which represents the eruptive products immediately following the lull in magma discharge on 15 September (Bonny et al., 2018) and reactivation of activity in the following 2 days. The bulk density of this sample is higher than any of the other tephra fall products from Holuhraun, and it is more crystal and microlite rich. Possibly the arrival and injection of this foam-forming magma was the trigger for the resumption of fountaining. Small pockets of ultra-vesicular foam are also present to

a very minor extent in the 1 September clast, this is possibly due to a similar resurgence of activity event as a minor eruption, lasting 4 hours, occurred at Holuhraun along these craters on 29 September before reactivation on 31 September with sustained activity for the next 6 months. This repose time and reactivation of the fissure, by a fresh pulse of melt into the system, could explain the glimpse of this texture on 1 September, during the initial stop-start phase of the eruption, before its reoccurrence on 17 September, following a waning and resurgence in MER. In both cases, the ultra-vesicular foam texture occurs as small pockets, bands or veins that generally mingle with other more mature melt domains whilst in a hot fluidal environment, in some places in the 17 September samples, this process is more dynamic and full mixing occurs (Figure 6. 13). It, therefore, follows that the resurgence or reactivation of activity is associated with a small pulse of hot fresh melt, with faster ascent rates, through the shallow conduit system. This fresh melt is rapidly driven to supersaturation, therefore, developing a starkly contrasting bubble nucleation, growth and coalescence signature compared to the slower ascending, more mature surrounding melt through which it veined or fingered prior to the foam developing. Due to the stiffness of mature vesicular foams and the fluidal boundary evidence suggesting easy mingling of the different domain types, the melts from which the different domains vesiculate must mingle prior to vesiculation of the foam (Figure 6. 17 and 6. 18).

The very mature melt- and crystal-rich texture (domain type C) increases throughout the eruption from the 1 and 6 September to the 8 October following a general steady decrease in MER. The exception to this pattern of steadily declining MER is the near-stop and resurgence event that erupted the 17 September pyroclasts, in which very mature, melt- and crystal-rich texture (domain type C) is the most dominant. The clasts erupted on 17 September are very dense compared to the other pyroclasts (Figure 6. 7 and Table 6. 1); they have a lower vesicularity and in thin section are rich in microlites and phenocrysts. As the mass-discharge rate drops exponentially from 9–15 September (Bonny et al., 2018), it follows that the shallow conduit system is dominated by melts that experience slower ascent rates or stagnation, which consequently have time to mature in terms of bubble relaxation but also to crystallise well-developed microlites, and the amount of fresh and rapidly rising melt is reduced. Whilst the eruption reached near shut-down from 15–16 September, the

maturing, slower ascending, melt in the shallow conduit could create a denser, mature crystal and melt rich plug-like region in the shallowest conduit. A sudden resurgence of vent activity and a waxing MER episode followed this 2-day near shut down period, with a fresh pulse of magma with a higher ascent rate mingling with this existing very mature, melt- and crystal-rich, texture and forming veins or bands of incipient ultra-vesicular foam when it subsequently vesiculated. Contrasting textures in the erupted pyroclasts on the 17 September 2014 record these two competing processes.

Fissure eruptions are episodic in nature, often exhibiting reactivation of vents after quiescence, or fluctuating levels in explosive intensities, therefore it is not surprising that the presence of ultra-vesicular foam textures has been noted by other studies on Icelandic and Hawaiian fissure eruption products. Notably, no hypothesis for the generation of these textures has yet been suggested but all occurrences are during fissure eruptions which display episodic fluctuations in MER with waning and waxing pulses. Parcheta et al. (2013) note very vesicular foams in the eruptive products from episode 9 of Mauna Ulu 1969 CE following a pulse of new magma into the east rift zone (Swanson et al., 1979). Stovall et al., 2012 note the presence of mingled more-vesicular textural domains creating heterogeneous clasts in episodes 15 and 17 of the Kīlauea Iki 1959 CE eruption, although these episodes were only hours apart. Stovall et al., 2012 also carried out major element geochemical analysis of these more vesicular textures, which are identical but volatile contents were not analysed. Moreland et al. 2019 note lineations of a very vesicular texture, running through some of the Eldgjá 936 CE samples. Whilst limited historical documentation exists for this eruption, detailed mapping of its tephra units (Larsen, 2000; Sigurðardóttir et al., 2015; Moreland et al., 2019) indicate sequentially explosive phases as activity propagated to the NE from the Katla central volcano, Iceland. This migration of activity to a new fissure would create significant lag-periods followed by MER resurgence. This study suggests that the previous studies which observed and documented comparable ultra-foam textures to those identified in the Holuhraun pyroclasts, are generated by similar processes despite the differences in tectonic environment and magmatic plumbing system. Moreland et al. (2019) also suggest that the ultrafoam domains act as a weakness which would fracture more easily than other areas which are less vesicular with thicker walls, dictating to some extent the

size of the lapilli clasts after fragmentation. Whilst this is plausible for the Eldgjá pyroclasts, in the Holuhraun eruption the ultra-vesicular foam probably only exists in an embryonic form prior and thus would not be extensive enough to facilitate this process.

A plot of the MER for the Holuhraun samples shown against the vesicularity data can be found in the supplementary material for this chapter (appendix C) for reference. It is not included here, as the Holuhraun eruptive activity, like many other fissure eruptions, is not a point source. It is therefore not appropriate to compare the vesicularity and MER of these events with point source eruptions such as the Etna summit events.

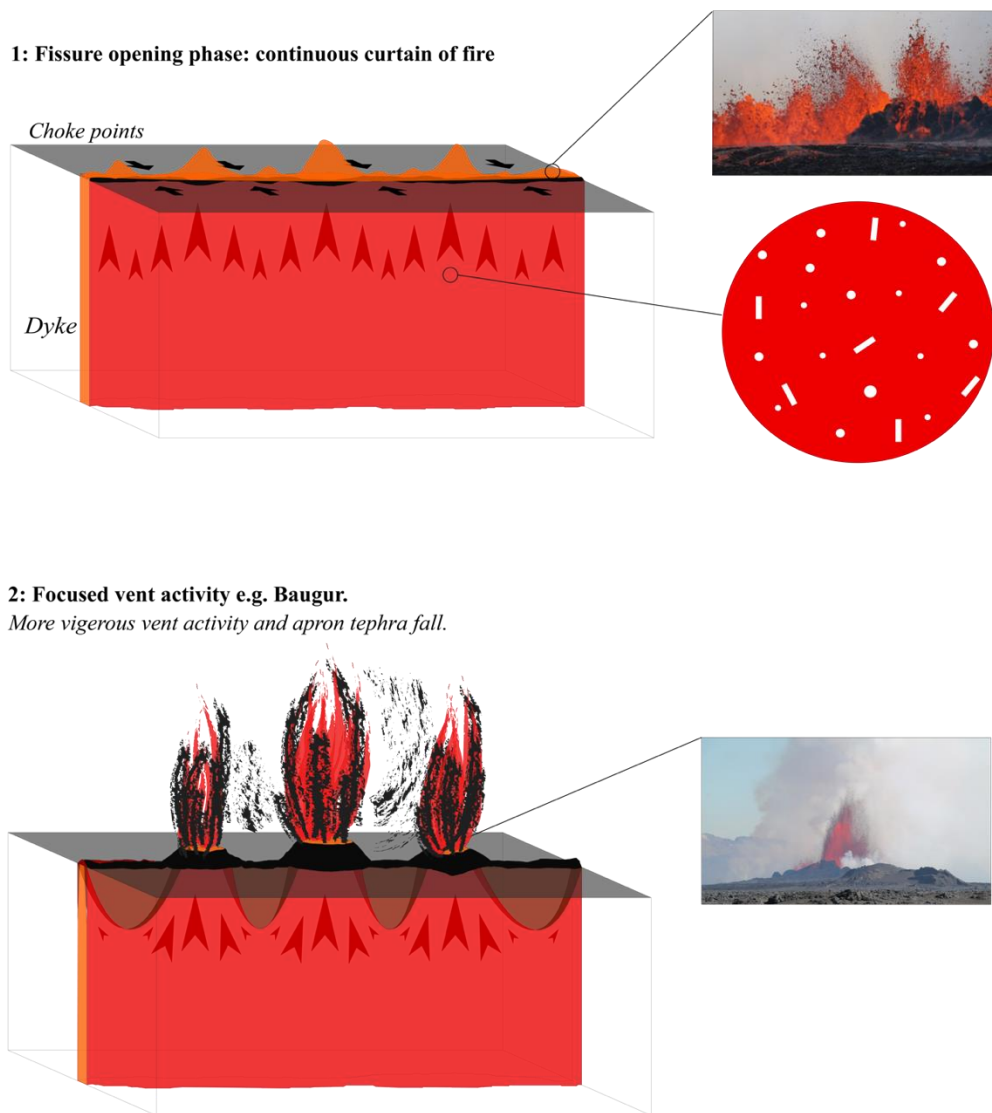
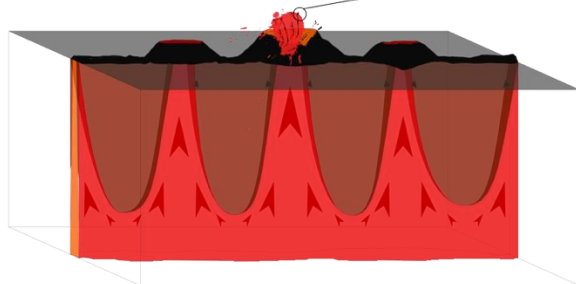


Figure 6. 17: (part A) Conceptual model of the evolution of Holuhraun 2014–15 CE’s shallow conduit system. A conceptual model for the evolution of the shallow conduit system during the Holuhraun eruption. Images of examples of vent activity for the Holuhraun eruption are provided as insets. Simplified schematic diagrams of the Holuhraun dyke and vent activity are displayed on the left, alongside zoomed-in examples of the magma at depth in accompanying circles. The magma is initially all red with a small population of rounded bubbles and phenocrysts. Stage 1 of activity) A long curtain of lava fountaining across the entire newly opened eruptive fissure. Stage 2) Discrete vents develop due to discrepancies in flow rate and conduit geometry, resulting in increased fountaining heights.

3a) Decreasing supply



3b) Pulse of new melt mingles with more mature textures

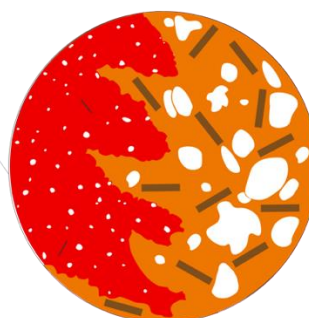
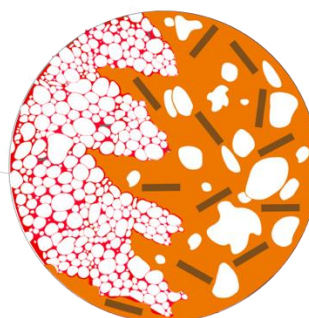
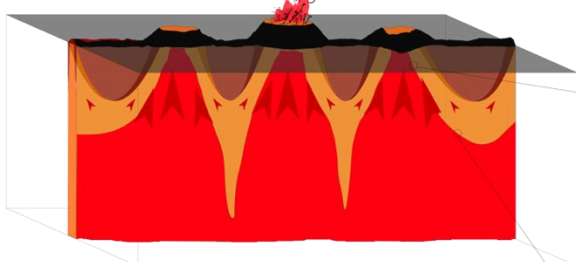


Figure 6. 18: (part B) Conceptual model of the evolution of Holuhraun 2014–15 CE's shallow conduit system. Stage 3a) The magma supply decreases and the eruptive activity changes accordingly to changes in bubble bursting and development of a lava pond whose level eventually drops completely. Stage 3b) The eruptive activity experiences a pulse of resurgence with an increase in fountain height due to a pulse of new melt. This is shown in the inset magma sketches with an orange melt with a mature vesicle population which is also crystal-rich rising slower through the shallow conduit with a pulse of fresh melt (red with a small vesicle population) with a higher ascent rate that mingles with the mature melt. As this package rises, the fresh melt batch vesiculates homogeneously, creating a stiff ultra-vesicular foam that forms bands within the mature melt.

The textural diversity present in the Holuhraun samples suggests that these pyroclasts are recording the existence of a gradational scale of the maturity of the melts, which develops due to subtle relative differences in ascent rates (Figures 6. 17

and 6. 18). These slower moving mature melts may then have subsequently mingled with a pulse of hot, fresh, faster-ascending before erupting. The proportion of these textures changes throughout the eruption, mirroring changes in the dominant processes in the shallow conduit at that period in the eruption; which, in turn, respond to episodic changes in MER. These processes impart distinct textural fingerprints on the pyroclasts themselves, including the presence or absence of an ultra-vesicular foam or a dominance of very mature melts. The distinct textural fingerprint of increasing eruptive intensity, is signified by the presence of an ultra-vesicular foam (Figure 6. 12), which could be used for other eruptions to identify if episodic changes in MER occurred during the event. This could be applied to poorly documented historical events or used to identify episodic intensity peaks following quiescence of activity in larger events such as FL or FB eruptions whose vent activity is less well understood due to limited historical FL data sets.

6. 6 Conclusions

The 2014–2015 CE 6-month long FL eruption at Holuhraun provided the first opportunity to document a low intensity and magnitude end-member FL eruption. Weakly explosive tephra fall producing activity was limited to the first 3 months of the eruption, and is predominantly confined to the first 4 weeks, with wider spread sporadic tephra fall occurring until mid-November.

Pyroclasts from key eruptive tephra fall phases, associated with distinct changes in the style of vent activity, preserve variations in shallow conduit processes which imparted heterogeneous VND, VSD and microlite contents on the primary melt prior to fragmentation in rapidly quenched clast rinds. Each type of domain has experienced differing ascent rates influencing bubble nucleation, growth and coalescence rates and imparting a distinct textural fingerprint. Internal, radial, cooling gradients within the pyroclasts in the fountains allowed the enhancement of primary melt heterogeneity of the Holuhraun melt seen in contrasting domain textures. The pre-existing heterogeneous melt and vesicle population forming distinct domains has been modified predominantly by post-fragmentation expansion. This adds to existing datasets which document the pervasiveness of post-fragmentation vesiculation in low-viscosity fountaining eruptions (Mangan and

Cashman, 1996; Stovall et al., 2011, 2012; Parcheta et al., 2013; Holt et al., 2019). Fluidal domain boundaries coupled with clear evidence of mingling, and in one case full mixing, of these different domains confirms that the mingling events that dictate the proportions of contrasting primary melts occurred prior to fragmentation, when all melts were hot and before vesiculation was advanced.

An increase in the proportion of more mature textural domains shows a broad correlation with a general decrease in MER throughout the eruption. During episodic changes in MER during the Holuhraun eruption, which occurred as stop-start episodes re-initiations or lulls in vent activity followed by a resurgence, an ultra-vesicular foam texture is present. Textural and geochemical data indicates that ultra-vesicular foams in this eruption are generated by melts associated with rapid ascent rates that are rapidly driven to volatile supersaturation and thus are more degassed (Table 6. 3). The presence of something resembling these ultra-vesicular foams has been identified in at least four other fissure eruptions in Iceland and Hawaii, all occurring during events with episodic shifts in MER. Identification and geochemical analysis of these textures in pre-historic or poorly recorded historic fissure eruptions, of all sizes, can help identify increasing MER after periods of activity quiescence.

Although the rinds from the heterogeneous clasts represent a mixture of shallow conduit histories their VSD and VND are similar to values from pyroclasts erupted during medium-high intensity phases at Kīlauea Iki 1959 CE and Mauna Ulu 1969 CE (Stovall et al., 2011, 2012; Parcheta et al., 2013).

6. 7 References

- Ágústsdóttir, T., Woods, J., Greenfield, T., Green, R. G., White, R. S., Winder, T., Brandsdóttir, B., Steinthórsson, S., and Soosalu, H. (2016). Strike-slip faulting during the 2014 Bárðarbunga- Holuhraun dike intrusion, central Iceland *Geophysical Research Letters*. 43. pp. 1495–1503.
- Bali, E., Hartley, M. E., Halldórsson, S. A., Gudfinnsson, G. H., and Jakobsson, S. (2018). Melt inclusion constraints on volatile systematics and degassing history of the 2014–2015 Holuhraun eruption, Iceland. *Contributions to Mineralogy and Petrology*. 173. (2), doi:10.1007/s00410-017-1434-1
- Bonny, E., Thordarson, T., Wright, R., Höskuldsson, A., and Jónsdóttir, I. (2018). The Volume of Lava Erupted During the 2014 to 2015 Eruption at Holuhraun, Iceland: A Comparison Between Satellite- and Ground-Based Measurements. *Journal of Geophysical Research: Solid Earth*. 123. (7), pp. 5412–5426.

doi:10.1029/2017JB015008

- Cashman, K. V. and Mangan, M. T. "Chapter 11b. Physical aspects of magmatic degassing II. Constraints on vesiculation processes from textural studies of eruptive products". In: *Volatiles in Magmas*, edited by Michael R. Carroll and John R. Holloway, Berlin, Boston: De Gruyter, 2018, pp. 447-478. doi:10.1515/9781501509674-018
- Costantini, L., Houghton, B. F., and Bonadonna, C. (2010). Constraints on eruption dynamics of basaltic explosive activity derived from chemical and microtextural study: The example of the Fontana Lapilli Plinian eruption, Nicaragua. *Journal of Volcanology and Geothermal Research*. 189. (3–4), pp. 207–224. doi:10.1016/j.jvolgeores.2009.11.008
- Eibl, E. P. S., Bean, C. J., Jónsdóttir, I., Höskuldsson, A., Thordarson, T., Coppola, D., Witt, T., and Walter, T. R. (2017). Multiple coincident eruptive seismic tremor sources during the 2014–2015 eruption at Holuhraun, Iceland. *Journal of Geophysical Research: Solid Earth*. 122. (4), pp. 2972–2987. doi:10.1002/2016JB013892
- Francalanci, L., Avanzinelli, R., Nardini, I., Tiepolo, M., Davidson, J. P., and Vannucci, R. (2012). Crystal recycling in the steady-state system of the active Stromboli volcano: A 2.5-ka story inferred from in situ Sr-isotope and trace element data. *Contributions to Mineralogy and Petrology*. 163. (1), pp. 109–131. doi:10.1007/s00410-011-0661-0
- Gardner, J. E., Thomas, R. M. E., Jaupart, C., and Tait, S. (1996). Fragmentation of magma during Plinian volcanic eruptions. *Bulletin of Volcanology*. 58. (2–3), pp. 144–162. doi:10.1007/s004450050132
- Gíslason, S. R., Stefánsdóttir, G., Pfeffer, M. A., Barsotti, S., Jóhannsson, T., Galeczka, I., Bali, E., Sigmarsson, O., Stefánsson, A., Keller, N. S., Sigurdsson, Bergsson, B., Galle, B., Jacobo, V. C., Arellano, S., Aiuppa, A., Jónasdóttir, E. B., Eiríksdóttir, E. S., Jakobsson, S., G.H. Guðfinnsson, G. H., Halldórsson, S. A., Gunnarsson, H., Haddadi, B., Jónsdóttir, I., Thordarson, T., Riishuus, M., Högnadóttir, T., Dürig, T., Pedersen, G. B. M., Höskuldsson, Á. and Gudmundsson, M. T. (2015). Environmental pressure from the 2014-15 eruption of Baröarbunga volcano, Iceland. *Geochemical Perspectives Letters*. 1. (1), pp. 84–93. doi:10.7185/geochemlet.1509
- Gonnermann, H.M., and Manga, M. (2003). Explosive volcanism may not be an inevitable consequence of magma fragmentation. *Nature*. 426, 432–435. doi:10.1038/nature02159
- Gonnermann, H. M., and Manga, M. (2007). The fluid mechanics inside a volcano. *Annual Review of Fluid Mechanics*. 39. pp. 321–356. doi:10.1146/annurev.fluid.39.050905.110207
- Gudmundsson, A. (2000) Dynamics of volcanic systems in Iceland: example of tectonism and volcanism at juxtaposed hot spot and mid-ocean ridge systems. *Ann. Rev. Earth Planet. Sci.*, 28, pp. 107-140
- Halldórsson, S. A., Bali, E., Hartley, M. E., Neave, D. A., Peate, D. W., Guðfinnsson, G. H., Bindeman, I., Whitehouse, M. J., Riishuus, M. S., Pedersen, G. B. M., Jakobsson, S., Askew, R., Gallagher, C. R., Guðmundsdóttir, E. R., Gudnason, J., Moreland, W. M., Óskarsson, B. V., Nikkola, P., Reynolds, H. I., Schmidt, J. and Thordarson, T. (2018). Petrology and geochemistry of the 2014–2015 Holuhraun eruption, central Iceland: compositional and mineralogical characteristics, temporal variability and magma storage. *Contributions to Mineralogy and Petrology*. 173. (8), pp. 1–25.

doi:10.1007/s00410-018-1487-9

- Hartley, M. E., and Thordarson, T. (2013). The 1874–1876 volcano-tectonic episode at Askja, North Iceland: Lateral flow revisited. *Geochemistry, Geophysics, Geosystems*. 14. (7), pp. 2286–2309. doi:10.1002/ggge.20151
- Hartley, M. E., Bali, E., Maclennan, J., Neave, D. A., and Halldórsson, S. A. (2018). Melt inclusion constraints on petrogenesis of the 2014–2015 Holuhraun eruption, Iceland. *Contributions to Mineralogy and Petrology*. 173. (2), pp. 1–23. doi:10.1007/s00410-017-1435-0
- Heliker, C., and Mattox, T. N. (2003). The first two decades of the Pu’u ‘Ō‘ō-Kūpaianaha eruption: Chronology and selected bibliography. *US Geological Survey Professional Paper*. 1676. pp. 1–20.
- Heliker, C., Swanson, D. A., Takahashi, T. J., Norton, G. A., Survey, U. S. G., and Paper, P. (2003). The Pu ‘u ‘Ö ‘ö-Kūpaianaha Eruption of Kīlauea Volcano , Hawai ‘i : The First 20 Years. *US Geological Survey Professional Paper*. 1676.
- Hjartardóttir, Á. R. (2008). Unpublished PhD thesis. The fissure swarm of the Askja central volcano. The University of Iceland.
- Hjartardóttir, Á. R., Einarsson, P., and Sigurdsson, H. (2009). The fissure swarm of the Askja volcanic system along the divergent plate boundary of N Iceland. *Bulletin of Volcanology*. 71. (9), pp. 961–975. doi:10.1007/s00445-009-0282-x
- Hjartardóttir, Á. R., and Einarsson, P. (2012). The Kverkfjöll fissure swarm and the eastern boundary of the Northern Volcanic Rift Zone, Iceland. *Bulletin of Volcanology*. 74. (1), pp. 143–162. doi:10.1007/s00445-011-0496-6
- Hjartardóttir, Á. R., Einarsson, P., Bramham, E., and Wright, T. J. (2012). The Krafla fissure swarm, Iceland, and its formation by rifting events. *Bulletin of Volcanology*. 74. (9), pp. 2139–2153. doi:10.1007/s00445-012-0659-0
- Hjartardóttir, Á. R., Einarsson, P., Gudmundsson, M. T., and Högnadóttir, T. (2016). Fracture movements and graben subsidence during the 2014 Bárðarbunga dike intrusion in Iceland. *Journal of Volcanology and Geothermal Research*. 310. pp. 242–252. doi:10.1016/j.jvolgeores.2015.12.002
- Holt, S. J., Carey, R. J., Houghton, B. F., Orr, T., McPhie, J., and Feig, S. (2019). Eruption and fountaining dynamics of selected 1985–1986 high fountaining episodes at Kīlauea volcano, Hawai‘i, from quantitative vesicle microtexture analysis. *Journal of Volcanology and Geothermal Research*. 369. pp. 21–34. doi:10.1016/j.jvolgeores.2018.11.011
- Houghton, B. F. and Wilson, C. J. N. (1989). A vesicularity index for pyroclastic deposits. *Bulletin of Volcanology*. 51. (6), pp. 451–462. doi:10.1007/BF01078811
- Houghton, B. F., and Gonnermann, H. M. (2008). Basaltic explosive volcanism: Constraints from deposits and models. *Chemie der Erde*. 68. (2), pp. 117–140. doi:10.1016/j.chemer.2008.04.002
- Houghton, B. F., Taddeucci, J., Andronico, D., Gonnermann, H. M., Pistolesi, M., Patrick, M. R., Orr, T. R., Swanson, D. A., Edmonds, M., Gaudin, D., Carey, R. J., and Scarlato, P. (2016). Stronger or longer: Discriminating between Hawaiian and Strombolian eruption styles. *Geology*. 44. (2), pp. 163–166. doi:10.1130/G37423.1
- Houghton, B. F., Tisdale, C. M., Llewellyn, E. W., Taddeucci, J., Orr, T. R., Walker, B. H. and Patrick, M. R. (2020). The Birth of a Hawaiian Fissure Eruption. *Journal of Geophysical Research: Solid Earth*, 126. doi:10.1029/2020JB020903
- IES eruption team field reports. Háskóli Íslands, Institute of Earth Sciences and The

- Icelandic Metrological Office (Veðurstofa Íslands). Accessed (17/03/2021) from: <https://en.vedur.is/earthquakes-and-volcanism/articles/nr/3071>
- IMO Holuhraun eruption reports. The Icelandic Metrological Office (Veðurstofa Íslands). Accessed (17/03/2021) from: <https://en.vedur.is/earthquakes-and-volcanism/articles/nr/3071>
- Ilyinskaya, E., Schmidt, A., Mather, T. A., Pope, F. D., Witham, C., Baxter, P., Jóhannsson, T., Pfeffer, M., Barsotti, S., Singh, A., Sanderson, P., Bergsson, B., McCormick Kilbride, B., Donovan, A., Peters, N., Oppenheimer, C., and Edmonds, M. (2017). Understanding the environmental impacts of large fissure eruptions: Aerosol and gas emissions from the 2014–2015 Holuhraun eruption (Iceland). *Earth and Planetary Science Letters*. 472. pp. 309–322. doi:10.1016/j.epsl.2017.05.025
- Jakobsson, S. P. (1979a). Petrology of Recent Basalts of the Eastern Volcanic Zone, Iceland. *Acta Naturalia Islandica*. 26.
- Jakobsson, S.P. (1979b) Outline of the petrology of Iceland. (Ágrip: Um bergfræði Íslands). *Jökull*. 29. pp. 57-73 (English full version) and 96-99 (Icelandic text only).
- Jakobsson, S., and Gudmundsson, M. T. (2008). Subglacial and intraglacial volcanic formations in Iceland. *Jökull*. 58. pp. 179–196.
- Jakobsson, S., Jonasson, K., Sigurðsson, A., (2008) The three igneous rock series in Iceland: a review. *Jökull*. 58. pp.117-138.
- Jóhannesson, H. and Sæmundsson, K. (1998) Geological Map of Iceland, 1:500,000. Bedrock Geology Icelandic Institute of Natural History and Iceland Geodetic Survey, Reykjavík.
- Jóhannesson, H. and Sæmundsson, K. (2009). Geological Map of Iceland. 1:600.000. Tectonics. *Náttúrufræðistofnun Íslands, Reykjavík (1st edition)*
- Jóhannesson, H. (2014) Geological Map of Iceland. 1:600.000. Bedrock. Náttúrufræðistofnun Íslands, Reykjavík.
- Jones, T. J., and Llewellyn, E. W. (2020). Convective tipping point initiates localization of basaltic fissure eruptions. *Earth and Planetary Science Letters*. 1. 116637. doi:10.1016/j.epsl.2020.116637
- Klug, C., and Cashman, K. V. (1994). Vesiculation of May 18, 1980, Mount St. Helens magma. *Geology*. 22. (5), pp. 468–472. doi:10.1130/0091-7613(1994)022<0468:VOMMSH>2.3.CO;2
- Landi, P., Métrich, N., Bertagnini, A., and Rosi, M. (2008). Recycling and “re-hydration” of degassed magma inducing transient dissolution/crystallization events at Stromboli (Italy). *Journal of Volcanology and Geothermal Research*. 174. (4), pp. 325–336. doi:10.1016/j.jvolgeores.2008.02.013
- Larsen, G. (2000). Holocene eruptions within the Katla volcanic system, south Iceland: Characteristics and environmental impact. *Jökull*. 49. (49), pp. 1–28.
- Lautze, N. C., and Houghton, B. F. (2008). Single explosions at Stromboli in 2002: Use of clast microtextures to map physical diversity across a fragmentation zone. *Journal of Volcanology and Geothermal Research*. 170. (3–4), pp. 262–268. doi:10.1016/j.jvolgeores.2007.10.011
- Loughlin, S. C., Aspinall, W. P., C, V.-B., Baxter, P. J., Braban, C., M, H., Schmidt, A., Thordarson, T., and Witham, C. S. (2012). Large-Magnitude Fissure Eruptions in Iceland: Source Characterisation. *British Geological Survey OpenFile Report*, pp. 1–136.
- <http://www.bgs.ac.uk/research/volcanoes/LakiEruptionScenarioPlanning.html%0Aapers3://publication/uuid/E5A6AE4C-D7D6-4563-AD7C-4B53F7033815>

- McBirney, A.R., and Murase, T. (1970). Factors governing the formation of pyroclastic rocks. *Bulletin of Volcanology*, 34, 372–384. doi:10.1007/BF02596762
- Mangan, M. T., and Cashman, K. . (1996). The structure of basaltic scoria and reticulite and inferences for vesiculation, foam formation, and fragmentation in lava fountains. *Journal of Volcanology and Geothermal Research*. 73. (1–2), pp. 1–18.
- Mangan, M. T., Cashman, K. V., and Newman, S. (1993). Vesiculation of basaltic magma during eruption. *Geology*. 21. (2), pp. 157–160. doi:10.1130/0091-7613(1993)021<0157:VOBMDE>2.3.CO;2
- Miller, J. (1989). Unpublished PhD thesis. The 10th century eruption of Eldgjá, southern Iceland. Nordic Volcanological Institute, Reykjavík University of Iceland., 8903.
- Moreland W.M, Thordarson T, Houghton B.F. and Larsen G, (2019). Driving mechanisms of subaerial and subglacial explosive episodes during the 10th century Eldgjá fissure eruption, southern Iceland. *Volcanica*.
- Namiki, A., and Manga, M. (2006). Influence of decompression rate on the expansion velocity and expansion style of bubbly fluids. *Journal of Geophysical Research: Solid Earth*. 111. (11), pp. 1–17. doi:10.1029/2005JB004132
- Namiki, A., and Manga, M. (2008). Transition between fragmentation and permeable outgassing of low viscosity magmas. *Journal of Volcanology and Geothermal Research*. 169. (1–2), pp. 48–60. doi:10.1016/j.jvolgeores.2007.07.020
- Orr, T. R., Poland, M. P., Patrick, M. R., Thelen, W. A., Sutton, A.J., Elisa, T., Thornber, C. R., Parcheta, C. and Wooten, K. M. (2015). Kilauea’s 5-9 march 2011 kamoamoā fissure eruption and its relation to 30+ years of activity from Pu’u ’Ō ’ō. In: *Hawaiian Volcanoes: From Source to Surface*. pp. 393–420. Carey, R., Cayol, V., Poland, M and Weis, D. (Editors). doi:10.1002/9781118872079.ch18
- Pálmason, G. and Sæmundsson, K. (1974) Iceland in Relation to the Mid-Atlantic Ridge. *Annual Review of Earth and Planetary Sciences*. 2. (1), pp. 25–50
- Papale, P. (1999). Strain induced magma fragmentation in explosive eruptions. *Nature*. 397, 425–428. Doi:10.1038/17109
- Parcheta, C. E., Houghton, B. F., and Swanson, D. A. (2013). Contrasting patterns of vesiculation in low, intermediate, and high Hawaiian fountains: A case study of the 1969 Mauna Ulu eruption. *Journal of Volcanology and Geothermal Research*. 255. pp. 79–89. doi:10.1016/j.jvolgeores.2013.01.016
- Parcheta, Carolyn E., Fagents, S., Swanson, D. A., Houghton, B. F., and Ericksen, T. (2015a). Hawaiian fissure fountains: Quantifying vent and shallow conduit geometry, episode 1 of the 1969–1974 Mauna Ulu eruption. *Geophysical Monograph Series*. 208. pp. 369–391. doi:10.1002/9781118872079.ch17
- Parcheta, C.E., Nash, J., Mitchell, K.L. and Parness, A. (2015b). Shallow Subsurface Structures of Volcanic Fissures. 2015 *AGU Fall Meeting abstract*.
- Parcheta, Carolyn E., Pavlov, C. A., Wiltsie, N., Carpenter, K. C., Nash, J., Parness, A., and Mitchell, K. L. (2016). A robotic approach to mapping post-eruptive volcanic fissure conduits. *Journal of Volcanology and Geothermal Research*. 320. pp. 19–28. doi:10.1016/j.jvolgeores.2016.03.006
- Pedersen, G. B. M., Höskuldsson, A., Dürig, T., Thordarson, T., Jónsdóttir, I., Riishuus, M. S., Óskarsson, B. V., Dumont, S., Magnusson, E., Gudmundsson, M. T., Sigmundsson, F., Drouin, V. J. P. B., Gallagher, C., Askew, R.,

- Gudnason, J., Moreland, W. M., Nikkola, P., Reynolds, H. I., and Schmith, J. (2017). Lava field evolution and emplacement dynamics of the 2014–2015 basaltic fissure eruption at Holuhraun, Iceland. *Journal of Volcanology and Geothermal Research*. 340. pp. 155–169. doi:10.1016/j.jvolgeores.2017.02.027
- Pfeffer, M. A., Stefánsdóttir, G., Bergsson, B., Barsotti, S., Galle, B., Ilyinskaya, E., Spina, A. La, Sigurðardóttir, G. M., and Jónasdóttir, E. B. (2015). Ground-based measurements of the emission rate and composition of gases from the Holuhraun eruption. *2015 EGU Abstract*. 17, 7373.
- Pfeffer MA, Bergsson B, Barsotti S, Stefánsdóttir G, Galle B, Arellano S, Conde V, Donovan A, Ilyinskaya E, Burton M, Aiuppa A, Whitty RCW, Simmons IC, Arason Þ, Jónasdóttir EB, Keller NS, Yeo RF, Arngrímsson H, Jóhannsson Þ, Butwin MK, Askew RA, Dumont S, Von Löwis S, Ingvarsson Þ, La Spina A, Thomas H, Prata F, Grassa F, Giudice G, Stefánsson A, Marzano F, Montopoli M, Mereu L. (2018). Ground-Based Measurements of the 2014–2015 Holuhraun Volcanic Cloud (Iceland). *Geosciences*. 8. (1), pp. 29. doi:10.3390/geosciences8010029
- Polacci, M., Corsaro, R. A., and Andronico, D. (2006). Coupled textural and compositional characterization of basaltic scoria: Insights into the transition from Strombolian to fire fountain activity at Mount Etna, Italy. *Geology*. 34. (3), pp. 201–204. doi:10.1130/G22318.1
- Porritt, L. A., Russell, J. K., and Quane, S. L. (2012). Pele’s tears and spheres: Examples from Kilauea Iki. *Earth and Planetary Science Letters*. 333–334. pp. 171–180. doi:10.1016/j.epsl.2012.03.031
- Richter, D. H., Eaton, J. P., Murata, K. J., Ault, W. U., and Krivoy, H. L. (1970). Chronological Narrative of the 1959-60 Eruption of Kilauea Volcano, Hawaii. *USGS Professional Paper*, 537-E. doi:10.1016/0198-0254(80)95902-6
- Rust, A. C., and Cashman, K. V. (2011). Permeability controls on expansion and size distributions of pyroclasts. *Journal of Geophysical Research: Solid Earth*. 116. (11), pp. 1–17. doi:10.1029/2011JB008494
- Sæmundsson, K. (1974) Fissure swarms and central volcanoes of the neovolcanic zones of Iceland. *Geological Society America Bulletin*. 85. pp. 495-504
- Sæmundsson, K. (1978) Fissure swarms and central volcanoes of the neovolcanic zones of Iceland. *Geological Journal Special Issue*. 10. pp. 415-432
- Sæmundsson, K. (1979) Outline of the geology of Iceland. *Jökull*, 29, pp. 7-28
- Sable, Julia E., Houghton, B. F., Del Carlo, P., and Coltelli, M. (2006). Changing conditions of magma ascent and fragmentation during the Etna 122 BC basaltic Plinian eruption: Evidence from clast microtextures. *Journal of Volcanology and Geothermal Research*. 158. (3–4), pp. 333–354. doi:10.1016/j.jvolgeores.2006.07.006
- Sable, J. E., Houghton, B. F., Wilson, C. J. N., and Carey, R. J. (2009). Eruption mechanisms during the climax of the Tarawera 1886 basaltic Plinian eruption inferred from microtextural characteristics-of the deposits. *Special Publications of IAVCEI*, 2, pp. 129–154. doi:10.1144/iavcel002.7
- Sahagian, D. L., and Proussevitch, A. A. (1998). 3D particle size distributions from 2D observations: Stereology for natural applications. *Journal of Volcanology and Geothermal Research*. 84. (3–4), pp. 173–196. doi:10.1016/S0377-0273(98)00043-2
- Schmidt, A., Carslaw, K. S., Mann, G. W., Wilson, M., Breider, T. J., Pickering, S. J., and Thordarson, T. (2010). The impact of the 1783-1784 AD Laki eruption on global aerosol formation processes and cloud condensation nuclei.

- Atmospheric Chemistry and Physics*. 10. (13), pp. 6025–6041. doi:10.5194/acp-10-6025-2010
- Schmidt, Anja, Ostro, B., Carslaw, K. S., Wilson, M., Thordarson, T., Mann, G. W., and Simmons, A. J. (2011). Excess mortality in Europe following a future Laki-style icelandic eruption. *Proceedings of the National Academy of Sciences of the United States of America*. 108. (38), pp. 15710–15715. doi:10.1073/pnas.1108569108
- Schmidt, A., Leadbetter, S., Theys, N., Carboni, E., Witham, C. S., Stevenson, J. A., Birch, C. E., Thordarson, T., Turnock, S., Barsotti, S., Delaney, L., Feng, W., Grainger, R. G., Hort, M. C., Höskuldsson, Á., Ialongo, I., Ilyinskaya, E., Jóhannsson, T., Kenny, P., Mather, T. A., Richards, N. A.D. and Shepherd, J. (2015). Satellite detection, long-range transport, and air quality impacts of volcanic sulfur dioxide from the 2014–2015 flood lava eruption at Bárðarbunga (Iceland). *Journal of Geophysical Research: Oceans*. 120. pp. 9739–9757. doi:10.1002/2015JC011107.
- Schneider CA, Rasband WS, Eliceiri KW (2012) NIH Image to ImageJ: 25 years of image analysis. *Nat Methods* 9:671–675. doi: 10.1038/nmeth.2089
- Shea, T., Houghton, B. F., Gurioli, L., Cashman, K. V., Hammer, J. E., and Hobden, B. J. (2010). Textural studies of vesicles in volcanic rocks: An integrated methodology. *Journal of Volcanology and Geothermal Research*. 190. (3–4), pp. 271–289. doi:10.1016/j.jvolgeores.2009.12.003
- Sinton, J., Grönvold, K., and Sæmundsson, K. (2005). Postglacial eruptive history of the Western Volcanic Zone, Iceland. *Geochemistry, Geophysics, Geosystems*. 6. (12). doi:10.1029/2005GC001021
- Sigurðardóttir, S. S., Gudmundsson, M. T., and Hreinsdóttir, S. (2015). Mapping of the Eldgja lava flow on Myrdalssandur with magnetic surveying. *Jökull*. 65. pp. 61–71
- Sigmundsson, F., Hooper, A., Hreinsdóttir, S., Vogfjörð, K. S., Ófeigsson, B. G., Heimisson, E. R., Dumont, S., Parks, M., Spaans, K., Gudmundsson, G. B., Drouin, V., Árnadóttir, T., Jónsdóttir, K., Gudmundsson, M. T., Högnadóttir, T., Fridriksdóttir, H. M., Hensch, M., Einarsson, P., Magnússon, E., Samsonov, S., Brandsdóttir, B., White, R. S., Ágústsdóttir, T., Greenfield, T., Green, R. G., Hjartardóttir, Á. R., Pedersen, R., Bennett, R. A., Geirsson, H., la Femina, P. C., Björnsson, H., Pálsson, F., Sturkell, E., Bean, C. J., Möllhoff, M., Braiden, A. K. and Eibl, E. P. S. (2014). Segmented lateral dyke growth in a rifting event at Bárðarbunga volcanic system, Iceland. *Nature*. 517 (7533). doi:10.1038/nature14111
- Sigmarsson, O., and Halldórsson, S. A. (2015). Delimiting Baroarbunga and Askja volcanic systems with Sr- and Nd-isotope ratios. *Jökull*. 65. pp. 17–28.
- Sparks, R. S. J. (2003). Dynamics of magma degassing. *Geological Society Special Publication*. 213. pp. 5–22. doi:10.1144/GSL.SP.2003.213.01.02
- Stefánsson, A., Stefánsson, G., Keller, N. S., Barsotti, S., Sigurdsson, Á., Thorlákssdóttir, S.B., Pfeffer, M.A., Eiríksdóttir, E.S., Jónasdóttir, E.B., von Löwis, S. and Gíslason, S.R. (2017). Major impact of volcanic gases on the chemical composition of precipitation in Iceland during the 2014–2015 Holuhraun eruption. *Journal of Geophysical Research – Atmosphere*. 122. JD024093. doi:10.1002/2015JD024093
- Stovall, W. K., Houghton, B. F., Gonnermann, H., Fagents, S. A., and Swanson, D. A. (2011). Eruption dynamics of Hawaiian-style fountains: The case study of episode 1 of the Kilauea Iki 1959 eruption. *Bulletin of Volcanology*. 73. (5),

- pp.511–529. doi:10.1007/s00445-010-0426-z
- Stovall, W. K., Houghton, B. F., Hammer, J. E., Fagents, S. A., and Swanson, D. A. (2012). Vesiculation of high fountaining Hawaiian eruptions: Episodes 15 and 16 of 1959 Kīlauea Iki. *Bulletin of Volcanology*. 74. (2), pp. 441–455. doi:10.1007/s00445-011-0531-7
- Swanson, D. A., Duffield, W. A., Jackson, D. B., and Peterson, D. W. (1979). Chronological narrative of the 1969-71 Mauna Ulu eruption of Kilauea Volcano, Hawaii. *U.S. Geological Survey Professional Paper*. 1056, 1056, 55 p.
- Thorarinsson, S., Einarsson, T. and Kjartansson, G. (1959): On the geology and geomorphology of Iceland. *Geografiska Annaler*. 41. pp. 143-153.
- Thorarinsson, S., Sæmundsson, K. (1979) Volcanic activity in historical time. *Jökull*. 29. pp. 29-32
- Thordarson, T. (2003). The 1783 – 1785 AD . Laki-Grímsvötn eruptions I: A critical look at the contemporary chronicles. *Jökull*. 53. pp. 1–10.
- Thordarson, T. (2020). Sulfur output by the 2014–15 flood lava eruption at Holuhraun, N-Iceland. *Goldschmidt 2020 abstract*. <https://doi.org/10.46427/gold2020.2594>
- Thordarson, T. and Self, S. (1993). The Laki (Skaftár Fires) and Grímsvötn eruptions in 1783-1785. *Bulletin of Volcanology*. 55. (4), pp. 233–263. doi:10.1007/BF00624353
- Thordarson, Th., Self, S., Óskarsson, N., and Hulsebosch, T. (1996). Sulfur, chlorine, and fluorine degassing and atmospheric loading by the 1783-1784 AD Laki (Skaftár Fires) eruption in Iceland. *Bulletin of Volcanology*. 58. (2–3), pp. 205–225. doi:10.1007/s004450050136
- Thordarson, T. and Self, S. (2003). Atmospheric and environmental effects of the 1783-1784 Laki eruption: A review and reassessment. *Journal Of Geophysical Research-Atmospheres*. 108. 4011
- Thordarson, T, Larsen, G., Steinthorsson, S., and Self, S. (2003b). The 1783–1785 AD Laki-Grímsvötn eruptions II: appraisal based on contemporary accounts. *Jökull*. 53. pp. 11–47.
- Thordarson, T., Self, S., Miller, D. J., Larsen, G. and Vilmundardottir, E. G. (2003a) Sulphur release from flood lava eruptions of the Veiðivötn, Grímsvötn and Katla volcanic systems, Iceland. In: C Oppenheimer, DM Pyle and J Barclay (eds.) Volcanic Degassing. pp. 103-121. *The Geological Society of London*.
- Thordarson, T., and Larsen, G. (2007). Volcanism in Iceland in historical time: Volcano types, eruption styles and eruptive history. *Journal of Geodynamics*. 43. (1), pp. 118–152. doi:10.1016/j.jog.2006.09.005
- Thordarson, T. and Höskuldsson, Á. (2008). Postglacial volcanism in Iceland. *Jökull*. 58. pp. 197–228.
- Tuffen, H., Dingwell, D.B., and Pinkerton, H. (2003). Repeated fracture and healing of silicic magma generate flow banding and earthquakes? *Geology*. 31, (12), pp. 1089–1092
- Walker, G.P.L. (1963) The Breiddalur central volcano, eastern Iceland. *Quarterly Journal of the Geological Society of London*. 119. pp. 29-63
- Walker, G.P.L. (1964) Geological investigations in eastern Iceland. *Bulletin Volcanologique* 27 (1). p. 351-363
- Walker, G.P.L. (1993) Basaltic-volcano systems. *Geological Society, London, Special Publications*. 76. pp. 3-38
- Webb, S.L., and Dingwell, D.B. (1990a). Non-Newtonian rheology of igneous melts

- at high stresses and strain rates: Experimental results for rhyolite, andesite, basalt, and nephelinite. *Journal of geophysical Research*. 95, 15695–15701
- Webb, S.L., and Dingwell, D.B. (1990b). The onset of non-Newtonian rheology of silicate melts. *Physics and Chemistry of Minerals*. 17. 125–132. doi:10.1007/BF00199663.
- Witt, T., Walter, T. R., Müller, D., Guðmundsson, M. T., and Schöpa, A. (2018). The Relationship Between Lava Fountaining and Vent Morphology for the 2014–2015 Holuhraun Eruption, Iceland, Analyzed by Video Monitoring and Topographic Mapping. *Frontiers in Earth Science*, 6. doi:10.3389/feart.2018.00235
- Wolfe EW, Neal CA, Banks NG, Duggan TJ (1988) Geologic observations and chronology of eruptive events. In: Wolfe EW (ed) The Pu'u 'O'o Eruption of Kilauea Volcano, Hawaii: Episodes 1 Through 20, January 3, 1993, Through June 8, 1984. *USGS Professional Papers*. 1463. pp. 1–97
- Zhang, T. (1999). A criterion for the fragmentation of bubbly magma based on brittle failure theory. *Nature*. 402, pp. 648–650. doi:10.1038/45210

Chapter 7: Shallow conduit processes during the Laki 1783–84 CE eruption

7.1 Introduction

Fountaining eruptions, producing incandescent and sustained jets of pyroclastic material, are evocative of eruptions at Kīlauea, Hawai‘i, but typify activity at many basaltic volcanoes worldwide, regardless of tectonic environment. Eruptions of this nature span a large range in magnitudes as well as smaller ranges in intensities and mass eruption rates.

Low magnitude and low intensity sustained fountaining is the most common style of vent activity during basaltic fissure eruptions and delineates the weakest end-member of explosive events. Based on historical observations and descriptions, the emergent phase during these events commonly comprises of a laterally near-continuous curtain-of-fire along a fissure’s length (100s metres to a few km) reaching metres–tens of metres high (Richter et al., 1970; Witt et al., 2018; Houghton et al., 2020), producing near-vent coarse grained pyroclastic fall deposits. If the eruption continues fountaining activity devolves from along the entire length of the fissure onto one or more point source vents, over hours to days (Richter et al., 1970; Witt et al., 2018). A corresponding increase in eruptive intensity occurs, producing low, moderate or high fountaining, as classified by Houghton et al. (2016). Moderate to high fountaining activity produces medial, sheet-like, fall tephra and proximal scoria cones. The increase in intensity appears to be an artefact of both vent localisation, where the magma is forced through a narrower vent as the eruption proceeds and increases in magma discharge. If localisation occurs whilst the eruption is waxing the increase in magma discharge drives an increase in fountaining height and intensity. At a constant or waning discharge rate, vent localisation plays a more dominant role in fountain height changes. Following this phase, a fissure eruption can evolve in two ways: (a) steadily declining fountain heights that are in phase with declining magma discharge, e.g., the Krafla Fires 1975–84 CE, Iceland or; (b) the eruption goes onto a pattern of eruption episodes during which seemingly random changes in fountain intensities and height are driven by increases in magma

discharge. A good example of the latter are the episodic and variable fountaining heights observed during episodic eruptions at Kīlauea in Hawaii, e.g., Kīlauea Iki 1959 CE (Richter et al., 1970; Stovall et al., 2011, 2012), Mauna Ulu 1969–74 CE (Swanson et al., 1979; Parcheta et al., 2013) Pu'u'Ō'ō 1983–86 CE (Wolff et al., 1988; Mangan and Cashman, 1996; Heliker et al., 2003; Heliker and Mattox, 2003).

Observations of historic low-discharge flood lavas (FL) ($>1\text{--}100\text{ km}^3$) i.e., Holuhraun 2014–15 CE (Bonny et al., 2018; Witt et al., 2018) suggest these events follow the pattern in behaviour described above but their greater volumes can be attributed to prolonged activity. Whilst events that represent the high-discharge and high-magnitude end-member of FL eruptions or indeed flood basalt (FB) eruptions ($100\text{--}10,000\text{ km}^3$) have never been observed; field studies indicate that vent or near-vent deposits consist of extensive early fountain-fed lavas and sheet-like tephra fall (Thordarson and Self, 1993; Thordarson et al., 1996; Brown et al., 2014; Moreland et al., 2019). This suggests a different sequence of activity compared to their lower intensity high-magnitude counterparts. Deposits from high-discharge events are consistent with rapid waxing with a “curtain-of-fire” fountain activity reaching sub-Plinian to Plinian intensities shortly after emergent activity along a short fissure. Within a few hours, fountaining height declines, accompanying decreasing magma discharge, and is possibly associated with vent localisation. This pattern is repeated in each fissure-opening episode during an eruption. This rapid ramping up to high fountaining heights and intense activity, over short timescales, is not dissimilar to two historical examples of sub-Plinian to Plinian basaltic fissure eruptions: the 1986 CE sub-Plinian eruption at Izu-Oshima, Japan which produced the highest recorded historical fountain heights (1,600 m) (Sumner, 1998) and a Plinian eruption at Mt. Tarawera, New Zealand in 1886 CE (Carey et al., 2007; Sable et al., 2009). It is important to note that the timescales and relative influence of vent localisation and changes in magma discharge rate on fountaining heights is not documented for either of these short-lived, small volume, events.

To fully understand the variability in eruptive style and intensity of basaltic fissure eruptions, multiple parameters influencing the ascending magma need to be considered, such as: mass-ascent rate; decompression rate; fluid dynamics (decoupled and/or coupled phase flow); melt geochemistry and thus viscosity; initial

volatile budget and redox state; behaviour of volatiles on ascent; outgassing; conduit geometry and stability. These produce complex feedbacks and rapid fluctuations that drive changes in eruptive dynamics and produce textural diversity in the eruptive pyroclasts. In practice, this means that the modulating role of shallow conduit processes on erupting magmas often can be inferred by vesicle numbers, shapes and sizes within the pyroclasts from these eruptions. This study looks at the relative influences of nucleation, growth and coalescence and collapse of bubbles, through textural analysis of pyroclasts which provide a snapshot of the melt at fragmentation and thus a window into the obscured shallow conduit. To date only two microtextural studies of sub-Plinian to Plinian basaltic fissure eruption products have been carried out: Eldgjá 939 CE, Iceland (Moreland et al., 2019) and Tarawera 1886 CE, New Zealand (Sable et al., 2009), as such, our understanding of the shallow conduit feedbacks that enable these rare basaltic events to achieve such high fountaining heights is limited.

7. 1. 1 Purpose

This study will expand upon the small existing subset of microtextural data on high-intensity sub-Plinian to Plinian basaltic fissure eruptions by analysing clasts from several eruptive phases of the 1783–84 CE Laki FL eruption. The results will be contextualised by comparing vesicle populations of contrasting intensity historical basaltic fissure events to assess any existing correlations. This will allow us to examine if the distinct differences in the pattern of eruptive behaviour between low-discharge and high-discharge events are independent of magnitude. Additionally, the effect of the over-printing effect of post-fragmentation bubble evolution on primary magmatic textures will be investigated to determine the extent to which primary textures persist after fragmentation in the fountain and upon deposition.

7. 1. 2 Previous work on high fountaining fissure eruptions

In contrast to silicic fragmentation, always associated with brittle failure at high tensile stress at or above a minimum bubble volume fraction, the parameters that induce the break-up of low viscosity magmas are fundamentally different. Instead, four other criteria can induce the fragmentation of basaltic magmas at much lower

vesicularities: (1) inertial, pull-apart, fluid dynamic forces, (2) strain-rate, (3) potential energy and (4) stress (Gonnermann and Manga, 2007; Namiki and Manga, 2008; Rust and Cashman, 2011; see Chapter 6 for more details). Laboratory experiments and numerical modelling have shown that the timing and degree of decompression, degassing, vesicle nucleation, growth, coalescence and outgassing are key to distinguishing between different styles of basaltic explosive volcanism (Namiki and Manga, 2006, 2008; Gonnermann and Manga, 2007). The timing and rates of these processes, and any temporal variations throughout an eruption, can be inferred by micro-textural vesicle analysis of pyroclasts. Quantitative micro-textural analysis is a powerful tool that fingerprints the modulating role of shallow conduit processes during a magma's ascent. Several studies have demonstrated that basaltic eruptions, which display vastly different eruptive behaviours, span a wide range in vesicle number densities (VND), size distributions (VSD) and volume distributions (VVD) (Cashman and Mangan, 1994; Polacci et al., 2006; Sable et al., 2006; Lautze and Houghton, 2008; Costantini et al., 2010; Stovall et al., 2011, 2012; Parcheta et al., 2013; Holt et al., 2019). Quantitative analysis of the products of high intensity, high-fountaining basaltic fissure events are however relatively limited, with just five studies covering eruptions of this nature, three in Hawai'i: Kīlauea Iki 1959 CE, Mauna Ulu 1969–74 CE and Pu'u'Ō'ō 1983–86 CE (Mangan et al., 1993; Cashman and Mangan, 1994; Mangan and Cashman, 1996; Stovall et al., 2011, 2012; Parcheta et al., 2013), one in New Zealand: Tarawera 1886 CE (Sable et al., 2009), and one in Iceland: Eldgjá 939 CE (Moreland et al., 2019). The latter two examples are the only existing high-intensity and high-magnitude fissure eruption studies, with Eldgjá representing the only existing microtextural FL study (Moreland et al., 2019). Unlike Eldgjá 939 CE, the 1783–84 CE event benefits from detailed contemporary accounts (Steingrímsson 1783a, 1783b, 1788; Eriksson, 1783) and a multitude of previous physical volcanological, petrological and geochemical studies (Thorarinsson, 1967, 1969, 1979, 1981; Óskarsson et al., 1984; Sigmarsson et al., 1991; Thordarson and Self, 1993; Thordarson et al., 1996, 2003; Bindeman et al., 2006; Guilbaud, 2006; Guilbaud et al., 2005, 2007; Passmore, 2009; Hamilton et al., 2010a, 2010 b; Passmore et al., 2012; Neave et al., 2013; Hartley et al., 2017). This enables variations in micro-textures seen in the stratigraphy to be linked to the driving mechanisms of the eruption, which modulate the temporal evolution of explosive vent activity, its style, and the peak periods of atmospheric volatile and aerosol

loading. This is of particular importance in regard to improving future hazard forecasting for a Laki-type event.

The observed variety of microtextural fingerprints identified by this study in a single lapilli clast and how these evolve with time throughout an eruption highlights the importance of quantitatively analysing the outer rinds, in isolation, if present, of pyroclasts from low viscosity melts. This provides accurate VND data sets for the state of the melt prior to fragmentation, rapidly quenched and unaffected by post fragmentation expansion, which can be used as a better proxy for explosivity in a variety of styles of basaltic eruptions. The discrete textural domains identified by small scale textural mapping of heterogeneities in basaltic pyroclasts also capture changing shallow conduit processes, which are responsible for rapid fluctuations in eruptive styles during fissure eruptions.

7. 1. 3 Geological setting

The 1783–84 CE Laki fissure is part of the Grímsvötn volcanic system, Iceland, and represents an ice-free branch of its 23 km wide and 100 km long embryonic fissure swarm (Jakobsson, 1979; Thordarson and Self, 1993) (Figure 7. 1). This system sits at the northern end of the Eastern Volcanic Zone (EVZ) (Figure 7. 1), which is responsible for more than 80% of Iceland's Holocene eruptions (Thordarson and Larsen, 2007; Thordarson and Hoskuldsson, 2008). The EVZ has been active for the last 2–3 Myr (Sæmundsson, 1974) and accommodates most of the spreading and rifting events as it gradually takes over from the Western Volcanic Zone (LaFemina et al., 2005). Flood lava eruptions, which are the building blocks of Iceland, are common throughout the Holocene in the EVZ where some of the largest such events on Earth have taken place (Vilmundardóttir, 1977; Larsen, 1984, 1979, 2000; Hjartarson, 1988; Thordarson and Self, 1993; Thordarson et al., 2001; Thordarson and Larsen, 2007; Thordarson and Hoskuldsson, 2008). Whilst events of this magnitude are rare, a 1-in-250-year event in Iceland, they have the potential to trigger hemisphere-wide climatic and environmental perturbations through the volatiles and aerosols they loft into the atmosphere. Consequently, infrequent high-intensity and high-magnitude FL eruptions in Iceland are considered a serious hazard

for Europe and have been the subject of a number of studies in recent years to improve hazard forecasting for these rare events (Loughlin et al., 2012).

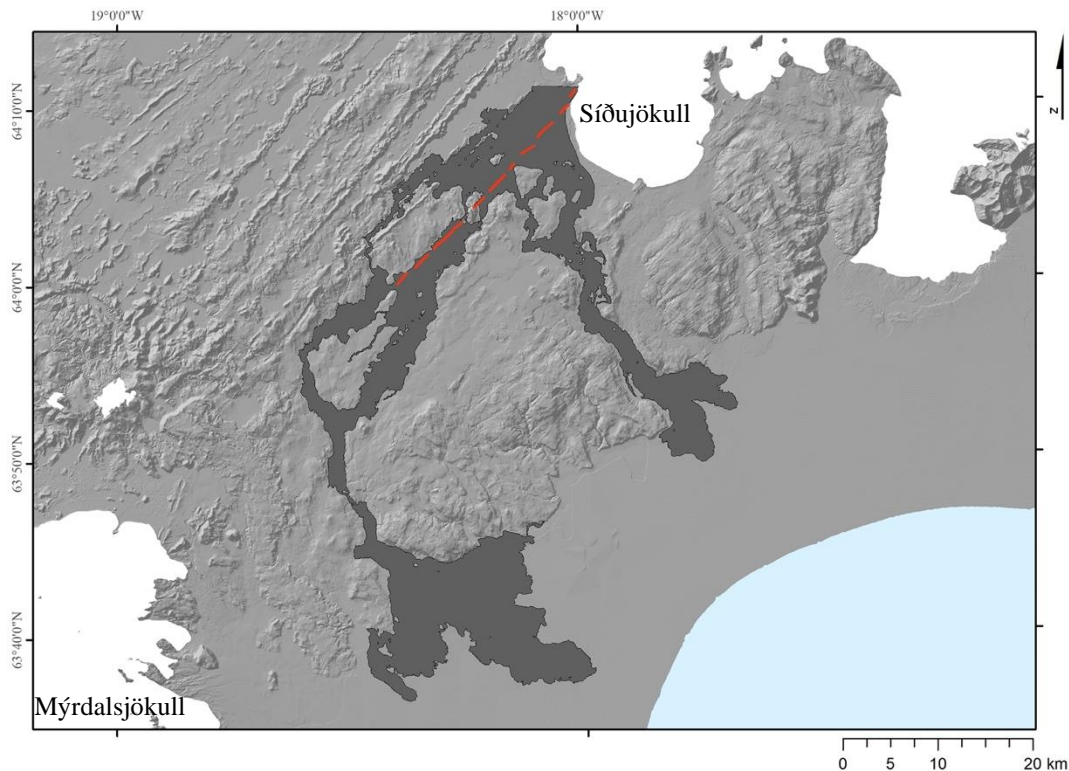


Figure 7. 1: Map of the Laki 1783–84 CE lava field and surrounding locations. ArcticDEM hillshade background, overlain with a dark grey outline of the total area of the Laki lava field, which spread from the Síða highlands to the lowlands through deep glacial river canyons, towards the sea shown in light blue. SW of the Vatnajökull ice-cap can be seen depicted in white, with the outlet glacier which Laki propagated underneath, Síðujökull, labelled for reference alongside Mýrdalsjökull to the SE. The location of the Laki fissure swarm is shown in red.

7. 1. 4 The 1783–1784 CE Laki eruption

The Laki eruption lasted for 8 months, from 8 June 1783 to 7 February 1784, during a large volcano-tectonic episode involving the Grímsvötn central volcano that lasted for more than 2 years (Steingrímsson 1788, Thordarson, 1990; Thordarson and Self, 1993; Thordarson et al., 2003a). The Laki eruption was the second largest historic FL eruption in Iceland. It had a devastating impact on the local population and may have directly and indirectly caused the death of > 2 million people across the Northern Hemisphere (Thordarson et al., 1996, 2003b; Thordarson and Self, 2001, 2003; Schmidt et al., 2011). The eruption started on 8 June 1783 in the Síða highlands (Figure 7. 1) and was preceded by 3–4 weeks of seismicity, which increased steadily until the onset of eruptive activity which lasted for 8 months (Steingrímsson 1783a, 1783b, 1788; Eriksson, 1783). Whilst this eruption produced

predominantly lava flows, 0.4 km³ of the 15.1 km³ (DRE) total eruptive products comprised tephra produced by initially explosive vent activity from 10 en-echelon fissures. These erupted sequentially in a stepwise fashion from the SW to the NE along the 29.5 km fissure system (Thordarson and Self, 1993; Thordarson et al., 2003a; Figure 7. 1; also see Chapters 4 and 5). Eruptive activity along the Laki fissure during each of the 10 fissure opening phases followed the same pattern: seismic swarms gave way to intense lava fountaining eruptive activity, with fountain heights of up to 1,500 m, lasting for hours to days, creating sheet-like, tephra fall deposits (Thordarson et al., 1993, 2003a; Thordarson, 2003). Activity subsequently waned into effusive activity feeding large lava flows which reached the lowlands. Explosive activity was predominantly magmatic, but three phreatomagmatic events also occurred when magma interacted with subaerial lakes or ice, creating 4 tuff cones out of the 140 vents along the mixed cone row (Thordarson and Self, 1993; Chapters 4, 5 and 7). These initial explosive phases produced proximal tephra aprons, with clear internal sub-unit stratigraphy, as well as distal air-fall sheets whose extent has been outlined by isopachs (Thordarson et al., 1993). Whilst the highly vesicular nature of the Laki tephra has been mentioned in previous studies, a comprehensive qualitative and quantitative VND, VVD and VSD analysis of the pyroclasts has not previously been conducted.

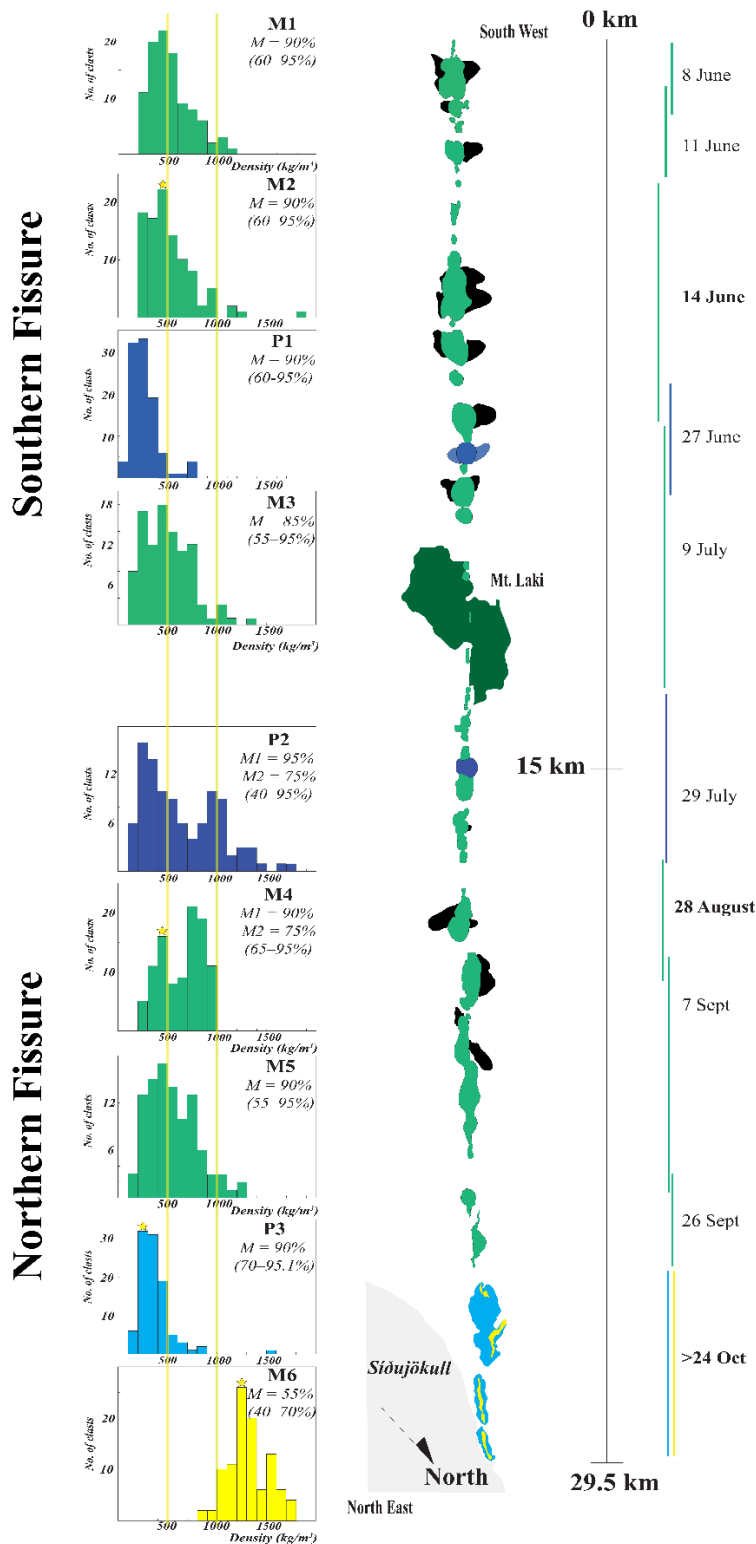


Figure 7. 2: Laki cone-row with fissure lengths, activity dates, and associated pyroclast density histograms of explosive phase tephra apron samples. Sample densities (left hand side) are displayed alongside the Laki crater row (scaled) and fissure length and initial activity date (righthand side). The Laki fissure is 29.5 km in length and consists predominantly of magmatic activity indicated by light green craters with black tephra aprons. Phreatomagmatic activity is shown in two shades of blue, dark blue indicates tuff deposits due to lake-magma interactions (Thordarson and Self, 1993; Thordarson et al., 2003a), and light blue indicates tuff cones produced by shallow subglacial eruptive activity. Thin yellow deposits can be observed in the centre of the subglacial tuff deposits, indicating ice-confined but sub-aerial magmatic spatter fed lavas which cap the sequence. Yellow/black lines are used to highlight the 500 and 1000 (kg/m^3) densities for comparison between samples. Corresponding ranges and modal vesicularity values are displayed for each sample in the upper right corner.

7.2 Methods

To capture changes in eruptive dynamics, modulated by shallow conduit processes, pyroclasts from previously identified and mapped out proximal tephra layers associated with different eruptive phases were sampled. These phases span the entire 8-month eruptive event and include both magmatic and phreatomagmatic activity. Pyroclasts were collected from 7 separate tephra pits along the 29.5 km fissure (Figure 7. 2). For the southern fissure proximal to medial soil horizons, which contain several Laki sub-unit layers, were used for sampling locations, as all of the tephra aprons from the southern fissures also contain tephra from episode 5. This forms a capping layer on top of all the tephra aprons from previous fissure opening phases 1–4 as episode 5 triggered reactivation of all the first 4 fissures as well as opening a new fifth; however, this is indistinguishable from the other proximal apron deposits beneath it. Each density sample consisted of at least 100 individual clasts between 16–32 mm. Eight samples were collected from the highest intensity eruptive activity, which forms the initial layer in the tephra aprons, from 8 separate fissure opening episodes for clast density/vesicularity analysis (Figure 7. 2).

Clast density measurements were carried out on the 100 largest clasts from each sample, following the procedure of Houghton and Wilson, 1989. First, samples were cleaned in an ultrasonic bath to remove any fine particles and dried in an oven at 40°C for at least 48 hours. Then, the clasts were weighed individually ($\omega_{\text{clast}}^{\text{D}}$, dry weight), and each clast was wrapped in polyethylene film (parafilm) to waterproof them, and the amount used recorded (ω_{parafilm}). Finally, each clast was immersed in deionised water, suspended in a wire cage, with a ballast of known and consistent weight (ω_{ballast}) and weighed again ($\omega_{\text{clast}}^{\text{W}}$, wet weight). The density of each clast (ρ_{clast}) was then calculated using Archimedes' principle following:

$$\rho_{\text{clast}} = \omega_{\text{clast}}^{\text{D}} / \omega_{\text{clast}}^{\text{D}} - (\omega_{\text{clast}}^{\text{W}} - \omega_{\text{ballast}} + \omega_{\text{parafilm}})$$

(Eq. 1)

A dense rock equivalent (DRE) value of 2830 kg m^{-3} for a Laki basalt calculated from major element concentrations was used when converting measured bulk density to density-derived vesicularity (ϕ) following:

$$\phi = (1 - (\rho_{\text{clast}} / \text{DRE}) * 100$$

(Eq. 2)

7. 2. 1 Textural Analysis

Three clasts of modal density were chosen from each of the ten bulk density histograms, along with additional outlier clasts representing the minimum and maximum density, to be made into polished thin sections for textural analysis. In total 30 clasts were made into polished sections, and initial qualitative petrological and microtextural observations were carried out to select which clasts are most representative of the textural diversity of each sample. Four out of 30 clasts were selected for quantitative vesicle size distribution and number density analysis and carbon coated with a thickness of $250 \text{ }\mu\text{m}$. The vesicle abundance and size distribution for these pyroclasts provide windows into shallow conduit processes by providing a snapshot of the vesiculation state quenched during and following fragmentation, which can be used to postulate the relative rates and significances of bubble nucleation and free growth, as well as the roles of vesicle coalescence and outgassing (Cashman and Mangan, 1994; Mangan and Cashman, 1996).

The four clasts chosen for detailed textural analysis were selected to represent the key stages of activity as the eruption evolved (Figure 7. 3), spanning 3 out of the 10 distinct fissure opening phases. Magmatic clasts have the prefix M, and phreatomagmatic clasts have the prefix P as well as a number corresponding to their identified tephra layers from Thordarson et al., 1993 and Chapter 5. One magmatic clast was selected from both the southern (M2) and northern fissures (M4), as well as two clasts from the final stages of the eruption, which initially occurred in a shallow subglacial environment (P3) and subsequently became subaerial in its waning stages (M6). Each of the clasts were selected from the modal peak of their respective density distribution (Figures 7. 2 and 7. 4):

- 1) M2: Eruptive episode 3 (14 June 1783 CE), Pele's-hair-rich base and intense activity noted in contemporary accounts and previous studies.
- 2) M4: eruptive episode 7, 25 August–1 September 1783 CE: this sample is from the first magmatic tephra apron produced from vents north of Mt. Laki. It occurs after a long period of quiescence compared to the fissure-opening phases in the southern part of the fissure system. This eruptive phase originated from fissure 7, 24 days after the activity at P2 (which in turn followed an extended period of quiescence, 17 days after M3). Longer lag times between fissure opening phases seems to be characteristic of the northern fissure, and the activity is more prolonged based on chronologies extracted from historical accounts.
- 3) P3: eruptive episode 10, approximately 24–25 October 1783 CE: this sample represents shallow subglacial eruptive activity along fissure 10 which created large tuff cones which were ice-confined at the very north of the Laki fissure (the last 3 km of the 29.5 km long Laki fissure, (see Chapters 4 and 5). The tuff cones are a mixture of fall and surge deposits littered with accretionary lapilli and armoured clasts. Large sub-angular to rounded lithics, from a glacially deposited and fluviially modified substrate, occur throughout the pyroclastic density current and coeval tephra fall sequence (see Chapter 5). The time frame for this activity is less well defined, occurring around 24–29 October and continuing for an unknown period. A possible tephra fall is described in the contemporary accounts on 25 October when sandy ash fell in the fire districts, which matches this crater's deposits well (see Chapters 4 and 5).
- 4) M6, eruptive episode 10, 24–25 October 1783 CE: this clast represents ice-confined magmatic activity as the pyroclastic material creating the tuff cones of P3 managed to isolate the vents from the water source, and spatter-fed lava flows and dense magmatic lapilli from the waning phases of the eruption is produced (see Chapter 5). This, like P3, occurs along fissure 10, for the last 3 km of the fissure system. The M6 clasts are much denser and more crystal-rich than earlier eruptive products, which makes sense as eruption wanes and more cooling and outgassing occurs, creating more syn-degassing crystallisation (see Chapter 5).

7. 2. 2 Image Acquisition

A JEOL-JSM-7001F Schottky Emission Scanning Electron Microscope at The Institute for Planetary Materials, Okayama University, Japan, was used to collect Back-Scatter Electron (BSE) images from each polished thin section. To fully capture textural variations of the vesicle populations, which span several orders of magnitudes, nests of overlapping images at different magnifications were taken. The pyroclasts from the Laki eruption are texturally complex and display a high degree of melt heterogeneity with domains characterised by distinct vesicle populations (for further details, see the Results section of this chapter). In order to accurately represent the observed textural heterogeneity within the Laki clasts, the method of Shea et al. (2010) was modified to include the whole thin section area mapped with 100x magnification BSE images collected with a 60% overlap. Internal SEM software (Mapxml) or software derived from UAV aerial image mapping (pix4D, using manual tie-points) was used to stitch the images without distortion into a whole clast map. The 100x full-pyroclast map replaces the flatbed scan and 50x magnifications in the Shea method, whereas the 250x and 500x magnification nest structures remain unchanged (Figures 7. 5 and 7. 6). The 250x and 500x magnifications were collected on a table-top Hitachi TM3000 SEM at The University of Iceland. The number of higher magnification images range from six to twelve depending on the heterogeneity of the sample, with more images taken for samples displaying a higher degree of textural complexity. Images analysed for the higher magnification nests were positioned to capture the relative proportions of different domains within the clast to ensure the data set included adequate numbers of nests to characterise each type of identified domain individually.

Image properties and scaling factors, alongside details of how the images were processed, are the same as those used for the Holuhraun clasts, and a detailed description of the processing method and any necessary image properties can be found in Chapter 6.

7. 2. 3 Geochemical Glass Analysis

Major element and volatile concentrations of basaltic glass from the Laki tephra was determined by electron microprobe analysis (EMPA), at The University of Iceland, using a JEOL JXA-8230 SuperProbe, with an acceleration voltage of 15 kV, corresponding to a 10 nA beam current with a diameter of 10 µm. EMP analysis followed the same set-up as described in further detail in the Holuhraun vesicularity Chapter 6.

7. 3 Results

7. 3. 1 Deposit characteristics

The tephra aprons from the Laki eruption form a proximal apron-like sheet which thickens towards the vent, forming shallow topography surrounding the scoria cone vents which divert spatter-fed lava flows. Due to the pre-existing landscape in the immediate vicinity of the Laki crater row, which consists of water-saturated heathland and older sub-glacially erupted deposits forming low-lying fells or eroded ridges, the internal stratigraphy of well-preserved tephra aprons can be easily accessed in proximal gullies. The orientation of explosive tephra apron deposits as they are traced away from the vents corresponds roughly to the wind direction during that opening phase (Head and Wilson, 1989), and thus the dispersal axis along which most of the tephra fell. Dispersal axes extracted from contemporary accounts (Steingrímsson, 1783a, 1783b, 1788; Eriksson, 1783), agree well with the orientation of proximal tephra aprons surrounding the Laki craters (Figures 7. 2 and 7. 3) (Thordarson et al., 1996, 2003a; Thordarson and Self, 1993; Thordarson, 2003). The Laki tephra deposits are well mapped and described in detail for fissure opening phases 1–6/7 by Thordarson and Self, (1993), however, sequences from fissure segments 7–10 of the fissure system which extends north of Mt. Laki are not well mapped, defined, or characterised. A new tephra apron for M5, episode 8, has been identified which extends N/NE of the craters and is distinct from M4, episode 7 (Figures 7. 2 and 7. 3), which is deposited to the SW (See Chapter 5) alongside previous unidentified magmatic and phreatomagmatic deposits from fissure 10 (see Chapter 5).

Magmatic proximal tephra aprons and medial tephra layers are black in colour, with a submetallic lustre, well-sorted, coarse, lapilli-sized clast supported units which also contain a medium to coarse ash matrix. They are rich in shiny black achneliths, with metallic blue-purple sheens and light- brown/yellow golden pumice, with subordinate amounts of lithics and matt black scoriaceous clasts. Pele's hairs and tears occur as a minor component in all the magmatic units, but notably, the high intensity activity in the opening phase of M2 (14–15 June 1783 CE), fissure eruptive episode 3, (Figures 7. 2 and 7. 3) resulted in a Pele's hair rich tephra layer at the base of this apron and also in the base of the medial M2 tephra layer which lies between M1 and P1.

Phreatomagmatic medial tephra layers are sandy-pale-brown in colour and are dominated by an abundant fine-ash-rich matrix, with subordinate, rounded, golden pumice lapilli. Vesicular achneliths, formed by hot magmatic gases fusing the outer clast surface of pumice clasts forming a fluidal outer skin (Thordarson et al., 1996), are absent in the phreatomagmatic units due to their interaction with external water. The phreatomagmatic lapilli clasts are also relatively round when compared to the magmatic clasts.

In the field, the phreatomagmatic deposits provide marker units in the proximal–medial tephra stratigraphy; this is particularly important for identifying the tephra units produced by the southern fissures. Due to the reactivation of all the previously active fissures during M3, the opening phases of M–3 and P1 cannot be sampled directly on the tephra apron near the vent as M3 lies unconformably on the top of all of these units. In places M3 is indistinguishable from the previous magmatic units thus obscuring the tephra apron stratigraphy. Consequently, sampling for these units is done in proximal–medial locations either from thick tephra layers preserved in local soil horizons or at the edges of aprons using phreatomagmatic markers, e.g., P1 (27 June 1783 CE, episode 4) overlies M2, separating it from the next magmatic unit M3 (Thordarson and Self, 1993; Thordarson et al., 2003a). P2 (29 July 1783 CE, episode 6) acts as a similar marker unit above M3 and prior to M4 deposition in soil horizons close to the northern fissure.

Angular juvenile and older wall-rock lithics occur in both the magmatic and phreatomagmatic units, but of particular interest are the sub-rounded lithics present in the P3 sequence (24–25 October 1783 CE, episode 10), at the crater (not traceable in its rarely identified tephra layer). These are derived from a fissile layer of fluvial-terminal-glacial origin that was ripped up during the crater-forming event along with lithic fragments from deeper in the conduit. Contemporary accounts of the eruptive activity from this phase initially suggested that the plume seen at this period of the eruption was from Grímsvötn, but further analysis suggests that it could easily be from fissure 10 (Chapter 5). Detailed isopach mapping of P3 has been impeded by the heavily glacially eroded surrounding terrain. Síðujökull is a surging glacier (Figures 7. 1, 7. 2 and 7. 4; see Chapter 5 for further details) and had a greater extent at the time of the eruption resulting in thick tillite and moraine sequences which removed or buried local tephra deposits. The P3 tephra layer has, however, now been identified in two locations: Nupahraun (near Illugilshnúkar) and eastern Geirlandsheiði (Figure 7. 1; and see Chapter 5 for further details), as a thin layer defining the top of the proximal-medial Laki tephra which at these locations displays internal sub-units. At Geirlandsheiði, these subunits are identified as M2, P1, M3, P2, M4, M5 and P3 (Figure 7. 3) and at Illugilshnúkar further to the NE (see Figure 7. 3), the subunits present are identified as P2, M4, M5 and P3. P3 occurs at these localities as a thin layer consisting of thicker coarse ash to very fine lapilli lenses connected by fine–coarse ash stringers (Figure 7. 3), indicative of this unit falling onto snow (Thordarson, pers. communication). Due to an abundance of fines in P3, and lack of lapilli clasts in medial tephra layer, its density sample was collected directly from the vent pyroclastic density current and coeval fall deposits (see Chapter 5).

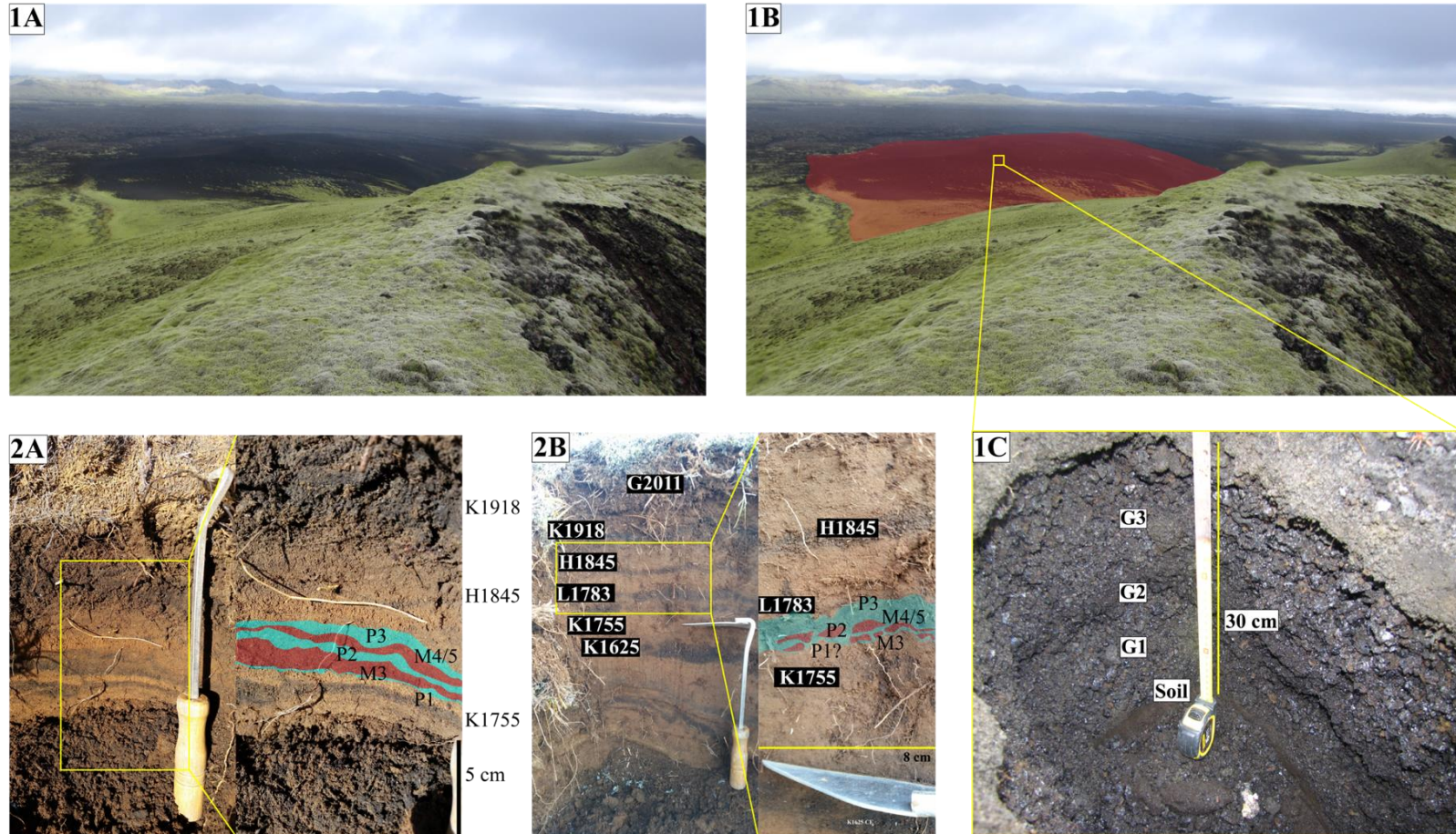


Figure 7. 3: Laki 1783–84 CE tephra layers in medial soil horizons and proximal tephra apron layering from a single eruptive phase. (1A) extensive black M5 apron tephra layer extending north-eastwards away from the green moss-covered crater, outlined in (1B) with red for clarity, with the inset outline for (1C) indicated by a yellow box. (1C) A tephra pit through the edge of M5 explosive apron tephra fall deposit to the soil layer underneath, 3 distinct layers with different grainsizes G1–3 (labelled) can be observed. (2A and B) Medial soil horizons in the Síða highlands, with coloured overlays highlighting distinct tephra magmatic (red) and phreatomagmatic (blue) sub-units within the Laki 1783–84 CE tephra layer, which are also labelled. Katla 1755 CE, Hekla 1845 CE, Katla 1918 CE and Grímsvötn 2011 CE are labelled for reference.

7. 3. 2 Clast density and bulk vesicularity

The average clast density for the Laki 1783–84 CE tephra ranged from 130–610 kg m⁻³, throughout the eruption from 8 June 1783 CE to approximately after and including the 24 October 1783 CE. This average density range corresponds to an average vesicularity range of 53–87 %, with errors reported to 1 std (Tables 7. 1a and 7. 1b). The clast density modal range of the tephra is 200–300 to 1500–1600 kg m⁻³, corresponding to a modal vesicularity range of 40–55 to 85–90 %.

Tables 7. 1a and 7. 1b:

	Av. Density (kg m ⁻³)	1 std	Av. Ves.	1 std	Distribution	Ves. Range	Min. Ves.	Max. Ves.	Modal Density (kg m ⁻³)	Modal Ves.
M1 (S. Fissure)	500	±21	81%	±7	Unimodal (+ve skew)	32%	59%	91%	400–500	85–90%
M2 (S. Fissure)	470	±26	82%	±9	Unimodal (+ve skew)	57%	35%	93%	400–500	85–90%
P1* (S. Fissure)	340	±14	87%	±5	Unimodal (slight +ve skew)	23%	71%	94%	200–300	85–90%
M3 (S. Fissure)	450	±25	82%	±9	Sawtoothed-Unimodal (+ve skew)	42%	53%	95%	200–300, 400–500	80% 90%
P2 (N. Fissure)	540	±38	77%	±13	Bimodal (+ve skew)	56%	37%	95%	200–300, 900–1000	65% 90%
M4 (N. Fissure)	610	±22	77%	±8	Bimodal (-ve skew)	28%	82%	93%	400–500, 700–800	75% 90%
M5 (N. Fissure)	554	±25	80%	±9	Bimodal (+ve skew)	40%	54%	94%	400–500, 700–800	75% 90%
P3 (N. Fissure)	340	±18	87%	±7	Unimodal (+ve skew)	56%	44%	95%	200–300	85–90%
M6 (N. Fissure)	130	±20	53%	±7	Unimodal-Jagged (slight +ve skew)	33%	36%	69%	1500–1600, 1200–1300	40% 55%

* From Zoë Decker's masters thesis, sample name: 20150925-003 Laki 4

Table 7. 1 a and b: Laki 1783–84 CE density and calculated bulk vesicularity data. Table 7.1a (above). Displaying measured density and calculated bulk vesicularity of the Laki clasts, Table 7. 1b (below, next page): displays the averages for the N and S explosive phases, as well as the waning stages of the eruption.

Southern Fissure	
Density Distribution	Unimodal, negatively skewed with dense tails
Modal Range	300–500 kg/m ³ (85–90% vesicularity)
Northern Fissure	
Density Distribution	Unimodal, negatively skewed with dense tails, and bimodal with dense tails
Modal Range	100–800 kg/m ³ (70–90% vesicularity)
Closing phase of the eruption	
Density Distribution	Unimodal, jagged
Modal Range	1300 g/m ³ (55% vesicularity)

The Laki fissure-opening episodes display distinct differences in density and bulk vesicularity passing from the SW to the NE of the long fissure system. Both magmatic and phreatomagmatic samples from the southern eruptive fissures (SW of Mt. Laki), i.e., episodes 1–5, from 8 June–9 July 1783 CE, are unimodal, positively skewed, and all samples have dense tails (Figures 7. 2 and 7. 4, Tables 7. 1a and 7. 1b). The average clast density for the SW fissures has a modal range from 200–300 to 400–500 kg m⁻³, corresponding to a modal vesicularity range of 80 to 90 %. The clast density distributions from eruptive episodes 1–4, M1–P1, displays a subtle shift towards lower densities from 400–500 to 200–300 kg m⁻³. The first two magmatic eruptive phases, M1 and M2, are denser than the first phreatomagmatic phase, P1, between M2 and M3. M1 and M2 are more positively skewed and also display more pronounced dense tails than P1, which has a tighter distribution. The sample from eruptive episode 5, M3, spans a broader range in density than the previous eruptive phases; it has a jagged unimodal distribution and pronounced dense tail. M3 has a modal density of 400–500 kg m⁻³ as the modal density decreases to similar values to M1 and M2.

To the NE of Mt. Laki, magmatic and phreatomagmatic northern fissure phases, i.e., episodes 6–8 (29 July–7 September 1783 CE), are bimodal and positively skewed (Figures 7. 2 and 7. 4; Tables 7. 1a and 7. 1b). The bimodality is more pronounced in episodes 6 and 7 (P2 and M4), whilst episode 8 (M5) has a saw-toothed unimodal distribution. The average clast density for the NE fissures has a modal density range from 200–300 to 700–800 kg m⁻³, corresponding to the modal vesicularity range of 70–75 to 85–90 %. The modal density of P2, is lower than the magmatic phases either side of this episode, which is similar to the phreatomagmatic phase, P1, in the SW Laki fissures. The dominant peak in the bimodal samples shifts to a higher density in M4, indicating greater proportions of higher clast vesicularities in the phreatomagmatic samples compared to the magmatic phase occurring in the next fissure opening. P2 spans the largest variation in density, with two modes at 200–300, and 900–1000 kg m⁻³, corresponding to modal vesicularities of 60–65 and 85–90 %, with a very pronounced dense tail. Episode 7 (M4) displays a much tighter bimodal distribution, with a slight negative skew, which is shifted towards higher clast densities when compared to P2 of 300–400 and 700–800 kg m⁻³ corresponding to modal vesicularities of 70–75 % and 85–90 %. Episode 8 (M5) has a unimodal

saw-toothed distribution with a main modal density peak at 300–400 kg m⁻³. The clast density distribution for M5 is shifted towards lower densities when compared to P2 and M4, although the modal peak is the same as the lower density peak for M4. Unlike M4, M5 has a pronounced dense tail.

The closing phases of the eruption in the very NE of the fissure system, i.e., episode 10, which occurred approximately from the 24 October 1783 CE onwards, are grouped separately from the other Laki explosive activity due to their sub-glacial to emergent ice-confined eruptive environment (Figures 7. 2 and 7. 4). The initial subglacial phreatomagmatic deposit from episode 10, P3, has a tight unimodal distribution, which is positively skewed and accompanied by a short, dense tail. P3 has a modal density range of 200–300 kg m⁻³, which corresponds to a modal vesicularity range of 85 to 90% (Tables 7. 1a and 7. 1b), indicating a shift towards lower densities as the activity progresses to the NE from the early northern fissure episodes. As this phase of the eruption evolves into the ice-confined magmatic activity, which captures the waning phases of the Laki eruption, a marked shift towards higher densities occurs. This late-stage magmatic activity, the M6 sample displays a unimodal distribution which has a jagged, broad shape with a marginal positive skew. M6 has a modal density range of 1200–1300 kg m⁻³, which corresponds to a modal vesicularity range of 55–60 % (Tables 7. 1a and 7. 1b). M6 has the highest modal density of all the Laki eruptive episodes analysed. The clasts from this sample contain a higher abundance of microlites, visible in hand sample. In thin section, the groundmass for the clasts in this sample is completely microcrystalline in places and contains mature euhedral microlite populations.

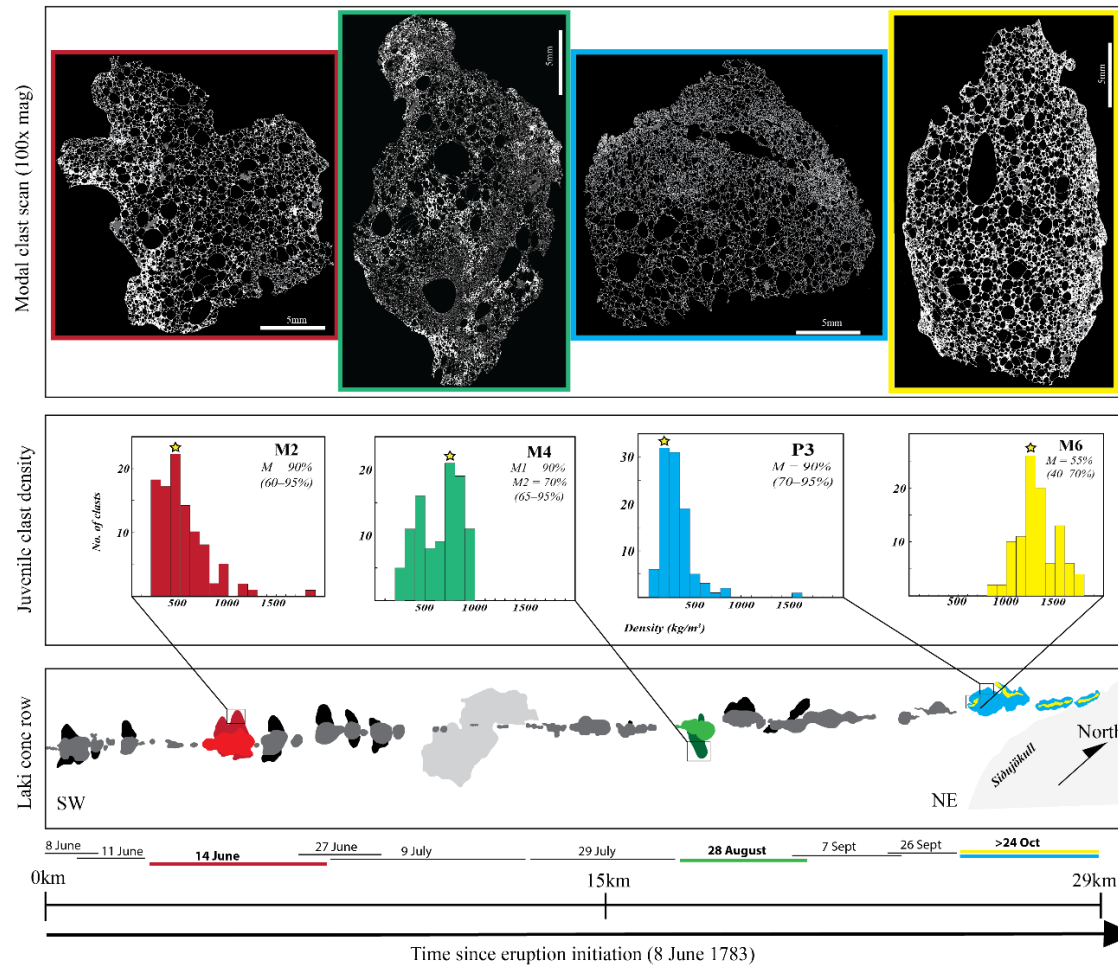


Figure 7. 4: Analysed phases of the Laki 1783–84 CE fissure opening phases. A panel compilation that indicates the evolution of several aspects of the Laki eruption (y-axis) through time (x-axis). The Laki fissure (bottom panel) is shown in grey, with the samples of interest highlighted in colour. M2 (red), M4 (green), P3 (blue) and M6 (yellow). The fissure is drawn to scale, and the glacier Síðjökull and north arrows are shown for orientation. The length of active fissures and their activity initiation date are shown below this panel. The middle panel displays the density histograms of samples collected for these phases. The very top panel displays images of the decoalesced analysed modal clast analysed from each of these eruptive phases.

7. 3. 3 Qualitative textural analysis and initial interpretations

All analysed clasts are composed of sideromelane, tachylite is present in unanalysed M4 and M5 samples, with varying microlite and phenocryst contents, although the latter has been measured as <6% for all samples. All the Laki clasts, regardless of eruptive environment, or degree of external water interaction, display mature and internally heterogeneous bubble textures. The majority of magmatic clasts are surrounded by a discontinuous, more rapidly quenched, outer rind containing an immature vesicle population which is absent in the phreatomagmatic clasts.

The observed pattern of a general increasing maturity of the vesicle population from the outer rind to the interior, in a semi-symmetrical arrangement (Figures 7. 5–7. 8), in the Laki pyroclasts occurs in a very similar fashion to vesicle populations in the Holuhraun pyroclasts (Chapter 6). Although this is less obvious in some of the Laki samples, the overall pattern from the outside to the clast interior is the same as Holuhraun (see Chapter 6): (1) an outer immature rind, (2) an interior rind (present in lower-intensity activity only, i.e., M6) and (3) inner mature foam (Figures 7. 5–7. 8).

7. 3. 3. 1 Post-fragmentation expansion

Pyroclasts displaying a rapidly quenched rind, coupled with an internally mature magmatic foam have been demonstrated by several studies at Kīlauea to result from post-fragmentation expansion of the interior vesicle population (Mangan and Cashman, 1996; Porritt et al., 2012; Stovall et al., 2011, 2012; Parcheta et al., 2013; Holt et al., 2019). This process has also been identified in the 2014–15 CE event at Holuhraun (Chapter 6). In all of these events this texture is generated by the ongoing post-fragmentation vesiculation, where hot and insulating sustained jets of gas create thermal gradients within the fluidal Laki pyroclasts in the fountains. This insulating environment permits varying rates of continued vesicle growth and development to maturity across the pyroclasts. Consequently, the rapidly quenched outer rind is the most representative of the vesicle population of the melt at fragmentation. However, unlike the Holuhraun and Hawaiian pyroclasts, a quenched rind is only present in some of the Laki magmatic eruptive episodes and always absent in the

phreatomagmatic phases; therefore, whilst quantitative textural analysis concentrates on the available outer rinds to identify the conduits of the melt at fragmentation, the whole-clast data sets from distinct eruptive phases are used for comparison.

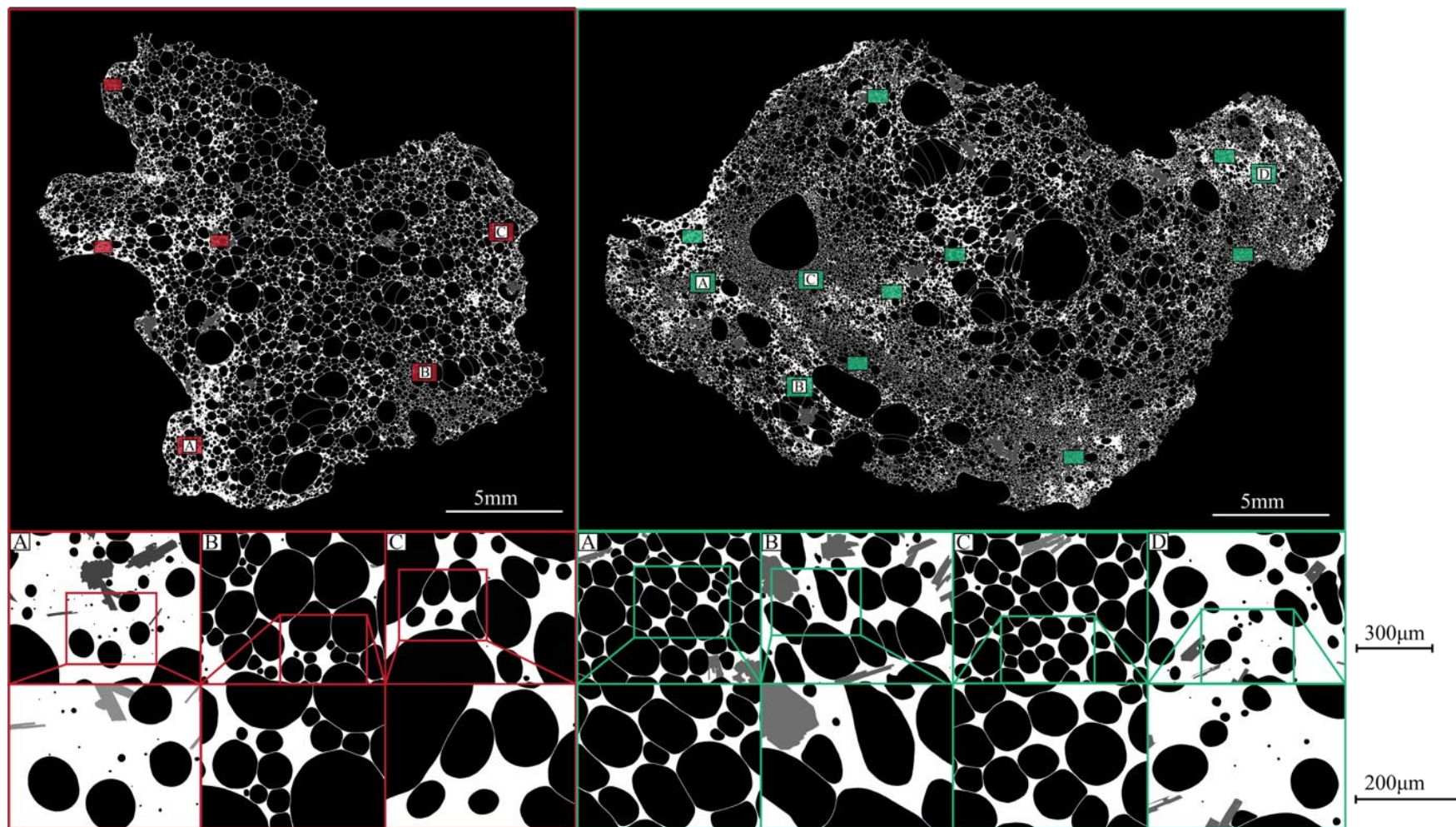


Figure 7. 5: SEM BSE images of texturally analysed pyroclasts from explosive tephra phases M2 and M4, Laki 1783–84 CE. These BSE images indicate the distribution of 250x and 500x magnification nests in M2 (left hand) and M4 (right hand) clasts. Underneath are SEM images at 250x and 500x that display examples of the different main textures found within the clasts. The location of the 500x magnification is indicated by a coloured box in the 250x images.

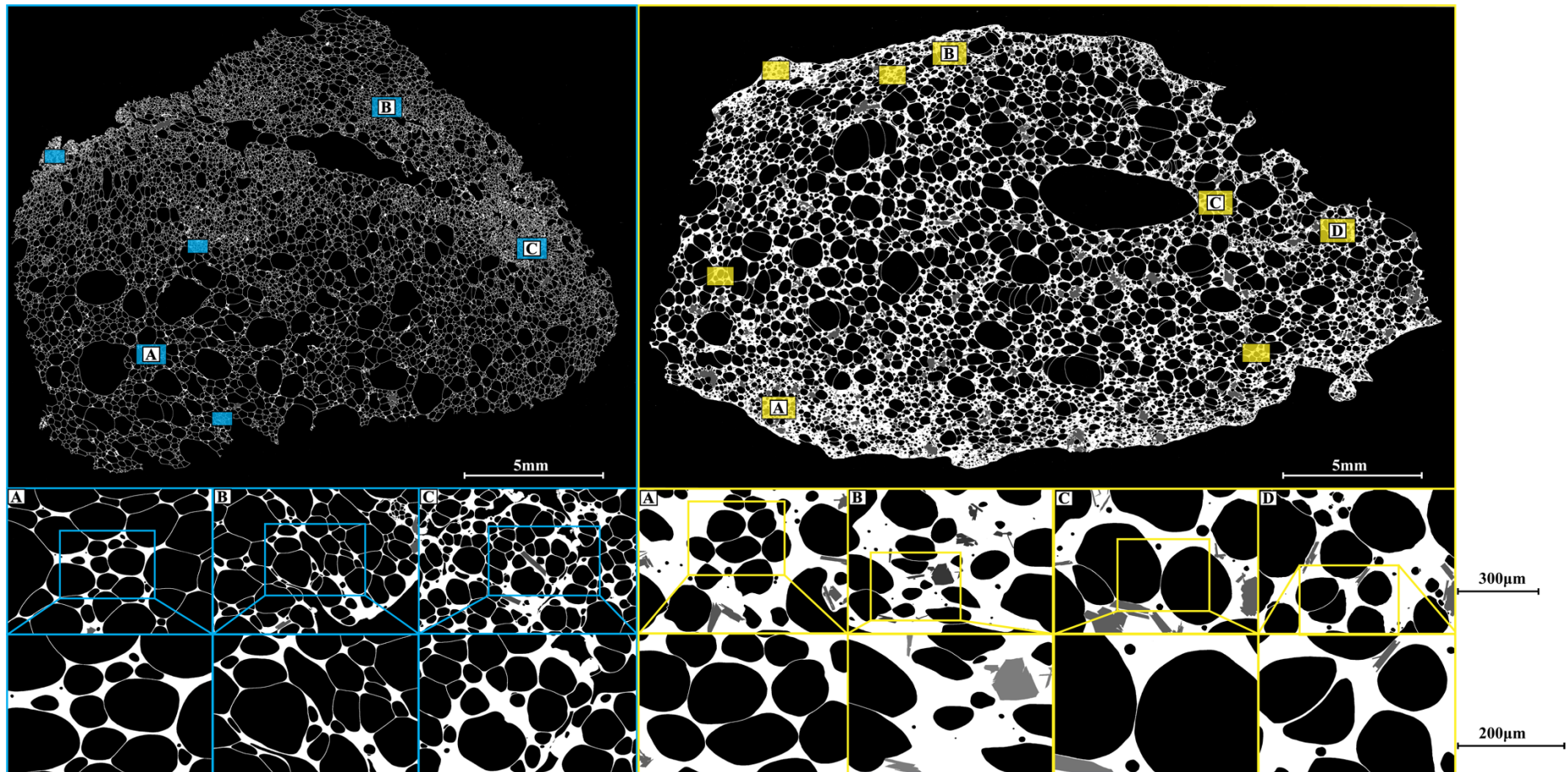


Figure 7. 6: SEM BSE images of texturally analysed pyroclasts from explosive tephra phases P3 and M6, Laki 1783–84 CE. These BSE images indicate the distribution of 250x and 500x magnification nests in P3 (left hand) and M6 (right hand) clasts. Underneath are SEM images at 250x and 500x that display examples of the different main textures found within the clasts. The location of the 500x magnification is indicated by a coloured box in the 250x images.

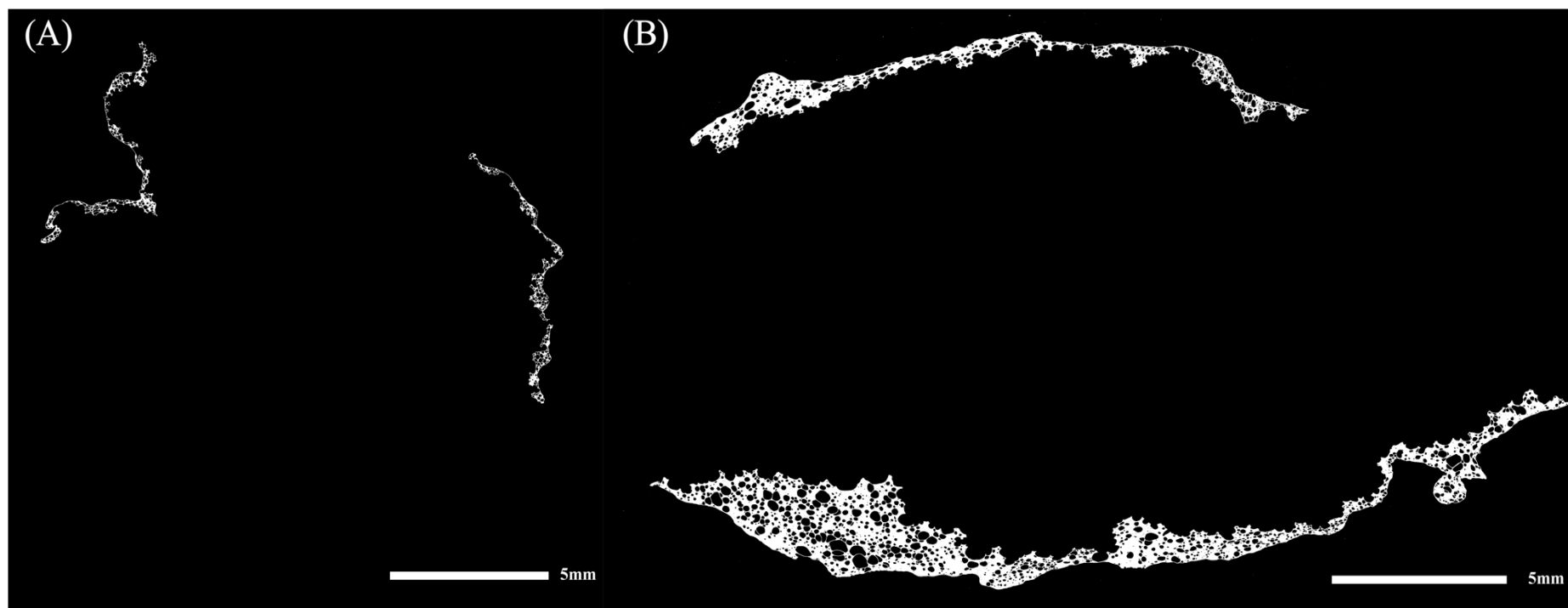


Figure 7. 7: Analysed rinds from M2 and M6 explosive tephra phase clasts, Laki 1783–84 CE. Outlines of the analysed melt rinds from ImageJ, the melt rich rinds are shown in white with any bubbles in black on a black background. From the top left across (A) M2 (9–10 July 1783 CE), (B) M6 (>25 October 1783 CE). These plots demonstrate the proportion of the rind in each sample, M6 towards the end of the Laki eruption has a higher degree of rind than the other samples

As with the Holuhraun pyroclasts, post-fragmentation expansion of the interior of the Laki pyroclasts has enhanced pre-existing, primary, textural heterogeneities not easily observed on a micro-scale in the rind. This process highlights evidence of the same patterns of shallow conduit mingling of different melt packages as analysed in the Holuhraun pyroclasts. For consistency, and because of their similar vesicle size distributions and number densities of these domains, the same terminology and classifications are used for the Laki clast domains as in the Holuhraun clasts (Chapter 6), whose key features are recapped below:

1) Mature vesicle texture (domain type 1): This mature texture contains a heterogeneous vesicle population, displaying evidence of several vesicle coalescence, nucleation, and growth events associated with vesicle shearing and deformation. The microlite population is not mature, mostly consisting of swallow-tailed laths. The vesicles in this domain had insufficient time to relax and therefore preserve disequilibrium textures; this vesicle and microlite population is generated by fast ascent rates, although not as fast as the ultra-vesicular foam texture.

2) Ultra-vesicular foam texture (domain type 2): A monodispersed, open-celled, polyhedral foam (Mangan and Cashman, 1996) comprising of small, rounded, bubbles with very thin bubble walls. It represents delayed disequilibrium vesiculation, whereby rapid ascent rates permit a high degree of volatile supersaturation prior to a late stage, short-lived, relatively homogeneous, burst nucleation event (Houghton and Gonnermann, 2008). N.B. As also observed in the Holuhraun clasts, it occurs as lenses or bands of well-developed foam throughout the Laki clasts in 2D, although these may connect in 3D. In the Laki clasts, there is a transitional texture that seems to result from the mingling of the mature and ultra-vesicular textures, forming a hybrid foam (Figure 7. 8, also see supplementary material appendix C).

3) Very mature, melt- and crystal-rich texture (domain type 3): The vesicle population present in this texture is strikingly smooth and elliptical, which reflects sufficient time for bubble relaxation, to simple shapes, suggesting a prolonged residence time in the shallow conduit prior to fragmentation. It is rich in mature, coarse, euhedral microlites relative to the mature and ultra-vesicular foam textures,

containing an immature and proportionally low microlite population. It represents a mature equilibrium texture, which didn't ascend as rapidly at shallow levels as the other vesicle textures present.

Again, as with Holuhraun pyroclasts, the proportions of these domains display differing degrees of dominance or in response to changes in ascent rate and therefore changes in shallow conduit processes at different stages of the event, which is addressed in full in the discussion (see Figures 7. 5–7. 8, 7. 11, 7. 14 and 7. 15). For the Laki eruption, this is more complicated than the observed changes in activity in the Holuhraun 2014–15 CE eruption, as Laki consisted of 10 distinct fissure opening episodes for each of which we are only analysing the initial, most explosive tephra fall. An additional layer of complexity for the Laki eruption exists alongside the temporal shift in eruptive activity seen in the opening phases, as there are changes in eruptive environment along-strike. Most of the eruptive activity was magmatic with localised phreatomagmatic activity present in both the SW and NE fissures due to interactions with surface water bodies (lakes). In the very NE of the fissure, during the final eruptive episode, there is evidence of shallow subglacial and ice-confined eruptive environments.

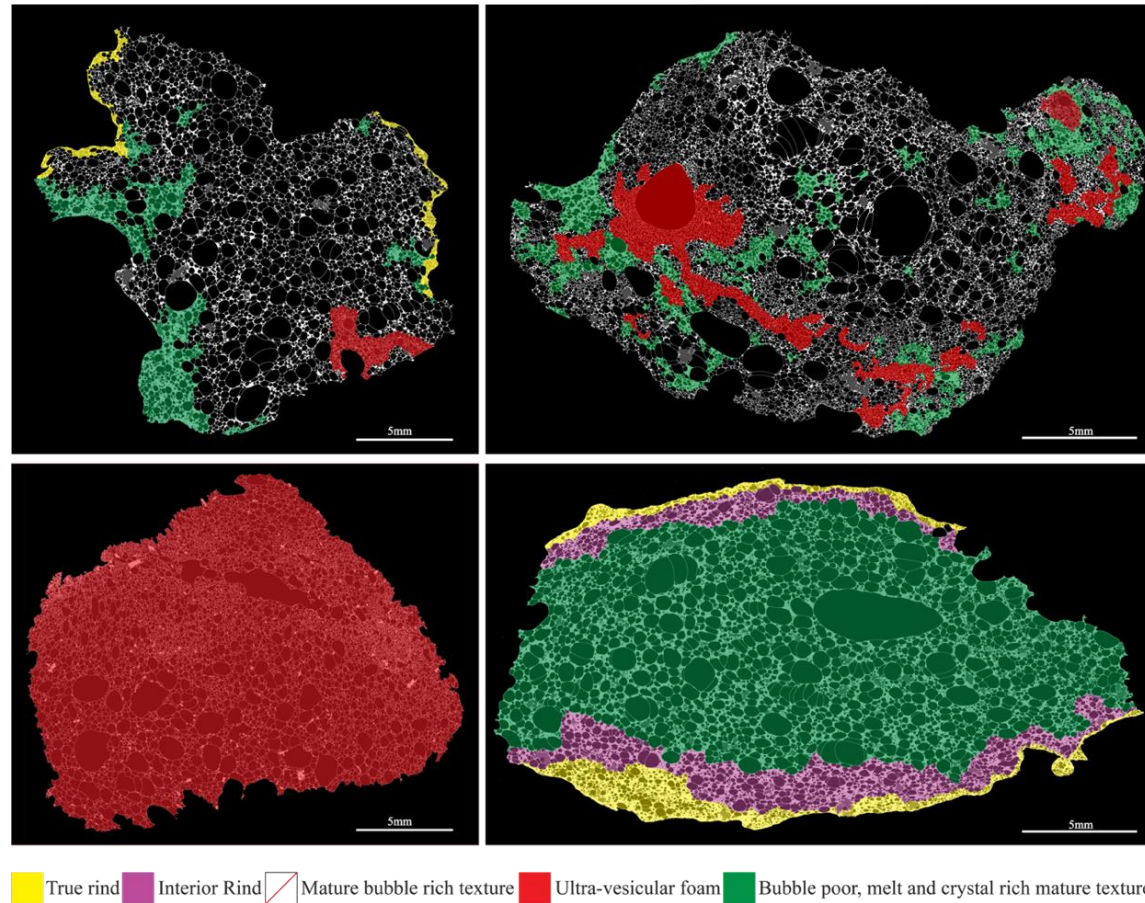


Figure 7. 8: Textural maps of domain proportions in Laki 1783–84 CE pyroclasts. Textural maps corresponding to descriptions of: (A) The rind shown in yellow, (B) interior rind shown in pink, as well a mature interior texture domain types 1–3: (1) Mature melt (no colour) (2) Ultra-vesicular foam shown in red and (3) Very mature melt, bubble poor and crystal rich shown in green. M2 and M6 both have a clear quenched rind, but it is better developed in M6. The proportions of (2) and (3) evolve throughout the eruption from <20% in M2, <35% in M4, (2) makes up 100% of P3 but is absent in M6, instead M6 entirely consist of (3) at varying stages of maturity captured by the immature vesicle textures in the thick outer and inner rinds. M6 represent the waning phase of the eruption, which would result in lower fountaining heights and the clasts spending less time in a hot insulating environment which corresponds to a thicker true rind and the presence of an interior thick rind.

7. 3. 4 Quantitative textural analysis

Quantitative textural analysis has been carried out on (1) the rinds, where available, e.g., M2 and M6, (2) specific textural domains that were large enough to be isolated, e.g., the ultra-vesicular foam and mature textures in M4, and (3) whole clast textural data for comparison.

7. 3. 4. 1 VND

Both of the Laki rinds have a low vesicularity, calculated from the ImageJ thin-section data sets, which ranges from 55.1% M2 to 34.58% in the M6 clasts, approximately 30% lower than the density derived vesicularity calculated for the whole clasts in both cases (Table 7. 2). Vesicle number densities (VND or N_V) for the two analysed lapilli clast rinds from the Laki eruption are very similar: M2 $2.67 \times 10^3 \text{ mm}^{-3}$ and M6 $3.15 \times 10^3 \text{ mm}^{-2}$, despite the large difference in MER and intensity/explosivity, which decreased exponentially between the initial eruptive fissures (i.e., M2) and final fissure eruptive episodes (i.e., M6) (Thordarson and Self, 1993; Thordarson et al., 1996). When these values are melt-corrected, i.e., adjusted to account for the volume of vesicles in reference to the melt (N_V^m) the corresponding values are slightly higher at 5.93×10^3 (M2) and $4.54 \times 10^3 \text{ mm}^{-3}$ (M6) (Table 7. 2), with M2 now displaying the higher VND.

Whole-clast N_V values span nearly an order of magnitude in range from 2.03×10^3 – $1.17 \times 10^4 \text{ mm}^{-3}$, where the subglacial sample P3 defines the upper boundary with the highest vesicle number density compared to the magmatic clasts which have a tight range from 2.03×10^3 – $2.42 \times 10^3 \text{ mm}^{-3}$. When whole clast values are adjusted to N_V^m , the vesicle number density all values increase, although to different extents M2 increases markedly whereas the increase is only marginal for M6, the range between the clasts also increases by a further order of magnitude 7.63×10^3 – $1.02 \times 10^5 \text{ mm}^{-3}$ (Table 7. 2). All whole clasts VND values are higher than their associated outer rinds, if available. Two textures are isolated in the interior foam in the M4 clast: (1) the mature texture is similar to the M4 whole clast, at $6.30 \times 10^3 \text{ mm}^{-3}$,

whereas (2) the ultra-vesicular foam texture has an order of magnitude larger at $2.03 \times 10^4 \text{ mm}^{-3}$ and is the highest value N_V^m amongst the Laki clasts.

Table 7. 2:

Sample	Date Erupted	Days into eruption	Density (g/cm ³)	Vesicularity	Vg/Vl	N _A (mm ⁻²)	N _V (mm ⁻³)	N _V ^m (mm ⁻³)
M2 rind	14–15 June 1783	7	N/A	55.1	0.5894000	116	2.67E+03	5.93E+03
M2	14–15 June 1783	7	0.412	85.5	5.8965517	53	2.42+E03	1.67E+04
M2 (interior)	14–15 June 1783	7	N/A		5.3071527			1.08E+04
M4 ultrafoam	25 August–1 Sept	79	N/A	77.34	3.4130627	244	4.61E+03	2.03E+04
M4 mature	25 August–1 Sept	79	N/A	67.98	2.1230481	92	2.02E+03	6.30E+03
M4	25 August–1 Sept	79	0.70	73.4	2.7593985	107	2.03E+03	7.63E+03
P3 (subglacial)	24 Oct	141	0.32	88.5	7.6956522	305	1.17E+04	1.02E+05
M6 rind	>24 Oct	>141	N/A	34.58	0.5285845	72	3.15E+03	4.54E+03
M6	>24 Oct	>141	0.9	68.2	2.1446541	59	2.74E+03	8.62E+03
M6 (interior)	>24 Oct	>141	N/A		1.6160696			4.08E+03

Table 7. 2: Vesicle number density data for selected rinds, whole clasts and interiors from Laki 1783–84 CE. See supplementary data, appendix A: Laki Clasts, for the complete data set.

7. 3. 4. 2 VVD

Vesicle volume distributions (VVD) (Figure 7. 9) show the volume fractions of a population within geometric size bins for the Laki clasts and, where available, accompanying rind pairs. Both the M2 and M6 Laki rinds have a unimodal distribution, with a slight negative skew and fine tails.

In the M2 rind >90 % of the void space is accounted for by vesicles with equivalent diameters from approximately 0.035–0.35 mm, with a modal peak between 0.15–0.25 mm. The M2 rind has a tight, markedly negative skewed distribution, around a 25 % volume fraction modal peak, a fine tail, with an abrupt drop off in large vesicle sizes when compared to the M6 rind. The M6 rind spans a greater range from 0.06–0.9 mm, with a modal peak at 0.15–0.25 mm, and whilst this is the same size bin as for M2 it has more subdued peak; with a small volume fraction, <10 %, attributed to the mode. This diverse vesicle population range occurs in the sample with the thickest rind (Figures 7. 5–7. 8) and creates a near-normal population which is very common in growth-driven size distributions; with a fine tail which is reduced compared to M2 and not extending into smaller vesicle sizes <0.01 mm. This is indicative of a vesicle collapse signature (Shea et al., 2010).

The Laki whole clasts span much larger ranges, which is expected for textures modified by post-fragmentation. In all cases, the whole clast volume distributions are offset from their rinds by 3–4 order of magnitude. The Laki whole clasts display both unimodal and weakly bimodal vesicle volume distributions, M2 and M6 are unimodal, and M4 and P3 are weakly bimodal. Despite its internal textural heterogeneity M2 is unimodal with a skewness close to zero, with an extended fine tail compared to its rind. M6, which is internally homogeneous, has a unimodal population that is negatively skewed, driven by the presence of a thick rind and inner rind M6 displaying a ripening of the mature texture through coalescence. The M4 whole sample, which is internally heterogeneous to a markedly greater extent than M2, is weakly bimodal, with a coarse tail and a slight fine tail; the modal peak, for the smaller bubble fraction, is well defined. P3, like M6, is internally texturally homogeneous. P3 consists solely of an ultra-vesicular foam at varying stages of maturity and displays a weakly bimodal VVD trend; with a more pronounced peak

than M6 in the smaller bubble size fractions, which can be attributed to the large areas of tightly packed small vesicles that exist within P3 around large scale internal fabric collapse features. These develop due to the opening of a permeable network via extensive coalescence and outgassing. The unimodality of these distributions is surprising given the internal textural heterogeneity of the samples, which contain starkly different vesicle textural domains.

Domains showing two textures were isolated in M4, the very mature foam and the ultra-vesicular foam. The very mature foam vesicles display a positive skew and have a broadly unimodal distribution with a slight fine tail. The dominance of large vesicles in this population indicates a very mature population. The ultra-foam vesicle distribution is tightly unimodal, with a very reduced fine tail producing a distribution very similar to the M2 rind. The modal peak from the M4 ultra-vesicular foam occurs at a smaller equivalent diameter, 0.22 mm, than for the mature texture, 0.3 mm, and is much more pronounced.

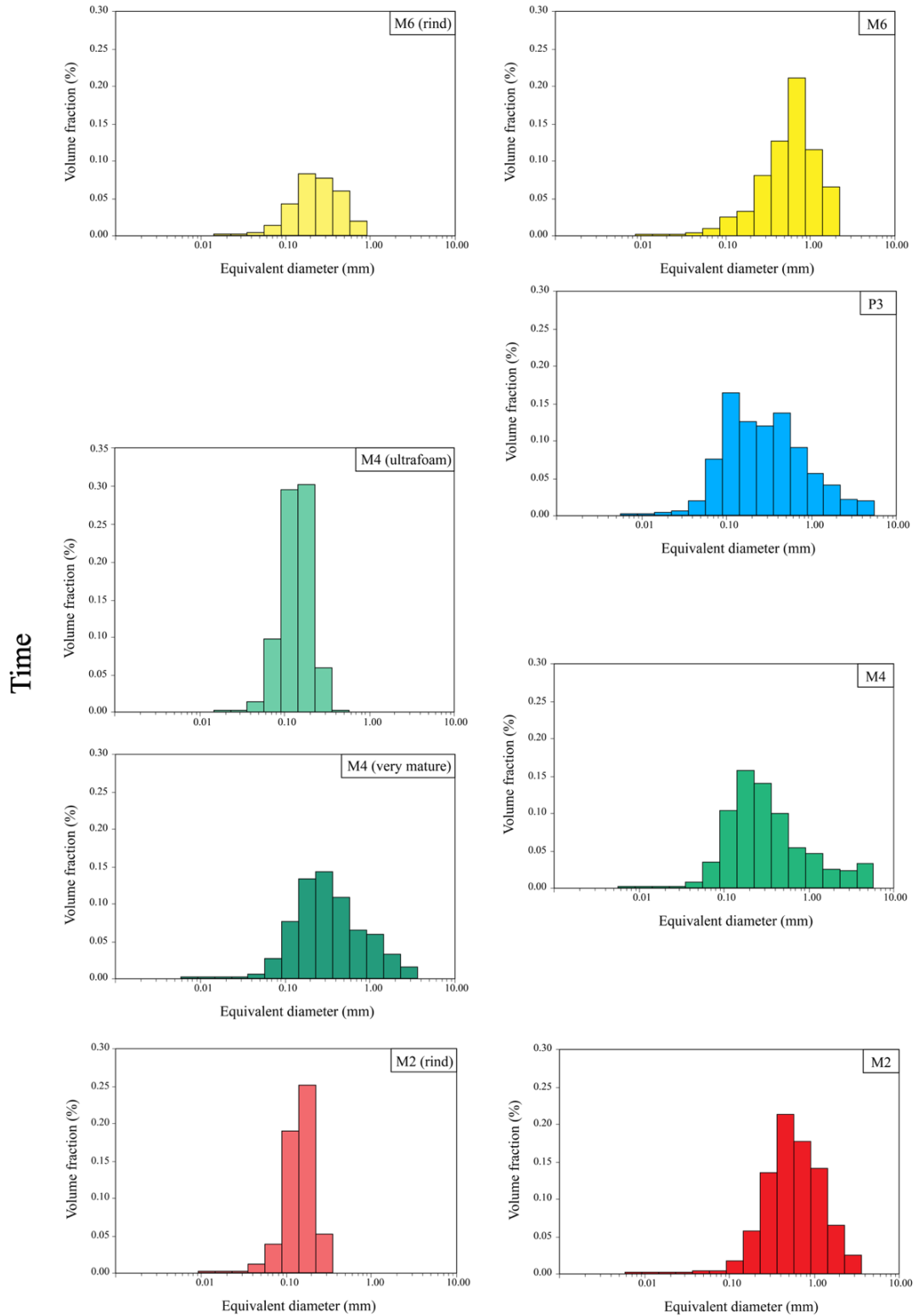


Figure 7. 9: Vesicle volume distributions from the Laki 1783–84 CE pyroclasts. Vesicle volume distributions show the volume fraction (%) weighted by their vesicle size bins (mm). The whole clast data is plotted on the right side of the figure with the corresponding rinds on the left. The data is present from the bottom upwards in a would-be stratigraphic time sequence.

7. 3. 4. 3 CVVD

Cumulative vesicle by volume distribution vs equivalent vesicle diameter plots (Figure 7. 10) produces sigmoid curves, which enable more direct comparisons than the VVD plots between different vesicle populations within a single pyroclast, as well as from time-series samples from the same eruption. Both of the Laki rinds produce sigmoidal curves; however, unlike the Holuhraun clast rinds, they do not display a similar curve shape.

Rinds: The M2 rind, which represents the melt erupted during a higher intensity eruptive fissure opening phase in the Laki eruption, has a much steeper sigmoid curve gradient than M6, driven by >80% of the cumulative vesicle volume is represented by a narrow vesicle size distribution from 0.09–0.2 mm. Steep and smooth sigmoid curves can indicate that this texture is generated by one phase of nucleation and growth, the rind in M2 does not include an embryonic version of either the ultra-foam or very mature texture and only captures the mature texture, so this may well be the case. The M6 rind, which represents the melt erupted during the closing stages of the final fissure opening episode, which was also the lowest eruptive intensity phase, has a much shallower and smooth, sigmoid curve. Greater than 80% of the cumulative vesicle volume is represented by a broad vesicle size distribution from 0.10–0.60 mm. The shallow M6 sigmoid curve also displays several prominent changes in slope, in the larger equivalent vesicle diameter sizes, matching the wide range in vesicle sizes recorded in the VVD distributions. Unlike M2, the M6 clast comprises solely of the very mature domain texture and therefore experienced the same shallow conduit history, captured in varying stages of maturity from the rind to the interior. Therefore, these changes in the slope of the CVVD curve indicate that this vesicle population in the M6 rind underwent coalescence, creating these larger populations.

Whole clasts: The M2 and M6 whole clast sigmoid curves have a markedly shallower gradient compared to their rinds, which is offset towards larger equivalent diameter vesicle size bins reflecting the contrasting immature vesicle population in the rinds and the mature, heterogeneous, interior vesicle textures. The mature interior

domains have undergone further post-fragmentation modification via growth, coalescence and further, although limited, nucleation.

Unlike Holuhraun, two analysed pyroclasts from the Laki eruption are texturally homogeneous, containing only one type of the domains present in other texturally heterogeneous clasts; as a result, the CVVD curves from these samples can be used to display the post-fragmentation evolution of a single texture. The M6 whole clast curve shows a small, distinct, bulge below the 20 percentile in the smaller vesicle size distributions, from 0.08–0.10 mm, associated with the presence of thicker outer and inner rinds in this clast. Whilst the M6 whole clast is offset to larger vesicle sizes, it maintains a similar gradient minus the bulges. Whilst this whole clast is offset towards larger bubble size bins than the M6 rind; the curves have a similar morphology and gradient, which is expected from growth-driven expansion of an existing more texturally homogeneous vesicle population. This can be seen clearly when comparing the M6 rind to the other Laki pyroclasts, such as M2, which displays a marked change in slope in the whole clast CVVD compared to its rind.

P3, which consists entirely of the ultra-vesicular foam texture (domain type 2; also see Chapter 6), spans the largest range in vesicle sizes of all the analysed clasts from 0.01–4.0 mm, producing a shallow slope sigmoid curve. P3 contains a higher proportion of smaller vesicles than either of the analysed rinds and whole clast samples. Its curve shows a notable early rise between 0.02–0.03 mm when compared to all the other analysed rinds, interior textures and whole clasts. P3 also displays notable changes in slope below the 50 percentile, at 0.10 mm, associated with distinct areas within the clast which record variations in ultra-vesicular foam maturity in response to post-fragmentation expansion.

The M4 whole clast curve has a larger range than M2 and M6, but not as large as P3, and displays clear evidence of multiple coalescence events, recorded by a shallowing off slope indicating an increase in the larger equivalent diameter vesicle populations above the 70 percentile.

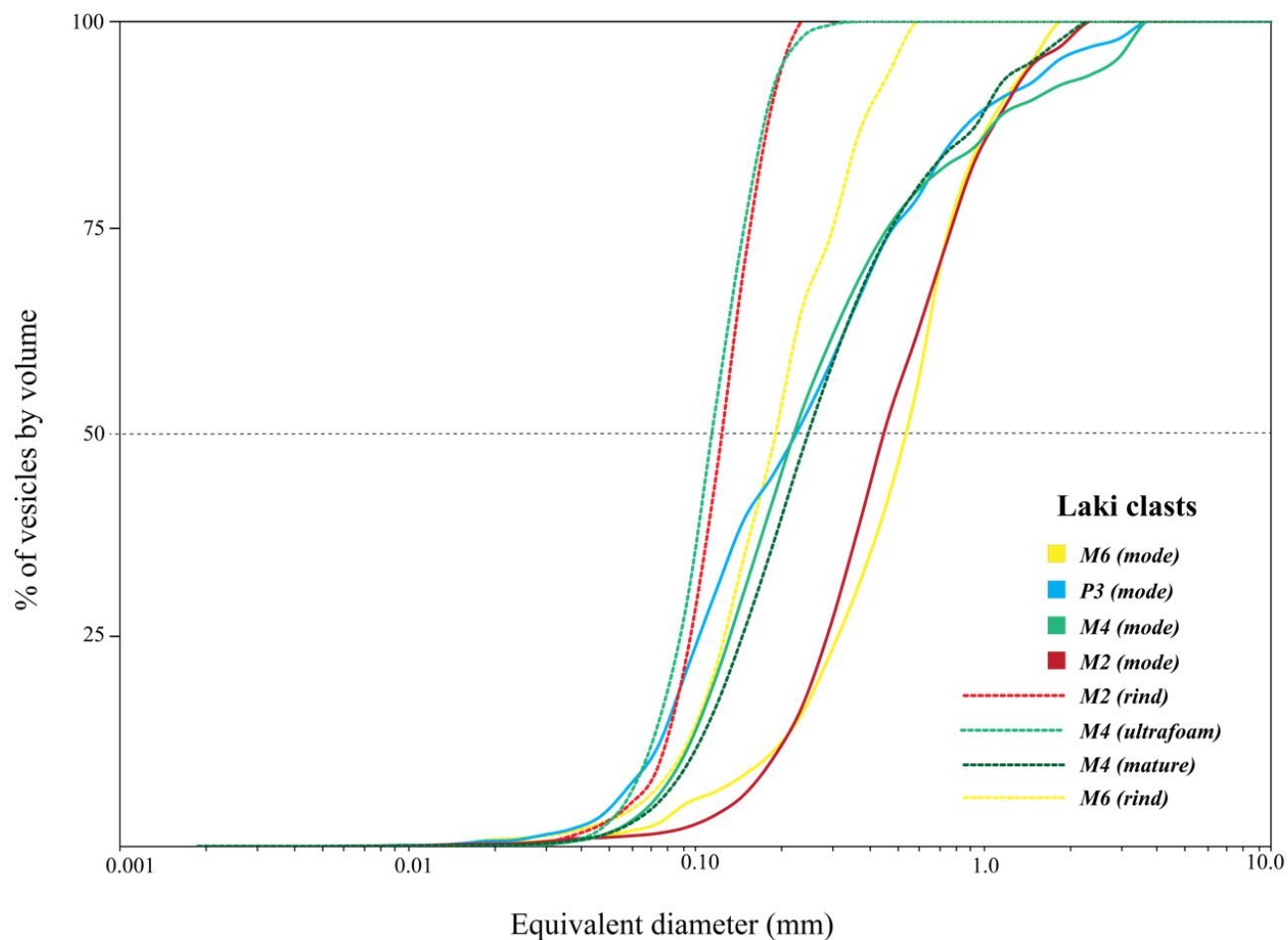


Figure 7. 10: Cumulative vesicle by volume distribution of textural analysis of Laki 1783–84 CE pyroclasts. Cumulative vesicle by volume distribution vs equivalent vesicle diameter plots produce curves that enable better direct comparisons between samples than VVD histograms. Here the rind data is plotted as dashed lines and the whole clasts as continuous lines of the same colour as the rinds. The M2 rind and M4 ultra-vesicular foam display a very similar curve shape and vesicle size range. The M6 rind is displaced to large vesicle size bins akin to the M4 mature texture for the bottom 50% of the sample but displays a steeper gradient than both of the M4 textures. Despite their textural differences, the M2 and M6 whole clasts display a very similar curve morphology, with a bulge at <10% for the M6 clast, probably due to the presence of a well-developed rind and interior rind, which drives up the proportions of smaller vesicles.

Isolated textures in heterogeneous clasts: Interestingly, the M4 ultra-vesicular foam curve replicates the M2 rind volume distribution with a very steep curve and minor offsets at the top and bottom of the curve. As the hypothesis for the formation of this texture is a sudden late nucleation event driven by volatile supersaturation, this form of curve is to be expected. The M4 ultra-vesicular foam contains higher proportions of the smallest and largest vesicles compared to the M2 rind populations; this is due to the extensive post-fragmentation expansion of this population in the interior of the clast.

M4 mature domain vesicle volume distributions are spread over a larger range in vesicle sizes in these populations and offset towards smaller vesicle sizes at the base of the curve, much like the M4 whole clast distribution. The M4 mature texture in isolation also displays changes in slope above the 75 percentile, indicating that there is evidence of coalescence in these larger vesicle size populations.

7. 3. 5 Glass geochemistry

To ascertain if these different textural end-members were linked to geochemical variations within the melts mingling in the shallow conduit throughout the Laki eruption, groundmass glass from all domain types was analysed, by EMP, from all of the texturally analysed clasts: M2, M4, P3 and M6. The different textural domains, that were mapped out and analysed in the quantitative and qualitative results sections, were targeted for analysis of major element and volatile element concentrations, e.g., sulfur (S) and chlorine (Cl). For each clast, 14–20 separate points were analysed for the rind, and between 10–40 separate points for the inner rind and each of the interior domains, averages are reported in Table 7. 3 (see supplementary material, appendix B: Laki EMPA bubble data, for the full data set).

Eruptive clasts from M2, M4 and P3 display the same major element geochemistry within statistical errors. Notably, whilst the major element concentrations are consistent throughout most of the different domains in the magmatic clasts there are differences in the S concentrations present in distinct domains. The ultra-vesicular foam (domain type 2, Figure 7. 8) displays markedly lower S concentrations than the

other analysed domains in both the M2 and M4 samples, which is relatively similar to the observations of its counterpart analysed in the Holuhraun clasts.

The difference in S concentration between the ultra-vesicular foam and the majority of other domains is approximately 100 ppm in the M2 clast, and >50 ppm in the M4 clast. Whilst the relative offset between the ultra-vesicular foam and other textural domains is different, in the Laki vs Holuhraun clasts, there is a commonality of the ultra-vesicular foam in both eruptions in terms of volatile content and VSD and VND. This suggests they were affected by similar shallow conduit processes: a melt package is driven to volatile supersaturation, associated with rapid ascent, relative to the other melt packages which form the other textures, triggering a late bursting nucleation event. An exception to this is a very low S concentration in an isolated pocket of mature vesicle texture referred to in Table 7. 3 as Mature (2), which is approximately 70 ppm lower than the ultra-vesicular foam and 150 ppm lower than the outer rind, mature and very mature domains. It is texturally unclear whether this is transitional or somehow related to the neighbouring ultra-vesicular foam.

Importantly, the magmatic to phreatomagmatic samples display a stark contrast in S concentration, with the phreatomagmatic, P3 clast, containing approximately 150–200 ppm higher S values in the analysed glass in most domains compared to the magmatic samples. However, P3 is mapped texturally as entirely ultra-vesicular foam (domain type 2; Figure 7. 8), which is, as mentioned previously, relatively more degassed than other domains of the clast. Therefore, the relative difference between P3 and magmatic ultra-vesicular foam S concentrations is more in the region of 300 ppm. The consistent discrepancy between the S concentration in magmatic and phreatomagmatic samples suggests that this shallow sub-glacially erupted sample has either been quenched before it could fully degas, via contact with external glacial melt water, or volatile loss was suppressed due to a higher overburden pressure from the glacier. Major element concentrations in the M6 clast indicate that the melt erupted during the closing phase of the final fissure opening event of the Laki eruption was slightly more evolved than previously erupted material during the same fissure activity, i.e., P3 or indeed earlier on in the eruption from different fissures. This does not correspond to an increase in S concentration;

instead, it displays S values which are similar to both M2 and M4 rinds and mature texture (domain type 1, Figure 7. 8). The M6 S values are extremely similar from the outer and inner rind to the interior of the clast; this extreme homogeneity is probably due to the clast consisting entirely of a single texture, the very mature texture (domain type 3, Figure 7. 8).

Table 7. 3: Basaltic glass analysis summary for all Laki clasts and their separate interior domains or concentric variations.

Clast	Texture	SiO ₂	TiO ₂	Al ₂ O ₃	FeO	MnO	MgO	CaO	Na ₂ O	K ₂ O	P ₂ O ₅	Totals	S ppm
M2	Rind	49.9	2.97	13.01	14.12	0.22	5.41	9.72	2.71	0.45	0.34	98.96	470
	Mature	49.8	2.97	13.13	14.08	0.22	5.29	9.78	2.83	0.47	0.33	98.85	476
	Very Mature	49.7	2.96	13.13	14.11	0.23	5.31	9.80	2.80	0.46	0.33	98.87	442
	Ultra-vesicular foam	50.0	2.96	13.09	13.92	0.23	5.29	9.78	2.83	0.45	0.35	98.89	357
M4	Potential Rind	49.9	3.06	12.68	14.46	0.23	5.20	9.56	2.77	0.48	0.36	98.83	456
	Mature	49.7	3.03	12.67	14.13	0.22	5.25	9.69	2.80	0.49	0.35	98.44	345
	Mature (2)	49.7	3.08	12.78	14.58	0.27	5.16	9.59	2.81	0.48	0.34	98.79	195
	Very Mature	49.7	3.07	12.75	14.45	0.23	5.20	9.61	2.82	0.48	0.35	98.72	442
	Ultra-vesicular foam	49.9	3.07	12.68	14.32	0.25	5.20	9.56	2.74	0.48	0.35	98.66	272
	Transitional	49.7	3.03	12.77	14.21	0.22	5.20	9.59	2.77	0.48	0.34	98.36	403
P3	Ultra-vesicular foam expanded	49.8	2.92	13.13	13.99	0.21	5.28	9.78	2.79	0.45	0.32	98.63	594
	Ultra-vesicular foam collapsed	50.0	2.95	13.15	14.04	0.22	5.26	9.79	2.85	0.46	0.34	99.09	647
M6	Rind	50.2	3.19	12.69	14.69	0.23	5.04	9.73	2.34	0.49	0.37	98.99	463
	Inner Rind	50.1	3.18	12.70	14.72	0.24	5.09	9.76	2.60	0.49	0.36	99.22	457
	Very Mature	50.2	3.21	12.70	15.04	0.24	5.10	9.78	2.36	0.50	0.35	99.43	465

Table 7. 3: EMPA groundmass glass geochemistry of analysed domains in the Laki 1783–84 CE pyroclasts. EMPA basaltic glass analysis of Laki pyroclasts. All data is an average of several analyses; see Supplementary data for the full data set (appendix B: Laki EMPA bubble data). All Major oxide data is reported in weight percent, with totals as the percentage sum of all oxides and volatiles measured. S, measured as parts per million, is the only volatile reported here; see supplementary data for full S data set. Cl elemental errors are too high to be presented in this data set. All analysis with a high elemental S error have been discarded.

7. 3. 8 Temporal changes in textures throughout the eruption

Similar to the Holuhraun pyroclasts, textural observations of the Laki pyroclasts (Figure 7. 8) clearly outline the heterogeneity in 2 out of the 4 samples. These clasts contain several domains with contrasting shallow conduit histories that have mingled at a relatively late stage prior to final fragmentation, thus recording three differing vesiculation histories within one clast. As with the Holuhraun samples, these domains are preserved despite post-fragmentation modification of vesicle populations; distinct primary textures have been accentuated and highlighted by post-fragmentation expansion. Unlike the Holuhraun pyroclasts, two Laki clasts: P3 and M6, have a texturally homogeneous interior. The clasts in question record this texture, preserved at different stages of maturity, due to post-fragmentation expansion, and thus even they are not strictly homogeneous throughout in terms of the size of the population. The dominance of certain distinct textural domains, or their proportions, vary temporally throughout the eruption, corresponding to trends in eruptive activity and lack thereof, i.e., changes in MER as well as new fissure opening phases and changes in eruptive environment. Whilst the degree of textural diversity present in the Laki pyroclasts and how this varies throughout the different fissure opening episodes in the Laki eruption, will be addressed in full in the discussion section; a brief numerical overview is presented below:

Immature vesicle textures (A and B, Figures 7. 7–7. 8) are only observed in two of the analysed clasts: (1) in M2, the immature texture form a very thin unbroken outer rind margin in two areas of the outer clast surface which represents <5 % of the clast area; (2) in M6, the immature texture is represented by both a thick outer rind which is continuous around all unbroken outer surfaces, as well as an extensive inner rind. The M6 sample contains the only example of an inner rind in the Laki clasts, unlike in Holuhraun, where it occurs in several clasts from different samples throughout the eruption. In M6 these make up approximately 15–20 % of the clast, which subdivides into approximately <8 % rind and 5–10 % inner rind. The M6 clast represents the very waning stages of the Laki eruption, with lower intensity fountaining. The interior of the M6 clast reached the glass transition faster than in the higher intensity eruptive phase M2 sample, as the low intensity fountaining in

M6 limits the time this clast experienced thermal insulation. Immature vesicle textures are absent in M4 and P3.

Temporally through the Laki eruption, over different fissure opening episodes, there are fluctuations in the proportions of contrasting textural domains, which evolved from melts with contrasting vesiculation histories (differing nucleation and growth rates), and subsequently mingled with the more dominant melt prior to fragmentation (Figures 7. 5–7. 8, 7. 14 and 7. 15). The Laki pyroclasts from earlier eruptive phases, M2 and M4, are dominated by a single vesicle texture (domain type 1, Figure 7. 8, see supplementary material, appendix C), which is produced by a common early shallow conduit history for the majority of the melt present in these clasts prior to fragmentation. In M2, this mature texture (domain type 1) makes up 80 % of the clast, which decreases to 70 % in M4. The difference in textural proportions from fissure opening phase 2, which produced M2, and fissure opening phase 6, which produced M4, is driven by the increase in the presence of the ultra-vesicular foam texture (domain type 2) from <5 % to 10 % of the sample (Figure 7. 8). This occurs alongside an increase of the very mature vesicle texture (domain type 3) from <10 % to 10–15 %.

The Laki pyroclasts from fissure 10, the final phase of Laki eruptive activity, which moves from a shallow subglacial eruptive environment to an ice-confined environment, do not display evidence of mingling of different melt domains; instead, they are texturally homogeneous. Critically, they do have homogeneous textures; P3 consists entirely of the ultra-vesicular foam (domain type 2), and M6 consists entirely of the very mature vesicle texture (domain type 3) (Figure 7. 8).

All magmatic clasts are achneliths with golden pumice interiors, changes in textural proportions in clast interiors in M2 and M4 not coupled by a variation in clast componentry or phenocryst populations (which sits at around 3 % for both of these samples). However, the phreatomagmatic P3 clasts do not have a hot gas fused outer film surface, and instead consists entirely of golden pumice and have a low phenocryst content of 0.5 %. The M6 clasts, like the other magmatic clasts, are achneliths with denser black basaltic pumice interiors; and display a slight increase in phenocryst content of 4.5 % but a marked increase in microlites which are visible in hand-sample with the naked eye.

7. 4 Interpretations and discussion

The bubble population present in the Laki rinds in the M2 and M6 clasts is the closest approximation of the melt textures present immediately prior to fragmentation at the most intense and least intense explosive phases of the Laki eruption during fissure opening phase 2 and 10, respectively.

No rinds were found in any of the P3 clasts; all of them have broken, none-fluidal, edges due to the thermally granulating effects of magma-water interactions (Moreland et al., 2019). As a result, any early-formed rind disintegrated when the melt from P3 interacted with external water during this shallow sub-glacial eruptive phase. Despite being magmatic, not enough rind exists in the M4 modal clast for separate statistical analysis either; as a result, no information could be extracted for the properties of the melt immediately prior to fragmentation in the shallow conduit for either of these phases.

7. 4. 1 Vesicle number density (VND) and variations in mass eruption rate (MER)

Plots of clast N_V^m against time-averaged mass discharge rate are often used as a rough proxy for eruptive intensity (in silicic samples), but this is complicated for basaltic, point-sourced, fissure events as the exact volume erupted from a given fissure geometry over a known period of time needs to be used. Episodic waxing and waning changes in MER further complicate this, as a result it is difficult to achieve anything more than an approximate estimate for fissure eruptions; the quality of which is even worse for relatively undocumented earlier historic events or for pre-historic eruptions, where the erupted patterns are unconstrained.

For the isolated point-source Laki clasts, there is no large discrepancy between the Holuhraun whole clast or the Laki magmatic whole clast samples, this also holds true for the rinds with the eruptions both displaying very similar N_V^m values (Figure 7. 11). The similarity of the Laki and Holuhraun clast N_V^m , despite Holuhraun representing the weaker intensity explosivity end-member for FL eruptions and Laki representing a high discharge, sub-Plinian intensity, event, cause both eruption N_V^m

data sets to plot in a very similar space to moderate–high fountaining events (Houghton et al., 2016) at Kīlauea Iki 1959 CE. The low N_V^m values for the Laki eruption are at odds with historical documentation in Eldrít suggesting sub-Plinian intensity fountaining activity, which has been confirmed by detailed isopach maps (Thordarson and Self 1993; Thordarson et al., 2003a), is further highlighted when comparing these samples to sub-Plinian basaltic fissure pyroclasts from the Eldgjá 939 CE eruption (Figure 7. 11). Whilst the Eldgjá data set (Moreland et al., 2019) does not separate clasts for time-averaged discharge point-source vents for different phases of the eruptions, due to the lack of detailed contemporary accounts, the data from this eruption more clearly displays a supportive trend for the coupled higher N_V^m and higher intensity hypothesis in basaltic clasts than the Laki data set. This suggests that in the Laki eruption, other fragmentation criteria such as inertia, stress and strain and larger bubbles not captured and recorded in pyroclasts are potentially playing a more dominant role in the Laki magma fragmentation than during the Eldgjá or Holuhraun events which have more typical N_V^m values for their time-averaged discharge rate.

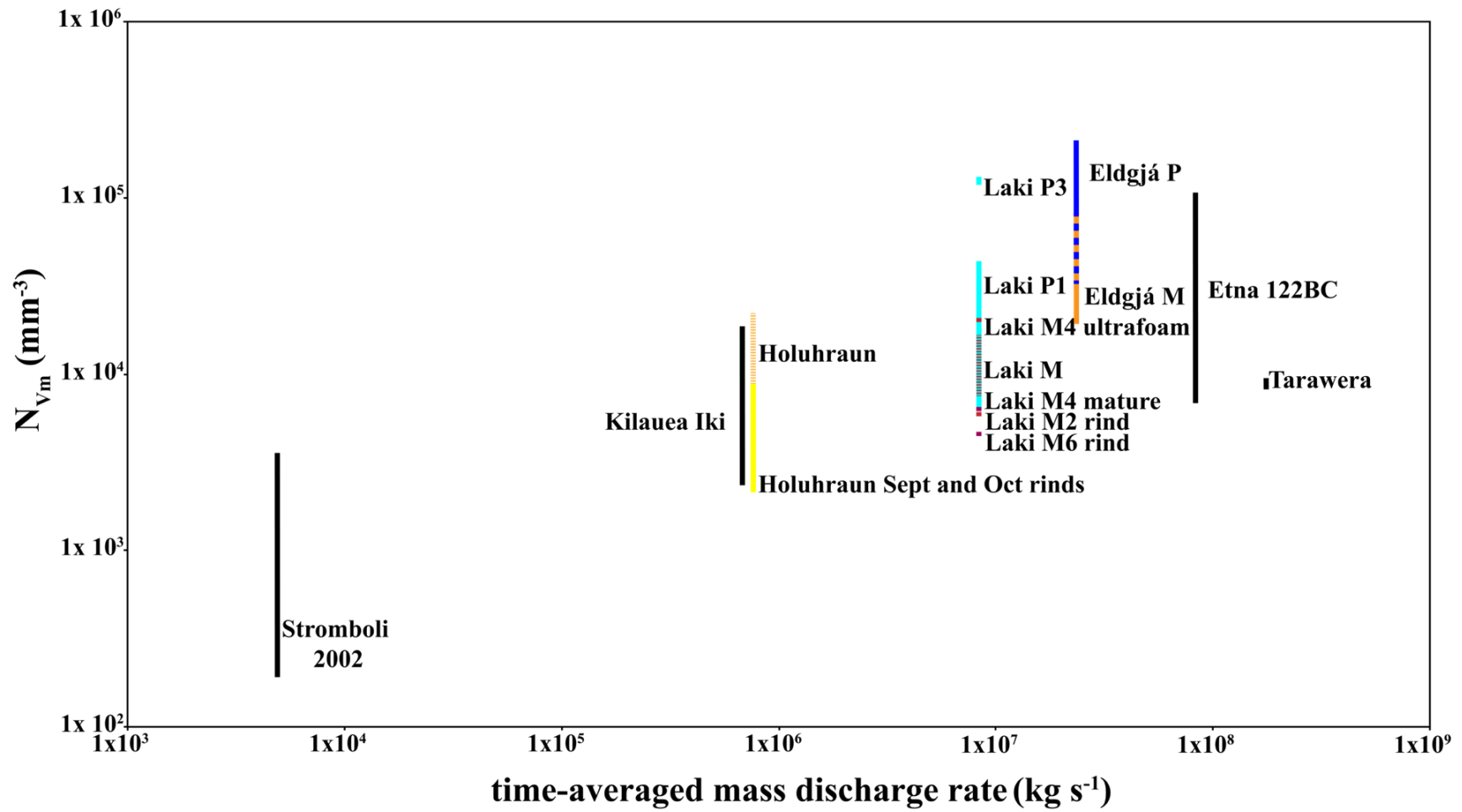


Figure 7. 11: Time-averaged mass discharge rate against vesicle number density for basaltic fissure eruptions. A comparison plot using point source discharge rates for Laki and Holuhraun and comparing the relative differences in N_{v^m} (mm^{-3}) which can be used as a proxy for eruptive intensity for certain events

A decrease in N_V^m between the M2 rind and the M6 rinds is clearly observed, which agrees with both the intensities inferred from the deposits and with the contemporary accounts, which indicate high-intensity phases during the first few months of the event (Thordarson and Self 1993, Thordarson et al., 1996, 2003a; Thordarson, 2003). Both P1 (Decker, 2017), the isolated M4 ultra-vesicular foam and P3 have elevated N_V^m values above the magmatic rinds and whole clasts. P1 is a heterogeneous textured clast and does not follow the same analysis undertaken in this study (carried out to eliminate textural bias), and as such, will not be considered further as the data set is skewed.

P3 displays the highest N_V^m values compared to any other Laki samples and consists entirely of the ultra-vesicular foam texture. This suggests that this phase was a high-intensity explosive phase formed by a very vesicular foam that interacted with a shallow overlying glacier tongue and external glacial meltwater (see Chapter 5). The activity captured by P3, for which there are no previous studies and limited contemporary documentation where it was initially interpreted as an explosive episode at the Grímsvötn central volcano (see Chapter 5), created the largest unconfined crater on the Laki cone-row and was clearly an intense event.

7. 4. 2 V_G/V_L

The volume contributed by the smallest vesicles in the CVVD plots is negligible, and so even a large number of these bubbles will have a negligible impact on the volume-based size distribution of the population, thus poorly representing trends at smaller scales of the population. However, this can be rectified by plotting VND, unaffected by the aforementioned issues, against vesicle-to-melt ratio (Gardner et al., 1996) to identify trends across the population at all scales (Stovall et al., 2011, 2012) (Figure 7. 13).

The rinds of the Laki samples consistently display lower number densities, seen as moderately lower N_V (mm^{-3}) values, but when these values are referenced to the melt fraction (N_V^m) this distinction is more exaggerated. VND for silicic samples is used as a proxy for the degree of volatile saturation at nucleation (Mangan et al., 1993;

Toramaru, 1995; Mangan and Cashman, 1996), which was also applied successfully to crystal-rich basaltic Plinian events (Sable et al., 2006). However, previous studies of Hawaiian basaltic fountaining events of differing intensities (Stovall et al., 2012; Parcheta et al., 2013) (also see Chapter 6) found a discrepancy between the VND for the rind and interior of the clasts. This highlights that for lower viscosity eruptions the competing processes of early nucleation (increasing VND) and post-fragmentation coalescence (reducing VND) have to be deconvoluted for the interior of the clasts, and that the rinds are much more representative of the melt at fragmentation.

The decrease between VND of the rinds from M2 to M6 samples could be due to increased post-nucleation evolution via growth or coalescence, which is scaled to the melt's residence time in the shallow conduit (Mangan et al., 1993). To examine these competing processes, a plot of VND against vesicle-to-melt ratio (V_G/V_L) (Gardner et al., 1996) can be used to distinguish between processes (Figure 7. 13) as well as identify trends across populations at all scales for the whole clasts as it represents trends in the smaller populations better than the CVVD data sets due to smaller vesicles contributing a negligible volume resulting in a minimal impact to the CVVD. How the clasts as a whole plot in VND and V_G/V_L space will also distinguish which post-fragmentation processes have a dominant influence on the clasts.

The M2 and M6 rinds plot in very similar VND vs V_G/V_L space. M6 is shifted towards coalescence/outgassing driven by a lower N_V^m and V_G/V_L number relative to M2, or the M2 clast towards a greater role for nucleation/growth relative to M6 (Figure 7. 13). M6 could indicate longer residence times in the shallow conduit, which promotes coalescence (tens of seconds) rather than growth (seconds) (Mangan et al., 1993). The M6 clast captures the waning phases of the eruption with low intensity spatter activity feeding small capping lava flows. The shift towards a lower N_V^m number, from the vigorous M2 activity which created a Pele's-hair-rich tephra layer to the M6 samples, could mirror a decrease in mass eruption rate, and thus longer shallow conduit residence times of the melt in these waning phases, which would favour coalescence. However, the M6 rind is offset both down and left of M2 on a trajectory that indicates the influence of both coalescence and outgassing

(Figure 7. 13). This again agrees with a lower ascent/mass discharge rate allowing coalescence. This is confirmed by textural observations in the samples with the presence of bubble collapse features in both the P3 and M6 samples (Figures 7. 12).

Both of the whole clast size distributions when compared to the rinds are offset on a trajectory that indicates growth and nucleation has modified all internal textures post-fragmentation from their original rind values, increasing both the V_G/V_L as well as the N_V^m (Figure 7. 13). The latter observation is interesting as Stovall et al. (2011, 2012) and Parcheta et al. (2013) both observed decreasing N_V^m from the rind to the core for the clasts, not an increase. However, for M6, there is a much smaller offset between the rind and whole clast than when compared to M2; and there are two competing processes at play here, which could be responsible for the difference: (1) nucleation (N) and growth (G), and (2) coalescence (C) and outgassing (O). If (1) N+G is wholly responsible, the M6 sample appears to have been modified to a lesser extent by post-fragmentation overprinting potentially due to the presence of an extensive outer rind and addition of the inner rind in M6. (1) agrees with this clast representing the waning phases of activity. However, M6 also displays textural relicts of process (2) outgassing in the form of collapsed, elongate and distorted vesicles as well as a frozen run-away coalescence event texture in the clast interior (Figure 7. 12). These processes competing with (1) lower the N_V^m and V_G/V_L values causing the sample to backtrack, along the same trajectory it travelled along, closer to its rind value. The whole clast values for M2 are complicated by the texture diversity. This study has outlined the presence of mingled or banded textures in full in previous sections; it, therefore, follows this clast's textural diversity did not form in situ. Instead, it is the result of differing melts, with different ascent histories that have mingled prior to fragmentation. Therefore, the N_V^m and V_G/V_L values of the whole clast cannot be used to define a single point on a single path of vesiculation. This is not the case for M6, which only contains a very mature, bubble-poor, melt- and crystal-rich texture (domain type 3), which is present in rind, interior rind and interior domains.

The issue of mingling is also a concern for the M4 clast, whose V_G/V_L and N_V^m values are artificially created through 3 separate textures mingling: two distinct mature heterogeneous melts and an ultra-vesicular foam, all of which are then

modified through post-fragmentation expansion. Whilst evolutionary trends cannot be inferred from these separate textures, as they are unrelated, they are plotted on the V_G/V_L plot for reference in terms of proportions of each adding to the whole clast. From the whole sample, the mature textures are displaced from the whole sample towards outgassing/ coalescence and outgassing (C+O), and the ultra-vesicular foam is displaced towards nucleation/ growth and nucleation (N/G+N). This agrees with the textural observations of the sample with ultra-vesicular foam domains representing a burst of nucleation generating a tight size distribution. The mature melt itself has regions with very few bubbles and a lot of microlites, as well as highly coalesced textures with thick melt walls, which may reflect outgassing.

The pattern of increasing VND and V_G/V_L values from the rind to interior in the M2 and M6 Laki clasts follows the same trend of post fragmentation expansion as demonstrated for the majority of the Holuhraun samples (Figure 7. 13, Chapter 6). As with Holuhraun, this trend from the rind to interior is the opposite of that observed in the Kilauea Iki 1959 CE samples (Figure 7. 13) from episodes 1, 16 and 17 (Stovall et al. 2011, 2012) and the 1969 CE Mauna Ulu samples (Parcheta et al., 2013).

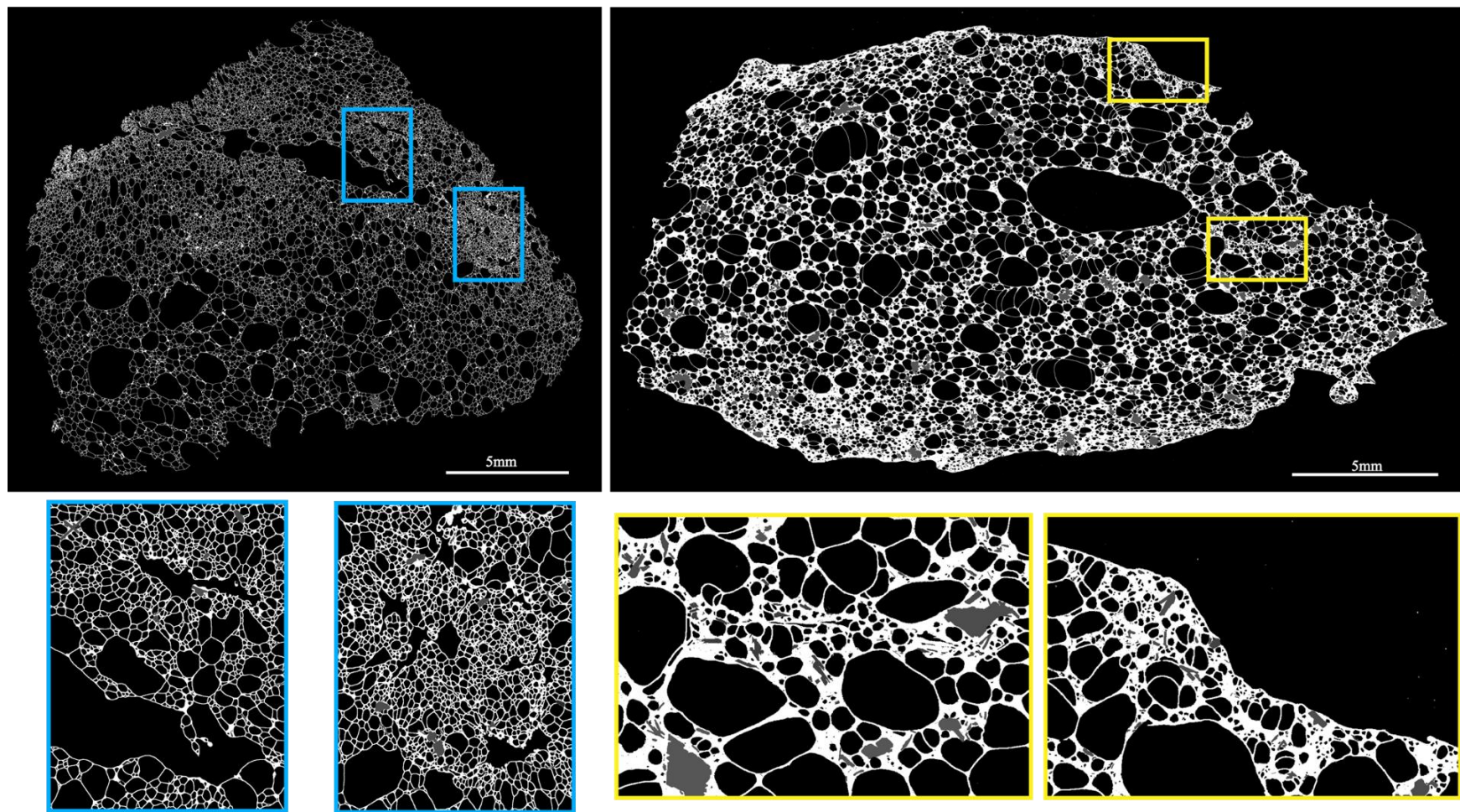


Figure 7. 12: SEM BSE images of collapse or outgassing features in P3 and M6 pyroclasts from Laki 1783–84 CE. Outgassing features in the last two phases of the Laki eruption: P3 (left-hand side, light blue) and M6 (right-hand side, yellow). In P3 large coalesced permeable networks have developed (top left), the foam around these areas shows scrunched and deformed collapse features (bottom right zoomed-in areas). In M6, these collapse features are less well defined in the mature melt texture, but deformed relicts of elongate vesicles are visible as rough linear features.

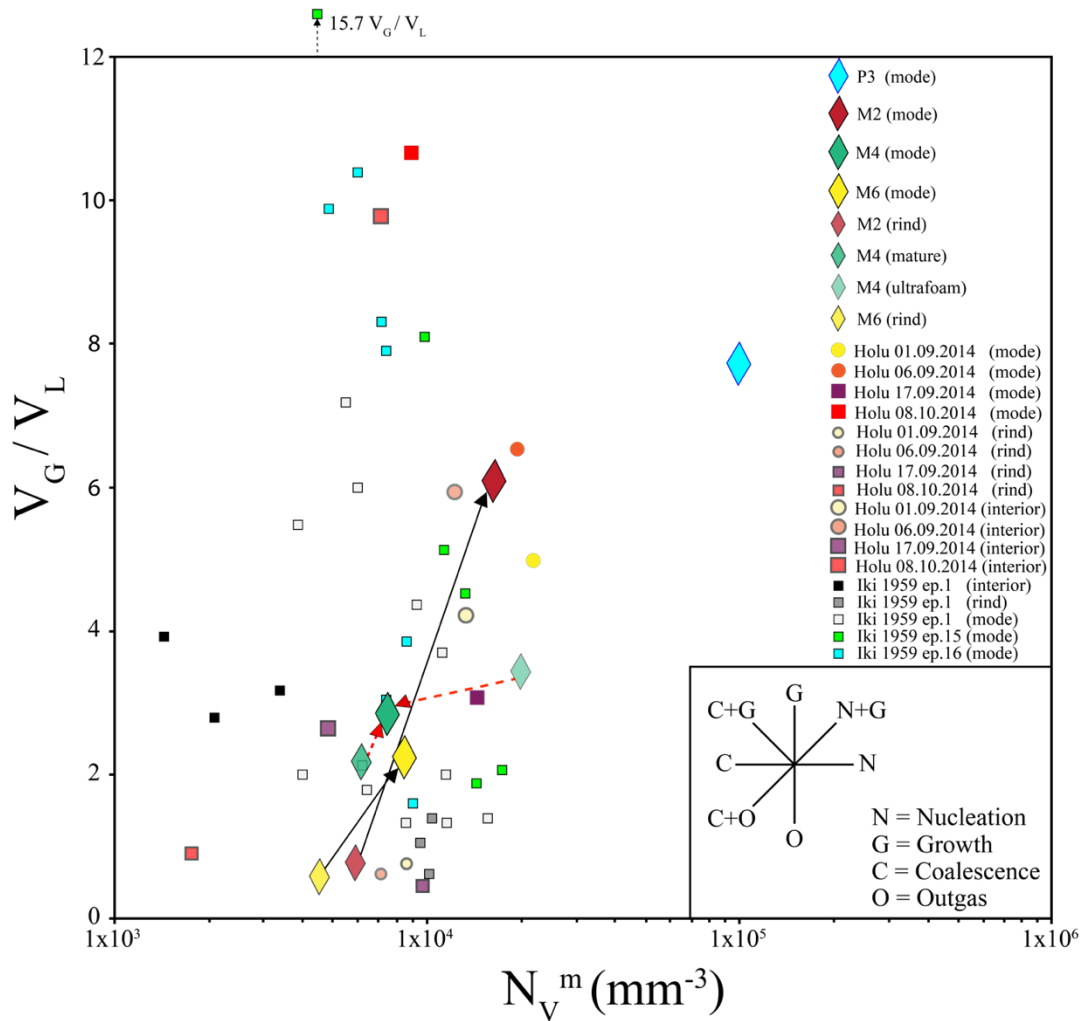


Figure 7. 13: VND against vesicle-to-melt-ratio of Laki pyroclasts. VND against vesicle-to-melt ratio (V_G/V_L) (Gardner et al., 1996) after Stovall et al. (2011, 2012). The compass inset refers to the different processes governing the trajectory line angle between the clast's rinds and whole clasts as well as between each other. This plot distinguishes the data sets from rinds (opaque symbols) from their whole clast counterparts (brightly coloured symbols of the same colour). Dark black lines indicate assumed trends from the rinds to the whole clasts. The dashed red lines for M4 ultra-vesicular foam and mature textures indicate a rough/potential mingling trajectory for these two post-fragmentation modified textures. The compass inset refers to a process governing the trajectory line angle between the clast's rinds and whole clasts as well as between each other. P3 has the highest VND and V_G/V_L number plotting high above any of the other rinds, whole clasts, or isolated interior textures. Kīlauea Iki 1959 CE pyroclast data from Stovall et al. (2011, 2012) for episodes 1, 15 and 16, as well as data from Holuhraun 2014–15 CE pyroclasts (Chapter 6) are plotted for reference.

P3, which represents shallow subglacial eruptive activity, has the highest V_G/V_L and N_V^m of all the Laki samples. Indeed, texturally it is more akin to reticulite, than subglacial phreatomagmatic samples, and clearly represents a fully vesiculated magmatic foam that has been quenched by glacial melt water after primary fragmentation (Chapter 5). This eruptive environment created a fine-ash-rich alternating sequence of pyroclastic density current and coeval fall deposits. Of particular interest is the textural homogeneity of this sample, P3 like M6, displays

only one of the four textures present in the Laki samples, but a different texture. P3 consists entirely of ultra-vesicular foam and seems to represent a conduit influx of homogeneous, actively vesiculating, melt during a sudden rapid ascent phase. This phase precedes the M6 activity, which caps the P3 sequence erupting from the same fissures, but the M6 melt is dominated by the mature melt- and crystal-rich texture with rounded coalesced bubbles. The offset of the M6 rind towards C+O, as well as its textural maturity, indicates slower ascent rates during the waning phase of the eruption, allowing for bubble wall relaxation and euhedral microlites to develop during a prolonged shallow conduit history of tens of seconds (Mangan et al., 1993).

7. 4. 3 Interpretations of observed temporal textural changes during the eruption

Models for temporal shifts in activity are constrained by the small number of clasts that could be analysed quantitatively. The earliest two clasts from fissure 2, M2, and fissure 6, M4, are dominated by mature vesicle textures (domain type 1), which represents a partially disequilibrium process texture. As the eruption progresses the very mature vesicle texture (domain type 3) increases in abundance, indicating equilibrium processes. The amount of ultra-vesicular foam (domain type 2) present in the samples corresponds to eruptive episodes which have experienced a long lag time between fissure opening phases. A lag time of 3 days between M1 and M2 results in a minor component of ultra-vesicular foam in the samples, whereas a lag time of 25 days between P2 and M4 results in a higher proportion of a banded and mingled ultra- vesicular foam present in the sample. A long lag time and a sudden new fissure opening event could provide the conditions needed in the shallow conduit for re-pressurisation and subsequent sudden decompression of the melt. As activity shuts down at a fissure, existing magma pathways to the surface become plugged with stagnating melt, creating higher overburden pressures for the magma still at depth; subsequently, a new fissure opens giving the magma feeding the Laki eruption a new pathway to the surface as it undergoes rapid decompression and rapid ascent rates. This would trigger a widespread homogeneous burst nucleation event, associated with volatile supersaturation, which could generate larger volumes of ultra-vesicular foam that mingled with slower-moving melt packages (Figures 7. 14 and 7. 15) in eruptive periods with a longer lag time between fissure opening phases.

P3, which erupts after the longest lag time, 6 weeks, consists only of ultra-vesicular foam representing a conduit flooding by melt undergoing a burst of late-stage bubble nucleation and rapid growth, which is interpreted as being due to high volatile supersaturation associated with the rapid ascent rates/decompression. This is immediately followed by eruptive activity M6, which caps the sequence, solely consisting of melt showing very mature textures (domain type 3), which display evidence of a cessation of bubble nucleation, relaxation of bubble walls and equilibrium crystallisation of microlites. This is the waning stages of the eruption. With lower mass-discharge rates and accompanying slower ascent rates, Laki was running out of the other melt types with a dwindling supply of fresh pulses of melt into the system. M6 clasts represent the end of the eruption, with only very mature texture (domain type 3) melt leftover in the conduit, which indicates slow ascent rates with ample bubble relaxation and crystallisation time. Bubble collapse textures suggest outgassing had begun prior to fragmentation in the shallow conduit during the eruptive phases, which emplaced P3 and M6 clasts.

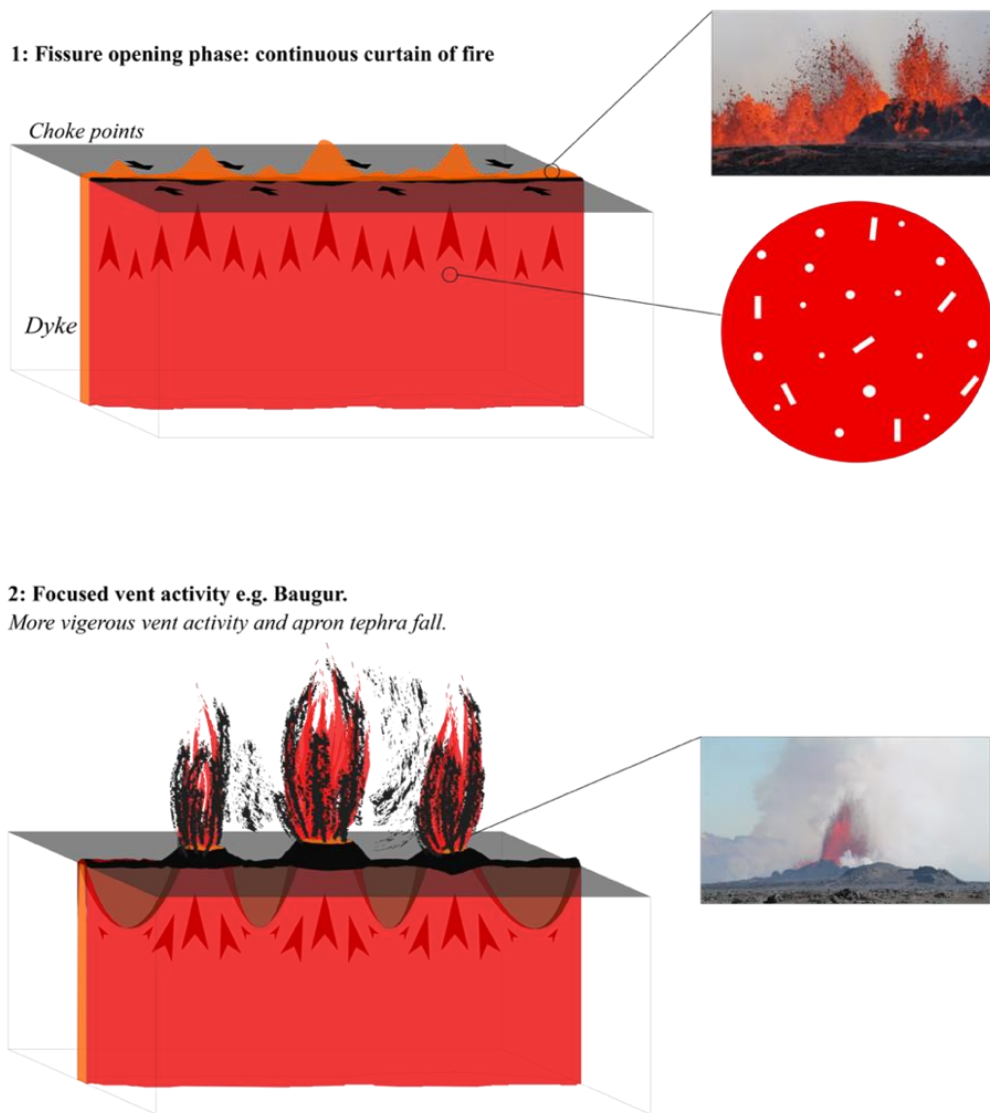
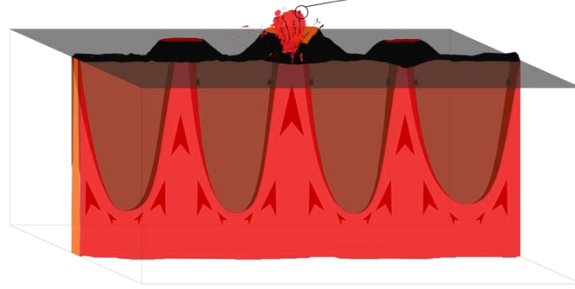


Figure 7. 14: (A) Conceptual model of the evolution of the shallow conduit system during the 1783–84 CE Laki eruption. A conceptual model for the evolution of the shallow conduit system during a single fissure opening phase in the Laki eruption. Images of examples of vent activity for the Holuhraun eruption are provided as insets. Simplified schematic diagrams of the Holuhraun dyke and vent activity are displayed on the left, alongside zoomed-in examples of the magma at depth in accompanying circles. The magma is initially all red with a small population of rounded bubbles and phenocrysts. Stage 1 of activity) A long curtain of lava fountaining across the entire newly opened eruptive fissure lasts for <1 hour in high-intensity fissure eruptions (Sumner et al., 1998). Stage 2) Waxing MER occurs in step with discrete vents developing along the fissure due to discrepancies in flow rate and conduit geometry, resulting in increased fountaining heights and an apron tephra fall phase.

3a) Decreasing supply



3b) Pulse of new melt mingles with more mature textures

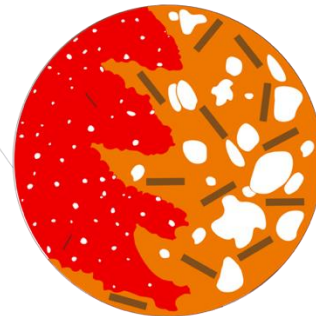
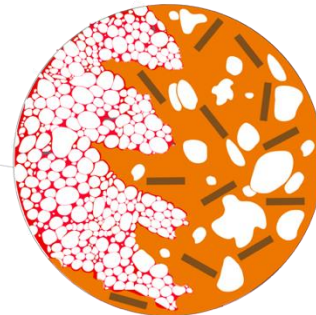
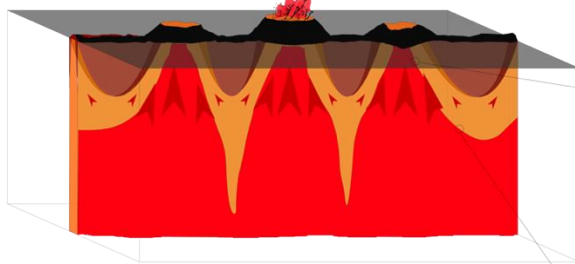


Figure 7. 15 (B) Conceptual model of the evolution of the shallow conduit system during the 1783–84 CE Laki eruption. Stage 3a) The magma supply decreases, and the eruptive activity changes according to changes in bubble bursting and development of a lava pond whose level eventually drops completely. Stage 3b) The eruptive activity experiences a pulse of resurgence with an increase in fountain height due to a pulse of new melt. This is shown in the circular inset magma sketches: A) an orange melt displaying a mature vesicle population which is also crystal-rich, rising slower through the shallow conduit with a pulse of fresh melt. B) red with a small vesicle population with a higher ascent rate that mingles with the mature melt. As this package rises, the fresh melt batch vesiculates homogeneously, creating a stiff ultra-vesicular foam that forms bands within the mature melt.

7. 5 Discussion

7. 5. 1 Correlating fountaining heights with N+G+C

The 1783–84 CE Laki eruption is the second-largest FL event in Icelandic history. It benefits from detailed contemporary accounts, which have provided unique opportunities to unravel the temporal evolution of the eruptive sequences. Alongside the style of eruptive activity, documented by contemporary accounts, variations in activity within individual fissure opening phases have been identified in the tephra deposits and lava flows the eruption emplaced. This has enabled the identification of peak periods of explosive activity, or periods of increased mass discharge rates, and the subsequent atmospheric and environmental impacts of such a sustained and polluting event.

VND is commonly used with silicic eruptions, as it scales to volatile supersaturation and thus ascent rate (Toramaru, 1995, 2006; Mourtada-Bonnefoi and Laporte, 1999, 2004), to approximate eruptive event explosivity. Previous studies focussing on basaltic Hawaiian activity of varying intensity (Stovall et al., 2011, 2012; Parcheta et al., 2013) found that the VND for rinds or rims of the clasts gave the best approximation for ascent rate. This was also identified for the Holuhraun 2014–15 CE, a low-intensity FL end-member event (Chapter 6), where rinds gave a better indication of the melt prior to fragmentation as the interior of the clasts had undergone similar post-fragmentation overprinting. Due to the vesicular nature of the rinds, fusing of the outer surface of the clast, by the hot gas stream in the fountains creating the achneliths, has only affected the very outer skin of the clast and not penetrated into the quenched rinds.

The M2 clast rind represents melt at fragmentation during the most explosive episode of Laki (Thordarson and Self, 1993; Thordarson et al., 2003a), and therefore most intensive phase of the entire Laki eruption. The M2 rind has a higher VND than the M6, rind which agrees with the weaker waning stages of the eruption that produced the M6 pyroclasts and fed the rheomorphic, spatter-fed, lava capping sequences (Chapter 5).

However, whilst contemporary accounts and previous studies (Thordarson et al., 1996; Thordarson and Self, 1993; Thordarson et al., 2003a) of tephra dispersal and fountaining height for the Laki event indicate that this eruption (VEI 4) was much more explosive than the 2014–15 CE event at Holuhraun, the N_V^m of the rinds for the Laki clasts are marginally lower than those calculated for the September Holuhraun rinds (see Chapter 6). VNDs from both rinds fall within the range of the Kilauea Iki 1959 CE and are between half and one order of magnitude less than the Eldgjá 393 CE basaltic Plinian eruption (Moreland et al., 2019). Moreland et al. (2019) did not isolate the rinds from the whole clast during analysis, but as shown with the Laki and Holuhraun VNDs, whilst there is some modification by post-fragmentation over-printing processes, the rinds and whole clast VNDs are still within the same order of magnitude. This indicates that whilst the interiors have been modified, as they roughly agree with the rind data sets, and we assume these first order estimates stand in the case of the Moreland et al. (2019) Eldgjá samples. VND and mass-eruption rate (MER) plots (Figure 7. 11) add little to the interpretation of the data set, as making direct comparisons with the intensities of point source volcanism with fissure eruptions which have multiple vents, or indeed fissures, active at the same time is extremely difficult.

For low viscosity magmas, larger bubbles (>1 m) can easily decouple from their original melt package, rising faster through the shallow conduit and potentially increasing the shear rate on the melt prior to fragmentation closer to the top of the shallow conduit; thereby changing the regime from bubbly to slug flow (Houghton and Gonnermann, 2008) in sub-Plinian events. This may account for the explosivity of these opening phases at Laki, which have rinds with an equivalent or lower N_V^m to those analysed from a weaker intensity (Holuhraun 2014–15 CE) event using exactly the same method and analyst. The textural results from Laki suggest that unlike Eldgjá, which displays higher N_V^m , the driving forces (i.e., inertia, stress, strain, or a larger bubble fraction), for such high fissure opening phase eruptive intensities are not captured in these pyroclasts.

7. 5. 2 Temporal changes in textures throughout the eruption, conditions of ascent/shallow conduit model and conduit geometry

Fissure eruptions have complex linear sub-surface geometries (Parcheta et al., 2015a, 2015b, 2016) and in Iceland are known to not be monogenetic in nature, e.g., Holuhraun I, II and 2014–15 CE (Hartley and Thordarson, 2013), Krafla fires 1975–84 CE (Sæmundsson, K. 1991; Einarsson, P. 1991b) and Mývatn fires 1724–29 CE (Sæmundsson, 1730; Grönvold, 1984). The complicated sub-surface geometry, e.g., flared, changing, or irregular inclination could exacerbate and influence differences in ascent rate across the conduit and therefore impose a delay of crucial seconds that influence the development of melt textures in the system, creating clasts with complicated internal textures. The ultra-vesicular foam texture could correspond to fresh pulses of melt from depth that undergo rapid decompression (Figures 7. 14–7. 15). This model matches the resurgence of activity documented during the Holuhraun eruption where the activity almost stopped, and a dense plug veined with an incipient ultra-vesicular foam was erupted immediately afterwards (see Chapter 6). The textural fingerprint of this process, although not fully understood, may be used to identify a similar episodic eruptive nature and peak explosivity or atmospheric volatile loading phases in FL eruptions of all magnitudes.

The variety in domains and their variable maturity could also be a factor of chaotic mingling of melt packages with different shallow conduit histories. The very mature, denser, textured melt (domain type 3) mingles with fresh mature and ultra-vesicular upwelling melt pulses (domain type 1 and 2) in the shallowest conduit and becomes incorporated/entrained creating the hybrid domain texture clasts. In the explosive opening phases of the Laki fissures melt packages rise at different rates in a chaotic conduit flow, the fastest ascending melt package results in this melt being volatile supersaturated and could form the ultra-vesicular foam (domain type 2) through a homogeneous burst nucleation event. This hypothesis is supported by the ultra-vesicular foam domains in M2 and M4 containing the lowest S concentrations, by 50–100 ppm when compared to all other textural domains suggesting they lost more S than domains which did not reach supersaturation. In M4, mature (2) also displays markedly lower S values, which are also consistently lower than the ultra-vesicular foam, however, it abuts an unanalysed ultra-vesicular foam domain and could be the result of an interaction with that domain or simply by an unmapped additional ultra-

vesicular foam texture. Buoyant but slower ascent rate blebs forming the mature disequilibrium texture (domain texture 1), which has not had time to relax, has indistinguishable S contents to the rinds of the clasts. Other blebs are texturally very mature (domain type 3), displaying relaxed bubble shapes and mature euhedral, and in some places zoned, microlite populations (Francalanci et al., 2012), indicating that this texture is in equilibrium and has had time to relax. The latter texture could have two methods of formation. The alternatives are that: a) it is a relic of partially degassed, downwelling/convecting melt (Jones and Llewellyn, 2020), which has partially been re-entrained into and mingled with, upwelling and actively vesiculating buoyant melts (domain types 1 and 2), creating hybrid textured, clasts upon fragmentation; or, b) it is the product of a third upwelling melt package which is ascending slower than domain types 1 and 2 and therefore has time to equilibrate. In the M2, M4 and M6 clast domains with this texture have indistinguishable S values to the rinds; therefore, the former hypothesis seems more likely, creating a large scale, relatively well-mingled, textural spread across the eruptive products which at the level of a single pyroclast record smaller scale heterogeneities.

At the very end of the Laki eruption, waning phases of the activity would likely form an overturning lava pond with bubble bursting activity, as observed at Holuhraun after November 2014 CE (see Chapter 6). This type of activity at the very final stages of fissure 10's life-span, fed mapped rheomorphic, spatter-fed, pāhoehoe flows which mantle the tuff cone (see Chapter 5; Figure 7. 16). Conduit filling with the very mature vesicle texture (domain type 3), which consequently dominates the associated eruptive products of the M6 phase, was in response to the reduction in the magma ascent rate towards the end of the eruption as the supply of new melt from below dwindles. Consequently, the bubbles in slow-moving melt have time to grow and coalesce, as well as relax into very stable morphologies. M6 has a mature microlite population, with the groundmass glass displaying more evolved geochemistries (Table 7. 3), in response to this extensive equilibrium crystallisation and melt textural maturation. Further EMP analysis of mapped domains in additional Laki clasts could be undertaken to verify this hypothesis fully.

In a large-scale propagating fissure eruption like Laki, changes in location of melt pathways along strike can also not be ruled out as new opening phases are initiated, but the subsurface geometry of an event like this is poorly constrained. Therefore, the very mature equilibrium texture could be associated with the role of sub-surface conduit geometry in influencing the shallow conduit dynamics.

7. 5. 3 Phreatomagmatic vs Magmatic activity

Unlike phreatomagmatic pyroclasts, which have experienced the suppression of volatile loss by early quenching due to external water entering the system prior to magmatic foam fragmentation, P3 is texturally similar to a mature and well-developed reticulite foam indicative of high ascent rate and fountaining activity. This texture requires homogeneous late nucleation resulting from a rapid decompression rate. Due to the location of the eruptive environment, the trigger for this decompression could either be purely associated with fissure opening or to the removal of the overlying shallow glacial tongue, and therefore, sudden change in overburden pressure. Moreland et al. (2019) postulated that thick ice from an outlet glacier from Mýrdalsjökull, overlying part of the Eldgjá fissure system did not provide sufficient overburden pressure to inhibit volatile exsolution and the phreatomagmatic phases reached full vesiculation and shared the same shallow conduit history as their magmatic counterparts. In the case of Eldgjá the presence of overlying ice and external meltwater did not add to the explosivity of the event but triggered thermal granulation through shock (Moreland et al., 2019). Síðujökull, the outlet glacier from Vatnajökull, which episode 10 of the Laki eruption propagated underneath (see Chapter 5), is a thin glacial tongue which would have been approximately 100 m thick at the time of the eruption, and thus is unlikely to provide sufficient change in overburden to generate rapid decompression due to ice melting (Figure 7. 16). The longer lag time in fissure opening between M5 and P3, up to 6 weeks, could provide a tectonically induced change in overburden pressure, that was sudden enough to produce eruptive products consisting solely of ultra-vesicular foam textures.

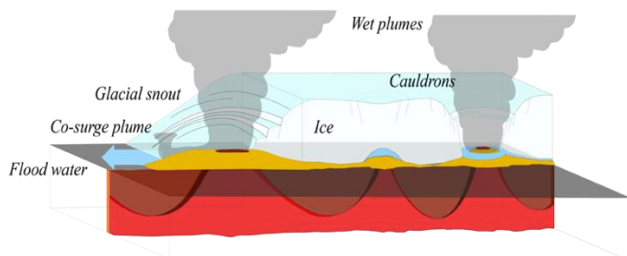
The presence of ice or glacial melt water has, however, partially suppressed degassing of the P3 tephra due to earlier quenching, with elevated S concentrations identified in the groundmass glass; which are 300 ppm richer than the ultra-vesicular foam in magmatic clasts and 150–200 ppm higher than all analysed magmatic clast domains (Table 7. 3).

Historic high-discharge and high-magnitude FL events are notable in size, but when compared to their ancient larger-scale counterparts, Flood Basalt (FB) eruptions, they are at least 4 orders of magnitude smaller. FB eruptions can contain a single lava flow with a volume of 2000 km³, often part of a compound flow field province >10,000 km³ emplaced over thousands of years (Rampino and Stothers, 1988; Self et al., 2005). However, regardless of magnitude, basaltic fissure eruptions maintain a similar style, nature, and emplace similar eruptive products. Therefore, by analysing pyroclasts from smaller scale, well-documented, modern analogues, we can improve our understanding of the eruption dynamics during large ancient FB events. This is important as FB eruptions are considered to induce significant atmospheric and climatic perturbations through the volatiles and aerosols they release and have a postulated association with the mass extinct events which punctuate Earth's geological record (Self et al., 2005).

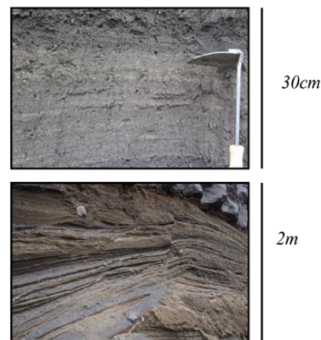
Subglacial and ice-confined case: P3 & M6

1: Shallow subglacial fissure eruption activity form bedded tuff cones.

At the snout of the glacier unconfined x-bedded tuff cones form, activity triggers jökulhlaups which drain from the glacier snout. Under thicker ice, tuff cones are ice-confined. Co-surge plume deposits accretionary lapilli in the interbedded surge and plume fall units.

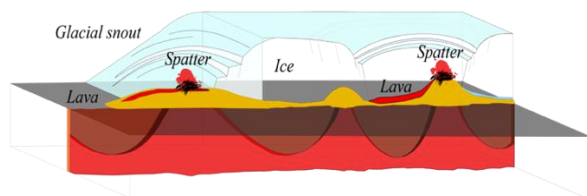


Tuff x-bed surge and fall units

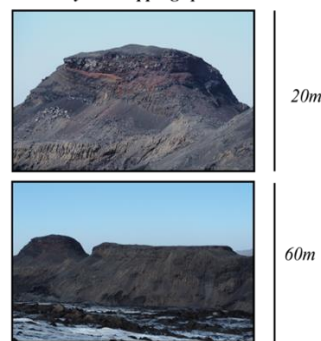


2: Tuff lithification enables vent isolation from water source, magmatic activity ensues.

At the glacier snout spatter fed lavas and dense scoria mantle the tuff sequences, magmatic activity (within the glacier margins) produces lavas that are laterally ice-confined.

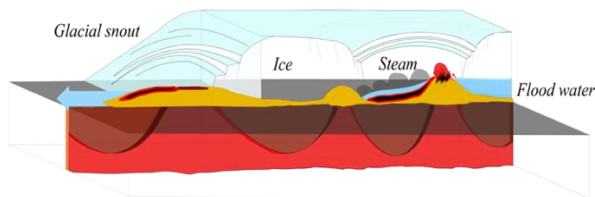


Transition to ice confined magmatic activity and capping spatter



3: Water pressure builds under the glacier, causing jökulhlaups

Flood water flows over active ice-confined lavas resulting in hackley jointed morphologies



Hackley jointed lava and jökulhlaup

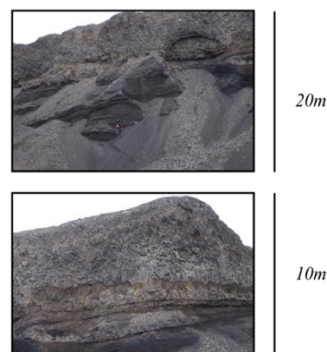


Figure 7. 16: Conceptual model of the evolution of shallow subglacial activity at fissure 10 during the Laki 1783–84 CE eruption. Part of schematic outline modified after Moreland et al. (2019). A fissure opens below the tongue of Síðujökull. At the glacier margin the craters are not confined laterally by the ice, forming ellipsoidal tuff cones comprising of pyroclastic surge layers cross-cutting each other. Where the ice is thicker, cauldrons form above this portion of the fissure with a body of meltwater below them, when the water reaches a high enough hydrostatic pressure, a jökulhlaup escapes from this region of the fissure. Subsequent activity is magmatic, although further north, the fissure continues to melt the surrounding glacier and episodic jökulhlaups disrupt the cooling spatter fed lava flows giving them hackley (rapid and disorganised) columnar jointing.

7. 5. 4 The influence of local tectonics

The episodic nature of the explosive phases from the eruptions is directly associated with variations in MER in response to recharge or changes in overburden pressure. However, the trigger and mechanisms which dictate fissure propagation during these high magnitude and high-intensity fissure eruptions, e.g., Vatnaöldur 870 CE, Eldgjá 939 CE, Veidivötn 1477 CE, and of course Laki 1783–84 CE remains poorly understood. All historic examples of high magnitude and high intensity events in Iceland display evidence of distinct explosive episodes associated with new fissure openings, as well as varying lag times between new fissure opening events.

Grímsvötn's fissure swarm is younger and less developed than Veidivötn's; as such, the region is less tectonically active and thus contains many fewer extensional fissures. The magma feeding the Laki eruption was stored at around 6–9 km depth, rapidly ascending on a timescale of days prior to fissure openings (Hartley et al., 2016). A less fractured surface crust may have resulted in a greater lithostatic overburden in the area prior to the eruption, resulting in the documented large earthquake swarms which precede each fissure opening phase as the Laki magma starts to ascend from depth. This rapid change in pressure during a new fissure opening phase, associated with a waxing MER may result in ultra-vesicular foams forming in these opening phase events that follow significant lag periods in activity. An overburden pressure change during the opening phase of fissure 10 due to the initial presence of ice could exacerbate the conditions required to generate only ultra-vesicular foam textures, i.e., the majority of all of the melt is rapidly ascending and is driven to volatile supersaturation.

7. 6 Conclusions

The 1783–84 CE 8-month long Laki eruption is the only well-documented historical high magnitude and high-intensity FL event in Iceland, thus providing a unique case study to contrast and compare the modulating role of shallow conduit processes on FL eruption style with more frequent, lower intensity and higher intensity basaltic fissure fountaining events of varying magnitude. N_v^m analysis of pyroclasts from 4 of its 9 explosive tephra fall units from separate fissure opening episodes, which

span: distinctive phases of the eruption or different eruptive environments, i.e., magmatic or phreatomagmatic, reveal discrete textural variations both temporally and between eruptive environments.

Comparing the rinds from the most explosive phase of the eruption, M2, and the waning phases of the eruption, M6, a clear relative decrease in N_v^m is observed. However, the N_v^m of both these clasts are marginally less than those calculated for the rinds analysed for the lower intensity 2014–2015 CE Holuhraun FL eruption pyroclasts and similar to those calculated for Kilauea Iki 1959 CE. This indicates that larger bubbles not captured by the pyroclasts alongside influences such as inertia, stress and strain are the main drivers of such explosive vent activity during the Laki eruption.

Disequilibrium and equilibrium textures were identified in the Laki pyroclasts, which were enhanced by post fragmentation expansion of the clast interiors. Post-fragmentation vesiculation highlights pre-existing distinct textural domains, which are the result of distinct melt packages with differing shallow conduit histories mingling prior to fragmentation creating a texturally heterogeneous erupted melt. Temporal variations in these textural proportions suggest a broad correlation between the extent of lag time between opening phases and the percentage of ultra-vesicular foam present, which is generated by disequilibrium processes. It is absent in the initial fissure-opening phase and increases throughout the eruption until the final episode, where it dominates within the conduit. Increasing quantities of very mature textures, caused by equilibrium processes, help identify periods of lower intensity fountaining activity; again, the proportions of this increases throughout the eruption in the magmatic clasts. Geochemical analysis of the groundmass glass in these textural domains within the clasts suggests that the textural differences are the product of melts with different geochemistries, as their major element compositions are nearly identical but instead record a difference in the shallow conduit history these melt packages experienced on ascent. An exception to this is the groundmass glass in M6 which is texturally more mature and has a slightly more evolved geochemistry, due to extensive microlite crystallisation towards the end of the eruption as the MER wanes.

The consistently lower S concentrations of the ultra-vesicular foam domains relative to the other melt textures present suggests this texture is generated by a rapid burst nucleation event in response to these melt packages being driven to volatile supersaturation through rapid ascent rates. This difference in volatile content is more pronounced in the Laki clasts than a similar contrast in the ultra-vesicular domains identified in the Holuhraun pyroclasts. However, the volatile content in the shallow sub-glacially erupted phreatomagmatic clast, P3, which consists entirely of ultra-vesicular foam, is up to 300 ppm higher than its counterparts in the magmatic clasts. This suggests that volatile loss during this phase of the eruption was suppressed due to the presence of the glacier; either through increased overburden pressure or early quenching of the melt through its interaction with external water prior to fragmentation. This sample is texturally very mature, with the highest N_v^m of all the Laki clasts, and whilst it has higher S concentrations, it also displays evidence of post-fragmentation expansion. Thus, further analysis is required to underpin the processes going on during the sub-glacially erupted portion of the Laki fissure.

7.7 References

- Bindeman, I. N., Sigmarsson, O., and Eiler, J. (2006). Time constraints on the origin of large volume basalts derived from O-isotope and trace element mineral zoning and U-series disequilibria in the Laki and Grímsvötn volcanic system. *Earth and Planetary Science Letters*. 245. (1–2), pp. 245–259. doi:10.1016/j.epsl.2006.02.029
- Brown, R. J., Blake, S., Thordarson, T., and Self, S. (2014). Pyroclastic edifices record vigorous lava fountains during the emplacement of a flood basalt flow field, Roza Member, Columbia River Basalt Province, USA. *Bulletin of the Geological Society of America*. 126. (7–8), pp. 875–891. doi:10.1130/B30857.1
- Bonny, E., Thordarson, T., Wright, R., Höskuldsson, A., and Jónsdóttir, I. (2018). The Volume of Lava Erupted During the 2014 to 2015 Eruption at Holuhraun, Iceland: A Comparison Between Satellite- and Ground-Based Measurements. *Journal of Geophysical Research: Solid Earth*. 123. (7), pp. 5412–5426. doi:10.1029/2017JB015008
- Carey, R. J., Houghton, B. F., Sable, J. E., and Wilson, C. J. N. (2007). Contrasting grain size and componentry in complex proximal deposits of the 1886 Tarawera basaltic Plinian eruption. *Bulletin of Volcanology*. 69. (8), pp. 903–926. doi:10.1007/s00445-007-0117-6
- Cashman, K. V. and Mangan, M. T. "Chapter 11b. Physical aspects of magmatic degassing II. Constraints on vesiculation processes from textural studies of eruptive products". In: *Volatiles in Magmas*, edited by Michael R. Carroll and John R. Holloway, Berlin, Boston: De Gruyter, 2018, pp. 447-478. doi:10.1515/9781501509674-018
- Costantini, L., Houghton, B. F., and Bonadonna, C. (2010). Constraints on eruption

- dynamics of basaltic explosive activity derived from chemical and microtextural study: The example of the Fontana Lapilli Plinian eruption, Nicaragua. *Journal of Volcanology and Geothermal Research*. 189.(3–4), pp. 207–224. doi:10.1016/j.jvolgeores.2009.11.008
- Decker, Z. (2017) Unpublished Thesis. The University of Iceland ‘Episode 4 of the 1783-84 Laki eruption: conduit processes and eruption dynamics of phreatomagmatic phase 1’
- Einarsson, P., (1991b). Umbrotin við Kröflu. (The eruption at Krafla). Í: Arnþór Garðarsson og Árni Einarsson (ritstjórar): Náttúra Mývatns. Hið íslenska náttúrufræðifélag, Reykjavík. pp. 95-139
- Eiríksson, J. (1783) Abstract from Erichsens writings, dated July 11, 1783 at Fljótastöðum Vestur-Skaftafells County. In: Einarsson, T., Guðbergsson, G. M., Gunnlaugsson, G. A., Rafnsson, S. and Þórarinnsson, S. (Editors.) Skaftáreldar 1783-1784: Ritgerðir og Heimildir. pp. 274-276. Mál og Menning Reykjavík.
- Francalanci, L., Avanzinelli, R., Nardini, I., Tiepolo, M., Davidson, J. P., and Vannucci, R. (2012). Crystal recycling in the steady-state system of the active Stromboli volcano: A 2.5-ka story inferred from in situ Sr-isotope and trace element data. *Contributions to Mineralogy and Petrology*. 163. (1), pp. 109–131. doi:10.1007/s00410-011-0661-0
- Gardner, J. E., Thomas, R. M. E., Jaupart, C., and Tait, S. (1996). Fragmentation of magma during Plinian volcanic eruptions. *Bulletin of Volcanology*. 58. (2–3), pp. 144–162. doi:10.1007/s004450050132
- Gonnermann, H. M., and Manga, M. (2007). The fluid mechanics inside a volcano. *Annual Review of Fluid Mechanics*. 39. pp. 321–356. doi:10.1146/annurev.fluid.39.050905.110207
- Grönvold, K. (1984). Myvatn Fires 1724-1729. Chemical composition of the lava. *Nordic Volcanological Institute Report, 1*.
- Guilbaud, M. N., Self, S., Thordarson, T., and Blake, S. (2005). Morphology, surface structures, and emplacement of lavas produced by Laki, A.D. 1783-1784. *Special Paper of the Geological Society of America*. 396. pp. 81–102. doi:10.1130/0-8137-2396-5.81
- Guilbaud, M. N. (2006). Unpublished PhD thesis. The Origin of Basaltic Lava Flow Textures. The Open University.
- Guilbaud, M. N., Blake, S., Thordarson, T., and Self, S. (2007). Role of Syn-eruptive Cooling and Degassing on Textures of Lavas from the ad 1783-1784 Laki Eruption, South Iceland. *Journal of Petrology*. 48. (7), pp. 1265–1294. doi:10.1093/petrology/egm017
- Hamilton, C. W., Thordarson, T., and Fagents, S. A. (2010). Explosive lava-water interactions I: Architecture and emplacement chronology of volcanic rootless cone groups in the 1783-1784 Laki lava flow, Iceland. *Bulletin of Volcanology*. 72. (4), pp. 449–467. doi:10.1007/s00445-009-0330-6
- Hamilton, C. W., Fagents, S. A., and Thordarson, T. (2010). Explosive lava-water interactions II: Self-organization processes among volcanic rootless eruption sites in the 1783-1784 Laki lava flow, Iceland. *Bulletin of Volcanology*. 72. (4), pp. 469–485. doi:10.1007/s00445-009-0331-5
- Hartley, M. E., and Thordarson, T. (2013). The 1874-1876 volcano-tectonic episode at Askja, North Iceland: Lateral flow revisited. *Geochemistry, Geophysics, Geosystems*. 14. (7), pp. 2286–2309. doi:10.1002/ggge.20151
- Hartley, M. E., Morgan, D. J., Maclennan, J., Edmonds, E. and Thordarson, T. (2016). Tracking timescales of short-term precursors to large basaltic fissure

- eruptions through Fe–Mg diffusion in olivine. *Earth and Planetary Science Letters*. 439. pp. 58-70. doi:10.1016/j.epsl.2016.01.018
- Hartley, M. E., Shorttle, O., MacLennan, J., Moussallam, Y., and Edmonds, M. (2017). Olivine-hosted melt inclusions as an archive of redox heterogeneity in magmatic systems. *Earth and Planetary Science Letters*. 479. pp. 192–205. doi:10.1016/j.epsl.2017.09.029
- Head III, J.W. and Wilson, L. (1989). Basaltic pyroclastic eruptions: influence of gas-release pattern and volume fluxes on fountain structure, and the formation of cinder cones, spatter cones, rootless flows, lava ponds and lava flows. *Journal of Volcanology Geothermal Research*. 37. pp. 261-271
- Heliker, C., and Mattox, T. N. (2003). The first two decades of the Pu' u 'Ö'ö-Kūpaianaha eruption: Chronology and selected bibliography. *US Geological Survey Professional Paper*. 1676. pp. 1–20.
- Heliker, C., Swanson, D. A., Takahashi, T. J., Norton, G. A., Survey, U. S. G., and Paper, P. (2003). The Pu ' u ' Ö ' ö-Kūpaianaha Eruption of Kīlauea Volcano , Hawai ' i: The First 20 Years. *U.S. Geological Survey Professional Paper*. 1676.
- Hjartarson, A. (1988). Þjorsárhraunið mikla - stærsta nútímahraun jarðar (The great Thjorsa lava: Earth's largest Holocene lava flow). (In Icelandic). *Náttúrufræðingurinn*, 58, pp. 1-16.
- Holt, S. J., Carey, R. J., Houghton, B. F., Orr, T., McPhie, J., and Feig, S. (2019). Eruption and fountaining dynamics of selected 1985–1986 high fountaining episodes at Kīlauea volcano, Hawai'i, from quantitative vesicle microtexture analysis. *Journal of Volcanology and Geothermal Research*. 369. pp. 21–34. doi:10.1016/j.jvolgeores.2018.11.011
- Houghton, B. F., and Wilson, C. J. N. (1989). A vesicularity index for pyroclastic deposits. *Bulletin of Volcanology*. 51. (6), pp. 451–462. doi:10.1007/BF01078811
- Houghton, B. F., and Gonnermann, H. M. (2008). Basaltic explosive volcanism: Constraints from deposits and models. *Chemie Der Erde*. 68. (2), pp. 117–140. doi:10.1016/j.chemer.2008.04.002
- Houghton, B. F., Taddeucci, J., Andronico, D., Gonnermann, H. M., Pistolesi, M., Patrick, M. R., Orr, T. R., Swanson, D. A., Edmonds, M., Gaudin, D., Carey, R. J., and Scarlato, P. (2016). Stronger or longer: Discriminating between Hawaiian and Strombolian eruption styles. *Geology*. 44. (2), pp. 163–166. doi:10.1130/G37423.1
- Houghton, B. F., Tisdale, C. M., Llewelin, E. W., Taddeucci, J., Orr, T. R., Walker, B. H. and Patrick, M. R. (2020). The Birth of a Hawaiian Fissure Eruption. *Journal of Geophysical Research: Solid Earth*. 126. . doi:10.1029/2020JB020903
- Jakobsson, S.P. (1979) Petrology of recent basalts of the Eastern Volcanic Zone, Iceland. *Acta Naturalia Islandica*. 26.103.
- Jones, T. J., Reynolds, C. D., and Boothroyd, S. C. (2019). Fluid dynamic induced break-up during volcanic eruptions. *Nature Communications*. 10. (1). doi:10.1038/s41467-019-11750-4
- Jones, Thomas J., and Llewelin, E. W. (2020). Convective tipping point initiates localization of basaltic fissure eruptions. *Earth and Planetary Science Letters*. 1. 116637. doi:10.1016/j.epsl.2020.116637
- La Spina, G., Arzilli, F., Llewelin, E. W., Burton, M. R., Clarke, A. B., de' Michieli Vitturi, M., Polacci, M., Hartley, M. E., Di Genova, D., and Mader, H. M.

- (2020). Explosivity of basaltic lava fountains is controlled by magma rheology, ascent rate and outgassing. *Earth and Planetary Science Letters*. 1. 116658. doi:10.1016/j.epsl.2020.116658
- LaFemina, P. C., Dixon, T. H., Malservisi, R., Árnadóttir, T., Sturkell, E., Sigmundsson, F., and Einarsson, P. (2005). Geodetic GPS measurements in south Iceland: Strain accumulation and partitioning in a propagating ridge system. *Journal of Geophysical Research: Solid Earth*. 110. (11), pp. 1–21. doi:10.1029/2005JB003675
- Larsen, G. (1984). Recent volcanic history of the Veidivötn fissure swarm, southern Iceland - an approach to volcanic risk assessment. *Journal of Volcanology and Geothermal Research*. 22. (1–2), pp. 33–58. doi:10.1016/0377-0273(84)90034-9
- Larsen, G. (1979). About the age of the Eldgjá lavas. *Náttúrufræðingurinn*. 49. pp. 1–26
- Larsen, G. (2000) Holocene eruptions within the Katla volcanic system, south Iceland: characteristics and environmental impact. *Jökull*. 49. pp.1–28.
- Lautze, N. C., and Houghton, B. F. (2008). Single explosions at Stromboli in 2002: Use of clast microtextures to map physical diversity across a fragmentation zone. *Journal of Volcanology and Geothermal Research*. 170. (3–4), pp. 262–268. doi:10.1016/j.jvolgeores.2007.10.011
- Loughlin, S. C., Aspinall, W. P., C. V.-B., Baxter, P. J., Braban, C., M. H., Schmidt, A., Thordarson, T., and Witham, C. S. (2012). Large-Magnitude Fissure Eruptions in Iceland: Source Characterisation. *British Geological Survey OpenFile Report*, pp. 1–136. <http://www.bgs.ac.uk/research/volcanoes/LakiEruptionScenarioPlanning.html%0Apapers3://publication/uuid/E5A6AE4C-D7D6-4563-AD7C-4B53F7033815>
- Mangan, M. T., and Cashman, K. (1996). The structure of basaltic scoria and reticulite and inferences for vesiculation, foam formation, and fragmentation in lava fountains. *Journal of Volcanology and Geothermal Research*. 73. (1–2), pp. 1–18.
- Mangan, M. T., Cashman, K. V., and Newman, S. (1993). Vesiculation of basaltic magma during eruption. *Geology*. 21. (2), 157–160. doi:10.1130/0091-7613(1993)021<0157:VOBMDE>2.3.CO;2
- Moreland W.M, Thordarson T, Houghton B.F. and Larsen G, (2019). Driving mechanisms of subaerial and subglacial explosive episodes during the 10th century Eldgjá fissure eruption, southern Iceland. *Volcanica*.
- Mourtada-Bonnefoi, C. C., and Laporte, D. (1999). Experimental study of homogeneous bubble nucleation in rhyolitic magmas. *Geophysical Research Letters*. 26. (23), pp. 3505–3508. doi:10.1029/1999GL008368
- Mourtada-Bonnefoi, C. C., and Laporte, D. (2004). Kinetics of bubble nucleation in a rhyolitic melt: An experimental study of the effect of ascent rate. *Earth and Planetary Science Letters*. 218. (3–4), pp. 521–537. doi:10.1016/S0012-821X(03)00684-8
- Namiki, A., and Manga, M. (2006). Influence of decompression rate on the expansion velocity and expansion style of bubbly fluids. *Journal of Geophysical Research: Solid Earth*. 111. (11), pp. 1–17. doi:10.1029/2005JB004132
- Namiki, A., and Manga, M. (2008). Transition between fragmentation and permeable outgassing of low viscosity magmas. *Journal of Volcanology and Geothermal Research*. 169. (1–2), pp. 48–60. doi:10.1016/j.jvolgeores.2007.07.020

- Neave, D. A., Passmore, E., Maclennan, J., Fitton, G., and Thordarson, T. (2013). Crystal-melt relationships and the record of deep mixing and crystallization in the ad 1783 laki eruption, Iceland. *Journal of Petrology*. 54. (8), pp. 1661–1690. doi:10.1093/petrology/egt027
- Óskarsson, N., Grönvold, K. and Larsen, G. (1984). The haze produced by the Laki eruption. (In Icelandic). In: Einarsson, T., Guðbergsson, G. M., Gunnlaugsson, G. A., Rafnsson, S. and Þórarinnsson, S. (Editors.) *Skaftáreldar 1783-1784 :Ritgerðir og Heimildir*. pp. 67-80. Mál og Menning: Reykjavík.
- Parcheta, C. E., Houghton, B. F., and Swanson, D. A. (2013). Contrasting patterns of vesiculation in low, intermediate, and high Hawaiian fountains: A case study of the 1969 Mauna Ulu eruption. *Journal of Volcanology and Geothermal Research*. 255. pp. 79–89. doi:10.1016/j.jvolgeores.2013.01.016
- Parcheta, Carolyn E., Fagents, S., Swanson, D. A., Houghton, B. F., and Ericksen, T. (2015a). Hawaiian fissure fountains: Quantifying vent and shallow conduit geometry, episode 1 of the 1969–1974 Mauna Ulu eruption. *Geophysical Monograph Series*. 208. pp. 369–391. doi:10.1002/9781118872079.ch17
- Parcheta, C.E., Nash, J., Mitchell, K.L. and Parness, A. (2015b). Shallow Subsurface Structures of Volcanic Fissures. 2015 *AGU Fall Meeting abstract*.
- Parcheta, Carolyn E., Pavlov, C. A., Wiltsie, N., Carpenter, K. C., Nash, J., Parness, A., and Mitchell, K. L. (2016). A robotic approach to mapping post-eruptive volcanic fissure conduits. *Journal of Volcanology and Geothermal Research*. 320. pp. 19–28. doi:10.1016/j.jvolgeores.2016.03.006
- Passmore, E. (2009). Unpublished PhD thesis. Feeding large eruptions: crystallisation, mixing and degassing in Icelandic magma chambers. The University of Edinburgh. pp. 1–379.
- Passmore, E., Maclennan, J., Fitton, G., and Thordarson, T. (2012). Mush disaggregation in basaltic magma chambers: Evidence from the ad 1783 Laki eruption. *Journal of Petrology*. 53. (12), pp. 2593–2623. doi:10.1093/petrology/egs061
- Polacci, M., Corsaro, R. A., and Andronico, D. (2006). Coupled textural and compositional characterization of basaltic scoria: Insights into the transition from Strombolian to fire fountain activity at Mount Etna, Italy. *Geology*. 34. (3), 201–204. doi:10.1130/G22318.1
- Porritt, L. A., Russell, J. K., and Quane, S. L. (2012). Pele’s tears and spheres: Examples from Kilauea Iki. *Earth and Planetary Science Letters*. 333–334. pp. 171–180. doi:10.1016/j.epsl.2012.03.031
- Rampino, M. R., and Stothers, R. B. (1988). Flood basalt volcanism during the past 250 million years. *Science*, 241. (4866), pp. 663–668. doi:10.1126/science.241.4866.663
- Richter, D. H., Eaton, J. P., Murata, K. J., Ault, W. U., and Krivoy, H. L. (1970). Chronological Narrative of the 1959-60 Eruption of Kilauea Volcano, Hawaii. *USGS Professional Paper*. 537-E. doi:10.1016/0198-0254(80)95902-6
- Rust, A. C., and Cashman, K. V. (2011). Permeability controls on expansion and size distributions of pyroclasts. *Journal of Geophysical Research: Solid Earth*. 116. (11), pp. 1–17. doi:10.1029/2011JB008494
- Sable, Julia E., Houghton, B. F., Del Carlo, P., and Coltelli, M. (2006). Changing conditions of magma ascent and fragmentation during the Etna 122 BC basaltic Plinian eruption: Evidence from clast microtextures. *Journal of Volcanology and Geothermal Research*. 158. (3–4), pp. 333–354. doi:10.1016/j.jvolgeores.2006.07.006

- Sable, J. E., Houghton, B. F., Wilson, C. J. N., and Carey, R. J. (2009). Eruption mechanisms during the climax of the Tarawera 1886 basaltic Plinian eruption inferred from microtextural characteristics-of the deposits. *Special Publications of IAVCEI*. 2. pp. 129–154. doi:10.1144/iavcel002.7
- Sæmundsson, J. (1730). Sandferdig Relation om det udi Island Brændenda Field Krabla, og andre der omkring liggende Smaae Felde, baade med Jordskielv (In Danish). In: Torden and Askefald, Copenhagen, Denmark, p 2
- Sæmundsson, K. (1974). Evolution of the axial rifting zone in Northern Iceland and the Tjörnes fracture zone. *Bulletin of the Geological Society of America*. 85. (4), pp. 495–504. doi:10.1130/0016-7606(1974)85<495:EOTARZ>2.0.CO;2
- Sæmundsson, K. (1978). Fissure swarms and central volcanoes of the neovolcanic zones of iceland. *Geological Journal Special Publications*. 10. pp. 415–432.
- Sæmundsson K. (1991). Jarðfræði Kröflukerfisins (In Icelandic). (Geology of Krafla volcanic system) In: Arnþór Garðarsson og Árni Einarsson (Editors): Náttúra Mývatns. Hið íslenska náttúrufræðifélag, Reykjavík. pp. 25–95 (In Icelandic).
- Schmidt, A., Ostro, B., Carslaw, K. S., Wilson, M., Thordarson, T., Mann, G. W., and Simmons, A. J. (2011). Excess mortality in Europe following a future Laki-style icelandic eruption. *Proceedings of the National Academy of Sciences of the United States of America*. 108. (38), pp. 15710–15715. doi:10.1073/pnas.1108569108
- Self, S., Thordarson, T. and Widdowson, M. (2005). Gas Fluxes from Flood Basalt Eruptions. *Elements*. 1. (5), pp. 283–287. doi:10.2113/gselements.1.5.283
- Shea, T., Houghton, B.F., Gurioli, L., Cashman, K.V., Hammer, J.E., and Hobden, B.J. (2010). Textural studies of vesicles in volcanic rocks: An integrated methodology. *Journal of Volcanology and Geothermal Research*. 190. pp. 271–289. doi:10.1016/j.jvolgeores.2009.12.003
- Sigmarrsson, O., Condomines, M., Grönvold, K., and Thordarson, T. (1991). Extreme Magma homogeneity in the 1783-84 Lakagigar eruption: origin of a large volume of evolved basalt in Iceland. *Geophysical Research Letters*. 18. (12), pp. 2229–2232.
- Steingrímsson J (1783a) A short compendium of the recent volcanic outburst in western part of Skaftafell county, dated at Prestbakki July 4, 1783. In: Einarsson, T., Guðbergsson, G.M., Gunnlaugsson, G.A., Rafnsson S. and Þórarinnsson, S. (editors.) Skaftáreldar 1783-1784: Ritgerðir og Heimildir. pp. 272-274. Mál og Menning: Reykjavík 1984.
- Steingrímsson J (1783b) Abstract from a letter to Reverend Bjarni Jónsson, dated August 31 1783 at Prestbakki. (In Icelandic). In: Safn til Sögu Islands, vol IV. pp. 69-70: Copenhagen.
- Steingrímsson J (1788) A complete description on the Síða volcanic fire, dated November 24 1788 at Prestbakki. (In Icelandic) In: Safn til Sögu Islands. IV. pp. 1-57: Copenhagen.
- Steingrímsson, J. and Ólafsson, S. (1783). A simple, but true narrative of the eruption in Skaftafell county in the year 1783, dated November 24 1788 at Kirkjubæjarklauster. (In Icelandic). In: Safn til Sögn Islands. IV. pp. 58-69: Copenhagen (in Icelandic).
- Stovall, W. K., Houghton, B. F., Gonnermann, H., Fagents, S. A., and Swanson, D. A. (2011). Eruption dynamics of Hawaiian-style fountains: The case study of episode 1 of the Kilauea Iki 1959 eruption. *Bulletin of Volcanology*. 73. (5), pp. 511–529. doi:10.1007/s00445-010-0426-z
- Stovall, W. K., Houghton, B. F., Hammer, J. E., Fagents, S. A., and Swanson, D. A.

- (2012). Vesiculation of high fountaining Hawaiian eruptions: Episodes 15 and 16 of 1959 Kīlauea Iki. *Bulletin of Volcanology*. 74. (2), pp. 441–455. doi:10.1007/s00445-011-0531-7
- Sumner, J. M. (1998). Formation of clastogenic lava flows during fissure eruption and scoria cone collapse: The 1986 eruption of Izu-Oshima Volcano, eastern Japan. *Bulletin of Volcanology*. 60. (3), pp. 195–212. doi:10.1007/s004450050227
- Swanson, D. A., Duffield, W. A., Jackson, D. B., and Peterson, D. W. (1979). Chronological narrative of the 1969-71 Mauna Ulu eruption of Kilauea Volcano, Hawaii. U.S. *Geological Survey Professional Paper*. 1056. 55 p.
- Thorarinsson, S. (1967). The Laki and Laki crater-row. *Náttúrufræðingurinn*, 37, pp. 27-57
- Thorarinsson, S. (1969). The Lakagíggar eruption of 1783. *Bulletin of Volcanology*. 33. pp. 910-929.
- Thorarinsson S (1979) On the damage caused by volcanic eruptions with special reference to tephra and gases. In: PD Sheets and DK Grayson (eds.) *Volcanic activity and human geology*. pp. 125-159. Academic Press: New York.
- Thorarinsson S (1981) Greetings from Iceland: ash-falls and volcanic aerosols in Scandinavia. *Geografiska Annaler*. 63A. pp. 109-118
- Thorarinsson S (1984) The Laki Fires. In: T Einarsson, GM Guðbergsson, GA Gunnlaugsson, S Rafnsson and S Þórarinnsson (eds.) *Skaftáreldar 1783-1784: Ritgerðir og Heimildir*. pp. 11-36. Mál og Menning: Reykjavík.
- Thordarson, T. (1990). Unpublished masters thesis. The eruption sequence and the eruption behaviour of the Skaftár Fires, 1783-85, Iceland: characteristics and distribution of eruption products. University of Texas at Arlington.
- Thordarson T, Self S (1993) The Laki (Skaftár-Fires) And Grímsvötn Eruptions In 1783-1785. *Bulletin Of Volcanology*. 55. pp. 233-263.
- Thordarson. T, Self, S., Óskarsson, N. and Hulsebosch, T. (1996). Sulfur, chlorine, and fluorine degassing and atmospheric loading by the 1783-1784 AD Laki (Skaftár Fires) eruption in Iceland. *Bulletin of Volcanology*. 58. (2–3), pp. 205–225. doi:10.1007/s004450050136
- Thordarson, T., Miller, D. J., Larsen, G., Self, S. and Sigurdsson, H. (2001). New estimates of sulfur degassing and atmospheric mass-loading by the 934 AD Eldgja eruption, Iceland. *Journal Of Volcanology and Geothermal Research*. 108. pp. 33-54
- Thordarson, T, and Self, S. (2001). Real-time observations of the Laki sulfuric aerosol cloud in Europe during 1783 as documented by Professor S. P. van Swinden at Franeker, Holland. *Jökull*. 50. pp. 65–72.
- Thordarson, T. (2003). The 1783-1785 A.D. Laki-Grímsvötn eruptions I: A critical look at the contemporary accounts. *Jökull*. 53. pp. 1-10
- Thordarson, T. and Self, S. (2003). Atmospheric and environmental effects of the 1783-1784 Laki eruption: A review and reassessment. *Journal Of Geophysical Research-Atmospheres*. 108, 4011
- Thordarson T, Larsen G and Steinthorsson S, Self S (2003a) The 1783-1785 A.D. Laki-Grímsvötn eruptions II: Appraisal based on contemporary accounts. *Jökull*. 53. pp. 11-48
- Thordarson, T., Self, S., Miller, D. J., Larsen, G. and Vilmundardottir, E. G. (2003b) Sulphur release from flood lava eruptions of the Veiðivötn, Grímsvötn and Katla volcanic systems, Iceland. In: C Oppenheimer, DM Pyle and J Barclay (eds.) *Volcanic Degassing*. pp. 103-121. *The Geological Society of London*.

- Thordarson, T. and Larsen, G. (2007). Volcanism in Iceland in historical time: Volcano types, eruption styles and eruptive history. *Journal of Geodynamics*. 43. (1), pp. 118–152. doi:10.1016/j.jog.2006.09.005
- Thordarson, T. and Höskuldsson, Á. (2008). Postglacial volcanism in Iceland. *Jökull*. 58. pp. 197–228.
- Toramaru, A. (1995). Numerical study of nucleation and growth of bubbles in viscous magmas. *Journal of Geophysical Research*. 100. (B2), pp. 1913–1931.
- Toramaru, A. (2006). BND (bubble number density) decompression rate meter for explosive volcanic eruptions. *Journal of Volcanology and Geothermal Research*. 154. (3–4), pp. 303–316. doi:10.1016/j.jvolgeores.2006.03.027
- Vilmundardóttir, E. G. (1977). Tungnárhraun Jarðfræðiskýrsla (The Tungnaá lava flows. A geological report, In Icelandic). *Orkustofnun Raforkuðeild*, 7702, 1–166.
- Witt, T., Walter, T. R., Müller, D., Guðmundsson, M. T., and Schöpa, A. (2018). The Relationship Between Lava Fountaining and Vent Morphology for the 2014–2015 Holuhraun Eruption, Iceland, Analyzed by Video Monitoring and Topographic Mapping. *Frontiers in Earth Science*. 6. doi:10.3389/feart.2018.00235
- Wolfe EW, Neal CA, Banks NG, Duggan TJ (1988) Geologic observations and chronology of eruptive events. *US Geological Survey Professional Papers*. 1463. pp. 1–97.
- Wolfe EW, editor (1988) The Puu Oo eruption of Kilauea Volcano, Hawaii: episodes 1 through 20. *US Geological Survey Professional Papers*. 1463, 251 pp

Chapter 8: Fingerprinting the mechanisms and timing of S released accompanying FL eruptions using novel chalcophile stable isotope proxies

8.1 Introduction

The volatile budget from a volcanic eruption predominantly consists of CO₂ and H₂O, with lower concentrations of sulfur (S), halogen species and associated metals. However, CO₂ and H₂O are thought to have a negligible short-term impact on atmospheric chemistry due to their high background abundances (Wignall, 2001; Self et al., 2005, 2008); hence, despite the relatively low eruptive concentrations of S, this is the only volcanic volatile species that has been observed to perturb the radiative balance of the atmosphere (Schmidt and Robock, 2015). Initially, at the vent and in a volcanic plume, SO₂ and H₂S are the most abundant S species present (Wallace and Edmonds, 2011), but relatively unreactive H₂S rapidly converts to SO₂ through oxidation by hydroxyl radicals (OH) in the highly oxidising, high-temperature, vent environment (Gerlach, 2004; Mather et al., 2008; Oppenheimer et al., 2011). Sulfur dioxide, if not deposited out of the plume, subsequently undergoes another conversion stage in the plume: oxidation via a reaction with OH radicals, produced by photolysis of ozone, to sulfate PM aerosols (SO₄²⁻) or to sulfuric acidic aerosols H₂SO₄ (Eatough et al., 1994) through a prior chain reaction from HOSO₂ to SO₃. Multiple parameters dictate the rate at which this conversion occurs, such as: ambient temperature; humidity; solar flux (Möller et al., 1980; Eatough et al., 1994; Carlsen et al., 2021); or whether the air is polluted (Hewitt, 2001), as chemical reactions or physical interactions occur with other particulate matter present (Carlsen et al., 2021). These aerosols absorb near-IR radiation and scatter it away from Earth's surface, inducing a surface cooling effect and creating thermal gradients that modify meteoric conditions (Robock, 2000; Robock and Oppenheimer, 2003; Edmonds and Mather, 2017). If injected into the stratosphere, the life span of both SO₂ (hours) and sulfate PM (SO₄²⁻) (days) increases to weeks and months-years, respectively, due to the slower removal processes associated with a low humidity environment. Thereby increasing their associated climatic and environmental impact.

Large and sustained injections of volcanic S can induce significant environmental degradation and health hazards through a tropospheric sulfur and halogen rich volcanic fog (vog), which also contains significant amounts of trace metals, acid rain and climatic perturbations, over the timescales of months-to-years, through upper troposphere-lower stratospheric sulfur aerosol loading (e.g. Thordarson and Self, 1993; 2001; Self et al., 2005; Thordarson et al., 2009; Schmidt et al., 2010, 2011; Oppenheimer et al., 2011; Wallace and Edmonds, 2011).

Of particular interest are basaltic eruptions, which produce a volatile load about an order of magnitude higher than explosive silicic eruptions (Devine et al., 1984). Explosive basaltic eruptions are easily capable of sub-Plinian to Plinian eruptive intensities that can achieve stratospheric injection levels, e.g., Fontana 60ka, 122BC Etna, Tarawera 1886 CE, Krakatoa 1883 CE (basaltic andesite), Katla 1918 CE and Grímsvötn 2011 CE (Self, 1992; Larsen, 2000; Sable et al., 2009; Costantini et al., 2010), but are generally much shorter-lived compared to their effusive counterparts. However, high-intensity and high magnitude basaltic flood lava (FL) eruptions, 1–100 km³ in DRE volume, produce volcanic plumes capable of stratospheric volatile loading during their higher intensity phases (Thordarson et al., 1996; Moreland et al., 2019). Analysis of the activity sequences of historical examples of eruptions of this nature in Iceland, such as the Laki 1783–84 CE and Eldgjá 939 CE events, show that they are capable of prolonged periods of volatile loading through discrete high-intensity phases that are days to weeks apart associated with new fissure opening activity. This style and intensity of eruptive activity maintains and prolongs the stratospheric S burden for longer than is expected for a single explosive phase. Consequently, modelling the hemispheric or global S dispersal from volcanic plumes within the atmosphere and stratosphere, as well as calculating the total S burden for previous high-intensity and high magnitude FL eruptions, to improve hazard and environmental assessments, has been a key research focus over recent decades (Sigurdsson, 1982; Thordarson et al., 1996, 2001, 2003a; Thordarson and Self, 1996, 2003; Self et al., 2005, 2006, 2008; Oppenheimer et al., 2011; Schmidt et al., 2011, 2015; Loughlin et al., 2012; Ilyinskaya et al., 2017). This is especially important for the European geographical area, which is vulnerable to unsafe S pollution levels from high magnitude and high-intensity FL events or low level S pollution events from high magnitude and low-intensity FL events in Iceland.

The partitioning of sulfur between magmatic fluids and melts controls the volatile budget of magmas, and thus total atmospheric S burden an eruption can have, as well as the speciation of sulfur released into the atmosphere upon eruption (Webster and Botcharnikov, 2011). How S partitions between vapour-melt phases is complicated, therefore to model this comprehensively for a given melt calculations of its S saturation threshold must include the effects of: temperature (T); pressure (P); melt composition; oxygen fugacity (f_{O_2}); and S fugacity (f_{S_2}) (Wallace and Carmichael, 1992; Scaillet and Pichavant, 2005; Moretti and Baker, 2008; Wallace and Edmonds, 2011, Barnes, 2012). The latter two parameters are particularly important as the redox state of the magma in question, prior to eruption, has a strong influence on the distribution of S between the melt and liquid/gas phase by controlling the amount of dissolved S that a melt can carry in solution at depth before the melt becomes S saturated. Experimental data demonstrates that upon decompression, as a basaltic magma ascends, the S strongly partitions into the gas phase (Edmonds and Mather, 2017), in particular for reducing conditions, e.g., MORB where S^{2-} becomes even less soluble in the melt phase during ascent.

In the last two decades, it has been possible to measure both the ratio of H_2S/SO_2 in gas fluxes for eruptions or quiescent outgassing (Mcgee et al., 2001; Burton et al. 2007; Christopher et al., 2010; Wallace and Edmonds, 2011) as well as the degassing budget to constrain patterns of volatile outputs through ground-based FTIR and DOAS analysis. This can be used alongside LiDAR or modified differential absorption LiDAR measurements of the plume to resolve gas mixture ratios (Oppenheimer et al., 2011), as well as ground-based electrochemical sensors such as a multi-gas or battery-powered filter packs used to characterise the chemistry of gases and aerosols present in the plume (Pfeffer et al., 2015; 2018; Ilyinskaya et al., 2017). However, high errors due to lack of IR sources means that not all S species that separated from the melt in a liquid or gas phase can be measured in the outgassing plume as some phases are not stable at atmospheric pressures and temperatures. For example, at magmatic temperatures and atmospheric pressures, e.g., during syn-eruptive degassing sulfate dissociates, forming SO_2 and O_2 (Behrens and Webster, 2011). This is also true for sulfides (FeS_2), which are broken down upon eruption and released into the gas phase (SO_2 as H_2S), thus increasing the total atmospheric S loading of the eruption in question, as well as releasing trace metals

associated with the sulfide phase into the atmosphere increasing the environmental impact of the eruption (Berlo et al., 2014; Gautheir et al., 2016; Brounce et al., 2017; Edmonds and Mather, 2017; Hartley et al., 2017; Longpré et al., 2017).

However, the speciation of S measured in volcanic plumes during atmospheric or stratospheric loading does not mirror the pre-eruptive redox state of the parent melt. Instead, the redox of the system and therefore the S speciation in the silicate melt and associated vapour or liquid phase are modified both upon decompression as the magma ascends to the surface (Anderson and Wright, 1972; Carmichael and Ghiorso, 1986; Wallace and Carmichael, 1992; Burgisser and Scaillet, 2007; Métrich et al., 2009; Métrich and Mandeville, 2010; Cottrell and Kelley, 2011; Gaillard et al., 2011; 2015; Gaillard and Scaillet, 2014; Moussallam et al., 2014, 2016, 2019; Brounce et al., 2017; Helz et al., 2017; Longpré et al., 2017) as well as upon eruption in the hot core of the volcanic plume as H₂S converts to SO₂ (Getahun et al., 1996; Hoshyaripour et al., 2012). In some circumstances, fO_2 determined by Mössbauer analysis of glass (Óskarsson et al., 1994) or XANES analysis of melt inclusions from rapidly quenched glassy tephra samples (Wallace and Edmonds, 2011; Moussallam et al., 2014, 2016, 2019; Shorttle et al., 2015; Hartley et al., 2017) yield information on the pre-eruptive redox conditions. However, if the melt in question is aphyric or the sample is old and weathered or altered then, the MIs cannot be analysed, and the species of S lost to the atmosphere cannot be determined, as the redox of the eruptive glasses does not reflect the conditions under which S species were lost to the atmosphere (Burgisser and Scaillet, 2007).

An emerging field utilizing redox sensitive novel stable isotope systems, of moderately volatile chalcophile elements such as zinc (Zn) and copper (Cu), alongside redox controlled volatile trace elements such as rhenium (Re), could potentially geochemically fingerprint the S speciation of the volatile phase released upon eruption. Using these novel data sets in combination with geochemical modelling and in-situ analytical techniques such as XANES, could provide another tool to advance our understanding of the evolution of redox conditions and S speciation of the melt and volatile phases that prevailed in the shallow conduit during syn-eruptive degassing and fragmentation. This helps to bridge a current gap between the measurable geochemical window into the melt at depth, provided by

melt inclusions, and the volatiles and aerosols measured in the eruptive plume by identifying, through analysis of the residual eruptive products the volatile and particulate species present prior to atmospheric dissociation.

For example, if S is lost as an oxidised volatile phase then the melt is depleted in the light Zn isotope, leaving the erupted melt with a heavy $^{66}\text{Zn}/^{64}\text{Zn}$ signature (Figures 8. 1 and 8. 2; Luck et al., 2005; John et al., 2008; Herzog et al., 2009; Chen et al., 2013; Chen, 2014). However, if S has been lost as a reduced volatile phase, with a Cu_3Cl_3 fluid component, the melt is expected to be depleted in the heavy Cu isotope and thus isotopically lighter with respect to $^{65}\text{Cu}/^{63}\text{Cu}$ (Figures 8. 1 and 8. 2). If an immiscible sulfide melt phase, which concentrates the light copper isotope, has formed, then they will have a lighter $^{65}\text{Cu}/^{63}\text{Cu}$ signature, relative to the melt (Figures 8. 1 and 8. 2; Halter et al., 2005; Markl et al., 2006; Moynier et al., 2006; Li et al., 2009; Savage et al., 2015). Thus, if additional sulfides are added to the melt it will have an increasingly lighter $^{65}\text{Cu}/^{63}\text{Cu}$ signature, but if they are removed the residual melt will have an heavier $^{65}\text{Cu}/^{63}\text{Cu}$ signature (Figures 8. 1 and 8. 2). To differentiate between sulfate fluid segregation and an SO_2 rich gas phase segregating from the melt trace elements which exhibit a similar behaviour to S, e.g., Re has been used to distinguish between gas and fluid oxidised loss S and therefore a heavy $^{66}\text{Zn}/^{68}\text{Zn}$ signature (Figure 8. 2).

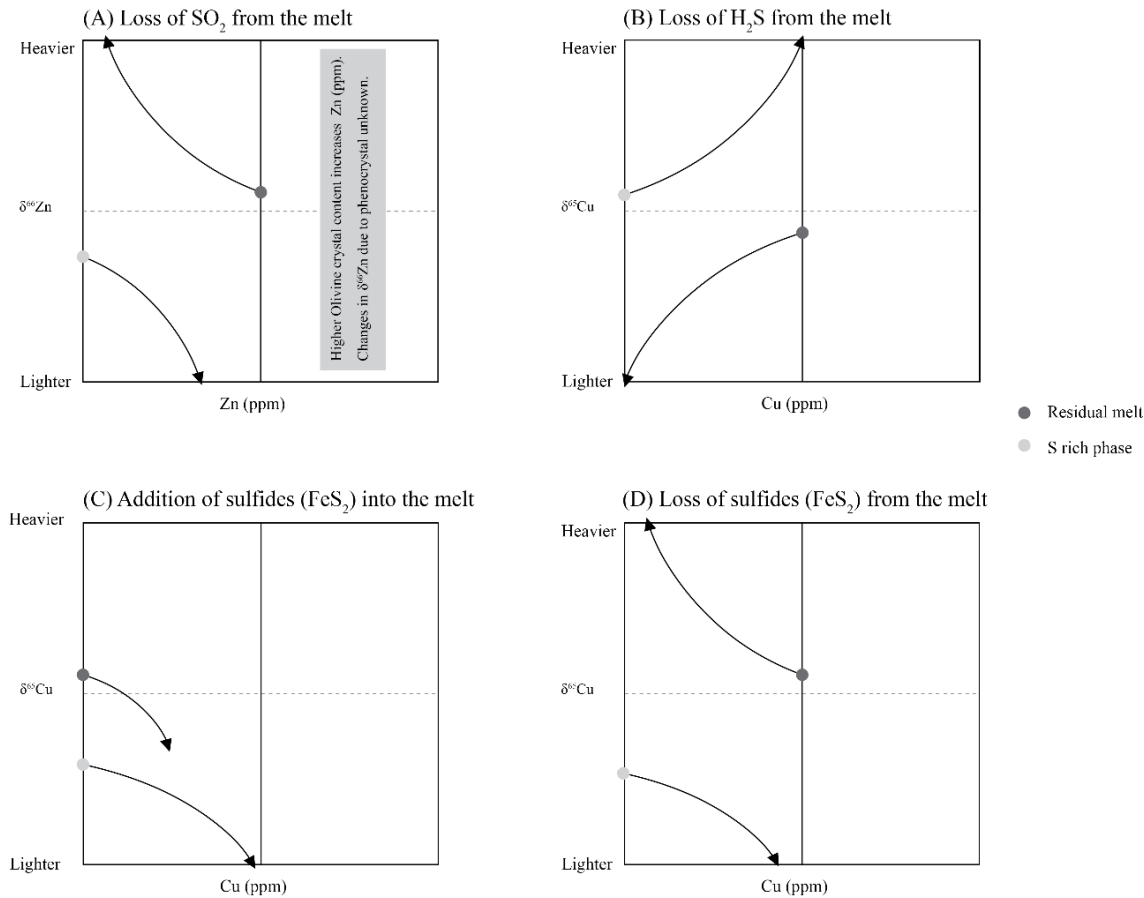


Figure 8. 1: A schematic of expected fractionation trends generated by Zn and Cu partitioning into oxidized and reduced S rich phases at magmatic temperatures during basaltic fissure eruptions. Each of the four quadrants (labelled A–D) displays the expected fractionation trends and the resultant isotopic fingerprints for $\delta^{66}\text{Zn}$ and $\delta^{66}\text{Cu}$ for different oxidized and reduced S rich phases and the residual melt. (A) Shows the expected trend of the residual melt towards heavier $\delta^{66}\text{Zn}$ as the lighter Zn isotope is preferentially partitioned into an oxidized S gas phase (SO_2) and Zn (ppm) is lost through degassing; (B) Shows the expected trend of the residual melt towards lighter $\delta^{66}\text{Cu}$ as the heavier Cu isotope is preferentially partitioned into a reduced S gas phase (H_2S) and Cu (ppm) is lost through degassing; (C) Shows the expected trend of the residual melt towards lighter $\delta^{66}\text{Cu}$ as sulfides rich in Cu (ppm), which the lighter Cu isotope preferentially partitions into, are added to the melt packages; (D) Shows the expected trend of the residual melt towards heavier $\delta^{66}\text{Cu}$ as sulfides rich in Cu (ppm), which the lighter Cu isotope preferentially partitions into, are lost from the melt packages.

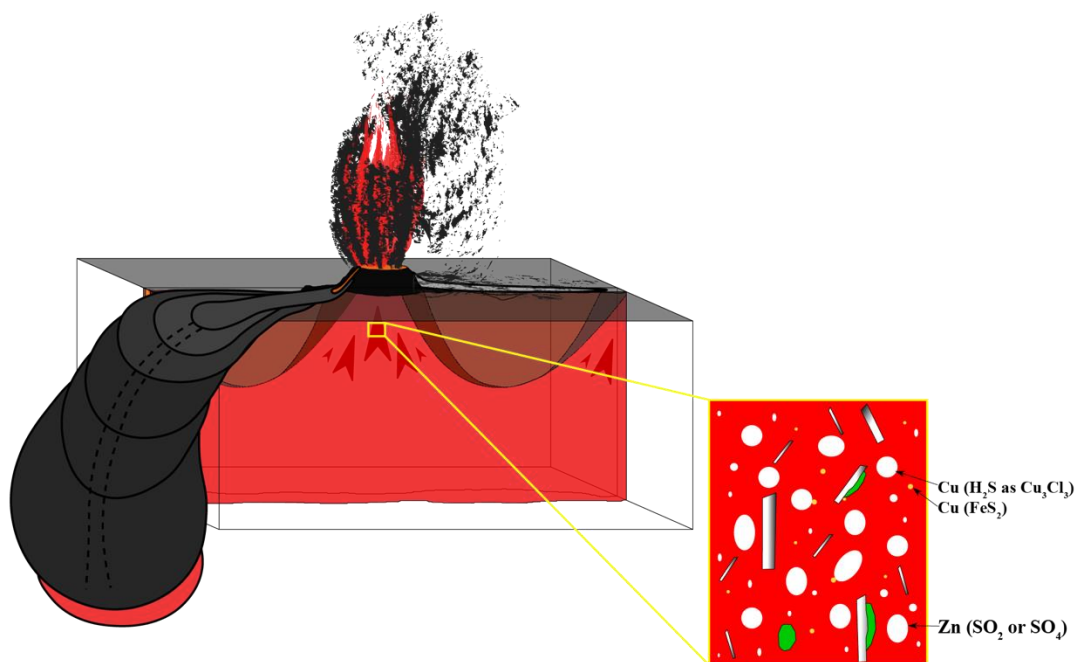


Figure 8. 2: An illustration of Zn and Cu partitioning into oxidized and reduced S rich phases. Schematic of a basaltic fissure eruption, and its eruptive products, with its shallow conduit system in cross-section. The inset displays a package of melt rising through the shallow conduit: melt is shown in red, bubbles in white, immiscible sulfide phases in yellow, plagioclase crystals in greyscale and olivine or pyroxene in green. This inset also highlights the partitioning behaviour of Cu and Zn during ascent, depending on the redox conditions of the system and which S species are present, which in turn results in the mass-dependant fractionation of these two stable isotope systems.

8. 1. 1 Previous work on Zn and Cu isotopic variations of terrestrial samples

Most previous chalcophile isotope studies have concentrated on determining the Zn isotopic composition of bulk silicate earth (BSE) (Herzog et al., 2009; Telus et al., 2012; Doucet et al., 2016; Liu et al., 2016; Mahan et al., 2017; Sossi et al., 2018; Wang et al., 2017) and Cu (Liu et al., 2015; Savage et al., 2015; Moynier et al., 2017) and the fractionation of these stable isotope systems during magmatic differentiation, hydrothermal and ore-forming processes. Our understanding of how these systems behave at magmatic temperatures and in response to degassing during eruptions is limited and mostly theoretical. Whilst previous work has identified mass-dependant fractionation of Zn stable isotopes induced by volatile loss during planetary formation events; there are few compelling examples of Zn fractionation due to degassing at magmatic temperatures during basaltic eruptions (Toutain et al., 2008; Chen et al., 2013; Chen, 2014; Liu et al., 2016). To date, there is only one published study that investigates Cu isotope evolution in an arc volcanic system, Niuatahi volcano, Tonga rear arc (i.e., Wang et al., 2019), which characterised a

number of complementary aspects of a volcanic system as a whole, e.g., hydrothermal system derived molten sulfur versus basaltic and dacitic lavas.

Whilst the sampling strategy adopted by these previous studies provides a broad perspective of each volcanic system, in terms of characterising differences in the isotopic composition of melts produced over the eruptive history or the differences between eruptive products and the accompanying hydrothermal system, neither of these strategies had the goal to systematically analyse one eruptive event and isolate the degassing induced mass-dependant fractionation fingerprint of Zn or Cu. In particular, these studies make comparisons of a limited number of samples from unrelated eruptions or parts of the lava field that may have been emplaced by very different vent activity rather than systematically analysing the spatial and temporal evolution of the eruptive products from a single event. The absence of any covariation of $\delta^{66}\text{Zn}$ isotopes with Zn concentrations and SiO_2 (wt %) in the eruptive products from Hekla central volcano highlights this concept well. Whilst this sample set captures the range of SiO_2 that the Hekla stratovolcano and associated fissure system has produced in the last 6000 years of its eruptive history (Savage et al., 2011), only 1 or 2 samples are analysed from each individual eruption within the system. This sample set is unsuitable for evaluating degassing induced isotope fractionation, as the melts in question are geochemically unrelated and have undergone different degrees of magmatic differentiation, mixing, and mingling with other magmas. As a result, they have different initial S concentrations and redox conditions, as well as experiencing different extents of degassing upon eruption response to different eruptive dynamics and intensities, as well as emplacement mechanisms.

Only if the eruptive history, and associated lava emplacement history, is well understood can the $^{65}\text{Cu}/^{63}\text{Cu}$ and $^{66}\text{Zn}/^{68}\text{Zn}$ variations be clearly related to degassing and distinguished from other effects. Lava flow fields are often compound, with multiple vents emplacing separate lava flow branches simultaneously, or discrete vents emplacing lava flows during distinct stages of the eruption associated with changes in eruption style and therefore degassing. Large scale late-stage lava flow resurfacing events have been observed in recent eruptions, e.g., Holuhraun 2014–15 CE (Pedersen et al., 2017), which complicates retrospective sampling as the

association between active channel migration, eruptive style and the resultant lavas emplaced is unclear.

This work focuses on two historical, well-documented, geochemically homogeneous, OIB FL eruptions. It aims to minimise the limitations of previous studies by isolating the effect of shallow conduit processes, such as syn-eruptive degassing, lava flow emplacement dynamics such as syn-emplacement degassing, and the evolution of the transport system in relation to vent activity; by documenting the effects of these processes on the Zn and Cu stable isotope systems. As of yet, a clear understanding of how these systems behave at magmatic temperatures and in response to different physical volcanological processes is not well constrained. This study will enable a greater understanding of the existing isotopic compositional ranges in eruptive products and how these systems behave during basaltic fissure eruptions. Establishing a detailed baseline dataset will enable better comparisons between crucial variations in isotopic compositions within samples from different parts of a volcanic system, i.e., intrusive versus extrusive rocks or the geothermal system, or between the isotopic fingerprint generated by different styles and intensities of eruptions. This has not been attempted with a large and diverse temporal and spatial sampling suite from a single eruptive event.

8. 1. 2 Geological Setting

A FL eruption occurs on average every 250 years in Iceland (Thordarson et al., 2003a); high-intensity and high magnitude FL events are associated with significant hemisphere-wide atmospheric and stratospheric volcanic pollution triggering environmental and climatic perturbations (Thordarson et al., 1996). Whilst the lower intensity end-member of the FL spectrum produces significant localised volcanic S and halogen pollution as well as intermittently elevating particulate or S levels in neighbouring countries (Schmidt et al., 2015). Iceland's proximity to Europe has direct implications for the health, environment and economy of dense European population centres and therefore, FL eruptions have been a particular focus for recent hazard assessments (Schmidt et al., 2011, 2012; Loughlin et al., 2012; Schmidt and Robock, 2015; Ilyinskaya et al., 2017; Carlsen et al., 2021).

Basaltic fissure eruptions span a wide spectrum in terms of intensity, magnitude, style, emplacement nature, and duration, producing comparable eruptive products, regardless of size. This enables smaller-scale, well-documented, FL eruptions to be used as modern analogues to improve our understanding of the atmospheric volatile loading and climatic impact associated with larger geological events such as flood basalt (FB, >100 km³) eruptions (Self et al., 1996; Chenet et al., 2007, 2008, 2009; 2003; Blake et al., 2010). Icelandic basaltic magmas are chosen for this study because they are S-rich and efficient at degassing their S load into the atmosphere (Edmonds and Mather, 2017).

Two small-scale historical, well-documented, Icelandic flood lava eruptions were chosen as modern analogue case studies (Figures 8. 3–8. 5):

- (1) The 2014–15 CE Holuhraun eruption, which created a lava field of 1.45 ± 0.04 km³, released 9.6 Mt SO₂ into the atmosphere (Gíslason et al., 2015; Pfeffer et al., 2015; 2018). The magma that fed the 2014–15 CE Holuhraun eruption is a moderately evolved olivine-tholeiite, sourced from 8 ± 5 km depth, and is compositionally indistinguishable from other historical basalts that have erupted from the Bárðarbunga–Veiðivötn system (Halldórsson et al., 2018). It contains <5% macrocrysts, which are predominantly composed of plagioclase with subordinate clinopyroxene and olivine, a quenched immiscible chalcopyrite sulfide phase and varying microlite contents which increase with distance from the vent, with the highest microlite contents associated with more mature, viscous, late-stage, lava morphologies (IES eruption team). Lava and tephra samples were collected throughout the 6-month long event capturing all stages of eruptive activity and analysed for whole rock major and trace element concentrations, taken with O, Pb, Sr and Hf isotopes; these data sets indicate that the magma feeding this eruption is compositionally homogeneous, generated by homogenisation of a compositionally variable mantle source (Halldórsson et al., 2018). A minor increase in the primitive crystal mush content, from a disrupted crystal mush at depth, in the very last eruptive products from Holuhraun has also been detected by the authors during field observations. Cumulate mush crystals

were dominated by plagioclase; they varied in size and had rounded resorption rims. Gabbroic fragments, dominated by plagioclase, were also observed in samples from early on in the eruption (Geiger et al., 2016); again, these had rims reacting with the carrier melt. Analysis of these gabbroic fragments identified that they displayed slightly lower $\delta^{18}\text{O}$ values when compared to bulk whole rock samples, suggesting they record melts that had incorporated hydrothermally altered crust. Samples containing disintegrated cumulate mush crystals or gabbroic fragments were avoided during sample selection as they do contain minor proportions of olivine, which could skew the Zn isotope data sets and distort trace element ratios in the samples selected for this study. Samples containing visible mush or gabbroic fragments were filtered out upon crushing during the sample preparation stage. They were also avoided in the field during post-eruption sampling. The Holuhraun eruption yielded unparalleled in-situ, airborne and satellite monitoring volcanological datasets, making it an ideal test case for characterisation of the isotopic variations, as we can directly relate any Zn or Cu stable isotope measurement to time-constrained observations. The majority of the eruptive activity from Holuhraun 2014–15 CE occurred along a 1.8 km long fissure, which started life as an open ‘curtain-of-fire’ and concentrated down within two days into discrete vents which were the focal point of the eruptive activity for its duration. This eruption is the low-intensity end-member for high magnitude eruptions, i.e., FL eruption, used in this study and due to its remote location and small size resulted in a limited local environmental impact.

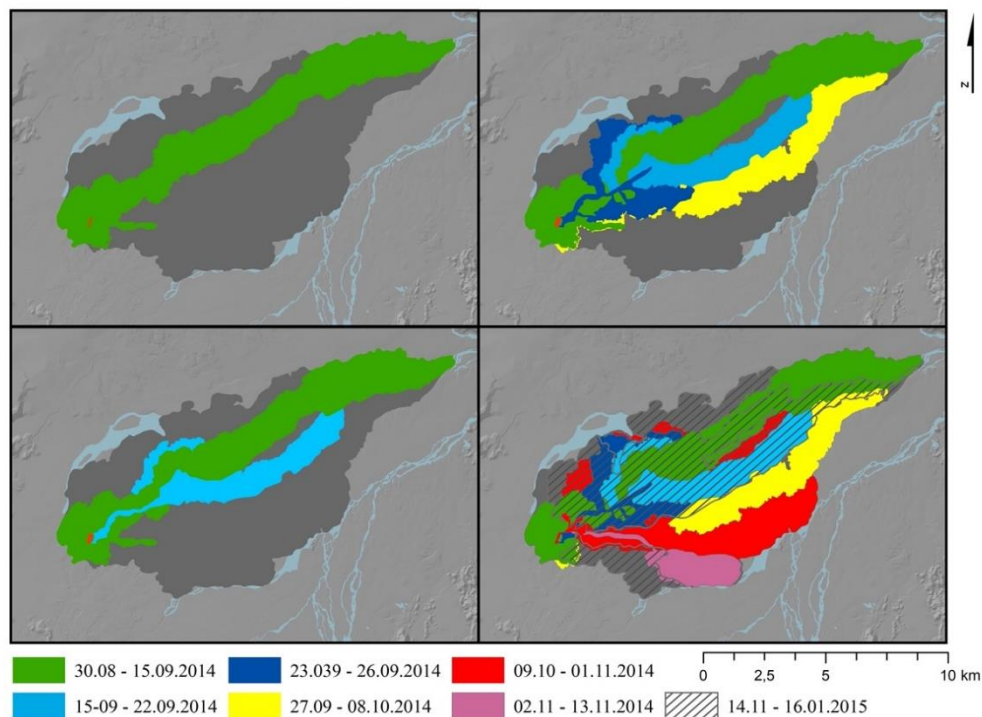
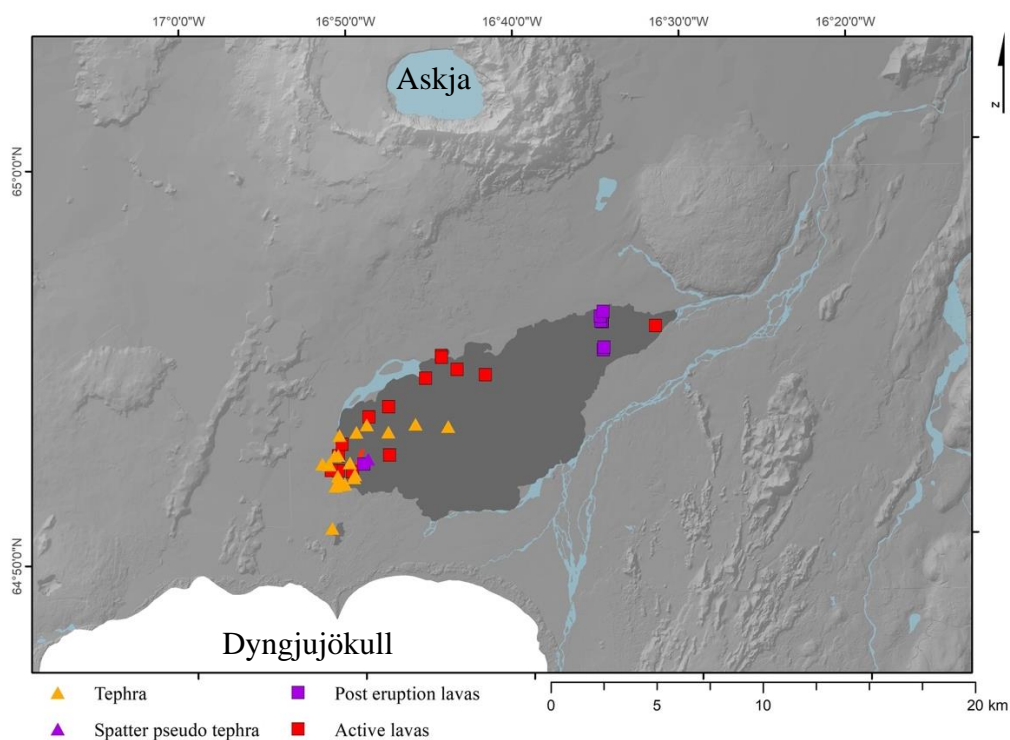


Figure 8. 3: (A: above). The temporal evolution of the Holuhraun 2014–15 CE flow field and sample locations. Samples analysed in this study, which correspond to the data table located in supplementary material, appendix B: Holuhraun Sample List. Some samples do not have a recorded GPS location. As indicated by the sample locations, the N, W and NE areas of the flow field were much more accessible than the southside due to the risk of jökulhlaups from Dyngjujökull.

Figure 8. 3: (B: below). Outline of the 2014–15 CE Holuhraun flow field after 27 February 2015 shown in grey, overlain on top of an Arctic DEM hillshade of the sandur it erupted onto. Four time periods are displayed, with their associated emplaced lava branches, to highlight the branching nature of flow emplacement, which is predominantly emplaced in a clockwise fashion. The initial branching of the flow field occurs coevally with changes in vent activity on 15 September 2014 occurs coevally.



(2) The 1783–84 CE Laki eruption which produced 14.7 km³ of lava and 0.4km³ of tephra (Thordarson and Self, 1993), as eruptive activity propagated along a 29–29.5 km long fissure (see Chapter 5). In total, it is thought to have released 120 Mt of SO₂ into the atmosphere (Fiacco et al., 1994; Thordarson et al., 1996; Thordarson and Self, 2001; Stephenson et al., 2003), thereof 100 Mt SO₂ into the lower stratosphere, producing a significant hemisphere-wide climatic and environmental impact (Sigurdsson, 1982, 1990; Wood, 1992; Thordarson and Self, 2001, 2003; Highwood and Stevenson 2003; Oman et al., 2006a, 2006b; Schmidt et al., 2010, 2012). The magma that fed the Laki eruption is a quartz tholeiite, containing <10% macrocrysts, predominantly composed of plagioclase with subordinate clinopyroxene and olivine, and like Holuhraun, its eruptive products contain a sulfide phase (see supplementary material, appendix B: Sulfides Tri Plot), with a calculated storage zone depth of 6–10 km. The limited elemental and isotopic (Pb, U, Th, Sr, Hf and O) variations throughout the eruptive products (Sigmarsson et al., 1991; Bindeman et al., 2006; Halldórsson et al., 2018) indicates that the magma feeding this 8-month long event was geochemically homogeneous. However, it is worth highlighting that the crystal cargo increases and becomes more primitive with time during the Laki eruption (Passmore, 2009; Passmore et al., 2012; Neave et al., 2013, 2017). The Laki eruption was much more explosive than Holuhraun, producing a plume capable of stratospheric loading (Thordarson and Self, 1993; Thordarson et al., 2003a, 2003b), its fissure system spans 29–29.5 km (see Chapter 5), and activity migrated along the fissure system in 10 distinct fissure opening episodes, from the SW towards the NE. Contemporary accounts documented in the Eldrít chronicles compiled and analysed by Thorarinsson (1967, 1969, 1984); Thordarson (2003); and Thordarson et al. (2003b), focus predominantly on the detailed scientific style of Jón Steingrímsson's accounts (Steingrímsson, 1783a, 1783b, 1788, 1901; Steingrímsson and Ólafsson, 1783). However, these studies also contain observations, maps and descriptions from subsequent Eldrít's written by: Björnsson (1783); Eiríksson (1783); Thorarinsson (1783); Pálsson (1783, 1793–1794); and Stephenson (1783, 1785, 1786). Taken together, these accounts provide scientifically important observations for reconstructing the eruptive activity. These are used in conjunction with

meteorological observations from elsewhere in Europe (Grattan and Pyatt, 1994; Grattan and Charman, 1994; Grattan and Brayshay, 1995; Grattan, 1998; Grattan and Sadler, 1999; Grattan et al., 1999; 2005; Thordarson and Self, 1993; 2001; 2003; Thordarson et al., 1996, 2003b), enabling a detailed reconstruction of the vent activity based on local tephra stratigraphy. The Eldrít chronicles and analysis of these accounts by Thordarson et al. (2003b), also provides sufficient resolution for the timing of the emplacement of lowland lava flows from the Laki eruption. The lava flow field has the added complication of the multiple vents and fissures, feeding it being active at the same time, and thus the known lowland arrivals are the only accurately dated lava flows as the highland record is unknown. The tephra layers from the 10 fissure opening episodes for the Laki eruption are given distinct names which define whether they are a magmatic (M) or phreatomagmatic (P) phase and their order, which includes 2 cone tephra from fissures (F) with no corresponding tephra layer: M1, M2, P1, M3, P2, M4, M5, F9, P3 (F10) and M6 (See Chapter 7). This modified the initial set up by Thordarson and Self. (1993), which uses strombolian (Sx) and tuff-cone (TC-x) for the different phases (x), as the activity is not strombolian this numbering system has been updated in this thesis (see Chapters 5 and 7).

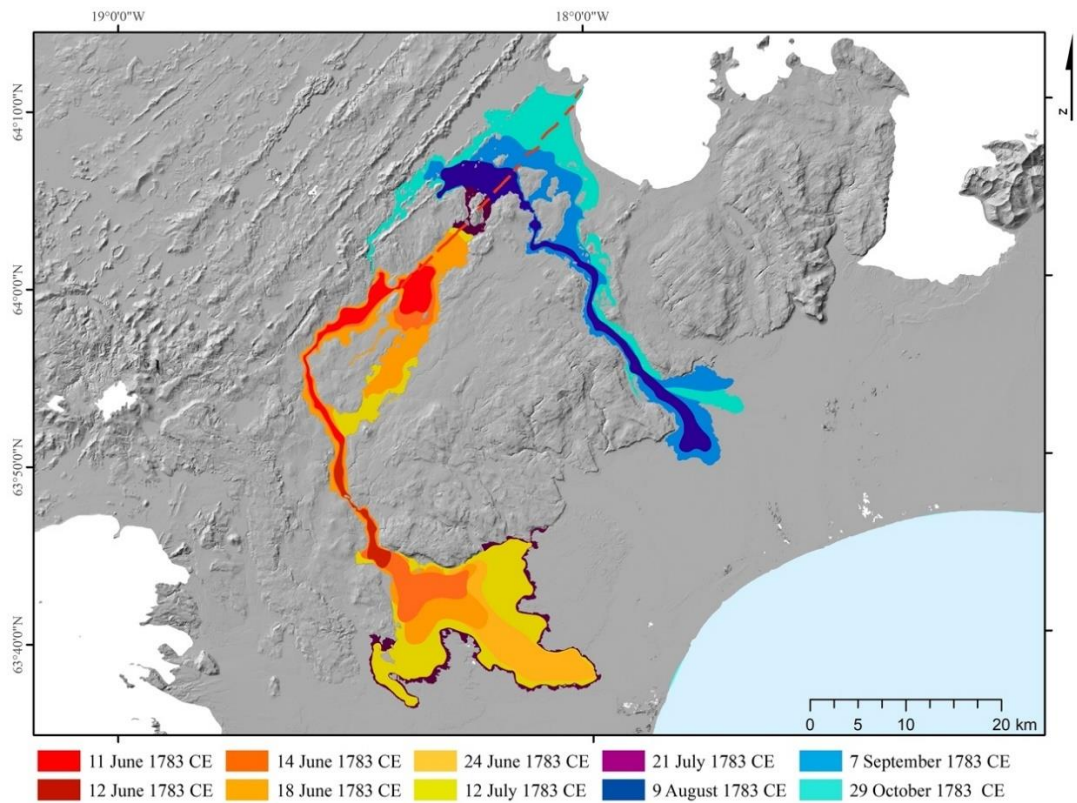
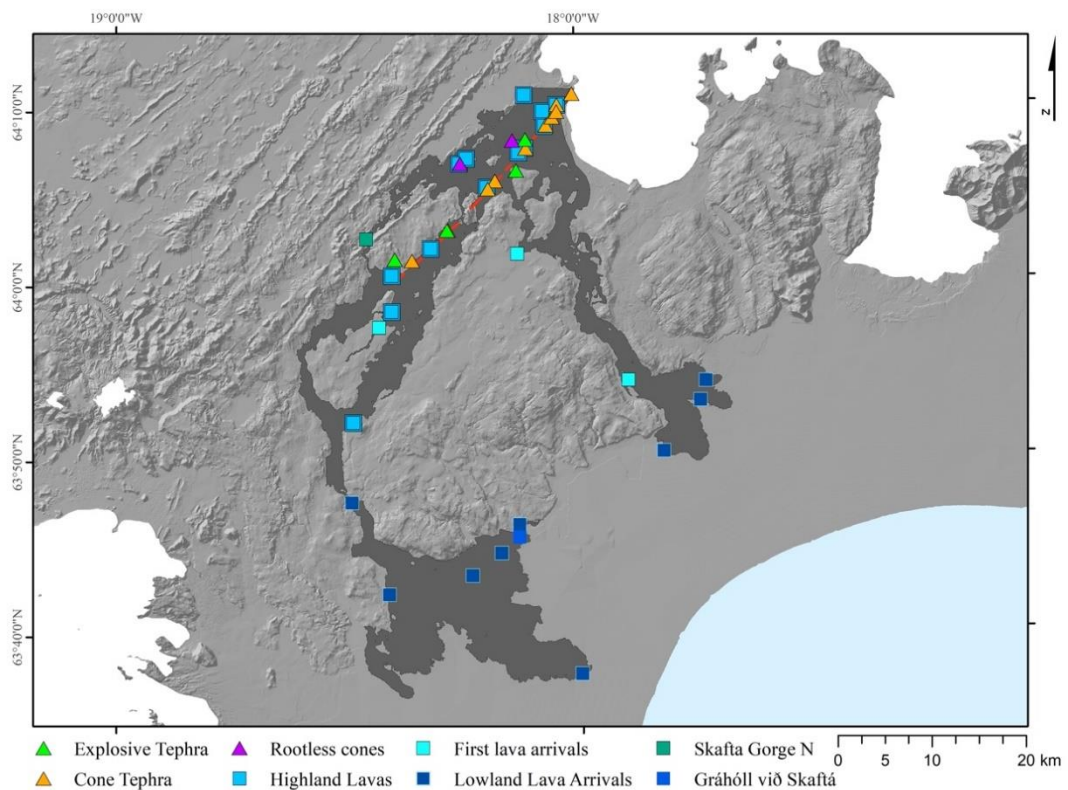


Figure 8. 4 (A: above): A georeferenced map of the temporal evolution of the Laki lava field and sample locations. Arctic DEM hillshade of the Laki area and its surroundings, overlain with the dated, Laki lava field arrivals to the lowlands, outlines taken from Thordarson et al. (2003b) were edited and georeferenced.

Figure 8. 4 (B: below): Arctic DEM hillshade of the Laki area and its surroundings, overlain with the outline of the final extent of Laki lava field, with the sample locations and types indicated throughout the flow field. For corresponding GPS points and sample names, see supplementary data, appendix B: Laki Sample List.



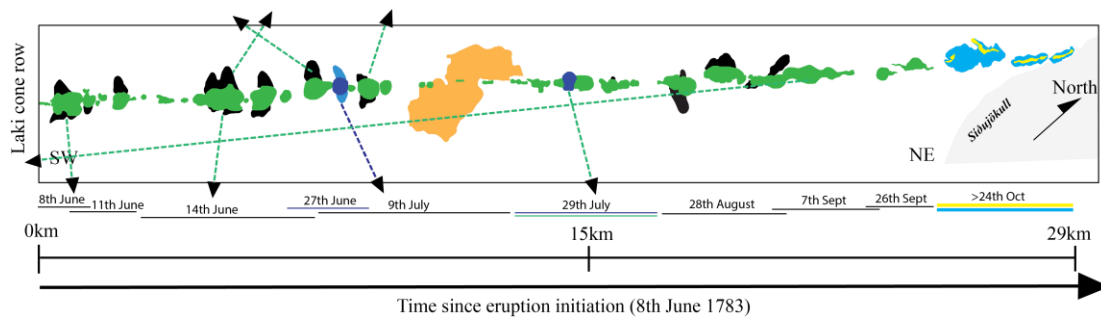


Figure 8. 5: Laki crater row, apron tephras and tephra dispersal axis. An outline sketch, to scale, of the Laki cone-row, modified from Thordarson and Self, (1993) using aerial images (from Loftmyndir). The length of individual fissure opening phases is indicated by the scale at the bottom of the figure, given alongside the date of initial opening phase activity just above the scale bar. Magmatic (M) cones are shown in green, with their tephra aprons outlined in black. Phreatomagmatic (P) cones have two colours: blue cones and light blue tephra aprons, which indicate surface lake generated phreatomagmatic tuff cones, and turquoise cones which, indicates sub-glacially generated phreatomagmatic tuff-cones. The small yellow features on the top of the latter indicate the location of ice-confined hackly lavas, which have undergone rapid cooling from external water interaction (assumed to be generated through interactions with jökulhlaups). Mt. Laki is shown in light orange. Blue and green dashed lines and black arrows indicate the dispersal axis of observed tephra fall, with locations of vents calculated by Thordarson and Self. (1993).

The relative geochemical homogeneity of these large volume eruptive events minimises the complication of Cu and Zn isotopic variations being due to a heterogeneous source composition; thereby making these well-documented and well-characterised FL events the perfect test site to apply and test these novel stable isotope proxies. Each of these eruptions offers a different aspect to capture the range of $\delta^{66}\text{Zn}$ and $\delta^{65}\text{Cu}$ values produced by an eruptive event during the stages of vent activity/dynamics and the associated changes in lava flow field emplacement regimes. Holuhraun erupted along a single fissure, whereas the Laki lava field was fed by multiple fissures. Despite the differences in eruptive intensity, with Laki producing fountains above 1400 m compared to the maximum fountaining height of 170 m observed at Holuhraun (IES eruption team reports), each of the Laki fissures went through relatively similar stages of activity to those observed for Holuhraun: an emergent fissure; explosive phase which wanes into predominantly lava effusion; and low-intensity bubble bursting or lava pond boiling before activity ceases. A large-scale detailed sampling campaign was undertaken to capture the range in eruptive products for both events in high resolution, which enables comparisons with the on-site monitoring data sets for Holuhraun 2014–15 CE and previous studies and contemporary accounts for Laki 1783–84 CE.

8. 2 Methods

8. 2. 1 Sampling methodology

In the case of the Holuhraun eruption, pristine lava selvages were collected from active or recently active lava fronts (Table 8. 1). The glassy lava selvages represent the naturally or manually quenched skin of the lava flow which records the volatile and microlite content at that point away from the vent, providing information on the lava channel and flow field development. Tephra was collected as it fell and alongside documented vent activity at the time (Figure 8. 6), with cone building tephra collected towards the end of the eruption.





	'A'a	Rubbly pāhoehoe	Slabby pāhoehoe	Spiny pāhoehoe
Description	A lava with brecciated flow tops and bases. The breccia consists of jumbles of blocky lava and irregular-shaped clinker.	A flow characterised by a flow top of pāhoehoe crustal rubble and a pāhoehoe base. The crustal rubble is up to several decimetre in size.	A flow characterised by a flow top of crustal slabs and a pāhoehoe base. The slabs are up to metres across and several decimetres thick.	A flow with a coherent crust, undisrupted at meter scale and with a spinose surface and characterised by longitudinal grooves and ridges over a flow field scale. Flows never display large amounts of volume growth via inflation.
Emplacement	The clinker is formed by viscous tearing of the chilled lava crust. The clinker is rafted towards the flow front where it is dislodged from the front in a caterpillar-track motion (Keszthelyi and Self, 1998, Harris et al., 2017).	Can be twofold (1) Pulses of lava disrupt the immature crust of a pāhoehoe flow, that is brecciated and transported on top of the flow (Keszthelyi et al., 2004; Guilbaud et al., 2005). (2) Breakout picks up loose breccia from the a'a flow that is carried on top of the flow.	Pulses of lava disrupt a mature crust of an inflated pāhoehoe flow and forms heaps of slabby clasts that raft on top of the flow (Macdonald, 1967; Swanson, 1973; Self et al., 2000).	Surface is formed by very slow but evident viscous tearing of the microlite rich lava in a break-out which as it oozes out and tears forms very fine Pele's Hair like spines on the surface. This flow type is susceptible to over inflation of, creating flower structures with outer surfaced turn 180°. It is often unpreserved over aerial scales.
				
Temperature s (FLIR data)	Ca. 995	Ca. 1005	Ca. 1050	
Velocity	≈ 30-60 m/hr	≈ 10-30 m/hr	≈ 400 - 800 m/hr	1-2 m/day
First time of observation	1 September/ 2 nd eruption day	1 September	31 August /1 st day of eruption	4 November
Location of activity	Active flow front.	Marginal and frontal break out.	Marginal and frontal break out. Primarily in proximal areas	Marginal and frontal break out. Primarily in proximal areas due to lower discharges.
Video	20140906_1523_GBMP	20140904_2221_GBMP	20140831_2033_RA	041114_1627_CRG

Table 8. 1 Key lava morphologies observed and sampled during Holuhraun 2014–15 CE. Active examples of the main lava morphologies observed and documented throughout the Holuhraun 2014–15 CE eruption. Key observations such as proximity to the vent, first time observed, velocity, and FLIR measured temperature is noted alongside key morphological characteristics. Images of the active lava fronts were taken by Dr. Gro. B. M. Pedersen (GBMP), Dr. Robert A. Askew (RA) and the author (CRG).



Figure 8. 6: Medial tephra fall from the Holuhraun 2014–15 CE eruption. Field images (capture by Dr. Bergrún Arna Óladóttir) of golden pumice, achneliths (fused outer surface golden pumice clasts), Pele’s tears and hairs on the dark Sandur, comprised of basaltic ash and rounded rock fragments from the glacial outwash plain. The size of golden pumice and achneliths varies from ash to large lapilli.

Sampling the Laki 1783–84 CE eruptive products was not as straightforward, target locations were selected utilising aerial and drone-based imagery alongside information from contemporary accounts (Eldrít chronicles, various authors) compiled and analysed by Thordarson et al. (2003b) and Thordarson (2003); to best capture different stages of lava flow advance down strike, through long-lived channels using changes in lava crust morphology. The tephra sampling strategy at Laki differed from the southern to northern fissures, which lie to the SW and NE of Mt. Laki respectively. The southern (S.) fissure tephra aprons cannot be used directly as during the 5th fissure opening phase (9–12 July, 1 month into the eruption) the entire S. fissure cone-row was reactivated, with tephra aprons from this episode falling directly onto older apron phases. To remove this complication, and a potential source of contamination of different tephra phases, a medial-proximal soil section containing a thick clear Laki tephra layer, and the target subunits, was used and each subunit separately ensuring no contamination from the layers above or below. The distinctive tephra layers from the following eruptions were used as stratigraphy marker units within the soil horizon to pinpoint the Laki tephra layers: Grímsvötn 2011 CE, Katla 1918 CE, Hekla 1845 CE, Veidivötn 1477 CE, Öräfajökull 1362

CE, Eldgjá 936 CE and Vatnaöldur-Törfajökull 870 CE (The Settlement layer), the presence of an intact sequence confirms that the stratigraphy was unaffected by secondary deposition/erosion or permafrost distortion (Figure 8. 7). The northern (N.) fissure tephra sampling focussed on the edge of proximal tephra aprons, which represent pyroclasts deposited downwind during the most explosive eruptive activity, and the variation that could be identified within a layered deposit associated only with activity from one fissure eruptive episode (Figure 8. 7). At this distance from the vent, the tephra apron is thinner but still clearly contains stratigraphic variations, present as sub-units with differing proportions of coarse or fine material and clear contacts between sub-units, which can be interpreted as subtle changes in vent activity. There is no stratigraphic evidence in the N. fissures of re-activation as the fissure opening events moved steadily, in a step-wise fashion, to the NE along the Laki cone-row, therefore these tephra aprons are not contaminated. However, because the soil layer is underdeveloped in this region, the very top of the unit which exhibited evidence of secondary erosion/deposition and weathering was excluded. For M4 (25 August–1 September) and M5 (7–14 September) enough variation in the stratified proximal apron tephra units can be observed to take 3 sub-samples from each of these deposits to see how degassing induced isotopic fractionation potentially varies within the life span of a single fissure. P3 erupted in a shallow subglacial environment (24–29 September), it is a cone building tephra sample from a co-surge and wet fall eruption phase; the tephra apron created by this event has been destroyed by the surrounding glacier as it was either deposited on ice or removed as the glacier re-advanced over the unconsolidated material. M6 erupted sometime after the wet phase of P3 stopped, as the vent isolated itself from the external water source, M6 represents the waning phases of the eruption. Tracing the cones from fissure 10, along strike to the NE they become increasingly ice-confined in morphology (see Chapter 5).

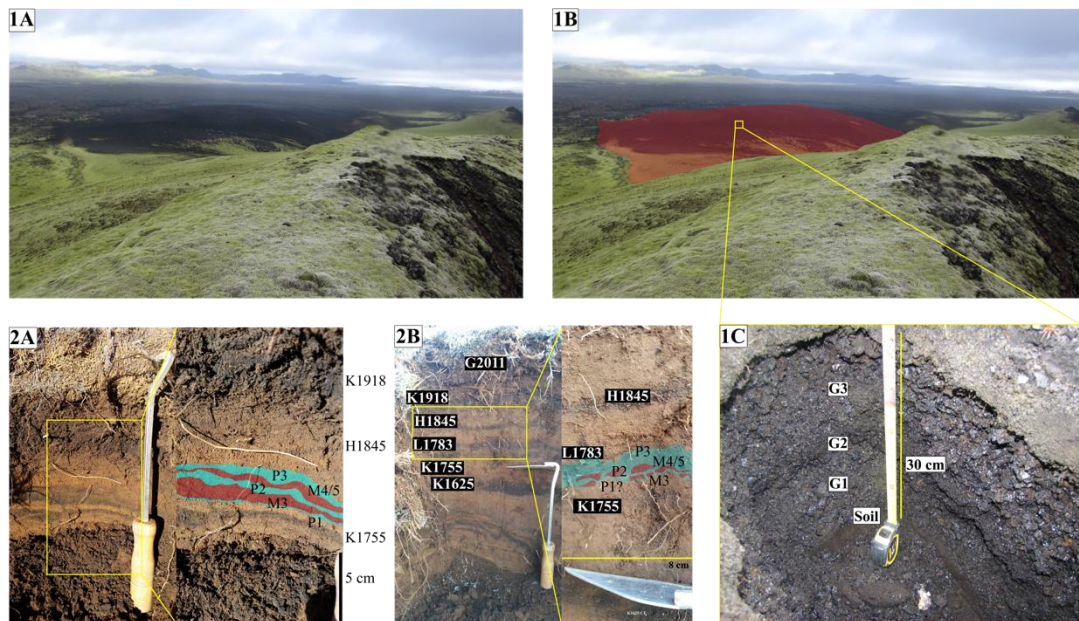


Figure 8. 7: Proximal Laki tephra aprons and internal layering and sub-units in medial Laki tephra in soil horizons. (1A) extensive black M5 apron tephra layer extending north-eastwards away from the green moss-covered crater, outlined in (1B) with red for clarity, with the inset outline for (1C) indicated by a yellow box. (1C) A tephra pit through the edge of M5 explosive apron tephra fall deposit to the soil layer underneath, 3 distinct layers with different grainsizes G1–3 (labelled) can be observed. (2A and B) Medial soil horizons in the Síða highlands, with coloured overlays highlighting distinct tephra magmatic (red) and phreatomagmatic (blue) sub-units within the Laki 1783–84 CE tephra layer, which are also labelled. Katla 1755 CE, Hekla 1845 CE, Katla 1918 CE and Grímsvötn 2011 CE are labelled for reference.

8. 2. 3 Sample preparation (major elements, trace elements, Cu and Zn)

All lava and tephra samples were selected to avoid visible biological material, then dried at 40°C in an oven for 72 hours, following IVHHN guidelines for volcanic ash sample preparation, to remove water and biological material before being processed without causing compositional changes. Samples were visually inspected when dry, and any samples with signs of alteration that could not be separated from pristine glass were discarded. Only the glassy rind and immediately adjacent material from the lava flow selvages was crushed and processed. Lava samples were cut using a diamond blade rock saw, and suitable fragments were then crushed. At every stage of processing rock fragments with contamination from any metallic surface, e.g., hammer/rock saw were removed. The tephra samples were crushed by hand using an agate mortar and pestle.

8. 2. 3. 1 Sample powdering (Cu and Zn, traces and majors)

Selected lava chips and crushed tephra were powdered using an agate ball mill at the rock preparation facility at Durham University. The mills were cleaned with water and then ethanol prior to and after running clean low-iron silica sand, this process is repeated between each sample. To pre-contaminate each ball-mill, a small quantity of sample was run for 5 minutes; this powder was agitated and discarded before the bulk sample was loaded and fully powdered (smooth when rubbed between a gloved finger and thumb).

8. 2. 3. 2 Sample analysis, Major elements:

Major element abundances, as well as CrO₃ and NiO concentrations, in bulk rock powder samples were obtained by wavelength-dispersive X-ray fluorescence spectrometry (Philips PW 2400) at the Institute for Planetary Materials, University of Okayama following the methodology outlined by Takei (2002). This analysis was carried out on fused glass beads containing lithium tetraborate flux at a ratio of 10:1. The totals reported are corrected to loss on ignition (LOI). The international standard BCR was analysed 3 times at the start of the analysis and twice after every 10 samples to track reproducibility and instrument drift. Two blank fused beads were also analysed at the start and the end of the analysis run. The Analytical errors (2 SD) for major element analysis were <5%.

8. 2. 3. 3 Sample dissolution (Cu and Zn and traces)

Eruptive products from both the 1783–84 Laki eruption and the 2014–15 event at Holuhraun contain potential small scale unavoidable heterogeneities inherent in natural samples. In the case of these basaltic lavas and tephra, they take the form of slight variations of: phenocrysts; immiscible sulfides; cryptic fragmentation induced incorporation of conduit material into vesicles in tephra samples; and sulfur rich melt stringers around phenocryst phases. Therefore, to ensure comparable data from each bulk rock powder aliquots for Zn, Cu, and trace elements were taken from the same digestion. All eruptive products, from both events, contained over 100 ppm for Cu and Zn; based on these ICP-OES concentrations (Halldorsson et al., 2018) and XRF

concentrations (Passmore, 2009), 60 mg of powder was digested for Zn and Cu stable isotope and trace element (ICP-MS) analysis collectively: 25 mg for Zn, 25 mg for Cu and 10 mg for traces.

The methodology, briefly summarised below, for the chemical purification of Zn in this study is outlined in detail by Moynier et al. (2006), and later adapted by Pons et al. (2011). Each sample was digested in concentrated HF and HNO₃ at a ratio of 2:1 ml in 7 ml PTFE Teflon screw cap beakers. They were then heated at 150 °C for 3 days in-between a normal and reversed hot block to create oven like, equal, heat distribution. The samples were subsequently dried down, but not baked, to an opaque gelatinous consistency. Then 0.5 ml of HNO₃ was added to the samples, which were refluxed at 120–150 °C overnight, before being dried down again. All samples were visually inspected using a binocular microscope before being evaporated at dryness to identify any anomalies in the digestion. At gel consistency, another 0.5 ml of HNO₃ was added, and samples continued to dry down to a gel again. This step was added to ensure all HF had evaporated as HNO₃ has a higher boiling temperature, and thus evaporates at a slower rate. This sequence of nitric acid reflux and dry downs inhibits the development of fluoride precipitates in the samples into which Zn would partition, causing mass fractionation. At this point 4 ml of concentrated (10.4 M) HCl was added, and the sample residue refluxed for >24 hours at 120 °C; the samples were placed in an ultra-sonic bath intermittently to aid any potential fluoride precipitates that had formed into solution (although no precipitates were observed). When the sample was fully in solution in concentrated HCl it was aliquoted by mass for Zn, Cu and trace element analysis. The equivalent of 10 mg of sample solution was taken for traces, dried down, and then taken up in 0.5 M nitric to be stored in 1.5 ml centrifuge tubes. 25 mg was taken for Cu analysis, dried down and stored in 7 ml Teflon beakers in 6 M HCl. For Cu, the samples are loaded onto the columns in 7 N HCl + 0.001% H₂O₂, the small amount of peroxide to ensure all the copper is present as Cu²⁺. Because H₂O₂ can degrade over time, the samples are further dried down retaken up in HCl and peroxide just prior to column chemistry. For Zn, the sample was brought back up in 3 ml of 1.5 M HBr, ready to be loaded onto the columns.

Alongside the sample rock powders, 3 duplicates of international standards (BCR-2, BIR-1 and BHOV-1) were put through the digestion and column chemistry as well as 7 procedural blanks.

8. 2. 3. 4 Sample analysis, trace elements:

The sample trace element concentrations were measured at The Department of Earth Sciences, Durham University by Inductively Coupled Plasma-Mass Spectrometry (ICP-MS). The trace element aliquot was dried down and taken back up in 0.5 M HNO₃ and spiked with 5 ppb In and Re and 20 ppb Be for use as internal standards. The spiked sample solutions were analysed on a Thermo Scientific X-SERIES-2 quadrupole ICP-MS, which was calibrated at the beginning of each analysis against multi-element synthetic standards prepared from high purity single-element standards. The external reproducibility for the following elements is <5 %: Sc, Ti, V, Ni, Cu, As, Rb, Sr, Y, Cd, Sb, Ba, La, Ce, Nd, and <10% for the follow elements: Sm, Eu, Gd, Tb, Ho, Tm, Lu, Li, Co, Pr, Dy, Er, and Yb. Tables of the trace and element data for all samples are provided in the supplementary information (Appendix B: Holuhraun Traces and Laki Traces). Aliquots of international reference standards BCR -2, BHVO-1 and BIR-1 were analysed alongside the Icelandic basalt samples, giving elemental concentrations which agree well with other published studies (Herzog et al., 2009; Moeller et al., 2012).

8. 2. 3. 5 Zinc Column Chemistry

The quantitative separation of Zn was achieved on shrink fit Teflon columns by anion-exchange chromatography using 0.5 ml of pre-cleaned BioRad AG1-X8, (200–400 µm mesh) resin. The resin was cleaned on the column by four alternating passes of 0.5 M HNO₃, and Milli-Q (MQ) ultrapure (18.2 MΩ) H₂O. Finally, the resin was pre-conditioned by loading 3 ml of 1.5 M HBr. The sample solution (also in 3 ml of 1.5 M HBr) was added to the column, following which the matrix was eluted in 3 ml of 1.5 M HBr, leaving behind ZnBr₃⁻. Zn was then recovered from the column via elution in 0.5 M HNO₃ which changes the speciation of Zn as it passes through the column to Zn²⁺, unbinding it from the resin and eluting it from the column. To ensure total purification of Zn from other sample matrix elements, each

sample was passed through the columns twice. Two sample replicates were also prepared to assess the reproducibility of the procedure and analysis.

8. 2. 3. 6 Copper Column Chemistry

The quantitative separation of Cu was achieved by anion-exchange chromatography using pre cleaned AG MP-1 anion-exchange resin (100–200 mesh, chloride form). The resin was cleaned on the column by 3 alternating passes of both 0.5 M HNO₃ and MQ. A final MQ pass is carried out after this pre-cleaning sequence before the column is pre-conditioned by loading 6 ml of 7 N HCl. The sample solution (1 ml of 7 N HCl +0.001% H₂O₂) is then added to the column. The first stage of matrix cations (that is, those with a much lower affinity for the resin than Cu²⁺, e.g., Mg, Ti, Ni etc) are eluted in 7 ml of 7 N HCl +0.001% H₂O₂, the purified Cu²⁺ is then eluted in 20 ml of 7 N HCl +0.001% H₂O₂. After the complete recovery of Cu from the column, Fe and Zn are eluted from the column using the alternating pre-cleaning passes of HNO₃ and MQ described at the start of the column procedure. This follows the original method outlined by Maréchal et al. (1999). As with Zn, the sample is passed through the columns twice to minimise the amount of matrix in the sample elute.

For both Cu and Zn column chemistry, the sample recovery rate was greater than 99%. Complete recovery for these column chemistry procedures is required to ensure the isotopic values measured are not the product of overprinted values due to procedural errors, e.g., fractionation on the column due to low elemental recovery (Maréchal et al., 1999).

8. 2. 3. 7 Mass spectrometry analytical set up for Cu and Zn isotope measurements

Zinc isotope ratio measurements were performed on a Thermo Scientific Plus MC-ICP-MS at Durham University, running in low-resolution mode. The samples, in a 0.5 M HNO₃ solution, were introduced via a PFA 50 nebuliser attached to a glass ESI SIS spray chamber at an uptake of 50 µl/min, giving a signal of 12.5 V (per ppm). To correct for potential instrument mass-bias and isobaric interference of ⁶²Ni on ⁶⁴Zn, this study follows an established standard-sample bracketing and empirical

external normalisation method (Maréchal et al., 1999, Mason et al., 2004, Chen et al., 2013). Prior to analysis the sample concentrations are diluted to match the pure 750 ppb AA-ETH Zn bracketing standard solution, and both are spiked with 70 µl of 350 ppb pure ETH Cu solution. AA-ETH Zn is used as the bracketing standard instead of JMC-Lyon due to the limited supply of the latter (Archer et al., 2017). The ETH standard has been calibrated against the international reference standards JMC-Lyon and IRMM-3702 and has an offset of 0.28 ± 0.02 ‰ for $\delta^{66}\text{Zn}$ relative to JMC-Lyon and is indistinguishable from IRMM-3702 (Archer et al., 2017). An offline Ni correction was applied to the data (Maréchal et al., 1999; Young, 2002; Chen, 2013) after it was Cu normalised (Mason et al., 2004). Values are reported in standard delta notation in per mil (eq. 1), and in keeping previous Zn isotope studies all data is published relative to the standard reference material JMC-Lyon this study follows suit with all $\delta^{66}\text{Zn}$ data corrected by +0.28 ‰.

$$\delta^{66}\text{Zn} = [({}^{66}\text{Zn} / {}^{64}\text{Zn}_{\text{sample}}) / ({}^{66}\text{Zn} / {}^{64}\text{Zn}_{\text{JMC-Lyon}}) - 1] \times 1000 \quad \text{eq. 1}$$

Each sample was analysed 3 times, with each measurement consisting of 30 cycles with an integration time of 3 seconds; an average of these 3 analyses is reported. IRMM-3702 was analysed every 10 samples, followed by the mono-component reference solutions Romil Zn A and B and a blank. The precision and accuracy of the methods were assessed using the international reference materials BIR-1, BCR-1, BCR-2 and BHOV-1 from UGSG, which, as stated previously were put through chemistry alongside the samples themselves undergoing the same method steps. The values obtained from these standards agree well with published data (Herzog et al., 2009; Bigalke et al., 2010; Moeller et al., 2012; Telus et al., 2012; Chen et al., 2013; Chen et al., 2015; Sossi et al., 2015; Liu et al., 2016; Inglis et al., 2017; Wang et al., 2017).

Seven masses were monitored during analysis which used the following Faraday cup configuration:

L3	L2	L1	C	H1	H2	H3
62 Ni	63 Cu	64 Zn	65 Cu	66 Zn	67 Zn	68 Zn

Copper isotope ratio measurements were performed on a Thermo Scientific Plus MC-ICP-MS at the University of St. Andrews running in low-resolution mode. The samples, in 1 ml 0.23 M HNO₃ solution, were introduced via an ESI microflow PFA nebuliser attached to a glass SIS spray chamber at an uptake of 75 µl/min, giving a signal of 4 V (on ⁶³Cu and ⁶⁰Ni, using 10¹¹ Ohm resistors). As for Zn, to correct for potential instrument mass-bias of ⁶⁴Ni, this study follows an established sample Ni doping, standard-sample bracketing, and empirical external normalisation method. The internationally certified reference standard for Cu ERM-AE633 was used as the internal bracketing standard during analysis; again, this is due to dwindling supplies of the previous international reference standard NIST SRM976. Prior to analysis, the sample concentrations were diluted to 75 ppb and doped with 200 ppb Ni. Each measurement consists of 22 cycles of 8.389 second integrations with a 3 second idle time. An offline log-normal Beta correction was applied to the measured Cu and Ni ratios, and a Ni interference correction was applied to the data; however, this did not change the data or its distribution or errors indicating that there was little Ni mass-bias interference, consequently the values presented in this study are not corrected for Ni interference. Values are reported in standard delta notation in per mil (e.g. 2). All previously published Cu isotope data is given relative to the standard reference material NIST SRM796, and this study follows suit with all δ⁶⁵Cu data corrected by -0.01‰ (the offset between ERM-AE633 and NIST SRM796) to enable comparisons between existing Cu isotope data (Moeller et al., 2012; Savage et al., 2015).

$$\delta^{65}\text{Cu} = \left[\left(\frac{{}^{65}\text{Cu}}{{}^{63}\text{Cu}}_{\text{Sample}} / \frac{{}^{65}\text{Cu}}{{}^{63}\text{Cu}}_{\text{NIST SRM976}} \right) - 1 \right] \times 1000 \quad \text{e.q. 2}$$

The precision and accuracy of the methodology were assessed using the international reference materials BIR-1, BCR-1, BCR-2 and BHOV-1, BHVO-2 from UGSG; which as stated previously were put through chemistry alongside the samples themselves, and their values agree with the published data (Li et al., 2009; Bigalke et al., 2010, 2011; Moynier et al., 2010; Chen, 2014; Chen et al., 2013; Savage et al., 2015)

Cup configuration:

L3	L1	C	H1	H2	H3
60 Ni	62 Ni	63 Cu	64Ni/64 Zn	65 Cu	66 Zn

The isotopic compositions of international standard reference materials (USGS) BIR-1, BHOV-1 and BCR-1 and -2 analysed in this study agree well with published values (Table 8. 6) (e.g., Herzog et al., 2009; Bigalke et al., 2010; Moeller et al., 2012; Telus et al., 2012; Chen et al., 2013; Sossi et al., 2015; Liu et al., 2016; Inglis et al., 2017; Wang et al., 2017; McCoy-West et al., 2018).

The reagents used to digest the silicate rock powders were distilled by sub-boiling at The Arthur Holmes laboratory facility Durham University using Teflon stills with the exception of ultra-pure (UpA) HBr, which was obtained from Romil. The total procedural blank from these in-house reagents and the facility was measured on the MC-ICP-MS at Durham University, using a PFA50 nebuliser and cinnabar spray chamber with an uptake of 90 $\mu\text{l}/\text{min}$, giving Zn concentrations between 4.0–9.8 ng. These variations are negligible as $>100 \mu\text{g}$ of Zn was processed for each sample. The presence of variations in the blank are thought to be explained by the presence of small quantities of a Zn rich compound found in the plastic items used in the clean laboratory, such as gloves or pipettes, and not due to variations in the purity of the reagents used.

8. 3 Results

Bulk whole-rock major, trace element, and Cu and Zn isotope data for Laki and Holuhraun are reported in Tables 8. 2–8. 5 respectively, the complete data set is presented in the supplementary material (see supplementary data, appendix B: Holuhraun Isotopes and Laki isotopes). The uniform geochemistry of the lavas and tephra, both temporally and spatially, of these two FL events yield, unsurprisingly, minimal variation in major element abundances in the 88 samples analysed (51 for 1783–84 CE Laki and 42 for 2014–15 CE Holuhraun) (Tables 8. 2–8. 5). Trace element variations in both the tephra and lava samples from both eruptions span a

typical range of Icelandic sub-aerial OIB basalts, with Zn and Cu concentrations for both eruptions in the range of 85–200 ppm for both Zn and Cu.

Sample Name	Days into eruption	Type	$\delta^{66}\text{Zn}$	2 SD	$\delta^{65}\text{Cu}$	2SD	Zn (ppm)	Cu (ppm)	SiO ₂ (wt%)	MgO (wt%)
H10	(-1)	Explosive tephra	0.161	0.021	/	/	98.00	150.20	/	/
ÁH 010914-01	1	Explosive tephra	0.197	0.026	0.07	0.08	89.62	138.00	49.73	6.89
SS 020914	2	Explosive tephra	0.189	0.029	0.05	0.05	127.5	194.30	49.86	6.86
JAS 040914-001	4	Explosive tephra	0.148	0.018	/	/	98.86	150.50	50.49	6.77
WM 1496-2 T	6	Explosive tephra	0.187	0.029	0.08	0.04	94.57	143.60	49.90	6.82
WM 1496-2 Pele's H/T	6	Explosive tephra	0.128	0.039	0.08	0.05	94.17	122.80	52.88	5.73
BAÓ 07092014-3	7	Explosive tephra	0.157	0.050	0.08	0.02	/	/	49.92	6.89
WM 1499-2	9	Explosive tephra	0.173	0.038	/	/	99.27	147.20	49.77	6.95
BAÓ 170914-01	17	Explosive tephra	0.159	0.070	0.13	0.04	118.0	171.10	49.52	6.90
BAÓ 210914 (67) T	21	Explosive tephra	0.182	0.022	/	/	98.74	159.60	49.35	6.97
TTJJCG 081014-02	38	Explosive tephra	0.213	0.034	0.06	0.03	97.76	148.60	49.77	6.91
MSR 161014-03	46	Explosive tephra	0.157	0.022	/	/	113.2	164.30	49.63	6.89
MSR 161014-03 repeat	46	Explosive tephra	0.150	0.029	/	/	113.2	164.30	49.63	6.89
MSR 291014-1	59	Explosive tephra	0.183	0.002	/	/	99.76	152.10	49.75	6.94
TTCG 041114-02 Snow	65	Explosive tephra	0.246	0.002	/	/	98.43	142.20	49.80	6.89
MSR 12112014-1	73	Explosive tephra	0.215	0.013	0.16	0.04	94.15	139.10	49.89	6.93
PN 120215-01	165	Cone tephra	0.145	0.033	0.07	0.01	94.80	142.30	49.46	6.98

Table 8. 2: Holuhraun tephra Cu and Zn isotopic variations. Holuhraun explosive and cone tephra Zn and Cu isotopic variations, alongside selected elemental concentrations and major element contents. / Indicates no $\delta^{65}\text{Cu}$ values or major/trace element concentrations for this specific sample.

Sample ID	Date emplaced	Type	$\delta^{66}\text{Zn}$	2 SD	$\delta^{65}\text{Cu}$	2SD	Zn (ppm)	Cu (ppm)	MgO (wt %)	SiO ₂ (wt%)
Sýni 81	0	Active lava	0.163	0.009	0.07	0.03	99.62	156.30	6.97	49.52
RCPW-2	1	Active lava	0.168	0.020	0.09	0.04	104.20	164.60	6.95	49.43
JG 040914-03	4	Active lava	0.199	0.038	0.08	0.04	98.52	152.10	6.92	49.57
06092014-08	6	Active lava	0.245	0.031	0.04	0.05	107.80	168.80	6.96	49.50
BAJ 07092014-5	7	Active lava	0.229	0.020	0.08	0.07	131.80	198.00	6.89	49.92
ÁH 170914-03	17	Active lava	0.166	0.045	0.06	0.03	112.20	168.40	6.96	49.39
BAÓ 210914-1	21	Active lava	0.185	0.013	/	/	111.40	169.60	6.90	49.45
WM 231014-01	53	Active lava	0.179	0.014	/	/	106.50	163.30	6.94	49.59
JG 111114-01	72	Active lava	0.189	0.010	0.14	0.03	97.64	148.80	6.97	49.29
MSR 271114-02	88	Active lava	0.209	0.017	/	/	112.50	170.90	6.95	49.21
ÁH 141209-04	105	Active lava	0.188	0.025	0.07	0.01	109.80	165.80	/	/
MSR 180115-1	140	Active lava	0.214	0.033	/	/	104.20	158.00	6.98	49.43
MSR 280115-02	150	Active lava	0.249	0.053	/	/	103.10	159.60	7.04	49.48
20150215#1	168	Active lava	0.215	0.005	/	/	100.10	149.30	6.96	49.27
MSR 170215-1	170	Active lava	0.206	0.014	/	/	101.60	155.50	6.93	49.30
Baugur Base	88	Resurface L	0.241	0.025	0.19	0.04	93.31	134.40	6.94	49.38
20160815-002 Spatter	105	Resurface L	0.261	0.025	/	/	98.62	137.50	6.89	49.54
20160815-003	140	Resurface L	0.255	0.030	/	/	88.75	129.30	6.98	49.34
20160815-006	150	Resurface L	0.261	0.030	/	/	103.60	158.50	/	/
20160815-007	168	Resurface L	0.262	0.019	/	/	94.83	145.90	6.96	49.40

Table 8. 3 Holuhraun lava Cu and Zn isotopic variations. Holuhraun active and post eruption lava sample Zn and Cu isotopic variations, alongside selected elemental concentrations and major element contents. / Indicates no $\delta^{65}\text{Cu}$ values or major/trace element concentrations for this specific sample.

Sample Name	Days into eruption	Type	$\delta^{66}\text{Zn}$	2 SD	$\delta^{65}\text{Cu}$	2SD	Zn (ppm)	Cu (ppm)	SiO ₂ (wt%)	MgO (wt%)
M1	1	Explosive tephra	0.146	0.007	0.17	0.07	119.9	101.20	49.77	5.67
M2 T	6	Explosive tephra	0.250	0.058	0.20	0.04	125.9	103.20	49.69	5.63
P1	17	Explosive tephra	0.270	0.031	0.13	0.04	133.6	115.00	49.54	5.65
M3 -011 T	31	Explosive tephra	0.260	0.011	-0.07	0.03	120.9	104.70	49.75	5.63
M1-3_P1 cone	34	Cone tephra	0.204	0.008	0.33	0.06	119.3	97.80	49.49	5.58
M4 Base	78	Explosive tephra	0.236	0.022	0.41	0.03	114.6	92.14	49.69	5.64
M4 middle	80	Explosive tephra	0.261	0.021	0.30	0.04	105.3	86.84	49.63	5.63
M4 Top	84	Explosive tephra	0.273	0.016	/	/	128.8	108.00	49.78	5.63
M5 (G3)	91	Explosive tephra	0.157	0.022	0.07	0.02	154	128.80	49.48	5.63
M5 (G2)	94	Explosive tephra	0.150	0.029	0.10	0.05	119.7	102.70	49.75	5.62
M5 (G2) Repeat	94	Explosive tephra	0.243	0.021	/	/	119.7	102.70	49.75	5.62
M5 (G1)	97	Explosive tephra	0.271	0.028	0.15	0.04	119.9	101.60	49.70	5.58
F9	110	Cone tephra	0.203	0.027	0.24	0.01	100.10	149.30	49.45	5.56
P3 Cone phase	138-140	Cone tephra	0.201	0.002	/	/	121.9	103.00	50.05	5.57
M6	>140	Cone tephra	0.201	0.038	0.16	0.04	134.3	119.20	/	/

Table 8. 4 Laki tephra Cu and Zn isotopic variations. Laki explosive and cone tephra Cu and Zn isotopic variations, alongside selected elemental concentrations and major element contents. / Indicates no $\delta^{65}\text{Cu}$ values or major/trace element concentrations for this specific sample.

Sample Name	Days into eruption	Type	$\delta^{66}\text{Zn}$	2 SD	$\delta^{65}\text{Cu}$	2SD	Zn (ppm)	Cu (ppm)	SiO ₂ (wt%)	MgO (wt%)
Hrossatunga 'A'ã - 01	6	Early lava	0.167	0.025	0.15	0.01	110.1	92.6	49.590	5.623
Bugar	48	Early lava	0.126	0.024	/	/	153.40	126.60	49.538	5.647
Grænháls-Brattland	66	Early lava	0.166	0.019	/	/	105.10	91.75	49.533	5.617
Hrossatunga 'A'ã - 03	4	Highland Lava	0.288	0.017	/	/	111.5	92.04	49.423	5.669
Leiðólfsfell-2	10	Highland Lava	0.278	0.022	/	/	117	98.71	49.746	5.612
Stakfell below RC	54	Highland Lava	0.254	0.003	0.14	0.06	120.8	103.1	49.701	5.611
Stakfell above RC	60	Highland Lava	0.243	0.009	/	/	152.4	132.8	50.655	5.742
M1-3 +P1 111016-002	4	Highland Lava	0.266	0.019	/	/	122.30	104.70	49.632	5.698
M1-3 +P1 131015-003a	12	Highland Lava	0.257	0.004	/	/	133	107.9	49.674	5.602
M4/P2 180916-013	66	Highland Lava	0.263	0.054	/	/	117.7	94.21	/	/
M5/F8 190916-017	>94	Highland Lava	0.238	0.036	/	/	122.1	95.59	/	/
F9-10 phh channel -008	>105	Highland Lava	0.275	0.021	/	/	120.8	103.9	49.577	5.623
P3/M6 101016-003	>140	Highland Lava	0.269	0.011	/	/	129.5	108.7	49.628	5.689
190814-003 Flow 2 top	91	Skaftá Gorge N	0.242	0.014	/	/	117.3	100.8	/	/
190814-001B (Selv)	60	Skaftá Gorge N	0.232	0.018	/	/	118.8	101.5	49.669	5.687
190814-001C (Selv)	51	Skaftá Gorge N	0.263	0.017	/	/	137.4	119.4	49.883	5.599
Skál	6	Lowland lava	0.236	0.072	0.11	0.03	132.80	113.30	49.458	5.639
Svínadalur- Múli	10	Lowland lava	0.241	0.001	/	/	126.80	106.30	49.582	5.605
Efri-fljótar Krókur 161017-01	16	Lowland lava	0.243	0.029	0.11	0.09	120.70	102.90	49.613	5.655
Gráhóll 'A'ã	23	Lowland lava	0.298	0.068	0.11	0.09	108.60	91.91	49.650	5.631
Gráhóll 'A'ã með Skaftá <small>fast OB</small>	35	Lowland lava	0.234	0.009	0.17	0.02	113.80	96.95	49.620	5.662
Eyjunni Á Skaftá	43	Lowland lava	0.244	0.018	/	/	118.10	101.50	49.783	5.649
Hraunból	54	Lowland lava	0.252	0.062	/	/	128.30	106.60	50.025	5.571
Brúnná	91	Lowland lava	0.287	0.031	0.19	0.04	115.80	99.31	49.498	5.732
Eldvatnkrókur	143	Lowland lava	0.262	0.011	/	/	125.20	106.30	49.830	5.631
Stakfell 001A+B	54	Rootless cone	0.279	0.03	/	/	168.2	142.8	49.751	5.616
Innrieyrar-Eldborgarraðir 025	91	Rootless cone	0.268	0.012	0.18	0.05	167.6	139.3	49.777	5.569

Table 8. 5: Laki lava Cu and Zn isotopic variations. Laki lavas, sub-categories used throughout this chapter indicated under type: early arrival; highland; Skaftá gorge; lowland; and rootless cones. Alongside the estimated date of emplacement (using Thordarson and Self, 1993) and their corresponding Cu and Zn isotopic variations, selected elemental concentrations and major element contents. / Indicates no $\delta^{65}\text{Cu}$ values or major/trace element concentrations for this specific sample.

USGS st.	d66Zn- norm (JMC-Lyon corrected)	2sd
BIR-1	0.26	0.26
BIR-1	0.25	0.25
BIR-1	0.22	0.22
BIR-1	0.23	0.23
BHVO-2	0.26	0.26
BHVO-1	0.31	0.31
BHVO-1	0.28	0.28
BCR-2	0.25	0.25
BCR-2	0.22	0.22
USGS st.	d65 Cu- Ni norm (NRST corr)	2sd
BHVO-2	0.09	0.04
BHVO-2	0.10	0.05
BHVO-2	0.13	0.02
BHVO-2	0.11	0.04
BHVO-2	0.13	0.05

Table 8. 6: International standards Zn and Cu isotopic ratios during analytical runs

When compared, the 2014–15 CE Holuhraun lava and tephra have, on average, 20 ppm higher Cu contents than those of 1783–84 CE Laki eruption, driven by the greater proportion of sulfides in the Holuhraun samples. On the other hand, the 1783–84 CE Laki lavas have 30–70 ppm higher Zn contents than the 2014–15 CE Holuhraun lavas, which is in keeping with 1783–84 CE Laki having marginally higher proportions of olivine phenocrysts. Concentration plots of Zn against immobile and incompatible elements such as Nb initially give an R^2 of around 0.7. However, when the tephra and lavas are separated into physical volcanological sub-groupings the R^2 values of Zn against Nb are >0.96 for both eruptions (see supplementary data, appendix B: Laki Traces). This strongly suggests that the Zn concentrations in the 250-year older 1783–84 CE Laki lavas have been little affected by weathering and other processes that control the Zn content in lava and tephra samples.

For both the 2014–15 CE Holuhraun and 1783–84 CE Laki eruptive products, Cu and Zn concentrations show a strong correlation, with an R^2 of >0.85 for the Holuhraun eruptive products and >0.93 for Laki eruptive products. Temporal Cu and Zn concentrations for the 2014–15 CE Holuhraun tephra and lavas alike display no correlation (Figures 8. 8 and 8. 9). However, there is an intriguing trend of two distinct Pb concentration trends in the Holuhraun lavas and tephra throughout the eruption when compared to Zn concentrations which do not vary temporally or spatially; however, when investigated further, this is an artefact of ICP-MS analysis and not associated with a particular batch sample digestion, giving false trends. Other trace elements have not been affected by these analytical errors and thus just the Pb data is discarded.

A similar trend of Pb against Zn exists in the Laki lavas and tephra; again, this is not associated with spatial and temporal variations, and again this is again due to analytical errors and not associated with a particular batch digestion as the Laki and Holuhraun samples were analysed at the same time. Unlike the lavas and tephra from Holuhraun, the Laki lavas and tephra show two distinct peak periods in Zn and Cu concentration at 50–60 days into the eruption and 85–95 days into the eruption but with no general temporal correlation (Figure 8. 8).

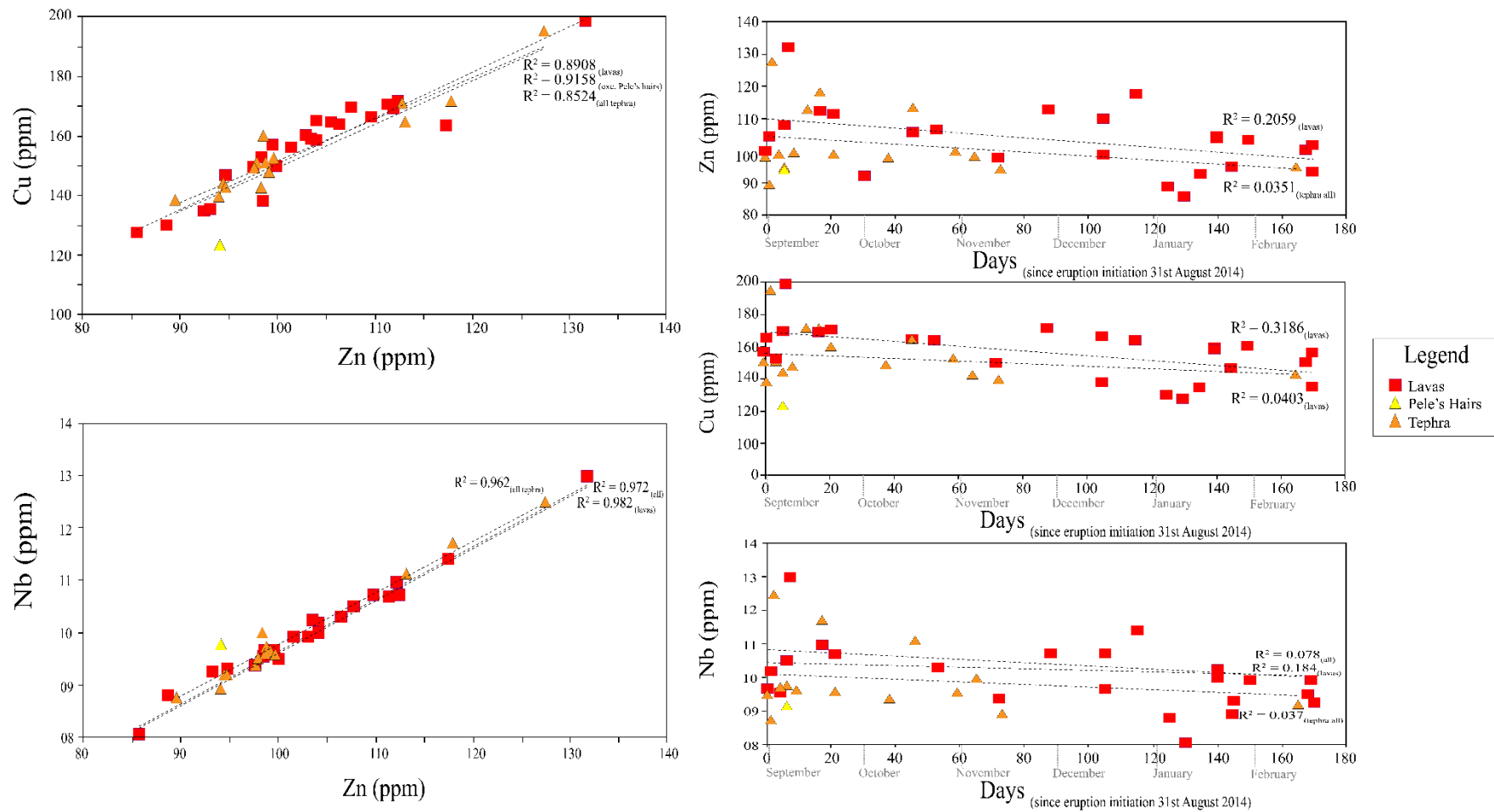


Figure 8. 8: Trace element temporal changes and co-variations in Holuhraun 2014–15 CE tephras and lavas. Selected trace element co-variation plots (left-hand side) and temporal variations in trace element plots (right-hand side) for the Holuhraun eruptive products: lavas (red boxes); explosive tephra (orange triangles); and Pele's hair (yellow triangle).

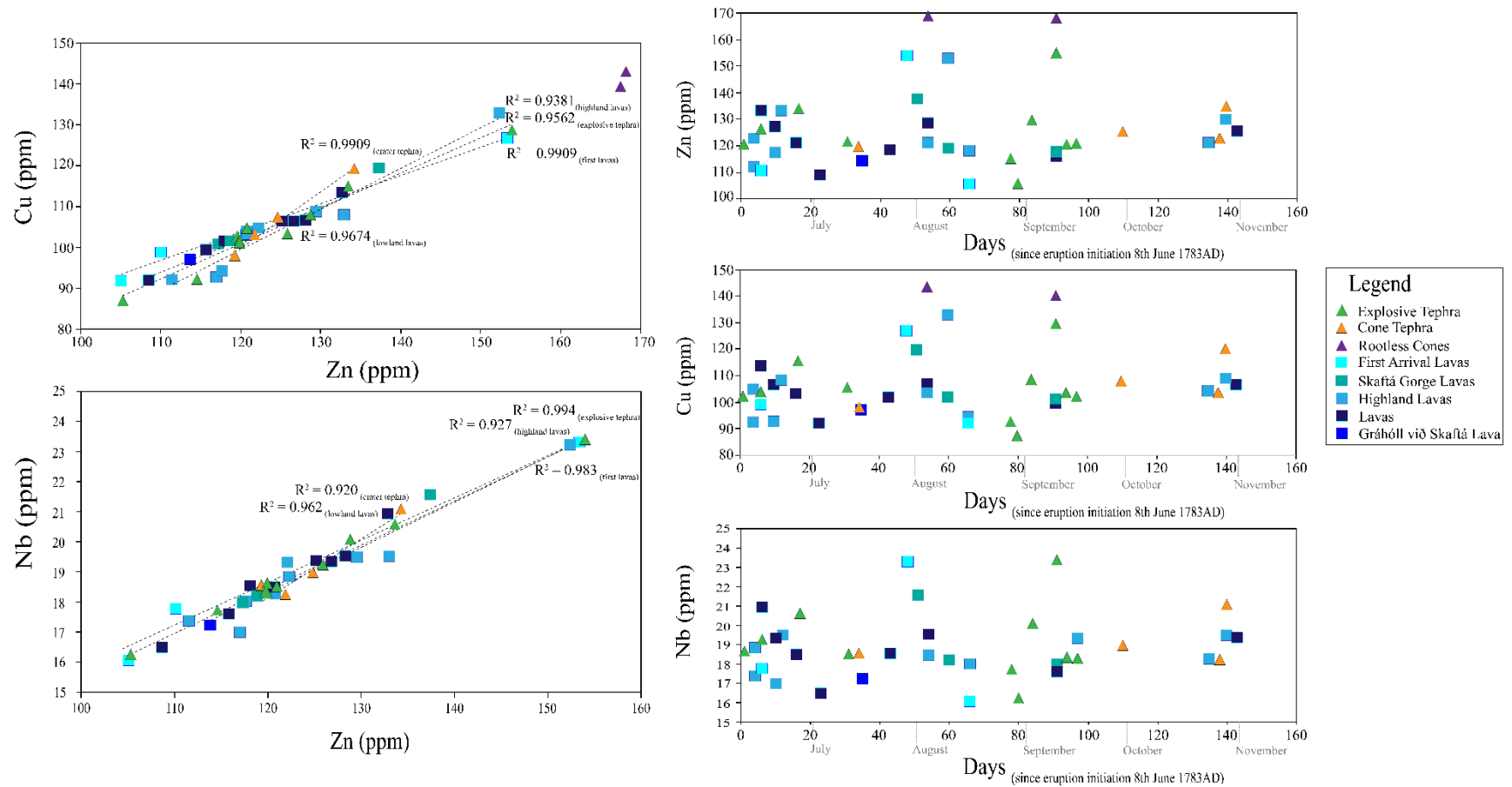


Figure 8. 9: Trace element temporal changes and co-variations in Laki 1783–84 CE tephra and lavas. Selected trace element covariation plots (left-hand side) and temporal variations in trace element (right-hand side) of the Laki eruptive products, lavas are shown in squares and tephra in triangles; see legend for details. The lavas are broken up into the subcategories: early, highland, lowland, Grárhóll Skaftá fast-moving break out, and Skaftá gorge N sequence.

For the 2014–15 CE Holuhraun eruptive products comparison of Cu and Zn concentrations against MgO (wt%) show no correlation (see supplementary material, appendix B: Holuhraun Traces, Holuhraun Majors and Holuhraun Isotopes). However, when isolating the Laki 1783–84 CE eruptive products into sub-groups: the cone tephra of the cone-row and first lavas N and S display strong covariance in Zn or Cu against MgO content with $R^2 > 0.97$. The lowland lava arrivals, highland lavas and rootless cones display no systematic variation of Zn and Cu concentrations with MgO content (see supplementary material, appendix B: Holuhraun Traces, Holuhraun Majors and Holuhraun Isotopes). In all of these cases, the MgO content displays an extremely narrow range, well within analytical error (Tables 8. 2 and 8. 3).

The ranges of trace element values and isotopic variations versus MgO content are discussed below, despite the narrow range found in MgO which is well within analytical error. These trends are not statistically robust, but with future analysis these data sets and potential trends can be added to.

8. 3. 1 Copper and Zinc isotopic signatures

The isotopic data obtained for all eruptive products from both events fall on a mass-dependant fractionation line of $R^2 = 1$, e.g., $^{68/64}\text{Zn} / \delta^{66/64}\text{Zn} = 1$ and $^{65}\text{Cu}/^{63}\text{Cu} = 1$ signifying that there are no artificial signatures due to sample processing causing mass-independant fractionation, or isobaric interferences for either isotope system during analysis. The 2014–15 CE Holuhraun and 1783–84 CE Laki lava and tephra samples have slightly heavier $\delta^{65}\text{Cu}$ when compared to BSE $\delta^{65}\text{Cu}$ 0.07 ± 0.10 ‰ (Savage et al., 2015) and moderately lighter $\delta^{66}\text{Zn}$ when compared to BSE $\delta^{66}\text{Zn}$ 0.28 ± 0.05 ‰ (Chen, 2014) and MORB/OIB $\delta^{65}\text{Cu}$ 0.06 ± 0.06 ‰ (Savage et al., 2015) and $\delta^{66}\text{Zn}$ 0.28 ± 0.06 ‰ (Liu et al., 2016) (Figures 8. 10 and 8. 11).

Initial values obtained from samples from both events demonstrate that both isotope systems display a high degree of scatter around the mean value for MORB with no distinct temporal or geochemical isotopic trends (see supplementary data, appendix B: Holuhraun Isotopes). However, when samples from each eruption are grouped in accordance with volcanological parameters such as tephra versus lava, temporal

variations dictated by vent activity, and lava channel development, trends and subtle covariations do emerge from the data. Due to sub-dividing the data sets for each eruption in this way, only some of the trends have enough samples within their sub-groups to be statistically robust.

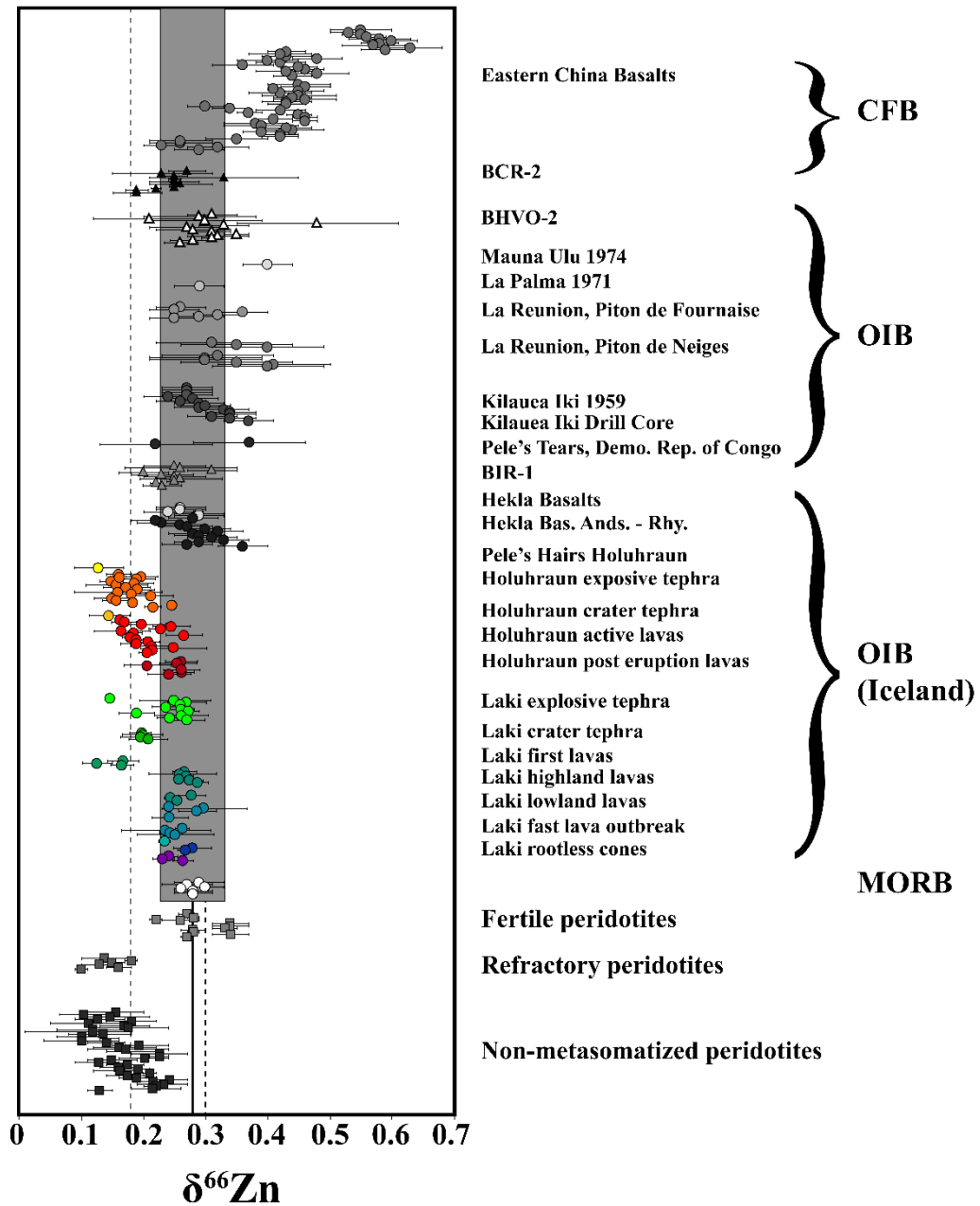


Figure 8. 10: Caltech $\delta^{66}\text{Zn}$ comparison plot of samples with existing data sets. Existing $\delta^{66}\text{Zn}$ data pertinent to this study displayed in Caltech plot: $\delta^{66}\text{Zn}$ variations of all existing published basaltic volcanics and peridotite samples, with their 2sd errors indicated by black lines, are displayed on the x-axis and spaced arbitrarily on a valueless y-axis (see supplementary data, appendix B: Zn Caltech Plot). BSE is indicated by the bold line at $\delta^{66}\text{Zn}$ 0.28 ± 0.06 ‰ (Wang et al., 2017), the range for MORB, within a 2sd error, is shown as an elongated grey box; dashed lines at $\delta^{66}\text{Zn}$ 0.31 ± 0.09 ‰, and 0.18 indicate the average values obtained for OIB and peridotites (Wang et al., 2017).

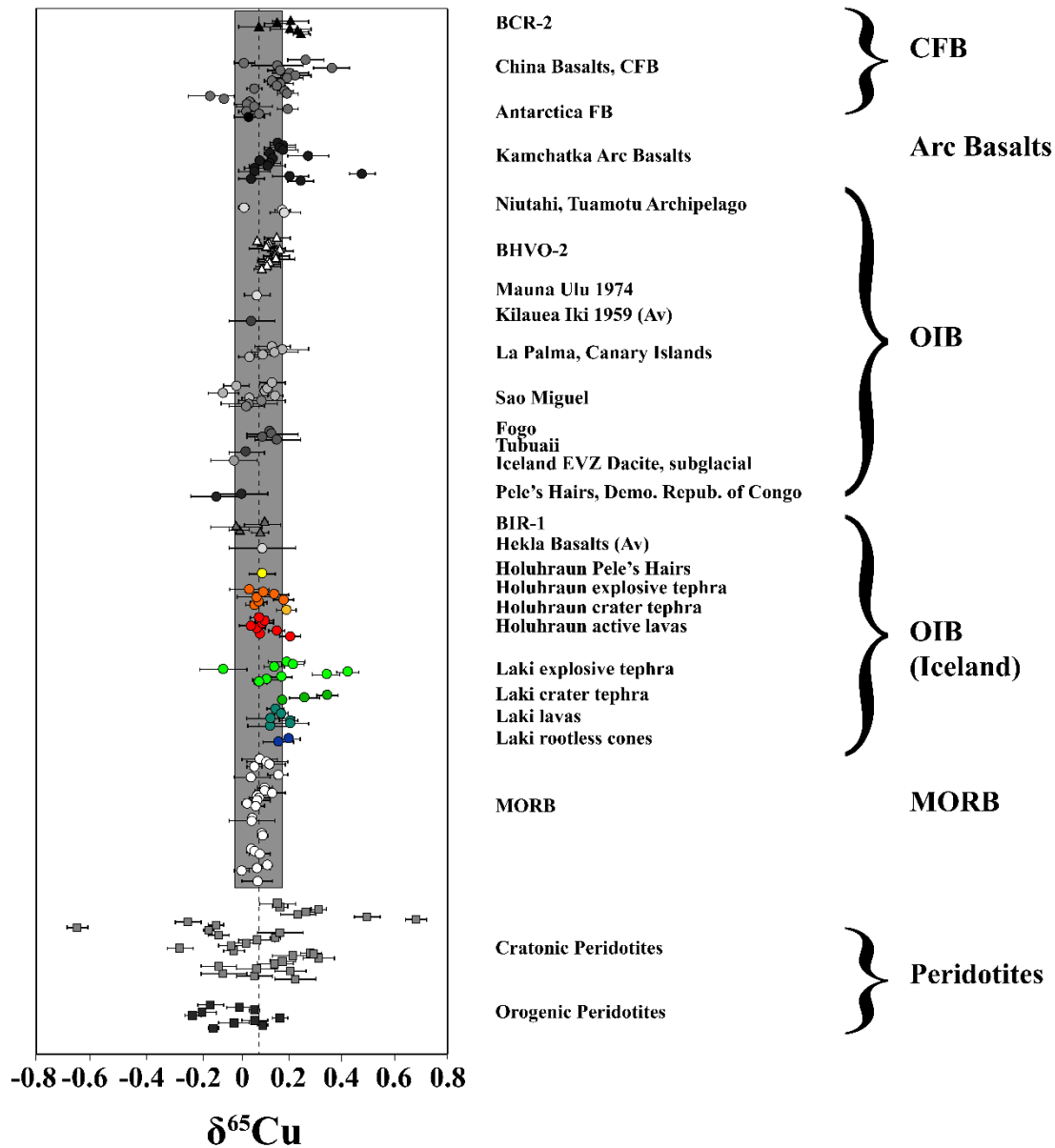


Figure 8. 11: Caltech $\delta^{65}\text{Cu}$ comparison plot of samples with existing data sets. Existing $\delta^{65}\text{Cu}$ data pertinent to this study displayed in Caltech plot: $\delta^{65}\text{Cu}$ variations of all existing basaltic volcanics and peridotite samples with their 2sd errors indicated by black lines, are displayed on the x-axis and spaced arbitrarily on a valueless y-axis (see supplementary data, appendix B: Cu Caltech Plot). BSE is indicated by a dashed black line at $\delta^{65}\text{Cu}$ 0.07 ± 0.10 ‰ (Savage et al., 2015), the range for OIB/MORB within 2sd error is shown as an elongated grey box $\delta^{65}\text{Cu}$ 0.06 ± 0.06 ‰ (Savage et al., 2015).

8. 3. 1. 1 Zn isotope variations:

8. 3. 1. 1. 1 Holuhraun 2014–15 CE

The Holuhraun eruptive products have a total range in $\delta^{66}\text{Zn}$ from 0.128–0.262. The heavier $\delta^{66}\text{Zn}$ values are predominantly seen in the lavas sampled after the eruption had finished, which capture late-stage resurfacing events of the flow field (Pedersen et al., 2017), which range from 0.241–0.262 $\delta^{66}\text{Zn}$. The samples collected throughout the eruption which represent tephra fall and active flow break-outs have a total $\delta^{66}\text{Zn}$ range from 0.128–0.249, when this is sub-divided further, the lavas span a range of 0.163–0.249 $\delta^{66}\text{Zn}$ and the tephra a larger range from 0.128–0.246 $\delta^{66}\text{Zn}$ including a Pele's hair (0.128 $\delta^{66}\text{Zn}$) and cone tephra sample (0.145 $\delta^{66}\text{Zn}$). If the latter two are removed, the explosive phase tephra spans a slightly smaller range from 0.148–0.246 $\delta^{66}\text{Zn}$; however, this is still a greater range than the lavas due to more samples having lighter $\delta^{66}\text{Zn}$ values (see Table 8. 2 and 8. 3).

Holuhraun lavas: Display two statistically resolvable trends towards heavier $\delta^{66}\text{Zn}$ with time (Figure 8. 12) in the actively sampled lava flows, which correlate well with a distinct change in mass-discharge rate and eruptive behaviour at the vent, and a change in the channel system observed on-site. A very strong covariance trend, with an R^2 of 0.9089 (although statistically weak as it is defined by 5 data points) exists between an increasingly heavier $\delta^{66}\text{Zn}$ in the lavas and days from the initiation of the eruption, which is also a proxy for distance from the vent and time spent in the transport system for the first 10–16 days of the eruption, suggesting an increase in the oxidised volatile loss of light Zn (Figure 8. 12). This phase of eruptive activity correlates with the first waxing mass eruption rate (MER), and discharge rate, peak phase from the 31 August–9 September (Bonny et al., 2018; also see Chapter 5). However, the trend does not correlate with the overall variations in Zn or Cu trace element content (Figures 8. 8 and 8. 12). From 10 September onwards, the MER exponentially decreases until 15 September, where it declines to its lowest flux since the first days of the event, and the eruption almost stopped. However, from 17 September onwards, the MER displays another waxing phase, peaking on 20 September before entering into a steadily decreasing MER phase until the eruption ended in February 2015 (Figure 8. 12). This second period from 17 September–27

February displays a clear, statistically weaker, covariance of $\delta^{66}\text{Zn}$ increasing with time, with an R^2 of 0.6746 again suggesting an increase volatile loss of light Zn with time. However, this time, it does not correlate with distance of the active lava fronts from the vent, as from 15 September onwards, the channel system branches creating a compound flow field with different transport systems active at different time periods, and also cases of older transport system reactivation later on in the eruption (Pedersen et al., 2017; Figure 8. 3). This trend of increasing ^{66}Zn occurs over a much longer timescale, 160 days, indicating at least some change in the transport system as partial channel insulation starts to occur. When viewed as a whole, the active lavas display no covariance (with an R^2 0.2272). There is no corresponding trend of $\delta^{66}\text{Zn}$ with Zn or Cu content in the molten and rapidly water quenched or recently naturally air quenched lava selvages. Likewise, there is no observable temporal trend in the post-eruption samples from transect of a lava flow outbreak which occurs as a direct resurfacing event, starting from the older levees of main active channel, and again no covariance trend of $\delta^{66}\text{Zn}$ with Cu and Zn content. Nevertheless, samples that were taken from the first surface outbreak itself display the lightest $\delta^{66}\text{Zn}$, when compared to the older 'A'ā channel levees, the resurfacing outbreak then develops a clear surface morphology with values moving towards a heavier $\delta^{66}\text{Zn}$; however, this increase is only shown by 3 data points and therefore is not statistically robust. This sampling transect, considering all samples and secondary spatter collected from closer to Baugur, exhibits a moderate trend towards heavier $\delta^{66}\text{Zn}$ with increasing MgO of R^2 0.7742 (Figure 8. 12); which could be due to the slight increase in olivine content in these later stage magmas, or a slightly more evolved melt chemistry, feeding the system towards the end of the eruption. Field and hand sample observations indicate that lava flows with a higher microlite content are produced towards the end of the eruption. At this stage the flow field is fed entirely from a rolling boil lava pond, undergoing convection and over-turning processes, creating an environment where crystals that were once microlite in size ($<100\ \mu\text{m}$) mature and grow; as well as further degassing induced crystallisation generating a new microlite phase. This lava then slowly drains into the flow field through the transport system, to feed late-stage lavas flows. From November onwards more viscous lava flow types dominate the active flow portions of the Holuhraun flow field (Pedersen et al., 2017; Table 8. 1), and these are very microlite crystal-rich and observed to

have a marginally higher FLIR derived temperature (attributed to the latent heat of crystallisation) than other viscous flows, e.g., ‘A’ā (IES eruption team field observations; Table 8. 1). An increase in the macrocryst content of the Holuhraun magma also occurred towards the very end of the eruption, with crystal mush xenocrysts also observed more frequently in hand-samples (C. R. Gallagher and K. W. Burton field observations).

*Holuhraun tephra*s: display no resolvable $\delta^{66}\text{Zn}$ trends either temporally or with Zn and Cu concentration or MgO content, although where tephra-lava sample pairs from the same day exist, the tephra always preserves a marginally lighter $\delta^{66}\text{Zn}$ (but within analytical uncertainty). The $\delta^{66}\text{Zn}$ values also generally become heavier with time in the explosive tephra phases, with the cone building phase tephra displaying a much lighter $\delta^{66}\text{Zn}$ value. The Pele’s hair sample (produced by the most vigorous vent activity, 6 September) gives the lightest $\delta^{66}\text{Zn}$ value and the lowest MgO, CaO, Al_2O_3 , and FeO_t contents, as well as the highest SiO_2 content (Table 8. 2 and supplementary material, appendix B: Holuhraun Isotopes). This is due to the lack of phenocryst phases in the Pele’s hairs samples, dictated by processes such as inertia, shearing, and strain acting upon the melt at fragmentation, which were highest during the highest MER phases; resulting in the highest explosive intensity of Holuhraun 2014–2015, that produced Pele’s hairs which have a very thin diameter. This sample drives a very weak covariation of $\delta^{66}\text{Zn}$ and MgO content (R^2 0.5502), in the early September tephra, which once removed do not display any covariation.

8. 3. 1. 1. 2 Laki 1783–84 CE

The Laki eruptive products have a total range in $\delta^{66}\text{Zn}$ from 0.126–0.298. This range of $\delta^{66}\text{Zn}$ values is predominantly dictated by lavas and rootless cone samples; however, the limited number of rootless cone samples have a narrow range in $\delta^{66}\text{Zn}$ compared to the lavas. The latter of which have a large range, from 0.126–0.298 $\delta^{66}\text{Zn}$, when samples from across the entire flow field are grouped together. Three particular lava flows sampled during the field campaign (Hrossatunga ‘A’ā -01, Bugar and Grænháls-Brattland; see Figure 8. 4) were emplaced by early peak discharge, explosive vent activity, and display the lightest $\delta^{66}\text{Zn}$ ranging from 0.126–0.167 (Figure 8. 13). Isolated sub-divisions of highland and lowland lavas display

very similar ranges in $\delta^{66}\text{Zn}$, with highland lavas spanning the range of 0.238–0.288 compared to 0.234–0.298 for the lowland lavas. Tephra fall spans a total range in $\delta^{66}\text{Zn}$ from 0.146–0.271, when this is subdivided into the highest eruptive intensity, explosive phase, apron tephra, the range stays the same; however, when the cone tephra sub-group is isolated a narrow range from 0.201–0.204 $\delta^{66}\text{Zn}$ is observed, although from a limited number of samples (Figure 8. 13).

Laki lavas: display clear vent activity related isotope signatures, initial lavas produced by an emergent curtain of fire active across a new fissure opening episode, these first lavas have a light $\delta^{66}\text{Zn}$ signature. In contrast, lavas fed by explosive activity phases, from established vents, display heavier $\delta^{66}\text{Zn}$ values. This trend exists regardless of distance from the vent, with highland and lowland (Síða district) lavas emplaced during periods of explosive activity, when the related June-July lava flow fronts are isolated (Figure 8. 13). When the first lavas, the Skaftá gorge sequence, lowland lavas and highland lavas are considered separately, none of these sample sub-groups display a resolvable temporal trend in $\delta^{66}\text{Zn}$. However, these lava samples do display good statistical trends of increasingly lighter $\delta^{66}\text{Zn}$ with increasing Zn content (Figure 8. 13) and Cu content (see supplementary data, appendix B: Laki Isotopes). The first lavas display strong trends of decreasing $\delta^{66}\text{Zn}$ with increasing Zn concentration (R^2 of 0.9853) and MgO content (R^2 of 0.9610), although they are a limited sample population size. The Skaftá gorge sequence lavas, lowland and highland lavas do not show a covariance of $\delta^{66}\text{Zn}$ with MgO content, and none of the Laki lavas display temporal trends of $\delta^{66}\text{Zn}$. However, strong trends exist with increasingly lighter $\delta^{66}\text{Zn}$ with higher elemental Zn content; in particular, the first lavas and Skaftá gorge sequence displays this trend well (R^2 of 0.9853 and 0.8623 respectively), with moderate trends displayed by the highland lavas (R^2 of 0.6395) and lowland lavas (R^2 of 0.6184). It should be noted here that whilst the Skaftá gorge and first lavas are of a limited sample number, the lowland and highland lava sub-groups contain between 8–10 samples and are thus more statistically robust.

Laki tephtras: display a clear temporal trend when considered in terms of their individual explosive fissure opening phases, each starting with lighter $\delta^{66}\text{Zn}$ values, which become heavier with time; however, there is no corresponding trend for $\delta^{66}\text{Zn}$

values against Zn or Cu concentrations with time (Figure 8. 13). The temporal variations are stronger for individual apron tephra phases, e.g., M4 and M5 (R^2 of 0.8715 and 0.8364 respectively), whereas where this detail of sampling was not possible in the S. fissure M1–3+P1 displays a very weak covariation (R^2 of 0.4597). The cone tephtras do not display a trend towards lighter $\delta^{66}\text{Zn}$ with time, but there is a strong covariance of the $\delta^{66}\text{Zn}$ with vent deposit activity through different eruptive phases with time (Figure 8. 13). The trend is always the same: each separate eruptive phase starts with lighter $\delta^{66}\text{Zn}$ values, which get heavier with time as the fissure activity eventually wanes; this trend occurs not only with time but also with Zn and Cu content (Figure 8. 13). Cone tephra values, taken from 10 cm below the cone surface, to avoid surface weathering, each represent the waning period of activity at the vent in question give a surprisingly consistent light $\delta^{66}\text{Zn}$ value of 0.201–204 $\delta^{66}\text{Zn}$ for all 4 cone samples analysed, which doesn't change with time (R^2 of 0.8560). When these narrow $\delta^{66}\text{Zn}$ values are compared to variations in Zn and MgO content, they display no covariance trends (Figure 8. 13).

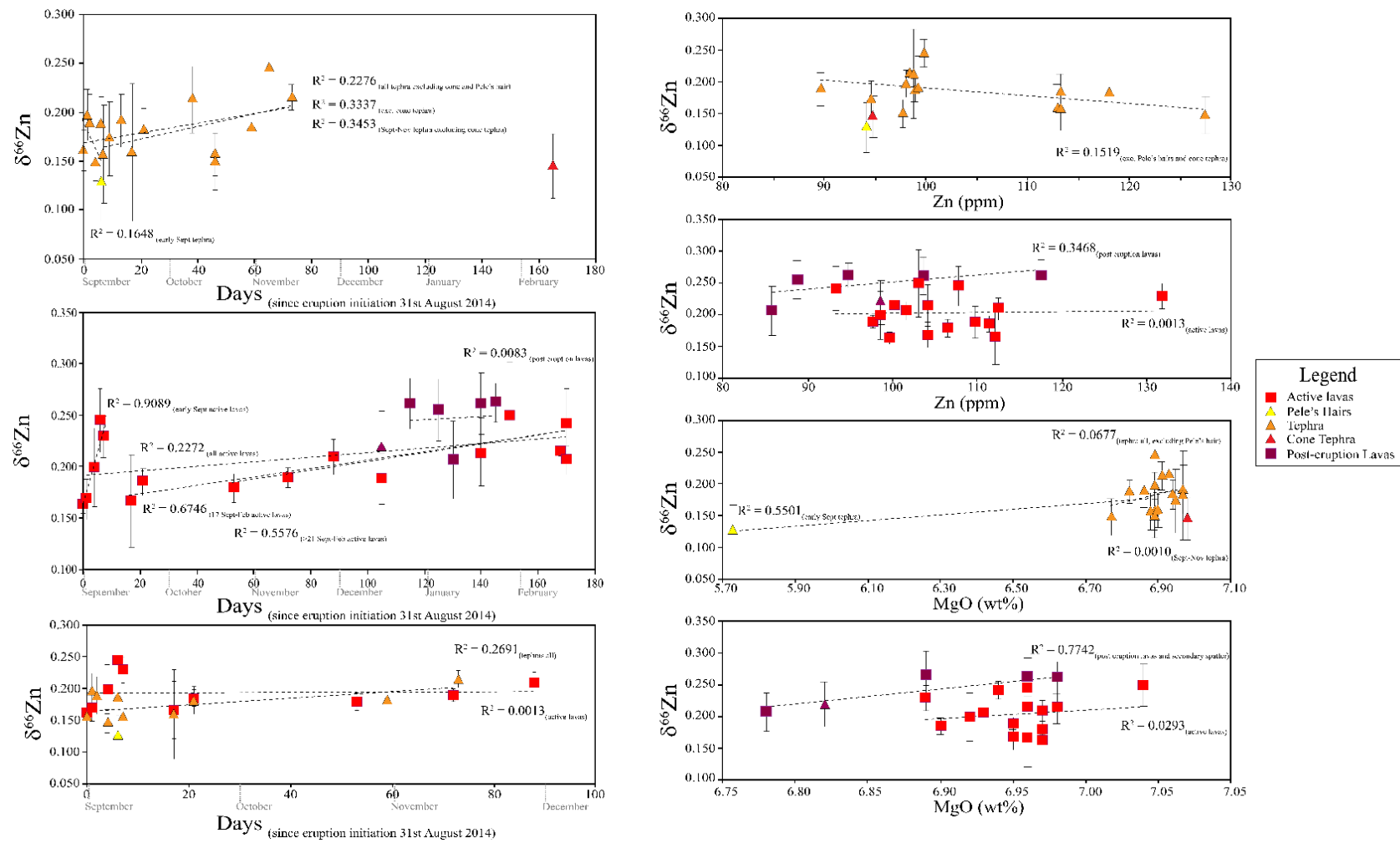


Figure 8. 12: Holuhraun $\delta^{66}\text{Zn}$ variations, temporal and key major and trace covariations in lavas and tephra. Holuhraun eruptive product $\delta^{66}\text{Zn}$ variations displayed temporally (left-hand plots) isolated by their sub-categories, all errors are 2sd. The top left-hand plot display temporal $\delta^{66}\text{Zn}$ tephra variations: explosive tephra (orange triangles); Pele's hair (yellow triangle); and cone tephra (red triangle). The left-hand middle plot displays temporal $\delta^{66}\text{Zn}$ variations in active lava (red squares) and post-eruption resurfacing lavas (dark red squares). The bottom left-hand plot only displays $\delta^{66}\text{Zn}$ variations for temporal tephra and lava pairs that exist within the data set; samples without a pair were excluded for clarity. The right-hand plots display the same sub-categories of eruptive products and their $\delta^{66}\text{Zn}$ variations against selected trace element (top and upper middle plots) or major elements (upper middle and bottom plots).

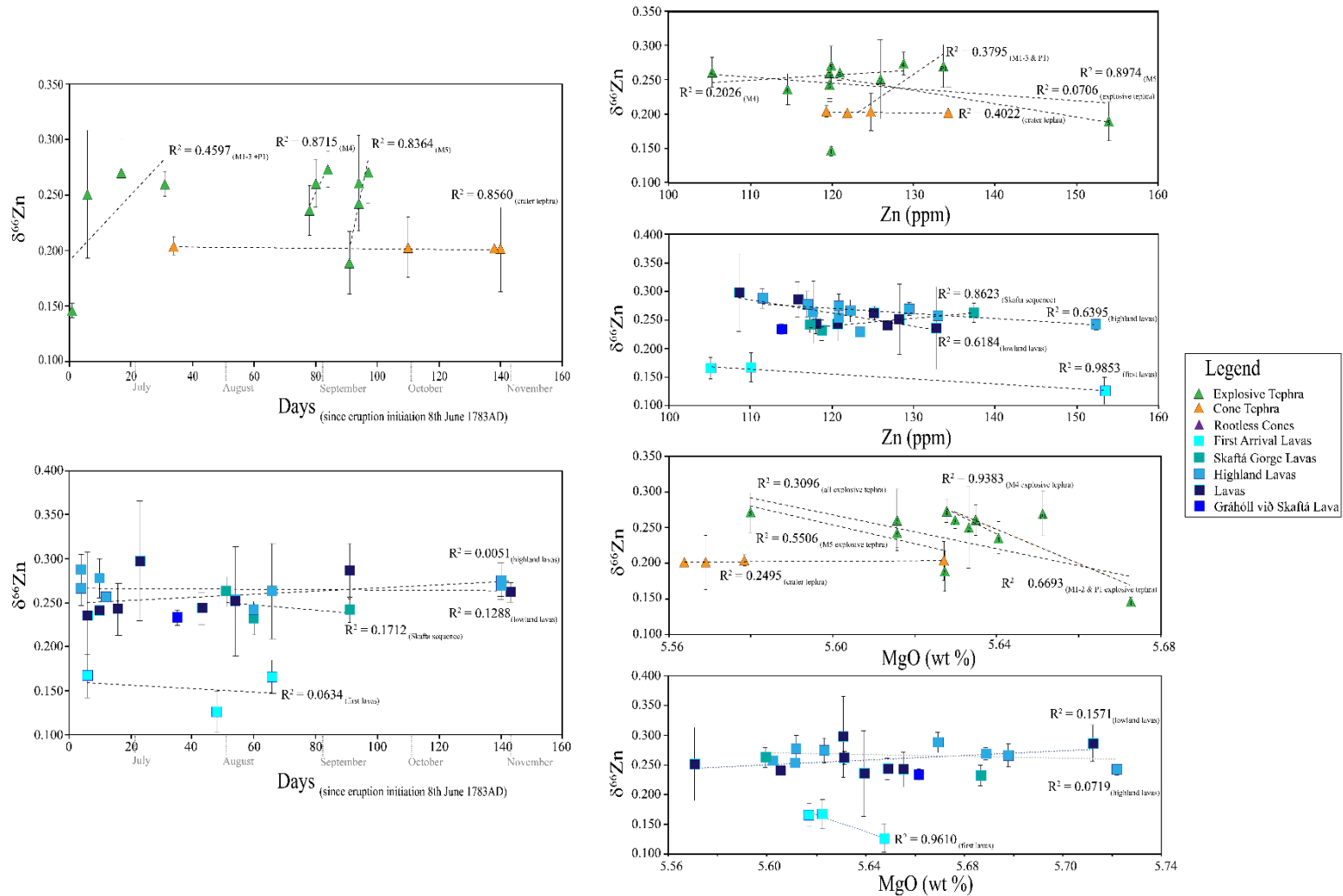


Figure 8. 13: Laki $\delta^{66}\text{Zn}$ variations, temporal and key major and trace covariations in lavas and tephra. Laki eruptive products $\delta^{66}\text{Zn}$ variations displayed temporally (left-hand plots) isolated by their sub-categories, all errors are 2sd. The top left-hand plot displays temporal $\delta^{66}\text{Zn}$ tephra variations: explosive tephra (green triangles) and cone tephra (orange triangles). The bottom left-hand plot displays temporal $\delta^{66}\text{Zn}$ variations in the Laki lavas. Sub-categories are as outlined before for previous figures, see legend for details. The right-hand plots display the same sub-categories of eruptive products and their $\delta^{66}\text{Zn}$ variations against selected trace element (top and upper middle plots) or major elements (lower middle and bottom plots)

8. 3. 2. 1. Cu isotope variations:

8. 3. 2. 1. 1. Holuhraun

The Holuhraun eruptive products have a total range in $\delta^{65}\text{Cu}$ from 0.03–0.19. When this is sub-divided into separate ranges for lavas and tephra, these display a near identical range within error: the lavas have a range in $\delta^{65}\text{Cu}$ from 0.04–0.19 and the tephra have a range in $\delta^{65}\text{Cu}$ from 0.03–0.17 within which the Pele's hair sample falls at 0.07 (Table 8. 3).

Holuhraun lavas: display a moderate temporal trend towards heavier $\delta^{65}\text{Cu}$ values (R^2 of 0.6177), as well as a strong trend of lighter $\delta^{65}\text{Cu}$ values with increasing Cu content (R^2 of 0.8860) (Figure 8. 14); the same, statistically weaker, trend exists with Zn content (see supplementary data, appendix B: Holuhraun isotopes). There is no trend of $\delta^{65}\text{Cu}$ values with MgO content for the lava samples.

Holuhraun tephra: If the cone tephra sample is excluded, there is no statistically robust temporal variation of $\delta^{65}\text{Cu}$ (R^2 of 0.3976), which is similar to the observations for $\delta^{66}\text{Zn}$ in the tephra samples. However, as with the lavas, the $\delta^{65}\text{Cu}$ values of the tephra indicate a tendency towards increasingly heavier $\delta^{65}\text{Cu}$ with time. When the cone tephra is included in the data set, unlike for $\delta^{66}\text{Zn}$, the trend of increasingly heavier $\delta^{65}\text{Cu}$ with time is moderate (R^2 of 0.6220). Notably, the Pele's hair sample has a heavier $\delta^{65}\text{Cu}$ than both the tephra and lavas sampled during this more vigorous fountaining phase. A strong covariance of heavier $\delta^{65}\text{Cu}$ and increasing MgO, Al_2O_3 , and CaO content exists in the explosive tephra samples if the Pele's hair sample is excluded (Figure 8. 14; see supplementary material appendix B: Holuhraun Isotopes), e.g., R^2 of 0.7420 for MgO content.

When the tephra and lava pairs are isolated from the other analysed samples, the temporal trends towards heavier $\delta^{65}\text{Cu}$ are stronger; the tephra displays an R^2 of 0.6957 and the lavas an R^2 of 0.8441. The lavas initially have lighter $\delta^{65}\text{Cu}$ values than the tephra, although this is within analytical error (Figure 8. 14).

8. 3. 2. 1. 2 Laki

The Laki eruptive products have a wide range in $\delta^{65}\text{Cu}$ from -0.07–0.41, which is driven entirely by the Laki tephra samples (Table 8. 4). When the Laki lavas and tephtras are isolated from each other, their ranges are different unlike, the Holuhraun samples (Figures 8. 14 and 8. 15). The range in $\delta^{65}\text{Cu}$ for the lavas is from -0.02–0.19 and from -0.07–0.41 for the tephtras (Table 8. 5). The latter has both a wider range and contains several markedly heavier $\delta^{65}\text{Cu}$ values. Laki lavas and tephtras display the opposite trends for $\delta^{65}\text{Cu}$, both temporally as well as elementally, but within the same range of values.

Laki lavas: display no temporal trend in $\delta^{65}\text{Cu}$ values (R^2 0.4381), although they generally become heavier with time (Figure 8. 15). A similar pattern of heavier $\delta^{65}\text{Cu}$ with increasing Cu and MgO contents is also evident, although again, this isn't statistically resolvable (R^2 of 0.4574 and 0.4316, respectively).

Laki tephtras: display the opposite trend to the lavas, with strong temporal trends towards lighter $\delta^{65}\text{Cu}$ values over time when different explosive phases are isolated, e.g., the S. and N. fissure explosive tephtras are separated (R^2 of 0.8518–0.9548). The N. fissure explosive tephtras can be divided further to isolate M5, which is the only sample sequence through a complete apron sample (Figure 8. 15) (R^2 of 0.8617). Cone build phase tephtras display a very strong temporal trend towards lighter $\delta^{65}\text{Cu}$ values (R^2 of 0.9457) (Figure 8. 15). All of these tephtra sub-groupings are limited statistically by a low sample number. Weak trends of lighter $\delta^{65}\text{Cu}$ values with increasing Cu content also exist for the same sub-groupings (R^2 of 0.5677) (Figure 8. 15). No statistically resolvable trends of $\delta^{65}\text{Cu}$ with MgO content are observed, with the exception of both M5, which displays a strong trend of marginally lighter $\delta^{65}\text{Cu}$ with MgO content (R^2 of 0.9910), and the cone tephtra, which displays a very weak covariation of lighter $\delta^{65}\text{Cu}$ with MgO content (R^2 of 0.4194).

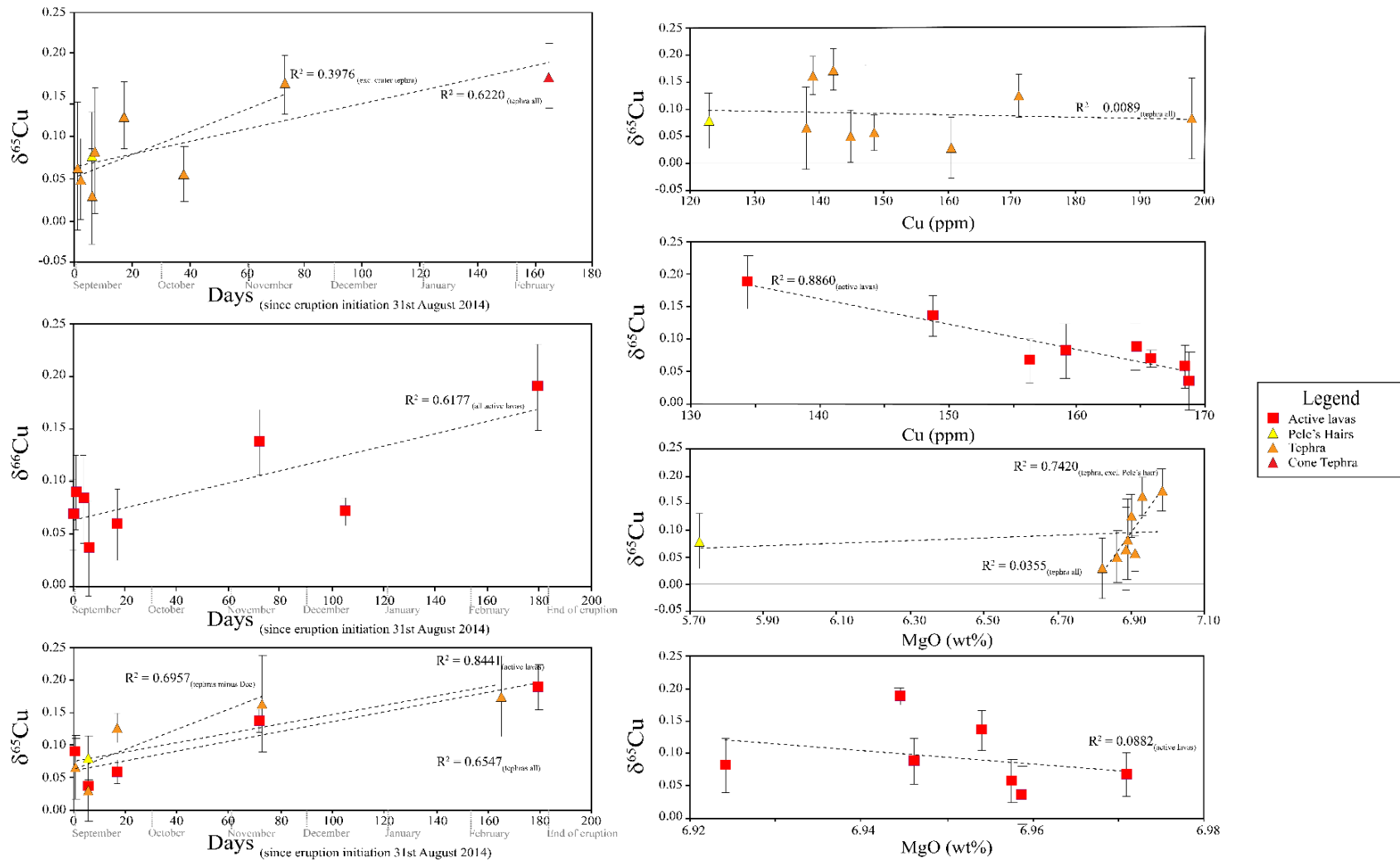


Figure 8. 14: Holuhraun 2014–15 CE $\delta^{65}\text{Cu}$ variations, temporal and key element covariations. Holuhraun eruptive products $\delta^{65}\text{Cu}$ variations displayed temporally (left-hand plots) separated by their sub-categories, all errors are 2sd. The top left-hand plot displays temporal $\delta^{65}\text{Cu}$ tephra variations: explosive tephra (orange triangles); Pele's hair (yellow triangle); cone tephra (red triangle). The middle left-hand plot displays temporal $\delta^{65}\text{Cu}$ variations in active lava (red squares). The bottom left-hand plot only displays temporal tephra and lava pairs $\delta^{65}\text{Cu}$ variations that exist within the data set, samples without a pair were excluded for clarity. The right-hand plots display the same sub-categories of eruptive products and their $\delta^{65}\text{Cu}$ variations against selected trace element (top and upper middle plot) or major elements (lower middle and bottom plot).

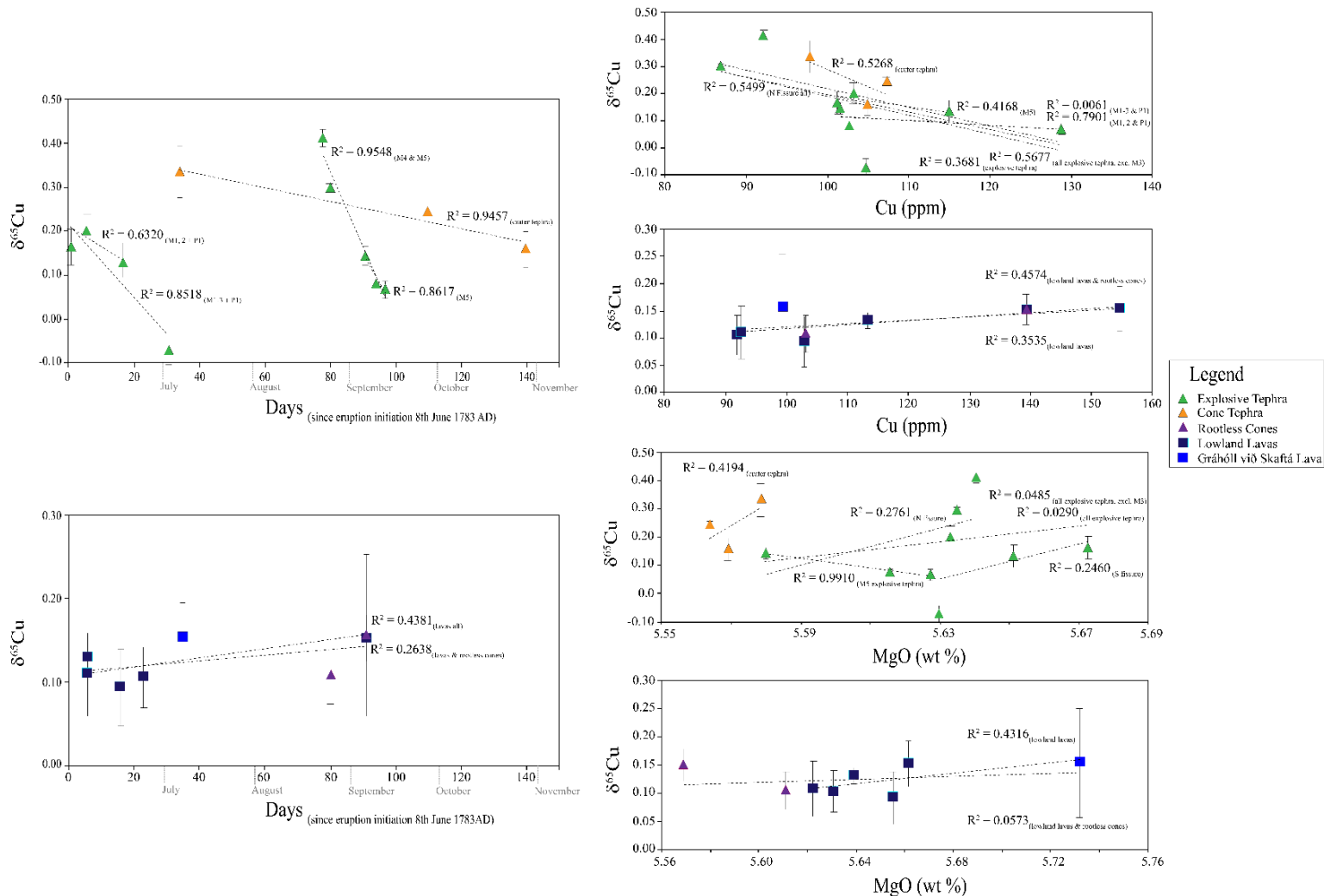


Figure 8. 15: Laki 1783–84 CE $\delta^{65}\text{Cu}$ variations, temporal and key element covariations. Laki eruptive products $\delta^{65}\text{Cu}$ variations are displayed temporally (left-hand plots) whilst separated by their sub-categories, all errors are 2sd. The top left-hand plot displays temporal $\delta^{65}\text{Cu}$ tephra variations: explosive tephra (green triangles) and cone tephra (orange triangles). The bottom left-hand plot displays temporal $\delta^{65}\text{Cu}$ variations in the Laki lavas, sub-categories are as follows: lowland and highland lavas (dark blue squares); rootless cone tephtras (purple triangles); and the fast-moving Gráhöll með Skaftá lava flow front break-out (lighter blue square). The right-hand plots display the same sub-categories of eruptive products and their $\delta^{65}\text{Cu}$ variations against selected elements (top and upper middle plots) or major elements (lower middle and bottom plots).

8. 3. 3. 1 Covariance of isotope systems:

8. 3. 3. 1. 1 Holuhraun: For the Holuhraun active lavas, there is an excellent covariance trend (R^2 of 0.7246) between both isotope systems, where both increase from light $\delta^{66}\text{Zn}$ and $\delta^{65}\text{Cu}$ values towards heavier $\delta^{66}\text{Zn}$ and $\delta^{65}\text{Cu}$ values if the samples taken during the most explosive phases of activity are excluded (Figure 8. 16); no trend is observed if the post-eruptive or explosive activity lava samples are included. Whilst the data set is limited temporally and spatially, and thus cannot provide the resolution needed for a statistically robust conclusion, the limited data set for all September samples plot in light $\delta^{66}\text{Zn}$ and light $\delta^{65}\text{Cu}$ isotope space (Figure 8. 16), with heavier $\delta^{66}\text{Zn}$ and heavier $\delta^{65}\text{Cu}$ values for lavas erupted after September. The tephra also display no resolvable trend when all samples are included; however, when the early September samples are isolated, they also display the same strong trend from light $\delta^{66}\text{Zn}$ and $\delta^{65}\text{Cu}$ to increasingly heavier $\delta^{66}\text{Zn}$ and $\delta^{65}\text{Cu}$ values (R^2 of 0.7726) (Figure 8. 16).

8. 3. 3. 1. 2 Laki: The Laki lavas display no isotopic covariation trend when considered as a whole data set. However, when the same previous sample sub-groupings are considered (where sample numbers allow), two strong isotope trends can be seen from light $\delta^{66}\text{Zn}$ and $\delta^{65}\text{Cu}$ to heavier $\delta^{66}\text{Zn}$ and $\delta^{65}\text{Cu}$ values for the N. fissure lavas (R^2 of 0.9683), which only marginally decreases when including the N. fissure rootless cone sample in the N. fissure lava samples (R^2 of 0.8759) (Figure 8. 16). The S. fissure lavas data set displays no resolvable isotope trend (R^2 of 0.3359) (Figure 8. 16). However, it is also important to note here that these values are not statistically robust due to the limit sample numbers in these sub-groupings. The tephra covariation plots of $\delta^{66}\text{Zn}$ and $\delta^{65}\text{Cu}$ are inconclusive when all tephra samples are assessed together, as well as when they are divided into N. and S. fissures (Figure 8.16). However, when isolated, the M5 tephra show the same trend from light $\delta^{66}\text{Zn}$ and $\delta^{65}\text{Cu}$ to increasingly heavier $\delta^{65}\text{Cu}$ and $\delta^{66}\text{Zn}$ (R^2 of 0.8681) that is observed in the N. fissure lavas. Notably, M5 is the only full sample sequence through a tephra apron for the $\delta^{65}\text{Cu}$ data set. Whilst the S. fissure displays no covariance, the very slight change in slope suggests these samples shift from heavier $\delta^{66}\text{Zn}$ and lighter $\delta^{65}\text{Cu}$ to lighter $\delta^{66}\text{Zn}$ and heavier $\delta^{65}\text{Cu}$ (Figure 8. 16), which is

the opposite to the M5 tephras. Cone tephras display a very strong isotopic covariation trend (R^2 of 0.9625), generated by the flat-line $\delta^{66}\text{Zn}$ values in all samples; (i.e., consistently no increasing oxidised S loss in these samples regardless of eruptive fissure). A shift towards increasingly heavier $\delta^{65}\text{Cu}$ values indicates either FeS_2 (immiscible sulfide fluid) loss fractionating Cu from the melt or decreasing degrees of degassing of a reduced volatile phase, e.g., H_2S (Figure 8. 16).

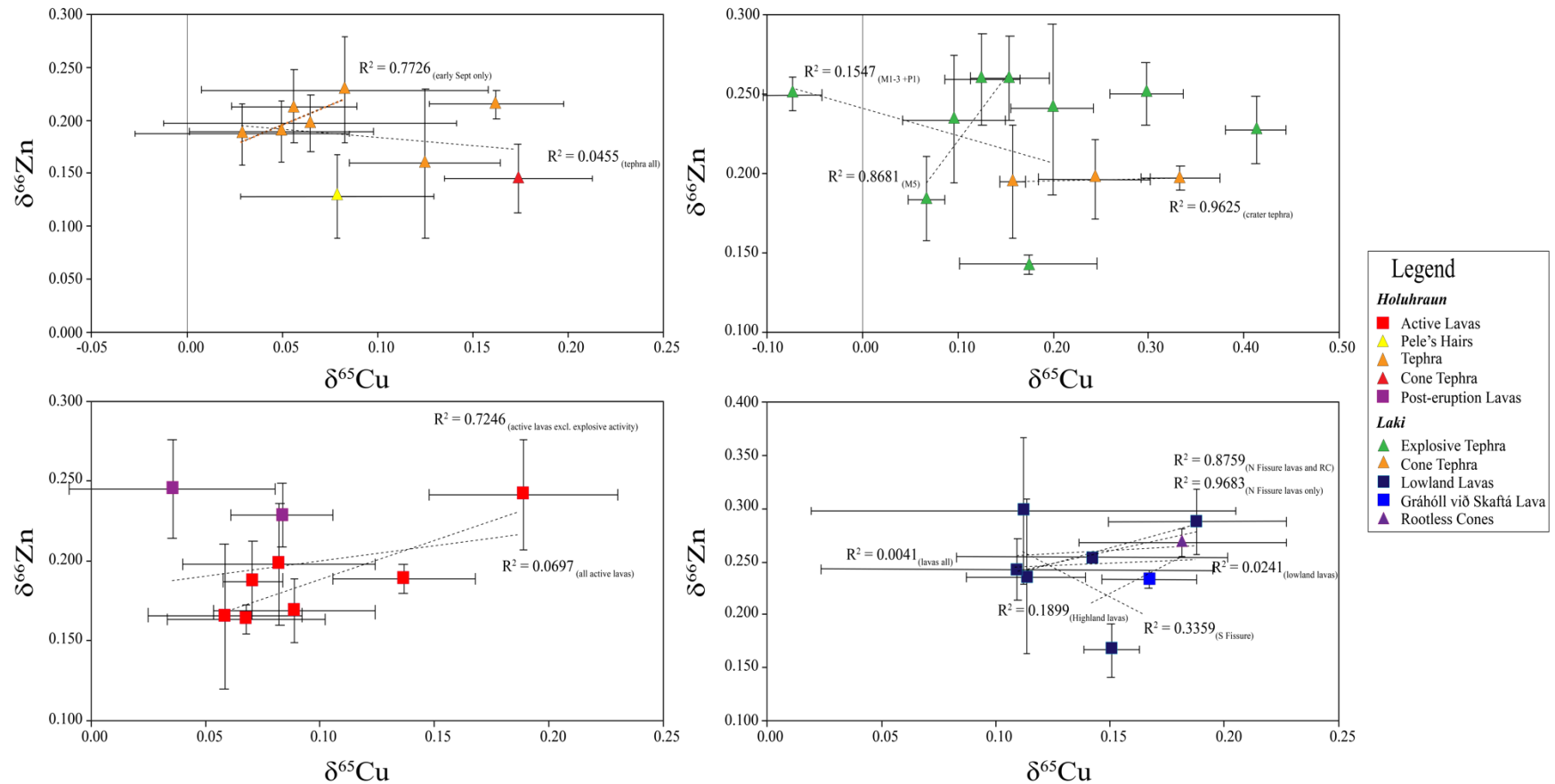


Figure 8. 16: $\delta^{66}\text{Zn}$ and $\delta^{65}\text{Cu}$ isotope covariations for Holuhraun 2014–15 CE and Laki 1783–84 CE tephra and lavas. The left-hand side plots depict Holuhraun tephra and lava $\delta^{66}\text{Zn}$ and $\delta^{65}\text{Cu}$ isotopic covariations. The top left-hand side plot displays $\delta^{66}\text{Zn}$ and $\delta^{65}\text{Cu}$ isotopic covariations in the Holuhraun tephra phases: explosive tephra (orange triangles); Pele's hair (yellow triangle); and cone tephra (red triangle). The bottom left-hand plot displays lava $\delta^{66}\text{Zn}$ and $\delta^{65}\text{Cu}$ isotopic covariations in active lava (red squares) and post-eruption lavas (purple squares). The right-hand side plots depict Laki tephra and lava $\delta^{66}\text{Zn}$ and $\delta^{65}\text{Cu}$ isotopic covariations. The top right-hand side plot displays $\delta^{66}\text{Zn}$ and $\delta^{65}\text{Cu}$ isotopic covariations in both explosive tephra (green triangles) and cone tephra (orange triangles). The bottom right-hand side plot displays $\delta^{66}\text{Zn}$ and $\delta^{65}\text{Cu}$ isotopic covariations in Laki lavas: lowland and highland lavas (dark blue squares); rootless cone tephra (purple triangle); and the fast-moving Gráhóll Skaftá lava flow front break-out (lighter blue square).

8. 4 Discussion

To recapitulate, for emphasis for the following section, the expected response of oxidised volatile loss of S is that the residual eruptive products will have heavier $\delta^{66}\text{Zn}$ values, as the light Zn isotope preferentially partitions into the volatile phase and is degassed. If S is lost as a reduced volatile species the residual eruptive products will have lighter $\delta^{65}\text{Cu}$ values as the heavy Cu isotope, preferentially partitions into the volatile phase, and is degassed. Whereas, if S is lost as a reduced particulate phase (i.e., as sulfides) this will result in the residual eruptive products having heavier $\delta^{65}\text{Cu}$ values, as the light Cu isotope preferentially partitions into the sulfide phase. If the eruptive products gain additional sulfides, the residual melt will have heavier $\delta^{65}\text{Cu}$ values.

A key limitation of this study is that there is no pristine un-degassed sample to compare with the data on partly degassed eruption products presented here. Alternatives such as hyaloclastite and pillow lavas within the same volcanic systems as the eruptions from this study are Plio-Pleistocene in age (Thordarson and Höskuldsson, 2008) and have experienced alteration which would affect $\delta^{66}\text{Zn}$ values and Zn concentrations as this element is mobile during low-temperature alteration; such as palagonisation due to high quantities of water and a distinct heat gradient. The best alternative for Holuhraun might be the Pele's hair sample which appears to have undergone the least amount of S loss. MORB $\delta^{66}\text{Zn}$ and $\delta^{65}\text{Cu}$ values are generally used within the isotope community as a reference for undegassed basaltic samples; in this case this is less than ideal as MORB generally represents depleted magmas, whereas 1783–84 CE Laki and 2014–15 CE Holuhraun magmas are enriched and fairly evolved basaltic melts (Passmore, 2009; Passmore et al., 2012; Hartley et al., 2017; Halldorsson et al., 2018). For this reason, this study is focused on the intra-flow field variations that result from resolvable physical volcanological processes. Iceland produces magmas with OIB chemistries, both 1783–84 Laki and 2014–15 Holuhraun sit within the axial rift of Iceland, namely the Eastern (EVZ) and Northern (NVZ) volcanic zones, respectively.

8. 4. 1 Zn isotope variations

8. 4. 1. 1 Holuhraun

Holuhraun tephra: $\delta^{66}\text{Zn}$ values do not display distinct temporal variations with trace element or major element concentrations; however, the explosive activity generated tephra samples generally seem to shift to heavier $\delta^{66}\text{Zn}$ values with time (Figure 8. 12). A single cone tephra sample, collected in February when the cone could be approached safely, captures the less intense cone building phase of the eruption; it has a very light $\delta^{66}\text{Zn}$ value compared to the rest of the tephra data set. This would suggest either a volatile gain in the system or, which is more likely, less efficient degassing of the cone tephra at this phase of more effusive activity. Notably this matches the trend observed in the Laki cone tephra phases which generally have lighter $\delta^{66}\text{Zn}$ values suggesting less oxidised volatile S loss. The Pele's hair sample has the lightest $\delta^{66}\text{Zn}$ of all the pyroclast samples (Figure 8. 12), representing a less efficient process of oxidised S loss during its formation. This may be associated with the thickness of the glass and mechanisms of formation, with more degassing occurring around the thin stretched hairs rather than the hairs themselves. This is not mirrored by the explosive tephra sample analysed from this day, consisting of a bulk sample of a natural abundance of lapilli sized clasts, collected in one locality at the same time so limiting the effects of slight variations S (ppm) vs vesicularity which could skew the Holuhraun tephra data set. A trend of higher S and lower vesicularity exists in the phreatomagmatic samples from P1 in the Laki eruption (Thordarson et al., 1996), but this is not applicable at Holuhraun as these samples are purely magmatic, although the difference in vesicularity and S content in these magmatic samples could be explored further. As observed from $\delta^{66}\text{Zn}$ values there is no trend found for $\delta^{65}\text{Cu}$ variations (either temporally or with trace element concentrations) in the Holuhraun tephra.

The explosive activity at Holuhraun is weaker but much more prolonged, over a period of days, compared to high-intensity explosive activity which was limited to hours–tens of hours at Laki. Both indicate a shift towards more efficient oxidised Zn loss with time; however, while this is very pronounced at Laki, it is much more subtle at Holuhraun, which may be the result of a difference in fountaining intensity

and thus the result of the modulation of eruptive style by shallow conduit dynamics (Figures 8. 12 and 8. 13).

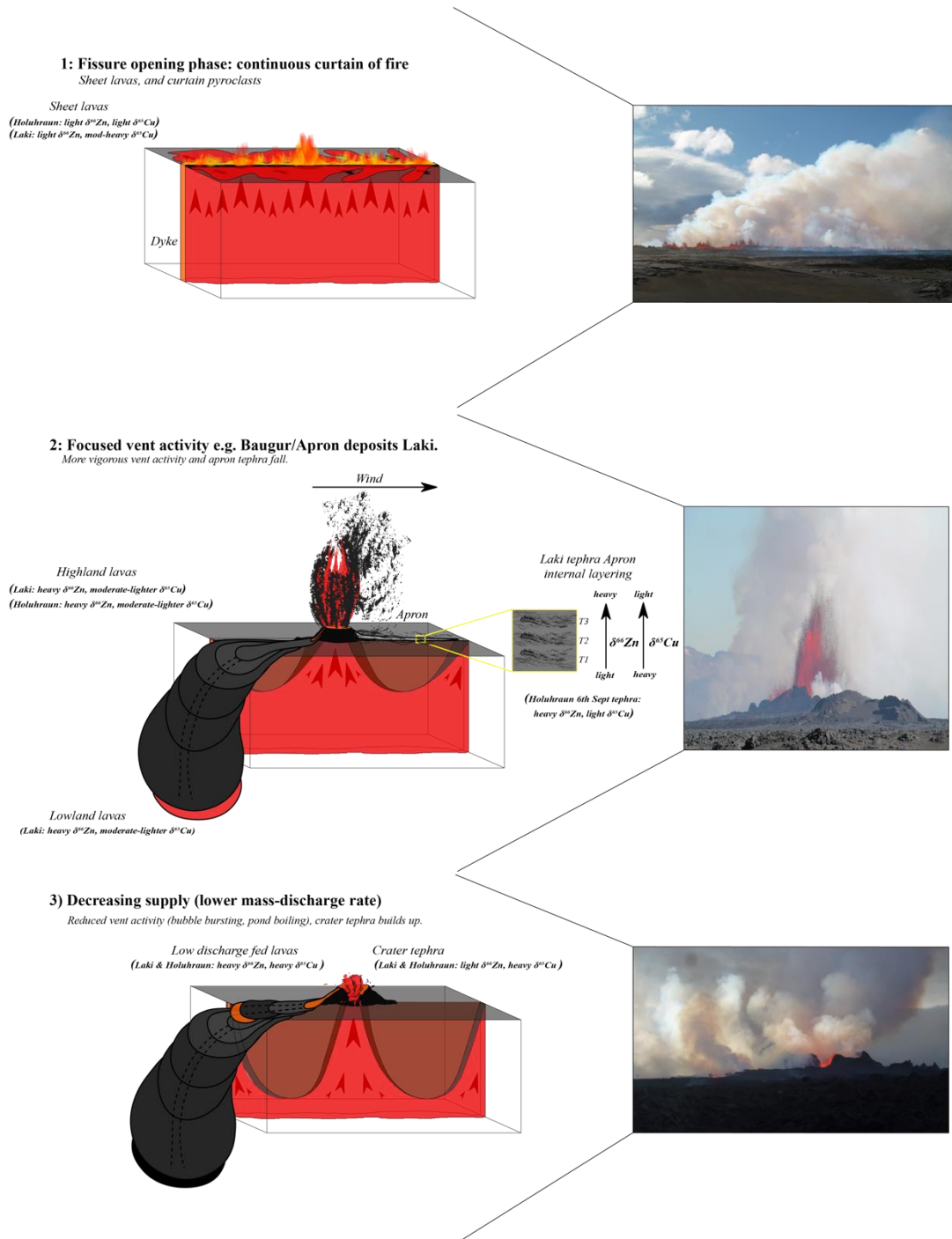


Figure 8. 17: Conceptual models for the generation of $\delta^{66}\text{Zn}$ and $\delta^{65}\text{Cu}$ isotope variations throughout both fissure eruptions. A simplified schematic model for the type of vent activity, lava flow field development, evolution of the lava flow transport system, and changes in subsurface geometry throughout the Laki and Holuhraun fissure eruptions is shown from the top-down on the left side of the figure. Corresponding examples of the evolution of vent activity intensity are shown alongside the schematic using examples of this activity from Holuhraun eruption, which are displayed to the right for reference. Although, the fountaining activity for the explosive tephra apron forming phases at Laki would have had much larger fountains, reaching 1400 m in height. (caption continues on next page).

(Caption continued). On the left hand-side, the conceptual model from the top-down shows: 1) Initial fissure opening episode. As melt rises through the dyke (shown as red in the subsurface), velocity gradients are generated due to subsurface geometry and thus is preferentially channeled through certain regions of the dyke. The melt feeds emergent curtain-of-fire eruptive activity at the surface, which is associated with fast-flowing sheet pāhoehoe lavas with no established channel system; 2) MER waves to highest intensity stage (the timescales for the process for Holuhraun versus Laki is very different). The activity devolves onto discrete vents above the highest velocity flow areas in the dyke, with areas with higher rheological properties developing at depth (shown in dark red), creating rheological gradients in the subsurface. Apron tephra fall is associated with this phase of activity. The hydrostatic head for the lava channel system is powerful enough to feed and emplace lavas far from the vent region; 3) MER decreases, and correspondingly the vent activity displays bubble bursting, discharge rates in the channel system decrease. Lavas use existing channel systems, and lava flow field resurfacing events occur through inflation events, or lavas nearer vent are emplaced on top of older flows.

Holuhraun lavas: As demonstrated in the Holuhraun Zn isotope result section, two positive temporal trends are observed in the measured $\delta^{66}\text{Zn}$ values. The first spans the first 10 days of activity (31 August–9 September), defining a steep positive trend of increasingly heavy $\delta^{66}\text{Zn}$ over a short time period that coincides with stepwise increase in magma discharge during the first waxing MER phase (Figures 8. 12, 8. 17, and 8. 18). The lighter $\delta^{66}\text{Zn}$ values indicate that the lavas formed at the beginning of the eruption are less degassed than the lavas formed during subsequent days up to 6 September (Figures 8. 12 and 8. 18). This trend is interpreted to indicate increasingly higher degrees of the volatile loss of light Zn with time during this period of waxing magma discharge (Figures 8. 12 and 8.18). This waxing MER phase and the corresponding increase in fountaining intensity, was also accompanied by a concentration of the fountaining activity onto the discrete vents that develop due to formation of choke points along the erupting fissure (Figure 8. 17). A reversal back to lighter $\delta^{66}\text{Zn}$ values around 17 September follows a major exponential drop in the magma discharge from 9–15 September (Figure 8. 18), and a near halt of the eruption on 15 September as revealed by vent activity consisting of very subdued periodic bubble bursting activity (IES eruption team, field reports) and relatively much denser eruptive tephra (see Chapter 6).

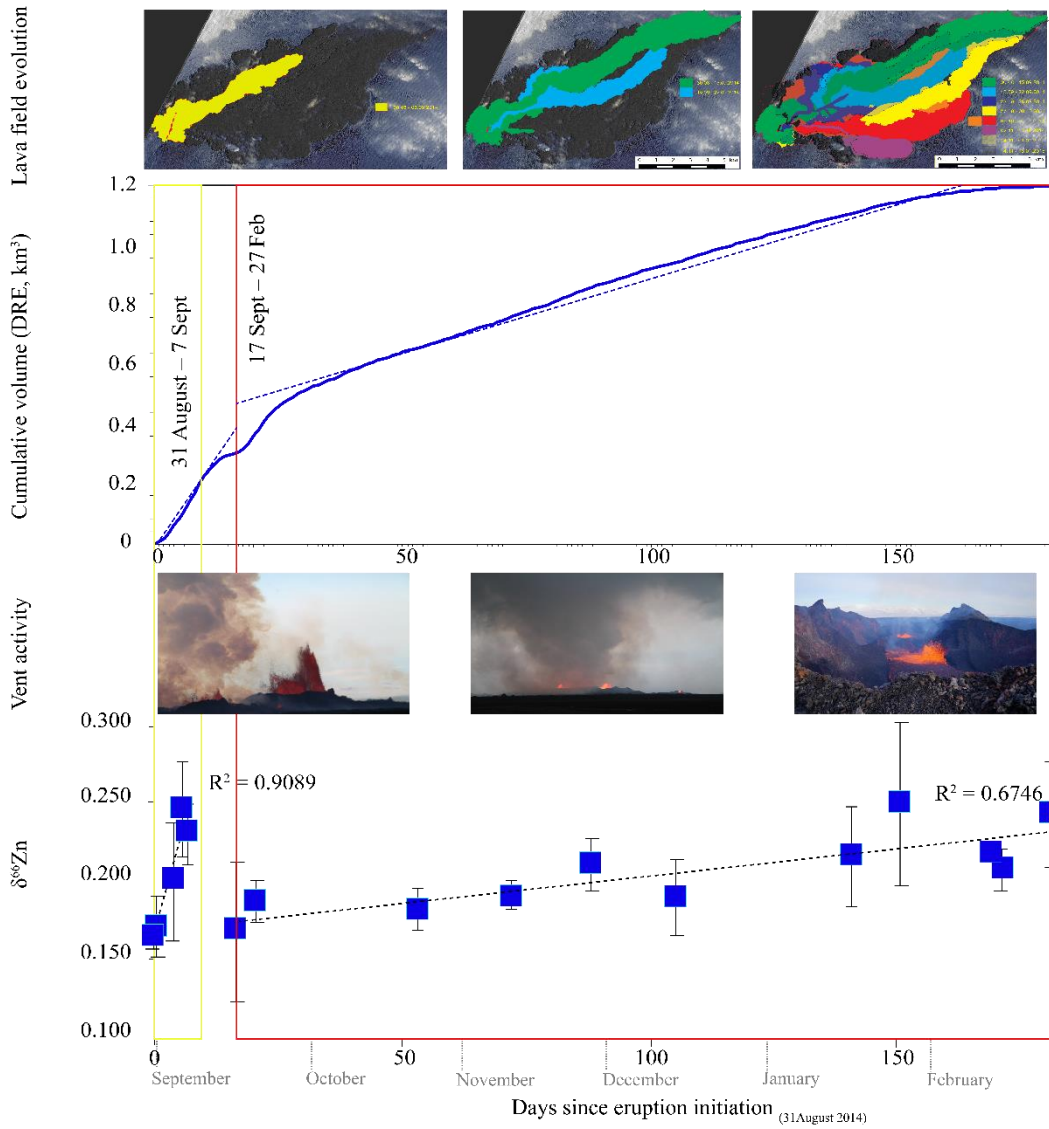


Figure 8. 18: Temporal $\delta^{66}\text{Zn}$ variations alongside physical volcanological data sets. Multi-panel figure showing the temporal $\delta^{66}\text{Zn}$ variations against key physical volcanological observations. From the bottom to the top, the following panels are displayed: (1) Temporal $\delta^{66}\text{Zn}$ variations from the active Holuhraun lavas (dark blue squares). Two trends are clear when these lavas are sub-categorised into early lavas (outlined by the yellow box) and later lavas (outlined by the red box). (2) Images that display key observed changes in vent activity throughout the Holuhraun eruption, which are associated with the highest MER vent activity on 6 September 2014, the lull in vent activity on 15–17 September 2014 and lava pond boiling towards the end of the eruption (February 2015). (3) A plot of temporal changes in cumulative lava volume output of the Holuhraun eruption (using dense rock equivalent, DRE) from Bonny et al. (2018) is displayed instead of time-averaged MER; as a shift in average lava discharge between the early lavas (outlined by the yellow box above) and later lavas (outlined by the red box) better isolates the shift in flow field development in response to exponential decreases in MER and near shut down in vent activity on the 15 September. (4) The temporal and spatial evolution of the Holuhraun flow field development shown as different georeferenced shapefiles for key phases of the eruption. Initially the flow field was fed by a single channel and was emplaced as one lava flow branch. After 15 September, in response to the change in MER or discharge, the flow field begins to branch and eventually develops into a complex compound flow field. Late-stage re-inflation and resurfacing breakouts from older channels are observed as opaque shapefiles.

The second sub-group spans the rest of the eruption, from 17 September–28 February after a lull in activity and period of low MER before a second waxing phase which starts on 17 September; which is defined by a shallower trend towards heavier $\delta^{66}\text{Zn}$, i.e., more degassed magma values, over a much longer time-span (Figures 8. 12, 8. 17, and 8.18). This agrees with the morphologies of lava outbreaks, or squeeze-outs emplaced from November onwards, which are generally more viscous. At this stage in the eruption, the first appearance of spiny pāhoehoe was observed: a microlite rich, viscous, and very degassed flow type associated with lava flow squeeze-outs or late-stage flow fed by an established lava pond (Pedersen et al., 2017). Direct comparisons between time spent in the channel or distance from the vent after 15 September, when the ‘A’ā lava reached its critical length, are extremely difficult as the flow field develops multiple different branches which advance further to the E and ESE as each new branch creates topography which the follow branch flows around (Figure 8. 3). Later in the eruption, a more insulated lava channel transport system also develops, inhibiting degassing during transport due to pressurisation. As a result, the different lava channel transport systems which exist prior to and post 15–17 September are difficult to compare, and therefore, this can only be made in general terms. The end of the eruption is dominated by reactivation and resurfacing events (Pedersen et al., 2016). This late-stage process may add to the increased scatter and relatively weaker trend which is observed in this second sub-grouping of the Holuhraun lavas (Figures 8. 12 and 8. 18). Importantly, these second-subgroup samples were collected from different active fronts from different flow branches, or resurfacing channel levee outbreaks, dictated by accessibility. Whereas the lavas sampled from 31 August–7 September were sampled along one, open channel fed, flow branch, with increasing distance from the vent with time (Figures 8. 3 and 8. 18) and thus define a tighter, more robust covariance trend of heavier $\delta^{66}\text{Zn}$ with time. During the early stages of the eruption, the channel could not crust over properly in this time period, and thus all these early lava samples that were collected are travelling in the same transport system.

Unlike Laki, the phenocryst/xenocryst cargo content of Holuhraun is very constant throughout, with rare gabbroic xenoliths observed (Gauthier et al., 2016; Halldórsson et al., 2018). Signs of very large, rounded crystal mush macrocrysts only appearing at the very end of the eruption; (Gallagher and Burton in field observation) which

were avoided during sampling. This observation is consistent with the limited range in Zn concentrations of the Holuhraun lavas (97.6–112.5 ppm, Table 8. 2).

This second sub-group could potentially be divided again with the period from 17–21 September defining a third isolated group, during which a second waxing MER phase occurs; creating a second peak intensity phase over a short period of time (Figures 8. 12 and 8. 18). However, this study does not have the sample resolution to cross-check this, as there are only two samples analysed which fall into this timeframe.

8. 4. 1. 2 Laki

Determining the primary Zn content for Laki is even more challenging as this eruption is 250 years old and has a well-developed biological layer above much of it consisting of mosses and lichens, which promote clay formation and alteration and weathering of the glassy surfaces potentially resulting in Zn remobilisation. However, when considered against immobile trace elements, in their volcanological groupings, there is an R^2 value of >0.97 , suggesting that weathering has not significantly affected the Zn content of these samples.

Unlike the Holuhraun eruptive products, most of the Laki lava and tephra subgroupings display a distinct but variable covariation of elemental Zn and Cu concentration with MgO content (see supplementary data, appendix B: Laki Traces, Laki Majors and Laki Isotopes). The first lava arrivals, highland lavas, and rootless cone samples display strong covariations, with weak covariations displayed by some of the explosive tephra sub-groupings. No covariation is observed between elemental Zn and Cu with MgO in the lowland lavas.

The rootless cone samples and first lava arrivals maintain this strong covariation trend when comparing $\delta^{66}\text{Zn}$ and MgO content (Figure 8. 13). However, both the highland lavas and cone tephra, which had strong Cu and Zn against MgO contents trend, do not display any observable covariation between $\delta^{66}\text{Zn}$ and MgO (Figure 8. 13). The sub-groupings of distinct phases of explosive apron tephra fall display some of the strongest $\delta^{66}\text{Zn}$ and MgO covariation trends, with increasingly lighter $\delta^{66}\text{Zn}$

values associated with increasingly higher MgO contents. This trend is consistent for the S. fissures explosive tephra and for each isolated apron tephra fall phase in the N. fissures. A distinct shift from relatively lower to higher MgO contents is seen with increasing heavier $\delta^{66}\text{Zn}$ each time, suggesting that the MgO contents become ever so slightly evolved during each eruptive episode alongside more efficiently degassed vent activity (Figure 8.13). If more syn-eruptive crystallisation is occurring during degassing, this may be contributing to this trend, with microlite rich bands observed in M4 and M5 tephtras (see Chapter 7). Petrological observations of more primitive macrocryst phases with time (Passmore, 2009; Passmore et al., 2012) should create a higher MgO content, unless they are not incorporated extensively into the tephra and instead are concentrated into the lava output from the vents.

Laki lavas: The lava sub-groupings display moderate–strong trends between elemental Zn concentrations and $\delta^{66}\text{Zn}$ values. The first lava arrivals and Skaftá gorge sequence display the strongest trends but are statistically weak as they each consist of 3 data points; whilst the lowland and highland lavas display only moderate covariance trends between elemental Zn concentrations and $\delta^{66}\text{Zn}$ values, each consist of 8–10 data points and thus is statistically more robust. As Zn has a relatively strong partition coefficient for olivine, of 1, samples with slightly higher proportions of olivine as macrocrysts or microlites would have higher Zn contents, with measurements revealing that olivine macrocryst phases contain around 100–200 ppm Zn. The Laki explosive and cone tephra elemental Zn concentrations and $\delta^{66}\text{Zn}$ values do not display a clear trend, with one exception, the M5 explosive tephra displays a strong trend, but this is mainly driven by one data point. This trend can potentially be explained by a slightly higher number of olivine macrocrysts in the portion of tephra powdered for M5 than in the other samples, not due to a general increase in macrocrysts in the magma feeding the eruption at this time. Although macrocryst content increases slightly towards the end of the eruption and these macrocrysts are more primitive (Passmore, 2009; Passmore et al., 2012). The Laki lavas in any subgroupings do not display any temporal trends throughout the eruption.

The Laki tephtras preserve a clear temporal trend towards heavier $\delta^{66}\text{Zn}$, i.e., more degassed apron tephra throughout the lifespan of explosive activity of a single

fissure opening episode (Figure 8. 17), evolving as follows: (1) The vent activity starts as a continuous curtain of fire across the length of the fissure; (2) Over a short timescale, within tens of minutes to hours (Sumner et al., 1998), the fountaining intensity of sub-Plinian phase intensity events increases to its maximum height due to a rapidly waxing mass-eruption rate (MER); (3) Choke points also develop along the fissure, where parts of the dyke shut down due to narrower sub-surface geometry in places, creating a stronger thermal gradient resulting in cooler, more microlite rich material, which moves slower and eventually clogs and chokes this part of the shallow subsurface fissure (Figure 8. 17). Here we liken this type of increased explosivity, due to a waxing MER and geometric factors in the conduit, to a “waterfall effect”: whereby this change in eruptive activity can be likened to water travelling in a river that suddenly goes over the edge of a waterfall and experiences changes in velocity, shearing, and strain rate. In response to changes in MER, and a much smaller conduit diameter, this subjects the melt to an increased strain rate and shearing, which studies have shown induces further degassing (Shields et al., 2014) in response to increasing fountaining intensity. This period of high intensity eruptive activity correlates with more efficient degassing of oxidised sulfur, and therefore each of these explosive phases displays a shift towards heavier $\delta^{66}\text{Zn}$ throughout these discrete episodes (Figures 8. 13 and 8. 17). As activity wanes from this initial sub-Plinian intensity, into predominantly lower intensity activity and effusive behaviour, towards the final stages of vent activity, i.e., the top tephra in the cone building phase, the degassing efficiency has decreased with consistently lighter $\delta^{66}\text{Zn}$ observed along the cone row at four different cones from different fissure episodes (Figures 8. 13 and 8. 17).

The Laki explosive apron tephra produced fissure opening phases that were sub-Plinian in intensity reaching >1400 m high, approximately 10 times higher than the weak-moderate fountaining phases observed at Holuhraun; which peaked at 170 m high during its most explosive phase 6–9 September (IES eruption team field report observations). A discrepancy between the two eruptions in the $\delta^{66}\text{Zn}$ of the tephra and lavas can be observed; with both the explosive and the cone tephtras from Laki reaching heavier $\delta^{66}\text{Zn}$ values than the Holuhraun tephra, which is also mirrored in some of the $\delta^{66}\text{Zn}$ values of the lava samples in the two eruptions (Figure 8. 17). If it is assumed that both eruptions have a similar initial $\delta^{66}\text{Zn}$ value prior to eruption, the

heavier $\delta^{66}\text{Zn}$ values suggest that the short-lived, hours long, higher intensity eruptive phases at Laki, are more efficient at degassing oxidised S at the vent compared to the weaker intensity explosive phases at Holuhraun; which lasted for several days, do not display a strong corresponding $\delta^{66}\text{Zn}$ trend. Higher fountaining heights during the apron tephra sub-Plinian intensity explosive phases, is consistent with the pyroclasts being transported for longer in the thermally insulating fountains, allowing post-fragmentation modification of the clasts, causing a thermal gradient inside the pyroclasts (see Chapters 6 and 7). However, textural and in-situ geochemical analysis of these post-fragmentation modified clasts indicates that the clasts mostly undergo growth drive expansion, due to pressure changes, rather than further volatile exsolution suggesting this is not the reason for the discrepancy in $\delta^{66}\text{Zn}$ values. Instead, a rapid increase MER during these more intense fissure opening phases at Laki, might drive the melt to volatile supersaturation enhancing degassing through burst homogeneous nucleation events. This agrees with textural findings in the Laki eruptive products (see Chapter 7), where an ultra-vesicular foam, with a low S groundmass glass concentration, was identified in M2 onwards in explosive tephra samples. An exception to this is M6 which captures the waning stage of the eruption, where this volatile supersaturation generated texture is absent (see Chapter 7). Whilst a similar ultra-vesicular foam was also identified in two of the Holuhraun samples after sudden increases in MER, on the 1 and 17 September, they are proportionally smaller in the samples and whilst they have a lower S content, it is not as pronounced as in the Laki samples (see Chapters 6 and 7). More intense fountaining activity, which occurs due to a waxing MER, during the Laki eruption displays a clear trend with increasingly heavier $\delta^{66}\text{Zn}$ (Figures 8. 13 and 8. 17). For both eruptions, the devolution of activity onto discrete vents and peak MER appear to increase the efficiency of oxidised S loss resulting in heavier $\delta^{66}\text{Zn}$ values. Early lavas from initial fissure opening phases, prior to the highest intensity explosive activity, display lighter $\delta^{66}\text{Zn}$ values; whereas all lavas fed by established explosive vent activity or later stage activity, which is dominated by lava effusion activity, have heavier $\delta^{66}\text{Zn}$ values, indicating further oxidised S loss (Figure 8. 17).

The range in $\delta^{66}\text{Zn}$ is smaller for the N. fissure explosive tephra, but it shows the same trend. A proposed explanation for this reduction in range is increased quantities of clearly degassed texturally mature, microlite and macrocryst rich melt in the N.

fissure eruptive products (seen in small quantities as early as M2, see Chapter 7). The texturally mature melt represents the remnants of a previously degassed melt batch that still exists in the dyke prior to a new fissure opening phase, with new explosive activity triggered by the injection of a fresh batch of melt represented in the erupted pyroclasts by an ultra-vesicular foam. The explosive apron phase tephra vary in Zn content by up to 50 ppm, which indicates either increased microlite content from a mature melt phase being mingled in varying degrees or macrocryst incorporation, again to varying degrees (Passmore, 2009).

The cone-forming phase tephra, produced after the explosive activity has mostly finished, are surprisingly uniform in their light $\delta^{66}\text{Zn}$ (with a range of 0.003‰) (Table 8. 4; Figures 8. 13 and 8. 17), indicating that the final layers of pyroclasts on the cones are relatively less efficiently degassed. These samples are produced when bubble bursting and lava pond boiling activity takes over, which is associated with lower MER and, therefore, lower eruptive intensities. The majority of the melt erupted at this time, during the cone building tephra phase, directly feeds the lava transport system. This degree of degassing of oxidised Zn is unchanged regardless of eruptive environment, as subaerial and shallow sub-glacially erupted samples alike have the same range of $\delta^{66}\text{Zn}$, despite EMPA analysis of P3 indicating volatile loss suppression due to a higher degree of quenching (see Chapters 5 and 7).

The similarity of isotopic values between sub-aerial and shallow subglacial cone tephra samples is also important, as the initial findings from Chapters 5 and 7 suggest the Laki magmatic foam interacted with late-stage water/ice once it was fully vesiculated, suggesting a consistent $\delta^{66}\text{Zn}$ in cone tephra is established through similar shallow conduit dynamics. However, the suppressed loss of S identified through EMPA analysis of the texturally analysed P3 clast (see Chapter 5 and 7) does not fit with this hypothesis of similar degrees of degassing in these samples. Further analysis of ice-water interaction samples from fissure 10 from the N. of Laki sequence are needed to investigate this further.

Importantly, this study finds a lack of $\delta^{66}\text{Zn}$ isotopic variations in the cone tephra, which are usually the only samples of pyroclastic deposits available for analysis from older eruptions. Therefore, cone tephra samples, rather than apron tephra, will

not give a good indication of the speciation of volatiles lost during explosive vent phases. The cone tephra only record the less explosive tephra phases, deposited during bubble bursting or lava pond boiling activity (Figures 8. 12–8. 17). Therefore, unless the corresponding medial or distal tephra from an older or less well-known eruption can be traced, variations in $\delta^{66}\text{Zn}$ imparted by volatile degassing cannot be discerned. Identifying tephra fall from explosive apron forming tephra phases for older eruptions in the field is more difficult than sampling cone tephra due to exposure, burial, or preservation issues. However, apron tephra sheets have been identified and sampled for both the Roza Member and Grande Ronde Member (Brown et al., 2015) of the Columbia River Basalt Group, a FB eruption, indicating that whilst harder to find these deposits can be sampled and analysed.

The majority of Laki lavas, when compared to the Holuhraun lava suite, display relatively heavier $\delta^{66}\text{Zn}$ values. Two statistically distinct separate lava groupings from the Laki lava field, highland lavas 1–5 km from the vent and lowland >20 km Síða district lavas, display moderate-heavy $\delta^{66}\text{Zn}$ values (Figure 8. 13). Whilst these are comparable to the degassed lavas fed by fountaining activity at Holuhraun, the caveat with a direct comparison is that the Holuhraun eruption was fed by one fissure and a clear sequence of eruptive activity related solely to that fissure, whereas the Laki lava flow field is fed by 10 fissures. Along the Laki cone-row multiple fissures were active at the same time, potentially during different stages in the evolution of vent activity, all feeding the flow field with active lava branches or channels potentially merging in the highlands or lowlands. This complicated activity sequence would distort or over-print primary isotopic signals by reducing the known conditions of sample formation either at the vent or along a single lava flow branch transport system, as mixing may have occurred to varying degrees at different stages. The result is a much more complicated compound flow field for Laki than Holuhraun. However, at least some of the Laki lavas are very likely to have been emplaced in exactly the same way as Holuhraun, with historical accounts stating that a fissure opening phase featured a short-lived (12–24 hours) sub-Plinian fountaining explosive phase with widespread sheet forming tephra fall that was followed by lava surge that passed through the distal part of the transport system days later (Steingrímsson, 1788; Thordarson and Self, 1993; Thordarson et al., 2003b) (Figure 8. 17). The hydrostatic pressures required to enable lava to travel from the vents to

the lowlands (>40km) would also demand more vigorous activity than bubble bursting/overturning lava pond to reach these distances.

Unlike at Holuhraun, where the early lavas from the curtain of fire activity were easily sampled, the initial Laki lavas with lighter $\delta^{66}\text{Zn}$ values are not captured well by this study as they are buried under later lava flow front advances (Figures 8. 13 and 8. 17). This would be the case if Holuhraun was sampled today, with early lava lying buried and inaccessible below the current flow field deposit. However, at three localities for Laki where the later lavas did not advance over the same area as the initial fissure opening phase lavas, the light $\delta^{66}\text{Zn}$ value of these relatively less degassed early lavas fed by curtain activity is preserved. Examples of these samples can be found at Hrossatunga ('A'ā -01) and Bugar/Grænháls-Brattland (S. and N. fissures respectively) (Figure 8. 17).

The lowland and highland lavas show a shallow covariation from heavier $\delta^{66}\text{Zn}$ towards moderately lighter $\delta^{66}\text{Zn}$ with increasing Zn content, consistent with either volatile gain into the system or a decrease in degassing efficiency of oxidised S with increases in Zn and Cu. There are two potential explanations for this:

- (1) The Laki lava field is fed not by one fissure whose activity wanes over time but by activity that propagates, opening new fissures and displaying a cycle of explosive activity followed by waning at each fissure. The explosive activity is the main source of lava surges within the lava field. This low-moderate fountaining activity, as seen in the Holuhraun 2014–15 CE event, produces relatively heavier presumably degassed $\delta^{66}\text{Zn}$ values. The lavas which reach the lowlands developed well-established (closed) transport channels which inhibited degassing due to transport pressurisation (Devine et al., 1984; Thordarson et al., 1996) (Figure 8. 17). Therefore, the relatively degassed, heavier $\delta^{66}\text{Zn}$, signature of these lavas must have been set close to or at the vent where the channel was open due to a high discharge rate from vigorous vent activity. This is in agreement with XANES data for the Laki lavas, which shows that oxidised S loss at the vents in explosive tephra phases leaves the erupted melt more reduced (Hartley et al., 2017). As explosive activity wanes, the fissures degassing becomes less efficient (i.e.,

light $\delta^{66}\text{Zn}$ cone building tephra), and increasingly lighter $\delta^{66}\text{Zn}$ is seen in the flow field along with increasing Zn content (Figures 8. 13 and 8. 17).

Alternatively,

- (2) The introduction of macrocrysts with olivine as a subordinate component, for which Zn has a partition coefficient of 1, would increase the Zn content (assuming 100–200 ppm for crystals). An increase of macrocrysts from the crystal mush-zone, accompanying drainage of the magma storage zone, is seen throughout the eruption (Passmore et al., 2012; Neave et al., 2013). The introduction of larger, well-developed microlites in larger proportions into the systems from the vents, which are shutting down, in response to low MER (Figure 8. 17), but still contributing to the lava flows, could be a way of increasing the Zn content in a degassed melt. There is also a rheological gradient around the macrocrysts which locally impedes degassing, on a microscale, with elevated S contents compared to normal groundmass glass (by up to 400 ppm) measured by this study in the melt around these crystals, which in turn promotes sulfide nucleation and growth. This might explain the similar increase in Cu content in the samples with higher Zn concentrations.

These trends can only be deciphered when we separate out the highland and lowland lavas; other target areas of interest, such as rootless cone fields and their associated lavas, are either too complex to understand in terms of transport system or there is not enough data to give a high enough resolution to say anything statistically robust.

For both the lavas and the tephra samples, the data sets cannot distinguish whether lighter $\delta^{66}\text{Zn}$ values result from the degassing of oxidised S as a volatile or aerosol phase. Future work comparing these values to Re trace element concentrations will be carried out to try and tease this apart due to its similar volatile behaviour to S.

XANES $f\text{O}_2$ data, from Hartley et al. (2017), for melt inclusions and matrix glass from 4 tephra samples and 5 lava selvages exist for the Laki eruption, although this data set indicates that a primary $f\text{O}_2$ has been overprinted by diffusion and re-equilibration with their external environment at magmatic temperatures. This study found that evolved Icelandic basalts, and indeed the Laki itself, are more oxidised

than previously thought and the lava selvages from this event track a progressively reducing and degassing carrier melt due to oxidised S loss (Hartley et al., 2017). This agrees well with this study's findings of $\delta^{66}\text{Zn}$ variability, which indicates some oxidised S loss during the Laki and Holuhraun eruptions, as well as reduced S loss from the degassed lava samples. Although to date, no Holuhraun melt inclusions have been analysed by XANES.

Other processes that could potentially produce the range of isotopic variation captured in the eruptive products from this study are: magma differentiation; mantle/source heterogeneity; and crustal contamination (addition of volatiles and change in composition, and therefore redox and S saturation). The former two processes which generate heterogeneities can be ruled out easily for Laki and Holuhraun from the previous Pb, Th, U, Hf and O isotopic studies, which indicate that both these eruptions are fed by homogenous melts (Sigmarsson et al., 1991; Bindeman et al., 2006; Halldórsson et al., 2018). The observation of increasing crystal mush content, and increasingly more primitive compositions throughout the Lakieruption, indicates some degree of heterogeneity in the melts (Passmore, 2009; Passmore et al., 2012). However, these crystals never exceed a bulk volume of 5-10% of the melt, and thus do not significantly change the overall chemistry of the erupted products. The latter process, which could result in the addition of volatiles, could be responsible for the initial isotopically lighter $\delta^{66}\text{Zn}$ values in both eruptions from the initial lavas and un-degassed Pele's hairs (Figures 8. 12– 8. 17). However, further work would be required to pick these variations apart, potentially using the Re-Os isotope system, which is highly sensitive to fractionation amongst minerals, as well as volatile loss.

8. 4. 2 Cu isotope variations

8. 4. 2. 1 Holuhraun $\delta^{65}\text{Cu}$ variations

Holuhraun lavas: display a strong covariation trend towards lighter $\delta^{65}\text{Cu}$ with increasing Cu content (Figure 8. 14). The increase in Cu content can be explained by the general gain of Cu into the system, through increasing the sulfide content, for which Cu has a high partition coefficient. At the same time, sulfides have lighter Cu

isotopic values which the higher Cu content samples all have. Increasing the sulfide content of the erupted melts could be achieved through two mechanisms: (1) immiscible sulfide phases are relatively dense and thus might be more prone to settling into the convecting lava pond, they would, therefore, be incorporated more readily into the melt feeding lava flows; or (2) there is an increase of immiscible sulfides in the erupted melt due to floatation/hitching of this phase onto the edge of bubbles rising through the conduit, thereby, transferring sulfides from a parent melt package through the shallow conduit (Mungall et al., 2015). The latter mechanism fits the Holuhraun data set best, as active lava samples taken earlier in the eruption have higher Cu content and lighter Cu isotope values than those emplaced later in the eruption. This process may also be responsible for the lower Cu content and heavier Cu isotope values later on in the eruption, with the same process having the reverse effect on melt batches erupted later on which have had their sulfides scavenged by more rapidly rising bubbles. No point counting was carried out to quantify variations in sulfide content in samples taken throughout the eruption lava, which would have verified this hypothesis; however, all analysed samples contain an immiscible sulfide phase (see supplementary material, appendix B: Sulfides Tri Plot). A shift from lighter $\delta^{65}\text{Cu}$ values and higher Cu contents towards heavier $\delta^{65}\text{Cu}$ values and lower Cu contents is observed throughout the eruption (Figure 8.14). This trend could be generated by higher proportions of faster moving pulses of melt, driven to volatile supersaturation and which experienced increased S degassing earlier in the eruption. As the MER wanes, the eruption is dominated by mature, slower-moving melts in the shallow conduit system, which has already lost the heavier Cu isotope in a reduced volatile S phase. This hypothesis is supported by textural observations of increasingly mature melts taking over the shallow conduit system with decreasing MER, as well as the lower S contents measured in domains of volatile supersaturation generated textures from waxing MER phases occurring earlier in the eruption (see Chapter 6). This earlier loss of a volatile reduced S phase, e.g., H_2S , could also take the form of large bubbles or bubble clusters that decouple from the melt and move at higher rise rates through the shallow conduit. Large bubble bursts of decoupled volatiles were observed during phases of lower intensity vent activity during the Holuhraun eruption (see Chapter 6). Field observations also noted reduced volatile S loss from the lava flow field during syn-degassing emplacement, and low oxygen environments near active lava flow fronts in the flow

field throughout the eruption. The detection of H₂S from syn-emplacement degassing of the lava flow field was frequently recorded on IES team gas meters. An Icelandic police team who were at the eruption site making field observations in December also reported a low oxygen environment causing their fingertips to turn white. These field observations are supported by data collected via XANES analysis of glassy lava selvages from basaltic fissure eruptions, which detected reduced conditions (Brounce et al., 2017; Hartley et al., 2017).

Holuhraun tephras: display no trend of $\delta^{65}\text{Cu}$ with Cu and Zn content (Figure 8. 14); however, like the Holuhraun lava samples, the tephra samples also display a statistically moderate trend of increasingly heavy $\delta^{65}\text{Cu}$ values with time (Figure 8. 14). As with the lava samples, similar processes could be responsible for this covariation trend, such as; (1) the loss of the heavy Cu isotope via a volatile reduced S phase, i.e., H₂S, occurring predominantly earlier in the eruption and decreasing over time; or (2) the earlier erupted melt gaining more sulfides from melt packages lower down in the lava column hitching a ride on bubbles. If this is due to increase sulfide contents, this would increase the eruption's atmospheric trace metal budget during its highest eruptive intensity, which is capable of delivering a plume to higher levels in the atmosphere, as these sulfide particulates oxidise and break down upon eruption (Berlo et al., 2014; Edmonds and Mather, 2017). Observed sulfide proportions in the Holuhraun melt changes temporally, and contain varying proportions of Cu, although chalcopyrite is the predominant sulfide form (Halldórsson et al., 2018; see supplementary material, appendix B: Sulfides Tri Plot). It is likely that a late-stage immiscible sulfide phase formed from the host magma during syn-eruptive degassing, rather than additional sulfides incorporated into the melt at depth from a different magmatic source which was ruled out by Halldórsson et al. (2018). Varying proportions of sulfides in the eruptive products may be due simply to a heterogeneous distribution within the melt itself, or volcanic processes such as; (1) sulfides hitching a ride with bubbles, moving faster through the conduit than their parental melt batch; or (2) settling or convecting sulfides in the vent area pond, which is predominantly feeding the lava flow field, and thus be preferentially incorporating sulfides into lavas rather than tephra. Both these processes would create the lighter $\delta^{65}\text{Cu}$ values observed in the earlier erupted Holuhraun samples through the addition of ^{63}Cu and an increase in elemental Cu concentration. The S

released by sulfide destabilisation during the Holuhraun eruption, as it converts to SO_2 and SO_4^{2-} or $\text{H}_2\text{SO}_4^{2-}$, may have varied with time, but it does not significantly increase the eruption's total atmospheric S budget, which is calculated from melt inclusion and eruptive glass S concentrations as there is no external melt at depth contributing extra sulfides to this eruption.

8. 4. 2. 2 Laki $\delta^{65}\text{Cu}$ variations

Laki tephtras: The Cu stable isotope data sets from the Laki tephra samples show a strong temporal trend with from initially heavier $\delta^{65}\text{Cu}$ towards lighter $\delta^{65}\text{Cu}$ values, which can be clearly observed both in the tephra layers sampled from proximal soil horizons for the S. fissures and through a time series of tephra apron samples from the N. fissures (Figure 8. 15). This is a much stronger trend than when the samples are grouped into S. fissure and N. fissure samples than for the $\delta^{66}\text{Zn}$ data. These trends in the S. and N. fissure samples, from initially heavier $\delta^{65}\text{Cu}$ towards lighter $\delta^{65}\text{Cu}$ values, could indicate the heavier Cu isotope is lost in a reduced volatile phase to increasing degrees with time, or the increasing addition of sulfides, and therefore generating a shift towards lighter Cu isotope values with time, for the S. and N. fissure tephtras separately (Figure 8. 15). For the latter hypothesis, the reverse could also be the case, where fewer sulfides are removed from the residual melt phases with time. Importantly, a complete time series through an individual tephra apron is only available for M5 samples, which show a strong temporal trend from heavier $\delta^{65}\text{Cu}$ towards lighter $\delta^{65}\text{Cu}$ values; unlike for the $\delta^{66}\text{Zn}$ samples where this is also observed for M4 due to higher sample numbers for the $\delta^{66}\text{Zn}$ analysis (Figures 8. 13 and 8. 15). In the case of $\delta^{65}\text{Cu}$ and $\delta^{66}\text{Zn}$, an isotopic “reset” towards initial values is observed for both the S and N fissure samples. Notably, in the case of the strong trend from heavy to lighter $\delta^{65}\text{Cu}$ values for the N. fissure tephra apron samples, which amalgamates data from both the M4 and M5 explosive phases, the starting value for the M5 explosive phase isn't “reset” back to the initially heavier $\delta^{65}\text{Cu}$ range as observed for the Laki $\delta^{66}\text{Zn}$ data sets for each complete apron phase time-series. Instead, the trend for the M5 data set continues towards increasingly lighter $\delta^{65}\text{Cu}$ directly from the M4 samples (Figure 8. 15). This suggests that the processes driving the samples towards lighter $\delta^{65}\text{Cu}$ values with time continue between these two eruptive phases. The addition of convecting sulfides from lava ponds in the vent,

from the M4 to M5 fissure phases is unlikely, as, at very shallow-surface levels, fissure segments from different eruptive phases are not likely to be connected. Earlier degassing of a reduced volatile S phase could generate this continued trend towards lighter $\delta^{65}\text{Cu}$ values with time, either at depth or as a decoupled volatile phase. Indeed, throughout the Laki eruption an increase in the proportions of mature melt textures present, which rose slowly through the shallow conduit is noted in Chapter 7, enabling more decoupling of faster moving volatile phases in larger bubbles, potentially removing more of the heavier Cu isotope in M5 compared to M4 through degassing of H_2S . Another textural variation as the eruption progresses noted in the Laki pyroclasts is the higher proportions of ultra-vesicular foam, generated by rapid rise rates driving this melt domain to volatile supersaturation, present after significant lag times between fissure opening phases (see Chapter 7). This may have generated further degassing heavier Cu in the M5 tephra compared to M4 and explain the continued trend towards lighter $\delta^{65}\text{Cu}$ values for the N. fissure tephra samples. Previous studies also suggest a difference in the explosivity, and therefore the MER, of the fissure opening phases throughout the eruption (Thordarson and Self., 1993; Thordarson et al., 2003b), which may also provide the conditions for larger bubbles to more easily decouple from their parent melt packages, again providing the mechanisms for heavier Cu isotope loss through H_2S degassing. Samples analysed for both M4 and M5, the only tephra apron samples taken as a sequence through individual aprons, both display a migration towards lighter $\delta^{65}\text{Cu}$ values during the explosive activity for these fissures. This either suggests further volatile loss of the heavy Cu isotope or the increasing addition of sulfides either through sulfide hitching a ride on bubbles or through density settling convection. As is the case for the $\delta^{66}\text{Zn}$ values for the Laki tephra apron samples, the $\delta^{65}\text{Cu}$ data sets aren't statistically robust as more samples are needed for these subgroups. In both cases, strong trends in an individual tephra apron are only defined by 3 or 4 data points.

There is a larger range of $\delta^{65}\text{Cu}$ for the Laki cone tephra samples compared to the flat line $\delta^{66}\text{Zn}$ values, with one of the cone tephra samples containing the second heaviest $\delta^{65}\text{Cu}$ composition of the Laki samples (Figure 8. 15). Temporally the cone tephra samples exhibit a very strong trend from heavy to light $\delta^{65}\text{Cu}$; this could either indicate an increasing gain of the light Cu isotope into the system with time or a

decrease in the volatile loss of the heavy Cu isotope with time. This trend from heavier to lighter $\delta^{65}\text{Cu}$ values of the Laki cone tephras could indicate, as with the Holuhraun lavas and tephras, an addition of ^{63}Cu into the samples through sulfides “hitching a ride” on the side of bubbles in the shallow conduit, increasing their quantity in melt batches which they didn’t originate from due to their higher buoyancy and therefore faster ascent rate (Mungall et al., 2015). Once in the vent region, as material feeding the more explosive activity is recycled, denser phases such as sulfides and crystals may be more prone to segregation and recirculation, thus entraining these phases, to a larger extent, into the melt feeding the lavas rather than the rapidly ascending high MER, more explosive eruptive phases forming the tephra aprons. A weak covariance trend from heavy to lighter $\delta^{65}\text{Cu}$, can be observed with increasing Cu content within a range of 40 ppm ($0.5677 R^2$; Figures 8. 14 and 8. 16); this would agree with the hypothesis of an increase in sulfides driving this trend. No significant visual temporal changes in sulfide content were observed, but again as with Holuhraun, this could be tested by point counting. For the N. fissure Laki samples, in particular M4, the samples have a much heavier $\delta^{65}\text{Cu}$ composition to start with. This could be explained by the long lag time between eruptive phases (see Chapter 5 and 7) (Thordarson, 2003; Thordarson et al., 2003b), which would generate a marked difference between the proportions present of mature melt and ultra-vesicular foams (see Chapter 7); with the mature texture containing more sulfides, or this explosive phase potentially having undergone less initial reduced S volatile loss. The wider range, and generally heavier $\delta^{65}\text{Cu}$ values, are driven solely by the explosive phase apron forming tephras from Laki (Table 8. 4), which is not dissimilar to a couple of samples previously analysed from explosive phase tephras from Mauna Ulu 1974 CE (Liu et al., 2015).

Laki lavas: A smaller set of Laki lava samples were analysed for Cu stable isotopes than for Zn isotopes. Samples with heavier $\delta^{65}\text{Cu}$ broadly have higher Cu and Zn concentrations, but no clear covariance trend exists; therefore, more samples are required to test this correlation properly. This trend is also the opposite of what is seen for Holuhraun, where $\delta^{65}\text{Cu}$ becomes lighter with increasing Cu and Zn, potentially due to an increase in sulfide content (Figures 8. 12–8. 17). This suggests that the samples which have both low Cu and light $\delta^{65}\text{Cu}$ have been driven to a reducing environment through the oxidised loss of S at the vents and subsequent

reduced Cu volatile phase loss, which is entirely consistent with the explosive tephra data set and with previous petrological and XANES studies (Moussallam et al., 2016; Hartley et al., 2017). These findings also agree with the low proportions of Fe-Ti oxides in the glass lava selvages in the Laki eruption (Thordarson et al., 1996), as reduced conditions would inhibit their crystallisation. Further supporting evidence for reducing conditions in the lava flows was also acquired during the Holuhraun eruption: with H₂S recorded on the field team gas meters at the lava margins (IES eruption team field reports), as well as low oxygen conditions and H₂S detection recorded by the specialised police unit stations at the eruption site in December who noted their fingertips turning white due to the lack of oxygen in the area by the active lava flows. Samples with relatively heavier $\delta^{65}\text{Cu}$ have not undergone as much reduced volatile loss of S; indeed, the samples with the heaviest $\delta^{65}\text{Cu}$ value is the same fast travelling lava flow break-out, upstream of the main active front, producing the relatively un-degassed sample of Gráhóll með Skaftá, which was documented by historical accounts (Thordarson and Self, 1993). Notably, the same Gráhóll með Skaftá sample also has an undegassed, light $\delta^{66}\text{Zn}$, signature.

8. 4. 3 $\delta^{66}\text{Zn}$ and $\delta^{65}\text{Cu}$ isotope covariations

8. 4. 3. 1 Holuhraun $\delta^{66}\text{Zn}$ and $\delta^{65}\text{Cu}$ covariation comparisons

Holuhraun tephra: Covariation plots of $\delta^{66}\text{Zn}$ and $\delta^{65}\text{Cu}$ for the explosive tephra samples from Holuhraun display no resolvable trends when the whole data set is compared. The highest intensity explosive activity at Holuhraun is represented by the 6 and 7 September 2014 samples, $\delta^{66}\text{Zn}$ and $\delta^{65}\text{Cu}$ covariations display the same fingerprint as the most explosive tephra $\delta^{66}\text{Zn}$ and $\delta^{65}\text{Cu}$ signatures at Laki of heavy $\delta^{66}\text{Zn}$ and light $\delta^{65}\text{Cu}$ (Figures 8. 16 and 8. 17). Notably, all the early September samples, during the initial waxing MER period sit in a similar quadrant in $\delta^{66}\text{Zn}$ versus $\delta^{65}\text{Cu}$ isotope space (Figure 8. 16). Although within this small sub-group of 5 samples a strong covariance trend is present from lighter $\delta^{66}\text{Zn}$ and light $\delta^{65}\text{Cu}$ towards heavy $\delta^{66}\text{Zn}$ and heavier $\delta^{65}\text{Cu}$ values. This suggests that for the mechanism that generates the increase in oxidised S loss, creating a trend towards heavy $\delta^{66}\text{Zn}$ in these samples, occurs at the expense of the process(es) that generate the light $\delta^{65}\text{Cu}$ values which could be driven either by sulfide gain to the system or by reduced

volatile S loss. The Pele's hair sample has a similar light $\delta^{65}\text{Cu}$ value but lies at a lighter $\delta^{66}\text{Zn}$ value which, as previously discussed, suggests that this sample experienced less oxidised S degassing despite occurring during a period of higher intensity and increasing shearing with the melt around the Pele's hair potentially degassing more as the lapilli sample for the same day has a heavier $\delta^{66}\text{Zn}$ value. Similarly, the cone tephra sample displays a less oxidised S degassed signature with a light $\delta^{66}\text{Zn}$ value but a much heavier $\delta^{65}\text{Cu}$ value, which could be generated by lower degrees of reduced S volatile loss or by sulfides being preferentially removed. The latter process fits the data set well, as it occurs during a period of activity dominated by a lower MER towards the end of the eruption, with vent activity defined by lava pond convection where sulfides could undergo density settling and be preferentially incorporated into the lava flow field. As with the Laki lava cone tephra, a light $\delta^{66}\text{Zn}$ signature for the Holuhraun cone tephra suggests that the mechanisms that these samples are formed by are governed by similar eruptive conditions and degrees of volatile loss.

Holuhraun lavas: The active Holuhraun lavas, when treated as a whole, display no covariance trend. However, a strong covariance trend from lighter $\delta^{66}\text{Zn}$ and light $\delta^{65}\text{Cu}$ exists in the Holuhraun active lavas, as long as the lavas from the more intense activity, higher MER, phases are excluded as these have elevated oxidised S loss signatures and therefore heavier $\delta^{66}\text{Zn}$ values. The limited data for all September active samples plot in similar $\delta^{66}\text{Zn}$ and $\delta^{65}\text{Cu}$ space, following a similar pattern to the Holuhraun early September tephra. However, this space is slightly different for the two types of samples; they all have similar $\delta^{65}\text{Cu}$ values but are differentiated by their $\delta^{66}\text{Zn}$ values, with lavas sitting in lighter $\delta^{66}\text{Zn}$ space suggesting that the tephra have undergone more oxidised S loss although this difference is within analytical error (Figure 8. 16). Whilst the Holuhraun September lava data set is limited temporally and spatially and thus cannot provide the resolution needed for a statistically robust conclusion, it does suggest that similar mechanisms of volatile S loss, and sulfide gain or loss exists throughout September. The post-eruptive lava samples, emplaced towards the very end of the eruption and fed by the waning stages of the lava pond, both plot in heavy $\delta^{66}\text{Zn}$ and lighter $\delta^{65}\text{Cu}$ space (Figures 8. 16 and 8. 17), which could be the result of the inclusion of more sulfides which had been convecting in the lava pond or higher degrees of reduced S volatile loss. They both

plot in heavy $\delta^{66}\text{Zn}$ space, suggesting these samples have undergone higher degrees of oxidised S loss than the September active samples despite their similar $\delta^{65}\text{Cu}$ values (Figure 8. 16).

8. 4. 3. 2 Laki $\delta^{66}\text{Zn}$ and $\delta^{65}\text{Cu}$ covariation comparisons

Laki tephra: As noted earlier, the explosive apron phase tephra covariation plots of $\delta^{66}\text{Zn}$ and $\delta^{65}\text{Cu}$ are inconclusive when assessed collectively, as well as when they are divided into N. and S. fissures (Figure 8. 16). However, when isolated, the M5 tephra display a strong trend from lighter $\delta^{66}\text{Zn}$ and light $\delta^{65}\text{Cu}$ to increasingly heavy $\delta^{66}\text{Zn}$ (Figure 8. 16); which suggests an increase in oxidised S loss alongside either the removal of sulfides or decreasing degree of reduced S loss. This indicates a change in the mechanisms of S loss throughout this fissure opening phase from more reduced to oxidising conditions or increased removal of sulfides from the system for later phases. The latter could occur due to them hitching a ride with bubbles and being incorporated into earlier erupted melts.

The Laki cone tephra display an excellent isotopic covariation trend (Figure 8. 16). This is a flat-line $\delta^{66}\text{Zn}$ values in all samples, which is combined with a shift towards increasingly heavier $\delta^{65}\text{Cu}$ values. This trend is generated by then consistently low $\delta^{66}\text{Zn}$ values, which do not display an increasing oxidised S loss in these samples, regardless of eruptive fissure phase or environment, as well as increasing FeS_2 (immiscible sulfide melt) loss fractionating Cu from the melt or decreasing degrees of degassing of a reduced volatile phase, e.g., H_2S (Figure 8. 16). This trend mirrors the exact same fingerprint as the single cone tephra sample analysed from the Holuhraun eruption. These variations can be explained either with sulfides that are circulating in the convecting lava, during these phases of low MER, that are potentially preferentially incorporated into the lavas, and not the small bubble burst fed cone tephra, or with sulfides which hitch a ride with bubbles and are erupted with earlier phases. However, a reduction in the loss of a reduced volatile S phase could also generate the variations observed in $\delta^{65}\text{Cu}$ values. Again, this is a very important finding as only variations in $\delta^{65}\text{Cu}$ values are observed in these samples, paired with remarkably consistent $\delta^{66}\text{Zn}$ values observed regardless of fissure phase or environment which has to be taken into account by future analysis of this type of sample.

Laki lavas: The same is true for the Laki lavas as for the tephra samples; the data sets, when viewed as a whole, display no covariation trends. However, when the same previous sample sub-groupings are considered in isolation, a strong covariation trend for the N. fissure lavas from light $\delta^{66}\text{Zn}$ and lighter $\delta^{65}\text{Cu}$ to heavy $\delta^{66}\text{Zn}$ and heavy $\delta^{65}\text{Cu}$ values can be observed. This marginally decreases when including the N. fissure rootless cone sample in the N. fissure lava samples (Figure 8. 16). This is the same trend that is displayed by the M5 tephtras, which are also from a N. fissure eruptive phase. However, it is important to note that these trends are not statistically robust due to low sample numbers.

8.5 Conclusions

This study is the first to find statistically resolvable variations in Zn and Cu isotopes as a product of degassing processes at the vent and associated lava field throughout eruption in two different intensity FL events: Holuhraun 2014–15 CE and Laki 1783–84 CE. Zinc and Copper isotopic values also appear to respond to variations in disequilibrium degassing processes (e.g., shallow conduit processes, such as increased proportions in ultra-vesicular foams and heavier $\delta^{66}\text{Zn}$ values) alongside equilibrium degassing during syn-emplacement of lava flows within basaltic samples from the same eruption. Whilst these initial constraints on volatile Zn and Cu loss during volcanic degassing are important, future work utilising well-documented eruptions spanning a range of: MER; varying flow field developmental stages; samples taken at several distances from the vent along the transport system; as well as considering eruptions from different tectonic settings is necessary to fully understand how $\delta^{66}\text{Zn}$ or $\delta^{65}\text{Cu}$ behave during degassing. Additional analysis for certain sub-groupings outlined in this chapter is also necessary to verify these findings with statistically robust trends; which, due to sampling and the limited scope of this project, require further work.

However, there are two significant caveats to be considered for this type of sample suite and data set: (1) The first is the lack of a known point zero for $\delta^{66}\text{Zn}$ or $\delta^{65}\text{Cu}$, or starting point, in terms of relatively un-degassed and un-weathered samples to compare this data set to. Whilst MORB can be used, it is not ideal as the mantle melting regime is not the same as those feeding the Icelandic OIB magmas. Hyaloclastites from Holocene age eruptions within the same volcanic systems in Iceland as Holuhraun and Laki have been subject to surface extensive weathering and palagonisation; and thus, whilst they are less degassed (volatile loss is not completely suppressed), they are likely to have altered $\delta^{66}\text{Zn}$ values and depletion in mobile trace element concentrations, e.g., Zn. (2) The second is that oxidised volatile versus oxidised particulate loss of S cannot be distinguished without comparing measured $\delta^{66}\text{Zn}$ values to volatile elements concentrations, such as rhenium (Re), in these samples; as Re behaves similarly to Zn during oxidised volatile S loss. This complementary analysis will be the focus of future work to underpin these differences properly.

8. 6 References

- Anderson, A. T., and Wright, T. L. (1972). Phenocrysts and glass inclusions and their bearing on oxidation and mixing of basaltic magmas, Kilauea volcano, Hawaii. *American Mineralogist*. 57. pp. 188–216.
- Archer, C., Andersen, M. B., Cloquet, C., Conway, T. M., Dong, S., Ellwood, M., Moore, R., Nelson, J., Rehkämper, M., Rouxel, O., Samanta, M., Ki-Cheol Shin, Ki-C., Sohrin, Y., Takano, S., and Wasylenki, L. (2017). Inter-calibration of a proposed new primary reference standard AA-ETH Zn for zinc isotopic analysis. *Journal of Analytical Atomic Spectrometry*. 32. pp. 415-419.
- Barnes, S. (2012) Sulfur in Magmas and Melts: Its Importance for Natural and Technical Processes, Economic Geology. Behrens, H. and Webster, J. D. (Editors). In: Sulfur in magmas and melts. *Reviews in Mineralogy and Geochemistry*, 73, doi:10.2113/econgeo.107.4.737.
- Barsotti, S., Jóhannsson, T., Hellsing, V. Ú., Pfeffer, M. A., Guðnason, T. Stefánsdóttir, G. (2015). Abundant SO₂ release from the 2014 Holuhraun eruption (Bárðarbunga , Iceland) and its impact on human health. *2015 EGU Abstract*, 17, 12886.
- Berlo, K., van Hinsberg, V. J., Vigouroux, N., Gagnon, J. E., and Williams-Jones, A. E. (2014). Sulfide breakdown controls metal signature in volcanic gas at Kawah Ijen volcano, Indonesia. *Chemical Geology*. 371. pp. 115–127. doi:10.1016/j.chemgeo.2014.02.009
- Behrens, H., and Webster, J. D. (2011). Studies of sulfur in melts - Motivations and overview. *Reviews in Mineralogy and Geochemistry*. 73. pp. 1–8. doi:10.2138/rmg.2011.73.1
- Bigalke, M., Weyer, S., and Wilcke, W. (2010). Stable Copper Isotopes: A Novel Tool to Trace Copper Behavior in Hydromorphic Soils. *Soil Science Society of America Journal*. 74. (1), pp. 60–73. doi:10.2136/sssaj2008.0377
- Bigalke, M., Weyer, S., and Wilcke, W. (2011). Stable Cu isotope fractionation in soils during oxic weathering and podzolization. *Geochimica et Cosmochimica Acta*. 75. (11), pp. 3119–3134. doi:10.1016/j.gca.2011.03.005
- Bindeman, I. N., Sigmarsson, O., and Eiler, J. (2006). Time constraints on the origin of large volume basalts derived from O-isotope and trace element mineral zoning and U-series disequilibria in the Laki and Grímsvötn volcanic system. *Earth and Planetary Science Letters*. 245. (1–2), pp. 245–259. doi:10.1016/j.epsl.2006.02.029
- Björnsson, E. 1783. Relation eins prests sem ár 1783 ferðaðist um sumarið á Suðurland frá Múlasýslu yfir Skaftafells bæði áfram og heimleiðis (Relation by one pastor, who travelled in the summer 1783 in Southern Iceland from Múlashire through Skaftafellshire back and forth). In T. Einarsson, G. M. Gudbergsson, G. Á. Gunnlaugsson, S. Rafnsson and S. Thorarinsson (eds.), *Skaftáreldar 1783–1784, Ritgerðir og Heimild- ir. Mál og Menning*, Reykjavík 1984, 295–297.
- Blake, S., Self, S., Sharma, K., and Sephton, S. (2010). Sulfur release from the Columbia River Basalts and other flood lava eruptions constrained by a model of sulfide saturation. *Earth and Planetary Science Letters*. 299. (3–4), pp. 328–338. doi:10.1016/j.epsl.2010.09.013
- Brounce, M., Stolper, E., and Eiler, J. (2017). Redox variations in Mauna Kea lavas, the oxygen fugacity of the Hawaiian plume, and the role of volcanic gases in

- Earth's oxygenation. *Proceedings of the National Academy of Sciences of the United States of America*. 114. (34), pp. 8997–9002. doi:10.1073/pnas.1619527114.
- Brown, R.J., Thordarson, T., Self, S. (2015). Disruption of tephra fall deposits caused by lava flows during basaltic eruptions. *Bull Volcanol* 77, 90 <https://doi.org/10.1007/s00445-015-0974-3>
- Burgisser, A., and Scaillet, B. (2007). Redox evolution of a degassing magma rising to the surface. *Nature*. 445. (7124), pp. 194–197. doi:10.1038/nature05509
- Burton, M., Mader, H. M. and Polacci, M. (2007). The role of gas percolation in quiescent degassing of persistently active basaltic volcanoes. *Earth and Planetary Science Letters*. 264. (1–2), pp. 46–60
- Carlsen, H.K., Ilyinskaya, E., Baxter, P.J., Schmidt, A., Thorsteinsson, T., Pfeffer, M. A., Barsotti, S., Dominici, F., Finnbjornsdottir, R. G., Jóhannsson, T., Aspelund, T., Gislason, T., Valdimarsdóttir, U., Breim, H. and Gudnason, T. (2021). Increased respiratory morbidity associated with exposure to a mature volcanic plume from a large Icelandic fissure eruption. *Nature Communications*. 12. 2161. doi:10.1038/s41467-021-22432-5
- Carmichael, I. S. E., and Ghiorso, M. S. (1986). Oxidation-reduction relations in basic magma: a case for homogeneous equilibria. *Earth and Planetary Science Letters*. 78. (2–3), pp. 200–210. doi:10.1016/0012-821X(86)90061-0
- Chen, H. (2014). Unpublished PhD thesis. Zinc and Copper Isotopic Fractionation during Planetary Differentiation. Washington University in St. Louis.
- Chen, H., Savage, P. S., Teng, F. Z., Helz, R. T., and Moynier, F. (2013). Zinc isotope fractionation during magmatic differentiation and the isotopic composition of the bulk Earth. *Earth and Planetary Science Letters*. 369–370. pp.34–42. doi:10.1016/j.epsl.2013.02.037
- Chen, S., Liu, Y., Hu, J., Zhang, Z., Hou, Z., Huang, F. and Yu, H. (2015). Zinc Isotopic Compositions of NIST SRM 683 and Whole-Rock Reference Materials. *Geostandards and Geoanalytical Research*. 40, (3), pp. 417–432.
- Chenet, A. L., Quidelleur, X., Fluteau, F., Courtillot, V., and Bajpai, S. (2007). 40K-40Ar dating of the Main Deccan large igneous province: Further evidence of KTB age and short duration. *Earth and Planetary Science Letters*. 263. (1–2), pp. 1–15. doi:10.1016/j.epsl.2007.07.011
- Chenet, A. L., Fluteau, F., Courtillot, V., Gérard, M., and Subbarao, K. V. (2008). Determination of rapid Deccan eruptions across the Cretaceous-Tertiary boundary using paleomagnetic secular variation: Results from a 1200-m-thick section in the Mahabaleshwar escarpment. *Journal of Geophysical Research: Solid Earth*. 113. (4). doi:10.1029/2006JB004635
- Chenet, A. L., Courtillot, V., Fluteau, F., Gérard, M., Quidelleur, X., Khadri, S. F. R., Subbarao, K. V., and Thordarson, T. (2009). Determination of rapid Deccan eruptions across the Cretaceous-Tertiary boundary using paleomagnetic secular variation: 2. Constraints from analysis of eight new sections and synthesis for a 3500-m-thick composite section. *Journal of Geophysical Research: Solid Earth*. 114. (6). doi:10.1029/2008JB005644
- Christopher, T., Edmonds, M., Humphreys, M. C. S., and Herd, R. A. (2010). Volcanic gas emissions from Soufrière Hills Volcano, Montserrat 1995–2009, with implications for mafic magma supply and degassing. *Geophysical Research Letters*. 37. (3), pp. 1–5. doi:10.1029/2009GL041325
- Cottrell, E., and Kelley, K. A. (2011). The oxidation state of Fe in MORB glasses and the oxygen fugacity of the upper mantle. *Earth and Planetary Science*

- Letters*. 305. (3–4), pp. 270–282. doi:10.1016/j.epsl.2011.03.014
- Courtillot, V. E., and Renne, P. R. (2003). On the ages of flood basalt events. *Comptes Rendus – Geoscience*. 335. (1), pp. 113–140. doi:10.1016/S1631-0713(03)00006-3
- Costantini, L., Houghton, B. F., and Bonadonna, C. (2010). Constraints on eruption dynamics of basaltic explosive activity derived from chemical and microtextural study: The example of the Fontana Lapilli Plinian eruption, Nicaragua. *Journal of Volcanology and Geothermal Research*. 189. (3–4), pp. 207–224. doi:10.1016/j.jvolgeores.2009.11.008
- Devine, J. D., Sigurdsson, H., Davis A. N. and Self, S. (1984). Estimates of sulfur and chlorine yield to the atmosphere from volcanic eruptions and potential climatic effects. *Journal of Geophysical Research*. 89. pp. 6309–6325
- Devine, D., and Island, R. (1984). Estimates of Sulfur and Chlorine yield to the atmosphere from volcanic eruptions and potential climatic effects. *Journal of Geophysical Research*. 89. pp. 6309–6325.
- Doucet, L. S., Mattielli, N., Ionov, D. A., Debouge, W., and Golovin, A. V. (2016). Zn isotopic heterogeneity in the mantle: A melting control? *Earth and Planetary Science Letters*. 451. pp. 232–240. doi:10.1016/j.epsl.2016.06.040
- Eatough, D. J., Caka, F.M. and Farber, R.J. (1994). The Conversion of SO₂ to Sulfate in the Atmosphere. *Israel Journal of Chemistry*. 34. (3-4), pp. 301-314. doi:10.1002/ijch.199400034
- Edmonds, M., and Mather, T. A. (2017). Volcanic sulfides and outgassing. *Elements*. 13. (2), pp. 105-110. doi:10.2113/gselements.13.2.105
- Eiríksson, J. (1783). Abstract from Erichsens writings, dated July 11, 1783 at Fljótastöðum Vestur- Skaftafells County. In: T Einarsson, GM Guðbergsson, GA Gunnlaugsson, S Rafnsson and S Þórarinnsson (eds.) Skaftáreldar 1783-1784: Ritgerðir og Heimildir. pp. 274-276. Mál og Menning Reykjavík.
- Fiacco Jr. R. J., Thordarson, T., Germani, M. S., Self, S., Palais, J. M., Whitlow, S. and Grootes, P. M. (1994). Atmospheric Aerosol Loading and Transport Due to the 1783-84 Laki Eruption in Iceland, Interpreted from Ash Particles and Acidity in the GISP2 Ice Core. *Journal of Quaternary Research*. 42. (3), pp. 231-240
- Gaillard, F., and Scaillet, B. (2014). A theoretical framework for volcanic degassing chemistry in a comparative planetology perspective and implications for planetary atmospheres. *Earth and Planetary Science Letters*. 403. pp. 307–316. doi:10.1016/j.epsl.2014.07.009
- Gaillard, F., Scaillet, B., and Arndt, N. T. (2011). Atmospheric oxygenation caused by a change in volcanic degassing pressure. *Nature*. 478. (7368), pp. 229–232. doi:10.1038/nature10460
- Gaillard, F., Scaillet, B., Pichavant, M., and Iacono-Marziano, G. (2015). The redox geodynamics linking basalts and their mantle sources through space and time. *Chemical Geology*. 418. pp. 217–233. doi:10.1016/j.chemgeo.2015.07.030
- Gerlach, T. M. (2004). Volcanic sources of tropospheric ozone-depleting trace gases. *Geochemistry, Geophysics, Geosystems*. 5. (9). doi:10.1029/2004GC000747
- Gauthier, P.-J., Sigmarsson, O., Gouhier, M., Haddadi, B., and Moune, S. (2016). Elevated gas flux and trace metal degassing from the 2014–2015 fissure eruption at the Bárðarbunga volcanic system, Iceland. *Journal of Geophysical Research: Solid Earth*. pp. 3782–3803. doi:10.1002/2015JB012111.
- Geiger, H., Mattsson, T., Deegan, F. M., Troll, Valentin, R., Burchardt, S., Gudmundsson, O., Tryggvason, A., Krumbholz, M., and Harris, C. (2016).

- Magma plumbing for the 2014–2015 Holuhraun eruption, Iceland. *Geochemistry Geophysics Geosystems*. 17. pp. 2953–2968. doi:10.1002/2015GC006205.
- Getahun, A., M. H. Reed, and R. Symonds. (1996). Mount St. Augustine volcano fumarole wall rock alteration: Mineralogy, zoning, composition and numerical models of its formation process. *Journal of Volcanology and Geothermal Research*. 71. pp. 73–107.
- Gíslason, S. R., Stefánsdóttir, G., Pfeffer, M. A., Barsotti, S., Jóhannsson, T., Galeczka, I., Bali, E., Sigmarsson, O., Stefánsson, A., Keller, N. S., Sigurdsson, Bergsson, B., Galle, B., Jacobo, V. C., Arellano, S., Aiuppa, A., Jónasdóttir, E. B., Eiríksdóttir, E. S., Jakobsson, S., G.H. Guðfinnsson, G. H., Halldórsson, S. A., Gunnarsson, H., Haddadi, B., Jónsdóttir, I., Thordarson, T., Riishuus, M., Högnadóttir, T., Dürig, T., Pedersen, G. B. M., Höskuldsson, Á. and Gudmundsson, M. T. (2015). Environmental pressure from the 2014-15 eruption of Baröarbunga volcano, Iceland. *Geochemical Perspectives Letters*. 1. (1), pp. 84–93. doi:10.7185/geochemlet.1509
- Guilbaud, M. N., Self, S., Thordarson, T., and Blake, S. (2005). Morphology, surface structures, and emplacement of lavas produced by Laki, AD. 1783-1784. *Special Paper of the Geological Society of America*. 396. pp. 81–102. doi:10.1130/0-8137-2396-5.81
- Guilbaud, M. N., Blake, S., Thordarson, T., and Self, S. (2007). Role of Syn-eruptive Cooling and Degassing on Textures of Lavas from the ad 1783-1784 Laki Eruption, South Iceland. *Journal of Petrology*. 48. (7), pp. 1265–1294. doi:10.1093/petrology/egm017
- Grattan, J. P. and Brayshay, M. (1995) An amazing and portentous summer: Environmental and social responses in Britain to the 1783 eruption of an Iceland volcano. *The Geographic Journal*. 161. pp. 125-134
- Grattan, J. P. (1998). The distal impact of volcanic gases and aerosols in Europe: a review of the 1783 Laki fissure eruption and environmental vulnerability in the late 20th century. In: Maund, J.G. and Eddleston, M. (eds) *Geohazards in engineering Geology*. pp. 7-53. *Geological Society*.
- Grattan, J. P., Rabartin, R., Self, S. and Thordarson, T. (2005). Volcanic air pollution and mortality in France 1783-84. *C. R. Geoscience*. 337. pp. 641-651
- Grattan, J. P. and Pyatt, F. B. (1994). Acid damage to vegetation following the Laki Fissure eruption in 1783 - an historical review. *Science of The Total Environment*. 151. (3), pp. 241-247. doi: 10.1016/0048-9697(94)90473-1
- Grattan, J.P. and Charman, D.J., (1994). Non-climatic factors and the environmental impact of volcanic volatiles: implications of the Laki Fissure eruption of AD 1783. *The Holocene*. 4. pp. 101-106
- Grattan, J. P. (1998). The distal impact of volcanic gases and aerosols in Europe: a review of the 1783 Laki fissure eruption and environmental vulnerability in the late 20th century. In: Maund, J.G. and Eddleston, M. (Editors). *Geohazards in engineering Geology*. pp. 7-53. *Geological Society*.
- Grattan, J. P. and Pyatt, F. B. (1999). Volcanic eruptions dry fogs and the European palaeoenvironmental record: localised phenomena or hemispheric impacts? *Global and Planetary Change*. 21. pp. 173-179
- Grattan, J. P. and Sadler, J. P. (1999). Regional warming of the lower atmosphere in the wake of volcanic eruptions: the role of the Laki fissure eruption in the hot summer of 1783. *Geological Society London Special Publications*. 161. (1), pp. 161-171. doi: 10.1144/GSL.SP.1999.161.01.11

- Grattan, J. P., Gilbertson, D. D. and Charman, D. J. (1999). Modelling the impact of Icelandic eruptions upon the prehistoric societies and environments of northern and western Britain. *Geological Society London Special Publications*. 161. (1), pp. 109-124. doi: 10.1144/GSL.SP.1999.161.01.08
- Halldórsson, S. A., Bali, E., Hartley, M. E., Neave, D. A., Peate, D. W., Guðfinnsson, G. H., Bindeman, I., Whitehouse, M. J., Riishuus, M. S., Pedersen, G. B. M., Jakobsson, S., Askew, R., Gallagher, C. R., Guðmundsdóttir, E. R., Gudnason, J., Moreland, W. M., Óskarsson, B. V., Nikkola, P., Reynolds, H. I., Schmidt, J. and Thordarson, T. (2018). Petrology and geochemistry of the 2014–2015 Holuhraun eruption, central Iceland: compositional and mineralogical characteristics, temporal variability and magma storage. *Contributions to Mineralogy and Petrology*. 173 (8). doi:10.1007/s00410-018-1487-9
- Halter, W. E., Heinrich, C. A., and Pettke, T. (2005). Magma evolution and the formation of porphyry Cu-Au ore fluids: Evidence from silicate and sulfide melt inclusions. *Mineralium Deposita*. 39. (8), pp. 845–863. doi:10.1007/s00126-004-0457-5
- Harris, A. J. L., Rowland, S. K., Villeneuve, N. and Thordarson, T. (2017). Pāhoehoe, ‘a‘ā, and block lava: an illustrated history of the nomenclature. *Bulletin of Volcanology*. 79. 7
- Hartley, M. E., Shorttle, O., MacLennan, J., Moussallam, Y., and Edmonds, M. (2017). Olivine-hosted melt inclusions as an archive of redox heterogeneity in magmatic systems. *Earth and Planetary Science Letters*. 479. pp. 192–205. doi:10.1016/j.epsl.2017.09.029
- Helz, R. T., Cottrell, E., Brounce, M. N., and Kelley, K. A. (2017). Olivine-melt relationships and syneruptive redox variations in the 1959 eruption of Kīlauea Volcano as revealed by XANES. *Journal of Volcanology and Geothermal Research*. 333–334. pp. 1–14. doi:10.1016/j.jvolgeores.2016.12.006
- Herzog, G. F., Moynier, F., Albarède, F., and Berezhnoy, A. A. (2009). Isotopic and elemental abundances of copper and zinc in lunar samples, Zagami, Pele’s hairs, and a terrestrial basalt. *Geochimica et Cosmochimica Acta*. 73. (19), pp. 5884–5904. doi:10.1016/j.gca.2009.05.067
- Hewitt, C. N. (2001). The atmospheric chemistry of sulphur and nitrogen in power station plumes. *Atmospheric Environment*. 35. (7), pp. 1155-1170. doi:10.1016/S1352-2310(00)00463-5
- Highwood, E.-J. and Stevenson, D.S. (2003). Atmospheric impact of the 1783–1784 Laki Eruption: Part II Climatic effect of sulphate aerosol. *Atmospheric Chemistry and Physics*. 3. pp. 1177–1189. doi:10.5194/acp-3-1177-2003
- Hofmann, C., Courtillot, V., Féraud, G., Rochette, P., Yirgu, G., Ketefo, E., and Pik, R. (1997). Timing of the ethiopian flood basalt event and implications for plume birth and global change. *Nature*. 389. (6653), pp. 838–841. doi:10.1038/39853
- Humayun, M. and Cassen, P. (2000) Processes determining the volatile abundances of the meteorites and terrestrial planets, In: R. M. Canup and K. Righter (eds.) *Origin of the Earth and Moon*, University of Arizona Press, Tucson, pp. 3-23.
- IES eruption team field reports. Háskóli Íslands, Institute of Earth Sciences and The Icelandic Metrological Office (Veðurstofa Íslands). Accessed (17/03/2021) from: <https://en.vedur.is/earthquakes-and-volcanism/articles/nr/3071>
- IMO Holuhraun eruption reports. The Icelandic Metrological Office (Veðurstofa Íslands). Accessed (17/03/2021) from: <https://en.vedur.is/earthquakes-and->

- Ilyinskaya, E., Schmidt, A., Mather, T. A., Pope, F. D., Witham, C., Baxter, P., Jóhannsson, T., Pfeffer, M., Barsotti, S., Singh, A., Sanderson, P., Bergsson, B., McCormick Kilbride, B., Donovan, A., Peters, N., Oppenheimer, C., and Edmonds, M. (2017). Understanding the environmental impacts of large fissure eruptions: Aerosol and gas emissions from the 2014–2015 Holuhraun eruption (Iceland). *Earth and Planetary Science Letters*. 472. pp. 309–322. doi:10.1016/j.epsl.2017.05.025
- Inglis, E. C., Debret, B., Burton, K. W., Millet, M., Pons, M., Dale, C. W., Bouilhol, P., Cooper, M., Nowell, G. M., McCoy-west, A. J., and Williams, H. M. (2017). The behavior of iron and zinc stable isotopes accompanying the subduction of mafic oceanic crust: A case study from Western Alpine ophiolites. *Geochemistry, Geophysics, Geosystems*. 18. (7), pp. 2562–2579. doi:10.1002/2016GC006735.
- Hoshyaripour, G. and Langmann, M. H. B. (2012). How does the hot core of a volcanic plume control the sulfur speciation in volcanic emission? *Geochemistry, Geophysics, Geosystems*. 13. (7), doi:10.1029/2011GC004020.
- Keszthelyi, L. and Self, S. (1998). Some physical requirements for the emplacement of long basaltic lava flows. *Journal of Geophysical Research: Solid Earth*. 103. (B11), p. 27447-27464. doi:10.1029/98JB00606
- Keszthelyi, L., Thordarson, T., McEwen, A., Haack, H., Guilbaud, M., Self, S. and Rossi, M. J. (2004). Icelandic analogs to Martian flood lavas. *Geochemistry Geophysics Geosystems*. 5. (Q11), 014. doi:10.1029/2004GC000758.
- John, S. G., Rouxel, O. J., Craddock, P. R., Engwall, A. M., and Boyle, E. A. (2008). Zinc stable isotopes in seafloor hydrothermal vent fluids and chimneys. *Earth and Planetary Science Letters*. 269. (1–2), pp. 17–28. doi:10.1016/j.epsl.2007.12.011
- Larsen, G. (2000) Holocene eruptions within the Katla volcanic system, south Iceland: characteristics and environmental impact. *Jökull*. 49. pp. 1–28.
- Li, W., Jackson, S. E., Pearson, N. J., Alard, O., and Chappell, B. W. (2009). The Cu isotopic signature of granites from the Lachlan Fold Belt, SE Australia. *Chemical Geology*. 258. (1–2), pp. 38–49. doi:10.1016/j.chemgeo.2008.06.047
- Liu, S. A., Huang, J., Liu, J., Wörner, G., Yang, W., Tang, Y. J., Chen, Y., Tang, L., Zheng, J., and Li, S. (2015). Copper isotopic composition of the silicate Earth. *Earth and Planetary Science Letters*. 427. pp. 95–103. doi:10.1016/j.epsl.2015.06.061
- Liu, S. A., Wang, Z. Z., Li, S. G., Huang, J., and Yang, W. (2016). Zinc isotope evidence for a large-scale carbonated mantle beneath eastern China. *Earth and Planetary Science Letters*. 444. pp. 169–178. doi:10.1016/j.epsl.2016.03.051
- Longpré, M. A., Stix, J., Klügel, A., and Shimizu, N. (2017). Mantle to surface degassing of carbon- and sulphur-rich alkaline magma at El Hierro, Canary Islands. *Earth and Planetary Science Letters*. 460. pp. 268–280. doi:10.1016/j.epsl.2016.11.043
- Loughlin, S. C., Aspinall, W. P., C, V.-B., Baxter, P. J., Braban, C., M, H., Schmidt, A., Thordarson, T., and Witham, C. S. (2012). Large-Magnitude Fissure Eruptions in Iceland: Source Characterisation. *British Geological Survey OpenFile Report*, pp. 1–136. <http://www.bgs.ac.uk/research/volcanoes/LakiEruptionScenarioPlanning.html%0Apapers3://publication/uuid/E5A6AE4C-D7D6-4563-AD7C-4B53F7033815>
- Luck, J. M., Othman, D. Ben, and Albarède, F. (2005). Zn and Cu isotopic variations

- in chondrites and iron meteorites: Early solar nebula reservoirs and parent-body processes. *Geochimica et Cosmochimica Acta*. 69. (22), pp. 5351–5363. doi:10.1016/j.gca.2005.06.018
- Macdonald, G. A. (1967). Forms and structures of extrusive basaltic rocks. In: Hess HH, Poldervaart A (editors) *The Poldervaart Treatise on rocks of basaltic composition*. Interscience, New York, pp. 1–61
- Mahan, B., Siebert, J., Pringle, E. A., and Moynier, F. (2017). Elemental partitioning and isotopic fractionation of Zn between metal and silicate and geochemical estimation of the S content of the Earth's core. *Geochimica et Cosmochimica Acta*. 196. pp. 252–270. doi:10.1016/j.gca.2016.09.013
- Maréchal C.N., Telouk P. and Albarède F. (1999) Precise analysis of copper and zinc isotopic compositions by plasma-source mass spectrometry. *Chemical Geology*. 156. pp. 251-273.
- Mather, T.A., Witt, M.L.I., Pyle, D.M., Quaylea, B.M., Aiuppa, A., Bagnato, E., Martin, R.S., Sims, K.W.W., Edmonds, M., Sutton, A. J. and Ilyinskaya, E. (2012). Halogens and trace metal emissions from the ongoing 2008 summit eruption of Kīlauea volcano, Hawai'i. *Geochimica et Cosmochimica Acta*. 83. pp. 292–323.
- Markl, G., Lahaye, Y., and Schwinn, G. (2006). Copper isotopes as monitors of redox processes in hydrothermal mineralization. *Geochimica et Cosmochimica Acta*. 70. (16), pp. 4215–4228. doi:10.1016/j.gca.2006.06.1369
- Mason, T. F. D., Weiss, D. J., Horstwood, M., Parrish, R. R., Russel, S. S., Mullane, E. and Coles, B. J. (2004). High-precision Cu and Zn isotope analysis by plasma source mass spectrometry; Part 2. Correcting for mass discrimination effects. *Journal of Analytical Atomic Spectrometry*. 19. (2), pp. 218-226
- McCoy-West, A. J., Fitton, J. G., Pons, M. L., Inglis, E. C., and Williams, H. M. (2018). The Fe and Zn isotope composition of deep mantle source regions: Insights from Baffin Island picrites. *Geochimica et Cosmochimica Acta*. 238. pp. 542–562. doi:10.1016/j.gca.2018.07.021
- Mcgee, K. A., Doukas, M. P., and Gerlach, T. M. (2001). Quiescent hydrogen sulfide and carbon dioxide degassing from Mount Baker, Washington. *Geophysical Research Letters*. 28. (23), pp. 4479–4482.
- Métrich, N., Berry, A. J., O'Neill, H. S. C., and Susini, J. (2009). The oxidation state of sulfur in synthetic and natural glasses determined by X-ray absorption spectroscopy. *Geochimica et Cosmochimica Acta*. 73. (8), pp. 2382–2399. doi:10.1016/j.gca.2009.01.025
- Métrich, N., and Mandeville, C. W. (2010). Sulfur in Magmas. *Elements*. 6. (2), pp. 81–86. doi:10.2113/gselements.6.2.81
- Moeller, K., Schoenberg, R., Pedersen, R. B., Weiss, D., and Dong, S. (2012). Calibration of the New Certified Reference Materials ERM-AE633 and ERM-AE647 for Copper and IRMM-3702 for Zinc Isotope Amount Ratio Determinations. *Geostandards and Geoanalytical Research*. 36. (2), pp. 177–199. doi:10.1111/j.1751-908X.2011.00153.x
- Möller, D. (1980). Kinetic model of atmospheric SO₂ oxidation based on published data. *Atmospheric Environment*. 14. (9), pp. 1067-1076. doi: 10.1016/0004-6981(80)90037-2
- Moreland W. M, Thordarson T, Houghton B. F. and Larsen G, (2019). Driving mechanisms of subaerial and subglacial explosive episodes during the 10th century Eldgjá fissure eruption, southern Iceland. *Volcanica*.
- Moretti, R., and Baker, D. R. (2008). Modeling the interplay of fO₂ and fS₂ along the

- FeS-silicate melt equilibrium. *Chemical Geology*. 256. (3–4), pp. 286–298. doi:10.1016/j.chemgeo.2008.06.055
- Moussallam, Y., Oppenheimer, C., Scaillet, B., Gaillard, F., Kyle, P., Peters, N., Hartley, M., Berlo, K., and Donovan, A. (2014). Tracking the changing oxidation state of Erebus magmas, from mantle to surface, driven by magma ascent and degassing. *Earth and Planetary Science Letters*. 393. pp. 200–209. doi:10.1016/j.epsl.2014.02.055
- Moussallam, Y., Edmonds, M., Scaillet, B., Peters, N., Gennaro, E., Sides, I., and Oppenheimer, C. (2016). The impact of degassing on the oxidation state of basaltic magmas: A case study of Kīlauea volcano. *Earth and Planetary Science Letters*. 450. pp. 317–325. doi:10.1016/j.epsl.2016.06.031
- Moussallam, Y., Longpré, M. A., McCammon, C., Gomez-Ulla, A., Rose-Koga, E. F., Scaillet, B., Peters, N., Gennaro, E., Paris, R., and Oppenheimer, C. (2019). Mantle plumes are oxidised. *Earth and Planetary Science Letters*. 527. 115798. doi:10.1016/j.epsl.2019.115798
- Moynier, F., Albarède, F., and Herzog, G. F. (2006). Isotopic composition of zinc, copper, and iron in lunar samples. *Geochimica et Cosmochimica Acta*. 70. (24), pp. 6103–6117. doi:10.1016/j.gca.2006.02.030
- Moynier, F., Abe, M. and Telouk, P. (2010). Experimental and theoretical investigation of isotope fractionation of Zn. *The Journal of Physical Chemistry A*.
- Moynier, F., Vance, D., Fujii, T. and Savage, P. S. (2017). The Isotope Geochemistry of Zinc and Copper. In: Non-traditional stable isotopes. *Reviews in Mineralogy and Geochemistry*. 82. (1), pp 543–600. Teng, F-Z., Watkins, J. M. and Dauphas, N. (Editors).
- Mungall, J. E., Brenan, J. M., Godel, B., Barnes, S. J., and Gaillard, F. (2015). Transport of metals and sulphur in magmas by flotation of sulphide melt on vapour bubbles. *Nature Geoscience*. 8. (3), pp. 216–219. doi:10.1038/ngeo2373
- Neave, D. A., Passmore, E., MacLennan, J., Fitton, G., and Thordarson, T. (2013). Crystal-melt relationships and the record of deep mixing and crystallization in the ad 1783 laki eruption, Iceland. *Journal of Petrology*. 54. (8), pp. 1661–1690. doi:10.1093/petrology/egt027
- Neave, D. A., Buisman, I., and MacLennan, J. (2017). Continuous mush disaggregation during the long-lasting Laki fissure eruption, Iceland. *American Mineralogist*. 102. (10), pp. 2007–2021. doi:10.2138/am-2017-6015CCBY
- Óskarsson, N., Helgason, Ö., and Steinthórsson, S. (1994). Oxidation state of iron in mantle-derived magmas of the Icelandic rift zone. *Hyperfine Interactions*. 91. (1), pp. 733–737. doi:10.1007/BF02064599
- Oman, L., Robock, A., Stenchikov, G.L. et al. (2006a). Modeling the distribution of the volcanic aerosol cloud from the 1783–1784 Laki eruption. *Journal of Geophysical Research*. 111. D12209.
- Oman, L., Robock, A., Stenchikov, G.L. and Thordarson, T. (2006b). High-latitude eruptions cast shadow over the African monsoon and the flow of the Nile. *Geophysical Research Letters*. 33. L18711.
- Pálsson, S. 1794. Ferðabók Sveins Pálssonar, Dagbækur og Ritgerðir 1791–1797. (The Travelogue of Sveinn Pálsson. Notebooks and essays through 1791–1797). 2nd edition, Örn og Örlygur, Reykjavík 1983, 813 pp. (First published by Snælandsútgáfan in 1945.)
- Pálsson, S. 1784. Historia ignis in oriente Islandiæ erump- entis Anno 1783, qvoad innotuit in tractu Skagafjörd- ensi, complectitur in se et effectus varios (The

- story of the earth fire which broke out in Eastern Iceland in the year 1783, as long as it was observed in Skaga- fjörður; concerning the progress of the eruption and its various effects). In T. Einarsson, G. M. Gudbergsson, G. Á. Gunnlaugsson, S. Rafnsson and S. Thorarinnsson (eds.), *Skaftáreldar 1783–1784, Ritgerðir og Heim- ildir, Mál og Menning*, Reykjavík 1984, 419–422.
- Pálsson, S. (1793 and 1794). Eldritið, viðbætir við lýsingar á Skaftáreldum 1783.? Book of Fire, additions to the descriptions of the Skaftár Fires (Laki eruption) 1783.
- Passmore, E. (2009). Unpublished PhD thesis. Feeding large eruptions: crystallisation, mixing and degassing in Icelandic magma chambers. The University of Edinburgh. pp. 1–379.
- Passmore, E., Maclennan, J., Fitton, G., and Thordarson, T. (2012). Mush disaggregation in basaltic magma chambers: Evidence from the ad 1783 Laki eruption. *Journal of Petrology*. 53. (12), pp. 2593–2623. doi:10.1093/petrology/egs061
- Pedersen, G. B. M., Höskuldsson, A., Dürig, T., Thordarson, T., Jónsdóttir, I., Riishuus, M. S., Óskarsson, B. V., Dumont, S., Magnusson, E., Gudmundsson, M. T., Sigmundsson, F., Drouin, V. J. P. B., Gallagher, C., Askew, R., Gudnason, J., Moreland, W. M., Nikkola, P., Reynolds, H. I., and Schmith, J. (2017). Lava field evolution and emplacement dynamics of the 2014–2015 basaltic fissure eruption at Holuhraun, Iceland. *Journal of Volcanology and Geothermal Research*. 340. pp. 155–169. doi:10.1016/j.jvolgeores.2017.02.027
- Pfeffer, M. A., Stefánsdóttir, G., Bergsson, B., Barsotti, S., Galle, B., Ilyinskaya, E., Spina, A. La, Sigurðardóttir, G. M., and Jónasdóttir, E. B. (2015). Ground-based measurements of the emission rate and composition of gases from the Holuhraun eruption. *2015 EGU Abstract*. 17. 7373.
- Pfeffer MA, Bergsson B, Barsotti S, Stefánsdóttir G, Galle B, Arellano S, Conde V, Donovan A, Ilyinskaya E, Burton M, Aiuppa A, Whitty RCW, Simmons IC, Arason Þ, Jónasdóttir EB, Keller NS, Yeo RF, Arngrímsson H, Jóhannsson Þ, Butwin MK, Askew RA, Dumont S, Von Löwis S, Ingvarsson Þ, La Spina A, Thomas H, Prata F, Grassa F, Giudice G, Stefánsson A, Marzano F, Montopoli M, Mereu L. (2018). Ground-Based Measurements of the 2014–2015 Holuhraun Volcanic Cloud (Iceland). *Geosciences*. 8. (1), 29. doi:10.3390/geosciences8010029
- Robock, A. (2000). Volcanic eruptions and climate. *Reviews of Geophysics*. 38. (2), pp. 191-219. doi:10.1029/1998RG000054
- Robock, A. and Oppenheimer, C. (2003). Volcanism and Earth's Atmosphere. Geophysical monograph. *American Geophysical Union*. 139. 368 p
- Rampino, M. R., and Stothers, R. B. (1988). Flood basalt volcanism during the past 250 million years. *Science*. 241. (4866), pp. 663–668. doi:10.1126/science.241.4866.663
- Sable, J. E., Houghton, B. F., Wilson, C. J. N., and Carey, R. J. (2009). Eruption mechanisms during the climax of the Tarawera 1886 basaltic Plinian eruption inferred from microtextural characteristics-of the deposits. *Special Publications of IAVCEI*. 2. pp. 129–154. doi:10.1144/iavcel002.7
- Savage, P. S., Georg, R. B., Williams, H. M., Burton, K. W. and Halliday, A. N. (2011). Silicon isotope fractionation during magmatic differentiation. *Geochimica et Cosmochimica Acta*. 75. (20), pp. 6124-6139
- Savage, P., Moynier, F., Chen, H., Shofner, G., Siebert, J., Badro, J., and Puchtel, I. S., (2015). Copper isotope evidence for large-scale sulphide fractionation

- during Earth's differentiation. *Geochemical Perspective Letters*. 1. pp. 53–64.
- Sayyed, M. R. G. (2014). Flood basalt hosted palaeosols: Potential palaeoclimatic indicators of global climate change. *Geoscience Frontiers*. 5. (6), pp. 791–799. doi:10.1016/j.gsf.2013.08.005
- Scaillet, B., and Pichavant, M. (2005). A model of sulphur solubility for hydrous mafic melts: Application to the determination of magmatic fluid compositions of Italian volcanoes. *Annals of Geophysics*. 48. (4–5), pp. 671–698. doi:10.4401/ag-3226
- Schmidt, A., Carslaw, K. S., Mann, G. W., Wilson, M., Breider, T. J., Pickering, S. J., and Thordarson, T. (2010). The impact of the 1783–1784 AD Laki eruption on global aerosol formation processes and cloud condensation nuclei. *Atmospheric Chemistry and Physics*. 10. (13), pp. 6025–6041. doi:10.5194/acp-10-6025-2010
- Schmidt, A, Ostro, B., Carslaw, K. S., Wilson, M., Thordarson, T., Mann, G. W., and Simmons, A. J. (2011). Excess mortality in Europe following a future Laki-style icelandic eruption. *Proceedings of the National Academy of Sciences of the United States of America*. 108. (38), pp. 15710–15715. doi:10.1073/pnas.1108569108
- Schmidt, A, Thordarson, T., Oman, L. D., Robock, A., and Self, S. (2012). Climatic impact of the long-lasting 1783 Laki eruption: Inapplicability of mass-independent sulfur isotopic composition measurements. *Journal of Geophysical Research Atmospheres*. 117. (23), pp. 1–10. doi:10.1029/2012JD018414
- Schmidt, A, and Robock, A. (2015). Volcanism, the atmosphere and climate through time. In: *Volcanism and Global Environmental Change*. pp. 195–207. doi:10.1007/9781107415683.014
- Schmidt, A., Leadbetter, S. and Theys, N., Carboni, E., Witham, C. S., Stevenson, J. A., Birch, C. E., Thordarson, T., Turnock, S., Barsotti, S., Delaney, L., Feng, W., Grainger, R. G., Hort, M. C., Höskuldsson, Á., Ialongo, I., Ilyinskaya, E., Jóhannsson, T., Kenny, P., Mather, T. A., Richards, N. A. D. and Shepherd, J. (2015). Satellite detection, long-range transport, and air quality impacts of volcanic sulfur dioxide from the 2014–2015 flood lava eruption at Bárðarbunga (Iceland). *Journal of Geophysical Research: Atmospheres*. 120. (18), pp. 9739–9757. doi:10.1002/2015JD023638
- Schmidt, A. (2015). Chapter 15 ‘Volcanic Gas and Aerosol Hazards from a Future Laki-Type Eruption in Iceland’. In: *Volcanic Hazards, Risks and Disasters*. Editor (s): John F. Shroder, Paolo Papale. doi:10.1016/B978-0-12-396453-3.00015-0.
- Self, S., Thordarson, T., Keszthelyi, L., Walker, G. P. L., Hon, K., Murphy, M. T., Long, P., and Finnemore, S. (1996). A new model for the emplacement of Columbia River basalts as large, inflated pahoehoe lava flow fields. *Geophysical Research Letters*. 23. (19), pp. 2698–2692.
- Self, S. (1992). Krakatau revisited: the course of events and interpretation of the 1883 eruption. *Geoscience Journal*. 28. (2), pp. 109–121.
- Self, S., Keszthelyi, L. P. and Thordarson, T. (2000). Discussion of: “Pulsed inflation of pahoehoe lava flows: implications for flood basalt emplacement”, by S.W. Anderson, E.R. Stofan, E.R. Smrekar, J.E. Guest and B. Wood. *Earth and Planetary Science Letters*. 168. pp. 7–18.
- Self, S., Thordarson, T., and Widdowson, M. (2005). Gas Fluxes from Flood Basalt Eruptions. *Elements*. 1. (5), pp. 283–287. doi:10.2113/gselements.1.5.283
- Self, Stephen, Widdowson, M., Thordarson, T., and Jay, A. E. (2006). Volatile

- fluxes during flood basalt eruptions and potential effects on the global environment: A Deccan perspective. *Earth and Planetary Science Letters*. 248. (1–2), pp. 518–532. doi:10.1016/j.epsl.2006.05.041
- Self, Stephen, Blake, S., Sharma, K., Widdowson, M., and Sephton, S. (2008). Sulfur and Chlorine in Late Cretaceous. *Science*. 319. pp. 1654–1657.
- Shields, J. K., Mader, H. M., Pistone, M., Caricchi, L., Floess, D., and Putlitz, B. (2014). Journal of Geophysical Research: Solid Earth Strain-induced outgassing of three-phase magmas during simple shear. 1, pp. 6936–6957. doi:10.1002/2014JB011111.
- Shorttle, O., Moussallam, Y., Hartley, M. E., Maclennan, J., Edmonds, M., and Murton, B. J. (2015). Fe-XANES analyses of Reykjanes Ridge basalts: Implications for oceanic crust's role in the solid Earth oxygen cycle. *Earth and Planetary Science Letters*. 427. pp. 272–285. doi:10.1016/j.epsl.2015.07.017
- Sigmarrsson, O., Condomines, M., Grönvold, K., and Thordarson, T. (1991). Extreme Magma homogeneity in the 1783-84 Lakagigar eruption: origin of a large volume of evolved basalt in Iceland. *Geophysical Research Letters*. 18. (12), pp. 2229–2232.
- Sigurdsson, H. (1982). Volcanic pollution and climate. *EOS Transactions of the American Geophysical Union*. 63. pp. 601–602.
- Sigurdsson, H. (1990). Assessment of the atmospheric impact of volcanic eruptions. *Geological Society of America, Special paper*. 247. pp. 99–110. In: Global Catastrophes in Earth History; An Interdisciplinary Conference on Impacts, Volcanism, and Mass Mortality. (Editors) Sharpton, V. L. and Ward, P. D.
- Sigurdsson, H. (1982). Volcanic pollution and climate: the 1783 Laki eruption. *EOS*. 63. pp. 601-602
- Sossi, P. A., Halverson, G. P., Nebel, O., and Eggins, S. M. (2015). Combined separation of Cu, Fe and Zn from rock matrices and improved analytical protocols for stable isotope determination. *Geostandards and Geoanalytical Research*. 39. (2), pp. 129–149. doi:10.1111/j.1751-908X.2014.00298.x
- Sossi, P. A., Nebel, O., O'Neill, H. S. C., and Moynier, F. (2018). Zinc isotope composition of the Earth and its behaviour during planetary accretion. *Chemical Geology*. 477. pp. 73–84. doi:10.1016/j.chemgeo.2017.12.006
- Stephensen, O. 1783. Abstract from prefect Stephensen letter to Erichsen, the deputy of the treasury, dated 15 August 1783. In T. Einarsson, G. M. Gudbergs- son, G. Á. Gunnlaugsson, S. Rafnsson and S. Thorarinsson (editoras.), *Skaftáreldar 1783–1784, Ritgerðir og Heimildir, Mál og Menning, Reykjavík* 1984, 279.
- Stephensen, M. 1785. Kort beskrivelse over den nye vul- cans Ildsprudelse i Vester- Skaptefields-Syssel paa Is- land i Aaret 1783. (A short description of the new Vol- canic eruption in Western Skaftafellshire in the year 1783). Nicolaus Möller, Copenhagen, 148 pp.
- Stephensen, M. 1786. Betænking over Indholdet af Chirurgi Jon Petersens Afhandling om Ildrögens kien- deligste Virkninger af Ildsprudningen 1783 saavidt Norder-Island angaaer (Comments on the contents of Dr. Jón Pétursson's essay on the effects of the volcanic haze from volcanic eruption in 1783 in North Iceland). *Islands Journal* 7, Þjóðskjalasafn Rtk. 42.2, fylgiskjöl nr. 104
- Steingrímsson J (1783a) A short compendium of the recent volcanic outburst in western part of Skaftafell county, dated at Prestbakki July 4, 1783. In: Einarsson, T., Guðbergsson, G.M., Gunnlaugsson, G.A., Rafnsson S. and Þórarinnsson, S. (editors.) *Skaftáreldar 1783-1784: Ritgerðir og Heimildir*. pp.

- 272-274. Mál og Menning: Reykjavík 1984.
- Steingrímsson, J. (1783b). Abstract from a letter to Reverend Bjarni Jónsson, dated August 31 1783 at Prestbakki. In: Safn til Sögu Íslands. IV. pp. 69-70: Copenhagen.
- Steingrímsson, J. and Ólafsson, S. (1783). A simple, but true narrative of the eruption in Skaftafell county in the year 1783, dated November 24 1788 at Kirkjubæjarklauster. In: Safn til Sögn Íslands. IV. pp. 58-69: Copenhagen (in Icelandic).
- Steingrímsson, J. (1788) A complete description on the Síða volcanic fire, dated November 24 1788 at Prestbakki. (In Icelandic) In: Safn til Sögu Íslands. IV. pp. 1-57: Copenhagen.
- Steingrímsson, Rev. J. (1907) Fullkomið rit um Síðueld (original manuscript transcribed). The National Archive of Iceland. In: Thórgunnar Skúladóttir (Editor) 'Fires of the Earth, The Laki Eruption 1783-1784. (1998). The University of Iceland Press and the Nordic Volcanology Institute.
- Stevenson, D.S., Johnson, C. E., Highwood, E.-J., Gauci, V., Collins, W. J., and Derwent, R. G. (2003). Atmospheric impact of the 1783–1784 Laki Eruption: Part I Chemistry modelling. *Atmospheric Chemistry and Physics*. 3. pp. 487–507, doi:10.5194/acp-3-487-2003
- Stothers, R. B., and Rampino, M. R. (1990). Periodicity in flood basalts, mass extinctions, and impacts; A statistical view and a model. In: *Global Catastrophes in Earth History; An Interdisciplinary Conference on Impacts, Volcanism, and Mass Mortality*, Virgil L. Sharpton, Peter D. Ward (Editors). *Geoscience World*.
- Sumner, J. M. (1998). Formation of clastogenic lava flows during fissure eruption and scoria cone collapse: The 1986 eruption of Izu-Oshima Volcano, eastern Japan. *Bulletin of Volcanology*. 60. (3), pp. 195–212. doi:10.1007/s004450050227
- Swanson, D. A. (1973). Pahoehoe Flows from the 1969–1971 Mauna Ulu Eruption, Kilauea Volcano, Hawaii. *GSA Bulletin*. 84. (2), pp. 615–626. doi: [https://doi.org/10.1130/0016-7606\(1973\)84<615:PFFTMU>2.0.CO;2](https://doi.org/10.1130/0016-7606(1973)84<615:PFFTMU>2.0.CO;2)
- Takei H. PhD thesis., 2002, Okayama University. Development of precise analytical techniques for major and trace element concentrations in rock samples and their applications to the Hishikari Gold Mine, southern Kyushu, Japan
- Telus, M., Dauphas, N., Moynier, F., Tissot, F. L. H., Teng, F. Z., Nabelek, P. I., Craddock, P. R., and Groat, L. A. (2012). Iron, zinc, magnesium and uranium isotopic fractionation during continental crust differentiation: The tale from migmatites, granitoids, and pegmatites. *Geochimica et Cosmochimica Acta*. 97. pp. 247–265. doi:10.1016/j.gca.2012.08.024
- Thordarson, T. (1990). Unpublished masters thesis. The eruption sequence and the eruption behaviour of the Skaftár Fires, 1783-85, Iceland: characteristics and distribution of eruption products. University of Texas at Arlington.
- Thordarson, T. (2020). Sulfur output by the 2014–15 flood lava eruption at Holuhraun, N-Iceland. *Goldschmidt 2020 abstract*. doi:10.46427/gold2020.2594
- Thorarinsson, Á. 1783. Hr. Provst Torarensens Beretning (Reverend Thorarensens Documentation). In T. Ein- arsson, G. M. Gudbergsson, G. Á. Gunnlaugsson, S. Rafnsson and S. Thorarinsson (eds.), *Skaftáreldar 1783–1784, Ritgerðir og Heimildir*, Mál og Menning, Reykjavík 1984, 280–283.
- Thorarinsson, S. (1967). *Skaftáreldar og Lakagíggar: Myndir úr jarðfræði Íslands VIII*

- (The Skaftár Fires and Laki cone-row: Illustrations from the geology of Iceland VIII). *Náttúrufræðingurinn*. 37. pp. 1–57.
- Thorarinsson, S. (1969). The Lakagígar eruption of 1783. *Bulletin of Volcanology*. 3. pp. 910–929.
- Thorarinsson, S., (1984). Annáll Skaftárelda (The annals of the Skaftá Fires). In T. Einarsson, G. M. Gudbergs- son, G. Á. Gunnlaugsson, S. Rafnsson and S. Thorarinsson (editors.), *Skaftáreldar 1783–1784, Ritgerðir og Heimildir, Mál og Menning*, Reykjavík 1984, 11–36
- Thordarson, T. and Self, S. (1993) The Laki (Skaftár-Fires) And Grímsvötn Eruptions In 1783-1785. *Bulletin Of Volcanology*. 55. pp. 233-263.
- Thordarson, T, and Self, S. (2001). Real-time observations of the Laki sulfuric aerosol cloud in Europe during 1783 as documented by Professor S. P. van Swinden at Franeker, Holland. *Jökull*. 50. pp. 65–72.
- Thordarson, T. and Self, S. (2003). Atmospheric and environmental effects of the 1783-1784 Laki eruption: A review and reassessment. *Journal Of Geophysical Research-Atmospheres*. 108. 4011
- Thordarson, Th., Self, S., Óskarsson, N., and Hulsebosch, T. (1996). Sulfur, chlorine, and fluorine degassing and atmospheric loading by the 1783-1784 AD Laki (Skaftár Fires) eruption in Iceland. *Bulletin of Volcanology*. 58. (2–3), pp. 205–225. doi:10.1007/s004450050136
- Thordarson, T., Miller, D. J., Larsen, G., Self, S. and Sigurdsson, H. (2001). New estimates of sulfur degassing and atmospheric mass-loading by the 934 AD Eldgja eruption, Iceland. *Journal of Volcanology and Geothermal Research*. 108. pp. 33-54
- Thordarson, T. (2003). The 1783-1785 A.D. Laki-Grímsvötn eruptions I: A critical look at the contemporary accounts. *Jökull*. 53. pp. 1-10
- Thordarson, T., Self, S., Miller, D. J., Larsen, G. and Vilmundardottir, E. G. (2003a) Sulphur release from flood lava eruptions of the Veiðivötn, Grímsvötn and Katla volcanic systems, Iceland. In: C Oppenheimer, DM Pyle and J Barclay (eds.) *Volcanic Degassing*. pp. 103-121. The Geological Society of London.
- Thordarson T, Larsen G and Steinthorsson S, Self S (2003b) The 1783-1785 A.D. Laki-Grímsvötn eruptions II: Appraisal based on contemporary accounts. *Jökull*. 53. pp. 11-48
- Thordarson, T. and Larsen, G. (2007). Volcanism in Iceland in historical time: Volcano types, eruption styles and eruptive history. *Journal of Geodynamics*. 43. (1), pp. 118–152. doi:10.1016/j.jog.2006.09.005
- Thordarson, T. and Höskuldsson, Á. (2008). Postglacial volcanism in Iceland. *Jökull*. 58. pp. 197–228.
- Thordarson, T., Rampino, M. R., Keszthelyi, L. P. and Self, S. (2009). Effects of megascale eruptions on Earth and Mars. In: Preservation of random megascale events on Mars and Earth: Influence on geologic history. *Special Paper of the Geological Society of America*. 453. pp. 37-53. doi: 10.1130/2009.453(04)
- Toutain, J. P., Sonke, J., Munoz, M., Nonell, A., Polvé, M., Viers, J., Freydier, R., Sortino, F., Joron, J. L., and Sumarti, S. (2008). Evidence for Zn isotopic fractionation at Merapi volcano. *Chemical Geology*. 253. (1–2), pp. 74–82. doi:10.1016/j.chemgeo.2008.04.007
- Wallace, P., and Carmichael, I. S. E. (1992). Sulfur in basaltic magmas. *Geochimica et Cosmochimica Acta*. 56. (5), pp. 1863–1874. doi:10.1016/0016-7037(92)90316-B
- Wallace, P. J., and Edmonds, M. (2011). The sulfur budget in magmas: Evidence

- from melt inclusions, submarine glasses, and volcanic gas emissions. *Reviews in Mineralogy and Geochemistry*. 73. pp. 215–246. doi:10.2138/rmg.2011.73.8
- Wang, Z. Z., Liu, S. A., Liu, J., Huang, J., Xiao, Y., Chu, Z. Y., Zhao, X. M., and Tang, L. (2017). Zinc isotope fractionation during mantle melting and constraints on the Zn isotope composition of Earth's upper mantle. *Geochimica et Cosmochimica Acta*. 198. pp. 151–167. doi:10.1016/j.gca.2016.11.014
- Wang, Z., Park, J. W., Wang, X., Zou, Z., Kim, J., Zhang, P., and Li, M. (2019). Evolution of copper isotopes in arc systems: Insights from lavas and molten sulfur in Niutahi volcano, Tonga rear arc. *Geochimica et Cosmochimica Acta*. 250. pp. 18–33. doi:10.1016/j.gca.2019.01.040
- Williams, H.M. and Archer, C. (2011) Copper stable isotopes as tracers of metal-sulphide segregation and fractional crystallisation processes on iron meteorite parent bodies. *Geochimica et Cosmochimica Acta*. 75. pp. 3166-3178.
- Webster, J. D., and Botcharnikov, R. E. (2011). Distribution of sulfur between melt and fluid in S-O-H-C-Cl-bearing magmatic systems at shallow crustal pressures and temperatures. *Reviews in Mineralogy and Geochemistry*. 73. pp. 247–283. doi:10.2138/rmg.2011.73.9
- Young, E. D., Galy, A. and Nagahara, H. (2002). Kinetic and equilibrium mass-dependent isotope fractionation laws in nature and their geochemical and cosmochemical significance. *Geochimica et Cosmochimica Acta*. 66. (6), pp. 1095–1104
- Wood, C. A. (1992) Climatic effects of the 1783 Laki eruption. In: Harington CR (ed) *The year without a summer?* Canadian Museum of Nature, Ottawa, p 58–7
- Wignall, P. B. (2001). Large igneous provinces and mass extinctions. *Earth Science Reviews*. 53. (1–2), pp. 1–33. [https://doi.org/10.1016/S0012-8252\(00\)00037-4](https://doi.org/10.1016/S0012-8252(00)00037-4)

Chapter 9: Synthesis and conclusions

9.1 Synthesis and conclusions

This project aimed to explore the mechanisms and timing of volatile loss from high magnitude basaltic fissure eruptions, by using a multidisciplinary approach to understand textural and isotopic variations in eruptive products for two historic Icelandic flood lava (FL) events as case studies: Holuhraun 2014–15 CE and Laki 1783–84 CE. Not only do these two eruptions occupy end-member eruptive styles of the spectrum of fountaining intensity from low-moderate Hawaiian fountaining to sub-Plinian intensity vent activity, they are also distinguishable by their order of magnitude difference in volume with activity predominantly feeding compound lava flow fields.

The questions addressed include: 1) the effect of eruptive environment on volatile loss, and the extent of influence of an overlying shallow sub-glacial tongue on eruptive products compared to a purely magmatic environment; the textural fingerprint of the evolution in mass eruption rate (MER) throughout the eruption and the preservation of equilibrium versus disequilibrium processes recorded in pyroclasts; 2) the speciation of S lost to the atmosphere throughout the eruption, and detectable changes in the efficiency of volatile loss as a function of the style of vent activity and eruptive environment as indicated by variations in Zn and Cu isotopic ratios; 3) the effect of single flow versus compound flow fields and changes in the insulation of the transport system on the variations in Zn and Cu isotopic ratios of lava samples as well as the impact of multiple vents feeding a single flow field on the Zn and Cu isotopic signature of eruptive products.

9.1.1 Eruptive environment

Chapter 5 This research is the first to identify exposed and fully preserved eruptive sequences from an historical shallow-subglacial–ice-confined basaltic fissure

eruption. Although this type of eruption is known to be common in Antarctica, their eruptive products are not preserved due to erosion or readvance of the local ice extent. The response of Earth's ice-bodies to climate change will result in more of these sequences being accessible due to exposure providing a window to understand these processes further from historical events rather than much older sequences where the eruptive activity type and duration, as well as environment or ice-thickness, is less well constrained. Using examples such as Laki 1783–84 CE to underpin changes in activity from a known and well characterised subaerial magmatic phase prior to propagation of activity under the ice also enables isolation of the purely ice or external water-magma related processes and interactions occurring throughout an eruptive event. Remote sensing resources like the Arctic DEM or similar high-resolution mapping can be used to target areas of interest in high altitude or high latitude regions for future research. Moreover, such eruptions can serve as analogues of similar volcanism occurring on Mars and further our understanding of the processes that occur on other planetary bodies. In the case of the Laki eruptive products, ice-confinement due to increased ice-thickness changes the aspect ratio of the deposit when tracing it from the SW to the NE; however, the level of interaction with external ice or water varies throughout the stratigraphy with clear evidence of fluctuating water levels. Geochemical and textural analysis of these eruptive products provides evidence of early quenching and thus suppression of volatile exsolution, with elevated sulfur (S) concentrations of up to 300 ppm, compared to the magmatic samples. Estimated ice-thicknesses based on eruptive sequences are shallow, approximately 100–150 m, which should not play a significant role in overburden pressure relating to volatile exsolution during eruption, but further analysis is required to completely rule this out. However, texturally immature and more mature magmatic foams coexist within the same pyroclastic samples, and whilst they have similar S values in these domains, texturally they are very different with mature textures indicating post-fragmentation expansion.

9. 1. 2 Textural maturity

Chapters 6 and 7 Explore temporal variations in the proportions of distinct textural domains identified in both the 1783–84 CE Laki and 2014–15 CE Holuhraun

pyroclasts. This textural heterogeneity is generated by the coeval presence of discrete melt packages of the same primary magma, that have experienced contrasting shallow conduit histories and differing ascent rates, which subsequently mingle prior to fragmentation. This textural fingerprint records the presence of discrete domains generated by equilibrium and disequilibrium processes, with the latter preserved as a low S content ultra-vesicular foam, formed by a burst nucleation event as the result of volatile supersaturation due to rapid ascent rates, occurring during episodic increases in MER during the eruptions. In the Laki pyroclasts, there is a broad correlation between the proportion of ultra-vesicular foam and the amount of lag time that exists between sudden waxing MER associated with sub-Plinian intensity opening. Whilst this texture has been noted in other basaltic fissure eruptions in Iceland and Hawaii, the reason for its generation has not been previously clarified nor its volatile content measured. The textural and geochemical presence of this texture in pyroclasts can be used to identify peak periods of eruptive intensity as well as pulsating fountaining behaviour in basaltic pyroclastic from less well documented or older eruptions, as well as identify peak explosive phases during higher magnitude, FB eruptions, to better characterise their explosive activity phases.

9.1.3 Post-fragmentation modification of primary textures

Chapters 6 and 7 Identified pervasive post-fragmentation expansion of the interior of the pyroclasts in both the 1783–84 CE Laki and 2014–15 CE Holuhraun eruptions, a phenomenon which has previously been noted in several textural studies of Hawaiian pyroclasts. A radial cooling gradient forms in the pyroclast as a result of the thermally insulating fountaining environment, from the rapidly outer quench rind to the interior. The outer rind consists of immature vesicle textures formed by a more rapidly quenched outer surface of the clast preserve the closest estimate to the melt prior to fragmentation. A more thermally insulated clast interior cools relatively slower and, as a result, the maturity of the vesicle population in the clasts increases in maturity in a semi-concentric arrangement when traced from the outer rind to the centre of the clast. Despite post-fragmentation modification of the primary vesicle texture, textural analysis indicates that the primary texture predominantly expands, enhancing primary textures, maintaining their diversity and distinct domains, rather

than over-printing these textures through other processes such as coalescence or further extensive nucleation.

Calculated vesicle number densities (N_v^m) for the rapidly quenched outer rinds of the 2014–15 CE Holuhraun pyroclasts are similar to other rind N_v^m values from similar intensity fountaining eruptions such as Kilauea Iki 1959 CE, with temporal variations in number density throughout the Holuhraun eruption corresponding to observed shifts in vent activity intensity. However, whilst the N_v^m values calculated for the 1783–84 CE Laki outer rinds indicate relative shifts towards decreasing number densities in intensity between the most explosive fountaining phases versus the waning stages of eruptive activity, the numbers are much lower than other analysed sub-Plinian events such as Eldgjá 939 CE. This suggests that the processes driving the sub-Plinian intensities of the Laki fissure opening phases are not reflected or captured in the eruptive pyroclasts, e.g. much larger bubbles or bubble clusters.

9.2 Chalcophile isotope variations in eruptive products

Chapter 8 This is the first research study to find statistically resolvable variations in chalcophile element isotopes, Zn and Cu, in response to volatile behaviour. Thus, these isotopes can potentially be used as a novel proxy for tracing the speciation of S loss during basaltic fissure eruptions, as well as to identify changes in degassing processes at the vent and associated lava field throughout a single eruption. This technique was applied successfully to two FL eruptions of differing fountaining intensities: Holuhraun 2014–15 CE and Laki 1783–84 CE identifying potential mechanisms of atmospheric and stratospheric S loading, as well as fingerprinting peak periods of volatile loss associated with different and well-constrained, vent activity. The majority of isotopic variations observed in the samples do not correlate to changes in major element concentrations, but some variations and trends are associated with changes in Zn and Cu concentrations.

Strong trends towards heavier $\delta^{66}\text{Zn}$ isotope values in tephras and lavas from both eruptions denote periods of higher degassing efficiency associated with periods of higher MER in both eruptions. Variations in isotope values in more explosive tephra

phases may be associated with disequilibrium degassing processes (e.g. shallow conduit processes, such as increased proportions in ultra-vesicular foams and heavier $\delta^{66}\text{Zn}$ values), alongside equilibrium degassing during cone build phase tephra and syn-emplacement of lava flows within basaltic samples from the same eruption.

Variations $\delta^{66}\text{Zn}$ and $\delta^{65}\text{Cu}$ occur throughout both eruptions and appear to track changes in oxygen fugacity, and therefore the speciation of S released, both in the flow field and at the vents. With varying proportions of sulfides predominantly dictating the variation in $\delta^{65}\text{Cu}$ observed in the vent products, with light $\delta^{65}\text{Cu}$ and a reduction in elemental Cu suggesting the volatile loss of H_2S in the lava field consistent with recently documented oxygen fugacity measurements from both Laki and other basaltic eruptions.

Temporal trends in both tephra and lavas for both isotope systems are more easily deciphered than spatial variations, which are solely associated with the development of the flow field. This study has highlighted the weaker isotope trends that occur in response to the development of compound flow fields with an evolving and complex, insulated versus open, transport system which changes at different localities throughout the eruption. This can be readily observed in the two Holuhraun trends where the early eruption samples taken from one advancing flow front display a much stronger trend than those from different flow branches from limited accessible areas of the flow field later in the eruption. The Laki lava field has an added layer of complexity with the active lava transport systems potentially being fed by several vents at once at varying stages of eruptive intensity as well as differing levels in insulation. This may explain the much weaker trends observed in this sample set compared to Holuhraun, as high-resolution flow field sampling of a well-constrained transport system is required to isolate these isotope signatures due to the complications arising from the development of several flow field branches in large volume compound flow fields. This observation is critical as it highlights the importance of well-constrained geological and physical volcanological observations in lava flow field sampling for isotopic studies. Therefore, if a corresponding explosive phase produced an apron tephra layer that cannot be used, extra care should be taken with sampling the correct lava values, and cone building phase tephra will not display variations in isotopic signatures which correspond to the

periods of peak degassing. Instead, cone phase tephra has isotopic values suggesting less efficient oxidised S degassing phases of the eruptive event during this phase of activity. More historical examples of varying intensity and magnitude events are required to fully constrain and understand how Zn and Cu behave during different eruptive activity.

This novel method could be applied to larger, less well-constrained, events such as older eruptions or individual FB units to identify S speciation upon degassing from the cone phase tephra and different flow field morphologies to identify the speciation of S lost in these events. Zinc and Copper isotope data sets from the 2014–15 CE Holuhraun and 1783–84 CE Laki FL events highlight the large variation in values that can be found in products from a single, geochemically homogeneous, eruption. Variations of this scale have implications for published data sets that use a small number of samples to ascertain the baseline values of these isotope systems for an eruptive event to assess the degree of degassing; as the isotopic fingerprint of eruptive dynamic processes, which evolve throughout an eruption, give very different values depending on which samples are analysed. This study highlights the need for, and importance of, large sample sets of different eruptive products, spanning different temporal and spatial variations, to fully understand the different isotopic signatures imparted on different eruptive products from a single event.

9.3 Future work

Although the work presented here contributes to our understanding of the mechanisms and timing of volatile loss during large volume basaltic fissure eruptions, it has also raised several outstanding questions that could be addressed by future work, which are outlined below:

- (1) What are the driving mechanisms of explosive activity during shallow subglacial eruptive activity, and how does the interaction with thin ice or alternatively its meltwater equivalent and hydraulic system beneath the glacier suppress volatile loss?
- (2) Is the ultra-vesicular foam texture and its driving disequilibrium process identified in these two eruptions present in other basaltic events? Visual

observations from published textural analysis of other basaltic fissure eruptions Eldgjá 939 CE as well as Mauna Ulu 1969 and Kilauea Iki 1959 suggest that texturally similar foams are present in clasts produced during pulsating or episodic fountaining behaviour. These textures may also record similar textural domains capturing the mingling of melts generated by disequilibrium or equilibrium shallow conduit processes prior to eruption. Geochemical analysis of these samples, as well as further textural and geochemical analysis of other basaltic fissure eruptions which are known to have episodic changes in MER, can be used to provide statistical weight to this hypothesis. This textural and geochemical fingerprint could then be used to identify peak periods in MER due to episodic fountaining behaviour in less well-constrained events or much older FB events to assess similarities in eruptive style or evolution of eruptive activity. Ultra-vesicular foam vs very mature texture proportions serve as markers of the evolution of the style of activity at the vent. The recent eruption at Fagradalsfjall, Geldingardalsgos 2021 CE, displayed pulsating, discrete, increases in fountaining intensity for at least part of the eruption could be used to see if this process is present in this eruption where, if MER is averaged, there is hardly any change.

- (3) Elemental mapping of the groundmass glass using fast diffusing elements such as lithium could be used to further investigate the disequilibrium versus equilibrium textural patterns in pyroclasts from eruptions where volatile supersaturation generated ultra-vesicular foam textures have been identified.
- (4) Vesicle number density analysis of the Laki pyroclast rinds, although limited, has indicated that there are other processes that are the main drivers for the sub-Plinian intensity of the opening phases of this event. To what degree do the tectonics of relatively embryonic fissure swarms in this portion of the EVZ contribute to this? Improving our understanding of the behaviour of larger bubbles or bubble clusters during sustained higher intensity sub-Plinian fountaining through increased image resolution, particle tracking in image frames, as well as time-lapse or slow-motion videos of future events, is key to understanding shallow conduit processes during more intense fountaining events using more frequent intense fountaining volcanoes such as Etna.

- (5) What controls the step-wise evolution of the vent system, i.e. un-zipping of the crust in the EVZ during high magnitude and high intensity Icelandic basaltic fissure eruptions such as Eldgjá and Laki? Why did no such thing take place in the 2014–15 CE Holuhraun eruption?
- (6) What dictates these periodic sub-Plinian opening phases, which are characteristic of these fissure unzipping episodes. Is it more tectonic or storage zone and recharge based?
- (7) Whilst this is the first study to identify mass-dependant fractionation of chalcophile isotopes, indicated by $\delta^{66}\text{Zn}$ and $\delta^{65}\text{Cu}$ variations in tephra and lava samples suggesting oxidized and reduced volatile loss at different stages of basaltic fissure eruptions; elemental Re concentrations are required to distinguish between volatile and particulate oxidized S loss.
- (8) Larger data collection and analysis for samples in the sub-groupings outlined in *Chapter 8* are also necessary to verify these initial findings with statistically robust trends, which due to sampling and the limited scope of this project require further detailed work.
- (9) Can chalcophile element stable isotope analysis of samples from less well constrained or older geological basaltic fissure eruptions be used to identify periods of peak eruptive intensity, or changes in eruptive environment, as well as the evolution of the flow field transport system? Before applying this method to larger and relatively unconstrained activity in flood basalt events, further testing on other well constrained basaltic fissure eruptions of varying magnitudes, and fountaining intensities, is required to gain a better understanding of how robust these variations are. This needs to be carried out not only in Iceland but across a variety of tectonic settings to acquire a basaltic volcanism data set that can be used in a global context.
- (10) Can other isotopic systems such as Fe and S be used alongside the novel Cu and Zn systems to help better constrain the volatile speciation during eruption? This can also be aided by in-situ XANES analysis of specific groundmass glasses of eruptive products, as well as utilising field plume chemistry measurements to build a complete picture of what's left versus what's lost, better enabling us to constrain the conditions of volatile speciation upon eruption.

- (11) Currently, there is no starting point in terms of an un-degassed control point sample to compare $\delta^{66}\text{Zn}$ and $\delta^{65}\text{Cu}$ isotopic variations with. Instead, only relative internal variations within eruptions can be compared, with assumptions made in terms of starting compositions for both of these isotope systems making it difficult to compare these datasets. Could analysis of un-weathered samples of relatively young subglacial pillow basalts from the same volcanic systems help constrain this further, or will partial degassing at these pressures, or alteration and therefore Zn mobility, always be an issue? In all likelihood, the geochemistry community will never have an absolute whole rock un-degassed starting point for these isotopic systems. Whilst MORB can be used, with these limitations in mind, it is not ideal for OIB or Arc setting magmas. With the possibility of future improvements in analytical techniques, in-situ Zn and Cu isotope measurements may be possible in melt inclusions (MIs), although as highlighted in recent XANES studies, only tephra oxygen fugacity and speciation measurements will be reliable indicators due to diffusion compromising MI in phenocrysts in lava flows.